

**Zbigniew Kotulski, Piotr Kowalczyk, Włodzimierz Sosnowski
(Editors)**

Selected Topics of Contemporary Solid Mechanics



INSTYTUT PODSTAWOWYCH PROBLEMÓW TECHNIKI
POLSKIEJ AKADEMII NAUK
WARSZAWA 2008

ISSN 0208-5658
ISBN 978-83-89687-35-7

Redaktor Naczelny:
prof. dr hab. Zbigniew Kotulski

Recenzenci:
doc. dr hab. Michał Basista
prof. dr hab. Tadeusz Burczyński
prof. dr hab. Krzysztof Dems
doc. dr hab. Krzysztof Doliński
prof. dr hab. Witold Gutkowski
prof. dr hab. Jan Holnicki-Szulc
dr hab. Piotr Kowalczyk
dr Tomasz Lekszycki
prof. dr hab. Zenon Mróz
prof. dr hab. Wiesław Ostachowicz
prof. dr hab. Piotr Perzyna
prof. dr hab. Henryk Petryk
prof. dr hab. Ryszard Pęcherski
doc. dr hab. Kazimierz Piechór
prof. dr hab. Wojciech Pietraszkiewicz
prof. dr hab. Maciej Pietrzyk
doc. dr hab. Stanisław Stupkiewicz
prof. dr hab. Jacek Tejchman
doc. dr hab. Krzysztof Wiśniewski

Instytut Podstawowych Problemów Techniki PAN

Nakład 400 egz. Ark. wyd. 30

Oddano do druku w lipcu 2008 r.

Druk i oprawa: Drukarnia Braci Grodzickich, Piaseczno, ul. Geodetów 47a

**Proceedings of the 36th Solid Mechanics Conference
Gdańsk, Poland, September 9–12, 2008**



36th SOLID MECHANICS CONFERENCE
Gdańsk, Poland
September 9–12, 2008

Scientific Committee

M. Basista	A. Garstecki	Z. Mróz	H. Petryk	W. Sosnowski
A. Borkowski	W. Gutkowski	W.K. Nowacki	R. Pęcherski	S. Stupkiewicz
T. Burczyński	M. Kleiber	J. Orkisz	W. Pietraszkiewicz	G. Szefer
K. Dems	W. Kosiński	J. Pamin	M. Pietrzyk	J. Tejchman
P. Dłużewski	J. Kubik	P. Perzyna	B. Raniecki	A. Tylikowski
	T. Łodygowski		K. Sobczyk	

Organizing Committee

W. Sosnowski (<i>Chairman</i>)	Sz. Imięłowski	G. Starzyński
Z. Kotulski (<i>Co-Chairman</i>)	P. Kowalczyk	R. Stocki
B. Lewandowska (<i>Scientific Secretary</i>)	K. Parkitna	T. Szolc
K. Twarowska (<i>Secretary</i>)	J. Rojek	

Sessions and their Organizers

Biomechanics (*P. Kowalczyk, T. Lekszycki, K. Piechór*)

Geomechanics (*Z. Mróz, J. Tejchman*)

Elastic-Plastic Continuum and Other Field Theories of Solids (*P. Perzyna, R. Pęcherski*)

Fracture and Damage Mechanics and Fatigue of Advanced Materials (*M. Basista, K. Doliński*)

Micromechanics (*H. Petryk*)

Thermomechanics, Phase Transitions and Shape Memory Materials (*S. Stupkiewicz*)

Mechanics of Structures and Optimization (*K. Dems, W. Gutkowski*)

Shells: Theory and Computations (*W. Pietraszkiewicz, K. Wiśniewski*)

Coupled Problems: Solid–Fluid, Thermo-Dynamics and Smart Structures (*J. Holnicki-Szulc, W. Ostachowicz*)

Computational Aspects of Solid Mechanics and Applications (*T. Burczyński, M. Pietrzyk*)

Copyright © by Institute of Fundamental Technological Research
of the Polish Academy of Sciences

Produced from camera-ready copies supplied by the authors

Warsaw 2008

Preface

This book contains extended abstracts of papers presented at the 36th Solid Mechanics Conference held in Gdańsk, Poland, on September 9–12, 2008. The Conference was organized by Institute of Fundamental Technological Research of the Polish Academy of Sciences. It follows the traditionally organized series of conferences initiated by the 1st Polish Solid Mechanics Conference in 1953. During the conferences a large number of prominent researchers visited Poland, presented their recent results and established permanent cooperation with Polish partners, often resulting with valuable joint research results. Such joint papers are also published in this volume.

The progress in mechanics, both theory and technology, is so rapid that every two years the Conference is organized we are forced to pay attention to new ideas in all areas of solid mechanics. This time the conference concentrated on such fields as: biomechanics, micromechanics, geo-mechanics, elastic-plastic continuum and other field theories of solids, fracture and damage mechanics and fatigue of advanced materials, thermomechanics, phase transitions and shape memory materials, mechanics of structures and optimization, shells – theory and computations, coupled problems – thermodynamics of solid–fluid systems, smart structures and computational aspects of solid mechanics and applications. These problems were presented in ten Solmech 2008 sessions and are now presented in ten main parts of this volume, with eight general lectures included in the parts according to their subject.

Two special sessions are dedicated to Professors Wojciech K. Nowacki and Bogdan Raniecki on the occasion of their 70 birthdays. They made significant scientific contributions to several branches of solid mechanics and educated a large number of researchers. Many friends and colleagues around the world have contributed to their Anniversary Solmech Sessions: Elastic-Plastic Continuum and other Field Theories dedicated to Professor Wojciech Nowacki and Thermomechanics, Phase Transitions and Shape Memory Materials dedicated to Professor Bogdan Raniecki.

The papers published in this volume are the result of extensive work of their authors, covering wide area of the contemporary mechanics. The publication would not be possible without consistent efforts of members of the Solmech 2008 Committees and the sessions' organizers. The editors are grateful to the authors of conference presentations for careful preparation of the manuscripts and all our colleagues involved in organization of the conference for their continued support and help.

Zbigniew Kotulski
Piotr Kowalczyk
Włodzimierz Sosnowski

Contents

Biomechanics

- 2 *R.O. Ritchie*
On the Fracture Mechanics of Bone and its Biological Degradation
- 4 *M. Kaczmarek*
Bio-poromechanics. Problems of Modelling Tissues and Biomaterials
- 6 *M. Itskov, A.E. Ehret*
An Anisotropic Micromechanically Based Viscoelastic Model for Soft Collageneous Tissues
- 8 *O.U. Colak, T. Hassan*
Cyclic Behavior of Ultra High Molecular Weight Polyethylene (UHMWPE) and Modeling
- 10 *A. John, P. Orantek*
Selected Applications of Interval and Fuzzy Analysis in Biomechanics
- 12 *E. Majchrzak, G. Kałuża, J. Poteralska*
Solution of the Cattaneo-Vernotte Bio-Heat Transfer Equation by Means of the Dual Reciprocity Method
- 14 *K. Piechór*
Travelling Waves in Two Mechanochemical Models of Tumor Angiogenesis
- 16 *M. Cieszko, W. Kriese*
Interaction of Ultrasonic Waves with Continuous Inhomogeneity of Porous Materials
- 18 *A. John, P. Orantek, P. Wysota*
The Numerical Modeling of Osteoporotic Changes in Selected Biomechanical Structures
- 20 *P. Kowalczyk*
Effect of Special Layers Shaping on Stress Distribution in Dental Restoration
- 22 *M. Kopernik, J. Nowak*
Numerical Modelling of the Opening Process of the Three-Coating Aortic Valve
- 24 *W. Gambin, P. Kowalczyk*
Analysis of Shrinkage Stresses in Light-Cured Dental Restorations
- 26 *I. Maciejewski, S. Chamera, T. Krzyzynski*
Application of Biomechanical Models in Design and Simulation of Active and Passive Vibration Damping
- 28 *M. Cieszko, Z. Szczepański*
Application of Micro Computer Tomography to Identification of Pore Structure Parameters of Porous Material

- 30 *P. Kowalczyk*
Orthotropic Model of Cancellous Bone. Application to Simulation of Adaptive Remodelling
- 32 *B. Nowak, M. Kaczmarek*
Modelling Bone-Implant Dynamics
- 34 *T. Lekszycki*
Modeling of Bone-Bioresorbable Graft Interaction
- 36 *U. Foryś*
Mutidimensional Lotka-Volterra Systems for Carcinogenesis Mutations
- 38 *M. Nowak*
On Some Properties of Bone Functional Adaptation Phenomenon Useful in Mechanical Design
- 40 *M. Gzik, D. Tejszerska*
Analysis of Influence of Human Head Movement on Cervical Spine Loading Conditions
- 42 *A. Dąbrowska-Tkaczyk*
Evaluation Method for Orthotropic Properties of Bone Tissue "in situ"
- 44 *B. Gambin, A. Gałka*
Rayleigh scattering of ultrasounds in cancellous bone
- 46 *B. Gambin, A. Gałka*
Fabric tensor and strength surface of bone-like materials

Computational Aspects of Solid Mechanics and Applications

- 48 *J.V. Wittenberghe, P. De Baets, W. De Waele*
Analysis of a Preloaded Conical Threaded Pipe Connection
- 50 *J. Ptaszny, P. Fedeliński*
Fast Multipole Evaluation of Domain Terms in Integral Equations of Two-Dimensional Elasticity
- 52 *J. Chróścielewski, M. Rucka, K. Wilde, W. Witkowski*
Modelling of Wave Propagation in Spatial Frame Elements — Numerical Simulations and Experimental Works
- 54 *W. Beluch, T. Burczyński, P. Orantek*
Evolutionary Identification of Laminates' Stochastic Parameters
- 56 *P. Orantek, T. Burczyński*
The Local Gradient Method Supported By Artificial Neural Network in Granular Identification Problems
- 58 *G. Kokot, A. John, W. Kuś*
The Complex Welding Process Simulation Using FEM, Parallel Computing and Grid Based Evolutionary Optimization
- 60 *S. Fialko*
Aggregation Multilevel Iterative Solver Based on Sparse Matrices Technique
- 62 *T. Rec, A. Milenin*
Numerical Modeling of Macro Segregation Evolution and Change of Stress–Strain State in Billet during Continuous Casting with Mechanical Soft Reduction

- 64 *J. Knabel, K. Kolanek, V.N. Hoang, R. Stocki, P. Tautowski*
Structural Reliability Analysis Using Object Oriented Environment STAND
- 66 *S. Czarnecki*
An Elastic Cube Subjected to Anti-Symmetrical Pressure Loading. Exact 3d Analytical Formulae Versus Numerical Solutions Based on Meshfree Method
- 68 *Y.M. Abushawashi, S.H. Eshtewi, A.M. Othman*
Convergence Behaviour for KPT Finite Elements
- 70 *I.M. González, H. Miguélez, A. Munoz*
ANN Approach for Modelling Orthogonal Cutting
- 72 *A. Zmitrowicz*
Contact Stresses — Models and Methods of Computations
- 74 *I. Pączelt, Z. Mróz*
Numerical Analysis of Some Steady State Wear Problems
- 76 *V. Pidvysotsky, R. Kuziak, M. Pietrzyk*
Physical and Numerical Simulation of Forging of Cu-Cr Alloy
- 78 *B. Szybiński, A. Wróblewski*
Numerical Analysis of Residual Stresses in Welds of Thick-walled Pressure Vessels
- 80 *A. Garwolińska, M. Kaczmarek*
Numerical Simulations of Laboratory and Field Tests of Permeability
- 82 *T. Bednarek, W. Sosnowski*
Computer Aided Design of Vibrating Structures Accounting for Material Fatigue and Reliability
- 84 *G. Działkiewicz*
Indirect Trefftz Solutions for Plane Piezoelectricity by Stroh Formalism and Collocation Technique
- 86 *N.C. Marín, M.H. Miguélez, J.A. Canteli, J.L. Cantero*
Lagrangian and ALE Approach for Predicting Residual Stresses in Orthogonal Cutting
- 88 *T. Łukasiak*
The Adaptive NEM-Delaunay Elements
- 90 *P. Orantek, A. Długosz, T. Burczyński*
Stochastic Identification in Thermomechanical Structures Using Evolutionary Algorithms
- 92 *M. Wójcik, J. Tejchman*
FE-Simulations of Dynamic Shear Localization in Granular Bodies Using an Arbitrary Lagrangian-Eulerian Formulation
- 94 *K. Jach, R. Świerczyński, M. Magier*
Numerical Analyses of Armour Steel Plates Penetration Process by Subcalibre Projectiles with Monolith and Segmented Penetrators
- 96 *G. Jurczak, P. Dłużewski, S. Kret, P. Ruterana*
Indium Clusters Evolution in a InGaN/GaN QW
- 98 *S. Ilic, K. Hackl*
Application of the Multiscale FEM to the Modeling of Composite Materials

Coupled Problems: Solid–Fluid, Thermo-Dynamics and Smart Structures

- 100 *M. Danielewski*
Mechano-Chemistry at Different Length Scales
- 102 *K. Frischmuth, W. Kosiński*
Hyperbolic Heat Conduction with Fuzzy Parameters
- 104 *W. Oliferuk, Z. Płochocki, O. Wysocka*
Pulsed IR Thermography for Detection of Material Defects
- 106 *M.B. Rahaei*
Comparison Lubricity Behaviour of Nanolaminated Ti₃SiC₂ and Solid Lubricants
- 108 *I. Radulescu*
Numerical Methods Involved in Lubricant Life Cycle Determination
- 110 *T.J. Hoffmann, M. Chudzicka-Adamczak*
Saint-Venant's Principle in Magnetoelasticity
- 112 *M. Cieszko, J. Kubik*
Propagation of Ultrasonic Waves in Inhomogeneous Materials
- 114 *A.V. Radulescu, F. Petrescu, I. Radulescu*
Tribological Aspects of the Solid–Fluid Interaction for Fresh and Used Lubricants
- 116 *E. Gavrilova*
Forced Gas–Structure Vibrations in a Rectangular Tank
- 118 *S.A. Lychev*
Coupled Dynamics Thermoviscoelastic Problem
- 120 *M.B. Rahaei*
Primary Evaluation of the Wear Behavior of the Combustion Synthesized TiC–NiAl Composite as Mechanical Seal Rings
- 122 *M. Cieszko, M. Kempński*
Description of Capillary Potential Curves of Porous Materials
- 124 *R. Wojnar*
Viscous Incompressible Flow in Porous Media
- 126 *S. Tokarzewski, J. Gilewicz*
Matrix Padé Bounds on Effective Transport Coefficients of Anisotropic Two-Phase Media
- 128 *G. Musielak, B. Świt*
Determination of Moisture Dependence of Material Coefficients for Macaroni Dough
- 130 *I. Dunajewski, Z. Kotulski*
Optimal Wireless Sensors Location for Widespread Structures Monitoring
- 132 *M.B. Rahaei, M. Kholghi, A. Shafiqe, M. Rahaei, M. Naghavi*
Self-Propagating High Temperature Synthesis of Bulk TiC–NiAl Composite
- 134 *M.B. Rahaei*
Comparison Mechanical Properties of Combustion Synthesized TiC–NiAl with Sintering Mechanical Seal Rings and Cutting Tools

Fracture, Damage Mechanics and Fatigue

- 136 *R. Kačianauskas*
The Discrete Element Method with Applications to Simulations of Granular Flow and Dynamic Fracture of Solids
- 138 *A. Bacigalupo, L. Gambarotta*
Modelling of Deformation and Damage of Heterogeneous Engineering Structures: Masonry Mechanics
- 140 *L. Nazarenko, L. Khoroshun, W.H. Müller, R. Wille*
Long-Term Microdamaging of Composites with Transversally Isotropic Components for Limited Function of Durability
- 142 *L. Stepanova*
Eigenspectra and Orders of Stress Singularity at a Mode I Crack in a Power-Law Medium
- 144 *O. Plekhov, N. Saintier, O. Naimark, T. Palin-Luc, R. Valiev, I. Semenova*
Thermodynamics of Plastic Deformation of Nanocrystalline Titanium
- 146 *B. Erzar, P. Forquin, J.R. Klepaczko*
Study of High Strain Rate Behaviour of Micro-Concrete
- 148 *G. Mejak*
Direct Numerical Computation of the Effective Material Properties of the Material with Random Distribution of the Microcracks
- 150 *K.P. Mróz, K. Doliński*
The New Fracture Criterion for Mixed-Mode Crack. The MK Criterion
- 152 *Z. Marciniak, D. Rozumek, C.T. Lachowicz*
The Energy Approach in the Calculation of Lives for High Cycle Fatigue
- 154 *L. Sosnovskiy, S. Sherbakov*
Model of Deformable Rigid Body with Dangerous Volume
- 156 *C.H. Wang*
Interfacial Thermal Stress Analysis of an Elliptical Inclusion with an Imperfect Interface in Anisotropic Plane
- 158 *J. Kozicki, J. Tejchman*
Simulation of Fracture Process in Concrete Elements with Steel Fibres Using Discrete Lattice Model
- 160 *W. Weglewski, M. Basista*
Modelling of Chemo-Damage in Concrete Due to Sulfate Corrosion
- 162 *J. Bobiński, J. Tejchman*
FE-Modelling of Concrete Behaviour under Mixed Mode Conditions with Non-Local and Cohesive Constitutive Models
- 164 *N. Pindra, V. Lazarus, J.B. Leblond*
Slight In-Plane Perturbation of a System of Two Coplanar Parallel Tensile Slit-Cracks
- 166 *Á. Kovács, Z. Vízváry, A. Kovács*
Strength Analysis of a Square-Form Perforated Microfilter
- 168 *A. Rusinek, J.A. Rodríguez-Martinez, J.R. Klepaczko*
Advanced Constitutive Relation for Numerical Applications: Modeling of Steels in a Wide Range of Strain Rates and Temperatures

- 170 *S. Shukayev, M. Gladskyi, K. Panasovskyi, A. Movaggar*
Damage Accumulation Model for Low Cycle Fatigue under Multiaxial Sequential Loading
- 172 *L. Jański, M. Kuna, M. Scherzer*
Simulations of Crack Growth in Piezoelectric Structures with Modern, Automatic and Efficient Finite Element Software
- 174 *A. Kaczyński, B. Monastyrskyy*
Thermal Stresses Around an Interface Rigid Circular Inclusion in a Bimaterial Periodically Layered Space
- 176 *I. Marzec, J. Tejchman*
FE-Analysis of the Behaviour of Concrete Elements with Coupled Elasto-Plastic-Damage Models with Non-Local Softening
- 178 *P. Kłosowski, Ł. Pyrzowski*
Identification and Validation of Material Parameters for Isotropic Damage Model in Viscoplastic Flow Conditions
- 180 *M.H.B.M. Shariff*
Extension of Isotropic Mullins Models to Anisotropic Stress-Softening Models
- 182 *P. Fedeliński*
Computations of Effective Elastic Properties of Solids with Microcracks Using the Boundary Element Method
- 184 *A.V. Zaitsev*
Nonlocal Conditions for the Transition Damage to a Localized Failure in Granular and Fibre-Reinforced Composites under Quasistatic Loading
- 186 *T. Jankowiak, T. Łodygowski, P. Sielicki*
Failure and fracture of concrete and brick walls imposed by explosion
- 188 *W.P. Jia, J.G. Wang, D.Y. Ju*
Effect of Strain Path Change on Microstructure and Properties of Hot-rolled Q235 Steel

Geomechanics

- 190 *H.O. Ghaffari*
Contact State Analysis by RST&NFIS Analysis
- 192 *E. Bauer, S.F. Tanton*
Shear Band Analysis of Weathered Broken Rock in Dry and Wet States
- 194 *C. Slominski, R. Cudmani*
The Influence of Soil Plugging on the Driving Resistance and Bearing Capacity of Open-Ended Steel Piles
- 195 *L.W. Morland*
Age–Depth correlation, grain growth and dislocation energy evolution, for three ice cores
- 196 *K. Wilde, M. Rucka, J. Tejchman*
Experimental and Theoretical Investigations of Silo Flow During Granular Flow
- 198 *J. Tejchman, W. Wu*
FE-Calculations of Stress Distribution under Prismatic and Conical Sandpiles Within Hypoplasticity

- 200 *J. Kozicki, J. Tejchman*
Comparative Modeling of Shear Localization in Granular Bodies Using a Discrete and Continuum Approach
- 202 *I. Panteleev, O. Plekhov, I. Pankov, A. Evseev, O. Naimark, V. Asanov*
Scaling Laws of Damage-Failure Transition in Rocks: from Laboratory Tests to Earthquakes
- 204 *A. Stankiewicz, J. Pamin*
Parametric Study of Gradient-Enhanced Cam-Clay Model
- 206 *X.T. Wang, W. Wu, J. Tejchman*
Update a Simple Hypoplastic Constitutive Model
- 208 *M. Pinheiro, R. Wan*
Incremental Plastic Response and Flow Rule Postulate under General Three-Dimensional Conditions
- 210 *Q.H. Jiang, C.B. Zhou, M.R. Yeung*
Three-Dimensional Discontinuous Deformation Analysis (3-d DDA) Coupled with Finite Element Method
- 212 *A. Sawicki, W. Świdziński*
Pre-Failure Behaviour of Granular Soils
- 214 *J. Rojek*
Simulation of Rock Cutting with Evaluation of Tool Wear
- 216 *J. Górski, J. Bobiński, J. Tejchman*
FE-Simulations of Size Effects in Granular and Quasi-Brittle Materials
- 218 *B. Wrana*
Identification of Damping in Soil by means of Morlet Wavelets
- 220 *R. Balevičius, R. Kačianauskas, Z. Mróz, I. Sielamowicz*
Comparison of Wall Pressures Measured in the Model Silo with DEM Simulation

Micromechanics

- 222 *H.L. Duan, J. Wang, B.L. Karihaloo*
Theory of Elasticity at the Nano-Scale
- 224 *P. Dłużewski*
Dislocations in Atomistic/Continuum Modelling of Semiconductor Structures
- 226 *N. Chiba, N. Ogasawara, C.R. Anghel, X. Chen*
A Substrate Effect of Hardness in Film/Substrate Indentation: Finite Element Study on 'Overshoot' Phenomenon of Hardness
- 228 *R. Pyrz, B. Bochenek*
Atomic-Continuum Equivalence: Atomic Strain Tensor
- 230 *K.C. Le, D. Kochmann, P. Sempiring*
Bridging Length-Scale in Continuum Dislocation Theory
- 232 *R. Staroszczyk*
A Migration Recrystallization Model for Polar Ice
- 234 *M. Kurza, H. Petryk*
The Energy Approach to Determining Plastic Deformation of Metal Crystals

- 236 *K. Kowalczyk-Gajewska*
Micromechanical Modelling of Metallic Materials of High Specific Strength Accounting for Slip-Twin Interactions
- 238 *Z. Poniżnik, V. Salit, M. Basista, D. Gross*
Modelling of Effective Elastic Properties of Interpenetrating Metal-Ceramic Networks
- 240 *H. Petryk*
Modelling of Microstructure Formation by Minimization of Incremental Energy Supply
- 242 *V.A. Eremeyev, W. Pietraszkiewicz*
On Natural Strain Measures of the Non-Linear Micropolar Continuum
- 244 *M. Svanadze*
Boundary Value Problems in the Two-Temperature Theory of Thermoelasticity of Binary Mixtures
- 246 *R. Oleśkiewicz, M. Neubauer, T. Krzyżynski*
Piezoelectric Switching Technique for Vibration Damping
- 248 *A.V. Manzhirrov, K.E. Kazakov*
Conformal Contact Between a Punch and a Layer with Thin Coating
- 250 *M. Hammoud, D. Duhamel, K. Sab*
A Coupled Discrete-Homogenized Approach to Study the Behavior of Ballast under Railways
- 252 *M. Janus-Michalska*
Micromechanical Model of Hyperelastic Behaviour of Cellular Materials

Elastic-Plastic Continuum and Other Field Theories

- 254 *L. Anand*
Mechanical Behavior of Bulk Metallic Glasses
- 256 *H.J. Luckner, S.P. Gadaj, W.K. Nowacki*
Mechanical Behaviour of TiAl Alloys During Static and Dynamic Deformations
- 258 *Z. Banach, W. Larecki*
Wave and Diffusive Phonon Heat Transport in Dielectrics and Semiconductors under High Thermal Loads
- 260 *K. Bartosz*
Hemivariational Inequalities Modelind Dynamic Contact Problems in Viscoelasticity
- 262 *A. Glema, T. Łodygowski, P. Perzyna, W. Sumelka*
Adiabatic Microdamage Anisotropy in Ductile Materials
- 264 *H.M. Shodja, H. Haftbaradaran*
Size Effect of an Elliptic Inclusion in Anti-Plane Strain Couple Stress Elasticity
- 266 *M.H. Pol, M.A. Akbari, G.H. Liaghat, A.V. Hosseini*
Analysis of Oblique Perforation of Conical and Ogive Projectiles into Thin Metallic Targets
- 268 *S.-Y. Leu*
On the Limit Internal Pressure of Hollow Cylinders of Strain Hardening Viscoplastic Materials

- 270 *Yu. Chernyakov, V. Shneider, D. Teslenko*
The Influence of History of Precritical Loading on Bifurcation of Process of Deformation of Elastic-Plastic Bodies
- 272 *Z. Nowak, W.K. Nowacki, P. Perzyna, R.B. Pęcherski*
Numerical Investigation of Localized Fracture in Polycrystalline Material (DH 36 Steel) During Dynamic Double Shear Loading Under Adiabatic Conditions
- 274 *Yu. Bayandin, O. Naimark*
Mesod defect Induced Mechanisms of Plasticity and Failure in Shocked Solids
- 276 *T. Żebro, K. Kowalczyk-Gajewska, J. Pamin*
A Gradient-Enhanced Coupled Damage-Plasticity Model in Large Strain Format
- 278 *R. Souchet*
On the Use of Gurson's Model in Continuum Damage Mechanics
- 280 *S. Sherbakov*
Three-dimensional Stress–Strain State of Roller-Shaft System in Conditions of Contact Interaction and Non-contact Bending of Shaft
- 282 *Yu.A. Chernyakov, A.S. Polishchuk*
On Comparison of Theory of Microstrains with Theories, Based on the Conception of Sliding
- 284 *S. Sherbakov, L. Sosnovskiy*
Influence of Stress–Strain State Caused by Non-Contact Forces on Formation of Contact Boundary Conditions
- 286 *C. Vallée, C. Lerintiu, D. Fortune, K. Atchonouglo, M. Ban*
Recovering the Bipotential of an Implicit Standard Material by Fitzpatrick's Method

Shells: Theory and Computations

- 288 *S. Shimizu, K. Hara*
Shear Behaviour of Hybrid Steel Girders
- 290 *V.A. Eremeyev, W. Pietraszkiewicz*
On Phase Transitions in Thermoelastic and Thermoelastoviscoelastic Shells
- 292 *H. Abramovich, V. Zarutsky*
Exact Solutions of Problems of Statics, Dynamics and Stability of Non-Closed Circular Cylindrical Shells Strengthened in One Direction by "Almost Regularly Placed" Ribs
- 294 *J. Pontow, D. Dinkler*
Evaluation of the Perturbation Sensitivity and the Limit Loads of Shells by the Perturbation Energy Concept
- 296 *R. Attarnejad, M. Eslaminia, A. Shahba*
A Novel Method for Static Analysis of Thin Curved Shells with Variable Thickness
- 298 *V. Kovalev*
An Asymptotic Approach to Problems of Scattering Acoustic Waves by Elastic Shells
- 300 *M.R. Khedmati, P. Edalat, M. Rastani*
Buckling/Collapse Behaviour of Cylindrical Shells in Bilge Region of Ship Hull Girders under Inplane Compression

- 302 *G. Geymonat, A. Münch*
Controllability for Thin Linearly Elastic Shells
- 304 *Ya. Grigorenko, S. Yaremchenko*
Stress State of Nonthin Noncircular Orthotropic Cylindrical Shells with Variable Thickness under Different Types of Boundary Conditions.
- 306 *K. Wisniewski, E. Turska*
On the Improved Membrane Part of Mixed Shell Elements
- 308 *S. Klinkel, W. Wagner*
A Piezoelectric Solid Shell Element Accounting for Material and Geometrical Nonlinearities
- 310 *V.D. Budak, A.Ya. Grigorenko, S.V. Puzyrev*
Free Vibrations of Orthotropic Shallow Shells of Variable Thickness on Basis of Spline-Approximation Method
- 312 *J. Górski, T. Mikulski*
Identification and Simulation of Shells Geometric Initial Imperfections
- 314 *W. Pietraszkiewicz, M.L. Szwabowicz, C. Vallée*
On Determining the Deformed Shell Midsurface From Prescribed Surface Strains and Bendings
- 316 *P. Kłosowski*
Membrane Shell Finite Element for Textile Fabric Modelling Numerical and Experimental Aspects
- 318 *J. Chróścielewski, I. Kreja, A. Sabik, W. Witkowski*
Composite Shells in 6-Field Nonlinear Shell Theory
- 320 *K. Myślecki, J. Oleńkiewicz*
Vibrations of Thick Plate by Boundary Element Method
- 322 *L. Kurpa, K. Lyubitsky*
R-Functions Method Applying to Large Deflection Analysis of Orthotropic Shallow Shells on Elastic Foundation
- 324 *R. Schlebusch, B. Zastrau*
On a Surface-Related Shell Formulation for the Numerical Simulation of Textile Reinforced Concrete Layers
- 326 *M.R. Khedmati, P. Edalat, M. Rastani*
A Numerical Investigation Into the Effects of Parabolic Curvature on the Buckling Strength of Deck Stiffened Plates
- 328 *C. Mardare*
Recovery of Displacement Fields From Stress Tensor Fields in Shell Theory
- 330 *J. Kruźecki, D. Trybuła*
Optimal Stabilization of Postbuckling Path for Conical Shells under External Pressure
- 332 *A.L. Bessoud, F. Krasucki, M. Serpilli*
Multimaterials with Shell-like Reinforcement
- 334 *I. Kreja*
Large Elastic Deformations of Laminated Cylindrical Panels under Point Load
- 336 *E. Harutyunyan*
Investigation of Oscillation Process of the Shell Element by Method of Finite Elements

- 338 *C. González-Montellano, E. Gallego, J. Morán, F. Ayuga*
The Effect of Patch Load on Corrugated Silo Walls
- 340 *A. Loktev, D. Loktev*
Dynamic Contact of the Elastic Impactor and Spherical Shell
- 342 *S.H. Sargsyan*
Theory of Micropolar Thin Elastic Cylindrical Shells
- 344 *P. Panasz, K. Wisniewski*
Nine-Node Assumed Strain Shell Element with Drilling Rotation
- 346 *G.D. Gavrylenko, V.I. Matsner*
Free Vibrations of Smooth Cylindrical Shells
- 348 *H. Altenbach, V.A. Eremeyev*
On the Mechanics of Functionally Graded Plates
- 350 *V. Kuznetsov, S. Levyakov*
Formulation of the Initial Invariant-Based Shell Finite Element Model Using the Plane Curve Geometry
- 352 *M. Bîrsan*
Some Problems Concerning the Deformation of Anisotropic Cosserat Elastic Shells

Mechanics of Structures and Optimization

- 354 *K.T. Han, Y. Jin*
Development of Forming Process of the Muffler Tube for Heavy Equipments
- 356 *P. Iwicki*
Comparison of Non-Linear Statical Analysis of Truss with Linear and Rotational Side Supports and 3D Roof Model
- 358 *A.V. Manzhurov, D.A. Parshin*
Raising of a Semi-Circular Vault
- 360 *T. Sokół*
Generalized Formulation of Eigenvalue Problem for Nonlinear Stability Analysis
- 362 *J. Melcer*
Shaking Experimental Investigation of Components for Fastening the Rails
- 364 *R. Jankowski*
Shaking Table Experimental Study on Structural Pounding during Earthquakes
- 366 *P.H. Piotrowski, R. Jankowski*
Prefabricated Structures under Earthquake Excitation: Damage and Failure of Connection Joints
- 368 *B. Błachowski, W. Gutkowski*
A Hybrid Continuous-Discrete Approach to Large Discrete Structural Optimization Problems
- 370 *K. Dems, J. Wiśniewski*
Optimal Fibers Arrangement in Single- and Multilayered Composite Materials
- 372 *K. Szajek, W. Kąkol, T. Łodygowski, M. Wierszycki*
Incorporating Two Optimization Algorithms into FEA Environment

- 374 *A. Garstecki, Z. Pozorski, R. Studziński*
Multi-Objective Optimal Design of Multi-Span Sandwich Panels with Soft Core, Allowing for Variable Support Conditions
- 376 *C. Iancu, A. Nioata*
Static FEA of Mechanical Complex Structures
- 378 *M. Chalecki, W. Nagórko*
A Nonasymptotic Modelling of Heat Conduction in Solids Reinforced by Short Fibres with Functional Gradation of Features
- 380 *L. Nunziante, M. Fraldi*
A Procedure for Defect Identification of Suspension Bridges Cables by means of Optical-Fibre Strain Measurements
- 382 *R. Górski, P. Fedeliński*
Free Vibration Analysis of Stiffened Plates by the Boundary Element Method
- 384 *W. Beluch, T. Burczyński, A. Długosz*
Evolutionary Computing in Multi-Objective Optimization of Laminates
- 386 *Sz. Imiełowski*
Energetic Approach to Stability of Beam-Columns Subjected to Deformation Dependent Loading
- 387 *A. Gorjipoor, A. Abedian*
Genetic Algorithm Optimization of Helicopter Blades Vibration Transition
- 388 *A. Khurana, S.K. Tomar*
Longitudinal Wave Response of a Chiral Slab Interposed Between Micropolar Solid Half-Spaces
- 390 *A. Le van, T.T.H. Nguyen*
A Weak Formulation for the Large Deformation Contact Problem with Coulomb Friction
- 392 *Q. Zhang, Ł. Jankowski*
Off-line Reconstruction of Dynamic Loads
- 394 *K. Lisowski*
Sparse Grid and Evolution-Type Algorithm in Shape Optimization for Beck's Column
- 396 *D. Bojczuk, M. Jabłoński*
Geometric Sensitivity Analysis of Truss and Frame Structures
- 398 *A. Bobylov, A. Zubko*
Application of the Stabilization Method for Analysis of Geometrically Non-Linear Forced Vibrations of Elastic Beams on Unilateral Winkler Foundation
- 400 *A. Myśliński*
Level Set Method in Structural Optimization
- 402 *B. Dyniewicz, C. Bajer*
Inertial Moving Loads

Thermomechanics, Phase Transitions and Shape Memory Materials

- 404 *F.D. Fischer, J. Svoboda*
Physics, Chemistry and Mechanics are Growing Together — the Role of Nonequilibrium Thermodynamics

- 406 *S. Stupkiewicz, H. Petryk*
Micromechanical Modelling of Pseudoelastic SMA Polycrystals under Non-proportional Loading
- 408 *H. Tobushi, E.A. Pieczyska, W.K. Nowacki, T. Sakuragi, Y. Sugimoto*
Torsional Deformation and Rotary Driving Characteristics of SMA Thin Strip
- 410 *E.A. Pieczyska*
Stress-Induced Martensite Transformation in TiNi SMA — Experimental Estimation of Energy Balance
- 412 *S. Starenchenko, I. Radchenko, V. Starenchenko*
Influence of Plastic Deformation on Structural Characteristics and Long-Range Order in Ni3Al Alloy
- 414 *S.J. Kowalski, A. Rybicki*
Estimation of Material Effort During Drying Processes
- 416 *W. Oliferuk, M. Maj*
Stress–Strain Curve and Stored Energy During Uniaxial Deformation of Polycrystals
- 418 *E.A. Pieczyska, H. Tobushi, W.K. Nowacki, T. Sakuragi, Y. Sugimoto*
Deformation Behavior of TiNi SMA Observed by Local Strain, Thermography and Transformation Band
- 420 *T. Inoue*
Transformation Plasticity. The Mechanism, Constitutive Equation and Applications
- 422 *E. Majchrzak, B. Mochnecki, J.S. Suchy*
Identification of Boundary Heat Flux on the External Surface of Casting
- 424 *E.A. Pieczyska, W.K. Nowacki, S.P. Gadaj, H. Tobushi*
TiNi SMA — Investigation of Stress-Induced Martensite Reverse Transformation, Independent of Thermal Influences of the Forward One
- 426 *S.V. Starenchenko*
Features of the Temperature-Induced and Deformation-Induced Order–Disorder Phase Transition
- 428 *S.J. Kowalski, A. Rybicki*
Stress Reverse and Residual Stresses in Dried Materials
- 430 *G. Ziętek, Z. Mróz*
Description of Cyclic Hardening of Material with Plasticity Induced Martensitic Transformation
- 432 *C. Urbina, S. De la Flor, F. Ferrando*
Thermal Cycling Effect on Different Two Way Shape Memory Training Methods in NiTi Shape Memory Alloys
- 434 *D.Y. Ju, X.D. Hu, Z.H. Zhao*
Inelastic Behaviour and Numerical Analysis in Twin-roll Casting Process of AZ31 Alloy
- 436 *J.A. Rodríguez-Martínez, A. Rusinek, D.A. Pedroche, A. Arias, J.R. Klepaczko*
Mechanical Behaviour of TRIP Steels Subjected to Low Impact Velocity at Wide Range of Temperatures
- 440 **Index of Authors**

**Extended Abstracts
of
Conference Lectures**

ON THE FRACTURE MECHANICS OF BONE AND ITS BIOLOGICAL DEGRADATION

R.O. Ritchie

Materials Sciences Division, Lawrence Berkeley National Laboratory, and
Department of Materials Science and Engineering, University of California, Berkeley
(*rortichie@lbl.gov*)

The age-related deterioration of both the fracture properties and the architecture of bone, coupled with increased life expectancy, are responsible for increasing incidences of bone fracture in the elderly segment of the population. In order to develop effective treatments, an understanding of the mechanisms underlying the structural integrity of bone, in particular, its fracture resistance, is essential. The origins of the toughness of human cortical bone (and dentin, a primary constituent of teeth and simple analog of bone) are described in terms of the contributing micro-mechanisms and their characteristic length scales in relation to the hierarchical structure of these mineralized tissues. It is shown that although structure at the nanoscale is important, it is microstructural features at the scale of one to hundreds of microns (*e.g.*, the Haversian systems present in the cortical bone of mammals and the tubule size and spacing in dentin) that are most important in determining fracture risk.¹⁻³ We specifically find that the origins of fracture resistance in materials such as bone are extrinsic, *i.e.*, associated primarily with crack growth, and are related to such toughening mechanisms as gross crack deflection and crack bridging (Figs. 1-2), both processes that are induced by preferential microcracking (at cement lines in bone and at unfilled tubules in dentin).³ In particular, our results, in terms of full nonlinear elastic crack-resistance curve measurements, show that human cortical bone is actually much tougher than has been previously thought, because it is largely associated with the growth, rather than the initiation, of cracking. In this context, realistic short-crack measurements of both initiation and growth toughneses performed on human and small animal bones and human and elephant dentin are used to evaluate the effects of aging and certain therapeutic treatments (*e.g.*, steroids and bisphosphonates). These measurements are combined with structure characterization using UV Raman spectroscopy, small-angle x-ray scattering and transmission electron microscopy and imaging studies involving two-dimensional *in situ* fracture tests performed in an environmental scanning electron microscope (including quantitative electron backscattering analysis) and three-dimensional *ex situ* examination of crack paths derived using synchrotron x-ray computed tomography (*e.g.*, Figs. 1-2)⁵, to determine the microstructural features that underlie the toughness of bone and teeth and how these properties can degrade with biological factors.^{2,4}

- ¹. R. K. Nalla, J. H. Kinney, and R. O. Ritchie, "Mechanistic fracture criteria for the failure of human cortical bone", *Nature Materials*, **2** (2003) 164-68.
- ². R. K. Nalla, J. J. Kruzic, J. H. Kinney, and R. O. Ritchie, "Effect of aging on the toughness of human cortical bone: Evaluation by R-curves", *Bone*, vol. **35**, 2004, pp. 1240-46.
- ³. J. W. Ager III, G. Balooch and R. O. Ritchie, "Fracture, aging and disease in bone", *Journal of Materials Research*, **21** (2006) 1878-92.
- ⁴. K. J. Koester, J. W. Ager III, and R. O. Ritchie, "The effect of aging on crack-growth resistance and toughening mechanisms in human dentin", *Biomaterials*, **29** (2008) 1318-28.
- ⁵. K. J. Koester, J. W. Ager III, and R. O. Ritchie, "'How tough is human bone? In situ measurements on realistically short cracks", *Nature Materials*, **7** (2008) in press.

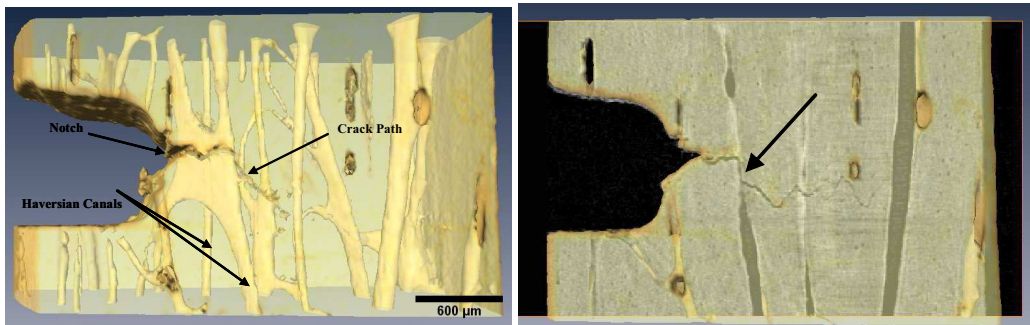


Fig. 1: Synchrotron x-ray computed tomography images of a crack path in human cortical bone (humerus, 37 yr donor) obtained in a notched 3-point bend geometry. The voxel size was $10\ \mu\text{m}$. The crack propagation direction (L-R in the images) was perpendicular to the long axis of the bone, i.e., in the transverse (breaking) orientation. A 3-D image showing the Haversian system is shown on the left, and a subsurface slice is shown on the right. The crack has extended approximately 1 mm from the notch and has undergone several deflections, which significantly increases the measured toughness. The arrow in the right-hand image shows that one such deflection occurs at a sub-surface Haversian canal. Examination of the full series of sub-surface slices found that all crack deflections observed at the surface could be associated with cement lines, lamellar boundaries, or Haversian canals present in the in the Haversian system. (after ref. 5).

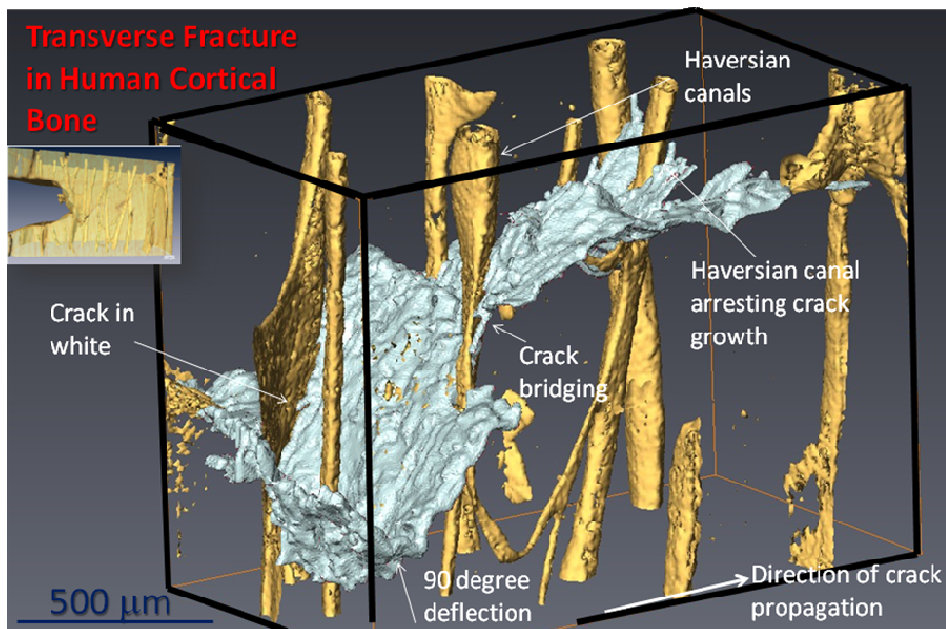


Fig. 2: Three-dimensional synchrotron x-ray computed tomography image of a crack path in human cortical bone (humerus, 37 yr donor), again in the transverse (breaking) orientation, showing the toughening obtained by crack deflection, and more importantly crack twisting, as the crack path encounters the interfaces of the Haversian canals (the cement lines). (Unpublished data from Advanced Light Source beamline 8.3.2: Barth and Ritchie).

BIO-POROMECHANICS. PROBLEMS OF MODELLING TISSUES AND BIOMATERIALS

M. Kaczmarek

Kazimierz Wielki University, Bydgoszcz, Poland

1. Motivation

Most biological (natural) materials and biomaterials (engineered materials replacing functions of tissues or organs) in their natural or working environment consist of solid skeleton filled with fluid. In case of tissues the skeleton is a complex hierarchical structure comprised of cells, vascular systems, mineral phase, etc (see e.g. [1]). The fluid in pore - extra cellular space is a composition of constituents plying different structural and biological roles within organisms. Biomaterials have usually less complex constitution and structure and as the result can realize less functions than biological materials, see Fig. 1.

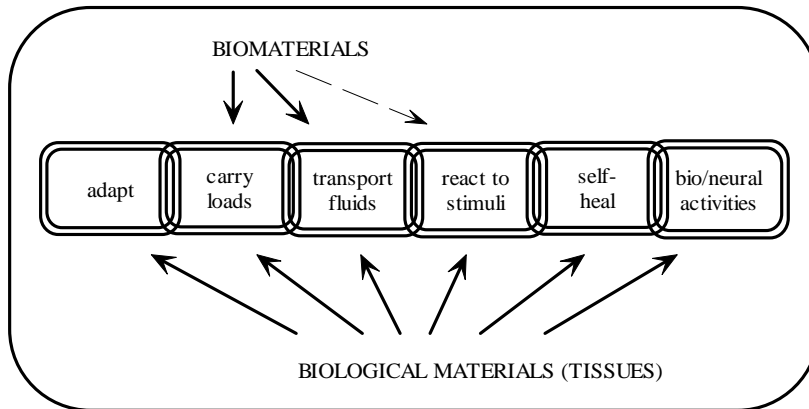


Fig. 1. Diagram showing functions of biomaterials and biological materials

The internal complexity of the materials of interest and range of phenomena and functions which are to be covered must determine useful modelling tools.

2. Poromechanics – a tool for modelling biological materials and biomaterials

Poromechanics is the coupled mechanical model of saturated porous materials which incorporates basic interactions between porous skeleton and pore fluid, including volumetric couplings, viscous and inertial interface forces. More advanced approaches try to include in the model characteristics of internal structure and information on properties of phases. Since its origin in the mature shape (the foundations of poromechanics were laid by M. A. Biot, see [2], [3], [4]) it has found number of successful applications for modelling rocks, soils, sound absorbing materials but also tissues (e.g. bones, muscles, cartilage, brain) and biomaterials (e. g. scaffolds, hydrogels). Among others the model was useful to predict division between phases of dynamically applied stress to bones and muscles followed by further redistribution of stress in time; It describes basic

properties of waves in bones and soft gels; It explains the evolution of deformation and porosity in diseased or injured brain. Despite that however there is a growing awareness that notions and equations of classical poromechanics when applied for modelling biological materials or biomaterials must be frequently supplemented with some components resulting from the particular material properties and functions.

From the mechanical point of view the material properties which cause the peculiarities of modeling tissues and biomaterials are: high porosity, anisotropy of mechanical and structural parameters, micro- and macro-inhomogeneity, complexity of interfacial conditions etc. They generate theoretical difficulties to find proper constitutive equations, boundary conditions and finally make credible simulations without known benchmark solutions. However, the least solved problems seem to be that which are related to elaboration of reliable experimental techniques which can determine numerous model parameters from tests made for usually small, inhomogeneous and anisotropic samples of materials. The problem is yet more striking when one realizes that material parameters determined in vivo, in situ (death tissue in its environment) and in vitro (death tissue removed from its environment) could be significantly different.

3. Discussion of applications

We will discuss some of the above problems as related to applications of poromechanics in modelling:

- 1) wave propagation through trabecular bones,
- 2) transport and deformation in brain, and
- 3) coupled chemo-mechanical behaviour of reactive gels.

In all the above cases the analysis will concentrate on proving high capability of poromechanics to describe phenomena which are specific for biological materials or biomaterials and also show limitations and unsolved topics within the approach. Connections of the modelling with predictive description, diagnostic applications as well as design of biomaterials will be highlighted. The discussion will be based on original results (see e.g. [5], [6]) and review of current literature and will be illustrated by simulations and results from experiments.

4. References

- [1] M. A. Meyers, P.-Y. Chen, A. Y.-M. Lin, Y. Seki (2008). Biological materials: Structure and mechanical properties, *Progress Mat. Science*, **53**, 1-2006.
- [2] M.A. Biot (1962). Mechanics of deformation and acoustic propagation in porous media: *J. Applied Physics*, **33**, 1482-1498.
- [4] T. Bourbie, O. Coussy and B. Zinszner (1987). *Acoustics of porous media*, Gulf Publ. Co.
- [3] J. Kubik, M. Cieszko, and M. Kaczmarek (2000). *Foundations of dynamics of fluid saturated porous materials*, IPPT Warsaw, (in Polish).
- [5] M. Kaczmarek, R.P. Subramanian, S.R. Neff (1997). The hydromechanics of hydrocephalus: steady-state solutions for cylindrical geometry, *Bull. Math. Biol.* **59**, 295–323.
- [6] M. Pakula, F Padilla, P Laugier, and M. Kaczmarek (2008). Application of Biot's theory to ultrasonic characterization of human cancellous bones: Determination of structural, material, and mechanical properties, *J. Acous. Soc. Am.* **124**, 4.

AN ANISOTROPIC MICROMECHANICALLY BASED VISCOELASTIC MODEL FOR SOFT COLLAGENOUS TISSUES

M. Itskov, A.E.Ehret

Department of Continuum Mechanics, RWTH Aachen University, 52056 Aachen, Germany

1. Introduction

Soft biological tissues are characterized in general by time dependent and in particular viscoelastic properties. This becomes apparent in mechanical testing where these materials reveal e.g. stress relaxation when stretched to a constant level and rate dependent hysteresis in cyclic loading. These characteristics depend on the direction of loading and are thus of anisotropic nature. In the present contribution, we propose a micromechanically motivated approach. The constitutive equations are based on the multiplicative decomposition of the stretch in fiber direction into an elastic and a viscous part. Anisotropy is taken into account by a non-uniform spatial distribution of the fiber-matrix units. Finally, the model is generalized to the three-dimensional case by integration over a unit sphere [1, 2, 3, 4].

2. Fiber-matrix unit

The passive mechanical properties of soft biological tissues are to a large extent determined by the histological structure of the extracellular matrix. The latter one includes fibrous constituents, primarily different types of collagen and the ground substance which contains a large amount of water. The typical J -shaped stress-strain curve of soft tissues is usually divided into a toe and a linear region. The increasing stiffness in the toe region is attributed to the orientation and uncoiling of collagen fibers. However, this fiber transition from a crimped to a straightened state needs rearrangement of the nearby ground substance [2]. Since the latter one is a highly viscous material, fiber straightening turns out to be a viscoelastic process.

2.1. One-dimensional model

The stretch λ in a fiber direction is multiplicatively decomposed into an elastic and a viscous part as $\lambda = \lambda_e \lambda_v$. While λ_v is associated with uncoiling and straightening of the fibers, λ_e describes the stretch in the collagen itself. Accordingly, the rheological model for the fiber-matrix unit can be illustrated in the case of small deformations by the following scheme (Fig. 1). Therein, $\Psi_v(\lambda_v)$ is the

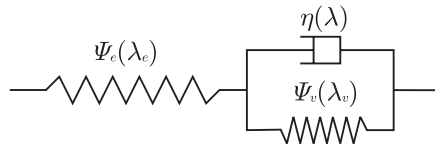


Figure 1. Rheological model for fiber-matrix unit.

strain-energy associated with fiber straightening and $\Psi_e(\lambda_e)$ is the collagen strain-energy which describes the linear region of the stress-strain curves. The dashpot element reflects the viscous properties of the ground substance and is characterized by a stretch dependent viscosity function $\eta(\lambda)$.

2.2. Anisotropic three-dimensional model

In order to obtain an anisotropic three-dimensional constitutive model, the free energy of the fiber-matrix unit is weighted by a directional distribution function and numerically integrated over a unit sphere (cf. [2, 3, 4]). While the stretches λ are assumed to be affine, the viscoelastic stretches λ_v in each integration point result from an evolution equation.

3. Application

We considered an incompressible biological tissue sample with fibers distributed around a preferred direction. Fiber dispersion was described by the von Mises distribution [5] where additionally a constant uniform ground distribution was added (cf. [1]). The strain-energy functions and the viscosity function were chosen according to

$$\Psi_v(\lambda_v) = \frac{k_1}{2k_2} \{ \exp [k_2(\lambda_v^2 - 1)] - 1 \}, \quad \Psi_e(\lambda_e) = c_1(\lambda_e - 1)^2, \quad \eta(\lambda) = d_1 \{ \exp [d_2(\lambda_c - 1)^2] \},$$

where k_1 , k_2 , c_1 , d_1 and d_2 denote material parameters. As proposed in [6], Ψ_v contributes only if $\lambda_v > 1$. For numerical integration over the unit sphere, a 61 integration points scheme [3] was utilized.

4. Conclusions

In this paper a viscoelastic model for the anisotropic behavior of soft tissues has been proposed. The model is based on the generalization of a one-dimensional model for the fiber-matrix interaction to the three-dimensional case. Anisotropy caused by non-uniform fiber distributions is easily included by a distribution function. The results suggest that many features of soft tissues are qualitatively well captured. For example, the strong increase in the hysteresis ratio with frequency compared to a moderate change in the storage modulus reported for some tissue types [7] can be obtained by the model.

5. References

- [1] Lanir Y.(1979). A structural theory for the homogeneous biaxial stress-strain relationship in flat collagenous tissues, *J. Biomech.*, **12**, 423-436.
- [2] Lanir Y. (1983). Constitutive equations for fibrous connective tissues, *J. Biomech.* **16**, 1-12.
- [3] Bažant Z.P., Oh B.H. (1986). Efficient Numerical Integration on the Surface of a Sphere. *ZAMM* **66**, 37-49.
- [4] Caner F.C., Carol I. (2006). Microplane Constitutive Model and Computational Framework for Blood Vessel Tissue. *J. Biomech. Eng.* **128**, 419-427.
- [5] Gasser T.C., Ogden R.W., Holzapfel G.A. (2006). Hyperelastic modelling of arterial layers with distributed collagen fiber orientations. *J. R. Soc. Interface* **3**, 15-35.
- [6] Holzapfel G.A., Gasser T.C., Ogden R.W. (2000). A New Constitutive Framework for Arterial Wall Mechanics and a Comparative Study of Material Models. *J. Elasticity* **61**, 1-48.
- [7] Mavrilas D., Tsapikouni T., Mikroulis D., Bitzikas G., Didilis V., Konstantinou F. and Bougioukas G. (2002). Dynamic mechanical properties of arterial and venous grafts used in coronary bypass surgery. *J. Mech. Med. Biol.* **2**, 329-332.

CYCLIC BEHAVIOR OF ULTRA HIGH MOLECULAR WEIGHT POLYETHYLENE (UHMWPE) AND MODELING

O. U. Colak¹ and T. Hassan²

¹ *Yildiz Technical University, Istanbul, Turkey*

² *State University of North Carolina, North Carolina, USA*

Abstract

Cyclic stress-strain responses of ultra high molecular weight polyethylene (UHMWPE) are investigated under different load control modes. Uniaxial and biaxial experiments are conducted under strain and stress controlled load reversals. One of the unified state variable models, Viscoplasticity Based Overstress (VBO) model for polymers [1] is used to simulate the recorded cyclic responses of UHMWPE. The model does not include any yield surface and loading and unloading conditions. Apart from many existing work in the literature, material parameters for VBO are determined using the genetic algorithm (GA) optimization procedure which is constituted using MATLAB Genetic Algorithm and Direct Search Toolbox.

Thermoplastics like ultra high molecular weight polyethylene (UHMWPE) have been used for a wide variety of applications, such as gears, unlubricated bearing, seals and in the field of biomechanics due to biocompatibility. Accurate prediction of stresses and deformation in service conditions is essential to the designer and finite element analyzer.

1. Experiments

For understanding the material behavior of UHMWPE under cyclic loading and evaluating a constitutive model for simulating cyclic responses, a set of material experiments under stress and strain controlled, uniaxial loading cycles are conducted. Tubular, dog-bone shaped specimens are machined from UHMWPE solid rods for conducting these tests. The strain-controlled uniaxial experiments involved monotonic loading up to 40% strain and cyclic loading with various strain-amplitudes. In both cases the prescribed loading rate is kept constant at 0.1%/second. Recorded axial stress-strain response from a cyclic strain-controlled experiment with 3% amplitude cycle is shown in Fig. 1. Stable hysteresis loop response is demonstrated by UHMWPE in this figure. The uniaxial stress-controlled cyclic experiments were conducted by prescribing various stress amplitudes and means, and loading rates. Response from such an experiment with the amplitude stress, 12.5 MPa prescribed at a rate of 0.77 MPa/ second is shown in Fig. 2. As the mean stress prescribed in this experiment is zero, no axial strain ratcheting is obtained. However, after ten such cycles when mean stress is increased to a nonzero value axial strain ratcheting is obtained (not shown).

2. Modeling

Cyclic behavior of UHMWPE in different grades and cross-linking has been the object of many researches in the field of biomechanics. Experimental studies have shown that strain softening is observed due to the morphology changes [2]. Even though there are some experimental studies in the literature, there are not many papers dealing with modeling of cyclic behavior of UHMWPE due to the difficulty of simulating viscous effects. In this work, VBO is used for modeling cyclic behavior of UHMWPE. Theory consists of two tensor values state variables, equilibrium and kinematic stress, and a scalar isotropic stress. Flow law is given in Eq.1. Inelastic strain rate is function of overstress which is the difference between Cauchy and equilibrium stresses ($\dot{o} = \dot{s} - \dot{g}$).

$$\dot{\mathbf{e}} = \dot{\mathbf{e}}^{el} + \dot{\mathbf{e}}^{in} = \frac{1+\nu}{CE} \dot{\mathbf{s}} + \frac{3}{2} \mathbf{F} \left[\frac{\Gamma}{D} \right] \left(\frac{\mathbf{s} - \mathbf{g}}{\Gamma} \right) \quad (1)$$

where \mathbf{s} and \mathbf{g} are the deviatoric part of the Cauchy ($\boldsymbol{\sigma}$) and the equilibrium stress (\mathbf{G}) tensor, respectively. The equilibrium stress (\mathbf{G}) is nonlinear, rate-independent and hysteretic. Its evolution equation in deviatoric form is given as:

$$\dot{\mathbf{g}} = \Psi \frac{\dot{\mathbf{s}}}{E} + \Psi \mathbf{F} \left[\frac{\Gamma}{D} \right] \left(\frac{\mathbf{s} - \mathbf{g} - \mathbf{g} - \mathbf{k}}{\Gamma} - \frac{\mathbf{g} - \mathbf{k}}{A} \right) + \left(1 - \frac{\Psi}{E} \right) \dot{\mathbf{k}} \quad (2)$$

where \mathbf{k} is the deviatoric kinematic stress, which is the repository for the modeling of the Bauschinger effect. A is the isotropic stress, rate independent contribution to the stress, which is responsible for modeling hardening or softening. The evolution equation for the kinematic stress in deviatoric form is,

$$\dot{\mathbf{k}} = \bar{E}_t \dot{\mathbf{e}}^{in} \quad (3)$$

where $\bar{E}_t = \frac{E_t}{1 - \frac{E_t}{E}}$ and E_t is the tangent modulus.

For more information about model, see Dusunceli and Colak [3].

3. Results

Simulation and experimental results of fully reversed symmetric cyclic loading under strain and stress-control modes is depicted in Fig.1 and 2.

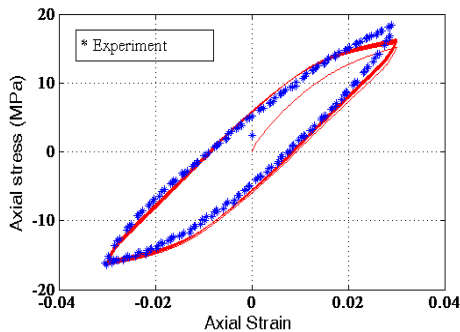


Fig.1 Strain controlled uniaxial loading at the strain rate of 1.E-3 /s.

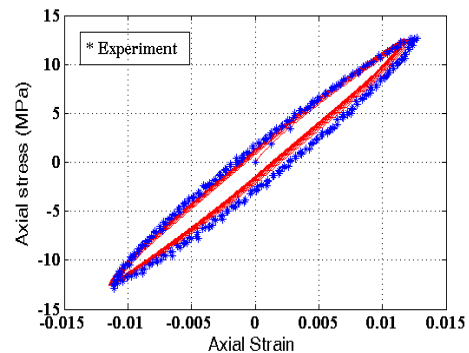


Fig.2 Stress controlled uniaxial loading at the stress rate of 0.77 MPa/s.

4. References

- [1] O. U. Colak and E. Krempl (2005). Modeling of the monotonic and cyclic Swift effects Using Isotropic Finite Viscoplasticity Theory Based on Overstress (FVBO), *International Journal of Plasticity*, 21, 3, 573-588.
- [2] A. Avanzini (2008). Mechanical characterization and finite element modeling of cyclic stress-strain behavior of ultra high molecular weight polyethylene, *Materials and Design*, 29, 330-343.
- [3] N. Dusunceli and O. U. Colak (2006). High density polyethylene (HDPE): Experiments and Modeling, *Mechanics of Time Dependent Materials*, 10, 331-345.

SELECTED APPLICATIONS OF INTERVAL AND FUZZY ANALYSIS IN BIOMECHANICS

A. John and P. Orantek

*Department for Strength of Materials and Computational Mechanics,
Silesian University of Technology, Poland*

1. Introduction

Bioengineering concerns many significant problems applied to the human body. The pelvic bone is one of the most important supporting elements in human pelvic joint but it is exposed to the injuries. Very often before and after surgical intervention the expertises about the stress, strain and displacement distributions in the pelvic bone are needed. For the safety of the patient there are only two possibilities available to derive mentioned values: model testing and numerical calculations. The numerical model should be prepared before numerical calculations [1,2,3]. Numerical calculations require the characteristics of the material properties and the material parameters from the beginning. Usually the literature is the source of the material parameters, but sometimes this data is not suitable for the implementation. This is a reason for the experimental investigations to identify these parameters [4,5,6]. It is well known that material properties of the living body depend on many factors: age, health, gender, environment and many others changing in time. As we are interested in results of analysis not only for a one patient but for a group of patients, we should assume an interval value of material parameters. In this paper the test of the interval and fuzzy analysis of the pelvic bone is presented. The interval and fuzzy analysis concerns material properties. The finite elements method is applied [7,8,9].

2. The interval and fuzzy analysis of the human pelvic bone

The human pelvic bone is restrained in pubic symphysis and on contact surface with sacral bone. It is loaded with force F acting in artificial acetabulum. Two cases of the linear elastic analysis were carried out. In the first case the material parameters are not position-depended. In the second case the selected material parameters depend on the position in the bone.

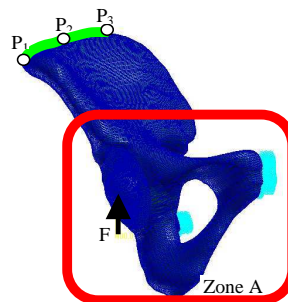


Fig. 1. The model of the human pelvic bone

For both cases the interval and fuzzy (two alpha-cuts-trapezoid) approaches are applied. It was assumed that for the interval analysis, the Young moduli of trabecular bone (in both cases) was constant and equal [1.8E8; 2.2E8]. The Young moduli of the cortical bone (in the first case) was modelled as the interval [1.8E10; 2.2E10]. In the second case the Young moduli of the cortical bone was equal to the interval [1.8E10; 2.2E10] in zone A (Fig.1) and was equal to [0.9E10; 1.1E10] in the bound B (between P1 and P3). In space between zone A and the bound B, the Young moduli was generated with the linear weight function.

In the fuzzy analysis case, the Young moduli of the trabecular bone (in both cases) was constant and equal to the fuzzy number (see Table.1). First the Young moduli of the cortical bone was modelled as the fuzzy number (see Table.1). The space between zone A and the bound B was determined with linear function.

The rest of parameter were assumed as the determine numbers.

Table 1. The fuzzy material parameters and displacements of point P₁

E1 [e+10] [Pa] cortical	E2 [e+8] [Pa] trabecular	Px ₁ [e-7] [mm]	Py ₁ [e-7] [mm]	Pz ₁ [e-7] [mm]
1.8 2.2	2.66 3.24	2.66 3.24	2.70 3.27	-3.34 -2.74
1.6 2.4	2.44 3.64	2.44 3.64	2.47 3.68	-3.76 -2.51

3. Conclusions

Arithmetic analysis enables evaluation of the selected characteristics (strain, stress and displacements) not only for a discrete deterministic material parameters, but for assumed interval. It satisfies reality more precisely. Obtained results can be useful to plan and assess quality of the surgical intervention. The surgeons can observe which states are dangerous for the patients.

4. Acknowledgement

The work was done as a part of project N51804732/3670 sponsored by Polish Ministry of Science and Higher School.

5. References

- [1] John A., Numerical analysis of solid and shell models of human pelvic bone. *Lecture Notes in Computer Science* 1988, Eds.: L. Vulkov, J. Waśniewski, P. Yalamov, Numerical Analysis and Its Applications, Springer-Verlag, Berlin Heidelberg, pp. 764-771, 2001.
- [2] John A., Orantek P., Computer aided creation of geometrical model of human pelvic bone. *Acta of Bioengineering and Biomechanics*, vol. 2, Supplement 2, pp. 217-220, 2001.
- [3] John A., Orantek P., Computer aided creation of numerical model of human pelvic bone. *Engineering Transactions*, vol. 51, No. 2-3, 215-226, 2003.
- [4] John A., Kuś W., Orantek P., Material coefficient identification of bone tissues using evolutionary algorithms. in: *Inverse Problems in Engineering Mechanics IV*. Masa.Tanaka (Ed.), Elsevier, 95-102, 2003.
- [5] Burczyński T., John A., Kuś K. Orantek P., Poteralski A., The evolutionary algorithm and hypersurface in identification of material coefficients in human pelvic bone. *Acta of Bioengineering and Biomechanics*, 5, Supplement 1, pp. 61-66, 2003.
- [6] Cowin S.C. (Ed.), *Bone mechanics handbook*. CRC Press, 2001.
- [7] Zienkiewicz, O.C. and Taylor, R.L., *The Finite Element Method*, Vol. 1: The Basis, fifth ed., Butterworth-Heinemann, Oxford, 2000.
- [8] Belytschko, T., Krongauz, Y., Organ, D., Fleming, M. and Krysl, P., *Meshless methods: An overview and recent developments*, Comput. Methods Appl. Mech. Engng, 139, pp. 3-47, 1996.
- [9] Owen, D.R.J., Feng, Y.T., Mak, K.W. and Honnor, M.E., *Computational modelling of large scale multiple fracturing solids and particulate systems*, *Computational Mechanics – New Frontiers for the New Millennium*, Proceedings of the First Asian-Pacific Congress on Computational Mechanics, Valliappan, S. and Khalili, N. Eds, Elsevier, Amsterdam, Vol. 1, pp. 117-126, 2001.

SOLUTION OF THE CATTANEO-VERNOTTE BIO-HEAT TRANSFER EQUATION BY MEANS OF THE DUAL RECIPROCITY METHOD

E. Majchrzak, G. Kałuża and J. Poteralska
Silesian University of Technology, Gliwice, Poland

1. Governing equations

According to the newest opinions the heat conduction proceeding in the biological tissue domain should be described by the hyperbolic equation (Cattaneo and Vernotte equation [1]) in order to take into account its nonhomogeneous inner structure. So, the following bio-heat transfer equation is considered

$$c \left(\tau \frac{\partial^2 T(x, t)}{\partial t^2} + \frac{\partial T(x, t)}{\partial t} \right) = \lambda \nabla^2 T(x, t) + Q(x, t) + \tau \frac{\partial Q(x, t)}{\partial t}$$

where c , λ denote the volumetric specific heat and thermal conductivity of tissue, $Q(x, t)$ is the capacity of internal heat sources due to metabolism and blood perfusion, τ is the relaxation time (for biological tissue it is a value from the scope 20-35 s), T is the tissue temperature, x, t denote the spatial co-ordinates and time. The function $Q(x, t)$ is equal to

$$Q(x, t) = G_B c_B [T_B - T(x, t)] + Q_m$$

where G_B is the blood perfusion rate, c_B is the volumetric specific heat of blood, T_B is the artery temperature and Q_m is the metabolic heat source. It should be pointed out that for $\tau = 0$ the equation reduces to the well-known Pennes bio-heat equation.

The equation is supplemented by the boundary conditions

$$\begin{aligned} x \in \Gamma_1: \quad T(x, t) &= T_b(x) \\ x \in \Gamma_2: \quad q(x, t + \tau) &= -\lambda \mathbf{n} \cdot \nabla T(x, t) = q_b(x) \end{aligned}$$

and initial ones

$$t = 0: \quad T(x, t) = T_0, \quad \left. \frac{\partial T(x, t)}{\partial t} \right|_{t=0} = 0$$

where Γ_1, Γ_2 are the surfaces limiting the domain, $q(x, t + \tau)$ is the boundary heat flux, $T_b(x)$, $q_b(x)$ are the known boundary temperature and the boundary heat flux and T_0 is the known initial temperature of the biological tissue.

2. Dual reciprocity boundary element method

For transition $t^{f-1} \rightarrow t^f$ the standard boundary element method leads to the integral equation [2]

$$\begin{aligned} B(\xi) T(\xi, t^f) + \int_{\Gamma} T^*(\xi, x) q(x, t^f) d\Gamma &= \int_{\Gamma} q^*(\xi, x) T(x, t^f) d\Gamma - \\ \int_{\Omega} \left[(c + \tau G_B c_B) \frac{\partial T(x, t)}{\partial t} + c \tau \frac{\partial^2 T(x, t)}{\partial t^2} - G_B c_B [T_B - T(x, t)] - Q_m \right] & T^*(\xi, x) d\Omega \end{aligned}$$

where ξ is the observation point, $B(\xi) \in (0, 1)$, $T^*(\xi, x)$ is the fundamental solution, $q(x, t^f) = -\lambda \partial T(x, t^f) / \partial n$ is the heat flux, $q^*(\xi, x) = -\lambda \partial T^*(\xi, x) / \partial n$.

In the dual reciprocity method the following approximation is proposed [2]

$$\left[(c + \tau G_B c_B) \frac{\partial T(x, t)}{\partial t} + c \tau \frac{\partial^2 T(x, t)}{\partial t^2} - G_B c_B [T_B - T(x, t)] - Q_m \right]_{t=t^f} = \sum_{k=1}^{N+L} \lambda a_k(t^f) \nabla^2 U_k(x)$$

where $a_k(t^f)$ are unknown coefficients, $P_k(x)$ are approximating functions fulfilling the equations

$$P_k(x) = \lambda \nabla^2 U_k(x)$$

and $N + L$ corresponds to the total number of nodes, where N is the number of boundary nodes while L is the number of internal nodes. After the mathematical manipulations one obtains

$$B(\xi) T(\xi, t^f) + \int_{\Gamma} T^*(\xi, x) q(x, t^f) d\Gamma = \int_{\Gamma} q^*(\xi, x) T(x, t^f) d\Gamma + \sum_{k=1}^{N+L} a_k(t^f) \left[B(\xi) U_k(\xi) + \int_{\Gamma} T^*(\xi, x) W_k(x) d\Gamma - \int_{\Gamma} q^*(\xi, x) U_k(x) d\Gamma \right]$$

where $W_k(x) = -\lambda \mathbf{n} \cdot \nabla U_k(x)$. This equation is solved in numerical way.

3. Example of computations

The biological tissue domain of dimensions $0.01 \text{ m} \times 0.01 \text{ m}$ ($L = 0.01 \text{ [m]}$) has been considered. The initial temperature of tissue equals $T_0 = 37 \text{ }^\circ\text{C}$. On the boundary $x_1 = 0$, $0 \leq x_2 \leq L$ the Dirichlet condition in the form $T_b(x_2) = 37 + (50 - T_0)x_2/L$ has been assumed, on the remaining part of the boundary the temperature $T_b = 37 \text{ }^\circ\text{C}$ can be accepted. The input data have been taken from [1]. The boundary has been divided into $N = 40$ constant boundary elements, at the interior $L = 100$ internal nodes have been distinguished. Time step: $\Delta t = 10 \text{ s}$.

In the Figures 1 and 2 the heating curves at three points (0.0035, 0.0035), (0.0055, 0.0055), (0.0075, 0.0075) from tissue domain for $\tau = 0 \text{ s}$ (Pennes equation) and $\tau = 20 \text{ s}$ (Cattaneo-Vernotte equation) are shown. The differences between the temperatures for these two models are visible.

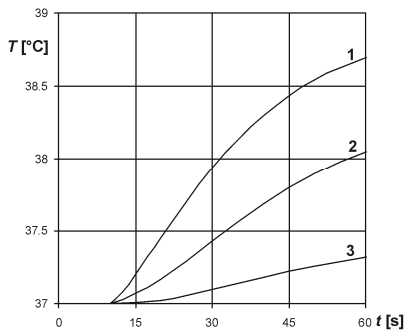


Fig. 1. Heating curves for $\tau = 0 \text{ s}$

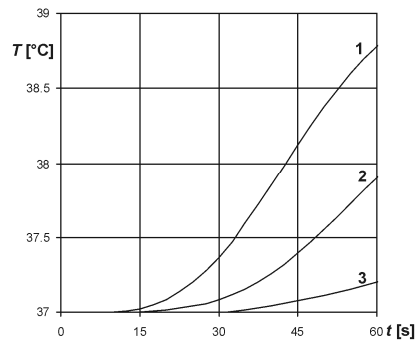


Fig. 2. Heating curves for $\tau = 20 \text{ s}$

4. References

- [1] J. Liu and L.X. Xu (2000). Boundary information based diagnostics on the thermal states of biological bodies, *Journal of Heat and Mass Transfer*, 43, 2827–2839.
- [2] P.W. Partridge, C.A. Brebbia, L.C. Wróbel (1992). *The dual reciprocity boundary element method*, CMP, London, New York.

TRAVELLING WAVES IN TWO MECHANOCHEMICAL MODELS OF TUMOR ANGIOGENESIS

K. Piechór

Institute of Fundamental Technological Research, Warszawa, Poland

1. Introduction

At the early stages of its formation the tumor secretes some chemical signals, called Tumor Angiogenic Factors, into the neighbouring extracellular matrix (ECM) to stimulate sprouting new blood vessels from the existing vascular system. This process is an example of the phenomenon called angiogenesis. The TAF when reach a blood vessel make the cells forming the outer layer, the endothelium, to move via chemotaxis into the direction of the tumor. The travelling endothelial cells cause some traction within the tissue inducing some deformations of it and changing its density, what in turn influences the motion of the endothelial cells themselves..

2. The model

In the mathematical model only four field velocities are taken into account. They are:

- $\mathbf{u}(t, \mathbf{x})$ - the displacement at time t of a point of ECM being initially at the position \mathbf{x} ,
- $N(t, \mathbf{x})$ - the density of ECM at time t and position \mathbf{x} ,
- $n(t, \mathbf{x})$ - the density of the endothelial cells at time t and position \mathbf{x} ,
- $r(t, \mathbf{x})$ - the concentration of TAF at time t and position \mathbf{x} .

The ECM is modelled as a visco-elastic continuum. It is assumed that the Reynolds number is small, consequently, the inertial terms are ignored. The body force balances the elastic force, the viscous force, and the cell traction within the ECM. The force balance equation reads

$$(1) \quad \nabla \cdot \left\{ \overbrace{\left[\frac{1-2\nu}{1-\nu} \boldsymbol{\varepsilon} - \beta_1 \nabla^2 \boldsymbol{\varepsilon} + \left(\frac{\nu}{1-2\nu} \theta - \beta_2 \nabla^2 \theta \right) \mathbf{I} \right]}^{\text{elastic force}} + \overbrace{\left[\mu_1 \frac{\partial \boldsymbol{\varepsilon}}{\partial t} + \mu_2 \frac{\partial \theta}{\partial t} \right]}^{\text{viscous force}} + \overbrace{\left[\tau s \mathbf{I} \right]}^{\text{traction}} \right\} = \overbrace{\left[\rho \frac{\partial \mathbf{u}}{\partial t} \right]}^{\text{body force}},$$

$s = s(n)$ is the traction stress, ν is the constant Poisson ratio, μ_1, μ_2 are the constant shear and bulk viscosities, β_1, β_2 are positive constants, \mathbf{I} is the unit matrix, and τ is a positive parameter characterising the strength of the traction τs , and ρ is a positive constant, $\boldsymbol{\varepsilon} = \frac{1}{2}(\nabla \mathbf{u} + \nabla \mathbf{u}^T)$ is the strain tensor, where T denotes the transpose, and $\theta = \nabla \cdot \mathbf{u}$ is the dilatation

The cells of ECM move only due to convection. Hence this equation is of the form

$$(2) \quad \frac{\partial N}{\partial t} + \nabla \cdot \left(\overbrace{N \frac{\partial \mathbf{u}}{\partial t}}^{\text{convection}} \right) = 0.$$

The EC cell density changes due passive convection, random diffusion, chemotaxis and haptotaxis. Due to the deformations of the ECM the diffusive flux is biased. Simply, scalar coefficient of diffusion is replaced by a tensor depending on the strain in the ECM. In our model we assumed for sake of some mathematical simplicity that the chemotactic flux is also biased by the same tensor. This assumption can be removed at the expense of more complicated formulae.. The equation of the EC density reads

$$(3) \quad \frac{\partial n}{\partial t} + \overbrace{\nabla \cdot \left(n \frac{\partial \mathbf{u}}{\partial t} \right)}^{\text{conection}} = \nabla \cdot \left[\overbrace{D \left(\mathbf{I} + \boldsymbol{\Phi} - \frac{\theta}{2} \mathbf{I} \right)}^{\text{biased diffusion and chemotaxis}} \cdot \left(\nabla n - \alpha \frac{n}{r} \nabla r \right) - \overbrace{n \nabla \gamma(N)}^{\text{haptotaxis}} \right],$$

where D , α are positive constants, and $\gamma(N)$ is the haptotactic function describing the adhesion of the endothelial cells to the ECM.

Finally, we assume that the TAF concentration changes in time due to diffusion and degradation, i.e. “consumption” by EC. The equation reads

$$(4) \quad \frac{\partial r}{\partial t} = \overbrace{d \nabla^2 r}^{\text{diffusion}} - \overbrace{F(n, r)}^{\text{degradation}}.$$

To close the system (1) – (4) we need to know the functional form of $s(n)$, $\gamma(N)$, and $F(n, r)$. We use the following models

$$s(n) = \frac{P_s n}{1 + k_s n^2}, \quad \gamma(N) = \frac{P_\gamma N}{1 + k_\gamma N},$$

and two models of the degradation function

$$(5) \quad F_I = knr \quad \text{and} \quad F_{II} = kn,$$

where $P_s, k_s, P_\gamma, k_\gamma, k$ are positive constants. The reason of considering two models given by F_I and F_{II} is that the “equations of state” like $s(n)$, $\gamma(N)$, etc. are known only in a very rough approximation. Frequently they are chosen for simplicity. We show that despite the small difference between F_I and F_{II} the corresponding travelling waves differ significantly.

We look for solutions of the system (1) – (4) in the form of travelling waves, i. e. the field quantities \mathbf{u}, N, n, r are assumed to be functions of one independent variable $\xi = \mathbf{k} \cdot \mathbf{x} - \sigma t$, where \mathbf{k} is a given constant vector, and σ is a positive constant, interpreted as the wave speed.

We prove that the wave propagates only in the direction of the vector \mathbf{k} . The main result of the paper is

Theorem *The endothelial cell density n and the TAF concentration r are well defined function on the real axis $(-\infty, \infty)$. They are positive, and for positive wave speed σ , $r(\xi)$ it is monotonically increasing in its domain. Moreover, they satisfy: for Model I*

$$n(\xi) = \begin{cases} n_- + o(1) & \text{as } \xi \rightarrow -\infty \\ O(e^{-\sigma \xi}) & \text{as } \xi \rightarrow +\infty \end{cases} \quad r(\xi) = \begin{cases} O\left(\exp\left(\frac{\sigma}{\alpha} \xi\right)\right) & \text{as } \xi \rightarrow -\infty \\ r_+ + o(1) & \text{as } \xi \rightarrow +\infty \end{cases}$$

and for Model II

$$n(\xi) = \begin{cases} O\left(\exp\left(\frac{\sigma}{\alpha} (\xi - 1)\right)\right) & \text{as } \xi \rightarrow -\infty \\ O(e^{-\sigma \xi}) & \text{as } \xi \rightarrow +\infty \end{cases} \quad r(\xi) = \begin{cases} O\left(\exp\left(\frac{\sigma}{\alpha - 1} \xi\right)\right) & \text{as } \xi \rightarrow -\infty \\ r_+ + o(1) & \text{as } \xi \rightarrow +\infty. \end{cases}$$

Hence, in the case of Model I the EC density has the form of a kink, whereas in the Model II its profile has the form of an impulse and vanishes at both ends. Therefore, such a wave cannot be accepted as a solution of the tumor angiogenesis problem; rather it corresponds to an *in vitro* vasculogenesis

Acknowledgement. This paper was partly supported by the Polish Ministry of Science and Higher Education Grant No 1 PO3A 01230.

INTERACTION OF ULTRASONIC WAVES WITH CONTINUOUS INHOMOGENEITY OF POROUS MATERIALS

M. Cieszko, W. Kriese

*Institute of Environmental Mechanics and Applied Computer Science,
Kazimierz Wielki University, Bydgoszcz, Poland*

1. Introduction

The problem of ultrasonic wave interaction with continuous inhomogeneity of material is of great importance for theory and applications. On the one hand such materials are commonly present in living systems, nature, building engineering and industry. The macroscopic inhomogeneity is often a result of their formation, production or processes taking place during their life (e.g. osteoporosis), exploitation (e.g. sedimentation of pollutions on filters) or interactions with environment (e.g. degradation of concrete surface). On the other hand the ultrasonic research of such materials, due to their non-invasive character, are more commonly applied in diagnostics and determination of pore structure parameters and material constants.

The aim of this paper is to apply the new method of description of ultrasonic wave interactions with macroscopic inhomogeneity of material to the analysis of wave reflection and transmission through a layer of porous material with inhomogeneous pore space structure (Fig. 1).

2. Formulation of the problem

We consider a one dimensional problem of wave interaction with material inhomogeneity caused by a layer of pores. It concerns interaction of waves in the air incident on a porous surface layer of an undeformable material with continuously changeable pore structure parameters (Fig. 1a), and waves in an elastic solid with a layer of pores in that medium (Fig. 1b). We assume that the local acoustical properties of the material are characterized by the impedance Z and the wave number k . These parameters, in general, are dependent on the spatial coordinate x and the wave frequency ω .

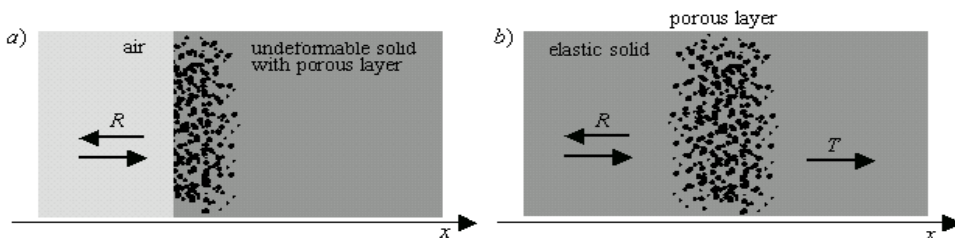


Fig. 1. The analyzed exemplary problems

Due to interaction with material inhomogeneity each wave propagating in such material generates the coupled backward wave. Therefore, the acoustical field in inhomogeneous material is defined by amplitudes T and R of the forward and backward waves, respectively.

In that case wave interaction with continuous inhomogeneity can be considered as multiple reflections and transition of the wave through the boundaries of infinitesimal layers. Such approach allows to derive the following system of equations for amplitudes T and R , [3]

$$\frac{dR}{dx} + ikR = \frac{dI}{dx}(2T + R) \quad , \quad \frac{dT}{dx} - ikT = \frac{dI}{dx}(2R + T) \quad ,$$

where $I = \ln(Z_o / Z) / 2$ and Z_o is constant.

Solution of these equations needs the parameters k and Z to be known functions of the spatial coordinate and wave frequency. In the paper such relations are obtained in two stages. First, both parameters are determined for homogenous materials and next their dependence on the spatial coordinate is postulated.

3. Acoustical characteristics of air-filled rigid porous material

To obtain the acoustical characteristics for air-filled rigid porous material, the one dimensional system of equations has been analyzed, [4]

$$\frac{\partial v}{\partial t} + a^2 \frac{\partial q}{\partial x} + \mu \frac{f_v^2}{K} v = 0 \quad , \quad \frac{\partial q}{\partial t} + \frac{1}{\delta^2} \frac{\partial v}{\partial x} = 0 \quad ,$$

where $q = (\rho - \rho_o) / \rho_o$, and f_v , δ , K are parameters of volume porosity, tortuosity and permeability, respectively. Quantity a stands for the wave velocity in bulk fluid, and μ for a kinematical viscosity.

The derived equations for the wave number and impedance of the air-filled rigid porous material take the form

$$k = \frac{\omega \delta}{a} P \quad , \quad Z = \rho_o a \frac{f_v}{\delta} P \quad ,$$

$$\text{where } P = 1 / \sqrt{2} \left(\sqrt{1 + \sqrt{1 + (\mu f_v^2 / K \omega)^2}} + i \sqrt{\sqrt{1 + (\mu f_v^2 / K \omega)^2} - 1} \right) .$$

Analysis of influence of parameters characterizing inhomogeneity of pore space structure on characteristics of reflected and transmitted waves was performed in the paper for different dependence of pore structure parameters on the spatial coordinate.

The similar analysis was performed for wave propagating in elastic solid with inhomogeneous layer of pores.

4. References

- [1] L. M. Brekhovskikh (1980). *Waves in Layered Media*. Academic Press, New York.
- [2] P. Filippi, D. Habault, J.P. Lefebvre, A. Bergassoli (1999). *Acoustics. Basic Physics, Theory and Methods*, Academic Press, San Diego.
- [3] M. Cieszko, J. Kubik. Propagation of Ultrasonic Waves in Inhomogeneous Materials (in press).
- [4] J. Kubik, M. Cieszko, M. Kaczmarek (2000). *Podstawy dynamiki nasyconych ośrodków porowatych*, Wyd. IPPT PAN, Warszawa.

THE NUMERICAL MODELING OF OSTEOPOROTIC CHANGES IN SELECTED BIOMECHANICAL STRUCTURES

A. John, P. Orantek, P. Wysota

Department for Strength of Materials and Computation Mechanics, Silesian University of Technology, Gliwice, Poland

Osteoporosis is metabolic disease of bone which causes progressive decrease of the osseous pulp and the changes of bone structure. Such weak bone is more susceptible on fractures. The early diagnosis of osteoporosis enlarges chance of the treatment. It is a big problem because disease progresses without symptoms – first symptoms appear when the loss of osseous pulp is big (about 30%) and it is the large risk of fractures. The treatment of osteoporosis usually depends on treatment of results - fractures and consists in providing analgesic and stabilization of places of fractures. It would be better to prevent that disease because lack of movement is causes of weakness of bones. Knowledge of physical properties of bone tissue is helpful in diagnosing of the diseases of the bone system (especially that properties change during progress of disease) [4].

From mechanical point of view the fracture of bone occurs in two cases:

- the correct structure of bone but the loads are so big that cause the stresses larger than stress limit,
- the disorders of bone structure caused decrease of strength properties of bone when normal activity of organism can result stresses larger than stress limit.

The paper concerns the second situation, which take place e.g. in osteoporosis. The most common preventive examinations are:

- densitometry of bone – method of representing of the bone density by using dual energy X-ray absorptiometry (DXA) ,
- computed tomography – method depending on mapping cross-section of bone; it makes possible localizing the places where is the considerable loss of osseous pulp.

These are standard examinations which gives enough information and to enable to make a correct decision in routine situations. However when data will be use to building of quantitative model of bone tissue these methods can be insufficient. Then it is necessary to perform Quantitative Computed Tomography [5].

To present the problem of the osteoporosis the strength analysis of the human hip joint were performed (health joint and the joint with osteoporotic changes). Numerical simulations give important information about behaviour of object on condition that numerical model is similar to analyzed structure (geometry, material properties and boundary conditions). During create geometry of the model date from coordinate measuring machine is used (it was concentrated on the pelvis bone). There is important the delimitation of material properties which are changed during osteoporosis. During examination the bone system as well as density phantom are X-rayed. The phantom is composed of regions representing specimens of bone density. The X-ray photographs are analyzed by use specialist software (the dependence between quantity of the absorbed radiation and the radiological density is used). The output density is standardized in Hounsfield scale (HU). Then the HU density is converted to the density of bone tissue. The next step is delimitation of material properties of bone tissue, especially elastic modulus (on the basis of experimental research the dependences between bone density and material properties were developed) [1, 2].

Because Computed Tomography gives cross-section for different places so material properties was delimited in the same places of bone (on the base of linear regression for measuring

points the calibration curve is created, it enable to calculate the properties for every voxel of photographs) - the more exact data from CT, the better representation of bone structure. This is important because bone is non-homogenous, especially pelvic bone, with regard to complex geometry and functions in organism, is characterized by changeability of material properties [5].

Delimitated properties were given to model. Next the boundary conditions were assumed.

The fixed was realized by use elements type bar type beam (during analysis the number and the stiffness of elements were changed). The boundary conditions were given both in the points and in the areas [3].

Strength calculations were performed in system MSC Patran/Nastran. The structure on the base of distributions of equivalent stresses, strains and displacements was analyzed. Obtained results can be helpful to estimated effort of pelvis and femoral bone and planning surgical interventions during treatment of injuries caused by osteoporosis.

The exemplary photographs with Quantitative Computed Tomography were presented in Fig.1. Examinations were performed in sagittal plate. Density phantom and the pelvic bone were X-rayed.



Fig.1. The images from computed tomography: a) density phantom, b) and c) pelvic bone

The work was done as a part of project N51804732/3670 sponsored by Polish Ministry of Science and Higher School.

REFERENCES

- [1] M. Binkowski, A. Dyszkiewicz, Z. Wróbel, “The analysis of densitometry image of bone tissue based on computer simulation of X-ray radiation propagation through plate model”, *Comput. Biol. Med.*, vol. 37, pp. 245-250, 2006.
- [2] A. Dąbrowska-Tkaczyk, J. Domański, Z. Lindemann, M. Pawlikowski, K. Skalski, “Stress and strain distributions in the bones of hip joint assuming non-homogenous bone material properties”, *Proc. of II Int. Conf. on Computational Bioengineering 2005*, vol. 2, pp. 263-275.
- [3] A. John, “Identification and analysis of geometrical and mechanical parameters of human pelvic bone”, *Scientific papers of SUT*, No 1651, Gliwice, 2004 (in Polish).
- [4] John A., Wysota P., *Selected problems of computer aided planing of surgical intervention in human skeletal system*, Finite Element Modeling in Biomechanics and Mechanobiology, Proceedings of the 2007 Summer Workshop of the European Society of Biomechanics, pp. 193 – 194, Dublin 2007.
- [5] L.M. McNamara, P.J. Prendergast, M.B. Schaffler, “Bone tissue material properties are altered during osteoporosis”, *Musculoskeletal Neuronal Interact*, vol. 5, pp.342-343, 2005.

EFFECT OF SPECIAL LAYERS SHAPING ON STRESS DISTRIBUTION IN DENTAL RESTORATIONS

P.Kowalczyk

Division of Applied Mechanics, Warsaw University of Technology, Warsaw, Poland

1. Introduction

One of the most popular materials used for restorations in dentistry are the resin-based composites reinforced by ceramic particles. In contrary to amalgam, the composites are mercury-free, do not require special cavity shaping and are esthetical. Photo-cured composites are one of the types of the resin-based composites. Typical features of the photo-polymerization process are: high speed of the polymerization, room temperature process, and limitation of the polymerization depth due to light absorption. Typical polymerization time of the photo-cured composite is 20 seconds for 2 mm thick layer. Fillings are made layer by layer. One of the main disadvantages of these materials is volumetric shrinkage that occurs during polymerization. It results in high residual stress in tooth and restoration, which can cause gaps between the tooth tissue and the filling. It may leads to microleakage and tooth decay. To ensure strong bonding between the tooth tissue and the composite restoration, bonding agents are used. The bonding agent is a photo-cured polymer with small viscosity. This material creates thin, approximately 0.01 mm layer on the tooth tissue and penetrates into it, and this creates kind of mechanical bonding. Adhesives bond with composite restoration chemically. For modern systems the bonding strength is 15 – 35 MPa [1]. Experiments reveal that the bonding strength of adhesives depends of cavity preparation before coating it with bonding agent. Existing of thin layer of bonding agent causes stresses reduction between composite filling and tooth tissue [2]. Most recently the effect of bonding agent is assumed to be negligible. Ausiello and coauthors had modeled the tooth under load with adhesive layer modeled with springs [3]. The tooth filling was assumed to be strain free, without polymerization shrinkage and residual stress.

Clinical practice reveals that shape of layers and method of layering are important [4]. In this study restoration of Class I is modeled with existing adhesive layer. Different shapes of composite layers and its influence on stress distribution in dental filling are taken into account.

2. Materials and methods

Premolar tooth was modeled with ABAQUS - the finite element method software. Mechanical properties of the tooth tissues (Young modulus E , and Poisson's ratio ν) are as follows: enamel $E = 80000$ MPa, $\nu = 0.33$; dentin $E = 18000$ MPa, $\nu = 0.31$; pulp $E = 2.07$ MPa, $\nu = 0.45$ [5]. The tooth tissues are assumed to be linearly elastic materials. Properties of the adhesive layer (UniFill) are: Young's modulus – 39100 MPa, assumed Poisson's ratio – 0.25 [6]. A 0.01 mm thick adhesive layer was modeled with cohesive elements. Properties of the resin-based composite (P50) are: Young's modulus – 20000 MPa, Poisson's ratio – 0.24 [4]. Polymerization shrinkage was modeled as analogical to thermal deformation. Total linear shrinkage of composite is $s_{max} = 0.008$. According to Versulis [4] shrinkage stress is developed after the gel point. Before this point all stresses are fully relaxed by the flowing of the material. Shrinkage value after the gel point is about $s_{post-gel} = 0.0022$. The filling material was modeled as linearly elastic with maximal linear shrinkage of 0.0022. The tooth and its restoration were modeled in assumption of axisymmetric model. Influence of adhesive layer is presented in Fig 1.

In these work, two shapes of horizontal layer are presented: a flat layers and a rounded layers. Moreover, a modification of the layering with additional vertical layer (called a pre-layer) is presented (Fig.2).

3. Results

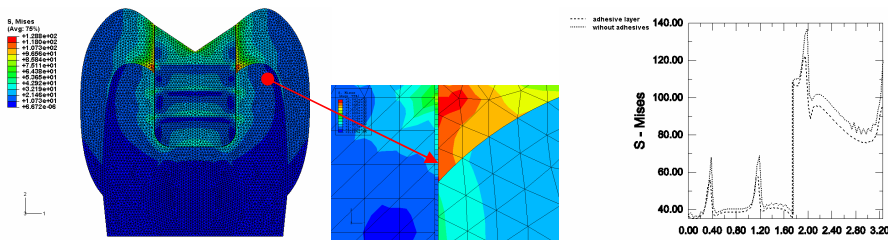


Fig. 1 Modeled adhesive layer with cohesive elements and plot of Huber-Mises stress in tooth tissue (adhesive layer reduces stresses of about 20%)

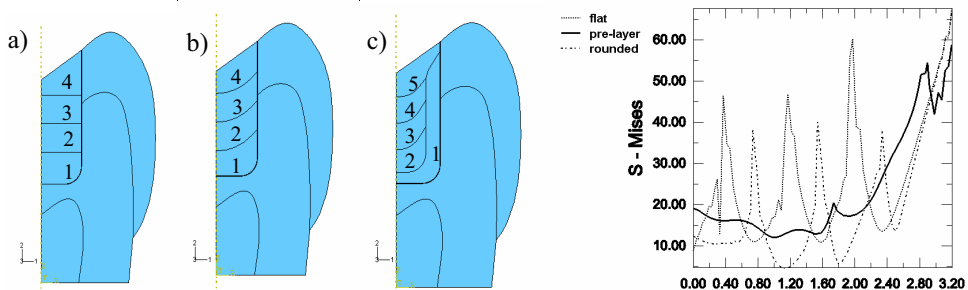


Fig. 2 Three types of layering techniques - a) flat, b) rounded, c) pre-layer, and plot of Huber-Mises stress along the right vertical wall of the cavity.

The horizontal rounded layers give smaller values of stresses along the cavity than flat layers. The lowest stress is achieved when an additional vertical layer is added. The pre-layer reduces significantly influence of the layers corners, and in consequence, stress accumulations near the adhesive layer. Unfortunately the pre-layer can increase stress at the top of restoration due to accumulation of the shear stresses at the top of the layer. To avoid this problem, the vertical layer should not reach the top of the cavity. The last horizontal layer should be extended on whole area of the cavity.

6. References

- [1] A. Takahashi, Y. Sato, S. Uno, P.N.R. Pereira, H. Sano (2002). Effect of mechanical properties of adhesive resins on bond strength to dentin, *Dental Materials* **18** 263-268
- [2] B.S. Dauvillier, P.F. Hubsh, M.P. Aarnts, A.J. Feilzer (2001). Modeling of viscoelastic behavior of dental chemically activated composites during curing, *Inc. J. Biomed Mater Res (Appl Biomater)* **58**: 16-26,
- [3] P. Ausiello, A. Apicella, C.L. Davidson (2002). Effect of adhesive layer properties on stress distribution in composite restorations – a 3D finite element analysis, *Dental Materials* **18** 295-303.
- [4] A. Versluis, W.H. Douglas, M. Cross, R.L. Sakaguchi (1996). Does an incremental filling technique reduce polymerization shrinkage stress?, *J. Dent. Res.* **75** 871-87
- [5] G. Couegnat, S.L. Fok, J.E. Cooper, A.J.E. Qualtrough (2006). Structural optimisation of dental restorations using the principle of adaptive growth, *Dental Materials* **22** 3-12.
- [6] A. Takahashi, Y. Sato, S. Uno, P.N.R. Pereira, H. Sano (2002). Effect of mechanical properties of adhesive resins on bond strength to dentin, *Dental Materials* **18** 263-268

NUMERICAL MODELLING OF THE OPENING PROCESS OF THE THREE-COATING AORTIC VALVE

M. Kopernik and J. Nowak

Akademia Górniczo-Hutnicza, Kraków, Poland

1. Introduction

The natural aortic valve, which is composed of three leaflets, works under the highest pressure in the circulatory system. In the case of irreversible failure, the valve is replaced with prosthesis. The tendency to create the mechanical valves, whose geometry is based on the real valves, is observed. These artificial organs are made of polyurethane (PU) and covered by TiN coatings to increase the biocompatibility. Development of the mathematical model of the TiN/PU/TiN aortic valve, which is connected with the earlier results obtained in [1] and based on physical formulas derived in paper [2], is the objective of the present work. Analysis of the sensitivity coefficients [1] calculated for the control parameters of the valve opening decided about the assumptions introduced in the new finite element (FE) model. The previous work [1] was dedicated to pure PU aortic valve. Since each of the identical leaflets of the real aortic valve has a three-coating structure, extending the analysis to structure is another objective of this project. The new model satisfies the basic conditions required for the mechanical construction of the aortic valve. The valve opening is used to determine the acceptable values of Young modulus and the thicknesses of outer coatings.

2. The FE model of TiN/PU/TiN aortic valve

The minimal buckling pressure is the basic parameter, which decides about the proper work of the aortic valve. According to Reul [2], this parameter depends on Young's modulus E , thickness of the leaflet d and aortic radius R . The conclusions of the sensitivity analysis for the pure PU aortic valve led to the new set of parameters of the model of the aortic valve ($R = 7$ mm, $d = 0.1$ mm and $E = 10$ MPa) [1], which gives the minimal value of the buckling pressure. In the present work this new construction of the valve has been tested for the three ratios between the thickness of the deposited outer coating and the thickness of the whole leaflet (1:100, 2:100 and 3:100). A search for the best value of the Young's modulus of the outer coating, which provides the minimal buckling pressure, was performed for each ratio. The buckling pressure, which is the loading of the leaflet and is a constant input parameter of the FE model in the present analysis, was taken 0.77 kPa and calculated for the pure PU leaflet with the optimal dimensions given above. The displacement of the TiN/PU/TiN leaflet reached in its characteristic point (Fig. 1a) is the output parameter of the model. The range of this displacement, which is assumed as proper and optimal, is 80-100% of that displacement for the pure PU leaflet. This defined range of the displacements is necessary to obtain the opening of the aortic valve.

3. Results and conclusions

The FE model of three-coating leaflet of aortic valve is generated in the ADINA FE code and is composed of 100 000 elements and 40 000 nodes, as it is shown in Fig. 1a. The displacements in the characteristic point of the leaflet for the valve opening are shown in Fig. 1b for the selected elastic moduli of outer coating and the geometrical ratio 1:100. The thicker is the outer coating and the bigger is Young's modulus, the smaller is the valve opening.

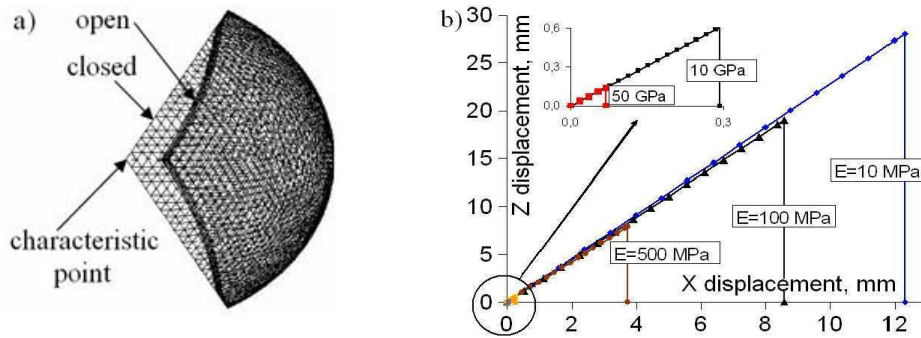


Fig.1. a) The FE model of three-coating leaflet of aortic valve in open and closed positions (top view), b) The valve opening for the selected elastic moduli and geometrical ratio 1:100.

Assuming the opening as the output of the FE model, the sensitivity coefficients of this parameter with respect to the Young's modulus of outer coating are calculated and plotted in Fig. 2a. Following these results, further calculations are dedicated to the remaining geometrical ratios (2:100, 3:100) and, especially to these elastic moduli, which have the meaningful values of sensitivity coefficients for the geometrical ratio 1:100. The valve opening for the set of elastic moduli and ratios (1:100, 2:100 and 3:100) is shown in Fig. 2b.

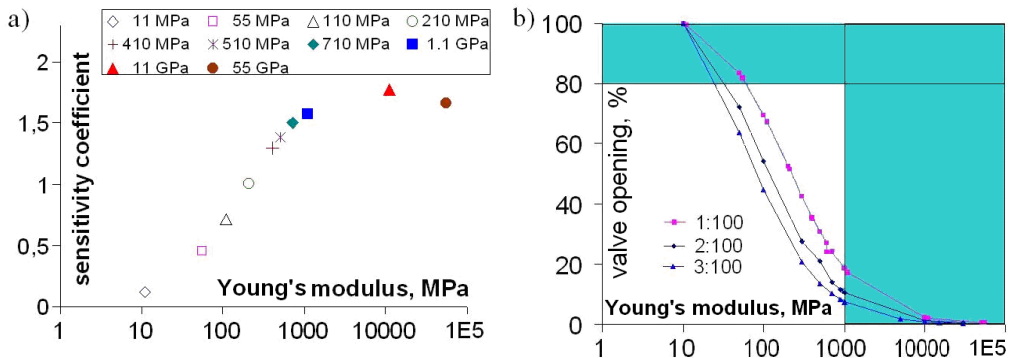


Fig.2. a) The sensitivity coefficients with respect to Young's modulus for geometrical ratio 1:100, b) The valve opening as function of the Young's modulus for all geometrical ratios.

Suggested approach is used to design the optimal values of elastic parameters and thicknesses of outer TiN coating of aortic valve using commercial FE code. The solution fulfills the conditions required for the analysed biomedical part.

4. References

- [1] M. Kopernik, D. Szeliga, J. Nowak (2007). Modelling of mechanical response of leaflet of aortic valve based on the sensitivity analysis of geometry and material parameters, *Proc. XVIIth Conf. CMM, Łódź-Spała*, CD ROM, 1-5.
- [2] D.N. Ghista, H. Reul (1983). Prosthetic aortic leaflet valve design: performance analysis of Avcothane leaflet valve, *Advance Cardiovascular Physiology*, **5**, 31-42.

Financial assistance of the MNiSzW, project no. N507 136 32/3962, is acknowledged.

ANALYSIS OF SHRINKAGE STRESSES IN LIGHT-CURED DENTAL RESTORATIONS

W. Gambin and P. Kowalczyk

Warsaw University of Technology, Warsaw, Poland

1. Introduction

Among the popular types of dental restorations are the photo-cured dental resin composite inlays. In spite of many qualities, one of the main disadvantages of the resin-based restorations is a shrinkage that occurs during the cure process. It results in high residual stresses in the restoration and the tooth, which can cause microleakages [1]. The most unfavourable stresses are the tensile and shear stresses located at the restoration-enamel interface. To reduce the shrinkage stresses, specific restorative techniques are used. One of them is applying the composite in a few layers instead of one layer. It appears a question whether the layering technique really reduces the polymerization shrinkage stresses [2]. To answer for this question, behaviour of cured polymer layers in the dental cave are described in terms of simplified analytical formulae. As the macroscopic measure of the conversion degree at time t , temporary volumetric shrinkage $s(t)$ is taken. In the case of the light-curing process, the volumetric shrinkage s depends on the light exposure H applied during the curing process. Simultaneously we observe evolution of Young's modulus E and Poisson's ratio ν . One can assume simple exponential functions describing s , E and ν as functions of H [3]. To simulate volumetric changes of the material, its temporary elastic properties are assumed and the thermal expansion analogy is used.

1. Model of the incremental filling

The tooth-cavity is assumed to be Class II, which may be modelled under the plain strain conditions as a rectangular opening (dimensions $2a \times b$), with rigid walls and bottom (Fig. 1). A full adhesion of restoration and the tooth tissues is assumed. The cave may be filled and next irradiated into two ways. One can fill the whole cavity before irradiation (Fig. 1a), or one can do it in two steps. At first, half of the prepared cavity is filled and irradiated (Fig. 1b). Next, the second layer is placed on the cured previously layer and irradiated (Fig. 1c).

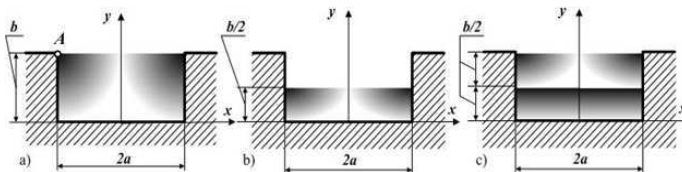


Fig. 1. Two ways of tooth-cavity restoration: in one step (a) and in two steps (b-c).

In our model, displacements of particles of considered resin layer, appearing during the curing process are expressed in terms of polynomials, prescribed at each point x of the layer. The polynomials satisfy the applicable boundary conditions at the walls and bottom of the cavity. The stress boundary conditions on the upper surface of the resin are satisfied approximately using the principle of minimum elastic energy. When half of the cavity is filled or irradiated, Young modulus E , Poisson ratio ν and the volumetric shrinkage s are introduced as step-functions prescribed on the whole cross-section of the filled cavity. As a consequence, the stresses, strains and displacements are given explicitly as combinations of polynomials and step-functions of s , E and ν . Such an approach enables to watch an influence of basic parameters describing the restoration process.

2. Results

Consider a case, when each of polynomials describing horizontal and vertical is determined by 9 coefficients, the cavity dimensions are $a = b = 1$ mm, $s = 0.01$, $E = 4800$ MPa and $\nu = 0.25$. Then, in the case of one-layer restoration, the tension stresses $\sigma_{xx}^{(1)}$ and the shear stresses $\sigma_{xy}^{(1)}$, along the cavity wall, are described by third order polynomials. For two layers restoration, the corresponding stresses $\sigma_{xx}^{(2)}$ and $\sigma_{xy}^{(2)}$ are described by combinations of third order polynomials and step-functions. The results are close to those obtained from FEM analysis with ABAQUS. In Figure 2, stresses $\sigma^{(1)}$ and $\sigma^{(2)}$ are presented as functions of non-dimensional variable $0 < \eta = y/b < 1$.

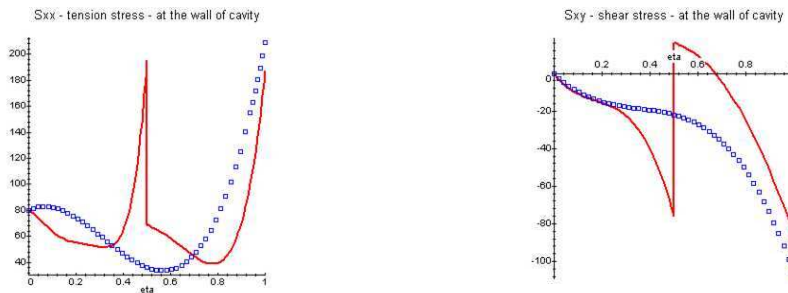


Fig. 2. Comparison of stresses $\sigma^{(1)}$ (point-lines) and $\sigma^{(2)}$ (continuous lines) at the cavity wall.

It is known from dental practice, that the point with the coordinate $\eta = 1$ (A at Fig. 1) is the most probable place where a leakage may appear. For this place, we have: $\sigma_A^{(2)} / \sigma_A^{(1)} = 0.89$, and $\sigma_A^{(2)} / \sigma_A^{(1)} = 0.80$. The result suggests that the layering of the composite material with successive irradiation may decrease maximal shrinkage stresses. Indeed FEM simulations of more realistic model of the restoration with one, two and four layers confirm this hypothesis (Fig. 3).

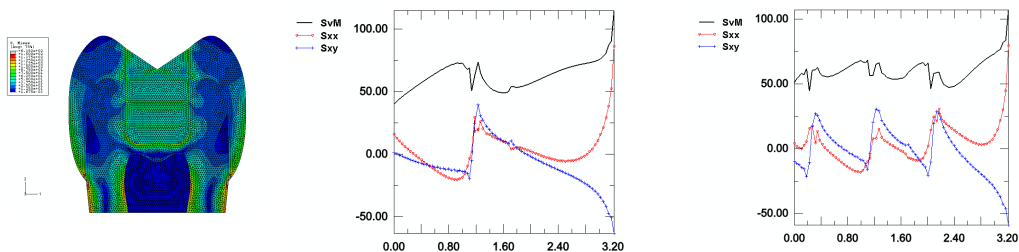


Fig. 3. FEM model of the 4-layers tooth restoration and stresses at the cavity wall for 2 and 4 layers.

Now, the comparison of stress components at the point A, gives the following results: $\sigma_A^{(2)} / \sigma_A^{(1)} = 0.88$, $\sigma_A^{(2)} / \sigma_A^{(1)} = 0.81$, $\sigma_A^{(4)} / \sigma_A^{(1)} = 0.83$, and $\sigma_A^{(4)} / \sigma_A^{(1)} = 0.76$.

6. References

- [1] D.N. Bardwell and S. Deliperi (2002). An alternative method to reduce polymerization shrinkage in direct posterior composite restorations, *JADA* 133.
- [2] A. Versluis, W.H. Douglas, M. Cross, R.L. Sakaguchi (1996). Does an incremental filling technique reduce polymerization shrinkage stress?, *J. Dent. Res.* **75** 871-87.
- [3] F.P. Jacobs (1992). *Rapid Prototyping & Manufacturing, Fundamentals of Stereolithography*, MI USA.

APPLICATION OF BIOMECHANICAL MODELS IN DESIGN AND SIMULATION OF ACTIVE AND PASSIVE VIBRATION DAMPING

I. Maciejewski, S. Chamera and T. Krzyzynski

Koszalin University of Technology,

*Institute of Mechatronics, Nanotechnology and Vacuum Technology,
Koszalin, Poland*

1. Introduction

Biomechanical models of human body are created for verification of vibration influence on individual parts of human body. By using those models, it is possible to estimate acceleration and frequency of vibrations, without necessity of experimental research. These experimental researches proved to be unreliable. Experiences of individual persons can be subjective and vary widely [4]. In biomechanical models, there are some elementary masses, connected by typical viscous-springy elements.

2. Physical models of the seat and of the human body

There are about 60 models, presented in scientific literature. Usually, there are discrete mechanical models, which consider lying, seating and standing position [3]. According to ISO and DIN standards there are other, simplified models. Those models present human body as sum of four masses in different configurations. In Fig. 1 models of human body, according to ISO and DIN are presented.

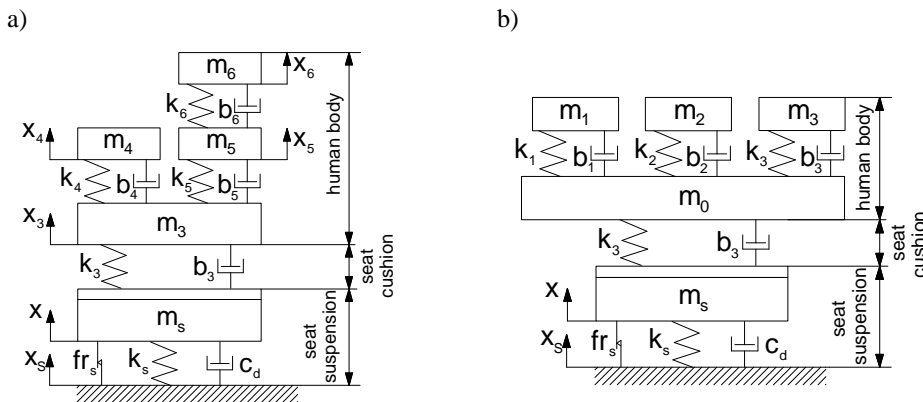


Figure 1. Physical models of the seat and the human body: bio-mechanical model ISO 5982 (a), bio-mechanical model DIN 45676 (b).

3. Simulation results

For evaluation of human body dynamical behaviour the white, band limited noise as excitation signal is used. The courses of power spectral densities of acceleration measured at the seat cushion (PSD) and transfer functions of suspension systems (T), are shown in Fig. 2. The presented simulation results are obtained for passive and active seat suspension system.

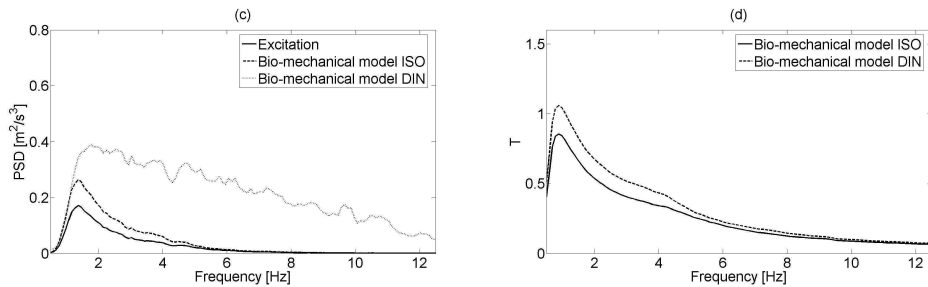


Figure 2. Simulated power spectral densities of acceleration (PSD) and transfer functions (T) of passive (a, b) and active seat suspension (c, d).

4. Conclusions

Values of power spectral density and transfer function, elaborated on the basis of simulation research, show that there are considerable differences between the system loaded by mass of modeled human body according to ISO 5982 and DIN 45676. Whereas, comparing dynamic properties of the seat, in use of two given biomechanical models, practically there is significant difference in the frequency range 0 – 5 Hz. Results of computer simulation show necessity of further investigations, for the purpose of uniform estimation of vibro-isolation properties. A model, which in the best way can reproduce dynamical behaviour of human body is needed.

5. References

- [1] DIN 45676 (2003). *Mechanische Eingangsimpedanzen und Übertragungsfunktionen des menschlichen Körpers*, Deutsches Institute für Normung.
- [2] ISO 5982 (2001). *Vibration and shock – Mechanical driving point impedance of the human body*, International Organisation for Standardization.
- [3] M., J. Griffin (2004). *Handbook of human vibration*, Elsevier Academic Press.
- [4] M. Nader (2001). *Modelowanie i symulacja oddziaływania drgań pojazdów na organizm człowieka*, Oficyna Wydawnicza Politechniki Warszawskiej.

APPLICATION OF MICRO COMPUTER TOMOGRAPHY TO IDENTIFICATION OF PORE STRUCTURE PARAMETERS OF POROUS MATERIAL

Mieczysław Cieszko, Zbigniew Szczepański

*Institute of Environmental Mechanics and Applied Computer Sciences
Kazimierz Wielki University, 85-064 Bydgoszcz, Chodkiewicza 30, Poland*

1. Introduction

Determination of the pore space structure parameters of porous materials is very important for applications. Porous materials are commonly present in: nature (e.g. the rocks, soils, wood), biology (e.g. bone tissue, lung, membranes) and technology (e.g. sintered metals, ceramics, aerogels and concretes). Their pore structure plays important role in many physical and chemical processes occurring in such materials: in transport of mass, momentum and energy, in wave propagation or chemical reactions. It also strongly influences mechanical properties of the skeleton.

There are many different methods used for identification of pore structure parameters: optical, dynamical (e.g. ultrasonic and vibration methods) and static (e.g. permeametry, gas pycnometry, electric spectroscopy and mercury porosimetry). To the static methods belongs also the Micro Computer Tomography (μ CT). It is very modern method of identification of microscopic structure of inhomogeneous materials. This allows to determinate their stochastic characteristics, macroscopic parameters of structure and also material constants.

The purpose of this paper is to apply the scans of microscopic geometry of human bones obtained by μ CT method to identification of their macroscopic pore structure parameters: volume porosity, permeability and tortuosity of pores and skeleton. These parameters, except the volume porosity, have been determined by simulations of microscopic processes of viscous fluid flow and electrical current passage through samples of bones. The simulations were performed using the COMSOL's Multiphysics environment assigned for solution of boundary value problems described by partial differential equations, by use of the finite element method.

2. Identification of microscopic geometry of pore space

Virtual models of microscopic geometry of porous samples of human bones were obtained in the paper applying the μ CT method. This method like tomography uses X rays to non-invasive identification of the three-dimensional internal structure of physical objects. It concerns e.g. small animals, tissues, microfossils and micro inhomogeneous materials like bones.

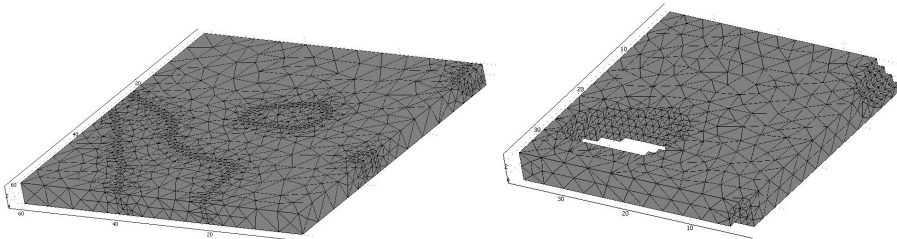


Fig. 1. Virtual 3D models of small slice of human bone identified by μ CT method.

The output data obtained from μ CT Takes form of three-dimensional 8 bits matrices that represent mass density of material in particular points of the sample. In the case of porous materials the identification of spatial distribution of the skeleton in the sample, such matrices have to be binarized. Next, they are used by specialized software to construct the virtual model of microscopic pore space geometry, enable for import by programs like COMSOL assigned for simulations of physical processes. The exemplary virtual 3D model of small slice of human bone identified by μ CT method is shown in Fig. 1.

3. Determination of macroscopic parameters of pore space structure

Three kinds of pore structure parameters are determined in the paper: volume porosity permeability and tortuosity of pores and skeleton. The volume porosity is calculated directly from geometrical relations given by 3D scans of samples whereas the permeability parameter and its directional characteristics are determined applying simulations of microscopic fluid flow in virtual model of porous material and Darcy law,

$$\mathbf{v} = -\frac{k}{\mu} \text{grad}(p),$$

describing this process at the macroscopic level.

To determine the value of the pore tortuosity parameter, the numerical simulations of an electric current passage through perfect conductor (e.g. electrolyte) filling pores of a non-conductive skeleton have been applied. It corresponds to the standard conductometric method of the tortuosity measurements in porous materials ([1], [2]).

These simulations enable calculation of formation factor,

$$F = \frac{\rho}{\rho_0},$$

that is the ratio of effective resistivity ρ of the conductor filling porous sample to specific resistivity ρ_0 of the bulk conductor. Due to relation, [3],

$$\delta^2 = f_v F,$$

the determination of volume porosity f_v and formation factor F , gives directly the value of pore tortuosity δ . The similar approach have been used for determination of the skeleton tortuosity and its directional characteristics.

References

- [1] Mac Carter W.J., Desmazes P. (1997). *Soil Characterization using Electrical Measurements*, Geotechnique, 47, 1, 179-183.
- [2] Łukowski J., Kaczmarek M. (2002). *Laboratory Methods of Determination of Pore Structure Parameters Formation Factor and Tortuosity of Permeable Media by electric Methods*, Engineering Transactions, 50, 4, 267-286.
- [3] Cieszko M. *Extended Description of Current Passage in Perfect Conductors Occupying Anisotropic Pore Space of Non-Conducting Porous Materials. Generalization of the Ohm's Law*, Engineering Transactions, (in the press).

ORTHOTROPIC MODEL OF CANCELLOUS BONE. APPLICATION TO SIMULATION OF ADAPTIVE REMODELLING

P. Kowalczyk

Institute of Fundamental Technological Research, Warsaw, Poland

1. Introduction

A numerical model that allows to simulate the process of anisotropic remodelling of cancellous bone is presented. The bone is treated as continuum with linear elastic orthotropic mechanical properties. Elastic constants and relative density are explicitly known functions of geometric parameters of microstructure. The parameters are nonuniformly distributed in the bone volume. The remodelling rule is an optimization problem in which the “cost” functional is a time rate of a certain global measure of bone quality at a given load state. Instantaneous rates of the parameters are supposed to minimize the functional. The numerically predicted evolution of the parameters is obtained from the time integration of the results of the instantaneous optimization problem.

2. Methods

Cancellous bone is a macroscopically continuous medium that exhibits orthotropic elastic properties within the physiological range of small deformations. Macroscopic mechanical properties are directly related to geometry and mechanical properties of trabecular microstructure. The latter are subject to evolution — this is the way bone adapts to changing (in the long time scale) mechanical conditions. For modelling of the evolution it is crucial to know (i) the mechanism of tissue changes and (ii) the way mechanical properties change along with the changes in microstructure.

Most constitutive models known for cancellous bone do not directly define the dependence between material constants and microstructure characteristics. In the following research, cancellous bone will be modelled with the use of the parametric constitutive model described by the author in [2]. In this model, macroscopic elastic constants are tabularized functions of certain geometric parameters $\{\mu_p\}$ — thicknesses of trabecular bars/plates and orientation angles of principal directions of orthotropy,

$$(1) \quad \sigma_{ij} = D_{ijkl} \varepsilon_{kl}, \quad D_{ijkl} = D_{ijkl}(\mu_p), \quad p = 1, N_p.$$

The functions are derived numerically for a family of idealized, repeatable bone-like microstructures.

Bone remodelling is understood as evolution of trabecular microstructure within the prescribed occupied domain Ω in a way ensuring the fastest possible improvement of bone quality at given loading conditions and at certain limitations resulting from bone physiology. In particular, it will be assumed here after [4] that bone quality is identified with the total strain energy accumulated at a given load and corresponding displacement field $u_i(\mathbf{x})$,

$$(2) \quad G[u_m, \mu_p] = \int_{\Omega} \frac{1}{2} u_{i,j} D_{ijkl}(\mu_p) u_{k,l} d\Omega$$

and thus the evolution of parameters $\dot{\mu}_p$ tends to minimize the rate of this functional

$$(3) \quad \Psi = \dot{G} = \int_{\Omega} \left[\frac{1}{2} u_{i,j} \left(\frac{\partial D_{ijkl}}{\partial \mu_p} \dot{\mu}_p \right) u_{k,l} + u_{i,j} D_{ijkl}(\mu_p) \dot{u}_{k,l} \right] d\Omega.$$

Employing the finite element discretization and introducing an incremental time integration procedure, we can replace the functional Ψ with its incremental approximate at the time interval $[t_n, t_{n+1}]$,

$$(4) \quad \Psi(\mathbf{q}_n, \Delta \mathbf{q}, \mathbf{m}_n, \Delta \mathbf{m}) = \Delta G = \frac{1}{2} \mathbf{q}_{n+1}^T \mathbf{K}(\mathbf{m}_{n+1}) \mathbf{q}_{n+1} - \frac{1}{2} \mathbf{q}_n^T \mathbf{K}(\mathbf{m}_n) \mathbf{q}_n,$$

where \mathbf{q} denotes nodal displacement vector, \mathbf{m} is an array of parameter values μ_p at element integration points, and \mathbf{K} is the stiffness matrix. Ψ is going to be minimized at the time interval with respect to the increment $\Delta \mathbf{m}$.

The minimization problem is subject to constraints: the equilibrium equation $\mathbf{K}_{n+1} \mathbf{q}_{n+1} = \mathbf{f}_{n+1}$, prescribed total mass, and physiological constraints on μ_p and $\dot{\mu}_p$. See details in [3].

The procedure has been implemented in an author's finite element code featuring design sensitivity analysis. Optimization at each time step is performed with the use of the HOPDM routine [1].

3. Results

Figure 1 presents results of computer simulation of mass and anisotropy distribution in a human femur (2D model). Initially bone is assumed uniformly filled with isotropic material. Application of three staggered load cases corresponding to real every day activities stimulates the remodelling process which finally leads to a distribution closely resembling patterns observed in natural bones.

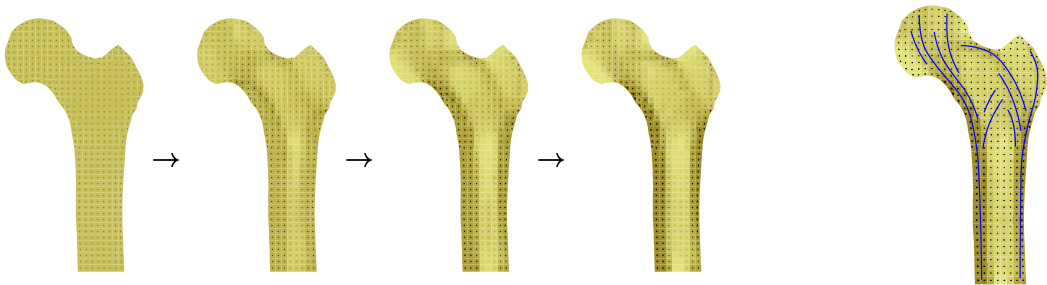


Figure 1. Evolution of mass and anisotropy in a F.E. model of a human femur.

4. References

- [1] J. Gondzio (1995). HOPDM (version 2.12) – A fast LP solver based on a primal-dual interior point method. *European Journal of Operational Research*, **85**, 221–225.
- [2] P. Kowalczyk (2006). Orthotropic properties of cancellous bone modelled as parameterized cellular material. *Computer Methods in Biomechanics and Biomedical Engineering*, **9**, 135–147.
- [3] P. Kowalczyk (2007). Computational model for anisotropic microstructure remodelling of cancellous bone. *17th International Conference on Computer Methods in Mechanics (CMM 2007)*, June 19–22, 2007, Łódź-Spała, Poland. CD-ROM Proceedings.
- [4] T. Lekszycki (1999). Optimality conditions in modeling of bone adaptation phenomenon. *Journal of Theoretical and Applied Mechanics*, **37**, 607–623.

MODELLING BONE – IMPLANT DYNAMICS

B. Nowak, M. Kaczmarek

*Institute of Environmental Mechanics and Applied Computer Science
Kazimierz Wielki University, Bydgoszcz, Poland*

Abstract

The aim of this paper is to consider dynamics of a system composed of bone and implant, with different quality of their attachment, using theoretical and experimental modal analysis. The studies are focused on development of a diagnostic tool based on the vibration technique.

Artificial bone replacements used for implants have become widely applied elements of treatments in orthopedic surgery for recent years. Destructive diseases or accidents call for prosthesis, which in many fields have achieved a certain degree of perfection, yielding pain-free functionality and longevity. However, gradual loosening of the implant-bone attachment integrity due to wear, bone regress (related to ageing or diseases) and micro-mechanical damage lead eventually to the failure of the replacement and thus to painful consequences: a repetition of the implanting surgery takes place under unfavourable conditions. On the other hand total costs of the healing are multiplied.

The existing methods of quality monitoring of implants are based either on the X-ray imaging or ultrasonic inspection (among them: standard radiography, contrast radiography and scyntigraphy). They are therefore impaired by shielding effects when complicated shapes of the prosthesis are needed. All methods above mentioned reveal not sufficient sensitivity and specificity when needed. Moreover, too frequent X-ray irradiation may lead to other serious injures.



Fig. 1. Mesh of substitute – simplified model.



Fig. 2. Mesh of anatomical model.

An alternative method of diagnosis is considered, based on the monitoring the integrity of the implant and bone by checking the changes of its vibrational characteristics. Unlike the ultrasonic inspection, which works on the principle of pulse dispersion and reflection for waves of certain frequency chosen for the tested tissue, the proposed method would rely on monitoring of the shifts of the frequency spectrum caused by the changes in the mechanical properties due to the deteriorating state of the system. A feasibility study for this relatively new method begins with the modelling of attachment integrity. This constitutes a starting point for both FE simulations using numerical modal analysis and experimental study based on vibrational techniques.

In the numerical part of the research two general types of models, taking into account geometry, are considered: substitute - simplified models which are grounded on beam model and anatomical models, fig. 1, based on real geometry of femur bone and implant. In this part of study called theoretical modal analysis Abaqus numerical environment is used to perform computations.

In the experimental study substitute-simplified systems are investigated using modal analysis which model the attachment. The set of dynamic parameters of the system is identified by measuring vibrations. The experimental tests are accomplished by introducing either impulse or harmonic excitation.

Analysis of numerical and experimental data which include: shifts in frequency spectrum, changes in eigenmode shapes, fluctuations of amplitude revealed significant changes in frame of proposed model of bone-implant integrity deterioration. It creates a starting point for determination of quantitative assessment of bone-implant integrity.

References

- [1] J. D. Keener, J. J. Callaghan (2003). Twenty-Five-Year Results After Charnley Total Arthroplasty In Patients Less Than Fifty Years Old, *Journal Of Bone And Joint Surgery*, **85**, A6, 1066-1072.
- [2] F. Katiamanis, D. D. Raftopoulos (1990). Determination of Mechanical Properties of Human Femoral Cortical Bone by Hopkinson Bar Stress Technique, *Journal of Biomechanics*, **23**, No 11, 1173-1184.
- [3] H.Yuehuei, A. Robert-Draughn (1996). *Mechanical Testing of Bone and Bone-Implant Interface*, CRC Press.
- [4] S. H. Park, J. B. Park, J. N. Weinstein, S. Loening (2004). Application of Extracorporeal Shock Wave Lithotripter in Orthopedics, *Journal of Applied Biomechanics*, **2**, Issue 2, 115-126.
- [5] K. Bathe (1996). *Finite Element Procedures*, Prentice Hall, New Jersey.
- [6] O.C. Zienkiewicz, R.L. Taylor (2000). *The Finite Element Method*, Vol. 1, 2, Butterworth, Oxford.

MODELING OF BONE – BIORESORBABLE GRAFT INTERACTION

T. Lekszycki

Institute of Fundamental Technological Research, Warsaw, Poland

1. Introduction

In recent orthopedic practice bioresorbable materials get more and more attention in bridging bony defects and filling bony losses. The application of such materials is associated with important advantages, among the others – it allows to avoid the usage of autogenic and allogenic implants associated with a risk of graft contamination and possibility of rejection as well as results in reduction of surgery invasiveness compared to cases of autogenic implants. Mathematical and computational models of effects present after graft implantation might be used in many situations, among the others – in surgery planning, in optimization of graft material characteristics, and in planning therapy after operation.

2. Modeling of tissue evolution in presence of resorbable material

Changes in bone after bioresorbable graft implantation are complex and not entirely known yet. Generally speaking there exist two major effects interacting with each other namely, tissue formation and remodeling and resorption of implanted graft. The interaction between them is of biological and mechanical nature. This is well known fact that bone adapts its micro structure and shape to variable in time mechanical loading what is known as functional adaptation. On the other hand the resorption of graft has sometimes significant influence in overall or local bone mechanical characteristics what evidently affects the activities of cells playing a fundamental role in the process of bone healing and adaptation after surgery. However graft resorption is not completely independent on its environment, it is also dependent of cells activity. Therefore these two effects can not be considered separately and models including both are needed.

3. Results

Mathematical description of simultaneous formation and remodeling of bone and resorption of bioresorbable graft was proposed. In this model three groups of bone cells are considered, one playing role of mechanical sensors, second responsible for tissue formation and the last for tissue resorption. These two simultaneous processes are affected by the third process - graft resorption which depends to some extent on cells activities. To derive necessary mathematical relations an approach proposed earlier by the author based on the hypothesis of optimal response of bone was used, see e.g. Lekszycki [1, 2]. They form nonlinear problem defined by a set of partial differential equations, integral inequalities, and algebraic inequalities and equations. It can be only solved numerically by incorporating finite element method to determine an actual state of system under examination with bone adaptation relations and graft resorption relations in one subroutine. This way the simulations of the process in bone after surgery are possible. Selected results of computer calculations will be presented to illustrate the application of proposed model in solution of practical

problems. Additional works are necessary and are being performed to compare effects of calculations with the clinical observations and results of experimental investigations.

6. References

- [1] T. Lekszycki (1999). Optimality conditions in modeling of bone adaptation phenomenon, *J. Theoret. Appl. Mech.*, **37**, 3, 148-167
- [2] T. Lekszycki (2002), Modelling of bone adaptation based on an optimal response hypothesis, *Meccanica*, **37**, 343 - 354

MULTIDIMENSIONAL LOTKA - VOLTERRA SYSTEMS
FOR CARCINOGENESIS MUTATIONS

Urszula Foryś

Faculty of Math. Inf. & Mech., University of Warsaw

Banacha 2, 02-097 Warsaw

urszula@mimuw.edu.pl

Abstract

In the paper $(n + 1)$ dimensional models describing carcinogenesis mutations are studied. The models are formulated on the basis of the Lotka–Volterra systems (food–chains and competition systems) with linear diffusion. We study the properties of the systems without diffusion (ODE systems), and with the Neumann boundary conditions as well as the Dirichlet ones. It occurs that the behaviour of solutions to the systems without diffusion and with the Neumann boundary conditions is similar, i.e. does not depend on diffusion coefficients, but strongly depends on the type of model. On the other hand, in the case of the Dirichlet boundary conditions this behaviour is related to the magnitude of diffusion coefficients. For sufficiently large diffusion coefficients it is similar for every model, i.e. the trivial solution which is unstable for zero diffusion gains stability.

1. The models

Depending on the environmental conditions we study the following systems of equations (compare [1] for detailed explanation):

$$\left\{ \begin{array}{l} \frac{\partial y_0}{\partial t} = d_0 \Delta y_0 + a_0 y_0 (1 - y_0) - \mu_1 y_0 y_1 \\ \frac{\partial y_i}{\partial t} = d_i \Delta y_i + a_i y_i (1 - y_i) + \eta_i y_i y_{i-1} - \mu_{i+1} y_i y_{i+1}, \quad i = 1, \dots, n-1, \\ \frac{\partial y_n}{\partial t} = d_n \Delta y_n + y_n + \eta_n y_n y_{n-1} \end{array} \right. , \quad (1)$$

$$\left\{ \begin{array}{l} \frac{\partial y_0}{\partial t} = d_0 \Delta y_0 + a_0 y_0 (1 - y_0) - \mu_1 y_0 y_1 \\ \frac{\partial y_i}{\partial t} = d_i \Delta y_i + a_i y_i (1 - y_i) + \eta_i y_i y_{i-1} - \mu_{i+1} y_i y_{i+1}, \quad i = 1, \dots, n-1, \\ \frac{\partial y_n}{\partial t} = d_n \Delta y_n + y_n - \eta_n y_n y_{n-1} \end{array} \right. , \quad (2)$$

$$\left\{ \begin{array}{l} \frac{\partial y_0}{\partial t} = d_0 \Delta y_0 + a_0 y_0 (1 - y_0) - \mu_1 y_0 y_1 \\ \frac{\partial y_i}{\partial t} = d_i \Delta y_i + a_i y_i (1 - y_i) + \eta_i y_i y_{i-1} - \mu_{i+1} y_i y_{i+1}, \quad i = 1, \dots, n-1, \\ \frac{\partial y_n}{\partial t} = d_n \Delta y_n - y_n + \eta_n y_n y_{n-1} \end{array} \right. , \quad (3)$$

with non-negative coefficients and non-negative initial functions $y_i(0, \omega) \geq 0$, y_i sufficiently smooth and $\omega \in \Omega \subset \mathbb{R}$, Ω is the open interval in \mathbb{R} (for simplicity), or Ω is open, convex, with smooth boundary $\text{bd } \Omega$ in three-variable space \mathbb{R}^3 . We study these systems with the homogenous Neumann (zero-flux) or Dirichlet (zero) boundary conditions.

2. Results

We start our analysis with the case without diffusion. In this case, in favourable conditions, that is for Eqs. (1), there is always unrestricted tumour growth and without any treatment the patient cannot survive. In the competitive conditions the dynamics can be similar to those obtained from Eqs. (1) but can be also different from it. If for every $t \geq 0$ there is $y_{n-1} < \frac{1}{\eta_n}$, that is the number of pre-malignant cells always stays at the level smaller than the threshold value $\frac{1}{\eta_n}$, then we observe unrestricted tumour growth. On the other hand, if y_{n-1} is bounded above this threshold, then the solution is attracted by the critical point \bar{y}^n with $y_n = 0$. In this system depending on the model parameters, we can also expect bi-stable behaviour, as in the typical competitive Lotka–Volterra system, compare e.g. [3]. The most stable behaviour we get for unfavourable conditions, described by Eqs. (3). For this model if the positive critical point \bar{y} exists, then it is globally attractive. If not, then we expect that one of the semi-trivial critical points is attractive, compare also the analysis for $n = 2$ in [2].

We also considered the influence of spatial arrangement due to diffusivity of cells. It occurs that for the case with diffusion the behaviour of the systems strongly depends on the boundary conditions. In the case of the Dirichlet boundary conditions the qualitative behaviour of solutions to every studied system for sufficiently large diffusion is the same — every solution tends to the trivial one for t tending to ∞ . On the other hand, the solution to the systems with the Neumann boundary conditions strongly depends on the system. In the author's opinion this suggests that either diffusion coefficients cannot be large or the Neumann boundary conditions better reflect the real process. In fact, even in the case of malignant cells occurrence we do not expect extinction of all cellular populations.

It should be marked that in every considered case there is no possibility to recovery, because the semi-trivial critical point which describes a healthy organism is always unstable. Therefore, we should try to target tumour cells parallelly increasing the competition coefficient η_n .

Acknowledgements. This paper was supported by the Polish Ministry of Science, grant No 1 P03A 028 30.

Bibliography

- [1] Ahangar R., Lin X.B., Multistage evolutionary model for carcinogenesis mutations, *Electron. J. Differ. Equ. Conf.* **10** (2003), 33-53.
- [2] Foryś U., Stability analysis and comparison of the models for carcinogenesis mutations in the case of two stages of mutations, *J. Appl. Analysis* **11** (2), (2005), 281-200.
- [3] Murray J.D., *Mathematical biology. 1, An introduction*, Springer-Verlag, New York, 2002.

ON SOME PROPERTIES OF BONE FUNCTIONAL ADAPTATION PHENOMENON USEFUL IN MECHANICAL DESIGN

M. Nowak

*Poznan University of Technology, Division of Machine Design Methods, Poznan, Poland
ul. Piotrowo 3, 60-965 Poznan, Poland, E-mail: Michal.Nowak@put.poznan.pl*

1. Introduction

Contemporary design methods include optimization procedures on each of design stage. In case of structural design the optimization assists the engineers from the earliest design idea up to the end of the design process. In case of the living entities all kind of the optimization must be simultaneous. The example of such simultaneous adaptation is the phenomenon of the trabecular bone remodeling process.

2. Trabecular bone remodeling process

There are many models of bone remodeling. In the Huiskes' 'regulatory model' [1] conception based on clinical observation of trabecular bone tissue behavior, the main assumption of this model is existence of homeostasis (perfect balance between bone gain and loss). This equilibrium can occur only in presence of mechanical stimulation. The network of osteocytes plays the role of sensors of the mechanical energy distribution along the trabecular bone tissue. The model used here postulates strain energy density (SED) on the surface of trabecular bone, as a scalar measure of mechanical stimulation and distinguished value of SED, corresponding to bone remodeling homeostasis.

3. The Principle of the Constant Strain Energy Density

The notable assumption of the presented model is existence of the homeostasis of the remodeling process described by the distinguished value of SED. It is interesting, that SED, as a energy measure, is also emphasized in optimization research, distant from biomechanical applications. In Pedersen's [2] considerations the optimal shape of the structure, minimizing the strain energy is thought.

The derivative of the total potential Π with respect to an arbitrary parameter h is:

$$(1) \quad \frac{d\Pi}{dh} = \frac{\partial U_\varepsilon}{\partial h}$$

For a local design parameter h_e that only changes the design in the domain e of the structure:

$$(2) \quad \frac{\partial U_\varepsilon}{\partial h_e} = \frac{\partial(\bar{u}_e V_e)}{\partial h_e}$$

where \bar{u}_e is the mean strain energy density in the domain of, and V_e is the corresponding volume.

Assuming two parameters h_i, h_j , the total volume V of the structure is:

$$(3) \quad \Delta V = \frac{dV}{dh_i} \Delta h_i + \frac{dV}{dh_j} \Delta h_j = 0$$

then the increment of the elastic energy:

$$(4) \quad \Delta U_\varepsilon = \frac{dU_\varepsilon}{dh_i} \Delta h_i + \frac{dU_\varepsilon}{dh_j} \Delta h_j$$

for design independent loads, and when only the local energies are involved:

$$(5) \quad \begin{aligned} \Delta U_\varepsilon &= \bar{u}_i \frac{dV_i}{dh_i} \Delta h_i + \bar{u}_j \frac{dV_j}{dh_j} \Delta h_j \\ \Delta U_\varepsilon &= -(\bar{u}_i - \bar{u}_j) \frac{dV_i}{dh_i} \Delta h_i \end{aligned}$$

and with the constant volume assumption the a necessary condition for optimality $\Delta U = 0$ with constraint $\Delta V = 0$ leads to the conclusion, that the strain energy densities must be equal. Similar, with all design parameters, the total energy change equation leads to the conclusion, that a necessary condition for optimality is constant value of the strain energy density. Thus for the stiffest design the energy density along the shape to be designed must be constant:

$$(6) \quad u_s = \text{const.}$$

4. Conclusions

From our resent research in the area of numerical simulation of bone remodeling phenomenon and studies on structural optimization, the astonishing conclusions can be formulated. The bone remodeling phenomenon is a biological realization of the optimal structure principle, requiring equal value of surface energy distribution. On the other hand, the optimization scenario based on the osteoclasts, osteoblasts activity and osteocytes mechanosensitivity assumption leads to the optimization results identical to these obtained by traditional optimization methods based on the minimal potential assumption [3].

6. References

- [1] Huiskes R. et al. (2000). Effects of mechanical forces on maintenance and adaptation of form in trabecular bone, *Nature* **404**, pp. 704-706.
- [2] Pedersen P., (2003). Optimal Design - Structures and Materials - Problems and Tools Book ISBN 87-90416-06-6.
- [3] Nowak. M, (2006). Structural optimization system based on trabecular bone surface adaptation, *Journal of Structural and Multidisciplinary Optimization*, Springer Berlin/Heidelberg, Volume **32**, Number 3, pp. 241-249.

ANALYSIS OF INFLUENCE OF HUMAN HEAD MOVEMENT ON CERVICAL SPINE LOADING CONDITIONS

M. Gzik, D. Tejszerska

Department of Applied Mechanics, Silesian University of Technology, Gliwice, Poland

1. Introduction

Anatomy and physiology of neck spine is quite well known but knowledge about biomechanical aspects as soft tissue mechanical influence on skeletal system is not satisfied. Especially correlation between spine movement, internal forces and muscles roles demands precise interdisciplinary researches, engaged medical and technical scientists. Activity of neck muscles is very important for head and cervical vertebrae movement during physiological and accidents situations. Many science institutions focus researches on neck muscles influence on head behaviour during situations corresponding to road accidents less attention concentrate on physiological aspects. Improvement of knowledge about correlation between dynamics, human body behaviour and internal cervical phenomena could contribute to the defence against spine failures. The best information about above mentioned correlation could be obtained during test on volunteers but experimenting on people is usually impossible because of its dangerous character moreover nowadays not exist suitable technique. Another way to study the behaviour of the human body and internal interactions during different situations is the mathematical modelling. This is proposal a non-invasive method [1,2].

The general aim of the presented researches is creation dynamical 3-dimensional model suitable for analysis of correlations between head movement and internal dynamical forces.

2. Modelling research

Modelling process was preceded by studies on anatomy of human cervical spine, properties of particular elements and kinds of living organisms modelling. 3-dimensional dynamical model of human cervical spine as author program was created on the basis of multibody methodology. Model consists of (figure 1a):

- head, seven cervical vertebrae are treated as 6 degrees of freedom rigid elements and immovable trunk, movement of the elements is depended on muscles, intervertebral discs, facet joints and ligaments activity,
- muscles are divided in two main groups: first deep muscles treated as non-linear spring damper elements and second group main muscles responsible for head and vertebrae movement. Muscles of second group are represented by forces calculating on the basis of optimization methods, coefficients was determined on the basis of experimental MRI and EMG methods,
- intervertebral disc is divided into isolated segments, representing anulus fibrosus as nonlinear spring element acting during extension and compression and nucleus pulposus as nonlinear spring - damper element acting only during compression,
- facet joints is treated as nonlinear spring – damper element taking into consideration relative motion possibility of connected vertebrae, additional resisting moment appears when physiological relative motion between neighbour vertebrae is exceeded,
- ligaments are divided in parallel strips acting as forces only during elongation,

The model was verified on the basis of experimental researches as comparison of vertebrae relative motion and action of muscles (figure 1b).. Necessary information about material parameters were obtained from tests on specimens of cadaver spines (figure 1c).

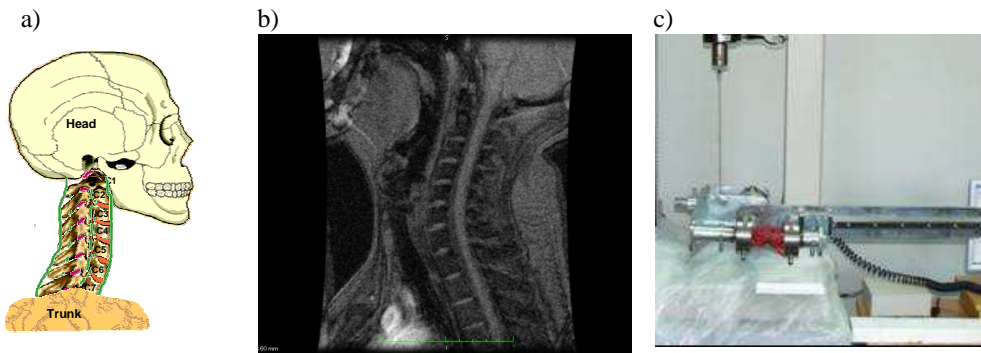


Figure 1 a) Model of human cervical spine.

Experimental research: b) MRI scans of cervical spine during movement in middle sagittal plane, c) test on spacers of cadaver spine with use of special device

3. Results

Two variants of spine loading were analysed: during physiological head flexion movement and during situation corresponding to car head-on collision (8kmph velocity of accident). Figure 2 presents maximal forces insight examples anatomical parts for two variants.

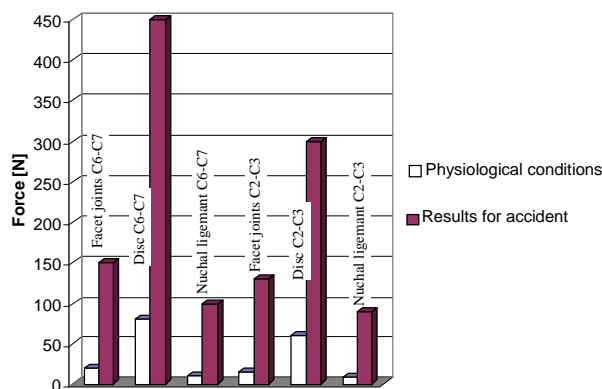


Figure 2 Comparison of maximal forces insight anatomical parts for physiological activity and accident situation

4. Conclusions

Neck muscles it is very complicated system. Analysis of biomechanical aspects of relations between movement, internal reactions and muscles forces demands to carry out common experimental and modelling researches. Presented model allows to carry out numerical simulation of dynamical forces inside anatomical parts of human cervical spine. Neck loading analysis in case of two variants physiological activity and car collision revealed increase of internal forces about five times.

5. References

- [1] R. Będziński (1997). *Biomechanika inżynierska. Zagadnienia wybrane*, Oficyna Wydawnicza Politechniki Wrocławskiej, Wrocław.
- [2] M. Gzik (2007). *Biomechanika kręgosłupa człowieka*, Wydawnictwo Politechniki Śląskiej, Gliwice.

EVALUATION METHOD FOR ORTHOTROPIC PROPERTIES OF THE BONE TISSUE “IN SITU”

A. Dąbrowska-Tkaczyk

*Institute of Mechanics and Design, Faculty of Production Engineering, Warsaw University of
Technology, Warsaw, Poland*

1. Introduction

A method for bone material properties evaluation of bone tissues „in situ” based on a CT images is presented. Calculations were made on the assumption that bone tissue was the orthotropic material. Calculation results obtained for chosen points of the femur section (trochanter minor) have been shown, as well.

2. Method

Computer tomography (CT) data on the patient, having the form of images of sections, were stored in the digital form DICOM (Digital Imaging and Communications in Medicine). They were then analyzed by means of the specialist software Mimics 9,0 to determine the distribution of radiological density C_T in terms the Hounsfield units [HU]. Those data make it possible to calculate other parameters of bone tissues, i.e. apparent density, Young modulus, shear modulus and Poisson’s ratio, for evaluation the values of compliance matrix $[b_{ij}]$ elements. The consecutive steps of bone material property calculations are presented in Fig. 1.

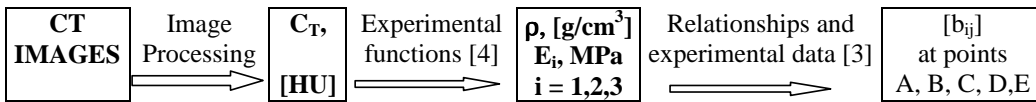


Figure 1. Method for evaluation of orthotropic properties of the bone tissue material “in situ.”

3. Measurements and calculations

Using the Mimics technique „profile lines” one obtains the curves representing the changes in radiological density C_T , [HU] (Fig 2b), along the lines marked in the picture of section (Fig.2a). The C_T values read off at characteristic points A, B, C, D, E, are shown in Table.1.

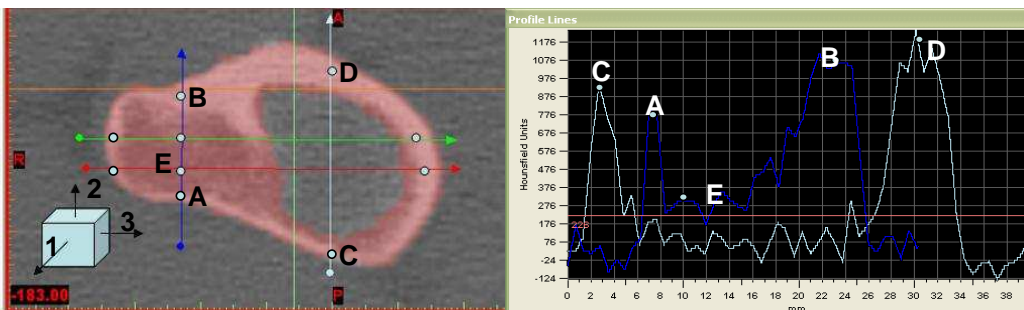


Figure 2. “Profile lines” technique for evaluation of radiological density at points A, B, C, D, E of the section through trochanter minor of the femur.

Basing on the C_T data, the values of apparent density were calculated. For the proximal femur the

relationship $\rho = f(\text{HU})$ represented by equation (1) [5] was employed.

$$\rho = 1,67 \cdot \text{HU} + 131 \quad [\text{kg/m}^3] \quad (1)$$

On the assumption that points A, B, C, D are situated within the area of cortical bone and after accepting suitable coordinate system the values of Young modulus: E_1, E_2, E_3 were calculated using equations (2), [5]. While since point E is situated within the spongy bone area equation (3) [5] should be applied.

$$E_1 = 0.014 \cdot \rho - 6.142, \quad E_2 = 0.009 \cdot \rho - 4.007, \quad E_3 = 0.010 \cdot \rho - 6.087, \quad [\text{GPa}], \rho[\text{g/cm}^3] \quad (2)$$

$$E_1 = 0,58 \cdot \rho^{1,30}, \quad E_2 = 0,01 \cdot \rho^{1,86}, \quad E_3 = 0,004 \cdot \rho^{2,01}, \quad [\text{MPa}], \rho[\text{kg/m}^3] \quad (3)$$

Other parameters characterizing material properties of the bone tissue; i.e., Poisson's ratio and values of the shear modulus G_{ij} can be calculated using formula (4), [1,4].

$$v_{ji} = v_{ij} \cdot \frac{E_j}{E_i}, \quad G_{ij} = \frac{E_i}{2(1 + v_{ij})} \quad i, j = 1, 2, 3; \quad i \neq j \quad (4)$$

The values of parameters: $v_{12} = 0,307, v_{23} = 0,622, v_{31} = 0,119$, for the cortical bone [4] and $v_{12}=v_{23}=v_{31}=v=0,2$ [2] for the spongy bone respectively, were taken from the literature for calculations the compliance matrix $[b_{ij}]$ elements. The calculations results for points A, B, C, D, E are presented in Table1.

	C_T , HU	ρ , g/cm ³	E_1 MPa	E_2 MPa	E_3 MPa	v_{21}	v_{32}	v_{13}	G_{12} MPa	G_{23} MPa	G_{31} MPa
A	776	0,959	7284	4624	3503	0,195	0,471	0,247	2786	1425	1565
B	1076	1,279	11765	7505	6704	0,196	0,556	0,209	4501	2313	2996
C	920	1,113	9435	6007	5039	0,195	0,522	0,223	3609	1852	2252
D	1170	1,386	13259	8465	7771	0,196	0,571	0,203	5072	2609	3472
E	326	0,479	1769	966	976	0,109	0,202	0,366	737	402	406

Table 1. Values of bone materials constants at points of the section through the trochanter minor

3. Conclusions

The introduced method makes it possible to calculate the parameters of orthotropic model of bone tissues in the organism ("in situ") on the basis of CT data. The results obtained for the plane sections can be transformed in to a 3D model [3] of the proximal femur .

6. References

- [1] R. Bak, T Burczyński , 2001, *Wytrzymałość materiałów z elementami ujęcia komputerowego*, WNT, Warszawa
- [2] Carter D., R, Beaupre G.,S. 2001, *Skeletal functions and form. Mechanobiology of skeletal development, Aging and Regeneration*. Cambridge University Press,
- [3] Dąbrowska-Tkaczyk A., Borkowski P. (2007) *Badanie rozkładów gęstości pozornej oraz rozkładów modułu Younga w modelach kości stawu biodrowego odtworzonych na podstawie obrazów CT*. W: J. Kubik, W. Kurnik, W.K. Nowacki (Red.), *Materiały I Kongresu Mechaniki Polskiej*, 8 str.
- [4] I.W. Knets, G.O. Pfafröd, J.Ž. Saylgozic, (1980) *Deformirowanije i razruszenije twierdych biologiczeskij tkaniej*. Zinatne, Riga
- [5] Rho, J.Y., Hobatho, M.C., and Ashman, R.B. (1995) "Relations of Mechanical Properties to Density and CT Numbers in Human Bone" *Medical Engineering and Physics*, Vol. 17, No. 5 347-355

RAYLEIGH SCATTERING OF ULTRASOUNDS IN CANCELLOUS BONE

B. Gambin , A. Galka

Institute of Fundamental Technological Research, Warsaw, Poland

1. Abstract

The paper is devoted to long wave propagation in composite material which is used as a model of cancellous bone. First, homogenized (macroscopic) properties of composite are calculated taking into account the multilevel structure of cortical bone. Next, the macroscopic properties of cancellous bone are calculated treated as two-phase composite built by trabeculae and marrow. Then, we deal with higher order terms in asymptotic expansion method of homogenization theory to take into account effects due to finite characteristic dimension of heterogeneities. Hence the scattering of waves which are long as compared to the dimension is determined.

2. Effective elastic properties of cancellous bone material

The mathematical homogenization of periodic media as well as stochastic media is based on assumption that an inhomogeneous medium behaves as a homogeneous one provided that macroscopic size, L , is infinitely large as compared to size l of its heterogeneities. The macroscopic behavior is described by effective (macroscopic) properties of a “homogenized” material, which are obtained in the case when the small dimensionless parameter $\varepsilon = l/L$ tends to zero.

The first step is to find the effective macroscopic elastic moduli of compact (cortical) bone by using reiterated homogenization method elaborated in [1]. Biological material like compact bone is characterized by several structural levels, cf. [2-4]. In this case three structural levels are of primary importance. At the lowest level, the lamellar structure is considered: collagen fibers are embedded in hydroxyapatite crystals. In a single lamella, all the collagen fibers have the same orientation but the orientation of these fibers can differ between two adjacent lamellae. The second level corresponds to a single osteon and of a part of the interstitial system, an osteon being a set of concentric lamellae, which surround the Haversian canal, cf. Fig. 1.

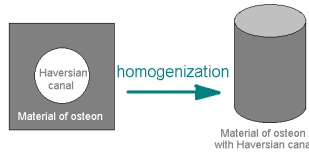


Fig. 1 . The method of calculation of effective material constants of osteon with Haversian canal.

At the highest level, compact bone is examined. The compact bone consists of large number of osteons embedded in the interstitial system. The osteons are packed tightly together, mutually parallel and oriented in the direction of the long axis of the bone, cf. Fig. 2.

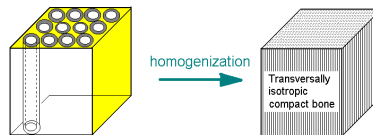


Fig. 2. Third step of calculations.

Consequently, three successive steps allow us to derive the final form of the *macroscopic elastic moduli of compact bone*. These moduli of compact bone are taken for moduli of trabecular component of cancellous bone. At the end the *effective properties of cancellous bone* are obtained as a result of homogenization applied to the two phase structure of the bone composed of fluid (marrow) and solid (compact bone) components.

3. Acoustic waves in cancellous bone

This study deals with long wave phenomena i.e. we assume that the wavelengths are large as compared with the characteristic size of pore dimension in trabecular structure of bone, but not infinitely large. This situation corresponds to wavelengths which are about 10-100 times greater than heterogeneities, i.e. $100 < \varepsilon < 10$. It is typical for ultrasounds excitations used in extended bone diagnostic techniques, cf. [5]. Thus, classical homogenization method must be enlarged to take into account higher order effects due to the size of inhomogeneities. It is done by using the formal asymptotic expansion method and preserving the terms proportional to successive powers of small parameter ε . Numerical results show, particularly, explicit dependence of velocities and polarizations on geometrical characteristics of trabecular structure, i.e. direction of anisotropy and volume fraction of marrow, cf. Fig. 3.

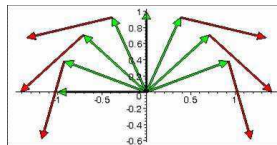


Fig. 3. Polarization vectors – red, wave vectors – green of the wave propagating in the direction along the length of the bone.

3. Results

All scattering effects are analyzed and polarization, dispersion and attenuation coefficients are visibly related to microstructure information about trabecula and marrow distributions. An example of layered structure being of great practical importance for ultrasounds diagnostic is studied in detail.

Acknowledgements

This work was supported by the grant - KBN No 4 T07A 003 27.

4. References

- [1] Allaire G., Briane H., 1996, Multiscale convergence and reiterated homogenization, Proc. R. Soc. Edinburgh, vol. 126A, 297-342.
- [2] Aoubiza B., Crolet J. M., Meunier, 1996, On the mechanical characterization of compact bone structure using the homogenization theory, J. Biomechanics, vol. 29, 1539-1547.
- [3] Cowin S. C., (ed.), 2001, Bone mechanics handbook, CRC Press, Boca Raton.
- [4] Crolet J. M., Aoubiza B., Meunier A., 1993, Compact bone: numerical simulation of mechanical characteristics, J. Biomechanics, vol. 26, 677-687.
- [5] Litniewski J, Nowicki A, Sawicki A., 2000, Detection of bone disease with ultrasound - comparison with bone densitometry, Ultrasonics 38 (1-8), 693-697.

FABRIC TENSOR AND STRENGTH SURFACE OF BONE-LIKE MATERIALS

B. Gambin, A. Galka

Institute of Fundamental Technological Research, Warsaw, Poland

1. Abstract

The porous microstructure plays an important role in the damage resistance of bones, [1], [3]. The aim of the paper is to establish the strength criterion for the bone-like porous material, which takes into account the porous geometry explicitly, Fig.1. Firstly, we define a new fabric tensor based on the mathematical homogenization theory to separate geometrical effects from mechanical ones. Next, we construct the strength surface using the introduced fabric tensor.

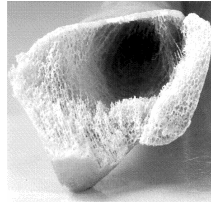


Fig.1. Anisotropic porous structure of a bone.

2. Fabric tensor based on the mathematical homogenization theory

The mathematical homogenization of periodic as well as stochastic media is based on the assumption that an inhomogeneous medium behaves as a homogeneous one, provided that macroscopic size L , is infinitely large as compared to the size l of its heterogeneities. The macroscopic behavior is described by effective (macroscopic) properties of a “homogenized” material, which are obtained in the case, when the small dimensionless parameter $\varepsilon = l/L$ tends to zero.

Let us assume that the local elastic properties described by the fourth order tensor, depend on the position \mathbf{x} belonging to the space occupied by a material body. The material body is composed of two-phase inhomogeneous material in the following way: $\mathbf{C}(\mathbf{x}/\varepsilon) = \mathbf{C}^{(2)} + (\mathbf{C}^{(1)} - \mathbf{C}^{(2)})\chi(\mathbf{x}/\varepsilon)$. Here $\mathbf{C}^{(1)}$, $\mathbf{C}^{(2)}$ are elastic properties of components, and $\chi(\mathbf{y})$ denotes a characteristic function of the set occupied by the component denoted by the index (1). Effective properties of the composite are given by:

$$\mathbf{C}^{eff} = \mathbf{C}^{(2)} + (\mathbf{C}^{(1)} - \mathbf{C}^{(2)}) \left\langle \chi \left(\mathbf{I}^{(4)} + \Gamma * (\mathbf{C}^{(1)} - \mathbf{C}^{(2)}) \chi \right)^{-1} \right\rangle,$$

where the components of 4th rank tensor $\Gamma_{ijkl}(y, y') = \partial_{(i}^y \partial_{j)}^y G_{(kl)}(y, y')$ compose the kernel of a integral operator. The operator can be defined by the Green function of the periodic boundary problem of elasticity for homogeneous material (2) if in a periodic structure of the composite was assumed. The brackets denote averaging over statistical ansamble or over the periodic cell. If $\mathbf{C}^{(1)} \rightarrow 0$, then the effective elastic properties of porous material with the skeleton described by $\mathbf{C}^{(2)}$ are given by the formula $\mathbf{C}^{eff} = \sqrt{\mathbf{C}^{(2)}} : \mathbf{T} : \sqrt{\mathbf{C}^{(2)}}$, where $\mathbf{T} = \mathbf{I}^{(4)} - \left\langle \chi \left(\mathbf{I}^{(4)} - \mathbf{A} * \chi \right)^{-1} \right\rangle$,

$\mathbf{A} = \sqrt{\mathbf{C}} : \mathbf{\Gamma} : \sqrt{\mathbf{C}}$. $\mathbf{I}^{(4)}$ - denotes unity in the space of the symmetric 4th rank tensors and two dots denote double contraction of the tensors. The tensor \mathbf{T} is called the *fabric tensor* and it can be rewritten in the following form: $\mathbf{T} = \mathbf{I}^{(4)} - \int_0^1 \frac{d\boldsymbol{\mu}(x)}{1-x}$. The measure $d\boldsymbol{\mu}(x)$, namely their moments, describe geometry of the porous structure. In what follows, the index (2) is omitted. Let us define two tensors, $\mathbf{T}_L = \sqrt{\mathbf{C}} : \mathbf{T} : (\sqrt{\mathbf{C}})^{-1}$ and $\mathbf{T}_R = (\sqrt{\mathbf{C}})^{-1} : \mathbf{T} : \sqrt{\mathbf{C}}$, which are called the left and right damage tensors, respectively. The names are justified by the relations $\boldsymbol{\sigma}^{eff} = \mathbf{T}_L : \boldsymbol{\sigma}$ and $\boldsymbol{\varepsilon}^{eff} = (\mathbf{T}_R)^{-1} : \boldsymbol{\varepsilon}$, where the first one is a stress relation between damaged (material with pores) and virgin material. It is assumed that strains are the same in damaged and virgin material and the second one is a strain relation between damaged and virgin material. Moreover, it is assumed that stresses are the same in both materials. The following relations also holds: $\mathbf{C}^{eff} = \mathbf{T}_L : \mathbf{C}$ and $\mathbf{T}_R = \mathbf{C}^{-1} : \mathbf{C}^{eff}$.

3. Strength surface

A homogenized failure criterion for an arbitrary two-phase elastic composite is formulated in [2]. The criterion incorporates an elegant first approximation to the microscopic stress fluctuation due to the interaction between the homogenized stress and the microstructure. To formulate homogenized criteria for trabecular bone, we assume that such criterion is known for the skeleton material i.e. compact bone, which is a component of composite. The criterion has the form of inequality for microstresses in the skeleton material: $\boldsymbol{\sigma}^{mikro} : \mathbf{\Pi} : \boldsymbol{\sigma}^{mikro} \leq 1$, where $\mathbf{\Pi}$ is given as 4th rank positively definite tensor. Now, the strength criterion of the trabecular bone, expressed by the 4th rank positively definite tensor, is given by the formulae

$$\mathbf{\Pi}^{eff} = (\mathbf{C}^{eff})^{-1} : \mathbf{C} : \mathbf{\Pi} : \mathbf{C} : [\nabla_c \mathbf{C}^{eff}] : (\mathbf{C}^{eff})^{-1},$$

where $[\nabla_c \mathbf{C}^{eff}]$ denotes so-called *phase gradient* of the effective tensor with respect to properties of compact bone material. It is the 8th rank tensor. The tensors \mathbf{C}^{eff} , $(\mathbf{C}^{eff})^{-1}$ denote stiffness and compliance effective tensors of the trabecular bone, respectively. The phase gradient is obtained from the solutions of a so-called local problem. In the case of periodic structure it is called “problem on the periodic cell”. The criterion is applied to macroscopic stresses in the trabecular bone. The strength criterion is given by the inequality $\boldsymbol{\sigma}^{makro} : \mathbf{\Pi}^{eff} : \boldsymbol{\sigma}^{makro} \leq 1$, where the equality defines the strength surface. Using the dependence on fabric tensor of effective elastic tensor introduced above, the influence of geometry on the strength criterion is analyzed with various assumptions concerning microstructure of bones.

Acknowledgements: The work was supported by the grant KBN No 4 T07A 003 27.

References

1. S. C. Cowin, Anisotropic poroelasticity: fabric tensor formulation, *Mechanics of Materials* 36 (2004), 665-677.
2. R. Lipton in: *Nonlinear Homogenization and Its Applications to Composites, Polycrystals and Smart Materials*, Eds: Ponte Castaneda P., Telega J.J., Gambin B., Kluwer Academic Publishers, Dordrecht, Boston, London, 2004, 169-192.
4. P. K. Zysset, A review of morphology-elasticity relationships in human trabecular bone: theories and experiments, *J. of Biomechanics* 36 (2003), 1469-1485.

ANALYSIS OF A PRELOADED CONICAL THREADED PIPE CONNECTION

J. Van Wittenberghe, P. De Baets and W. De Waele
Laboratory Soete, Ghent University, Belgium

1. Introduction

In the oil and gas industry, steel threaded pipe connections are commonly used e.g. as couplings between drill pipes, risers and pipelines. Due to environmental influences, like waves and vortex induced vibrations in offshore applications, these tubular structures are subjected to both static and dynamic loading conditions. To maintain a secure connection, the couplings are installed with a preload to avoid them coming apart. To introduce the preload on the connection, conical threaded connections or rotary shouldered connections are used. These connections are installed by applying the so-called make-up torque.

Due to the combination of the preload and external loading the stress distribution in the connection is complex. Additionally, the stress distribution depends on the coupling's geometry (pipe dimensions and thread type) and material properties (coefficient of friction between the threads). The resulting stress concentrations can initiate fatigue cracks and cause a premature failure of the connection. The influence of the different geometrical and material parameters on the connector's applicability and service life are not well known. However, improved pipe connections are necessary to meet new industrial needs.

This study aims to get a better understanding on the influence of the different parameters on the connection's performance through finite element analyses of different connection types. In this paper the analysis of an API line pipe connection is presented.

2. Modeling of threaded pipe connections

The stress distribution in the connection is calculated by finite element analysis (FEA). A widely used method to model threaded pipe connections is by the use of 2D axisymmetric models [1], [2]. This approach does not take into account the thread helix nor the exact run-out region. However it is known from [3] and [4] that 2D axisymmetric models give accurate results compared to full 3D models. Moreover, axisymmetric models are less time-consuming and hence finer element meshes can be calculated.

FEA were carried out using the software package ABAQUSTM. An elastic-plastic material model of AISI 4340 HSLA steel is used. This material has a yield strength of 800 MPa.

To model the preload an initial overlap is given to the male and female part of the connection (pin and box), corresponding to the specified number of make-up turns according to the API standard [5]. This overlap is shown in figure 1 together with a detail of the model's mesh.

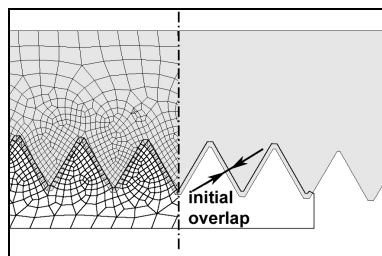


Figure 1: Detail of model mesh and initial overlap to model the make-up torque.

During the first step of the analyses, the overlapping surfaces of pin and box are brought into contact. This results in the von Mises stress distribution as shown in figure 2 a). The stress at the tip of the pin is a hoop stress of about 450 MPa.

An additional external axial load is applied on the connection giving the stress distribution of figure 2 b). As can be expected from [1], the highest stress concentration is located at the root of the last engaged thread of the pin. This stress concentration is mainly caused by axial stress, while the stress state at the tip of the pin is caused by hoop stresses from make-up and opening between the threads of the pin and box.

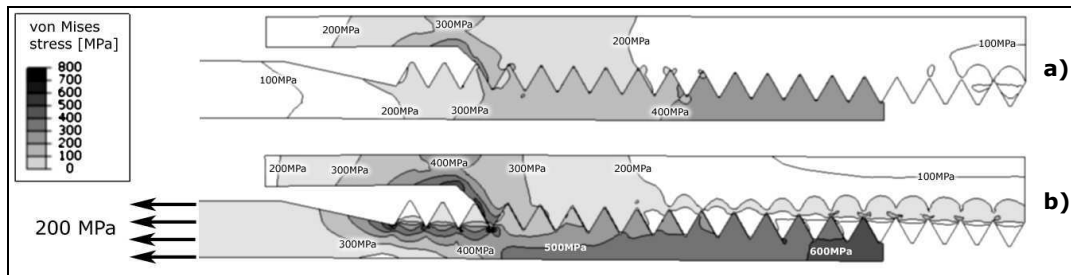


Figure 2. Stress distribution resulting from a) make-up, b) make-up + 200 MPa axial load.

When the wall thickness of the box is increased, the box becomes more rigid. This increases the hoop stresses in the pin. If on the other hand, the wall thickness of the pin is increased, the acting hoop stress on the pin will decrease while the hoop stress in the box will increase.

It can be seen in figure 2 b) that the box has an unthreaded extension at the left side. Due to a combination of hoop stress and bending of the extension, an additional stress concentration is introduced where it is connected to the threaded section of the box. When this extension is left out however, the opening between the threads under load increases together with the hoop stress in the pin, reducing the connection's strength.

It was observed that the opening between pin and box threads is significantly influenced by the coefficient of friction between the threads. Since a larger opening will decrease the static pull-out strength of the connection, it is important to have accurate data of the coefficient of friction. However, this data is generally not present and can only be determined experimentally.

4. Conclusions

A finite element analysis of a preloaded conical threaded connection is presented. Results are consistent with data known from literature. The strength of the connection depends on both geometrical and material properties. The coefficient of friction between the threads should be determined experimentally to predict the connection's behavior accurately.

6. References

- [1] E.N. Dvorkin and R.G. Toscano (2003). *Finite element models in the steel industry, Part II: Analyses of tubular products performance*, Computers and Structures, **81**, 575–594.
- [2] L. Bertini, M. Beghini, C. Santus and A. Baryshnikov (2006). *Fatigue on drill string conical threaded connections, test results and simulations*, 9th Int. Fatigue Congress, Atlanta, USA.
- [3] J.J. Chen, Y.S. Shih (1999), *A study of the helical effect on the thread connection by three dimensional finite element analysis*, Nuclear Engineering and Design, **191**, 109–116.
- [4] A. Zhong (2007), *Thread Connection Response to Critical Pressures*, ABAQUS Users' Conference, Paris, France, 690-706.

FAST MULTIPOLE EVALUATION OF DOMAIN TERMS IN INTEGRAL EQUATIONS OF TWO-DIMENSIONAL ELASTICITY

J. Ptaszny and P. Fedelinski

*Department for Strength of Materials and Computational Mechanics
Silesian University of Technology, Gliwice, Poland*

1. Introduction

Application of the fast multipole method (FMM [1]) reduces the complexity of the boundary element method (BEM) analysis. Reference [2] gives a review on applications of the fast multipole boundary element method (FMBEM) and directions of further research, which should be carried out. Among others, a fast evaluation of domain integrals is mentioned. Reference [3] gives a comparison of efficiency and accuracy of different methods applied to evaluation of such integrals, for both Poisson and Helmholtz equations. Four methods were considered, namely: particular solution, dual reciprocity, direct integration and multipole method [4]. It is shown, that the domain integration methods are more efficient and provide better accuracy than the other ones, in spite of necessity of discretization of the domain. In Reference [5] analysis of gradient materials by the BEM, using the classical fundamental solutions of two-dimensional elasticity, is presented. The method requires evaluation of domain integrals. Results of the analysis are compared to the ones obtained using isoparametric finite element method (FEM). It is shown, that the BEM is more accurate than the FEM in the cases of stress concentration and distorted internal cells (finite elements). In Reference [6] a FMBEM application to analysis of elasto-plastic plates is presented. Linear or quadratic boundary elements and constant triangle internal cells are used. In the present work, a FMBEM analysis of elastic plates loaded by volume forces is presented. Here, quadratic boundary elements and quadratic triangle internal cells are used.

2. Fast multipole boundary element method

The linear elasticity problem can be described using an integral equation. In this equation, boundary and volume integrals occur, which are dependent on the fundamental solutions of Navier-Lamé operator [7]. Boundary integrals depend also on boundary displacements and traction forces, and the volume integral depends on a known field of body forces. The boundary of analysed structure is discretized, and for each boundary node as the collocation point the integrals are evaluated. In order to calculate the volume integrals, the domain of analysed body is discretized, using internal cells. Thus, a linear system of algebraic equations is obtained. The conventional algorithm has complexity $O(N \times (M + N))$, where N is the number of boundary elements and M is the number of internal cells. The complexity is reduced to $O(N + M)$ by hierarchical grouping of influences coming from integration points. A tree structure of clusters, containing groups of boundary elements and internal cells is formed. The integrals evaluated for clusters located far enough from collocation points are expanded into multipole series, near to integration points. The coefficients (multipole moments) of the expansion are transformed by shifting the expansion points to larger clusters. The integrals are also expanded near to collocation points (local expansion). The local moments are formed from the multipole ones, and then the influences are distributed to smaller clusters, by shifting the expansion points. Finally, the far-field terms of potentials are evaluated for each collocation points, using the local moments. The near-field terms of potentials are calculated directly. The operations lead to obtaining the matrix-vector products. The matrices are not built explicitly, so the system of equations is solved iteratively. More details can be found in References [1, 2, 3, 6, 8].

3. Computer code

A FMBEM code for analysis of elastic plates, loaded statically by traction and volume forces, is developed [8]. The boundary of the structure is discretized using three-node quadratic boundary elements and the domain is discretized using six-node quadratic internal cells. The regular boundary integrals are calculated using the Gauss quadrature. The singular boundary integrals are calculated using logarithmic Gauss quadrature or rigid body movement method, respectively. The regular domain integrals are calculated using 7-point Gauss cubature, and the singular ones are regularized using transformation to the polar coordinates. The system of equations is solved using the preconditioned GMRES.

4. Numerical example

A rotating disk loaded by centrifugal forces was analysed. Results were obtained using three versions of the BEM. In the first version, all integrals were calculated directly. In the second one, only the volume integrals were calculated by using expansions. In the third version, the expansions were used for calculation of all the integrals. An influence of the number of the expansion terms on the error of displacements and stresses were analysed. The efficiency of the three considered versions of the BEM was also analysed.

5. Conclusions

The accuracy and the effectiveness of the FMBEM can be adjusted to a particular problem by changing the number of the expansions terms, dependently on the case, whether only displacements, or also stresses are to be analyzed. The application of the method to the evaluation of the volume integrals gives capability of effective analysis of a broader range of deformable structures, e.g. made of elastoplastic materials, gradient materials, etc.

6. References

- [1] L. Greengard and V. Rokhlin (1987). A fast algorithm for particle simulations, *J. Comput. Phys.*, **73**, 325-348.
- [2] N. Nishimura (2002). Fast multipole accelerated boundary integral equation methods, *Appl. Mech. Rev.*, **55**, 299-324.
- [3] M.S. Ingber, A.A. Mammoli and M.J. Brown (2001). A comparison of domain integral evaluation techniques for boundary element methods, *Int. J. Numer. Meth. Engng*, **52**, 417-432.
- [4] J. Barnes and P. Hut (1986). A hierarchical $O(N \log N)$ force-calculation algorithm, *Nature*, **324**, 446-449.
- [5] V. Minutolo, E. Ruocco and T. Colella (2006). Isoparametric FEM vs. BEM for elastic functionally graded materials, *Advances In Boundary Element Techniques VII*, International Conference on Boundary Element Techniques BETEQ VII, Eds B. Gattmiri, A. Sellier and M.H. Aliabadi, Paris, 263-266.
- [6] P.B. Wang and Z.H. Yao (2007). Fast multipole boundary element analysis of two-dimensional elastoplastic problems, *Commun. Numer. Meth. Engng*, **23**, 889-903.
- [7] C.A. Brebbia and J. Dominguez (1992). *Boundary elements an introductory course*, McGraw-Hill, New York.
- [8] J. Ptaszny and P. Fedelinski (2007). Fast multipole boundary element method for analysis of linear-elastic plates, *First Congress of Polish Mechanics*, Eds J. Kubik, W. Kurnik and W.K. Nowacki, Warsaw, CD-ROM, 8 pages.

MODELLING OF WAVE PROPAGATION IN SPATIAL FRAME ELEMENTS – NUMERICAL SIMULATIONS AND EXPERIMENTAL WORKS

J. Chróścielewski, M. Rucka, K. Wilde and W. Witkowski
Gdansk University of Technology, Gdańsk, Poland

1. Introduction

Wave propagation in structures is a subject of intensive investigation. One of the possibilities of the wave propagation modelling is the Spectral Element Method (SEM), developed by Patera [1] in 1984 in the context of fluid dynamics. The main idea of the SEM is use of one high-order polynomial for each domain [2].

In this study a spectral frame N -node finite element appropriate for analysis of wave propagation phenomena in engineering structures build from spatial frames is presented. The element is elaborated in linear range. Each node of the element is endowed with six engineering dofs. The kinematical assumptions of Timoshenko beam theory are employed. Associated with the formulation of the element, is the temporal integration scheme. Special emphasis is put on the accuracy and efficiency of the time integration to ensure reasonable simulation times. The algorithm uses accelerations as the primary variables and the mass matrix of an element is integrated using Lobatto quadrature rule. Consequently, it can be recast in a form of the pseudo diagonal matrix and substantial efficiency in computation times can be gained.

2. Formulation

The time integration scheme does not use the stiffness matrix. On the local element level, under the assumptions of classic Timoshenko beam theory, the element load vector \mathbf{r} and mass matrix \mathbf{M} are derived. The damping matrix \mathbf{C} is formulated under the hypothesis of proportional damping. Then, it is possible to find the element inertia force vector \mathbf{b} and damping force vector \mathbf{c} . While transforming the above matrices and vectors to the global frame coordinates, the transformation of the internal nodes is omitted, leaving them in the local frame coordinates. This is justified by the fact the wave propagation in local frame (along element axis) is of the primary interest. By writing the dynamical equilibrium condition, the following equation is obtained with respect to increment of acceleration $\delta\ddot{\mathbf{q}}$

$$(1) \quad [\mathbf{M} + \Delta t \gamma \mathbf{C}] \delta\ddot{\mathbf{q}} = \mathbf{p}_{n+1} - \mathbf{b}_{n+1}^{(i)} - \mathbf{c}_{n+1}^{(i)} - \mathbf{r}(\mathbf{q}_{n+1}^{(i)} + (\Delta t)^2 \beta \delta\ddot{\mathbf{q}}), \quad \beta = 1/4, \quad \gamma = 1/2$$

where \mathbf{p} is the element external load vector, n denotes the time step, i is the label for iteration and Δt is the time step. Simple iteration method is then used to obtain correction of $\delta\ddot{\mathbf{q}}$

$$(2) \quad \delta\ddot{\mathbf{q}} = [\mathbf{M} + \Delta t \gamma \mathbf{C}]^{-1} (\mathbf{p}_{n+1} - \mathbf{b}_{n+1}^{(i)} - \mathbf{c}_{n+1}^{(i)} - \mathbf{r}(\mathbf{q}_{n+1}^{(i)})).$$

Obviously, if \mathbf{M} and \mathbf{C} are pseudo-diagonal the time integration scheme becomes efficient. The iterative process **Błąd! Nie można odnaleźć źródła odwołania.** is terminated when equilibrium condition

$$(3) \quad \mathbf{j}_{n+1}^{(i+1)} = \mathbf{p}_{n+1} - \mathbf{b}_{n+1}^{(i+1)} - \mathbf{c}_{n+1}^{(i+1)} - \mathbf{r}(\mathbf{q}_{n+1}^{(i+1)}) \rightarrow \mathbf{0}.$$

is satisfied in some sense.

3. Experiments and numerical simulations for rod

The investigations were carried out for a steel rod [3] of the length 1 m, height 8 mm and width 8 mm (Fig. 1). The boundary condition was assumed as pinned-pinned. The experimentally determined material properties were found to be: Young's modulus $E = 195$ GPa and mass density $\rho = 7563$ kg/m³. The rod was subjected to a dynamic load applied in the half of the rod length. The response was recorded at the same point as the load. The measurements were made using piezoelectric plate transducers Noliac CMAP11. The excitation signal was chosen as sine wave of frequency 40 kHz modulated by the Hanning window.

The spectral element with 101 nodes was applied for modelling of the rod. The time step was assumed as 10^{-8} s. The minimum number of nodes for proper response modelling is 101 (above 12 nodes per wavelength). The comparison with the experimental results is given in Fig. 1. It is noted, that both numerical simulations are in good agreement with the experimental data.

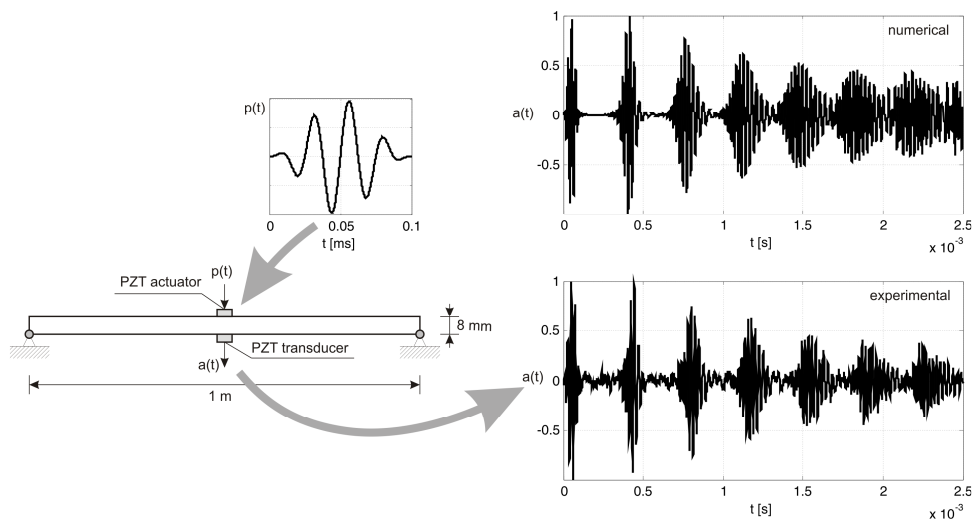


Figure 1. Steel rod, comparison of experimental and numerical solutions

4. Conclusions

The study on modelling of wave propagation in frame elements leads to the following conclusions and suggestions:

- The integration of the equations of wave propagation can be efficiently conducted due to the pseudo-diagonal mass matrix
- Application of GLL nodes in both natural and geometric coordinates requires 12 nodes per wavelength.

5. References

- [1] T. Patera (1984). *A spectral element method for fluid dynamics: laminar flow in a channel expansion*. Journal of Computational Physics **54**, 468-488.
- [2] C. Pozrikidis (2005) *Introduction to Finite and Spectral Element Methods using MATLAB*[®]. Chapman & Hall/CRC.
- [3] M. Rucka, W. Witkowski, K. Wilde, J. Chróścielewski (2007) Wave propagation in steel truss girder for structural health monitoring. III ECCOMAS Thematic Conference on Smart

EVOLUTIONARY IDENTIFICATION OF LAMINATES' STOCHASTIC PARAMETERS

W. Beluch¹, T. Burczyński^{1,2} and P. Orantek¹

¹*Department for Strength of Materials and Computational Mechanics, Silesian
University of Technology, Gliwice, Poland*

²*Institute of Computer Modelling, Cracow University of Technology, Cracow, Poland*

1. Introduction

Laminates are a group of fibre-reinforced composites made of many stacked and permanently joined layers (plies). Laminates have great strength/weight ratio and it is possible to obtain desired properties of laminate by manipulating the components materials, stacking sequence, fibers orientation and layer thicknesses.

The aim of the paper is to identify material constants in multi-layered, fibre-reinforced laminates. Simple and hybrid (with laminas made of different materials) laminates are considered. The hybrid laminates are in a form of interply hybrids, with plies composed of two different materials [1]. The internal layers are made of a low-strength and less expensive material while the outer layers are made of a more expensive but better material.

Usually, laminates can be treated as orthotropic thin plates with four independent elastic constants: axial Young's modulus E_1 , transverse Young's modulus E_2 , axial-transverse shear modulus G_{12} and axial-transverse Poisson ratio ν_{12} .

2. Formulation of the stochastic identification problem

A non-linear stochastic optimization problem is a searching for a random vector [4]:

$$(1) \quad \mathbf{X}(\gamma) = [X_1(\gamma), X_2(\gamma), \dots, X_i(\gamma), \dots, X_n(\gamma)]$$

which minimizes the objective function $F(\gamma) = F[\mathbf{X}(\gamma)]$ and satisfies the constraints:

$$(2) \quad P[g_j(\mathbf{X}) \geq 0] \geq p_j, j = 1, 2, \dots, m$$

where: $(\Gamma, \mathfrak{F}, P)$ - the probability space; Γ - the space of elementary events; \mathfrak{F} - σ -algebra of subset of the set Γ ; P - the probability defined on \mathfrak{F} .

In the present paper evolutionary algorithm (EA) is used as the optimization method [2]. The vector $\mathbf{X}(\gamma)$ (chromosome) consists of random genes. Each gene is represented by a random variable. It is also assumed that each gene has a n -dimensional Gaussian distribution function and that random genes are independent random variables. Eventually, the original stochastic problem can be reduced to the deterministic one. Random chromosome $\mathbf{X}(\gamma)$ is replaced by a deterministic chromosome $ch(\mathbf{x})$. Each gene x_i is a stochastic variable represented by a mean value m_i and a standard deviation σ_i [3].

Identification can be treated as the minimization of the objective function F with respect to the vector of the design variables \mathbf{x} :

$$(3) \quad \min : \left[F(\mathbf{x}) = \sum_{k=1}^N \left| \frac{\hat{\mathbf{q}}_k - \mathbf{q}_k}{\hat{\mathbf{q}}_k} \right| \right]$$

where: $\mathbf{x} = (x_k)$ - the parameters representing the identified constants; $\hat{\mathbf{q}}_k$ - the measured values of state fields; \mathbf{q}_k - the values of the same state fields calculated from the solution of the direct problem; $k = 1..N$, N - the number of sensor points.

The \mathbf{x} vector has the form: i) for simple laminates: $\mathbf{x} = (E_1, E_2, G_{12}, \nu_{12})$; ii) for hybrid laminates: $\mathbf{x} = (E_1^1, E_2^1, G_{12}^1, \nu_{12}^1, \rho^1, E_1^2, E_2^2, G_{12}^2, \nu_{12}^2, \rho^2)$ (superscripts specify the material number).

Direct problems for the identification tasks are solved by means of a finite element method software (MSC.PATRAN/NASTRAN). To reduce the number of sensor points, the modal analysis methods are employed. In present paper the eigenfrequencies are used as the measurement data. The numbers of plies, their thicknesses, fibres orientation and the number of layers made of each material are assumed to be known. External layers hybrid laminates are made of material M_e and the core layers are made of material M_i . The number of layers made of each material is also known.

3. Numerical example

A rectangular simple laminate 0.5x0.2m with one of shorter sides fixed is made of the glass-epoxy. Each ply of the symmetrical laminate has the same thickness $h_i=0.002\text{m}$. The stacking sequence of the symmetrical laminate is: (0/45/90/-45/0/90/0/90)s. The plate is divided into 200 4-node plane finite elements. The first 10 eigenfrequencies of the plate are the measurement data. It is assumed that measurements are random variables with the Gaussian distribution. The measurements were repeated 200 times to collect data. The population in EA consists of 200 chromosomes of 4 genes each. The identification results after 1000 generations are collected in Table 1.

	E_1 [Pa]		E_2 [Pa]		ν_{12}		G_{12} [Pa]	
	m	σ	m	σ	m	σ	m	σ
Min	2.00E10	0.00E9	4.00E9	0.00E9	0.00	0.00	2.00E9	0.10E8
Max	6.00E10	0.30E9	9.00E9	0.30E9	0.50	0.10	6.00E9	0.70E8
Actual	3.86E10	0.12E9	8.28E9	0.20E9	0.26	0.02	4.14E9	0.50E8
Found	3.92E10	0.11E9	8.14E9	0.17E9	0.27	0.04	4.07E9	0.22E8

Table 1. A simple laminate - identification results.

4. Final conclusions

An identification method based on the stochastic representation of the identified parameters has been presented. The Evolutionary Algorithm has been employed to solve the identification task for simple and hybrid laminates. Positive identification results have been obtained for both kinds of laminates.

5. Acknowledgments

The research is partially financed from the Polish science budget resources as the research project and the Foundation for Polish Science (2005-2008).

6. References

- [1] S. Adali et.al. Optimal design of symmetric hybrid laminates with discrete ply angles for maximum buckling load and minimum cost, *Composite Structures*, **32**, 409–415, 1995.
- [2] J. Arabas. *Lectures on Evolutionary Algorithms*, WNT, 2001 (in Polish).
- [3] P. Orantek and T. Burczyński. The identification of stochastic parameters in mechanical structures, *CMM-2007 Conference Proceedings*, CD-Edition, Lodz-Spala, 2007.
- [4] K. Sobczyk. *Stochastic Wave Propagation*. PWN, Warsaw, 1984.

**THE LOCAL GRADIENT METHOD
SUPPORTED BY ARTIFICIAL NEURAL NETWORK
IN GRANULAR IDENTIFICATION PROBLEMS**

P. Orantek¹ and T. Burczyński^{1,2}

*1) Department for Strength of Materials and Computational Mechanics,
Silesian University of Technology, Poland*

2) Cracow University of Technology, Artificial Intelligence Department, Poland

1. Introduction

The identification problems belong to inverse problems and concern the determination of mechanical systems by finding same material, shape and topology parameters and boundary conditions from the knowledge of the responses to given excitations. Such problems are mathematically ill posed.

One of the well known optimization methods are the gradient methods: (i) steepest descent method, (ii) conjugate gradient method, (iii) variable metric gradient method and etc. This methods in the previous stages of investigation were used.

This paper describes a new conception of application of the local gradient method supported by artificial neural network in granular identification problems. The following systems are considered as the granular models (i) interval numbers, (ii) fuzzy numbers and (iii) random variables. The proposed local method was examined for testing bench-mark. Next, the algorithm was applied for identification problem in mechanical structures. The paper presents the application of the algorithm in finding the shape, material coefficients and boundary conditions of the granular mechanical structures.

2. The formulation of granular identification problem

Consider an elastic body which occupies the domain Ω bounded by boundary Γ . The body is restrained by granular boundary conditions and loaded by granular forces. The material parameters are also assumed as the granular numbers. The body can contains some defects described by granular parameters also. The number, shapes and sizes of the defects are unknown.

The aim of the identification problem is to find the parameters described the set of defects. The identification problem is expressed as the minimization of the special minimizing function. The function contains the physical values which can be measured in the special selected sensor points. The sensor points are located on the surface of the body. As the measured values means here: (i) displacements under static loading, (ii) displacements under dynamical loading, (iii) eigenfrequencies and etc.

3. The local gradient method supported by artificial neural network

The proposed local optimization method is a combination of the classical gradient method and the artificial neural network. In the first step of the algorithm a set (cloud) of points in the function domain is generated. In the aim of realize the optimization process the network is constructed.

In each iteration of the optimization algorithm a few steps are performed.

In the first step the set of training vectors of the network is created. In the first iteration the set is created on basis of the cloud of points. The coordinates of points play the role of the input values of the network, the fitness values in points play the role of output value of the network.

In the second step the network is trained.

In the next, third step, the optimization process is carried out. The gradient method of optimization is used. The network as the fitness function approximation is used. The gradient of the fitness function on the basis of the artificial neural network is computed also.

For a point, which is a result of optimization (found in step 3), the actual fitness function is computed.

In the last step the stop condition is checked. In the case, in which the condition is true, the point is treated as the result of the optimization process. If this condition is false, this point is added to the training vector set and the next iteration is carried out (go to step 1).

This approach for deterministic problems (testing bench-mark and mechanical identification problems) was used.

In the present paper the artificial neural network is used as the computation tool of the sensitivity analysis of the granular fitness function.

4. Conclusions

An effective intelligent technique based on the gradient methods, artificial neural networks and granular approach has been presented. This approach in the granular optimization problems in mechanical structures can be applied. The following granular problems were solved in the identification of the (i) defects, (ii) boundary conditions and (iii) material parameters.

The results were satisfactory.

In future the influence of the parameters on the sensitivity of the algorithm (the number of the trainign vectors, number of the layers and number of the neurons in the hidden layers) should be tested.

In future presented algorithm will be connected with the granular evolutionary algorithm. This idea for deterministic problem was applied. Due to fusion evolutionary algorithms with the gradient method supported by artificial neural network the optimization time was decreased even to 50%.

5. Acknowledgement

The work was done as a part of project N502 4573 33 sponsored by Polish Ministry of Science and Higher Education.

6. References

- [1] A. Bargiela, W. Pedrycz, Granular Computing: An introduction. Kluwer Academic Publishers Boston/Dordrecht/London 2002.
- [2] H.D.Bui, Inverse Problems in the Mechanics of Materials: An Introduction. CRC Pres, Boca Raton 1994.
- [3] L. Chen, S.S.Rao, Fuzzy finite element approach for vibrating analysis of imprecisely defined systems. Finite Elements in Analysis and Design. 1977, vol. 27, pp. 69-83.
- [4] E. Czogała, W. Pedrycz, Elementy i metody teorii zbiorów rozmytych. PWN, Warszawa 1985.
- [5] J. Kacprzyk, Zbiory rozmyte w analizie systemowej. PWN Warszawa 1986.
- [6] A. Papoulis, Probability, Random Variables, and Stochastic Processes. McGraw Hill, New York 1991
- [7] A. Piegat, Modelowanie i sterowanie rozmyte. Akademicka Oficyna Wydawnicza EXIT, Warszawa 2003.
- [8] D. Rutkowska, M. Piliński, L. Rutkowski, Sieci neuronowe, algorytmy genetyczne i systemy rozmyte. PWN Warszawa-Łódź 1997.
- [9] R. Schaefer, Podstawy genetycznej optymalizacji globalnej. Wydawnictwo Uniwersytetu Jagiellońskiego, Kraków, 2002.
- [10] L.A. Zadeh, Fuzzy sets, Information and Control, Vol.8, 1965.

THE COMPLEX WELDING PROCESS SIMULATION USING FEM, PARALLEL COMPUTING AND GRID BASED EVOLUTIONARY OPTIMIZATION

G. Kokot, A. John, W Kuś

Silesian University of Technology, Gliwice, Poland

1. Introduction

A complex numerical simulation of a welding process using the finite element method [1,2] is presented in the paper. Results for full coupled thermo-mechanical problem are prescribed. As the simulation and optimization of welding is very time and resource consuming the parallel calculation technique (the domain decomposition method (DDM)) and grid based evolutionary optimization are applied.

The objective of the welding simulation is to study the temperature generated during the welding process and investigate residual stresses in the component after welding. Such results give the possibility to determine properties of materials in welding zones, stress and strain state of welded parts. From other side it is possible to perform optimization process looking for welding parameters (welding speed, welding power source etc.) or initial shape of welded sheets according to displacement state (welding of thin metal sheets with stiffeners – T joints). Those results are the base for fatigue analysis too.

2. Welding simulation

Welding is one of the most commonly used join process but till now it is still difficult to simulate it in standard CAE systems based on finite element method. In most of them this requires the writing of specialized, additional user subroutines for specific boundary conditions (a heat source, a weld path, a filler element treatment, a material behaviour etc.) what makes it difficult and inconvenient in use. It causes the simulation of welding is extremely difficult. From other side such a simulation gives a lot of information very important for engineers. An undesirable side-effect of welding is the generation of residual stresses and deformations in the component and the quality of the weld has a substantial impact on the fatigue life of the structure. These resultant deformations may render the component unsuitable for further use. Also, the residual stresses form the input for subsequent manufacturing or structural processes.

Considered simulation allows to determine the cooling period from 800°C to 500°C (so-called cooldown rate $t_{8/5}$) [2], which is used to model the strength parameters in a heat-affected zone. Finding the optimal value of $t_{8/5}$ is one of the primary goal of simulation and optimization of the welding process [3]. Obtained results can be also the base for optimization process of welding parameters for e.g. thin metal sheets with T stiffeners (cars body, airplane panels, shipbuilding, frame construction) and for a fatigue analysis of welded structures.

It should be mentioned that nearly full set of welding parameters are considered during simulation. Those parameters are: moving heating source, velocity, source power, cooling temperature and time, shape of the source, heat input, weld flux etc.

3. Results

In the fig. 1. results for complex simulation for welding are presented. The results consider all the simulation mentioned above.

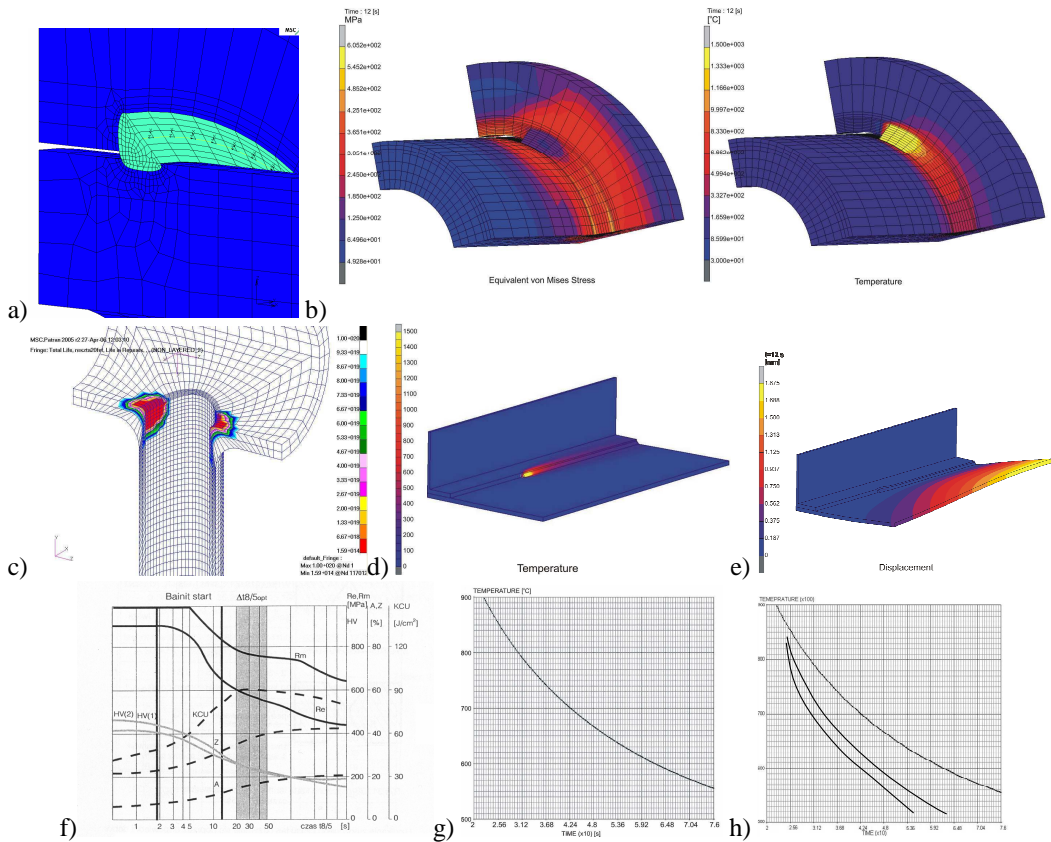


Fig. 1 The complex set of results of the welding process simulation: a. the model, b. von Mises stresses and temperature distribution during welding, c. fatigue analysis results, d., e. results of optimization of T join, f. cooldown rate $t_{8/5}$ in the HAZ – the reference diagram, g. calculated $t_{8/5}$, h. example of $t_{8/5}$ after optimization of welding parameters.

Using modern CAE systems connected with parallel and grid based evolutionary computing it is possible to perform an advanced complex simulation of welding process and analysis of welded parts. It is possible to perform: a static linear analysis of welded components, a coupled thermo-mechanical simulation of welding process, fatigue analysis of the welded component, an optimization process of welding parameters etc. [2,3].

4. References

- [1] Goldak J., Chakravarti A., and Bibby M., A New Finite Element Model for Welding Heat Sources, Metallurgical Transactions B., Volume 15B, June 1984, 299 – 305.
- [2] Kokot G., John A., Górká J. Welding process simulation using FEM. Proc. of the 17-th International Conference on Computer Methods in Mechanics CMM-2007, on CD, Lodz-Spala, 2007.
- [3] Kokot G., John A., Kuś W., Grid based evolutionary optimization of strength parameters in heat affected zone of welded joints, 8th. World Congress on Computational Mechanics (WCCM8), 2008, (accepted paper).

AGGREGATION MULTILEVEL ITERATIVE SOLVER BASED ON SPARSE MATRICES TECHNIQUE

S. Fialko^{1,2}

¹ *Cracow University of Technology, Cracow, Poland*

² *Software company SCAD Soft, Kiev, Ukraine*

1. Introduction

An efficient iterative method for solution of large-scale linear equation sets with sparse positive definite matrices is considered. These problems appear in static analysis of finite element problems of structural and solid mechanics.

Realistic design models often produce ill-conditioned large-scale problems. This fact essentially restricts the application area of iterative methods, especially to problems of structural mechanics.

The main idea of this research is to develop an iterative method stable against ill-conditioning, which allows us to compete with sparse direct finite element solvers during the calculation stage of the analysis. This investigation continues the previous researches of author [3 – 6]. A combination of two powerful ideas – the aggregation multilevel preconditioning for preconditioned conjugate gradient method AMIS [2 - 5] and the sparse incomplete Cholesky factorization preconditioning [6] is the basis of the present research.

2. Aggregation multilevel preconditioning for preconditioned conjugate gradient method.

A lot of problems of structural mechanics are ill-conditioned; the respective models have bar substructures and specific finite elements (rigid links, compatible nodes and so on). This fact forces us to reject the multi-grid approach and to prefer to use the preconditioned conjugate gradient (PCG) method with aggregation multilevel preconditioning. This approach combines advantages of both PCG and multilevel methods and allows us to create an iterative approach stable against ill-conditioning. The aggregation approach [2-5] has a clear mechanical interpretation, creates a coarse level model due to imposed local rigid links, allows us to analyze bar structures, continuous structures and combined ones. It also takes into account special finite elements. The application of element-by-element technique to creation of the coarse level stiffness matrix, a restriction-prolongation procedure [3-5], and implementation of the sparse direct solver to keep a relatively large size of coarse level model (till 100 000 – 200 000 equations) [5] allows us to improve the prediction of slow-convergent low modes and accelerate the convergence.

The next important issue is a correction of the interpolated solution vector. The need for it arises when extending the coarse level (aggregated model) solution onto the fine level (finite element model). In previous versions of the AMIS solver, a few steps of the inner iteration procedure (a preconditioned quickest descent method) were applied to damp quickly oscillating residuals. The symmetrical Gauss-Seidel preconditioning as well as incomplete Cholesky factorization by position ICCG0 one were implemented. But in some practical problems a lock of convergence occurs: the coarse level model leads to a fast reduction of the relative norm of residual vector, $\text{err} = \|\mathbf{r}_k\|_2 / \|\mathbf{b}\|_2$, where \mathbf{b} is a load vector, to about 10^{-2} , and then the convergence still slows down.

In the present research we apply a sparse incomplete Cholesky factorization preconditioning [6] to improve the correction abilities of the inner smoothing iterations. The following results

demonstrate an essential improvement of robustness of AMIS_SICPS (an aggregation multilevel iterative solver with sparse incomplete Cholesky preconditioning during smoothing) method.

3. Numerical example

A large-scale design model (multi-storey building) comprises 1 956 634 equations (tab. 1) and has 3 load cases. The efficiency of several solvers is compared. Designations: BSD MFM is a block sparse direct multi-frontal method [6], ICCG0 is an incomplete Cholesky conjugate gradient by position solver, SICCG is a sparse incomplete Cholesky conjugate gradient by value solver [6], AMIS_SICPS is the approach suggested here. The convergence tolerance is $\text{tol} = 10^{-4}$. A PC Pentium IV (RAM 2.0 GB, CPU 2.40 GHz) has been used.

Method	Computation time	Memory storage, MB	Number of iterations
BSD MFM	2 h 20 min	7.2 GB – size of factored matrix	-
ICCG0	3 h 12 min	0.5 GB	8470 / 7944 / 7368
SICCG	27 min 25 s	1.5 GB	562 / 520 / 509
AMIS SICPS	13 min 20 s	1.76 GB	31 / 31 / 30

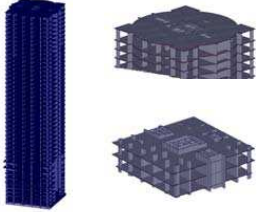


Table 1. Comparison between methods

An essential part of the solution time (about 40%) BSD MFM method is spent for slow input/output disk operations because the size of the factored matrix exceeds the core memory capability significantly. The serial ICCG0 method demonstrates a slow convergence due to ill-conditioning of the design model. The SICCG method has a good stable convergence for this problem (the rejection parameter $\psi = 5 \times 10^{-9}$ and the post-rejection one $\psi = 10^{-6}$). But the best results are demonstrated by the AMIS_SICPS method (the same values for rejection and post-rejection parameters are used).

6. References

- [1] A. Brandt (1977). Multi-level adaptive solutions to boundary-value problems. *Mathematics of Computations*, **31**, № 138, 333–390.
- [2] V.E. Bulgakov, G. Kuhn (1995). High-performance multilevel iterative aggregation solver for large finite-element structural analysis problems. *Int. j. Num. Methods Eng.*, **38**, 3529-3544.
- [3] S. Fialko (2002). Aggregation Multilevel Iterative Solver for Analysis of Large-Scale Finite Element Problems of Structural Mechanics: Linear Statics and Natural Vibrations, *R. Wyrzykowski et al. (Eds.): PPAM 2001, LNCS 2328*, Springer-Verlag Berlin Heidelberg, 663–670.
- [4] S. Fialko (2000). High-performance aggregation element-by-element Ritz-gradient method for structure dynamic response analysis, *Computer Assisted Mechanics and Engineering Sciences*, **7**, 537-550.
- [5] S.Yu. Fialko (2004). Application of iterative solvers in finite element analysis of structural mechanics. Linear statics and natural vibrations. *Proceedings of 8-th international conference "Modern building materials, structures and techniques". May 19–22, Vilnius, Lithuania*, 721–725.
- [6] S. Fialko (2006). Sparse incomplete Cholesky conjugate gradient iterative solver for analysis of large-scale problems of structural and solid mechanics. *Proceedings of 35-th Solid Mechanics conference. Krakow, September 4–6*, 379–380.

**NUMERICAL MODELING OF MACRO SEGREGATION EVOLUTION AND CHANGE OF STRESS-
STRAIN STATE IN BILLET DURING CONTINUOUS CASTING WITH MECHANICAL SOFT
REDUCTION**

T.Rec, A.Milenin

AGH University of Science and Technology, Kraków, Poland

One of the fundamental problems concerning continuous casting process (CCP) is formation of segregation of chemical elements in a cross-section of billet. It has significant influence on mechanical properties and microstructure of final products. The possibility of decrease of macrosegregation by deformation of billet in a semi-solid state (Soft Reduction, SR) was presented in [1]. Parameters of SR process (time and value of strain) significantly influence ratio of segregation together with the parameters of continuous casting process. The purpose of this paper is to optimize the parameters of SR using numerical modeling. In recent publications, several approaches for CCP modeling are presented [2-3], however neither of them takes into account all factor of SR.

The full numerical model of CPP processes should consists of the following components:

- model of the heat transfer phenomenon and crystallization processes;
- model of thermal stresses evolution;
- model of influence of constructive mechanism of the CCM on metal;
- the segregation evolution model [4];
- model of SR process;
- model of damage.

In order to model crystallization process, the heat transfer equation was used and modified by the method of effective specific heat. The elasto-plastic theory of plasticity was used for simulation of mechanical processes.

In present work three variants of simulation are considered: W1 – without SR and W2, W3 – with SR. Simulation conditions were equivalent to industrial conditions of continue casting (300x400mm bloom, St3S steel). SR prescribed before the end of crystallization process, for W2 SR started 1103s after beginning of CPP, and W3 – SR started 593s after beginning of CPP. Intensive cooling in mould follows to fast temperature decrease on the surface of ingot what induces beginning of solidification process. During the first steps of crystallization process, the carbon concentration decreases from 0.14% to 0.053% on the surface of ingot for each variant. In succeeding stages the carbon concentration increases due to backward diffusion phenomenon. The concentration attains maximum value when the last liquid fraction is crystallizing in the ingot. Maximum carbon concentration in center line billet was 0.292%, after crystallization process 0.278% for variant W1. The final difference between the surface and the center of ingot was 0.0575%. For W2 variant, deformation caused displacement some part of carbon to upper layer of liquid metal and decreased concentration of carbon after solidification in center line ingot (center – 0.185%, outside surface – 0.136% difference of concentration – 0.0492%). In W3 variant, deformation was prescribed considerably early then in variant W2 (when in ingot share liquid phase was grate). It caused on increase of carbon segregation as in variant W2 (center – 0.192%, surface – 0.137%, difference of concentration– 0.0546%).

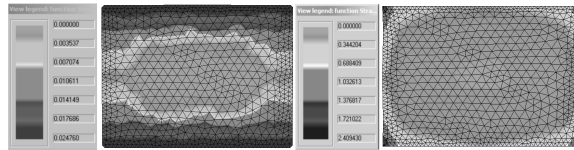


Fig. 1. Distribution of strain intensity in the cross-section in continuous cast billet, after finish of solidification process; a) for W1 variant; b) for W2 variant.

The strain intensity in billet during continue casting with SR is determined. The SR process essentially influences the distribution of strain intensity. Bending and straightening of billet cause that maximal values of strain intensity are attained on the ingot surfaces - W1 variant (fig. 1a). In the W2 variant strain intensity concentrates in ingot corners. (fig. 1b). The results presented in fig. 1 show an essential influence of SR on strain distribution. Therefore, a proper fracture model of billet during SR is so important and it was developed and added to the model of CCP in present paper. The forecast of the brings fracture on ingot surface was based on the theory of fracture described in literature [5 – 6]. In this model, as a key-parameter of fracture, the resource of plasticity ψ is proposed:

$$\psi = \frac{\varepsilon_i}{\varepsilon_p(k, \mu_\sigma, T)} < 1$$

where: ε_i – strain intensity; ε_p – critical strain before fracture metal as a function of parameters $k = \sigma/\sigma_s$ and Lode coefficient μ_σ ; σ – mean stress; σ_s – yield stress; T – temperature.

The function $\varepsilon_p(k, \mu_\sigma, t)$ was determined in experimental investigations at Gleeble simulator. The critical strain was determined based on experimental tensile test and SICO test. For determination of empirical parameters of function $\varepsilon_p(k, \mu_\sigma, t)$ the inverse analysis was used. For simulation of tests the FORGE3 software was used.

References:

- [1] K. Isobe, Y. Kusano, S. Noguchi ea (1995). *Improvement of segregation of continuously cast billet by soft reduction*, Porc. Near-Net-Shape Casting in the Minimills, Vancouver, 179-192.
- [2] M. Bellet (2007). *Two-phase multiscale FEM modelling of macrosegregation formation in steel slabs*, 9th International Conference on Numerical Methods in Industrial Forming Processes, June 17-21, 2007 Porto, 1369-1374.
- [3] А.А. Миленин (2005). *Проблемы моделирования напряженно-деформированного состояния металла при непрерывном литье заготовки*, В кн. Современные проблемы металлургии: «Системные технологии», 576 с, 15-23.
- [4] A. Milenin, T. Rec (2008). *Model matematyczny odkształcenia w maszynie COS wlewka w stanie półciekłym*, Mat. 15 Konf. Informatyka w Technologii Metali, Korbeltów, 55-64
- [5] F. Grosman., M. Tkocz (2004). *Zastosowanie funkcji odkształcalności granicznej do prognozowania utraty spójności materiału*. Mat. 11 Konf. Informatyka w Technologii Metali, Zakopane, 339÷346.
- [6] A. Bogatow (1996). *Osobennosti reologiczeskogo povedenija i razruszenija metalla pri monotonnoj i znakoperemnoj deformaciji. Plasticzeskaja deformacija stalej i splawów*, Moscow, 90÷98.

STRUCTURAL RELIABILITY ANALYSIS USING OBJECT ORIENTED ENVIRONMENT STAND

*J. Knabel, K. Kolanek, V. Nguyen Hoang, R. Stocki, and P. Tuzowski
Institute of Fundamental Technological Research, Warsaw, Poland*

1. Introduction

Dealing with uncertainty is an essential part of the structural design process. Traditionally uncertainties are taken into account by means of safety factors specified by appropriate design codes. For most of the typical problems this approach allows to obtain safe structures, however the actual safety level of such designs is hard to estimate. On the other hand, a progressive increase of computational capabilities and development of reliability analysis methods and specialized software allows for more rational treatment of inherent uncertainties of material parameters, structural geometry and the applied loads. The contemporary “computer aided” reliability analysis provides a valuable tool for designers and decision makers by enabling them for more realistic estimation of the probability of structural failure, identification of the weakest elements and evaluation of their influence on the safety of entire structure.

The structural reliability analysis can be performed by a number of software packages, such as ANSYS PDS and DesignXplorer, CalREL/FERUM/OpenSees, COSSAN, NESSUS, PERMAS-RA/STRUREL, PHIMECA-SOFT, PROBAN, PROFES, UNIPASS, all of them reported in the special issue of Structural Safety journal [1]. The structural reliability analysis usually requires many evaluations of the so-called failure function, which is defined by means of selected structural responses. Since these responses are most often computed using the finite element (FE) method therefore, a reliability analysis system must interact with the FE analysis program. This is usually realized in two alternative ways: either the reliability and FE codes are closely integrated (linked) or reliability analysis code have interface enabling it to modify and read input and output data files, respectively, of a third-party FE analysis system or other structural analysis program.

Although the first approach has unquestionable advantages such as easy access to FE model parameters or a common graphical user interface etc., it restricts application of reliability analysis to problems supported by the integrated FE analysis code. The second solution gives possibility of performing the reliability analysis for any problem, provided that the corresponding FE computations can be executed from the command line. This approach is often preferred and used in most of the systems listed above.

The key to success in developing any large software package is a proper organization of its code facilitating future modifications and allowing it to be simultaneously developed by many programmers. The code architecture should also facilitate integration of new algorithms into the existing environment. Such a flexibility is offered by object oriented programming and therefore it was C++ that was chosen as a programming language for creating reliability analysis software STAND (Stochastic Analysis and Design), developed in the Institute of Fundamental Technological Research (IFTR) of Polish Academy of Sciences. By analyzing reports in [1] it can be concluded that only few from the above listed programs benefit from using object oriented paradigm.

The graphical user interface implemented in STAND is easy to use and provides the interface to the external computational programs by the concept of data files parsing. Parameters of, say, FE model can be easily identified and linked to random variables in the stochastic model by simply highlighting appropriate fields in a template input file. Similar approach was employed in COSSAN [2] and PROFES [3], for instance. Analogous method is employed for collecting the FE analysis results. As it was mentioned, this type of interface is suitable only for the FE programs that can be

run from the command line and read text input data files as well as produce results in the text format. This, however, is the case for most of the commercial and research oriented FE codes.

2. STAND environment description

So far, these are mainly time invariant component reliability problems that can be addressed with STAND. In addition to standard reliability analysis methods like FORM, SORM, crude Monte Carlo, unimodal importance sampling or mean value first order method STAND offers multimodal adaptive importance sampling method (MAISM), developed recently in IFTR. MAISM proved to be very efficient in dealing with noisy nonlinear limit state functions (LSFs), see [4].

The basic statistical analysis is available in STAND as well. It is based on two sampling methods: crude Monte Carlo and a very efficient descriptive sampling design - optimal Latin hypercube (OLH), see [5]. OLHs can be either created during the problem execution or, if available, loaded from the attached large database of pre-generated OLH designs.

Some of reliability analysis algorithms implemented in STAND take advantage of parallel computing, which now becomes the standard in commercial codes. Thus the tasks performed with STAND can be submitted on a single PC as well as on parallel computers, which should be a default choice for real life problems involving computationally expensive FE simulations.

STAND has been successfully employed in crashworthiness reliability analysis of the welded sheet metal car components. Due to manufacturing imperfections and fatigue deterioration significant number of spot welds may be missing in operational vehicle. This effect may significantly reduce strength of an important car component such as thin-walled s-rail. A great number of joints makes precise stochastic modeling of spot welds unreasonable. Thus, it was proposed to model the uncertainty of element connections by adding a random noise to LSF. However reliability analysis problem defined in this way is very difficult to solve. This is not only due to difficulties with assessing failure probability for noisy LSFs, but also due to time consuming FE analysis that is involved. An effective method for solving this class of problems was implemented in STAND, see [4]. In the considered example there were assumed 8 random variables corresponding to metal sheet thicknesses, the initial velocity of impacting mass and material parameters. The failure event was defined as insufficient energy absorption.

The second example demonstrates capabilities of STAND integration with third party FE analysis programs. Influence of geometrical imperfections on the buckling behavior of a cylindrical shell presented in the ABAQUS example problems manual (example 1.2.6.) has been studied. In the original example imperfections are modeled using a linear combination of the eigenvectors of the linear buckling problem. For the purpose of stochastic analysis coefficients of the linear combination are assumed to be random variables. Then it was possible to estimate probability that the buckling load of the investigated cylindrical shell is lower than an assumed value. Application of STAND to the modified example problem of widely used FE code clearly illustrates its integration possibilities.

6. References

- [1] M.F. Pellissetti, G.I. Schueller (2006). On general purpose software in structural reliability – an overview. *Structural Safety*, **28**, 3–16.
- [2] G.I. Schueller and H.J. Pradlwarter (2006). Computational stochastic structural analysis COSSAN – a software tool, *Structural Safety*, **28**, 68–82.
- [3] Y.-T. Wu, Y. Shin, R.H. Sues, A. Cesare~Mark (2006). Probabilistic function evaluation system (PROFES) for reliability-based design, *Structural Safety*, **28**, 164–195.
- [4] R. Stocki, P. Tuzowski, J. Knabel. Reliability analysis of a crushed thin-walled s-rail accounting for random spot weld failures, *International Journal of Crashworthiness*, in print
- [5] M. Liefvendahl, R. Stocki (2003). A study on algorithms for optimization of Latin hypercubes. *Journal of Statistical Planning and Inference*, **136**, 3231-3247.

**AN ELASTIC CUBE SUBJECTED TO ANTI-SYMMETRICAL PRESSURE LOADING.
EXACT 3D ANALYTICAL FORMULAE VERSUS NUMERICAL SOLUTIONS
BASED ON MESHFREE METHOD**

S. Czarnecki

*Division of Applied Computer Science in Civil Engineering, Faculty of Civil Engineering,
Warsaw University of Technology, Warsaw, Poland*

1. Introduction

Many Finite Element Method (FEM) solvers do not accurately predict stresses, particularly at interfaces of the elements due to the piecewise continuous nature of the displacement field assumed in FEM formulation. Moreover, the well known difficulties in adaptive analysis using FEM (especially in 3D problems) justify attempts to develop alternative numerical methods, e.g. Mesh Free Methods (MFree). This paper refers to the two versions of the MFree algorithms, namely Radial Point Interpolation Method (RPIM) and Moving Least Squares (MLS) method. The hitherto existing versions of 3D MFree suffer from the drawbacks like relatively small number of numerical examples of quantitative analysis (e.g. lack of comparisons of the numerical solutions with the exact 3D solutions) and lack of the fast search procedures in constructing the influence (or support) domains with irregular and non-convex boundaries. The aim of the present paper is to put forward an improved version of the Element Free Galerkin (EFG) formulation for the numerical approximation of the 3D boundary value problems of linear elasticity. The monomial basis functions from the Pascal pyramid used with the radial basis functions in RPIM and with the non-singular weight functions in MLS method are implemented in computing the shape functions and their derivatives. Well known properties, advantages and disadvantages of both the formulations are discussed in many papers and monographs (see e.g. [2], [4]) but most of the work related to the development of EFG has been focused on two-dimensional applications. On the other hand, the numerical results in three-dimensional EFG method (very often coupled with FEM) are rarely presented (see e.g. [1]). In the present paper, for benchmarking purposes, three various numerical solutions for a linear-elastic and isotropic cube subject to an anti-symmetrical pressure loading are shown and compared. First and second numerical result are obtained by RPIM and MLS methods. The Kronecker delta function property in RPIM allows a direct imposition of essential boundary conditions, but the use of non-singular weight functions in MLS approximation does not allow for a direct imposition of essential boundary conditions, hence EFG formulation with Lagrange Multipliers is implemented. Third solution is shown in the analytical form found by G. Jemielita [3].

2. Numerical and analytical solution

Consider a 3D elastic body $\Omega \subset \mathbb{R}^3$. In the meshfree method used, the global interpolation (in RPIM) and the global approximation (in MLS) $\mathbf{u}^h = \mathbf{u}^h(\mathbf{x}) = [u_x^h(\mathbf{x}), u_y^h(\mathbf{x}), u_z^h(\mathbf{x})]^T$ ($\mathbf{x} = [x, y, z]^T \in \Omega$) of the displacement field are calculated from the formula $\mathbf{u}^h(\mathbf{x}) = \sum_I \Phi_I(\mathbf{x}) \mathbf{u}_I$ where $\Phi_I = \Phi_I(\mathbf{x})$ is the diagonal matrix of the shape functions corresponding $N = N(\mathbf{x})$ nodes in the support domain of the point \mathbf{x} and \mathbf{u}_I is the vector of the displacement parameters of the node I . The exact analytical formula for the displacement field $\mathbf{u} = \mathbf{u}(\mathbf{x}) = [u_x(\mathbf{x}), u_y(\mathbf{x}), u_z(\mathbf{x})]^T$ of the elastic isotropic cube $a \times b \times h$ subject to the loading anti-symmetrical with respect to the middle

plane $z = 0$ load $\mathbf{t} = \mathbf{t}(\mathbf{x}) = [t_x(\mathbf{x}), t_y(\mathbf{x}), t_z(\mathbf{x})]^T$ applied on the top and bottom free sides can be written as (see [3])

$$(1) \quad u_x(\mathbf{x}) = \left[\alpha_1 A_1 z \cosh(pz) + B_1^1 \sinh(pz) \right] \sin\left(\alpha_1 x + \frac{\pi}{2}\right) \sin(\alpha_2 y)$$

$$(2) \quad u_y(\mathbf{x}) = \left[\alpha_2 A_1 z \cosh(pz) + B_1^2 \sinh(pz) \right] \sin(\alpha_1 x) \sin\left(\alpha_2 y + \frac{\pi}{2}\right)$$

$$(3) \quad u_z(\mathbf{x}) = \left[p A_1 z \sinh(pz) + B_1^3 \cosh(pz) \right] \sin(\alpha_1 x) \sin(\alpha_2 y)$$

where $t_x = t_y = 0$, $t_z(x, y, h/2) = t_z(x, y, -h/2) = 0.5 q \sin(\pi x/a) \sin(\pi y/b)$. In the above three expressions (1), (2), (3) all coefficients depend (in a rather complicated way) on the known components a , b , h defining the sizes of the cube, material constants E , ν (Young modulus, Poisson ratio) and load parameter q . The cube is simply supported on the remaining (unloaded) four vertical boundary planes along z and x axes or z and y axes. The material parameters used in analysis are: $E = 3.0 \cdot 10^6 [N/m^2]$, $\nu = 0.3$. A uniform nodal distribution with the total number of nodes equal to 1241 and with the $8 \times 8 \times 8 = 512$ background mesh of hexahedron cells for integration is employed. The basis functions of quadratic order from the Pascal pyramid are used. The original search procedure guarantees that exactly 15 from among at least 20 nodes are visible from each integration point. Dimensionless lengths of the sides of the support domain in all x , y and z directions are set as equal to 3 and the 6-point Gauss integration scheme is adopted. The value of the load parameter $q = 1.0 \cdot 10^6 [N/m^2]$. The length a , width b and height h of the cube are equal to 0.9 [m].

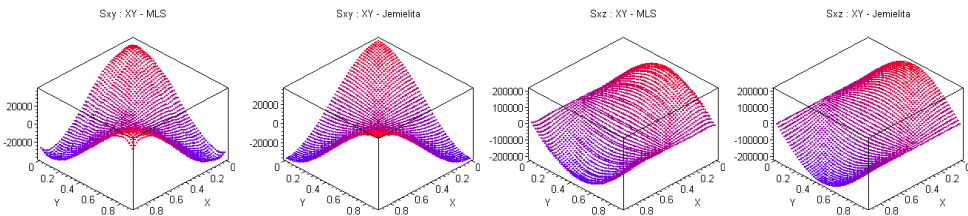


Fig. 1. Shear stress distributions σ_{xy} , σ_{xz} through a cross section $z = 0.225$ [m] of the square block – MLS (first and third figs) and exact analytical solution (second and fourth figs).

The proposed version of the EFG formulation clearly demonstrates robustness of the algorithm and its ability to produce accurate and numerically reliable results.

Acknowledgement. The paper was prepared within the Research Grant no T07A 038 30.

3. References

- [1] W. Barry, S. Saigal (1999). A Three-Dimensional Element-Free Galerkin Elastic and Elastoplastic Formulation, *Int. J. Numer. Meth. Engng.* **46**, 671–693.
- [2] T. Belytschko, Y. Krongauz, D. Organ, M. Fleming, P. Krysl (1996). Meshless methods: An overview and recent developments, *Comput. Methods. Appl. Mech. Engng.*, **139**, 3–47.
- [3] G. Jemielita (1982). Thick plates with applied shear traction, *not published* (in Polish).
- [4] G.R. Liu (2003). *Mesh Free Methods. Moving Beyond the finite Element Method*, CRC Press LLC.

CONVERGENCE BEHAVIOUR FOR KPT FINITE ELEMENTS

Y. M. Abushawashi¹, S.H. Eshtewi² and A.M. Othman³
^{1,2} Mechanical Engineering Dept and ³ Civil Engineering Dept.
 Al-Fateh University/ Tripoli, Libya
 E: mail- seshtewi@hotmail.com

1. Abstract

Triangular elements are more versatile than rectangular elements; they can be used for the analysis of plates having various boundary shapes. The use of triangular finite elements for the solution of plate bending under Kirchhoff assumptions is considered. An investigation about the convergence behaviour of two KPT elements representing the nature of conformal and non-conformal elements performed.

The KPT elements chosen to show the influence of increase the nodal field variables and the interpolation function order to obtain the continuity requirement for C^1 problems. The numerical examples performed in this work to clarify the advantage of using higher order element in terms of the rate of convergence compared with the lower order element.

2. Introduction

For the well known plate bending governing equation we can apply the first step of the Galerkin formulation approach by minimizing the residual R .

$$(1) \quad R = \frac{\partial Q}{\partial x} + \frac{\partial Q}{\partial y} + p_o$$

$$(2) \quad \int_A R \cdot N_i \cdot dA = 0$$

After substituting element trial solution, the general expression can be written in a matrix form as: $[K]\{w\} = \{F\}$ Where

$$(3) \quad K_{ij} = \int_A D \left[\frac{\partial^2 N_i}{\partial x^2} \frac{\partial^2 N_j}{\partial x^2} + \nu \frac{\partial^2 N_i}{\partial x^2} \frac{\partial^2 N_j}{\partial y^2} + \frac{\partial^2 N_i}{\partial y^2} \frac{\partial^2 N_j}{\partial y^2} + \nu \frac{\partial^2 N_i}{\partial y^2} \frac{\partial^2 N_j}{\partial x^2} + 2(1-\nu) \frac{\partial^2 N_i}{\partial x \partial y} \frac{\partial^2 N_j}{\partial x \partial y} \right] dA$$

$$F_i = - \oint_S N_i Q_n ds + \oint_S M_n \frac{\partial N_i}{\partial n} ds - \oint_S N_i \frac{\partial M_{ms}}{\partial s} ds + [N_i M_{ms}]_s - \int_A N_i p dA$$

The parent element will have its own coordinate system (ξ, η) , to convert the upper integral forms to this coordinate system we write:

$$(4) \quad dA = Jac \cdot d\xi \cdot d\eta \quad \text{Where } Jac \text{ is the Jacobian determinant.}$$

As we notice the plate bending element still capable to represent the element field variables with satisfactory amount of accuracy even for the elements of non-conforming type. This element is one of the first elements where used for plate bending problems and it shows a good convergence results for three nodes nine DOF KPT element.

Note that no complete polynomial available to represent nine degrees of freedom, the complete cubic polynomial will have ten unknowns (P_3). One of the choices we have is that one of the terms $\xi^2 \eta$ or $\xi \eta^2$ is omitted. In this case we use the following polynomial for our displacement interpolation weighing functions.

$$(5) \quad N = a_1 + a_2 \xi + a_3 \eta + a_4 \xi^2 + a_5 \xi \eta + a_6 \eta^2 + a_7 \xi^3 + a_8 \xi^2 \eta + a_9 \eta^3$$

To obtain the nine unknowns ($a_i, i=1, 2, \dots, 9$) we need to define the condition of the nodal weighing values (N_i).

Three nodes eighteen DOF KPT element (six degrees of freedom per node) is one of the conformal plate bending elements. The compatibility requirements for CI problems require the above six field variables to be continuous at the corner nodes. Here we meet the same complexity that we have seen in the nine DOF triangle element, where also there are no complete polynomials available to represent eighteen DOF. The complete quadric polynomial (P_4) has only fifteen terms.

The following suggested polynomial is complete up to terms of fourth order and contains three terms of fifth order. The last three terms are chosen to force the normal derivative on each side to be cubic in ξ and η , on other hand the parabolic variation of the normal slope is not uniquely defined by the two end nodal values and hence resulted in the non-conformity [4].

$$(6) \quad N = a_1 + a_2\xi + a_3\eta + a_4\xi^2 + a_5\xi\eta + a_6\eta^2 + a_7\xi^3 + a_8\xi^2\eta + a_9\xi\eta^2 + a_{10}\eta^3 + a_{11}\xi^4 + a_{12}\xi^3\eta + a_{13}\xi^2\eta^2 + a_{14}\xi\eta^3 + a_{15}\eta^4 + a_{16}(\xi^5 - 5\xi^3\eta^2) + a_{17}(\xi^2\eta^3 - \xi^3\eta^2) + a_{18}(\eta^5 - 5\xi^2\eta^3)$$

3. Numerical Results

The numerical results for the simply supported and clamped square plates where obtained for deferent number of elements, the plate geometry, physical properties and uniformly distributed load are chosen to be within the *Kirchhoff* assumptions. The plates are $1m \times 1m \times 13mm$, $E=200GPa$ and $\nu=0.3$ under uniformly distributed load of $0.1 MPa$. The maximum deflection results of the first element insures the convergence as the number of elements increasing in the simply supported and clamped plates, this is also true for the second element.

The figure shows that in terms of both total degrees of freedom and number of elements the higher order element presents better performance and convergence rate for the simply supported plate and for other cases.

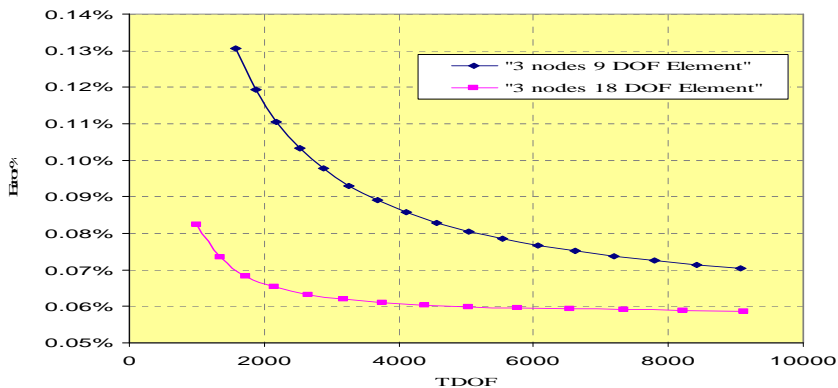


Figure 1. Simply Supported Plate Results (TDOF vs Error %)

4. References

- [1].S. S. Rao (1999), "The Finite Element Method in Engineering", Third edition, Butterworth Heinemann.
- [2].K. Bathe (1996), "Finite Element Procedures", Prentice Hall New Jersey.
- [3].K. C. Rocky, H. R. Evans, D. W. Griffiths and D. A. Nethercot (1990), "The Finite Element Method, A Basic Introduction", Crosby Lockwood Staples, London.
- [4].G. Dhatt. and G. Touzot (1984), "The Finite Element Method Displayed", John Wiley and Sons.

ANN APPROACH FOR MODELLING ORTHOGONAL CUTTING

I.M. González, H. Miguélez, A. Muñoz

Department of Mechanical Engineering, Universidad Carlos III, Madrid, Spain

1. Introduction

Machining is a complex process involving very large strains and strain-rates, which cause large temperature increase. Since most process variables are difficult to measure, analytical and numerical modelling of chip formation are versatile and reliable approaches to obtain local information on some variables on the workpiece and the cutting tool [1].

Recently, artificial neural networks (ANN) have been used to simulate cutting, since this technique is fairly robust and frequently converges to the desired solution. The main drawback of ANN the need of large data points for training and validation. [2] Using results obtained from validated numerical models to train the network, diminishes the experimental work significantly. Finite element analysis has played an important role in simulating and understanding the metal cutting process by having an insight look at what is going on during cutting, which is hard to achieve by experimental or analytical methods.

The aim of this paper is to simulate cutting with a radial basis function network (RBFN). This is not commonly used in cutting simulation, although it has some advantages when compared with multilayer perceptron (MLP) neural networks. The neural network is trained with results obtained from numerical model, mainly cutting forces and shear angle. This work presents briefly the numerical model used in the generation of data, the characteristics of the ANN approach and its training and validation. Results showed the ability of the neural network to predict accurately cutting parameters.

2. Numerical model

A plane strain A.L.E. model was developed in ABAQUS/Explicit. A thermo-mechanical coupled analysis was developed, with CPE4RT element type (see ABAQUS manual). These are plane strain, quadrilateral, linearly interpolated, and thermally coupled elements with automatic hourglass control and reduced integration, for A.L.E. formulation. The workpiece material was modelled using the Johnson-Cook (JC) constitutive model. The physical properties and the constants of the JC model for the work-piece material (AISI 316L) and the properties of tool material (Kennametal K313) have been found in recent work in literature [3]. The tool is fixed and the cutting speed is applied to the workpiece. Cutting takes place in plane strain conditions and continuous chip formation are assumed. Details of the A.L.E. model are shown in [4].

3. Neural network

Simulation of cutting processes is mostly achieved with multilayer perceptron (MLP) neural networks. However, MLP networks suffer from local minima problems and long computation time. The radial basis function network (RBFN) is an alternative network that has been reported to be faster and at times more accurate, as compared to a MLP neural network [5].

RBFN is a feed-forward network that is often used as a multidimensional interpolation technique. A RBFN is a local network whereas the MLP performs a global mapping. The basic architecture of the RBFN has three layers. The input layer composed of the vector of input variables. The hidden layer transforms the data from the input space by applying a non-linear function. Frequently, a Gaussian function is used. Finally, the output layer that applies a linear combination of the hidden layer outputs.

A common learning strategy for RBFN is the hybrid learning. However, this procedure has an important drawback because the radial basis centers are arbitrary selected. Here, the orthogonal

least square (OLS) algorithm will be used as learning method (see, [6]). This algorithm allows selecting a suitable center from a large set of candidates. The learning and validation steps will be performed by using a cross-validation (CV) technique. This technique allows selecting the best model when the amount of data is limited. The CV is a method for estimating a generalization error based on resampling. In CV the data set is split into two parts. The first part is denoted as training set and is used to fitting the model. The second part is denoted as validation set and is used to measure how well the model fits this new data, that is, to compute the prediction error. The best model is the one with the smallest average prediction error, computed based on all (or some) different ways of data splitting. Different types of CV have been proposed in the literature. In this work, the Monte Carlo cross-validation (MCCV) proposed by [7], is used.

4. Results

The input variables of the model are the rake angle X_1 and the friction coefficient, X_2 . The output variables are the cutting force, Y_1 , thrust force, Y_2 and shear angle, Y_3 . The values of the input variables are $X_1 = -6, 0, 6, 8$ and $X_2 = 0, 0.5, 0.1, \dots, 0.4$. A set of $n = 30$ multivariate observations are used. From this set, a sample of $n_v = 5$ is extracted to be used as validation subset. Then, the learning subset has $n_l = 25$ observations. For each candidate model, a total of $B = 10000$ subsets of n_v are randomly extracted. The OLS method is used as learning algorithm.

The results obtained shows that the best model is a RBFN with 4 hidden units. The total average mean square error using the validation subsets is $MSE = 0.0011$. The average mean square error for each predicted variable is: $MSE(Y_1) = 0.0026$, $MSE(Y_2) = 0.0006$ and $MSE(Y_3) = 0.0002$.

6. Acknowledgments

The authors acknowledge to the Ministry of Science and Technology of Spain, the financial support obtained for this work with the Project CYCIT DPI2005-08018

7. References

- [1] H. Miguélez, R. Zaera, A. Rusinek, A. Moufki, A. Molinari, Numerical modelling of orthogonal cutting: influence of cutting conditions and separation criterion, *Journal de Physique IV*, **134** (2006) 417-422.
- [2] D. Umbrello, G. Ambrogio, L. Filice, R. Shivpuri, An ANN approach for predicting subsurface residual stresses, and the desired cutting conditions during hard turning, *Journal of Materials Processing Technology* **189** (2007) 143–152
- [3] M. Nasr, E.G. Ng, M.A. Elbestawi, Modelling the effects of tool-edge radius on residual stresses when orthogonal cutting AISI316L, *International Journal of Machine Tools & Manufacture*, **47**, (2007) 401–411.
- [4] M.H. Miguélez, R. Zaera, A. Molinari, R. Cheriguene, A. Rusinek, Residual stresses in orthogonal cutting of metals: the effect of thermomechanical coupling parameters and of friction, *Journal of Materials Processing Technology*, (submitted 2008)
- [5] S. Chen, C. Cowan and P (1991). Grant. Orthogonal Least Squares Learning Algorithm for radial Basis Function Networks, *IEEE Trans. Neur. Netw.*, **2**, 302-309.
- [6] J. Shao (2003). Linear Model Selection by Cross-Validation, *J. Amer. Stat. Assoc.*, **88**, 486-494.
- [7] S. Haykin (2007). *Neural networks: A comprehensive foundation*, 7 ed. Prentice Hall, Harlow.

CONTACT STRESSES - MODELS AND METHODS OF COMPUTATIONS

A. Zmitrowicz

Institute of Fluid-Flow Machinery, Gdańsk, Poland

1. Introduction

Contact stresses are forces acting between contacting bodies or between the body and a foundation. They are identified as normal pressure and tangential traction. A potential contact area between two bodies can be divided into the following states: separation (non-contact), sticking and slipping. In the most cases the contact stresses, the size of the contact region, the distribution of contact zones of slip and adhesion cannot be predicted a priori.

There has been little progress toward general models for contact phenomena. The reason for this lies in the significant complexity of the phenomenon. Descriptions applied in classical mechanics are very simple and they do not include present experimental facts. The purpose of this contribution is to review general and simplified forms of constitutive laws of normal traction and friction, and to review computational methods used in calculations of the normal pressure and friction [5]. They are described in the framework of continuum mechanics, FEM and other methods.

2. The normal traction

Mechanics considers two models of mechanical interactions i.e. forces and analytical relations describing restrictions of deformations, i.e. geometrical and kinematical constraints. Unilateral contact constraints are as follows: two contacting bodies cannot penetrate each other, cannot pull on each other and are either separated or pressed on each other (so-called Signorini conditions). To reduce the computational effort for contact pressure computation, in some problems, contact stresses are formulated directly from kinematical considerations. The contact conditions are frequently modeled by nonlinear springs (and viscous dampers) which connect solids (e.g. Winkler-type contact laws). Such model may, however, correspond to severely ill-conditioned system of motion equations since very stiff springs must then be used to simulate no-slip and no-clearance gap conditions. Other methods are following: stiffness approach, flexibility approach, normal compliance, normal damped response, bond or gap elements, interfaces materials, etc.

3. The tangential traction

The tangential components of the contact traction (shear traction) are governed by friction laws. Friction forces depend on motions of the bodies, and they are not known in advance. For vanishing sliding velocity (case of sticking), the tangential traction is a resting force governed by the equation of equilibrium. The law of Amontons and Coulomb is commonly taken as the friction law in the case of slipping.

4. Development of ideas and modeling of friction

It should be noticed that many identically significant reasons have an influence on friction. We take into account the following parameters: normal pressure, sliding velocity, surface temperature, time of contact, surface roughness, presence of wear debris, extreme environments. There are materials and ranges of the contact parameters, especially for their extreme values, whose constitutive relations for friction should be considered as various nonlinear functions with respect to the parameters. Friction plays a crucial role for many mechanical systems. In special applications, more sophisticated models are desirable to accurately model the contact phenomena, e.g. in

vibrating systems, in materials processing, in rubbers and polymers, in geomechanics, in bioengineering, in living systems.

The genesis of friction is not clearly known. Mechanical and atomistic theories of the origins of friction are used at present, and friction modeling is based on observations from macro- to micro-scale. In the subject literature, there are phenomenological, micromechanical, atomic-level and multi-scale friction models. In [2,3,4] a family of non-classical friction laws have been proposed. These friction laws include anisotropy and heterogeneity effects. Anisotropy means that there are distinguished directions of sliding. Heterogeneity means that there are distinguished points at the contact surface. Kinematics of sliding can initiate microstructural and frictional changes in the surface and near-surface material (self-organization and structural adaptation). As in continuum mechanics the central topic for the friction constitutive models are conditions of material objectivity, the Second Law of Thermodynamics and conditions of symmetry.

5. Predictions of contact stresses

Different approaches can be applied to calculations of contact stresses and to satisfaction of kinematic contact constraints on displacements of the contacting bodies. Since both forces and displacements in the contact area are unknown, additional relations are needed to describe them. Powerful formulations of problems with constraints on certain solution variables (e.g. unilateral and contact problems) can be obtained by utilization of the classical variational formulations and the following techniques: Lagrange multipliers, penalty function, perturbed Lagrangian method, augmented Lagrangian method [1]. They are so called active strategies. These methods are designed to fulfill the constraint equations in normal direction to the contact area. For the tangential part we need constitutive equations. Most standard finite element codes use two active strategies i.e. the Lagrange multipliers and the penalty method [1].

6. Adhesion and impacts mechanics

Adhesion is the phenomenon that occurs when a normal tensile force must be done to separate two surfaces from contact (after being compressed together). The adhesive normal force depends on the initially normal pressure and a coefficient of adhesion (the law of Rabinowicz and Frémond). Impacts occur if the solids come into contact among each other or against the foundation. Short-time impacts, one can describe using an impulse model for impacts. The colliding solids change their velocities discontinuously (the law of Newton and Poisson). Wave theory is appropriate for the description of collisions against flexible structures.

7. References

- [1] P. Wriggers (2002). *Computational Contact Mechanics*, John Wiley & Sons Ltd., Chichester.
- [2] A. Zmitrowicz (2003). Glaciers and laws of friction and sliding, *Acta Mechanica*, **166** (1-4), 185-206.
- [3] A. Zmitrowicz (2006). Models of kinematics dependent anisotropic and heterogenous friction, *International Journal of Solids and Structures*, **43** (14-15), 4407-4451.
- [4] A. Zmitrowicz (2006). Sliding path curvature dependent friction and wear, In *Analysis and Simulation of Contact Problems*, Series: Lecture Notes in Applied and Computational Mechanics, Vol. 27, P.Wriggers, U. Nackenhorst (eds), Springer, Berlin, Heidelberg, 369-370.
- [5] A. Zmitrowicz . Contact stresses: a review of models and methods of computations, *Journal of Theoretical and Applied Mechanics*, in press.

NUMERICAL INVESTIGATION OF SOME STEADY STATE WEAR PROBLEMS

I. Páczelt¹ and Z. Mróz²

¹ University of Miskolc, Miskolc, Hungary

² Institute of Fundamental Technological Research, Warsaw, Poland

1. Introduction

In many practical industrial applications it is very important to predict the form of wear shape, contact stresses. Usually, the contact shape evolution is simulated numerically by integrating the wear rate expressed in terms of relative slip velocity and contact pressure. A steady state is then predicted by the incremental integration procedure with account for contact shape and pressure variation. However, much more effective procedure can be developed by postulating minimization of the contact response functional. It was shown in the previous our papers [1-2] that the total wear dissipation power at the contact interface provides the steady wear regimes by applying the stationary conditions. In the later case the stationary of the functional gives the contact stress distribution and the rate of the rigid body movement.

In the work by Páczelt and Mróz [1-2] the optimal shapes generated by wear process were analyzed by postulating minimization of the wear dissipation power. It was shown that the contact shape evolution tends to a steady state satisfying the minimum principle of the wear dissipation rate.

The specific modified Archard wear rule is assumed for wear rate in normal direction on contact surface. Very important, that in general contact conditions the vector of wear rate is not normal to the contact surface and has tangential component. A fundamental assumption is now introduced, namely, *at the steady state the wear rate vector is collinear with the rigid body wear velocity of body which has rigid body like displacement*. It is demonstrated that the wear dissipation power at the contact surface is minimal in the steady state of the wear process and in many cases corresponds to the uniform wear rate. In the normal direction the Signorini contact conditions are valid. The Coulomb dry friction models are investigated. The temperature effects and heat generated at the frictional interface in our investigation is considered.

It is assumed that the displacements and deformations are small, the material of the contacting bodies are elastic. The discretization of the contacting bodies was performed by the displacement based on p -version of finite elements [2] assuring fast convergence of the numerical process and accurate specification of geometry for shape optimization.

2. Contact optimizations problems

Without the restriction of generality, let us consider the contact problem of two elastic bodies B_α , ($\alpha=1,2$) with the usual boundary and loading conditions. The boundary portion $S_c^{(\alpha)}$ will be called the potential zone of contact. In this part of the bodies the shape may be modified. In the normal direction the Signorini contact conditions are valid. The Coulomb dry friction models are investigated. In the analysis of wear problem, usually the elastic portion of relative tangent velocity is much smaller than the rigid body motion induced velocity, thus the effect of elastic component of tangent relative velocity can be neglected in the wear analysis. The temperature effects and heat generated at the frictional interface in our investigation is considered [3]. The contact conditions are checked at the Lobatto integration points of the contact elements during the solution process.

Assume the isotropic wear rule in the form [1]

$$\dot{w}_i = \beta_i (\tau_n)^{b_i} \|\dot{\mathbf{u}}_\tau\|^{a_i} = \beta_i (\mu p_n)^{b_i} \|\dot{\mathbf{u}}_\tau\|^{a_i} = \beta_i (\mu p_n)^{b_i} v_r^{a_i} = \tilde{\beta}_i p_n^{b_i} v_r^{a_i}, \quad i=1,2$$

The material parameters β_i, a_i, b_i specify the wear rates of two contacting bodies and $\tilde{\beta}_i = \beta_i \mu^{b_i}$, $v_r = \|\dot{\mathbf{u}}_r\|$ is the relative velocity between two bodies, μ is the coefficient of friction. In general contact conditions the vector of wear rate is not normal to the contact surface and has tangential components. This vector specifies the shape transformation and tangential motion of the worn material. To analyze this transformation, let us define first the contact stress of interaction of bodies B_1 and B_2 , thus

$$\mathbf{p} = \mathbf{p}_1 = -\mathbf{p}_2 = -p_n(\mathbf{n}_c \pm \mu \mathbf{e}_{\tau_1}) - \mu_d p_n \mathbf{e}_{\tau_2} = -p_n \tilde{\mathbf{n}}_c,$$

where μ is the friction coefficient specifying the shear stress in sliding direction and μ_d is the friction coefficient associated with transverse wear velocity. The unit vectors $\mathbf{e}_{\tau_1}, \mathbf{e}_{\tau_2}, \mathbf{n}_c$ constitute the local reference triad on S_c . Here \mathbf{n}_c is the unit normal to the contact surface of body B_1 , \mathbf{e}_{τ_1} is the tangent unit vector coaxial with the sliding velocity and \mathbf{e}_{τ_2} is the transverse tangent unit vector.

A fundamental assumption is now introduced, namely, *at the steady state the wear rate vector is collinear with the rigid body wear velocity of B_1* , so that

$$\dot{\mathbf{w}}_R = \dot{\mathbf{w}}_{1,R} + \dot{\mathbf{w}}_{2,R} = \dot{w}_R \mathbf{e}_R, \text{ where } \mathbf{e}_R = \frac{\dot{\lambda}_F + \dot{\lambda}_M \times \Delta \mathbf{r}}{\|\dot{\lambda}_F + \dot{\lambda}_M \times \Delta \mathbf{r}\|}.$$

The generalized wear dissipation power for the case of wear of two bodies

$$D_w^{(q)} = \sum_{i=1}^2 \left(\int_{S_c} (\mathbf{p}_i \cdot \dot{\mathbf{w}}_i)^q dS \right)^{1/q} = \sum_{i=1}^2 C_i^{1/q},$$

where q is the control parameter, usually $q \geq 0$. Assume that the contact pressure $p_n(\mathbf{x})$ and the friction induced shear stress $\tau_n = \mu p_n(\mathbf{x})$ satisfy the global equilibrium conditions for the body B_1 , so we have $\mathbf{f} = \mathbf{0}$, $\mathbf{m} = \mathbf{0}$. The Lagrangian functional at $b = b_1 = b_2$ is

$$L_{D_w}^{(q)} = L_{D_w}^{(q)}(p_n, \dot{\lambda}_F, \dot{\lambda}_M) = D_w^{(q)}(p_n) + (b+1) \dot{\lambda}_F \cdot \mathbf{f} + (b+1) \dot{\lambda}_M \cdot \mathbf{m}$$

and satisfying the stationary condition of the Lagrange functional, the contact pressure distribution has the next form

$$p_n = \left(\frac{\dot{\lambda}_F \cdot \tilde{\mathbf{n}}_c + (\dot{\lambda}_M \times \Delta \mathbf{r}) \cdot \tilde{\mathbf{n}}_c}{\left[(\tilde{\beta}_1 v_r^{a_1})^q C_1^{\frac{1-q}{q}} + (\tilde{\beta}_2 v_r^{a_2})^q C_2^{\frac{1-q}{q}} \right]} (1 \mp \mu \tan \chi)^{-q} \right)^{\frac{1}{(b+1)q-1}}$$

where χ is the angle between \mathbf{n}_c and \mathbf{e}_R . The given non-linear equations can be solved by applying Newton-Raphson technique. Minimization of this functional with equilibrium constraints for body B_1 at $q=1$ gives results for steady state wear process of arbitrary shape of contact surface

Some specific examples will be presented. It is shown that the thermal distortion effects essentially the optimal contact shape associated with the steady state

3. References

- [1] I. Páczelt and Z. Mróz (2005). On optimal contact shapes generated by wear, *Int. J. Numer. Meth. Engng.* **63**, 1310-1347.
- [2] B. Szabó and I. Babuska (1991). Finite element analysis, Wiley-Interscience, New York.
- [3] P. Ireman, A. Klarbring and N. Strömberg (2002). Finite element algorithms for thermoelastic wear problems, *European Journal of Mechanics A/Solids* **21**, 423-440.
- [4] I.G. Goryacheva and M.H. Dobuchin (1988). Contact problems in tribology (in Russian), Mashinostroenie, Moscow.
- [5] P. Wriggers and C. Mieke (1994). Contact constraints within thermomechanical analysis - a finite element model. *Comput. Methods Appl. Mech. Engng* **113**, 301-319.

PHYSICAL AND NUMERICAL SIMULATION OF FORGING OF Cu-Cr ALLOY

V. Pidvysotsky¹, R. Kuziak¹ and M. Pietrzyk²

¹ Institute for Metallurgy, Gliwice, Poland

² Akademia Górniczo-Hutnicza, Kraków, Poland

1. Introduction

Development of the hot forging technology for copper alloys, which are characterized by high mechanical properties, is a goal of research in several laboratories. Repeatability of properties is the advantage of these alloys. Cu-Cr alloys are characterized by particularly high exploitation properties for a variety of applications combined with dependence of electrical conductivity on applied heat treatment. Various methods of thermomechanical processes are possible for this alloy and quite different properties are obtained depending on the parameters of this process. Thus, the technology design for Cu-Cr forgings has to combine obtaining required shape with control of microstructure and properties. The technology design is usually supported by physical and numerical simulations. This work is focused on application of both kinds of simulations.

2. Rheological model

Accuracy of numerical simulations depends on the correctness of description of boundary conditions and material properties. The latter problem is considered in this work. Although the rheological models are well explored for various steels, there is still lack of models for copper alloys. Thus, the prime objective of this work is performing uniaxial compression tests for the Cu-Cr alloy at temperatures 500-1000°C and strain rates 0.1-100 s⁻¹, application of the inverse analysis [1] to the interpretation of results of those tests and development of the rheological model for the applicable for the investigated range of parameters. Three states of the alloy, yielding different mechanical response during deformation, were considered. A) samples after super saturation annealing at 1000°C; B,C) samples after hot extrusion, followed by different preheating processes: B) heating to the test temperature, maintaining for 120 s and deformation; C) heating to 950°C, maintaining for 300 s, cooling to the test temperature, maintaining for 60 s and deformation. Inverse analysis yielded the flow stress independent of the influence of such disturbances as friction or deformation heating for all investigated cases. Analysis of results showed [2] that oscillations in the material response occur for low Zener-Hollomon parameters for samples B and C.

Microstructure of the samples was investigated prior to deformation and after each test. Correlation between flow stress and microstructure was determined, see selected results in Fig. 1. Investigation of the deformed samples has shown that their structure depends strongly on the initial state of the material. Under the same deformation conditions, as extruded samples heated to the test temperature were subject to dynamic recrystallization (DRX) during deformation. Their structure was fully recrystallized with finer grains while lowering deformation temperature and increasing strain rate. In the other specimens, the DRX was not easily initiated during deformation below 900°C and their microstructure was partly recrystallized. The solute drag effect of Cr atoms exerted on the recrystallization nuclei boundaries is a possible reason of different behaviour of the samples. Chromium effect on the stacking fault energy is an alternative reason. In the extruded samples all chromium precipitated out of the solution. The precipitates were relatively large and they did not affect the recrystallization process substantially. Thus, the super-saturated samples exhibit the greatest effect of Cr on the recrystallization. Samples reheated to 950°C prior the deformation show the intermediate effect, and the effect of Cr is almost negligible in the extruded samples. Flow stress models accounting for the microstructure were determined using inverse analysis.

3. Modelling industrial forging process

FE code with the developed flow stress model was used for simulation and analysis of the industrial forging with following parameters: stock diameter 60 mm, mass of the forging 1.2 kg and die 2000 kg, initial temperature 900°C, die energy 70 kJ, die displacement 850 mm, die velocity 5 m/s. View of the die and the preform is shown in Fig. 2. Various variants of the process were considered. Selected results for the material after extrusion (variant B) only are discussed below. One example showing how simulation allows to eliminate faults is presented.

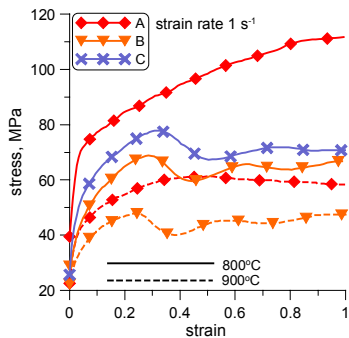


Figure 1. Flow stress for different initial state of the samples.

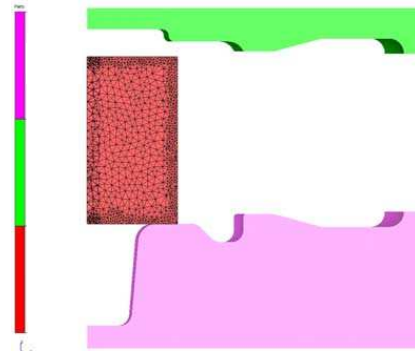


Figure 2. View of the die and the preform.

Simulation of the one stage closed die forging has shown that fault occurs at the surface. Therefore, upsetting is performed first and is followed by the forging. Three reductions in upsetting (10, 15 and 20 mm) are considered. Forging after upsetting with 10 mm reduction resulted in fault of the product (Figure 3a). Under filling of the die was obtained when 20 mm reduction was applied in upsetting (Figure 3c). Proper forging was obtained for 15 mm reduction in upsetting (Figure 3b).

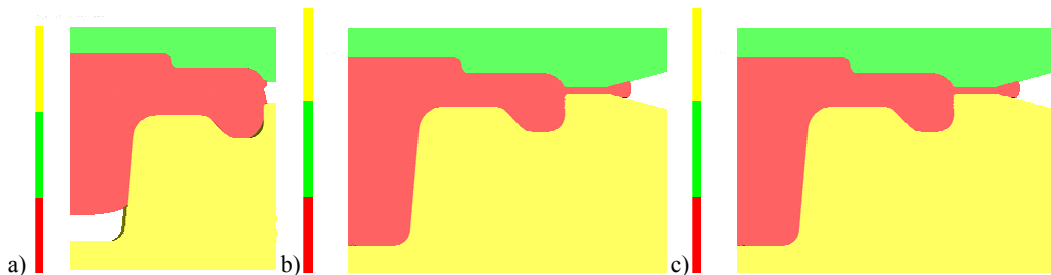


Figure 3. Die filling for various reductions in upsetting: a), 10 mm, b) 15 mm, c) 20 mm.

4. Conclusions

Rheological model of the CuCr alloy accounting for the state of microstructure was developed. Various variants of the industrial forging were simulated and the capability of the model to support technology is shown. 15 mm reduction in upsetting before forging is selected in the considered case as giving the best quality of the forging.

5. References

- [1] D. Szeliga, J. Gawad, M. Pietrzyk, Inverse Analysis for Identification of Rheological and Friction Models in Metal Forming, *Comp. Meth. Appl. Mech. Engrg.*, **195**, 2006, 6778-6798.
- [2] M. Pietrzyk, R. Kuziak. Model reologiczny miedzi chromowej w procesach obróbki plastycznej na gorąco, *Obróbka Plastyczna Metali*, **19**, 2008, in press.

NUMERICAL ANALYSIS OF RESIDUAL STRESSES IN WELDS OF THICK-WALLED PRESSURE VESSELS

B. Szybiński¹, A. Wróblewski²

¹ *Institute of Machine Design Cracow University of Technology, Poland*

² *Institute of Applied Mechanics, Cracow University of Technology, Poland*

1. Introduction

Failures caused by fatigue in welded structures result in substantial costs each year all over the world. The premature fracture is often attributed to existence of residual stresses, which have their source in welding technology. Application of concentrated source of heat, high temperature gradients, phase and volume changes during the process make this problem difficult to analyze. Additional changes of material constants and yield stress values lead to a nonlinear problem, which should be analyzed as coupled [1, 2]. Also experimental assessment of residual strains or stresses in welds is rather limited due to high cost of investigations. The above observation influenced the development of various numerical methods and codes focused on weld simulation. This problem attracts many researchers since seventies of the past century. The first successful trials can be found in papers [3-6]. The extensive review of numerical modelling and simulation of welding process is presented in [7].

Nowadays there are several codes based on the Finite Element approach oriented to weld simulation, as for example: SYSWELD[®], MSC Marc/Mentat[®]. It is also possible to use the universal FE code ANSYS[®], in which the authors perform the simulations. Below the results of welding simulation of two plates are presented. The thickness of plates was chosen in such a way that the weld can be made in a single pass. Further calculation will be preformed for a thick-walled cylindrical chamber, where the welding process becomes more complex – needs more passes, preheating before welding and heat treatment after welding.

2. Numerical modelling of welds

Welding is one of the most common methods of joining elements made of low carbon or alloy steels. This method involves many different phenomena and results in complex stress and strain state in structures. Appearance of high temperature gradient in the process, phase and volume changes in joined materials and simultaneous changes of material constants are the main source of residual strains and stresses. Additional complication arises from the movement of the heat source along the weld path during the manufacturing process. This causes that the thermal problem should be regarded as a transient one. Finally, the analysis is performed in two basic steps. The thermal analysis is the first one. Locally applied heat source causes thermal dilatation resulting from thermal expansion. This is supplemented by the volume changes due to phase transformations. All these phenomena result in deformation, which is usually permanent due to rapid reduction of the yield stress with temperature increase. The thermal analysis is followed by the mechanical calculation made on the base of the temperature distribution. The whole analysis is nonlinear and is performed in several steps.

3. Results of exemplary numerical simulation

The problem of welding of thin plates is usually analysed as two dimensional [8, 9]. In the present paper the whole structure was modeled as three dimensional and the weld was made in one pass. At the beginning of the process the full geometry was defined and then the procedure of element annihilation was utilized. Next the sub-volumes on the weld path were animated with the

velocity corresponding to the velocity of welding. The exemplary results of such approach are shown in Figure 1. Here the distribution of temperature and residual strains at the end of the welding process are presented. As it can be seen, the residual strains are located in vicinity of the heat-affected zone, which confirms the earlier observations [8, 9].

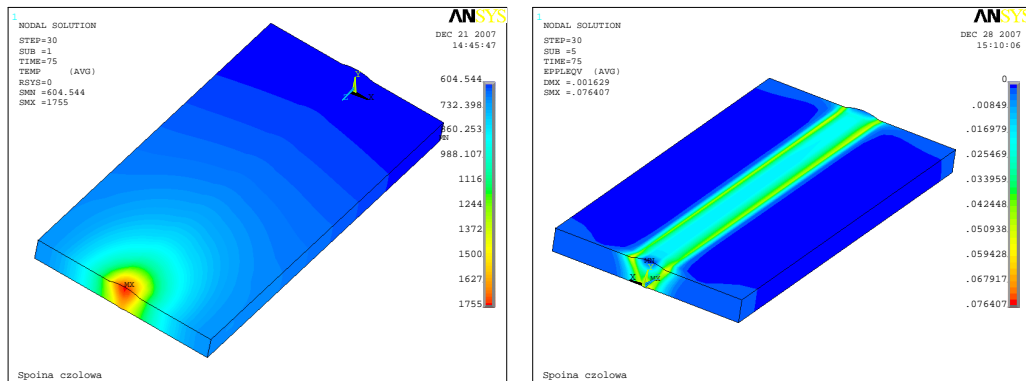


Figure 1 Distribution of temperature and residual strains in two plate welding process

The preliminary investigations show, that the standard finite element code ANSYS enables the simulation of welding process, and it has been decided to use it in modelling of welds in more complex, thick-walled structures.

Acknowledgement

Grant PB-1353/T02/2007/32 is gratefully acknowledged.

4. References

- [1] K. Easterlink (1983), *Introduction to the Physical Metallurgy of Welding*, 1st Ed., Butterworths.
- [2] L. Karlsson (1986), *Thermal stresses in Welding*, in R.B. Hetnarski (ed.), *Thermal stresses*, vol.1, Elsevier Science Publishers.
- [3] E.F. Rybicki, D.W. Schmueser, R.B. Stonesifer, J.J. Groom, H.W. Mishler (1978). A finite element model for residual stresses in girth-butt welded pipes, *ASME J.Pressure Vessel Technology*, **100**, August, 256-262.
- [4] E.F. Rybicki, R.B. Stonesifer (1979). Computation of Residual Stresses due to Multipass Welds in Piping Systems, *ASME J.Pressure Vessel Technology*, **101**, 149-154.
- [5] Y. Ueda, H. Murakawa (1984). Applications of computer and numerical analysis techniques in welding research, *JWRI*, **13/2**, 165-174.
- [6] J. Goldak (1989). Modeling thermal stresses and distortions in welds, *Proc. of the 2nd I.Conf. on Trends in Weld. Res.*
- [7] L-E. Lindgren (2001). Finite Element Modeling and Simulation of Welding, (Part 1, 2 and 3), *J. of Thermal Stresses*, **24**, 141-192, 195-231, 305-334.
- [8] S. Dobrociński, W. Kiełczyński (2005). Modelowanie i badanie pól naprężeń w połączeniach spawanych, *Biuletyn Instytutu Spawalnictwa*, **5**, 154-160.
- [9] L. Flis (2006). Wykorzystanie MSC MARC/Mentat do symulowania spawania cienkich płyt, *Zeszyty Naukowe Akademii Marynarki Wojennej*, Rok **XLVII** Nr **2** (165), 23-35.

NUMERICAL SIMULATIONS OF LABORATORY AND FIELD TESTS OF PERMEABILITY

A. Garwolińska, M. Kaczmarek

*Institute of Environmental Mechanics and Applied Computer Science
Kazimierz Wielki University, Bydgoszcz, Poland*

1. Background

Surrounding environment strongly influences the durability of concrete structures. A first symptom of deterioration of concrete structure is an increase of the permeability of its cover layer. Increase of permeability causes deeper and faster ingress of water and aggressive agents which accelerates the deterioration of deeper layers of concrete. Thus, the evaluation of permeability of concrete cover plays significant role in prediction of its quality.

Description of number of different field tests of permeability can be found in literature [1,2,5]. Most of them and few other specific techniques [3,4] can be used in laboratory. In general, there is a possibility to test permeability with liquid or gas but in case of the high-performance concrete, liquid tests are practically not possible. Such concrete is almost completely water-resistant and gas methods are preferred.

2. Aims and method

The paper deals with modeling transient flow of compressive gas in porous materials. Mathematical model describing the phenomenon including viscous interaction and Klinkenberg effect was formulated. Simulations by Finite Element Method in COMSOL environment assuming different boundary and initial conditions are shown and results are analyzed.

3. Results and discussion

A number of simulations within model describing transient phenomenon of compressible fluid flow in porous media were performed assuming that initially in the gas reservoir:

- a. The pressure is significantly lower (technical vacuum) than in the pore space of tested material (suction),
- b. The pressure is few times higher (overpressure) than in the pore space of tested material (pumping).

Such conditions correspond to the main groups of presently used practical methods in laboratory and field permeability testing.

Since laboratory tests are made on samples with sealed lateral surface then the fluid flows along the axis of the sample and the corresponding model of flow is one dimensional (1D). In turn most field tests rely on configurations for which gas flows both in axial and radial directions and then the two dimensional model (2D) is appropriate. The results shown in this paper refer to transient flow of compressible gas in concrete for both cases.

The simulations show that the influence of Klinkenberg coefficient on pressure distribution in the porous material is essentially greater in case (a) than in case (b). The same undergoes for the time dependence of pressure in the reservoir. The facts can be justified by a physical argument that the longer mean free path (more rarefied gas) the stronger slippage effect must appear.

Taking into account that the most convenient for measurement is observation of pressure changes versus time in the gas reservoir Figure 1 presents distributions of changes in reservoir pressure for 1D and 2D cases. In both simulations the same material constants and geometry were

assumed. The initial pressure in reservoir was equal five times the pressure in the pore space of tested material.

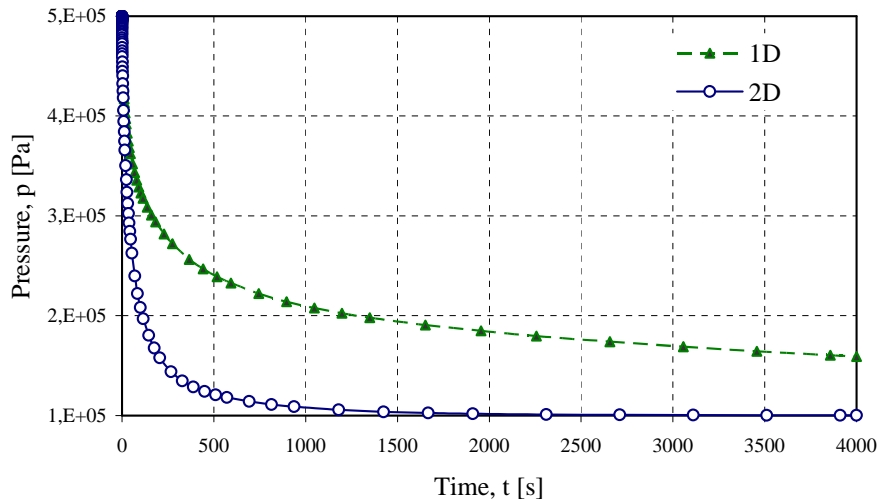


Figure 1. Distributions of pressure changes in reservoir for one and two dimensional simulation of compressible fluid flow in porous media

4. Final remarks

The paper presents simulations of one and two dimension transient flow of compressive gas in porous material. Material constants, initial pressures in pore space of tested material and reservoirs as well as the geometrical conditions of simulated problems are assumed in the way corresponding to practice in laboratory and field tests of concrete permeability. The obtained results show great importance of testing conditions for time dependence of pressure in reservoir and pressure distribution in the porous material. A particular sensitivity to testing conditions shows the Klinkenberg effect. Currently experimental works are made to verify the results obtained from simulations.

6. References

- [1] P. A. M. Basheer (1993) *A brief review of methods for measuring the permeation properties of concrete in situ*, Proc. Instn Civ. Engrs Struct Bldgs, 99 74-83.
- [2] J.W. Figg, *Methods of measuring the air and water permeability of concrete*, Magazine of Concrete Research 25(85) 213–219.
- [3] D. R. Gardner, A. D. Jefferson, R. J. Lark (2007) *An experimental, numerical and analytical investigation of gas flow characteristics in concrete*, Cement and Concrete Research 38 (2008) 360-367.
- [4] M. Kaczmarek (2008) *Approximate Solutions for Non-stationary Gas Permeability Tests*, Transp. Porous Med, accepted for publication.
- [5] R.J. Torrent (1992) *A two-chamber vacuum cell for measuring the coefficient of permeability to air of the concrete cover on site*, Materials and Structures 25 358-365.
- [6] Yu-Shu Wu, K.Pruess (2000) *Integral solutions for transient fluid flow through a porous medium with pressure-dependent permeability*, International Journal of Rock Mechanics and Mining Sciences 37 51-61.

COMPUTER AIDED DESIGN OF VIBRATING STRUCTURES ACCOUNTING FOR MATERIAL FATIGUE AND RELIABILITY

T. Bednarek^{1,2} and W. Sosnowski^{1,2}

¹ *Institute of Fundamental Technological Research, Warsaw, Poland*

² *Kazimierz Wielki University, Bydgoszcz, Poland*

The numerical method for prediction of fatigue life of structure is presented. The finite element modeling and damage parameter calculation are based on algorithm described originally in [1].

As an example the optimization of double – disk rotor shaft system, presented if Figure 1, based on sensitivity analysis followed by the fatigue life estimation of optimized shaft is considered. The objective of optimization is to avoid resonance, which can cause excessive stresses leading to premature fatigue cracks. Sensitivities of eigenvalues with respect to design variables are calculated by the Direct Differentiation Method (DDM) [2,3]. The optimization is performed with the objective to move natural frequencies as far as possible from resonance frequency. Next the shaft system is dynamically loaded. Fluctuation of stress established from FEM analysis by numerical code FEAP [4] are stored, cycles are counted by rainflow method and next fatigue life estimation is performed. Design parameters are diameters of selected shaft parts.

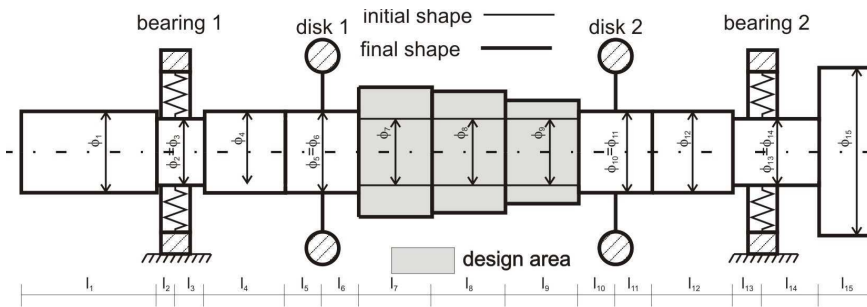


Figure 1. Double – disk rotor shaft system before and after optimization.

Damage accumulation hypothesis is used in order to take into account all components of dynamic load [5]. An accumulated damage caused by all cycles in block can be calculated.

The idea of the equivalent amplitude stress described in [6] is used, in order to calculate the number of cycles to failure of the analyzed structure loaded by arbitrary non-symmetric load with any stress ratio .

Fatigue durability may be expressed by number of cycles to expected failure N or hours of safety work of the structure [7]. Design life and probability based fatigue factors are calculated as so called Factor of Strength (FOS). It shows how much the component is over or under strength in terms of Finite Element Analysis (FEA) stresses.

The FOS is the ratio of the strength of material to the working stress. The FOS value is calculated using the Goodman mean stress correction. Referring to Figure 2, which shows the Goodman line in coordinates (S_a, S_m) , the FOS is given by

$$FOS = \frac{OB}{OA} \quad (1)$$

Effects of unloading on fatigue life is also calculated [8]. The simplified reliability analysis makes use of fuzzy set approach to the basic fatigue data such as material data, load parameters etc. [8].

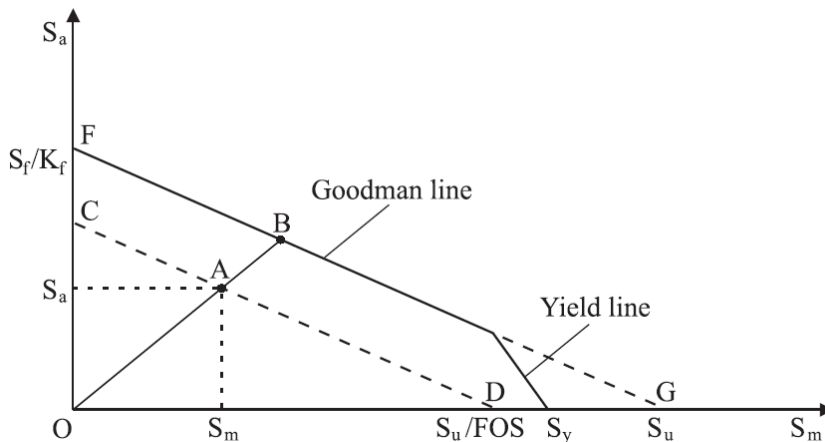


Figure 2. Factor of Strength based on Goodman line. S_a - stress amplitude, S_m - mean stress, S_y - yield stress, S_u - ultimate tensile strength, K_f - stress concentration factor.

Short summary

Present work deals with optimization performed on the basis of exact sensitivity.

Optimization with objective to avoid resonance allows to eliminate undesirable vibration, noise and considerable increase fatigue life.

Equivalent amplitude stress is very effective tool in fatigue analysis in engineering cases, when fatigue data are provided only for stress ratio $R = -1$, but also in dynamic fatigue analysis where rainflow algorithm is used.

- [1] Oller S., Salomon O., Onate E., A continuum mechanics model for mechanical fatigue analysis, *Computational Material Science*, vol. 32, 2005.
- [2] M. Kleiber, H. Antunez, T. D. Hien, P. Kowalczyk, *Parameter sensitivity in nonlinear mechanics*, John Wiley & Sons, Chichester, 1997
- [3] Sosnowski W. and Kleiber M., A study on the influence of friction evolution on thickness changes in sheet metal forming, *Journal of Materials Processing Technology*, Vol. 1-4, pp. 469-474, 1996
- [4] Zienkiewicz O.C. and Taylor R.L. *The Finite Element Method* 5th edition, BH 2000
- [5] H. Jakubczak, *Uncertainty of data in the fatigue life assessment of structural components*, Oficyna Wydawnicza Politechniki Warszawskiej, Warsaw, 2002
- [6] I. Marczevska, T. Bednarek, A. Marczewski, W. Sosnowski, H. Jakubczak and J. Rojek, Practical fatigue analysis of hydraulic cylinders and some design recommendation, *Int. Journal of Fatigue*, Vol 28/12 pp 1739-1751, 2006
- [7] N. E. Frost, K. J. Marsh, L. P. Pook, *Metal fatigue*, Dover publications, INC, Mineola, New York, 1999.
- [8] T. Bednarek, *Computer aided design of vibrating structures accounting for material fatigue and reliability*, PhD Dissertation, in print

INDIRECT TREFFTZ SOLUTIONS FOR PLANE PIEZOELECTRICITY BY STROH FORMALISM AND COLLOCATION TECHNIQUE

G. Dziatkiewicz

*Department of Strength of Materials and Computational Mechanics,
Silesian University of Technology, Gliwice, Poland*

1. Introduction

The coupled field analysis of piezoelectric materials requires solution of continuum mechanics and continuum electrodynamics equations [1,3]. Practically, the process of solving the boundary – value problems is realized using the numerical methods. The most popular are: the finite element method (FEM) and the boundary element method (BEM). The FEM requires the whole region discretization; in the BEM, in many cases, only the boundary is discretized. Hence, in these both methods the mesh of finite and boundary elements is required. Recently, there can be noticed a development of the meshless methods, which do not need the time-consuming mesh generation process. One of the meshless methods is the indirect Trefftz collocation method [1,4,6,7].

In the Trefftz method, the solution of the boundary-value problem is approximated by the series of the T-complete functions [4,7]. These functions satisfy the system of the governing equations, i.e. the homogenous system of the elliptic differential equations of the linear piezoelectricity. The piezoelectric materials are modelled as: homogenous, anisotropic linear-elastic and linear – dielectric [3]. Even for the transversal isotropic ceramic piezoelectric material, the form of the partial differential operator makes the determination of the T-complete functions quite complicated. The quite similar problem exists, when the fundamental solution is being determined. The Stroh formalism is a powerful and elegant analytic technique for anisotropic elasticity, which is expanded to the linear piezoelectricity in this case. The Stroh formalism allows to obtain both the fundamental solution and the T-complete functions [3,5].

2. The Stroh formalism and the T-complete functions

Since piezoelectric materials are anisotropic, the determination of the fundamental solutions and the T-complete functions are rather complicated, even for the transversal isotropic model of the material. In the Stroh formalism, it is assumed, that the field of the generalized displacements (the mechanical displacements and the electric potential) has a form of product of the unknown complex vector and the analytic complex function [3]. Then, the formalism requires the solution of the special eigenvalue problem with respect to the material constants of the piezoelectric material. The general solution, which is the base of the T-complete functions set, can be expressed by using the eigenvalues, eigenvectors (of the special eigenvalue problem) and arbitrary complex vector and arbitrary analytic complex function. The orientation of the polarization direction is also taken into account using this formalism. The eigenvalues and eigenvectors, related to these constants, are specially transformed according to the polarization direction.

3. The collocation technique

When the set of the T-complete functions is determined, the solution of the boundary-value problem can be approximated by the superposition of these functions [1,4,7]. The superposition of the T-complete functions satisfies the governing equations, but does not satisfy the mechanical and electric boundary conditions. This problem leads to the minimization problem of the boundary residuals [1]. The unknowns are the coefficients of the superposition of the T-complete functions,

which describe the wanted mechanical and electric fields. The collocation method assumes that the residuals vanish at the boundary points. The resulting system of algebraic equations is usually solved by using the least square method [1,6].

4. Least square method and regularization technique

The indirect Trefftz collocation approach usually requires the solution of the overdetermined system of equations, which determines the unknown coefficients of the superposition of the T-complete functions [1,6]. The matrix of the system of equations is usually nearly singular and ill-conditioned [4]. For a system of equations with these properties, a singular value decomposition (SVD) solver is one of the most popular solution. The SVD allows to regularize the solution with the minimal norm [2]. In numerical computations, the nearly singular and the ill-conditioned matrix has no rank exactly equal to the mathematical rank. The numerical rank is smaller than the mathematical rank, because of small nonzero singular values. When the matrix has very small nonzero singular values, then a norm of the solution is very large. To remove this effect, the least singular values must be neglected, so the new solution is called the truncated singular value decomposition solution [2]. The truncation number is a regularization parameter in this method. In the present work the L – curve method is used for to determine the optimal truncation number.

5. Numerical examples

The indirect Trefftz collocation method program for plane boundary – value problem of linear piezoelectricity is developed. Results for some simple boundary – value problems are compared to analytical and BEM solutions. The numerical examples demonstrate a good agreement of the Trefftz method solutions with the exact and BEM solutions.

6. Conclusions

The point-collocation technique has the simplest algorithm among the others Trefftz methods and is therefore the most computationally – efficient approach [4]. This is also truly meshless boundary method and no integration is carried out in this technique. The Trefftz method uses regular functions, this is an important advantage when the indirect Trefftz method is compared with other boundary methods [7]. The necessity of regularization is some kind of drawback, but the SVD method ensures accurate and stable results.

7. References

- [1] W.G. Jin, N. Sheng, K.Y. Sze, J. Li (2005). Trefftz indirect method for plane piezoelectricity, *Int. J. Num. Meth. Eng.*, **63**, 139-158.
- [2] L. Marin, L. Elliot, D.B. Ingham, D. Lesnic (2002). Boundary element regularisation methods for solving the Cauchy problem in linear elasticity, *Inv. Probl. Eng.*, **10**, 335-357.
- [3] E. Pan (1999). A BEM analysis of fracture mechanics in 2D anisotropic piezoelectric solids, *Eng. Anal. Bound. Elem.*, **23**, 67-76.
- [4] A. Portela and A. Charafi (1997). Programming Trefftz boundary elements, *Adv. Eng. Soft.*, **28**, 509-523.
- [5] Q.-H. Qin (2003). Variational formulations for TFEM of piezoelectricity, *Int. J. Sol. Struct.*, **40**, 6335-6346.
- [6] N. Sheng, K.Y. Sze, Y.K. Cheung(2006). Trefftz solutions for piezoelectricity by Lekhnitskii's formalism and boundary-collocation method, *Int. J. Num. Meth. Eng.*, **65**, 2113-2138.
- [7] Z. Xiaoping and Y. Zhen-han (1995). Some applications of the Trefftz method in linear elliptic boundary-value problems, *Adv. Eng. Soft.*, **24**, 133-145.

LAGRANGIAN AND ALE APPROACH FOR PREDICTING RESIDUAL STRESSES IN ORTHOGONAL CUTTING

N.C. Marín, M.H. Miguélez, J.A. Canteli, J.L. Cantero

Department of Mechanical Engineering, Universidad Carlos III, Madrid, Spain

1. Introduction

Machining is a complex process involving very large strains and strain-rates, which cause large temperature increase. Improvement of tool performance and quality surface requires good understanding of the process. Since most process variables are difficult to measure, analytical and numerical modelling of chip formation are versatile and reliable approaches to obtain information on some local variables of the workpiece and the cutting tool [1,2]. Finite element analysis has provided an insight look at what is going on during cutting, which is difficult to achieve by experimental or analytical methods. Eulerian, Lagrangian and Arbitrary Lagrangian-Eulerian (A.L.E.) techniques have been used to simulate orthogonal cutting. [3,4]. In Lagrangian analysis, the computational grid deforms with the material whereas in Eulerian analysis it is fixed in space. The Lagrangian calculation embeds a computational mesh in the material domain and solves for the position of the mesh at discrete points in time. Two distinct methods, the implicit and explicit time integration techniques, could be used to implement these analyses. A.L.E. is a relatively new modelling technique in machining, including a combination of the Lagrangian and Eulerian approaches without having their drawbacks. It was firstly introduced to model the cutting process by the end of the last decade. This approach became popular due to its implementation in commercial finite element codes. Explicit dynamic A.L.E. formulation is very efficient for simulating highly non-linear problems involving large localized strains.

The residual stress field in a machined surface is one of the most important factors influencing the surface quality. In fact, residual stress distribution can affect the workpiece material behaviour during service loading (fatigue, fracture, stress corrosion) [5]. Residual stresses are produced by mechanical and thermal phenomena associated with the process of chip formation. The nature of residual stresses depends not only on machining parameters such as cutting speed, feed rate, depth of cut, but also on the tool geometry and the lubrication conditions.

In this work, orthogonal cutting is modelled with ALE approach (ABAQUS/Explicit code) and Lagrangian approach (DEFORM-2DTM code). The aim of this paper is predicting residual stresses after orthogonal cutting, comparing general and specific codes. The study is focused on AISI 316L a difficult-to-machine material, because of high strain hardening effects and low thermal conductivity [6]. Advantages and drawbacks of both codes are analyzed.

2. Numerical models

A plane strain A.L.E. model was developed in ABAQUS/Explicit. A thermo-mechanical coupled analysis was developed, with CPE4RT element type (see ABAQUS manual). These are plane strain, quadrilateral, linearly interpolated, and thermally coupled elements with automatic hourglass control and reduced integration, for A.L.E. formulation. In DEFORM-2DTM, the workpiece was initially meshed with 10000 isoparametric quadrilateral elements. The tool was modeled as rigid and meshed with 6000 elements.

For both models, the cutting velocity is 120 m/min and the feed used was 0.1 mm. The clearance angle, rake angle and the edge radius are 10°, 0° and 0.02, respectively. Analysis was carried out in two steps. In the first step, cutting was modelled at constant cutting speed and steady state conditions were reached. In the second step, the workpiece was unloaded and cooled. The residual stress distribution was obtained in a section of the workpiece corresponding to stationary conditions during cutting. The workpiece material was modelled using the Johnson-Cook (JC) constitutive model [7].

3. Results

Fields of residual stress in direction x (the direction of cutting speed) after unload and cooling obtained with DEFORM-2D, is shown in figure 1(a). Residual stress is tensile in machined surface, the level is around 900 MPa. Distribution of residual stress in depth into workpiece obtained with ABAQUS/Explicit is shown in figure 1 (b). The level of tensile residual stress in machined surface is higher with this code.

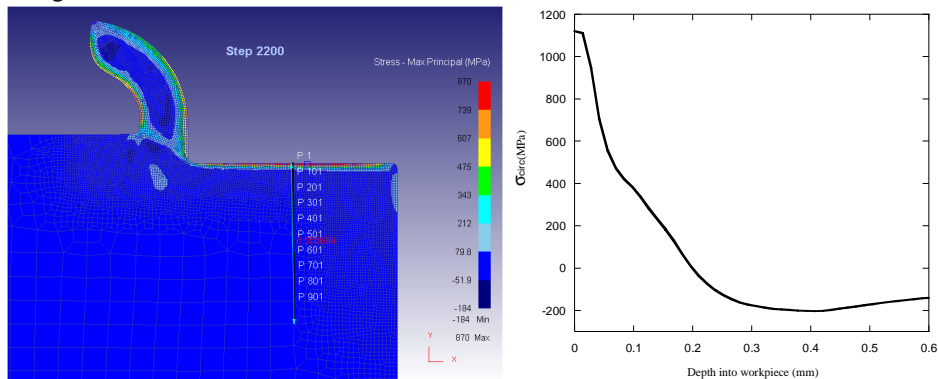


Figure 1. (a) Fields of residual stress (circumferential) obtained with DEFORM-2D. Circumferential stress obtained in depth in workpiece with ABAQUS/Explicit.

In Lagrangian formulation using DEFORM-2DTM, the mesh should be very fine around the tool tip, this fact increases the computational cost of the simulation. In the ALE model a specific mesh should be defined for a given tool geometry, being necessary to make some iterations to obtain the initial geometry of the chip able to deform to the final shape of the chip. Changes in tool geometry imply the development of a new initial geometry for the chip.

4. Acknowledgments

The authors acknowledge to the Ministry of Science and Technology of Spain, the financial support obtained for this work with the Project CYCIT DPI2005-08018

5. References

- [1] A. Moufki, A. Molinari, D. Dudzinski, Modelling of orthogonal cutting with a temperature dependent friction law, *J. Mech. Phys. Solids*, **46** (10) (1998) 2103-2138.
- [2] H. Miguélez, R. Zaera, A. Rusinek, A. Moufki, A. Molinari (2006), Numerical modelling of orthogonal cutting: influence of cutting conditions and separation criterion, *J. Phys IV*, **134**, 417-422.
- [3] M. Bäker, Finite Element Simulation of Chip Formation, Shaker Verlag, Aachen, 2004.
- [4] M. Barge, H. Hamdi, J. Rech, J.M. Bergheau, Numerical modelling of orthogonal cutting: influence of numerical parameters, *J. Mat. Process. Tech.* **164-165** (2005) 1148-1153.
- [5] K. Okushima, Y. Kakino, A study on the residual stress produced by metal cutting, *Memoirs of the Faculty of Engineering, Kuyoto* **34** (1972) 234-248.
- [6] M.N.A. Nars, E.G. Ng and M.A. Elbestawi (2007). Modeling the effects of tool-edge radius on residual stresses when orthogonal cutting AISI 316L, *Int. J. Mach. Tools & Manuf.*, **47**, 401–411.
- [7] D. Umbrello, R. M'Saoubi and J.C. Outeiro (2007). The influence of Johnson-Cook material constants on finite element simulation of machining of AISI 316L steel, *Int. J. Mach. Tools & Manuf.*, **47**, 462–470.

THE ADAPTIVE NEM – DELAUNAY ELEMENTS

T. Łukasiak

The Faculty of Civil Engineering, Warsaw University of Technology, Poland

1. Abstract

Meshless methods utilized in numerical solution of boundary problems have recently been widely investigated by many authors. The explicit connectivity between nodes does not exist for such methods. Therefore due to computational efforts in remeshing steps for FEM, the meshless methods seem to be an attractive alternative for adaptive process in computational mechanics. The Natural Element Method (NEM) proposed by Traversoni (1994), Brown and Sambridge (1995) [1] is treated as a meshless method. The shape functions for the NEM are constructed with help of the Voronoi diagram, which describes so called natural neighbours for each node P_i placed in the domain Ω . There are two main kinds of approximation for the NEM, the “non-sibsonian” with the Laplace coordinate [2] built on basis of the first order Voronoi diagram (1), and approximation with the Sibson functions [3] constructed with the help of locally created the second order Voronoi diagram (2).

$$(1) \quad V_i = \{ \mathbf{x} \in R^n : d(\mathbf{x}, P_i) < d(\mathbf{x}, P_k) \forall i \neq k, \forall \mathbf{x} \in \Omega \}$$

$$(2) \quad V_{ij} = \{ \mathbf{x} \in R^n : d(\mathbf{x}, P_i) < d(\mathbf{x}, P_j) < d(\mathbf{x}, P_k) \forall i \neq j \neq k, \forall \mathbf{x} \in \Omega \}$$

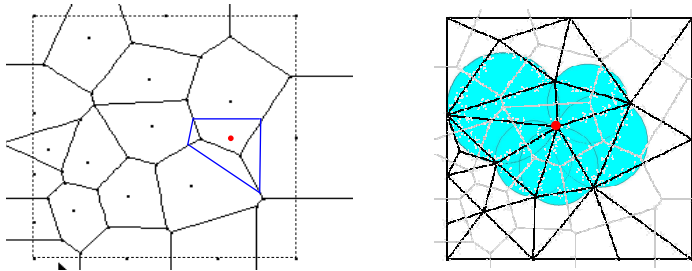


Fig 1) a) The Voronoi diagram (first order, and locally second order),
b) Delaunay triangles and support domain for selected node.

For both approximations the support domain of the shape function for the node P_i is the union of all the circumcircles about that node. In this work the Delaunay tessellation dual to the Voronoi diagram is utilized. The global stiffness matrix is obtained by summing over each Delaunay triangle instead the triangularized Voronoi region as in [4]. For each Delaunay triangle the proper stabilized numerical integration [5] is applied, i.e. 1 or 2-points Gauss quadrature along each edge of the triangle. For such an integration only values of the shape function are required, not the derivatives as usual. The error in energy norm (3) (or norm) of the solution is calculated by the local projection of the solution values over the Delaunay triangles.

$$(3) \quad Err = \left\| \mathbf{u}^h - \bar{\mathbf{u}} \right\| \quad \text{where} \quad \bar{\mathbf{u}} = \sum_k B_k \mathbf{u}^h(\mathbf{x}_k)$$

\mathbf{u}^h is the NEM solution in Ω and B_k – bilinear shape functions for 3-node triangle.

In the adaptive procedure the new size of the Delaunay element is calculated from

$$(4) \quad h_i^{new} = h_i \left(\eta \frac{\|\mathbf{u}^h\|}{\|\mathbf{u}^h - \bar{\mathbf{u}}\|_i} \frac{\sqrt{A_i}}{\sqrt{A}} \right)^{1/p}$$

and new nodes are placed. Firstly at the edges of the Delaunay triangle and then if required in its interior.

For the proposed routine of the adaptive process with NEM the results (the energy norm) for the 2D linear elasticity problem (plane stress problem) (fig.2) and for the assumed permissible energy error level $\eta=1\%$ are presented in tab.1. The “real” energy ($\|\mathbf{u}^R\| = 3.48077$) was calculated for the uniformly divided domain to 400 elements (8-node finite elements) in AnSys system. The initial and the ultimate nodes location for adaptive process are shown in fig. (2).

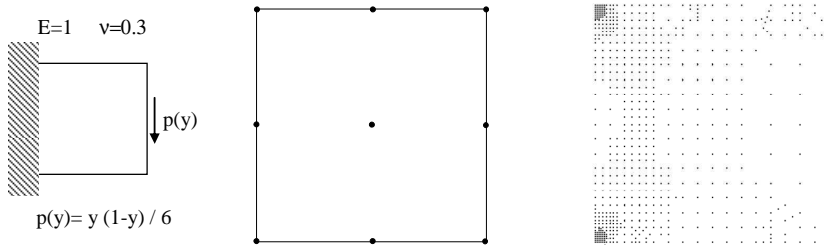


Fig 2) The test problem. The initial and the final set of nodes

Nodes	$\ \mathbf{u}^h\ $	Err	$Err / \ \mathbf{u}^h\ $ [%]	$Err / \ \mathbf{u}^R\ $ [%]
9	4.9287	2.8049 E 00	56.91	80.58
25	3.8187	6.7136 E-01	17.58	19.29
81	3.5844	2.0144 E-01	5.62	5.79
224	3.5184	6.9518 E-02	1,98	2.00
444	3.5045	3.7097 E-02	1.06	1.07
636	3.5001	2.7658 E-02	0.79	0.79

Table.1. Result for unity square test problem.

2. References

- [1] Sukumar N., Moran B., Belytschko T.(1998). The natural element method in solid mechanics. *Int. J. Numer. Meth. Engng.*, **43**, 839-887.
- [2] Belikov VV, Ivanov VD, Kontorovich VK, Korytnik SA, Semenov AYu. (1997). The non-Sibsonian interpolation: a new method of interpolation of the values of a function on an arbitrary set of points. *Comput Meth Math Phys*, **37**, 9–15.
- [3] Sibson R. (1980). A vector identity for the Dirichlet Tessellation., *Math Proc Cambridge Philos Soc* **87**, 151–155.
- [4] Yvonnet J., Coffignal G., Ryckelynck D., Lorong P., Chinesta F. (2006). A simple error indicator for meshfree methods based on natural neighbors. *Computers and Structures*, **84**, 1302-1312.
- [5] Chen JS., Wu CT, Yoon S., Youk Y., (2001). A stabilized conforming nodal integration for Galerkin mesh-free methods. *Int. J. Numer. Meth. Engng.*, 2001, **50**, 435-466.

STOCHASTIC IDENTIFICATION IN THERMOMECHANICAL STRUCTURES USING EVOLUTIONARY ALGORITHMS

P. Orantek¹, A. Długosz¹ and T. Burczyński^{1,2}

¹ *Department for Strength of Materials and Computational Mechanics
Silesian University of Technology, Konarskiego 18a, 44-100 Gliwice*

² *Institute of Computer Modelling, Cracow University of Technology,
Warszawska 24, 31-455 Cracow*

1. Introduction

The thermomechanical processes belong to coupled problems in which interaction between mechanical and thermal field is considered. It is very convenient for identification, because measuring both quantities: displacements and temperatures simultaneously is more effective than measuring only one with the use of the same numbers of sensor points [2].

The identification problem can be formulated as the minimization of some objective functional (fitness function) which depends on measured and computed state fields such as displacements, strains or temperature. In order to obtain the unique solution of the identification problem one should find the global minimum of the objective functional.

In the present paper the parameters of thermomechanical systems are modelled by random variables with a Gaussian probability density function. The applications of evolutionary computation to such problems require some modifications of the algorithm. Genes should be modelled by random numbers and the potential solutions of the optimization problem are represented by stochastic individuals in the form of random vectors. Modified evolutionary operators of mutation, crossover and selection are proposed.

2. Stochastic identification problem

The aim of the stochastic identification is to find a random vector $\mathbf{X}(\gamma)$:

$$(1) \quad \mathbf{X}(\gamma) = [X_1(\gamma), X_2(\gamma), \dots, X_i(\gamma), \dots, X_n(\gamma)]$$

which minimizes an objective function $F(\gamma) = F[\mathbf{X}(\gamma)]$ subjected to m constraints $P[g_j(\mathbf{X}) \geq 0] \geq p_j, j = 1, 2, \dots, m$

where: (Γ, \mathcal{F}, P) is a probability space, Γ is a space of elementary events, \mathcal{F} is σ -algebra of subset of the set Γ , P is the probability defined on \mathcal{F} .

In order to solve the identification problem an evolutionary algorithm (EA) is used. Each individual is a multidirectional vector consisting of random variables (genes) with the Gaussian density probability function. Each gene is represented by the two moments: (i) the mean value m_i and (ii) standard deviation σ_i .

The evaluation of the fitness function can be done by solving the stochastic boundary-value problem, for instance: stochastic boundary element method SBEM [1] or the stochastic finite element method SFEM [3].

The original stochastic problem can be also reduced to the series of the deterministic one. In this work for each individual several direct problems are solved on the basis of input random variables. The moments of the displacement and temperature fields are evaluated on the basis of the 200 deterministic tasks. An fitness function is expressed by minimization of the following functional:

$$(2) \quad \min : \left[F(\mathbf{x}) = \sum_j w_j \sum_i (x_i - \hat{x}_i)^2 \right]$$

where: x_i - the measured quantity (temperature or displacement), \hat{x}_i - quantity computed for the structure with the parameters generated by the evolutionary algorithm, w_j - is appropriate weight. Direct problems of thermoelasticity for the identification task are solved by means of the finite element method (FEM) [5].

3. Numerical example

In this example thermal boundary conditions are identified. It is assumed that identified ambient temperature T^∞ and heat convection coefficient α are random variables. The structure under thermomechanical loading presented in Figure 1a is considered. One surface of the box is supported, whereas on the opposite load P is applied. On the supported surface of the structure the temperature T is applied. The third type thermal boundary condition (convection) is specified on the internal surface (identified random variables T^∞ and α). The stochastic fitness function is evaluated on the basis of measured displacements and temperatures in boundary sensor points, which are random variables with the Gaussian distribution. Table in Figure 1b contains limitations of the design variables, actual values of parameters and obtained results.

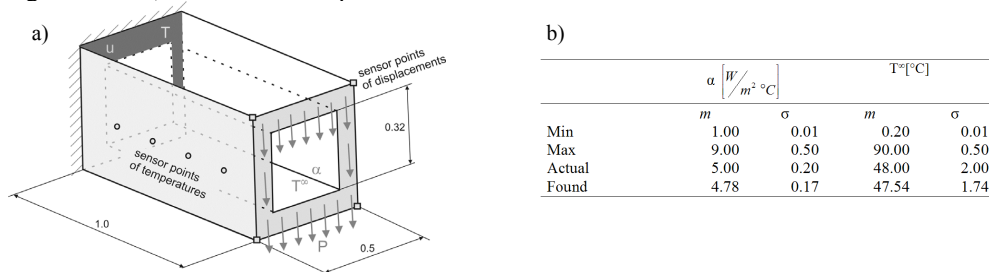


Figure 1. a) Geometry of the structure. b) The results of the stochastic identification

4. Conclusions

An effective intelligent technique based on the stochastic evolutionary algorithm has been presented. This approach can be applied in the optimization and the identification of systems that are in the random conditions. The obtained results demonstrate good accuracy comparing to exact solution. Numerical computations of thermoelasticity problems using finite element usually is time consuming, especially with more complicated models.

5. Acknowledgements

The work was done as a part of project N502 4573 33 sponsored by Polish Ministry of Science and Higher Education.

6. References

- [1] T. Burczyński, *Metoda elementów brzegowych w mechanice*, WNT, Warszawa 1995.
- [2] T. Burczyński, A. Długosz, Application of boundary element method in identification problems of thermoelasticity, *Electronic Journal of Boundary Elements*, vol 3, 2002.
- [3] M. Kleiber T. D. Hien, *The Stochastic Finite Element Method*. John Wiley & Sons. 1992.
- [4] P. Orantek, T. Burczyński The granular computing in uncertain identification problems, *Computer Assisted Mechanics and Engineering Sciences*, vol. 14 no.4, 2007, pp. 695-704.
- [5] O.C. Zienkiewicz, R. Taylor, *The Finite Element Method*, Vol.1-3, Butterworth, Oxford 2000.

FE-SIMULATIONS OF DYNAMIC SHEAR LOCALIZATION IN GRANULAR BODIES USING AN ARBITRARY LAGRANGIAN-EULERIAN FORMULATION

M. Wójcik and J. Tejchman

Gdańsk University of Technology, Gdańsk, Poland

1. Introduction

Algorithms of continuum mechanics usually use two descriptions of motion: the Lagrangian and Eulerian one [1]. In a pure Lagrangian formulation each individual node of the computational mesh is permanently connected to the same material points during motion. There are no convective effects and the material derivative reduces to a simple time derivative. Such formulation allows an easy tracking of free surfaces and interfaces between different materials, and treatment of materials with history-dependent constitutive relations. The formulation, however, is restricted to a certain deformation range because the element mesh may be severely distorted or entangled due to the fact that elements deform with the material. Thus, the FE-analysis usually loses accuracy, size of the time increment has to be significantly reduced or simply terminates due to convergence problems. A remeshing may not be even efficient. In a pure Eulerian formulation, the computational mesh is fixed spatially and the continuum moves with respect to the grid (elements retain their original shape). The convective effects appear because of the relative motion between the deforming material and computational grid, which makes the analysis computationally expensive. The formulation leads to difficulties when free surface conditions, prescribed boundary conditions or deformation history dependent material properties are considered as the element mesh is not connected to the material. In order to combine the advantages of both formulations and to minimize their limitations, an Arbitrary Lagrangian-Eulerian formulation (ALE, in short) has been developed [1], where state variables are a function of the referential coordinates (not connected to material points). In the ALE method, the mesh is neither connected to the material nor fixed to the spatial coordinate system (nodal displacements are uncoupled from material displacements) but it can be prescribed in an arbitrary manner. As a result, a mesh velocity has to be computed in order to compute the mesh. Grid points on the surface move with the mesh velocity, but these points must remain on the free surface. Since the mesh is not connected to the material, a remap of state variables has to be performed. The freedom in the mesh movement helps to handle greater distortions than would be allowed by a Lagrangian method with more resolution than that afforded by an Eulerian approach.

In our paper, a so-called uncoupled ALE-method was used [2], [3], where the deformation process was split into a pure Lagrangian and a pure Eulerian phase combined with a smoothing approach. This approach [2], [3] has some advantages with respect to the full coupled ALE-approach [1], where both nodal point and material values are calculated by solving a global assembled set of equations. The uncoupled approach simplifies this problem since the Lagrangian approach can be used and the stiffness matrix does not contain any convective terms. Thus, it is not necessary to describe the mesh velocity in a set of equations.

2. FE-analysis

Our dynamic FE-analysis was carried out with a non-local hypoplastic constitutive model, which is able to describe the essential properties of granular bodies during shear localization in a wide range of pressures and densities [4], [5]. Due to the presence of a characteristic length of micro-structure (by application of non-local terms), the model can simulate the formation of shear zones with a certain thickness and related size effects. It includes barotropy (dependence on pressure level), pycnotropy (dependence on density), dilatancy and contractancy and material

softening during shearing of a dense material. This law describes the evolution of effective stress tensor with the evolution of rate of deformation tensor by isotropic linear and non-linear tensorial functions. In contrast to elasto-plastic models, a decomposition of deformation components into elastic and plastic parts, the formulation of a yield surface, plastic potential, flow rule and hardening rule is not needed. A characteristic length was taken into account in hypoplasticity by means of a non-local theory. It is enough to treat non-locally the local modulus of deformation rate to obtain mesh-independent FE-results [4], [5]. The constitutive relationship requires totally 9 material constants.

The calculations of shear localization were carried out for 2 different dynamic problems using an explicit FE-formulation: plane strain compression and confined granular flow in silos. First, the calculations were carried out for a plane strain compression test. The following parameters were varied: loading velocity, initial void ratio, characteristic length of micro-structure and specimen size. Attention was paid to a deterministic dynamic size effect and thickness of a shear zone inside the deformed granular specimen. Some comparative analyses were also carried out using a pure Lagrangian approach.

The results show that inertial forces influence the shear zone formation. The calculations with a slow loading velocity were compared with corresponding quasi-static laboratory tests performed at Karlsruhe University [6]. A satisfactory agreement was achieved between numerical and experimental results.

Second, the FE-studies were performed for granular silo flow in a bin and hopper with a controlled or free outlet velocity [7]. Both, the initial void ratio and wall roughness were varied. The wall roughness was described by different Coulomb wall friction. The FE-results were compared with corresponding laboratory tests [8], [9]. A good agreement with respect to the shape of propagating internal shear zones inside the flowing solid was obtained between experiments and calculations. An uncoupled ALE-approach enabled us to avoid large mesh distortions during flow at the silo outlet.

4. References

- [1] T. Belytschko, W.K. Liu, B. Moran (2000). *Nonlinear Finite Elements for Continua and Structures*. Wiley, Chichester.
- [2] C. Linder (2003). An arbitrary Lagrangian-Eulerian finite element formulation for dynamics and finite strain plasticity models. *PhD Thesis*, University of Stuttgart.
- [3] C. Stoker (1999). Developments of the Arbitrary Lagrangian-Eulerian Method in non-linear Solid Mechanics. *PhD Thesis*, University of Twente.
- [4] J. Tejchman (2004). Comparative FE-studies of shear localizations in granular bodies within a polar and non-local hypoplasticity. *Mechanics Research Communications* **31/3**, 341-354.
- [5] J. Tejchman (2006). Effect of fluctuation of current void ratio on the shear zone formation in granular bodies within micro-polar hypoplasticity. *Computers and Geotechnics*, **33**, 1, 29-46.
- [6] I. Vardoulakis (1977). Scherfugenbildung in Sandkörpern als Verzweigungsproblem. *PhD thesis*, Institute for Soil and Rock Mechanics, University of Karlsruhe, 70.
- [7] M. Wójcik and J. Tejchman (2007). Numerical simulations of granular material flow in silos with and without insert. *Archives of Civil Engineering*, LIII, 2, 293-322.
- [8] J. Tejchman (1997). Modelling of shear localisation and autogeneous dynamic effects in granular bodies. *Publication Series of the Institute of Soil and Rock Mechanics*, University Karlsruhe, 140, 1-353.
- [9] R.L. Michalowski (1984). Flow of granular material through a plane hopper. *Powder Technology* **39**, 29-40.

NUMERICAL ANALYZES OF ARMOUR STEEL PLATES PENETRATION PROCESS BY SUBCALIBRE PROJECTILES WITH MONOLITH AND SEGMENTED PENETRATORS

K. Jach¹, R. Świerczyński¹ and M. Magier²

¹ *Institute of Optoelectronics, Military University of Technology, Warsaw, Poland*

² *Military Institute of Armament Technology, Zielonka, Poland*

The penetration of segmented projectiles has become an area of considerable interest in penetration mechanics due to its speculated enhanced penetration efficiency. A segmented projectile is a cylindrical rod where the main material is separated by spacers, which are usually made of another material.

According to above restrictions, in the model of the subcalibre projectile with segmented penetrator (constructed by Military Institute of Armament Technology), was applied penetrator rod composed of the two tungsten alloy pieces connected by screwed steel muff (fig.1). The main destination of this solution is increasing the defeat possibilities of the composite (steel-ceramic) armour of the modern combat tanks.

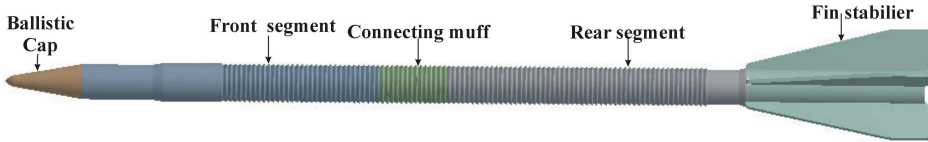


Fig.1. Subcalibre projectile with segmented penetrator

Composite armour (fig.2) is a type of vehicle armour consisting of layers of different material such as metals, plastics, ceramics or air. Most composite armour is lighter than their all-metal equivalent, but instead occupies a larger volume for the same resistance to penetration. It is possible to design composite armour stronger, lighter and less voluminous than traditional armour, but the cost is often prohibitively high, restricting its use to especially vulnerable parts of a vehicle.

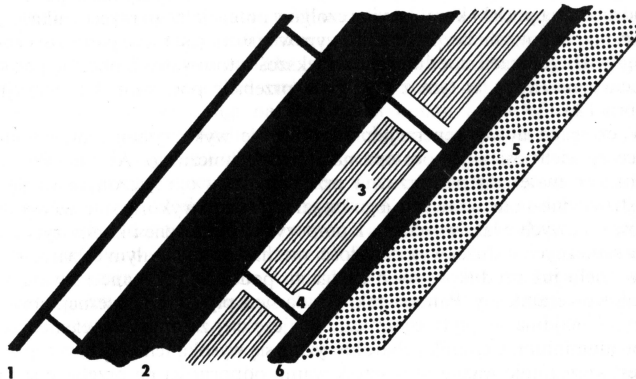


Fig.2. The cross-section of the typical composite armour.: 1 — front thin-walled plate, 2 — main steel plate, 3—ceramic elements, 4 — light alloy box, 5 — laminate layer, 6 — inertial steel plate.

In theoretical assumptions front segment of the penetrator, which hit the composite armour, is consumed during stationary hydrodynamic penetration process. The destination of the connecting muff is elimination of the shock wave propagated in front of the penetrator; which is transmitted to

the rear of the rod during hit. This wave, by the generation of the plastic deformations, has negative influence to the strength of the penetrator. In this way is possible that the structurally undisturbed rear segment could perforate the ceramic element and inertial layers of the composite armour.

Using a mathematical-physical model and computer code, a series calculation tests were performed concerning the problem of modeling of tungsten monolith and segmented rods penetrating steel targets. The computer simulations have been showed for two variants W2 – W3 (see table 1).

Variants number	Type of penetrator	Steel target thickness
W2	monolith	50 cm
W3	Two-segmented with steel connection muff	50 cm

Table 1. Configuration of the successive variants

In this paper, we present the computer modeling results of a steel armour plate's penetration by subcalibre projectiles with a monolith and segmented penetrators (tungsten alloy) accelerated to the velocity 1550 m/s. We used the most recent version of the free point's method. The results were compared to relevant experimental results. It is show that using this method we have obtained good consistency of the theoretical and experimental results

INDIUM CLUSTERS EVOLUTION IN A InGaN/GaN QW

G. Jurczak¹, P. Dłużewski¹, S. Kret² and P. Ruterana³

¹ *Institute of Fundamental Technological Research PAS, Warsaw, Poland*

² *Institute of Physics PAS, Warsaw, Poland*

³ *SIFCOM, UMR6176, CNRS-ENSICAEN, Caen, France*

Nitride semiconductors (GaN, AlN and InN) have been extensively studied due to its superb optoelectronic properties. Blue light-emitting devices or ultra-high frequency transistors compose only two of the wide range of technical applications. Nitrides are grown on various substrates with large misfits what may lead to a high density of defects or a strong composition fluctuations at the atomic scale. In particular, an active area for a blue LED or blue lasers are made of a multiple GaN/InGaN/GaN quantum wells (QW) and presence of the indium rich clusters in a QW area is reported, see Fig. 1. From this point of view, the knowledge about the cluster formation mechanism, its evolution and their role on the optical properties of the nitride based heterostructures is crucial. To this end, a quantitative high resolution transmission microscopy (HRTEM) is coupled with a stress induced diffusion in a finite element method (FEM).

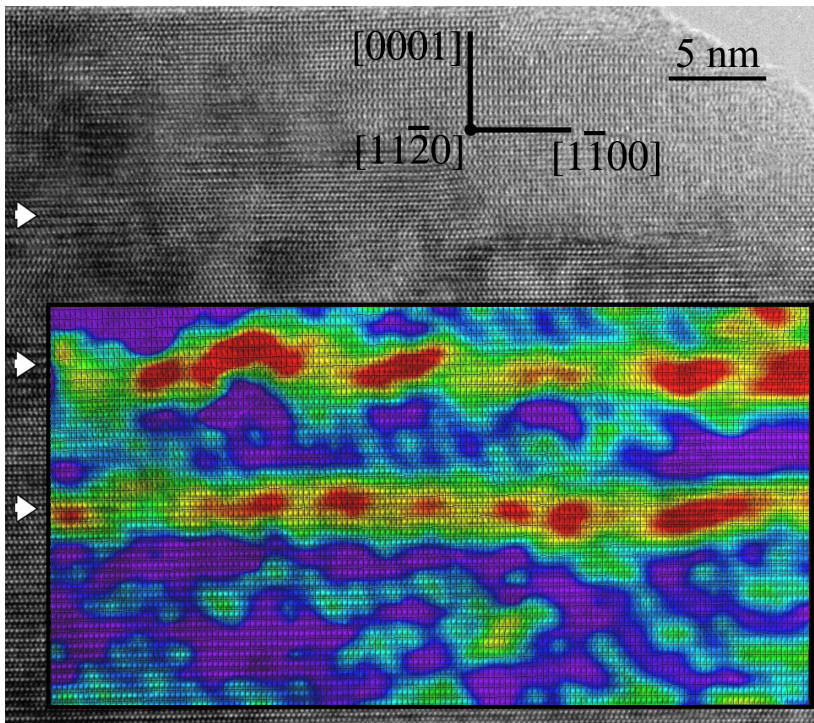


Fig. 1. HRTEM image of the MOCVD InGaN/GaN heterostructure. Black frame denotes evaluation area for a lattice distortion.

On the basis of the real indium clusters in InGaN/GaN QW a computer simulation has been performed for the stress induced diffusion process. Taking into account the geometry, position and composition of indium clusters as a starting configuration for FE initial-boundary problem we calculated subsequent configurations of indium cluster tending to the normalization of stresses. The elastic energy stored in HRTEM sample and its evolution in time has been analyzed. In particular, different position of the clusters towards the samples free surface (TEM sample) were analyzed to find the most preferable configuration taking into account elastic energy of the sample, see Fig. 2.

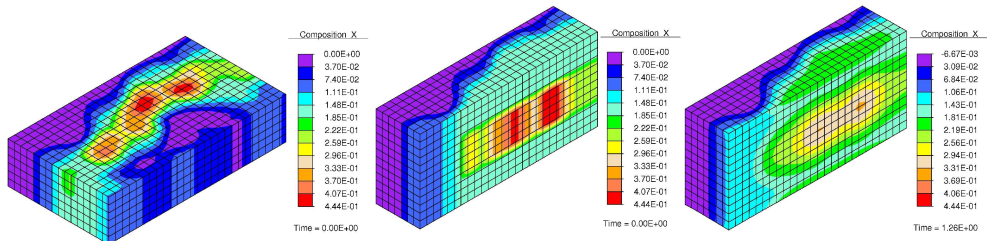


Fig. 2. FEM modeling of stress induced diffusion in a InGaN/GaN QW. Initial and final configuration.

References

- [1] G. Jurczak, G. Maciejewski, S. Kret P. Dłużewski and P. Ruterana (2004). Modelling of indium rich clusters in MOCVD InGaN/GaN multilayers, *J. Alloy Comp.*, **382**, 10-16.
- [2] P. Dłużewski (2005). Nonlinear Field theory of Stress Induced Diffusion in Crystalline Solids, *Defects and Diffusion Forum*, **237-240**, 107-114.

APPLICATION OF THE MULTISCALE FEM TO THE MODELING OF COMPOSITE MATERIALS

S. Ilic and K. Hackl

Institute of Mechanics, Ruhr University Bochum, Germany

The multiscale FEM is a numerical method based on the theory of homogenization, with the specific principle that real material properties have to be replaced by effective ones obtained by the examination of a RVE [6]. The terminology "macro" relates to the examined body, while "micro" relates to the RVE describing the material structure thereby the macroquantities are defined using the concept of the volume average and the coupling of the scales requires Hill's macrohomogeneity condition to be satisfied. Transformation of the latter condition leads to the definition of the boundary conditions at microscale and in that way to the closed formulation of the boundary value problem related to this level. The contribution examines materials with periodic and random microstructure, explaining three examples in detail.

The first example simulates the behavior of microporous nonlinear material. Here, a tension test of a plate is considered at macroscale, while a square RVE with an elliptical pore is chosen to describe the material properties. Given a random microstructure, the RVE is assumed to have a different orientation in each Gauss' point. The material investigation is illustrated by three groups of tests with different lengths of the semi-major axis of the pore. Each time, ellipticity is changed in an interval $[0, 1]$ where the lower limit corresponds to pores with zero thickness and the upper limit to circular ones. The results show that in the moment when pores appear, even if their thickness can be neglected, the material parameters decrease at once; furthermore, with pore growth, Young's and bulk modulus undergo a monotonous decrease while Poisson's ratio increases. Calculations also show that voids with elongated shape have a more significant influence on material weakening than voids whose shape is close to the circular one.

The second example looks at modeling solution-precipitation creep, which is a diffusional process occurring in polycrystals if pressure and temperature are in the specific range [3, 4, 5]. For this problem, firstly a continuum-mechanical model is proposed where the deformation is decomposed into an elastic and an inelastic part and the total power is written as a superposition of total elastic power and dissipation. The elastic energy is chosen in the standard form, dependent on the Helmholtz free energy, while the dissipated energy is formulated particularly for the process of solution-precipitation creep. It depends on the normal velocity of the crystal boundary due to precipitation or solution of material and on the velocity of material transport within the crystal interfaces. One of the main properties of this model is that the difference between the normal component of the Eshelby stress tensor and its smooth approximation becomes the driving force of the process. Such behavior is already endorsed by the experiments showing that under homogeneous pressure acting on one side of a rectangular crystal, solution-precipitation creep occurs only in edge zones of the sample. Another advantage of the proposed model is that in contrast to other procedures, continuity of stress in triple points is not required. Preliminary results for the behavior of polycrystals are obtained using the Taylor model and show that solution-precipitation creep leads to the elongation of the crystal shape. FEM-based methods are used for more realistic simulations and to estimate the change in effective material parameters over time. Here the most important simulations are those concerning materials with completely random structure and materials with regular structure consisting of hexagonal crystals.

The motivation behind developing the model for the RVE of cancellous bone, which is the last example presented in this contribution, is to investigate the process of osteoporosis, whose main indicators

are the decrease and partial disappearance of the solid phase [1, 2]. The important feature of the model is that the presence of the fluid phase necessitates dynamic interrogation and analysis in the complex domain. According to the geometry of the microstructure it is assumed that the RVE has a cubic form and that it consists of the solid frame and of viscous blood marrow filling the core of the frame. The effective elasticity tensor and the parameters of materials with different microstructure are calculated as the final results at microscale. Comparison of the real parts of material parameters with the experimental results shows good agreement. The calculations at macrolevel are illustrated by simulating the ultrasonic test where the attenuation coefficient is calculated as a final result, using the ratio of amplitudes of particle oscillations. The obtained numerical values are much smaller than the experimental ones so that an improvement of the model of the RVE is envisaged. Two main ideas for overcoming the problem consist of assuming a new geometry of the solid phase of the RVE, and introducing wave scattering on the interface of the phases.

From the previous overview it can be seen that, although limited by the requirements concerning the size of the RVE, the multiscale FEM can still be applied to modeling composite materials with very diverse microstructures. The examples presented here confirm in particular that the method can be applied efficiently in modeling nonlinear materials with a regular structure and a random structure, which mostly exceeds the abilities of analytical solutions and other numerical methods.

1. References

- [1] J.L. Buchanan, R.P. Gilbert and K. Khashanah (2002). Recovery of the poroelastic parameters of cancellous bone using low frequency acoustic interrogation, In A. Wirgin (ed.), *Acoustic, Mechanics, and the related Topics of mathematical Analysis*, World Scientific, 41-47.
- [2] J.L. Buchanan, R.P. Gilbert and K. Khashanah (2004). Determination of the parameters of cancellous bone using low frequency acoustic measurements, *J. Comput. Acoust.*, **12**(2), 99-126.
- [3] K. Hackl and S. Ilic (2005). Solution-precipitation creep – continuum mechanical formulation and micromechanical modelling, *Arch. Appl. Mech.*, **74**, 773-779.
- [4] S. Ilic and K. Hackl (2005). Solution-precipitation creep – micromechanical modelling and numerical results, *PAMM*, **5**, 277-278.
- [5] S. Ilic and K. Hackl (2006). Multiscale FEM in modelling of solution-precipitation creep, *PAMM*, **6**, 483-484.
- [6] J. Schröder (2000). *Homogenisierungsmethoden der nichtlinearen Kontinuumsmechanik unter Beachtung von Stabilitäts Problemen*, Habilitationsschrift, Universität Stuttgart.

MECHANO-CHEMISTRY AT DIFFERENT LENGTH SCALES

M. Danielewski

*Interdisciplinary Centre for Materials Modeling, Faculty of Materials Science and Ceramics
AGH University of Science and Technology, Al. Mickiewicza 30, 30-059 Cracow, Poland*

Abstract

Following Darken [1], Brenner [2] and Öttinger's [3] theories we recently postulated that the volume velocity defines the local material velocity at nonequilibrium [4]. It allowed fixing the unique frame of reference for all internal transport processes, thermodynamics in general. This frame of reference allows the use of the Navier-Lamé equation of mechanics of solids. Proposed modifications of Navier-Lamé and energy conservation equations are self-consistent with the literature for solid-phase continua dating back to the classical experiments of Kirkendall and their interpretation by Darken. No basic changes are required in the foundations of linear irreversible thermodynamics except recognizing the need to add volume density to the usual list of extensive physical properties undergoing transport in every continuum.

We define the volume density and using the Euler's and Lagrange theorems derive: the volume continuity equation, the equation of motion and energy conservation equations. We present the equivalence of presented and Darken methods when Darken restriction are introduced and the consistency of the Newton laws with thermodynamics. The method fulfills the following conditions:

1. The local acceleration of the mixture depends on its mass, not on its internal energy.
2. The local centre of mass position is not be affected by any diffusion process (mass diffusion, heat transport, internal friction etc.).
3. The volume velocity (v , i.e., the material velocity) is a unique internal frame of reference for all processes: diffusion, deformation, viscosity, heat transport etc.
4. The nonbalanced diffusion fluxes affect the local volume velocity.

The following equations govern the transport in compressible multicomponent mixtures. The volume continuity equation:

$$\operatorname{div} \left(\sum_{i=1}^r c_i \Omega_i v_i \right) = 0,$$

where $\Omega_i(N_1, \dots, N_r; T, p)$ denotes the partial molar volume. The mass conservation law:

$$\frac{\partial c_i}{\partial t} + \operatorname{div}(c_i v_i) = 0;$$

the equation of motion:

$$\rho \frac{Dv}{Dt} \Big|_v = \operatorname{Div}(\sigma^e + \sigma^p) - \sum_{i=1}^r c_i \operatorname{grad} \mu_i^{ch} - \rho \operatorname{grad} V^{ext},$$

where μ_i^{ch} is the chemical potential. The mechanical and thermal energy conservation equations:

$$\sum_{i=1}^r c_i \frac{D\mu_i^*}{Dt} \Big|_v = \sigma^e : \operatorname{Grad} v + v \sum_{i=1}^r c_i \operatorname{grad} \mu_i^{ch} + \sum_{i=1}^r c_i v_i^d \operatorname{grad} \mu_i^*,$$

$$\rho \frac{DT_S}{Dt} \Big|_v = \sigma^p : \text{Grad } v - \text{div } J_q - \sum_{i=1}^r c_i v_i^d \text{grad } \mu_i^* .$$

where μ_i^* is the mechano-chemical potential. The last terms in above equations describe the fact that diffusion (entropy production) does not affect internal energy of the mixture. Namely, that entropy is produced at the expense of mechanical energy of the mixture.

The drift velocity is the unique frame of reference for the diffusion and the volume continuity equation allows defining it quantitatively:

$$\text{div} \left(\sum_{i=1}^r c_i \Omega_i v_i \right) = \text{div} \left(v^{drift} + \sum_{i=1}^r c_i \Omega_i v_i^d \right) = \text{div} \left(v^{drift} + \sum_{i=1}^r \Omega_i J_i^d \right) = 0 .$$

The local momentum density depends on the diffusion of mass as well as on all other transport processes. The momentum due to the diffusion can be locally compensated by the Darken velocity. In such a case the overall volume velocity in the momentum balance is: $v = v^\sigma + v^r$ and complete the condition, that the local acceleration of the body depends on its mass, not on its internal energy and that the local centre of mass position is not affected by diffusion.

The method is applied to investigate the Planck-Kleinert Crystal hypothesis [5]. Crystal is the ideal cubic fcc crystal formed by Planck particles. In this type of quasi-continuum the energy, momentum and mass transport are described by the presented above classical balance equations and volume continuity equation. It will be shown that transverse wave can be interpreted as the electromagnetic wave and its velocity equals the velocity of light. The quasi-stationary collective movement of mass in the crystal is equivalent to the *particle* (body) and such an approach enables derivation of the Schrödinger equation. The interstitial Planck particles (defects) create a deformation that is equivalent to the gravity field and the computed value of G is within the accuracy of experimental data. The model predicts four different force fields in the crystal lattice.

The consequence of the equation of internal energy conservation is the existence of waves involving temperature but not the mechanical potential variations. They are analogous to “the second sound” described by Landau and Lifshitz [6].

References

- [1] L.S. Darken (1948), *Trans. A.I.M.E.*, **174** 184-198.
- [2] H. Brenner (2006), *Physica A*, **370** 190-211.
- [3] H.C. Öttinger (2005), *Beyond Equilibrium Thermodynamics*, Wiley, New Jersey.
- [4] M. Danielewski, B. Wierzba (2008), *Physica A*, **387** 745–756.
- [5] M. Danielewski (2007), *Z. Naturforsch.*, **62a** 564-568.
- [6] L.D. Landau and E.M. Lifshitz (1987), *Fluid Mechanics*, 2nd ed., Butterworth-Heinemann, Oxford.

HYPERBOLIC HEAT CONDUCTION WITH FUZZY PARAMETERS

K. Frischmuth¹ and W. Kosiński^{2,3}

¹*Institute of Mathematics, University of Rostock, 18051 Rostock, Germany*
kurt.frischmuth@uni-rostock.de

²*Department of Computer Science, Polish-Japanese Institute of Information Technology,*
ul. Koszykowa 86, 02-008 Warsaw, Poland

³*Kazimierz Wielki University in Bydgoszcz*
Institute of Environmental Mechanics and Applied Computer Science
ul. Chodkiewicza 30, 85-064 Bydgoszcz
wkos@pjawst.edu.pl

We consider a heat conductor for which the heat transfer model [2, 6] with the semi-empirical temperature is used. In real-life problems material coefficients and parameters used in mathematical modelling can be just vague. For instance at 15 K for NaF crystals, where the first and second sound waves have been observed, known measurements of material parameters (cf. [4] and the literature cited there) show large volatilities of observed quantities. Hence to model this one can go to an extended model in which some material coefficients and data are fuzzy. In this paper we assume them in the form of ordered fuzzy numbers appearing in the new model introduced by the second author (W.K.) with two coworkers in 2002 in [7, 9, 10, 11, 12]. Our aim is to investigate waves described by the hyperbolic model of heat conduction [1, 3] to give solutions of the coupled system of fuzzy differential equations. Some defuzzification operators [7, 9] are proposed in order to get crisp numerical results.

Fuzzy numbers as a particular case of fuzzy sets were introduced by Zadeh in 1965 [14]. They have entered the applications area such as control theory or economy. In most applications the so called (L, R) -numbers with two shape functions L and R , proposed by Dubois and Prade in 1978 as a restricted class of membership functions, are commonly used together with triangular and trapezoidal fuzzy numbers [5]. Arithmetic operations on fuzzy numbers have been developed with both the Zadeh's extension principle [15, 16] and the α -cut with interval arithmetic methods [5].

The concept of convex fuzzy numbers has been introduced by Nguyen [13] in order to improve calculation and implementation properties of fuzzy numbers. However, the results of multipl operations on the convex fuzzy numbers are leading to the large growth of the fuzziness, and depend on the order of operations since the distributive law, which involves the interaction of addition and multiplication, does not hold there.

Recently introduced and developed main concepts of the space of ordered fuzzy numbers (OFN) by the second author and his coworkers solved several drawbacks of both (L, R) as well as the convex fuzzy numbers. In this approach the concept of membership functions has been weakened by requiring a mere *membership relation*.

By an ordered fuzzy number A we mean an ordered pair (f, g) of functions such that $f, g : [0, 1] \rightarrow \mathbf{R}$ are continuous. The new model of fuzzy numbers has a lot of useful mathematical properties, in the particular the arithmetic of ordered fuzzy numbers is similar to that known for real numbers. Moreover, we are getting rid of the main problem in a classical fuzzy numbers - the unbounded increase of inaccuracies with next calculations.

Now, we apply the concept to the heat conduction problem mentioned above. Following [2, 6] a scalar internal state variable β is introduced. For β a kinetic equation is proposed. Then the heat flux q is given in terms of gradients of the absolute temperature θ and β . Taking gradients of the both

sides of the kinetic equation one obtains an evolution equation for $g = \nabla\beta$

$$(1) \quad g_{,t} = \gamma\theta_{,x} - \gamma g.$$

Throughout this present paper we restrict ourselves to the simplest case where β itself does not appear explicitly in that equation, i.e., we postulate a linear kinetic equation.

In the previous paper [4] we assumed that θ is small enough so the heat capacity c_v and the conductivity κ have been regarded as constants (measured at some reference temperature θ_0). In the present paper we assume that they are ordered fuzzy numbers.

In the previous paper we have discussed the case of fuzzy ordinary differential equations (FODE) [8]. Now the governing system becomes a system of fuzzy partial differential equations (FPDE) for which numerical calculations are performed. The results are discussed from the point of view of their physical applicability. Some defuzzification operators [9] are proposed, which map fuzzy numbers into reals in order to give an appropriate physical interpretation for the results obtained.

References

- [1] V. A. Cimmelli and K. Frischmuth, *Determination of material functions through second sound measurements in a hyperbolic heat conduction theory*, Mathl. Comput. Modelling, **24**(12) (1996), 19.
- [2] V. A. Cimmelli and W. Kosiński, *Nonequilibrium semi-empirical temperature in materials with thermal relaxation*, Arch. Mech., **43** (6),(1991), 753–767.
- [3] K. Frischmuth and V. A. Cimmelli, *Numerical reconstruction of heat pulse experiments*, Int. J. Eng. Sc., **33** (1995), 2, 209.
- [4] K. Frischmuth and V. A. Cimmelli, *Coupling in thermo-mechanical wave propagation in NaF at low temperature*, Arch. Mech. **50** (4), 1998, 703–713.
- [5] A. Kaufman, M. M. Gupta, *Introduction to Fuzzy Arithmetic*, Van Nostrand Reinhold, New York, 1991.
- [6] W. Kosiński, *Elastic waves in the presence of a new temperature scale*, In: *Elastic Wave Propagation*, M. F. McCarthy and M. Hayes (eds.), Elsevier Science (North Holland), New York, pp. 629–634, 1989.
- [7] W. Kosiński, *On defuzzification of ordered fuzzy numbers*, In: *ICAISC 2004, 7th Int. Conference, Zakopane, Poland, June 2004*, L. Rutkowski, Jörg Siekmann, Ryszard Tadeusiewicz, Lofti A. Zadeh (Eds.), LNAI, vol. 3070, pp. 326–331, Springer-Verlag, Berlin, Heidelberg, 2004.
- [8] Kosiński W., Koleśnik R., Prokopowicz P., Frischmuth K., *On algebra of ordered fuzzy numbers*, in Atanassov K. T., Hryniewicz O., Kacprzyk J., (Eds.) *Soft Computing – Foundations and Theoretical Aspects*, (Warszawa: Akademicka Oficyna Wydawnicza EXIT) 291–302.
- [9] W. Kosiński, U. Markowska-Kaczmar, *An evolutionary algorithm determining a defuzzification functional*, Task Quarterly, **11**(1-2), 2007, 47–58.
- [10] W. Kosiński, P. Prokopowicz, *Algebra of fuzzy numbers*, *Algebra liczb rozmytych* (In Polish): Matematyka Stosowana, **5**(46), 2004, 37–63.
- [11] W. Kosiński, P. Prokopowicz, D. Ślęzak, *Fuzzy numbers with algebraic operations: algorithmic approach*, In: *Intelligent Information Systems 2002*, M. Kłopotek, S. T. Wierzchoń, M. Michalewicz (Eds.), Proc.IIS'2002, Sopot, June 3-6, 2002, Poland, pp. 311-320, Physica Verlag, Heidelberg, 2002.
- [12] W. Kosiński, P. Prokopowicz, D. Ślęzak, *Ordered fuzzy numbers*, Bulletin of the Polish Academy of Sciences, Ser. Sci. Math. **51**(3), 2003, pp. 327-338.
- [13] H.T. Nguyen, *A note on the extension principle for fuzzy sets*, J. Math. Anal. Appl., **64**, (1978), 369–380.
- [14] L. A. Zadeh, *Fuzzy sets*, Information and Control, **8**(3), 1965, 338–353.
- [15] L. A. Zadeh, *The concept of a linguistic variable and its application to approximate reasoning, Part I*, Information Sciences, **8**(3), 1975, 199–249.
- [16] L. A. Zadeh, *The role of fuzzy logic in the management of uncertainty in expert systems*, Fuzzy Sets and Systems, **11**(3), 1983, 199–227.

PULSED IR THERMOGRAPHY FOR DETECTION OF MATERIAL DEFECTS

W. Oliferuk, Z. Płochocki and O. Wysocka
Institute of Fundamental Technological Research,
Polish Academy of Sciences, Świętokrzyska 21,
00-049 Warsaw, Poland

1. Introduction

The application of IR thermography to detect flaws in the subsurface layer of the tested material needs a thermal stimulation of its surface. One of the most common thermal stimulation method used in the nondestructive material testing is the pulsed IR thermography. It is based on monitoring of the temperature distribution on the material surface during its self-cooling after stimulation. The surface temperature distribution is disturbed by the flaws inside the tested material. This disturbance as an indicator of flaw presence can be used. Thus, it is necessary to know the time dependence distribution of the temperature on the surface of the sound material. This dependence is known when the surface of the tested material is uniformly heated by an impulse with infinitesimal duration [1, 2]. In this paper the layer of the examined material is approximated by a semi-infinite body and the self-cooling process of semi-infinite uniform body after stimulation by a rectangular impulse with a finite duration is considered. The criterion of long time regime approximation is formulated and verified experimentally.

2. Time dependence of temperature field on semi-infinite body surface heated uniformly by the heat impulse of constant strength with a finite duration

When the surface of a tested material is heated uniformly, we can limit the analysis to the one-dimensional differential heat conduction equation. Then we have:

$$(1) \quad \frac{\partial T}{\partial t} = \alpha \frac{\partial^2 T}{\partial z^2} + \frac{w}{c\rho}$$

where α is the thermal diffusivity of the material, c is the specific heat, ρ is the material density, w is the volume density of the heat impulse power absorbed, t and z are coordinates time and distance, respectively. Then the initial boundary conditions are as follows:

$$(2) \quad T(0, z) = T_0, \quad \frac{\partial T}{\partial z}(t, 0) = 0 \quad \text{and} \quad T(t, \infty) = T_0.$$

The solution of the differential equation of heat conduction for the initial boundary conditions as above is as follows:

$$(3) \quad \Delta T(t) = \frac{2Q_s(\tau)}{c\rho\sqrt{\pi t\alpha}} \left(\sqrt{\frac{t}{\tau}} - \sqrt{\frac{t}{\tau} - 1} \right)$$

Thus, it has been shown that when the surface of the tested material was heated uniformly by the heat impulse with the finite duration time τ and the time of the surface self-cooling $t \gg \tau$, then:

$$(4) \quad \Delta T(t) \sim \frac{1}{\sqrt{t}}$$

Deflection from the form of Eq. (4) indicates a presence of flaws in the tested material, because defects change thermal diffusion process. On logarithmic scales the graph of the function given by Eq. (4) is a straight line with slope $-\frac{1}{2}$.

3. Experiments, results and discussion

Experiment was performed on the specimen containing a simulated delamination. The specimen was made of two austenitic steel plates. In one of them (3.6 mm thick) the flat bottom hole has been drilled. The second plate was 2 mm thick and it has been stuck to the previous one. It allowed us to obtain the simulated delamination located at the depth of 1 mm. The surface of the specimen was heated uniformly by a conventional IR lamp of 500 W during 3 seconds. A temperature distribution on the surface during its self cooling process was measured by IR camera (ThermaCam 595) with a frame rate 50 Hz.

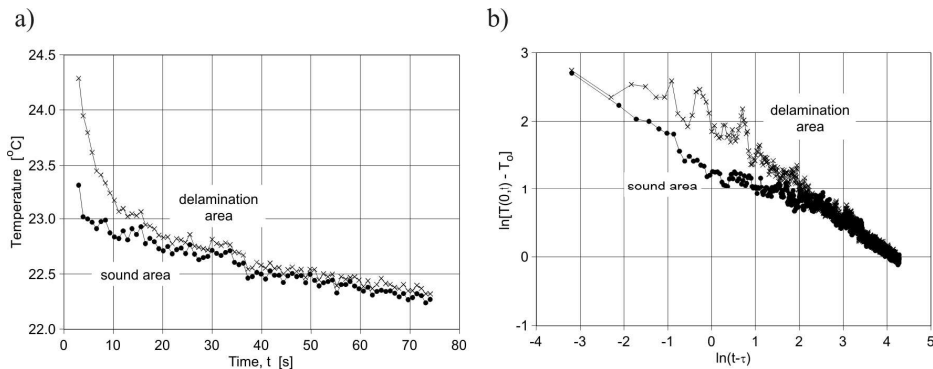


Fig. 1. a) The time evolution of the average temperature for the surface zones over defect and over sound material; b) Logarithmic time evolution of the surface temperature after the end of uniform heating for the surface zones.

In Fig. 1b the diagram $\ln[T(0,t) - T_0]$ vs. $\ln(t - \tau)$ for the sound and delamination zone is presented. The term $T(0,t)$ is average surface temperature of two investigated zones and $T_0 = 21.7^\circ\text{C}$ is the temperature of the tested surface before heating. It is seen that the slope of the graph line corresponding to the sound zone is nearly $-\frac{1}{2}$. This confirms correctness of the derived formula (4) and of the taken assumption. A deflection from the $-\frac{1}{2}$ slope, as the indicator of a presence of flaws under a tested area of the material surface can be used.

It has been shown that monitoring of temperature field on the material surface after its uniform thermal stimulation by a heat impulse of a finite duration makes possible to detect flaws under tested surface.

4. References

- [1] A. V. Luikov (1968). *Analytical Heat Diffusion Theory*, Academic Press, 377–398.
- [2] H. S. Carslaw, J. C. Jaeger (1959). *Conduction of Heat in Solids*, 2nd ed., Clarendon Press, 50–92.

COMPARISON LUBRICITY BEHAVIOUR OF NANOLAMINATED Ti_3SiC_2 AND SOLID LUBRICANTS

M. B. Rahaei

Materials and Energy Research Center, Tehran, Iran

1. General

In this research, the lubricity behavior of Ti_3SiC_2 was investigated by using a pin-on-disc a sliding wear test with a AISI 52100 steel. In the pin-on-disc test, samples show the low friction coefficient (μ), especially in low loads. Microscopic observations show a lubricating layer on samples surfaces that the result of decreasing of μ due to the lubricating behavior. In a high load, samples shows increase in μ ($\approx 200N$) and wear rate in 80 N loads, approximately. The results showed that Ti_3SiC_2 has a lubricity behavior in low loads ($< 80 N$) and can be used as a solid lubricant. Then lubricity behavior of this compound was then evaluated in comparison with graphite and MoS_2 solid lubricant. Likewise lubricity mechanisms are layer structure in compounds, and constituted permanent and lubricant oxide layer on surface of samples.

2. Introduction

The ternary compound, nanolaminated Ti_3SiC_2 is known that has many of the best properties of both metals and ceramics, such This unique combination of properties makes Ti_3SiC_2 a likely candidate for structural applications at elevated temperatures [6, 7], such as turbine blades and stators, heavy duty electric contacts, bearings, etc [4].

A number of useful publications have been written on the use of solid lubricants for space applications. Realistically, the most likely candidates are in the following categories: - Soft metal films: especially Pb, but also Ag and Au, - Lamellar solids: e.g., MoS_2 and WS_2 , and - Polymers: such as PTFE films and glass fiber reinforced composites. Many other candidates could also be considered, but these are the primary choices [3]. Solid lubricants are useful for conditions when conventional lubricants are inadequate [2]. The friction coefficients of solid lubricant materials are of about 0.06 to 0.15 depending upon humidity and sliding conditions [1]. However, currently, reports on the tribological behavior of Ti_3SiC_2 are limited, especially lubricity and wear rate in high load. In the present paper evaluate the tribology behavior (lubricity and wear) of Ti_3SiC_2 ternary compound against 52100 steel pin in low and high loads, then compared with graphite and MoS_2 solid lubricants. The unit cell of Ti_3SiC_2 that compose a nanolayered structure, and graphite and MoS_2 solid lubricants, as shown in Fig. 1.

3. Experimental procedure

The contracted phases of the Ti_3SiC_2 were characterized employing XRD-Philips X'pert-MPD and Microstructure observation by SEM-XL30. The macro-hardness was evaluated by a Vickers diamond indenter at load 50 N using the following formula in Eq. 1. The wear rate (wear coefficient in mm^3/Nm) was calculated under opposite frame: $\Delta m / (p.F.L)$. Then compared with graphite and MoS_2 slid lubricants.

4. Results and discussion

according to XRD analysis, (Fig. 1), As can be seen in the SEM represented at Fig. 3, the product was not uniform, some regions rich in the ternary Ti_3SiC_2 phase, and some being a two-phase mixture of TiC and few amount and Ti–Al binary phases was detected. The results of friction test are listed in Table 1 in various loads, likewise in sliding distance curves, in the pin-on-disc test (Fig 2). It was found that the material undergoes a critically transition stage where the friction coefficient (μ), increases linearly of 0.06 to 0.35 in 200 N load. A change in wear mechanism is initial observed at high load, especially in load over 200 N, that increase (COF and wear rate). The final result show that a low wear rate in 80N load ($< 10^{-6}$) and low COF in low load ($< 200N$) (Fig. 2). Therefore proposed this compound can use as solid lubricant in load lower than 80 N.

Table. (1). Friction coefficient and wear rate for Ti_3SiC_2 sample in various normal load.

Load (N)	10	40	80	120	160	200	240	280
COF (μ)	0.06-0.08	0.06-0.1	0.06-0.1	0.06-0.12	0.06-0.12	0.06-0.12	0.3-0.4	0.35-0.39
WR $\times 10^5$ (mm ³ /Nm)	2	6	12.2	20.3	21.3	25.6	198	182

In table (2) had come friction coefficient of for Ti_3SiC_2 sample in comparison MoS_2 and graphite solid lubricant. The result shows that nanolayered Ti_3SiC_2 has lubricity behavior in higher loads without humid environment, also can use in higher temperature in comparison MoS_2 in low load, because of don't decompose.

Table. (1). Friction coefficient and wear rate for Ti_3SiC_2 sample in various normal load.

Load (N)	10	40	80	120	160	200	240	280
Ti_3SiC_2	0.06-0.08	0.06-0.1	0.06-0.1	0.06-0.12	0.06-0.12	0.06-0.12	0.3-0.4	0.35-0.39
Graphite	0.24	0.16	0.05-0.12	Failure				
MoS_2	0.05-0.15	0.05-0.15	0.05-0.15	0.05-0.15	0.05-0.15	0.05-0.15	0.05-0.15	0.05-0.15

5. Conclusion

In this work, the tribology behavior of Ti_3SiC_2 /steel friction pairs was investigated. This compound showed low COF $\approx 0.06-0.12$ in low load ($<200N$) and a critically behavior in 200 N load, which that change wear mechanism of tribochemical to abrasion. Likewise illustrated low wear rate $\approx < 10^{-6}$ in load lower than 80 N. lubricity mechanisms in low load was composed permanent oxide layer (tribochemical mechanism) and layered structure, but in high load has abrasion mechanism and plastic deformation. Therefore nanolaminated Ti_3SiC_2 can be used as a solid lubricant in low load, and high temperature due to constituted a passive layer in high loads. In comparison if that MoS_2 has lubricity behaviour in high loads but in high temperature decomposed. Also in comparison graphite has lubricity behavior without a humid environment.

6. References

- [1] R. L. Fusaro (2001). Preventing Space craft Failures Due to Tribological Problems, National Aeronautics and Space Administration, 43.
- [2] H. E. Sliney (1991). Solid Lubricants. NASA Technical Memorandum, 38.
- [3] Yi Zhang (2002). Ti_3SiC_2 -a self-lubricating ceramic, Mat. Letters, 55, 285-289.

NUMERICAL METHODS INVOLVED IN LUBRICANT LIFE CYCLE DETERMINATION

I. Radulescu

S.C. I.C.T.C.M. S.A. Bucharest, Romania

1. Introduction

The paper proposes a method for the lubricants wear degrees diagnosis, based on determination of the rheological properties, specially about the reducing of the viscosity values during the time. The experimental stand used for measuring the rheological parameters of the lubricants is a cone and plate viscometer, which offers absolute viscosity determination with precise shear rate and shear stress information.

In order to estimate the wear degree of the used oils, a theoretical relation is proposed [1], which establish the variation of the viscosity versus the equivalent distance covered by the motor vehicle:

$$\eta = \eta_0 e^{-Kd} \quad (1)$$

The two parameter characteristics are the initial viscosity η_0 for the fresh oil and the wear intensity coefficient K . These values are determined using the regression analysis method.

2. Experimental procedure

Experimental investigations were undertaken with the aim to check the assumed theoretical method. They were carried out at the ambient temperature of 20 °C, for three types of oils, which lubricate motor vehicles with different wear degrees:

- ELF EXCELLIUM LDX 5W-40 from a Diesel motor vehicle with 130000 km way;
- ELF PERFORMANCE EXPERTY 10W-40 from an essence motor vehicle with 38000 km way;
- ELF COMPETITION ST 10W-40 from an essence motor vehicle with 80000 km way.

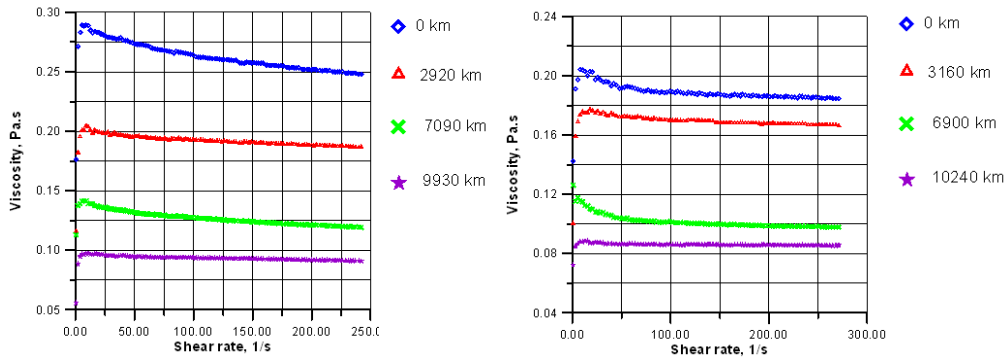
For each type of oil, the mean life time recommended by the producers is 10000 km, [2]. During this period, a few samples of lubricants have been collected, corresponding at different wear degrees: for fresh oil (at 0 km) and for used oil (approx. at 3000 km, 7000 km and 10000 km).

3. Results

Two typical rheograms, obtained with the Brookfield cone and plate viscometer, for two tested oils, are presented in Figure 1, a and b. In these figures, four curves are presented, corresponding for different wear degrees of the tested oils. It can observe that the viscosity decreases with equivalent distance of the motor vehicle, and clearly depends of the oil type.

The experimental data have been numerical analyzed using the regression analysis method, in order to obtain the mean values of the viscosity, for fresh and used oils (see Table 1). The same table presents the values of the correlation coefficient, which is an indicator of the correlation level between the theoretical Newtonian model and the experimental data.

In order to obtain the main values of the initial viscosity η_0 for the fresh oil and the wear intensity coefficient K (see Eq. 2), the data from Table 1 are numerically treated and the results are presented in Table 2.



a. ELF EXCELLIUM LDX 5W-40 oil b. ELF PERFORMANCE EXPERTY 10W-40 oil
 Figure 1. Experimental rheogram for tested oils

Type of oil	Wear degree	Equivalent distance, km	Viscosity, Pa.s	Correlation coefficient
ELF EXCELLIUM LDX 5W-40	Fresh oil	0	0.186	0.963
	Used oil	2920	0.167	0.982
		7090	0.086	0.991
		9930	0.099	0.994
ELF PERFORMANCE EXPERTY 10W-40	Fresh oil	0	0.253	0.957
	Used oil	3160	0.189	0.978
		6900	0.122	0.989
		10240	0.092	0.995
ELF COMPETITION ST 10W-40	Fresh oil	0	0.229	0.968
	Used oil	2850	0.164	0.975
		7100	0.118	0.988
		9870	0.068	0.990

Table 1. Regression parameters for tested oils

Type of oil	Initial viscosity, Pa.s	Wear intensity coefficient, km ⁻¹	Correlation coefficient
ELF EXCELLIUM LDX 5W-40	0.188	$7.793 \cdot 10^{-5}$	0.811
ELF PERFORMANCE EXPERTY 10W-40	0.254	$10.092 \cdot 10^{-5}$	0.996
ELF COMPETITION ST 10W-40	0.234	$11.582 \cdot 10^{-5}$	0.964

Table 2. Main values of the initial viscosity and wear intensity coefficient

4. Conclusions

Analyzing the experimental results obtained with this rheological method, it can be observed an important tendency of viscosity decreasing during the working time. Using the determination of the two characteristic parameters, the initial viscosity η_0 for the fresh oil and the wear intensity coefficient K , a new criteria for the wear degree of the oils is obtained.

5. References (selected)

[1] Czarny, R. "A study of thixotropy phenomen in lubricating greases", EUROTRIB' 89, Vol. IV, Helsinki, sept.1989, pp. 198-203
 [2] *** ELF Lubricants, www.lubricants.elf.com/lub/lubroot.nsf/

SAINT-VENANT'S PRINCIPLE IN MAGNETOELASTICITY

T. J. Hoffmann, M. Chudzicka-Adamczak

Poznań University of Technology, Institute of Applied Mechanics, Poznań, Poland

Toupin's version of Saint-Venant's principle in linear elasticity is generalized to the case of linear magnetoelasticity. That is, it is shown that, for a straight prismatic bar made a linear magnetoelastic material end loaded by a self-equilibrated system at one end only, the internal energy stored in the portion of the bar which is beyond a distance s from the loaded end decreases exponentially with the distance s .

Mathematical versions of Saint-Venant's principle in linear elasticity due to Sternberg, Knowles, Zanaboni, Robinson and Toupin have been discussed by Gurtin [1] in his monograph. Later developments of the principle for Laplace's equation, isotropic, anisotropic, and composite plane elasticity, three-dimensional problems, nonlinear problems, and time-dependent problems are summarized in the review articles by Horgan and Knowles [2] and by Horgan [3]. In this paper we prove an analogue of Toupin's version of Saint-Venant's principle for linear magnetoelasticity. For a linear elastic homogeneous prismatic body of arbitrary length and cross-section loaded on one end only by an arbitrary system o self-equilibrated forces, Toupin [4] showed that the elastic energy $U(s)$ stored in the part of the body which is beyond a distance s from the loaded end satisfies the inequality

$$(1) \quad U(s) \leq U(0) \exp \left[-\frac{(s-l)}{s_c(l)} \right].$$

The characteristic decay length $s_c(l)$ depends upon the maximum and the minimum elastic moduli of the material and the smallest nonzero characteristic frequency of free vibration of a slice of the cylinder of length l . Inequalities similar to (1) have been obtained by Batra [5] for linear elastic piezoelectric prismatic bodies and by Borrelli & Patria [6] for a semi-infinite magnetoelastic cylinder on the asymptotic behaviour of the Dirichlet integral of the magnetic field and of the elastic energy.

Here we consider a linear theory of magnetoelasticity (for infinitesimal strain) in which only the ponderomotive force remains non-linear in presence of a magnetic field. We assume that the elastic body is homogeneous, isotropic and electrically conducting [7], [8], [9], [10].

Let the finite spatial region occupied by the magnetoelastic body be V , the boundary surface of V be S . the unit outward normal of S be n_i , and S be partitioned as

$$(2) \quad \begin{aligned} S &= S_u \cup S_T = S_E \cup S_B, \\ 0 &= S_u \cap S_T = S_E \cap S_B. \end{aligned}$$

Physically, S_u, S_T are, respectively, parts of the boundary S on which mechanical displacements and tractions are prescribed. S_E is the part of S which is in contact with electrode, hence the tangential electric field vanishes on it, and S_B the parts of S on which the magnetic induction is prescribed. The governing equations and boundary conditions for static magnetoelasticity in rectangular Cartesian coordinates in SI units are:

$$\begin{aligned}
(3) \quad & \partial_i \tilde{T}_{ij} = 0, \quad \varepsilon_{ijk} \partial_j E_k = 0, \quad \partial_k D_k = 0, \quad \text{in } V, \\
& \varepsilon_{ijk} \partial_j H_k = j_i, \quad \partial_k B_k = 0, \quad \text{in } V, \\
& j_k = \sigma E_k, \quad D_k = \varepsilon E_k, \quad B_k = \mu H_k, \quad \text{in } V, \\
& \tilde{T}_{ij} = t_{ij} + T_{ij}, \quad t_{ij} = c_{ijkl} \varepsilon_{kl}, \quad T_{ij} = B_i H_j - \frac{1}{2} \delta_{ij} B_k H_k, \quad \text{in } V, \\
& \varepsilon_{ij} = \frac{1}{2} (\partial_i u_j + \partial_j u_i), \quad \text{in } V, \\
& u_i = \tilde{u}_i \quad \text{on } S_u, \quad n_i \tilde{T}_{ij} = \tilde{t}_j \quad \text{on } S_T, \\
& \varepsilon_{ijk} n_j E_k = 0 \quad \text{on } S_E, \quad n_i B_i = 0 \quad \text{on } S_B,
\end{aligned}$$

where u_i is the mechanical displacement, t_{ij} the mechanical stress tensor, T_{ij} the Maxwell stress tensor, ε_{ij} the strain tensor, E_k the electric field vector, D_k the electric displacement vector, H_k the magnetic field vector, j_k the current vector, B_k the magnetic induction vector, ε, μ, σ the electromagnetic material constants, c_{ijkl} the elastic moduli, ε_{ijk} the permutation tensor, δ_{ij} the unit tensor, ∂_k the spatial derivative, \tilde{u}_i and \tilde{t}_j are the prescribed boundary mechanical displacement and traction vectors.

References

- [1] M. E. Gurtin (1972). *The Linear Theory of Elasticity*, Handbuch der Physik, Vol. VIa/2, ed. C. Truesdell, Springer-Verlag, Berlin, Heidelberg, New York.
- [2] C. O. Horgan, J. K. Knowles, (1983). *Recent developments concerning Saint-Venant's principle*, *Advances in Applied Mechanics*, Vol. 23, edited by J. W. Hutchinson and T. Y. Wu, Academic Press, New York pp. 179-269.
- [3] C. O. Horgan (1989). *Recent developments concerning Saint-Venant's principle: an update*. *Appl. Mech. Rev.* pp. 295-303.
- [4] R. A. Toupin (1965). *Saint-Venant's principle*, *Arch. Rat. Mech. Anal.* **18** pp. 83-96.
- [5] R. C. Batra, J. S. Yang (1995). *Saint-Venant's Principle in Linear Piezoelectricity*, *J. of Elasticity* **38** pp. 209-218.
- [6] A. Borrelli, M. C. Patria (1997). *Decay and other estimates for a semi-infinite magnetoelastic cylinder: Saint-Venant's Principle*, *Int. J. Non-Linear Mech.* **32** pp.1087-1099.
- [7] W. Nowacki (1966). *Dynamic Problems of Thermoelasticity* (in Polish), PWN Warszawa.
- [8] G. A. Maugin (1988). *Continuum Mechanics of Electromagnetic Solids*, North Holland.
- [9] A. C. Eringen, G. A. Maugin (1990). *Electrodynamics of Continua*, Vol. 1. Springer-Verlag.
- [10] T. J. Hoffmann (2002). *Mechanical Aspects of Magnetoelasticity* (In Polish), Wydawnictwo Politechniki Poznańskiej, Poznań.

This work is supported by the Poznan University of Technology Project No. 21-206/2008 BW.

PROPAGATION OF ULTRASONIC WAVES IN INHOMOGENEOUS MATERIALS

M. Cieszko, J. Kubik

*Institute of Environmental Mechanics and Applied Computer Science,
Kazimierz Wielki University, Bydgoszcz, Poland*

1. Introduction

The problem of ultrasonic wave interaction with continuous inhomogeneity of material is of great importance for theory and applications. Such materials are commonly present in living systems, nature, building engineering and industry. They are often strongly micro inhomogeneous, form multicomponent systems and processes of their growth, production or destruction often lead to their macro inhomogeneity. The techniques of experimental investigation of such materials, widely developed in recent years, are ultrasonic methods. They allow non-destructive determination of materials coefficients and parameters, evaluation of their state and proceeding processes. However, there is a lack of papers devoted to description and analysis of interaction of ultrasonic waves with continuous inhomogeneity of the material, and existing monographs (e.g. [1], [2]) consider this problem in simple acoustical systems characterized only by the wave number.

The aim of this paper is to present the new method of description and analysis of one dimensional problems of ultrasonic wave interaction with continuous inhomogeneity of materials characterized by dependence of the wave number and the impedance of a medium on the spatial coordinate.

2. Formulation of the problem

We consider one dimensional problem of plane harmonic wave propagation of frequency ω in an arbitrary material with inhomogeneity of acoustical properties that are locally characterized by the impedance z and the wave number k . These parameters, in general, are complex functions of spatial coordinate x and wave frequency ω (Fig. 1).

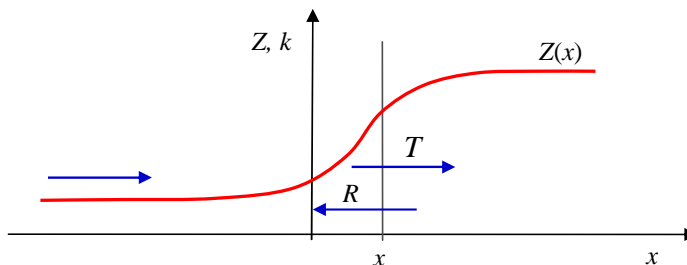


Fig.1. Exemplary distribution of local impedance in material with continuous inhomogeneity of acoustical properties.

Due to interaction with material inhomogeneity each wave propagating in such material generates the coupled backward wave. Therefore, the acoustical field in inhomogeneous material is defined by amplitudes T and R of the forward and backward waves, respectively.

3. Solution of the problem

Equations describing the acoustical field in inhomogeneous material have been obtained considering such medium as a system of homogeneous infinitesimal layers with stepwise changeable acoustical properties approximating functions $k(z)$ and $Z(x)$. In this case wave interaction with continuous inhomogeneity can be considered as multiple reflections and transitions of wave through the boundaries of infinitesimal layers and the acoustical field in the material, characterized by amplitudes T and R , as the superposition of waves propagating in each direction. The obtained equations have the form

$$\frac{dR}{dx} + ikR = \frac{dI}{dx}(2T + R) \quad , \quad \frac{dT}{dx} - ikT = \frac{dI}{dx}(2R + T)$$

where $I = \ln(Z_0/Z)/2$ and Z_0 is constant. From these equations results that only inhomogeneity of medium impedance induce the backward wave.

3. Analysis of exemplary problem

To illustrate the wave interaction with continuous inhomogeneity of the material the special case of inhomogeneous material has been considered. It is composed of two homogeneous halfspaces separated by a layer of inhomogeneous material of thickness L (Fig.3).

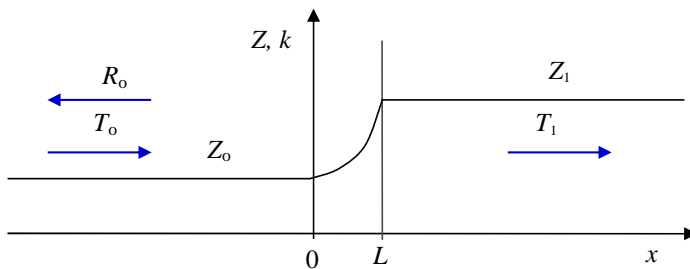


Fig.2. The exemplary medium with continuous inhomogeneity of impedance.

We assume that wave number k is constant in the whole system and impedance of the medium is continuous and changes only within the layer according to the expression

$$Z = Z_0 \exp(\alpha x) = Z_0 (Z_1 / Z_0)^{x/L} \quad , \quad \alpha = \ln(Z_1 / Z_0) / L \quad .$$

In this case the system of equations becomes linear, and due to continuity of impedance, a wave propagating in such medium is reflected only by impedance inhomogeneity in the layer. It enables the analysis of influence of this inhomogeneity on acoustical characteristics of reflected and transmitted waves.

4. References

- [1] L. M. Brekhovskikh (1980). *Waves in Layered Media*. Academic Press, New York.
- [2] P. Filippi, D. Habault, J.P. Lefebvre, A. Bergassoli (1999). *Acoustics. Basic Physics, Theory and Methods*, Academic Press, San Diego.

TRIBOLOGICAL ASPECTS OF THE SOLID-FLUID INTERACTION FOR FRESH AND USED LUBRICANTS

A. V. Radulescu¹, F. Petrescu² and I. Radulescu³

¹ *University "POLITEHNICA" Bucharest, Romania*

² *TECHNICAL University of Civil Engineering of Bucharest, Romania*

³ *S.C. I.C.T.C.M. S.A. Bucharest, Romania*

1. Introduction

The paper presents the tribological aspects of the solid-fluid interaction, in order to obtain a new evaluation method for the lubricant durability. Its purpose is the development of a fast diagnoses method for the liquid lubricants, with minimal investments and a high precision level, easy to use, [1].

The principal result of this project is a new, efficient, performed and ecological methodology, for the evaluation and quantification of the wear degree and lubricants durability. In addition, it is important that a new complex device must be obtained for diagnosis of lubricants oils "life reserve". The project assures a modern laboratory and creates new premise for developing new approach directions for the lubricants durability problems, [2].

2. Experimental procedure

The test programme, using a TIMKEN equipment, had in view the influence of the lubricant state of degradation, considering the tribological behavior of the friction couple during the working time. Thus, six parallelepiped samples and twelve cylindrical samples were used. Each one of the parallelepiped samples has two active plane surfaces, made of OLC45-heat-treatable steel, and the final mechanical working process of the active surfaces was rough grinding. The cylindrical samples were made also of OLC45-heat-treatable steel and the final mechanical working process was finish grinding.

The length of the linear contact obtained in this way (cylinder/plane) is 12,7 mm and it corresponds to the parallelepipedic sample width. All the tests were carried out in the presence of two lubricants, 15W40 oil and LHP 46 oil, in fresh and used state. The cylinder-plane friction couple was immersed in a tank filled with this lubricant; also, during all tests, the oil temperature was kept to a constant value ($T = 40^{\circ}\text{C}$) and the same relative velocity ($v = 3,83\text{ m/s}$) was used. Tests were carried out using three values of the normal load F_n (30 N, 40 N and 50 N) and, during the tests, the wear trace (width and depth) were measured. Finally, pictures of the damage area were obtained with NEOPHOT 21 metallographic microscope.

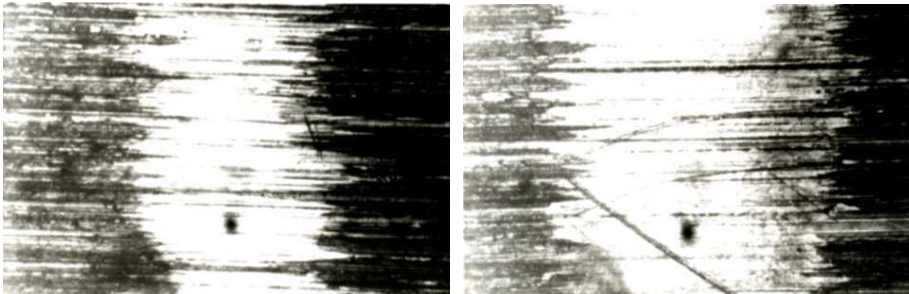
3. Results

The results of the experiments are presented in Table 1; Figures 1 and 2 show the microscopically pictures.

Proof No.	Load [N]	Lubricant	State of the lubricant	Width of the wear trace [mm]	Depth of the wear trace [mm]
1	50	15W40	fresh	1,230	0,015
2			used	1,512	0,023
3		LHP 46	fresh	1,230	0,015
4			used	1,688	0,025
5	40	15W40	fresh	1,045	0,012
6			used	1,132	0,018

Proof No.	Load [N]	Lubricant	State of the lubricant	Width of the wear trace [mm]	Depth of the wear trace [mm]
7	30	LHP 46	fresh	1,008	0,011
8			used	1,383	0,018
9		15W40	fresh	0,832	0,008
10			used	1,014	0,012
11		LHP 46	fresh	0,895	0,007
12			used	0,998	0,014

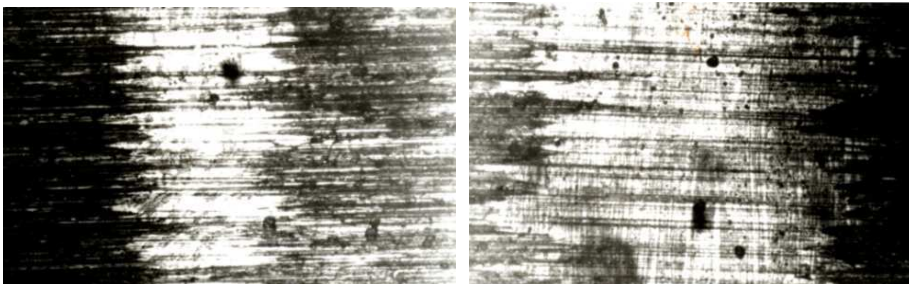
Table 1. Experimental results.



a. Fresh lubricant

b. Used lubricant

Figure 1. Wear trace for 15W40 oil



a. Fresh lubricant

b. Used lubricant

Figure 2. Wear trace for LHP 46 oil

4. Conclusions

The tribological method proposed is able to diagnose the state of degradation of the lubricants, with high precision and accuracy. As a signaled conclusion - the wear degree of the friction couples which utilizes used lubricants is more important than the same which utilizes fresh lubricants.

5. References (selected)

- [1] Hutching, I. M., Tribology – Friction and Wear of Engineering Materials, Edward Arnold, Great Britain, 1992.
- [2] Lockwood, F. E., Dally, R., Lubricant Analysis, ASTM Handbook, ASM International, Metals Park, OH, Vol. 18, 1992.

FORCED GAS-STRUCTURE VIBRATIONS IN A RECTANGULAR TANK

E. Gavrilova

St. Ivan Rilski University of Mining & Geology, Sofia, Bulgaria

1. Introduction

Rectangular thin elastic plates are often used as structural components closing or covering parallelepiped cavities filled with compressible fluid (gas) and subjected to dynamic loads. Such mechanical systems are applicable in the glass-skin technology of tall buildings, as outside skin plates of supersonic air crafts, as covers of different tanks in chemical industry, etc. In [1] the method of Bubnov-Galerkin together with the method of the crossed strips of G. Warburton is used and it is elaborated in the form of an easy scheme for application to the dynamic problem about the stationary vibrations of a special fluid-structure interaction system. It consists of a thin elastic plate, inserted into a rectangular orifice of an arbitrary wall of a parallelepiped tank, filled with an acoustic fluid.

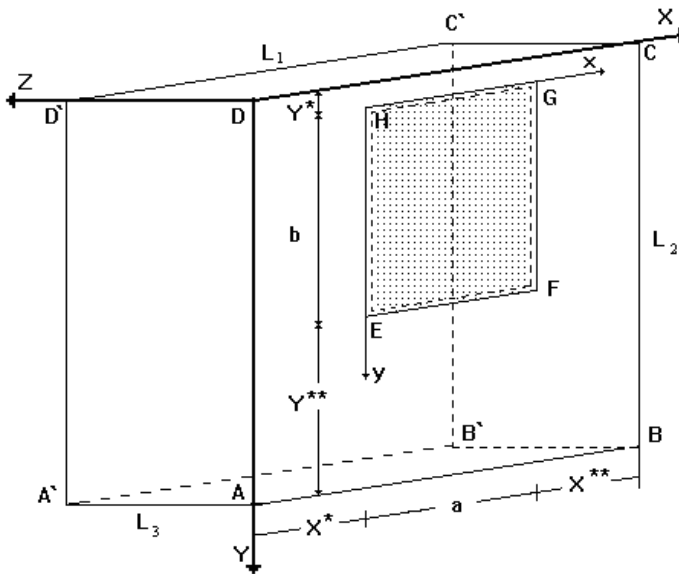


Figure 1. The geometry of the gas-structure interaction system under consideration

2. Formulation of the problem

Thin linearly elastic rectangular plate EFGH with sizes a and b and surface S is inserted into an orifice of the absolutely rigid wall ABCD of a rectangular parallelepiped tank, all its other walls are absolutely rigid (Figure 1). The tank volume is filled with gas with given sound velocity and mass density. The mass density per unit area of the plate, the flexural rigidity, the thickness, Young's modulus of elasticity and Poisson's ratio of the elastic plate material are given. Two rectangular co-ordinate systems DXYZ and Hxyz are used (see Figure 1). The problem about the stationary forced vibrations of the gas and the elastic plate under the action of a source, being situated in the gas tank, is under consideration. Let the source have a range of sizes which are small

in comparison with the lengths of the excited waves: then it is possible to be accepted as a point source. It is supposed that the productivity and the frequency of the source are given and are not influenced by the earlier excited waves. The problem is considered in a linear approximation without giving an account of the dissipating forces. Then the velocity potential function of the gas motion and the function, describing the middle surface vibrations of the plate, satisfy corresponding partial differential equations with boundary conditions which describe the way of supporting of the elastic plate as well as some compatibility condition [1].

3. Analytical solution

The point source is presented by the Dirac delta function. The velocity potential function of the gas motion and the function, describing the middle surface vibrations of the elastic plate, are separated into space-dependent modes and time-dependent terms, where the trial functions as well as the wave numbers or the dispersion equations are chosen correspondingly to the supporting conditions along the four plate edges [1]. After satisfying the compatibility condition and using the Bubnov-Galerkin method, some infinite system of nonhomogeneous algebraic equations about the unknown coefficients is obtained. Taking the determinant of the homogeneous system equal to zero, the equation about the determination of the natural frequencies of the considered gas-structure interaction system is obtained.

4. Numerical calculations

The theoretical solution is very complicated - that is why an approximate solution is made at based on ignoring diffraction by the elastic plate waves. The approximate solution can be used when the frequencies of the source are not close to the resonance frequencies of the gas-structure interaction system and when the cavity is filled with air.

Some numerical examples are made and they are represented graphically. If the frequency of the source tends to zero, very strong increase of the amplitudes appears except at the resonance points. The approximate formula cannot be used if there is a heavy liquid in the rectangular tank.

5. Conclusions

In this paper a closed rigid rectangular parallelepiped tank is filled with gas as a part of one of its walls is a thin linearly elastic rectangular plate. The problem about the stationary forced vibrations of the gas and the elastic plate under the action of a source, being situated in the gas tank, is under consideration. A combination of the use of the method of the crossed strips of G. Warburton and the method of Bubnov-Galerkin is made to investigate the dynamic behavior of this gas-structure interaction system in the cases of arbitrary supporting conditions of the plate. Some numerical examples are given which demonstrate the necessity of taking into account which part of the spectrum of the natural frequencies of the elastic plate the forced frequency is located in.

6. References

- [1] E.G. Gavrilova (1994). *Hydroelasticity of Thin-walled Prismatic Structures with Elastic Inclusions. PhD Thesis*, BAS IM, Sofia.

COUPLED DYNAMICS THERMOVISCOELASTIC PROBLEM

S. A. Lychev

Samara State University, Dept. of Continuum Mechanics, Samara, Russia

In the present study a closed solution of coupled dynamics thermoviscoelastic problem for finite body is obtained. The solution is of the form of spectral expansion to the biorthogonal eigenfunction system of non-self-adjointed differential pencil, generated by the initial–boundary value problem under consideration. The representation of spectral expansion is obtained by special non-symmetrical integral transformation [1,2].

Consider the coupled equations of viscoelastic motion and heat conduction in cylindrical coordinate system (r, φ, z) :

$$(1) \quad \begin{pmatrix} \mathcal{L}_1 & -\gamma\mathcal{L}_2 \\ 0 & \nabla^2 \end{pmatrix} \mathbf{y} + \begin{pmatrix} \mathcal{L}'_1 & 0 \\ -\eta\mathcal{L}_3 & -1/\kappa \end{pmatrix} \frac{\partial}{\partial t} \mathbf{y} + \begin{pmatrix} -\rho\mathcal{E} & 0 \\ 0 & 0 \end{pmatrix} \frac{\partial^2}{\partial t} \mathbf{y} = \mathbf{f},$$

wherein $\mathbf{f} = (-X_r, -X_\varphi, -X_z, -\omega)$ is prescribed vector-function, defined by volumetric force and heat sources intensity, \mathcal{E} is identity operator, $\mathcal{L}_1, \dots, \mathcal{L}_3$ are the following differential operators:

$$\mathcal{L}_1 = \begin{pmatrix} \left(\mu(\nabla^2 - \frac{1}{r^2}) + (K + \frac{\mu}{3}) \frac{\partial}{\partial r} \left(\frac{\partial}{\partial r} + \frac{1}{r} \right) \right) & \frac{K + \mu/3}{r} \frac{\partial}{\partial \varphi} \left(\frac{\partial}{\partial r} - \frac{1}{r} \right) - \frac{2\mu}{r^2} \frac{\partial}{\partial \varphi} & (K + \frac{\mu}{3}) \frac{\partial^2}{\partial r \partial z} \\ \frac{2\mu}{r^2} \frac{\partial}{\partial \varphi} + \frac{K + \mu/3}{r} \frac{\partial}{\partial \varphi} \left(\frac{\partial}{\partial r} + \frac{1}{r} \right) & \mu(\nabla^2 - \frac{1}{r^2}) + \frac{K + \mu/3}{r^2} \frac{\partial^2}{\partial \varphi^2} & \frac{K + \mu/3}{r} \frac{\partial^2}{\partial \varphi \partial z} \\ (K + \frac{\mu}{3}) \frac{\partial}{\partial z} \left(\frac{\partial}{\partial r} + \frac{1}{r} \right) & \frac{K + \mu/3}{r} \frac{\partial^2}{\partial z \partial \varphi} & \mu \nabla^2 + (K + \frac{\mu}{3}) \frac{\partial^2}{\partial z^2} \end{pmatrix},$$

$$\mathcal{L}'_1 = \mu' \begin{pmatrix} \left(\nabla^2 - \frac{1}{r^2} + \frac{1}{3} \frac{\partial}{\partial r} \left(\frac{\partial}{\partial r} + \frac{1}{r} \right) \right) & \frac{1}{3r} \frac{\partial}{\partial \varphi} \left(\frac{\partial}{\partial r} - \frac{1}{r} \right) - \frac{2}{r^2} \frac{\partial}{\partial \varphi} & \frac{1}{3} \frac{\partial^2}{\partial r \partial z} \\ \frac{2}{r^2} \frac{\partial}{\partial \varphi} + \frac{1}{3r} \frac{\partial}{\partial \varphi} \left(\frac{\partial}{\partial r} + \frac{1}{r} \right) & \nabla^2 - \frac{1}{r^2} + \frac{1}{3r^2} \frac{\partial^2}{\partial \varphi^2} & \frac{1}{3r} \frac{\partial^2}{\partial \varphi \partial z} \\ \frac{1}{3} \frac{\partial}{\partial z} \left(\frac{\partial}{\partial r} + \frac{1}{r} \right) & \frac{1}{3r} \frac{\partial^2}{\partial z \partial \varphi} & \nabla^2 + \frac{1}{3} \frac{\partial^2}{\partial z^2} \end{pmatrix},$$

$$\mathcal{L}_2 = \left(\frac{\partial}{\partial r} \quad \frac{1}{r} \frac{\partial}{\partial \varphi} \quad \frac{\partial}{\partial z} \right)^T, \quad \mathcal{L}_3 = \left(\frac{\partial}{\partial r} + \frac{1}{r} \quad \frac{1}{r} \frac{\partial}{\partial \varphi} \quad \frac{\partial}{\partial z} \right), \quad \nabla^2 = \frac{\partial^2}{\partial r^2} + \frac{1}{r} \frac{\partial}{\partial r} + \frac{1}{r^2} \frac{\partial^2}{\partial \varphi^2} + \frac{\partial^2}{\partial z^2},$$

K, μ are the elastic modulus; γ, η are the thermomechanical constants; κ is the thermal conductivity coefficient, ρ is the density, μ' is the viscosity modulus.

The boundary conditions \mathcal{D} are arbitrary on lateral area and have some restrictions on end faces (to admit the separation of variables, see [3]):

$$(2) \quad \mathcal{D} = \{ \mathbf{y} | \mathbf{y} \in L_2^4, \mathcal{B}\mathbf{y} = 0, \mathbf{y} = O(1) \},$$

$$\mathcal{B}\mathbf{y} = \begin{pmatrix} \mathcal{B}_1 \mathbf{y} \Big|_{r=R} \\ \mathcal{B}_2 \mathbf{y} \Big|_{z=0} \\ \mathcal{B}_2 \mathbf{y} \Big|_{z=H} \\ [\mathbf{y}]_0^{2\pi} \end{pmatrix}, \quad \mathcal{B}_1 = \begin{pmatrix} \vartheta \frac{\partial}{\partial r} + \frac{\lambda}{r} & \frac{\lambda}{r} \frac{\partial}{\partial \varphi} & \lambda \frac{\partial}{\partial z} & -\gamma \\ \frac{\partial}{\partial z} & 0 & \frac{\partial}{\partial r} & 0 \\ \frac{1}{r} \frac{\partial}{\partial \varphi} & \frac{\partial}{\partial r} - \frac{1}{r} & 0 & 0 \\ 0 & 0 & 0 & \frac{\partial}{\partial r} \end{pmatrix}, \quad \mathcal{B}_2 = \begin{pmatrix} 0 & 0 & 1 & 0 \\ \frac{\partial}{\partial z} & 0 & \frac{\partial}{\partial r} & 0 \\ 0 & \frac{\partial}{\partial z} & \frac{1}{r} \frac{\partial}{\partial \varphi} & 0 \\ 0 & 0 & 0 & \frac{\partial}{\partial r} \end{pmatrix},$$

wherein $[\mathbf{y}]_0^{2\pi} = \mathbf{y} \Big|_{\varphi=0} - \mathbf{y} \Big|_{\varphi=2\pi}$, $\vartheta = 4(\mu + \mu' \partial / \partial t) / 3 + K$, $\lambda = K - 2(\mu + \mu' \partial / \partial t) / 3$. Initial values are defined by initial distributions of temperature, displacements and velocities.

The obtained solutions of problem (1), (2) are of the form of spectral expansions based on complete biorthogonal sets of eigenfunctions (and perforce associated functions), corresponding to the conjugate pairs of matrix operator pencils $\mathcal{L}_\nu, \mathcal{L}_\nu^*$:

$$\mathcal{L}_\nu = \mathcal{A}_0 + \mathcal{A}_1 \nu + \mathcal{A}_2 \nu^2, \quad \mathcal{L}_\nu^* = \mathcal{A}_0^* + \mathcal{A}_1^* \bar{\nu} + \mathcal{A}_2^* \bar{\nu}^2,$$

$$\mathcal{A}_0^* = \begin{pmatrix} \mathcal{L}_1 & 0 \\ \gamma \mathcal{L}_3 & \nabla^2 \end{pmatrix}, \quad \mathcal{A}_1^* = \begin{pmatrix} \mathcal{L}'_1 & \eta \mathcal{L}_2 \\ 0 & -1/\kappa \end{pmatrix}.$$

Here \mathcal{A}_i^* are conjugate to \mathcal{A}_i differential operators, defined in the domain \mathcal{D}^* , that defined by boundary operator \mathcal{B}^* :

$$\mathcal{B}^* \mathbf{y} = \begin{pmatrix} \mathcal{B}_1^* \mathbf{y} \Big|_{r=R} \\ \mathcal{B}_2^* \mathbf{y} \Big|_{z=0} \\ \mathcal{B}_2^* \mathbf{y} \Big|_{z=H} \\ [\mathbf{y}]_0^{2\pi} \end{pmatrix}, \quad \mathcal{B}_1^* = \begin{pmatrix} \vartheta \frac{\partial}{\partial r} + \frac{\lambda}{r} & \frac{\lambda}{r} \frac{\partial}{\partial \varphi} & \lambda \frac{\partial}{\partial z} & \nu \eta \\ \frac{\partial}{\partial z} & 0 & \frac{\partial}{\partial r} & 0 \\ \frac{1}{r} \frac{\partial}{\partial \varphi} & \frac{\partial}{\partial r} - \frac{1}{r} & 0 & 0 \\ 0 & 0 & 0 & \frac{\partial}{\partial r} \end{pmatrix}.$$

The coefficients of expansions referred to as transforms one can obtain by applying direct integral transformation to (1), resulting in the reduction initial boundary value problem to the sequence of initial problems for ODEs in image space [1,2]. It enable us to represent the solution of (1), (2) as follows:

$$(3) \quad \mathbf{y} = \sum_{i=1}^{\infty} \left[\left(\langle \mathcal{A}_1^* \mathbf{k}_i^* + \bar{\nu}_i \mathcal{A}_2^* \mathbf{k}_i^*, \mathbf{y}_0 \rangle + \langle \mathcal{A}_2^* \mathbf{k}_i^*, \dot{\mathbf{y}}_0 \rangle \right) \exp(\bar{\nu}_i t) + \int_0^t \langle \mathbf{f}(\tau), \mathbf{k}_i^* \rangle \exp(\bar{\nu}_i(t - \tau)) d\tau \right] \mathbf{k}_i \mathcal{Q}_i^{-1}.$$

One can found $\mathbf{k}_i, \mathbf{k}_i^*$ by solving the coupled set of boundary eigenvalue problems:

$$\mathcal{L}_\nu \mathbf{k} = 0 \quad (\mathbf{k} \in \mathcal{D}), \quad \mathcal{L}_\nu^* \mathbf{k}^* = 0 \quad (\mathbf{k}^* \in \mathcal{D}^*).$$

In equation (3) \mathcal{Q}_ν is the normalizing matrix and ν_i ($i = 1, \dots, \infty$) are the elements of pencil discrete spectrum. The constructible representation of normalizing matrix \mathcal{Q}_ν and the exact method for evaluation of corresponding quadratures are described in [4, 5]. Note, that biorthogonal relations [3] here are in the form

$$\langle \mathcal{A}_1 \mathbf{k}_i, \mathbf{k}_j^* \rangle + (\nu_i + \nu_j) \langle \mathcal{A}_2 \mathbf{k}_i, \mathbf{k}_j^* \rangle = 0, \quad \langle \mathcal{A}_0 \mathbf{k}_i, \mathbf{k}_j^* \rangle - \nu_i \nu_j \langle \mathcal{A}_2 \mathbf{k}_i, \mathbf{k}_j^* \rangle = 0.$$

It is important to note, that, unlike well-known transformation technique (Laplace transform, etc.), that uses numerical approach for inversion, proposed method admit to obtain solution in closed analytical form and to develop effective algorithmic realization of computer simulation. It usability for the analysis of the non-stationary, high frequency loadings on several particular examples is elucidated [1–4].

- [1] Senitsky Y.Ed. Generalized biorthogonal finite integral transforms and their application to non-stationary problems of mechanics *Physics-Doklady. American Institute of Physics* **vol.40. N4**, 1995
- [2] Lychev S.A., Senitskii Y.Ed: Nonsymmetric finite integral transformations and their application to visco-elasticity problem. *Vestnik of Samara State University* **Special Issue**:16–38, 2002.
- [3] Lychev S.A.: Coupled dynamic thermoelastic problem for a finite cylinder. *Vestnik of Samara State University* **4(30)**:112–124, 2003.
- [4] Senitskii Y.Ed, Lychev S.A.: The method for computation of finite integral transformation kernel norm and its application. *Izv. Vuz. Matematika* **8**:60–69, 1999.

PRIMARY EVALUATION OF THE WEAR BEHAVIOR OF THE COMBUSTION SYNTHESIZED TiC-NiAl COMPOSITE AS MECHANICAL SEAL RINGS

M. B. Rahaei

Materials and Energy Research Center, Tehran, Iran

1. General

In this research, the wear behavior of combustion synthesized TiC-NiAl composite was evaluated in comparison sintered SiC specimens as relevant materials for use in pumps (Hard Face Part of Mechanical Seals), because of low cost and simplicity of combustion synthesis process. Therefore wear behavior of samples was determined by pin on disk test against a 52100 steel pin under dry condition as well as in aqueous environment of a pump.

2. Introduction

SiC belongs to this group of materials and is well known for its high hardness, the relatively high strength, a high melting point and a good corrosion resistance [2, 3]. The most reliable and economic way to control fluid leakage from industrial equipment such as centrifugal pumps, agitators, automotive engines, compressors, turbines and mixers is to isolate the rotating shaft and its housing with a mechanical seal [4, 5]. In compared to the sintering methods for fabrication of seals, combustion synthesis is a simple, low cost and energy conservative process [1]. In seal ring for pumps, lubrication and wear resistance properties are important factors [6, 7]. Also as TiC-NiAl has good properties such as wear resistance and low density [8], therefore combustion synthesized TiC-NiAl was evaluate in comparison sintering SiC in wear test and durability test for use as seal rings in pumps.

3. Experimental procedure

The combustion synthesized TiC-NiAl composite and sintering SiC was prepared. The outer diameter and the inner diameter of the samples were 3.2 and 2.5 mm, respectively. Fig. 1 is shown seal ring sample of sintered SiC and combustion synthesized TiC-NiAl.



Figure 1. Sintering SiC and combustion synthesized TiC-NiAl seal ring samples.

The constituted phases of the samples were characterized employing X-ray diffraction (XRD-Philips X'pert-MPD) and microstructure was observed using by Scanning Electron Microscopy (SEM-XL30). Macro hardness and micro hardness of specimens measured by criterion RA and Vickers respectively.

For evaluated lubricity and wear behavior, wear test was conducted on an oscillating pin on disk tester for combustion synthesized TiC-NiAl and sintering SiC samples, in contrast to AISI 52100 steel pin according to AISI M. Gee 32 [7, 9, 10]. weight loss and friction coefficient of samples were measured under 20, 240, and 280 N loads in pin on disk wear test in 1000 m sliding distance with 0.07 m/s linear velocity. Furthermore weight losses of samples were measured in durability test in pump.

4. Results and discussion

Hardness and density samples are shown in table 1. Result of hardness and density almost were similar to result of other researches [1, 8]. Likewise, in figure 4 has been come friction coefficient of TiC-NiAl in 200 N loads, which has low friction coefficient similar to SiC in wear test. Table 2 shows the coefficient of friction of SiC and TiC-NiAl in various loads in wear test. Coefficient of friction of TiC-NiAl samples change in various loads and are low, especially in low loads similar to working condition that is suitable for use in pump as seal ring.

Figure 5, (a) shows the weight loss curve of both SiC and TiC-NiAl in 240 N loads during sliding distance (every 100 m) in (pin on disk) wear test. Also figure 5, (b) shows friction coefficient curve of samples in 200 N loads during sliding distance. Due to weight loss and friction coefficient in TiC-NiAl sample is low and almost similar to SiC seal ring during sliding distance in wear test, So TiC-NiAl was proper to evaluate in durability test in pump.



Figure 5. a. Weight loss, b. friction coefficient of both TiC-NiAl and SiC samples in wear test.

Table 3 shows the weight loss of samples in wear test via 240 N loads in 1000 m distance and durability test for 30 days continuous work in pump in aqueous conditions at 0.5 MPa pressure.

Seal ring samples	Weight loss after pin on disk test	weight loss after durability test in pump
SiC	1.7×10^{-3} gr	0.0855 gr
TiC-NiAl	2.1×10^{-3} gr	0.0896 gr

Table 3. Weight Loss in samples in wear test and testing for durability in pump.

The result shows that weight loss of TiC-NiAl is low in wear test and durability test in pump similar to SiC. Therefore TiC-NiAl is proper for use in a pump as mechanical seal ring.

5. Conclusions

Experimental results showed that combustion synthesized TiC-NiAl has friction coefficient and weight loss close to sintered SiC in wear test and durability test in pump. Also hardness result showed that TiC-NiAl has high hardness and low density like SiC for use in pump. Therefore primary evaluation showed that TiC-NiAl composite has acceptable primary condition for use in as mechanical seal rings in aqueous environment.

6. References

- [1] L. Harmon (2002). Silicon carbide bushings help seal less pump prevent production losses, *Materials and Design*, **3**, 577-581.

DESCRIPTION OF CAPILLARY POTENTIAL CURVES OF POROUS MATERIALS

M. Cieszko, M. Kempieński

Institute of Environmental Mechanics and Applied Computer Science, Bydgoszcz, Poland

1. Introduction

The capillary potential curve determine the relationship between the volume and pressure of the mercury intruding against the capillary forces into pores of a sample of porous material. Such relationship is the direct result of measurements conducted with a help of the mercury porosimeter and is a base for the standard method of determination of the pore size distribution. These distributions are important characteristics of microscopic structure of the pore space of porous materials. They enable one to determine the basic macroscopic parameters of such materials (e.g. the volume porosity, permeability or the internal surface) which play important role in many physical and chemical processes occurring in permeable porous materials (e.g. filtration, transport of mass, momentum and energy, wave propagation or chemical reactions).

The aim of this paper is to formulate the description of capillary potential curves of porous materials based on microscopic and macroscopic model of the mercury intrusion into porous material. In the microscopic description the chain model of pore space architecture has been used, whereas the macroscopic description has been based on the diffusion model of the intrusion process.

The analysis of influence of parameters characterizing pore size distribution on the capillary potential curve was performed for both microscopic and macroscopic models the intrusion process. The influence of the capillary diffusion coefficient on the form of this curve was illustrated. These models have been used to identify the pore size distribution of selected natural and model materials.

2. Microscopic model of mercury intrusion in a porous layer

In the microscopic description of pore space of porous material the pores are modeled as cylindrical pipes (links) with random distribution of their diameter D and length s , described by the density of probability $\psi(D,s)$. In this case, the pore space structure of porous medium is determined by two independent factors: the pore size distribution and the way of their connection, called here the architecture of the pore space, [1]. Consequently, even for the same pore diameter distribution, the pore space structure may be different. Regarding the pore architecture, one can distinguish three kinds of models of the pores space structure: the capillary, chain and network models. In the capillary model, the links of the same diameters are joined in series and form long capillaries of the constant diameter, crossing the whole material. The diameters of different capillaries have random values. In the chain model the links are randomly combined in series, creating the capillaries of step-wise changing cross-section. In the network model, the randomly connected links form a spatial net. The capillary and chain models are the limiting models of the network model describing the curves of capillary potential.

The expression describing the capillary potential curves for porous materials with the capillary pore architecture takes the form

$$(1) \quad \frac{V_L(p)}{V_o} = \int_{D^*}^{\infty} \vartheta(D) dD ,$$

where $D^* = 4\sigma \cos(\theta)/p$, is the critical diameter of link in which the menisci is in equilibrium at a given pressure, $\vartheta(D) = D^2 \bar{\psi}(D)/\bar{D}^2$ describes the volumetric distribution of pore diameters, whereas $\bar{\psi}(D)$ is the pore diameters distribution and \bar{D} stands for its mean value.

For the chain model of pore space architecture we have

$$(2) \quad \frac{V_L(p)}{V_o} = \left[2\beta(1 - \exp(-\frac{1}{\eta\beta})) - \frac{1}{\eta} \exp(-\frac{1}{\eta\beta}) \right] \int_{D^*}^{\infty} \vartheta(D) dD,$$

where

$$(3) \quad \beta = \frac{\bar{D}_N / \bar{D}}{(1 - \eta)N}, \quad \eta = \int_{D^*}^{\infty} \bar{\psi}(D) d(D),$$

whereas $N = L/a$ and a is the mean value of pore length.

3. Macroscopic model of mercury intrusion in a porous sample

The other possibility of description of mercury intrusion into a porous layer gives the diffusive model of capillary transport in porous media. In such model the quasistatic process of inviscid fluid intrusion caused by progressive increase of pressure is considered at the macroscopic level like non-stationary process of diffusion. For the simplest case equation describing fluid distribution in porous material takes the form, [2],

$$(4) \quad \frac{\partial \rho}{\partial p} - \text{div}(C(\rho) \text{grad}(\rho)) = 0,$$

where $C(\rho)$ stand for coefficient of capillary diffusion of inviscid fluid in porous material.

Solution of equation (4) for fluid intrusion into porous layer (at constant C) and for boundary condition obtained from the microscopic model is given by expression, [4],

$$(5) \quad \rho(x, p) = \bar{\rho} \left[1 - \frac{4}{\pi} \sum_{m=0}^{\infty} \frac{1}{2m+1} \exp\left(-\frac{(2m+1)^2 \pi^2}{L^2} Cp\right) \sin\left(\frac{(2m+1)\pi x}{L}\right) \alpha \right].$$

In this case the capillary potential curve takes the form

$$(6) \quad \frac{V_L(p)}{V_o} = \left[1 - 8 \sum_{m=0}^{\infty} \frac{1}{(2m+1)^2 \pi^2} \exp\left(-\frac{(2m+1)^2 \pi^2}{L^2} Cp\right) \right] \int_{D^*}^{\infty} \vartheta(D) dD.$$

The derived expressions (1), (2) and (6) have been used in the analysis of influence of pore size distribution and capillary coefficient of diffusion on the capillary potential curve. Both types of models were applied to interpretation of such curves obtained by mercury intrusion method for samples of model and natural materials.

4. References

- [1] M. Cieszko, M. Kempniński, *Determination of Limit Pore Size Distributions of Porous Materials from Mercury Intrusion Curves*, Engng. Trans., 54, 2, 143-158, 2006.
- [2] M. Cieszko, *Diffusive Model of Capillary Transport in Porous Materials. Transport in Porous Media*, (in press).
- [3] F.A.L. Dullien, *Porous Media*, Academic Press, New York 1979.
- [4] Z.M. Jarzębski, *Diffusion in Materials and Alloys*, (in Polish), Slask Publishers, 1987.
- [5] A.E. Scheideger, *The Physics of Flow Through Porous Media*, Univ. Press, Toronto 1957.

VISCOUS INCOMPRESSIBLE FLOW IN POROUS MEDIA

R. Wojnar

Institute of Fundamental Technological Research PAS, Warszawa

1. General

Our aim is to extend the Darcy law to a range of higher speeds of flow, and to derive a number of properties of such a flow. First, we note that the laminar flows occur for the large values of Reynolds number. Next, it is shown that viscosity scaling for small capillaries in a porous medium is not related to the Reynolds number, and the Darcy law, applicable not only to the stokesian seepage, is obtained using the Navier–Stokes equations for the steady case. Finally, a non-homogeneous porous medium, consisting of two different porous components is selected to show that for such a composite so called the Dykhne hypotheses are satisfied and a square root formula for the effective permeability is obtained.

2. The laminar flow

Consider steady flow in a pipe of arbitrary cross-section, the same along the whole length of the pipe. Let \mathbf{v} denote the velocity, p – pressure, η – viscosity. Moreover, let t denote the time and \mathbf{x} – the position. We take the axis of the pipe as the x_3 axis. The fluid velocity is along the x_3 axis, and is a function of x_1 and x_2 only. We have $\partial v_i / \partial t = 0$, $v_1 = v_2 = 0$ and $v_3 \equiv v$. Hence, the left-hand side of the Navier-Stokes equation vanishes. If η is constant then $\partial p / \partial x_1 = \partial p / \partial x_2 = 0$ and

$$\frac{\partial p}{\partial x_3} = \eta \left(\frac{\partial^2 v}{\partial x_1^2} + \frac{\partial^2 v}{\partial x_2^2} \right) \quad (*)$$

In general, fluid flow in a pipe crosses the threshold from laminar to turbulent flow when Reynolds number R reaches about 2000, $R = \rho u d / \eta$; ρ – the fluid density, u – the mean velocity over the pipe cross-section, and d – its mean diameter. For the water ($\rho = 1 \text{ g/cm}^3$, $\eta = 0.01 \text{ g/cm s}$) flowing in a pipe with the diameter $d = 1 \text{ mm}$ we reach such value of R with the mean velocity $u = 2 \text{ m/s}$. Laminar flow has actually been observed even to Reynolds number $R \approx 50\,000$, what gives $u = 50 \text{ m/s}$. The velocity of blood in aorta (in pulsatile regime) is of the order $u = 4 \text{ m/s}$.

3. Scaling in laminar flow

Let the cross-section of a pipe be an equilateral triangle of side a . We put $x = x_1$, $y = x_2$ and $z = x_3$. The solution of the equation (*) is

$$v = - \frac{2}{\sqrt{3}} \frac{H}{a} \frac{1}{\eta} \frac{dp}{dz} \quad \text{where} \quad H = y \left[\left(\frac{\sqrt{3}}{2} a - y \right)^2 - 3x^2 \right]. \quad \text{Hence} \quad Q = \frac{\sqrt{3}}{320} a^4 \frac{1}{\eta} \frac{dp}{dz}$$

and Q denotes the discharge, it is the volume of fluid passing each second through the pipe.

Next, we divide each side of cross-section into two equal parts, introduce into the parallel rigid walls with infinitesimal thickness, and obtain four smaller pipes similar to the original one. After n such divisions $Q_n = Q/2^{2n}$ and Q_n vanishes as number of divisions n goes to infinity. To conserve the total discharge we should reduce the viscosity of fluid by factor ε^2 , where $\varepsilon = 1/2^n$. In reality, instead of η it is the pressure gradient which scaled.

4. Homogenisation of stationary laminar flow in porous composite

Consider stationary laminar flow in a porous medium of dimension L with periodic structure (elementary cell with dimension l) and introduce the fraction $\varepsilon = l/L$. According to an asymptotic development method we put for the pressure p^ε and velocity \mathbf{v}^ε the expansions

$$p^\varepsilon = p^{(0)}(x, y) + \varepsilon p^{(1)}(x, y) + \varepsilon^2 p^{(2)}(x, y) + \dots \quad \mathbf{v}^\varepsilon = \mathbf{v}^{(0)}(x, y) + \varepsilon \mathbf{v}^{(1)}(x, y) + \varepsilon^2 \mathbf{v}^{(2)}(x, y) + \dots,$$

where $y = x/\varepsilon$, substitute to the laminar flow equation (*), and compare terms at the same power of ε . Term with ε^{-1} provides $\partial p^{(0)}/\partial y_3 = 0$ what means $p^{(0)} = p^{(0)}(x)$. To satisfy equation with power ε^0 , we put $p^{(0)} = \xi(y)(-\partial p^{(0)}/\partial x)$ and $\mathbf{v}^{(0)} = \chi(y)(-\partial p^{(0)}/\partial x)$ where χ satisfies

$$\left(\frac{\partial^2 \chi}{\partial y_1^2} + \frac{\partial^2 \chi}{\partial y_2^2} \right) = -1 + \frac{\partial \xi}{\partial y_3}$$

After averaging the velocity over the elementary cell we get the Darcy law

$$\langle \mathbf{v}^{(0)} \rangle = \langle \chi(y) \rangle \left(-\frac{\partial p^{(0)}}{\partial x_3} \right)$$

derived not from the Stokes but from the Navier–Stokes equation for the steady laminar flow.

5. Stationary flow in two-dimensional two-component porous composite

The solid part of the system contains two overlapping domains of distinctly different permeabilities, K_1 and K_2 . In geology, the low permeability medium corresponds to block matrix with primary porosity, surrounded by fractures, and the high permeability continuum corresponds to rock fractures (secondary porosity). In biology we observe, for example, pores of different size in plant tissues or in animal bones, cortical and trabecular. If such systems are planar and the following Dykhne assumptions are satisfied: (i) considered fields are 2-dimensional, (ii) the flow is stationary and has the potential, (iii) statistical symmetry and isotropy of the composite is assured, then the square root formula for the effective property holds.

Define vector \mathbf{f} as 2-dimensional gradient of pressure field, $f_\alpha = -\partial p/\partial x_\alpha$ where $\alpha = 1, 2$.

The Darcy law has the form $v_\alpha = K f_\alpha$ where K is a permeability. On the another hand, curl of \mathbf{f} as of the potential vector, vanishes, it is $f_{2,1} - f_{1,2} = 0$ and the assumption that the flow is incompressible gives $v_{\alpha,\alpha} = 0$ or $f_{1,1} + f_{2,2} = 0$. Thus the conditions of Dykhne are satisfied and $K^{eff} = \sqrt{K_1 K_2}$. This is the formula for effective permeability if the domains with permeabilities K_1 and K_2 are statistically equivalent. It gives the effective values also in the case when the Hagen–Poiseuille flow and Darcy flow are mixed together.

6. Acknowledgements

This work was supported by the grant KBN No 4 T07A 003 27.

7. References

- [1] L. Landau i E. Lifszic (1958). *Mechanika ośrodków ciągłych*, tłumaczył z ros. Roman Żelazny, PWN, Warszawa.
- [2] É. Sanchez-Palencia (1980). *Non-homogeneous media and vibration theory*, Springer, Berlin.
- [3] A. M. Dykhne (1970). Conductivity of a two-dimensional two-phase system, *Zhurnal Eksperimentalnoi i Teoreticheskoi Fiziki* **59**(7), 110-115.

MATRIX PADÉ BOUNDS ON EFFECTIVE TRANSPORT COEFFICIENTS OF ANISOTROPIC TWO-PHASE MEDIA

S. Tokarzewski¹, J. Gilewicz²

¹*Institute of Fundamental Technological Research, Warsaw, Poland*

²*Centre de Physique Théorique, CNRS, Luminy Case 907, 13288 Marseille Cedex 09, France*

The prediction of macroscopic coefficients Υ of two-phase composites, if properties γ_1 and γ_2 and microstructures of their constituents are known, is one of the most important problems of mechanics of inhomogeneous media. Due to the difficulty of calculating of effective material constants Υ exactly, there has been much of interest in obtaining bounds on Υ .

It is well known that effective transport coefficients Υ of two-phase composites such as thermal and electrical conductivities, dielectric constants, magnetic permeabilities and diffusion coefficients have a matrix Stieltjes function representation $\mathbf{f}(z)$

$$(1) \quad \mathbf{f}(z) = \frac{(\Upsilon - \mathbf{I})}{z} = \int_0^1 \frac{d\gamma(u)}{1 + zu}, \quad z \in \mathbb{C} \setminus (-\infty, -1), \quad d\gamma(u) \geq 0, \quad \mathbf{f}(-1) \leq \mathbf{I},$$

where \mathbf{I} and $z = \frac{\gamma_1}{\gamma_2} - 1$ denote the unit matrix and the isotropic non-dimensional characteristic of constituents. We assume that we know matrix coefficients $\mathbf{f}_j^{(k)}$ up to p_j order in matrix Taylor expansions at z_j , $z = z_j \in \mathbb{C} \setminus (-\infty, -1)$, $j = 1 \dots N$, i.e.

$$(2) \quad \mathbf{f}_j^{(k)}, \quad j = 1, \dots, N, k = 1, \dots, p_j,$$

where

$$(3) \quad \mathbf{f}(z_j) = \mathbf{f}_j^{(0)}, \quad \left. \frac{\partial \mathbf{f}(z_j)}{\partial z} \right|_{z=z_j} = \mathbf{f}_j^{(1)}, \dots, \quad \left. \frac{\partial^{(p_j)} \mathbf{f}(z_j)}{\partial z^{(p_j)}} \right|_{z=z_j} = \mathbf{f}_j^{(p_j)}.$$

We seek the matrix function $\mathbf{F}_{n+2}(z; \alpha, \beta)$ estimating $\mathbf{f}(z)$ in the form a sum of simple matrix fractions given by:

$$(4) \quad \mathbf{F}_{n+2}(z; \alpha, \beta) = \sum_{k=1}^K \mathbf{A}_k^{\frac{1}{2}}(\alpha, \beta) (\mathbf{I} + z\mathbf{B}_k(\alpha, \beta))^{-1} \mathbf{A}_k^{\frac{1}{2}}(\alpha, \beta) + \alpha^{\frac{1}{2}} (\mathbf{I} + z\beta)^{-1} \alpha^{\frac{1}{2}},$$

where

$$(5) \quad K = E((n+1)/2) \text{ and if } n \text{ even } \mathbf{B}_{n/2}(\alpha, \beta) > \mathbf{0} \text{ or if } n \text{ odd } \mathbf{B}_{n/2}(\alpha, \beta) = \mathbf{0}.$$

Here $\mathbf{A}_k(\alpha, \beta)$, α , $\mathbf{B}_k(\alpha, \beta)$, β are two-dimensional matrices satisfying matrices inequalities

$$(6) \quad \mathbf{A}_k(\alpha, \beta) > \mathbf{0}, \quad \alpha > \mathbf{0}, \quad \mathbf{B}_k(\alpha, \beta) > \mathbf{0}, \quad \beta > \mathbf{0},$$

while n denotes the number of independent input data given by (3). The coefficients $\mathbf{A}_k(\alpha, \beta)$ and $\mathbf{B}_k(\alpha, \beta)$ are determined by the assumption that $\mathbf{F}_{n+2}(z; \alpha, \beta)$ (matrix multipoint Padé approximant) and $\mathbf{f}(z)$ (matrix Stieltjes function) have matrix Taylor expansions coinciding up to p_j order at z_j , $j = 1, \dots, N$. The main results of this paper present the following matrix relations. By $\phi_{n+1}(z_0)$, $n = 1, 2, \dots$, we denote the matrix bounds on $\mathbf{f}(z_0)$.

For $n = 0$

$$(7) \quad \phi_1(z_0) = \left\{ \alpha^{\frac{1}{2}} (\mathbf{I} + z_0\beta)^{-1} \alpha^{\frac{1}{2}}; \quad \alpha = (\mathbf{I} - \beta), \quad \mathbf{0} \leq \beta \leq \mathbf{I}, \quad (\mathbf{0} \leq \alpha \leq \mathbf{I}, \quad \beta = \mathbf{0}) \right\}.$$

For $n = 1, 2, 3, \dots$

$$(8) \quad \phi_{n+1}(z_0) = \{\mathbf{F}_{n+2}(z_0, \alpha, \beta); \alpha = \alpha_n(\beta)\},$$

where

$$(9) \quad \alpha_n(\beta) = \begin{cases} \alpha_{\mathbf{A}_n}(\beta), & \mathbf{0} \leq \beta \leq \beta_1^{(n)}, \\ \alpha_{\mathbf{F}_{n+2}}(\beta), & \beta_1^{(n)} \leq \beta \leq \beta_2^{(n)}, \end{cases} \quad \text{if } n \text{ is odd}$$

or

$$(10) \quad \alpha_n(\beta) = \begin{cases} \alpha_{\mathbf{F}_{n+2}}(\beta), & \mathbf{0} \leq \beta \leq \beta_1^{(n)}, \\ \alpha_{\mathbf{A}_n}(\beta), & \beta_1^{(n)} \leq \beta \leq \beta_2^{(n)}, \end{cases} \quad \text{if } n \text{ is even.}$$

Here $\beta_1^{(n)}, \beta_2^{(n)}, \dots, \beta_n^{(n)}$ are roots of the equation

$$(11) \quad \alpha_{\mathbf{F}_{n+2}}(\beta) - \alpha_{\mathbf{A}_n}(\beta) = \mathbf{0}, \quad n = 1, 2, 3, \mathbf{0} = \beta_0^{(n)} < \beta_1^{(n)} < \beta_2^{(n)} < \dots < \beta_n^{(n)} < \beta_{n+1}^{(n)} = \mathbf{I}.$$

The matrix functions appearing in (9) and (10)

$$\alpha = \alpha_{\mathbf{A}_n}(\beta) \text{ and } \alpha = \alpha_{\mathbf{F}_{n+2}}(\beta)$$

satisfy the matrix relations

$$(12) \quad \mathbf{A}_n(\alpha, \beta) = \mathbf{0} \text{ and } \mathbf{F}_{n+2}(-1, \alpha, \beta) = \mathbf{I},$$

respectively. Coefficients $\mathbf{A}_n(\alpha, \beta)$ are determined by the system of equations

$$(13) \quad \mathbf{f}(z) - \mathbf{F}_{n+2}(z, \alpha, \beta) = O((z - z_j)^{p_j}), \quad j = 1, 2, \dots, N, \quad n = \sum_{j=1}^N p_j.$$

The matrix Padé bounds $\phi_n(z_0), n = 0, 1, 2, \dots$ determined by relations (7)-(13) are new. For the scalar case they coincide with the relevant ones reported in literature [1, 2]. Zero order bounds $\phi_1(z_0)$ on $\mathbf{f}(z_0)$ determined by (7) are calculated and depicted in Fig. 1.

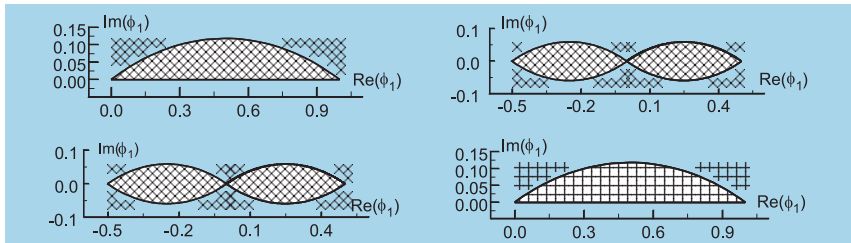


Fig. 1: Matrix Padé bounds $\phi_1(z_0)$ on admissible values of a matrix Stieltjes function $\mathbf{f}(z_0)$, $z_0 = 1 - i$ representing the effective anisotropic transport coefficient $\boldsymbol{\Upsilon}$ of two-phase medium. The bounds $\phi_1(z_0)$ are calculated from one information only, i.e. $\mathbf{f}(-1) \leq \mathbf{I}$.

As an example of applications the effective conductivity of a rectangular array of cylinders is solved by means of matrix Padé bounds. Results are presented in a number of tables and graphs.

Acknowledgment This work was supported by the Ministry of Science and Higher Education (Poland) through the Grant Nr 4 T07A 053 28.

[1] G.W. Milton, The Theory of Composite, Cambridge Monographs on Applied and Computational Mathematics, Cambridge University Press, 2002.
 [2] S. Tokarzewski, Multipoint continued fraction approach to the bounds on effective transport coefficients of two-phase media. IFTR Reports, 4: 3–171, 2005.

DETERMINATION OF MOISTURE DEPENDANCE OF MATERIAL COEFFICIENTS FOR MACARONI DOUGH

G. Musielak¹ and B. Świt²

¹ *Poznań University of Technology, Poznań, Poland*

² *Sulzer Chemtech, Wysogotowo, Poland*

1. Introduction

One of the most popular human food – macaroni is produced of dough by forming and drying. The drying is the most important and the most difficult part of macaroni production. It influences sensorial, physico-mechanical and even feeding features of product. During drying the material shrinks and this could cause permanent deformations and even fracturing of macaroni. Up to now there are only few publications devoted to the mechanical behaviour of macaroni dough during drying e.g. [1-3].

During drying of macaroni dough its moisture content (dry basis) change from about 0.28-0.32 to 0.1-0.12. In that range the material is initially visco-elastic and finally brittle-elastic. The material coefficients of the material change in that range almost thousandfoldly. The aim of the work is to determine moisture dependence of some material constants of macaroni dough, in particular Young modulus, viscous equivalent of Young modulus and strength of the material. It is assumed that the material is Maxwell visco-elastic one.

2. Experiments

The experiments consisted of three parts: samples preparation, extension test and final drying. Examined material was dough appropriated to popular macaroni production [4]. Because there are no norms devoted to the extension of dough, the samples shape was similar to the normalized shape of samples made of plastic. The dough was carefully mixed. Then the samples were shaped with the use of prepared matrix. Next they were slowly dried to demanded moisture content and isolated during 24h to ensure uniform moisture content inside material. The samples were put to extension test with the 1 N/s load rate. After disruption of sample a small part of sample from the disruption region was weighed. Next the piece of sample was dried to dry mass and weighed once again to establish moisture content (dry basis) of the sample during extension test.

4. Results

Because it is assumed that the material is Maxwell visco-elastic one, the strain of the material ε is the sum of elastic strain $\varepsilon^{(e)}$ and viscous one $\varepsilon^{(v)}$

$$\varepsilon = \varepsilon^{(e)} + \varepsilon^{(v)}$$

These two strains obey Hook and Newton models

$$\varepsilon^{(e)} = \frac{\sigma}{E} \quad \frac{d\varepsilon^{(v)}}{dt} = \frac{\sigma}{\Gamma}$$

The Young modulus E and its viscous equivalent Γ were estimated using above equations. Strength of the material is taken directly from the test (the maximal stress during test).

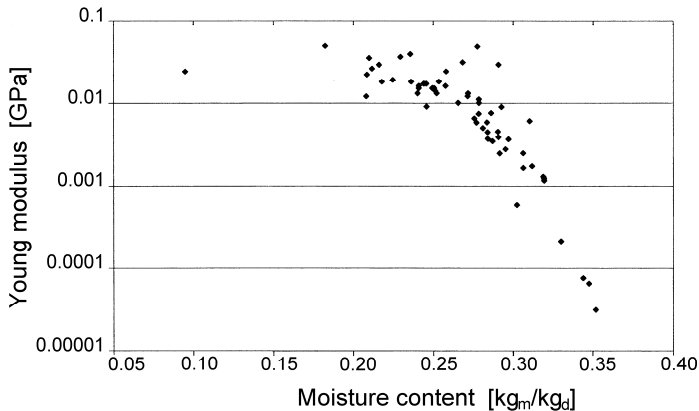


Figure 1. Young modulus versus moisture content (dry basis).

As exemplary result the Young modulus versus moisture content (dry basis) is shown on the figure 1. We obtained that the material parameter highly depends on moisture content and change its value from about 0.00003 GPa for 0.35 kg/kg moisture content to about 0.05 GPa for 0.18 kg/kg moisture content. The other two examined material parameters also highly depend on moisture content.

5. Acknowledgements

This work was carried out as a part of research project 32-266/08-DS of Department of Chemical Technology, Poznań University of Technology.

6. References

- [1] R. Pęczalski, P. Laurent, J. Andrieu, J.C. Boyer and M. Boivin (1996). Drying-Induced Stress Build-up within Spaghetti, *Proceedings of the 10th International Drying Symposium*, Cracow, Poland, 30 July – 2 August 1996, Vol. B, 805–816.
- [2] S.J. Kowalski and B. Mielniczuk (2006). Drying Induced Stresses in Macaroni Dough, *Drying Technology*, **24**(9), 1093–1099.
- [3] B. Mielniczuk (2007). Mathematical Modelling and Experimental Examination of Stress Development in Materials Dried Convectively and by Microwaves, *PhD Thesis*, Poznań University of Technology, Poznań, Poland. (in Polish)
- [4] Polish Norm PN-A-74131.

OPTIMAL WIRELESS SENSORS LOCATION FOR WIDESPREAD STRUCTURES MONITORING

I. Dunajewski¹, Z. Kotulski²

¹ *Kazimierz Wielki University, Bydgoszcz, Poland*

² *Institute of Fundamental Technological Research, Warsaw, Poland*

1. Formulation

Structures and environmental monitoring are important factors of proper work of intelligent structures and they have a strong effect on their safety. Traditionally, the structure's state was registered by human observers or remote measurement devices connected directly to event recorders. Modern telecommunication technology enables application of wireless sensor networks [1] for monitoring, making possible extremely increase spatial density and temporal frequency of observations. Such sensors are both measurement devices and a communication network nodes broadcasting their own signal and retransmitting signals obtained from neighbors. Thus, they constitute a self-organizing P2P network that collects measurements and transmits them to managing or analytic centre.

2. Measurement conditions constraints

Design of a monitoring system for a structure requires adequate selection of sensor's locations. Since usually the number of sensors is fixed, equal n , their locations must be optimally selected to obtain the best observation result for such limited resources. Depending on a concrete task, system designers use different optimality criteria for the sensors' locations [2]. For instance, they can be uniform distribution of sensors over the structure, non-overlapping information criterion, highest sensitivity criterion, minimal correlation of measurements criterion, etc. These criteria usually take into account properties of a mechanical phenomenon measured and usability of the received data for a certain engineering task, e.g. structure control. However, in modern wireless sensors networks more criteria, mainly following from wireless communication conditions must be taken into account [3]. Such criteria are usually independent of structural optimality criteria, what force the monitoring system designers to use multiple criteria optimization [4] to select best locations for sensors at structural elements or in the environment.

The purpose of this paper is to propose a procedure that can optimally design wireless sensor networks for widespread structures monitoring in uncertain environmental conditions.

3. Topologies and communication conditions constraints

Optimal deployment of wireless sensors should first of all ensure the best communication efficiency possible as well as appropriate wear and failure resistance. The basic type of wireless sensor networks has a homogenous structure. Due to the requirements of a monitored structure, a network with (privileged) supernodes and (auxiliary) communication nodes, or a combination of both, can be applied.

The main criteria to be taken into account with the application of wireless technology are the criteria that have an effect on the lifespan of a sensor network such as the criterion of the minimum power consumption for data transmission, distance minimization to the node collecting data from the paths, optimal data transmission path criterion, load minimization measured, for example, by the

mean traffic value carried by the node (the necessity to use network resources evenly). The optimal deployment of nodes should also take into consideration the requirement of alternative path availability in case of a failure (each node has to have more than just one neighbor), the requirement of avoiding communication obstacles and also cost-effectiveness, to this extent limiting the number of sensors, and so on.

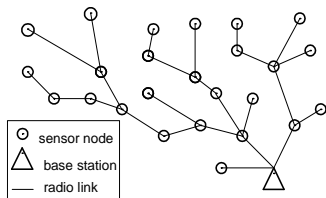


Fig.1. Homogenous network

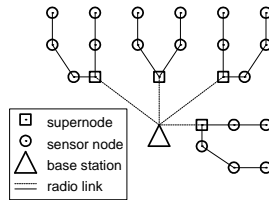


Fig.2. Network with supernodes

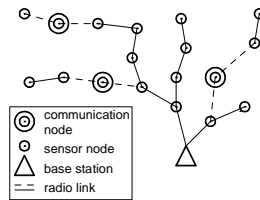


Fig.3. Network with communication nodes

Depending on the applied topology, these criteria have varied significance. For example, in a supernode network it is possible to invalidate the criterion of the even use of resources since the most loaded nodes can be replaced by supernodes, or the application of communication nodes can significantly mitigate the criterion for avoiding terrain obstacles, etc.

4. Criteria of optimality

The paper proposes a phased-in approach (in three stages) to problem formulation for optimization of the deployment of nodes of wireless sensor network for widespread structures monitoring. As the result of the first level of calculation a space of available solutions due to the quality of measurements criterion (mechanical) depending on the required measurement objective emerges. The second stage of the optimization effects in the establishment of the number of measure nodes with the criteria of the installation costs and replacement of each of the nodes in case of its failure taken into consideration. The third stage of the analysis is to optimize the deployment of sensors with a defined number of nodes with the maximum life-span of the network criterion taken into consideration, i.e. with the aim of the minimization of the distance of routes and avoiding the necessity of overloading of individual nodes.

The purpose of the performed analysis is to determine the acceptable locations of nodes of the wireless sensor network and then to decide on the preferred locations of nodes from the set of non-dominated solutions.

5. References

- [1] E. Gaura and R. Newman (2006). *Smart MEMS and Sensor Systems*, Imperial College Press, London.
- [2] Z. Kotulski (1990). Optimization of Sensors' Location in a Stochastic Extrapolation Problem, *J. Sound & Vibration*, **138**(3), 351–363.
- [3] B. Książkowski and Z. Kotulski (2005). On scalable security model for sensor networks protocols, in: R.J. Scherer, P. Katranuschkov, S.-E. Schapke [eds], *CIB-W78 2005, 22nd Conference Information Technology in Construction*, Dresden, CIB Publ. No. 304, 463-469.
- [4] M. Ehrgott (2005). *Multicriteria Optimization*, 2nd ed. Springer, Berlin.

SELF-PROPAGATING HIGH TEMPERATURE SYNTHESIS OF BULK TiC-NiAl COMPOSITE

M. B. Rahaei¹, M. Kholghi², A. Shafiyee², M. Rahaei², M. Naghavi¹

¹*Materials and Energy Research Center, Tehran, Iran*

²*Isfahan University of Technology, Isfahan, Iran*

1. Abstract

This study was based on production of TiC-NiAl by combustion synthesis method. TiC-NiAl composite was fabricated by reaction of $Ti + Al + Ni + C \rightarrow TiC-NiAl$ assistant heated coil on top surface of green body along with a medium 100 MPa pressure to obtain a bulk sample. The constituted phases were characterized by XRD and microstructure observation has been done with SEM. The density of the synthesized bulk samples was measured according to the Archimedes method. Micro and macro hardness, and fracture toughness of samples were measured by a vickers diamond indenter. Isostatic Pressing along with thermal reaction like to a thermomechanical process result in bulk TiC-NiAl composite.

2. Introduction

In recent years, many methods, such as sintering [4], hot pressing [5], hot isostatic pressing [6], spark plasma sintering (SPS) and solid-state reaction [7], have been developed to produce TiC-NiAl composite in bulk form sample. Combustion synthesis in powder metallurgy processes has been in attention, because it offers advantages as economics and process simplicity. Also the very high reaction rates and elimination of the need for high temperature furnaces used in conventional material fabrication due to the self generation of heat required for the process. Considering their low density and their high wear resistance and refractoriness, compounds of the system Al-Ni-Ti-C can be used to produce high temperature wear resistance components. This paper describes studies of combustion synthesis of bulk TiC-NiAl via SHS in its wave propagation mode, with pseudo hot isostatic pressing.

3. Experimental procedure

A homogeneous powder blend includes Ti, Al, Ni and C within the molecular ratio 1:1:1:1 in a low energy ball milling. The dried reactants were cold pressed into square pellets by a press at 30 MPa. For the SHS wave propagation experiments, a slightly compacted Ti-C-Ni-Al blend was inserted into a vertically placed stainless steel cylinder. A heated coil at one end ignited the pellets and self-sustained from this heated end to the full sample due to the highly exothermic reaction. The compact was immediately pressed just after wave passed, the products was in hot and soft condition too (delay time ≈ 5 s). The pressure (100 MPa) was kept for 10 s. Figure 1 is a schematic of the SHS/PHIP setup.

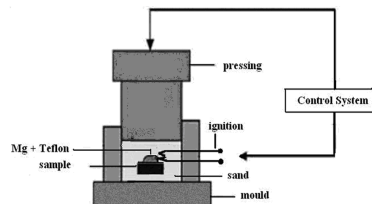


Figure 1. The schematic illustration of the SHS/PHIP setup.

The dense products were then sectioned with cutter and grinded for microstructure and mechanical analysis. The constituted phases of the synthesized TiC-NiAl samples were characterized employing X-ray diffraction (XRD-Philips X'pert-MPD) and microstructure observation by scanning electron microscopy (SEM-XL3). Micro-hardness of dense samples was measured under 5 N loads, with vickers diamond indenter. The macro-hardness was evaluated by a Vickers diamond indenter at loads of 50 N. The fracture toughness was calculated using the following formula in equation 2. The density of the synthesized bulk samples was measured by using water, according Archimedes test method [3].

4. Results and discussion

For obtained a highly homogeneous starting mixture used a tumbler mill (low energy mill) with election a low time, because prevent mechanical alloying within milling [7].

The SHS reaction of the system Al-Ni-Ti-C was followed by powder reaction sample. TiC-NiAl composite was fabricated by combustion reaction of $\text{Ti} + \text{Al} + \text{Ni} + \text{C} \rightarrow \text{TiC-NiAl}$. Figure 2 gives an overview of the recorded diffraction patterns as the reaction proceeds, which that compose TiC and NiAl phases.

With attention to high exothermic reaction (≈ 183 Kj/mole) of Ti and C, composed TiC, and then done reaction Al and Ni, because of lower exothermic reaction (≈ 118 Kj/mole) [1, 2]. Likewise NiAl has role of bonding phases. SEM observation is shown in figure 3. Product is composed of small, round TiC particles embedded in continues matrix of NiAl which TiC phases adhering by assistant NiAl intermetallics to compose a continues structure. Also exist slightly pore in sample similar to HIP process [4]. This result was similar to other researcher which fabricated this compound by hot isostatic pressing and spark plasma sintering [4, 7, 9].

Mechanical properties tests are put into table 1. These mechanical properties is almost similar to result of other researchers that produce by other process like sintering [4, 10-12].

compound	Relative density (%)	density	Micro hardness (HV ₅)	Macro hardness (GPa)	Fracture toughness (MPa√m)
TiC-NiAl	97.6	5.174	1077	9.95	7-10

Table 1. The mechanical properties of TiC-NiAl sample.

5. Conclusions

The SHS reaction of the quaternary system Al-Ni-Ti-C has been started with the synthesis of Ti and C to compose TiC, and then followed by melting and reaction of Al and Ni. The final product is composed of small, round TiC particles embedded in a continuous matrix of NiAl. Results show excellent properties of TiC-NiAl, >95% dense samples with density ≈ 5.17 gr/cm³, micro hardness ≈ 1077 Hv₅, macro hardness ≈ 9.95 GPa and fracture toughness ≈ 8.5 MPa√m. Furthermore primary evaluation has been shown by combustion synthesis can produce TiC-NiAl composite in bulk shape that has suitable mechanical properties in comparison with sintering samples.

6. References

- [1] J.M. John and H.J. Feng (1995). Combustion Synthesis of Advanced Materials Part I: Reaction Parameters, *Progress in Materials Science*, **39**, 243-273.
- [2] J.M. John and H.J. Feng (1995). Combustion Synthesis of Advanced Materials Part II: Classification, Application and Modelling, *Progress in Materials Science*, **39**, 275-316.

COMPARISON MECHANICAL PROPERTIES OF COMBUSTION SYNTHESIZED TiC-NiAl WITH SINTERING MECHANICAL SEAL RINGS AND CUTTING TOOLS

M. B. Rahaei

Materials and Energy Research Center, Tehran, Iran

1. Abstract

The main aim in this study is based on replacement possibility of combustion synthesis procedure with conventionally sintering method for fabrication some of the mechanical seal rings and cutting tools, because of simplicity and economic of this procedure. As TiC-NiAl composite has excellent wear resistant, it was chosen as a relevant material for mechanical seals and cutting tools. Therefore microstructure and their mechanical property of combustion synthesized TiC-NiAl composite such as hardness and fracture toughness was compared with those of usual compounds of cutting tools and mechanical seal rings, like silicon carbide, alumina and tungsten carbide-cobalt that be produced by sintering method. The primary evaluation of mechanical properties shows that TiC-NiAl has acceptable hardness and fracture toughness in comparison SiC, Al₂O₃ and WC-Co. Therefore by combustion synthesis method can produce some of materials with mechanical properties similar to the mechanical seal rings and cutting tools.

2. Introduction

Cutting tools are made from very hard materials and have been applied in wide variety of turnery industries and machining operations. For cutting tools, these sintering materials usually include tungsten carbide and alumina. Cutting materials for extreme requirements (for example, interrupted cuts or machining of high strength materials) can consequently not be made from one single material, but may be realized by composite materials. This tools produce by hot press and hot isostatic pressing of carbide mixture (cemented carbide) [1, 2].

Mechanical seals are machine elements specially designed to prevent fluid leakage from pressurized chambers in fluid (gas or liquid) transport systems at high temperature or to avoid hot lubricant outflow in general equipment moving parts. Many different materials and combinations of them have been successfully tested and are routinely used today in the industry. In an engineering sense, the term generally refers to a class of materials that are characterized by their high hardness, high stiffness, low thermal expansion, and good wear resistance. For mechanical seals, these include silicon carbide, tungsten carbide and alumina. Other materials such as silicon nitride are used in special applications. These tools can be synthesized by sintering method [3, 4].

The self-propagating high-temperature synthesis procedure has low energy consumption and has large potentials for industrial applications due to the high productivity and the very simple equipment involved [5]. Due to excellent wear behavior of TiC-NiAl [6], in this paper mechanical properties of combustion synthesized TiC-NiAl in comparison with sintering alumina, silicon carbide and cemented carbide samples was evaluated for use in cutting tools and high temperature mechanical seals.

3. Experimental procedure

The dense samples were sectioned with wire cut and grinded for microstructure observation and mechanical property analysis. The constituted phases of the synthesized TiC-NiAl samples, alumina, silicon carbide and cemented carbide were characterized employing X-ray diffraction (XRD-Philips X'pert-MPD) and microstructure observation by scanning electron microscopy (SEM-S360 and SEM-XL3) equipped with EDS Analyzer. Micro-hardness of dense samples was

measured under 5 N load, with Vickers diamond indenter. Macro-hardness was evaluated by a Vickers diamond indenter at loads of 50 N.

The fracture toughness was measured by the Vickers indentation method. Indentation test was conducted on polished samples with a load between 200 N to 300 N that held for 15 s.

The density of the synthesized bulk samples was measured by using water, according Archimedes test method [2].

4. Results and discussion

Fig. 1 gives an overview of the recorded diffraction patterns of the sintering SiC. As it can be seen in Fig. 1, XRD pattern shows that SiC phase is in SiC seal ring sample.

Furthermore SEM observations as seen in Fig. 5, shows continuous structure for sintering SiC, alumina, cemented carbide and combustion synthesized TiC-NiAl. Moreover low pore density and relatively same sizes were in samples too.

Mechanical properties tests of samples are put into table. 1. As it is shown TiC-NiAl composite has high hardness and fracture toughness in acceptable limited in sintering samples of cutting tools and mechanical seal rings.

compound	Relative density	density	Micro hardness (HV _{0.5})	Macro hardness (Gpa)	Fracture toughness (MPa√m)
SiC	~ 95.6	3.06	2443	21.6	2-3.5
Al ₂ O ₃	~ 95	3.675	1010	12.02	3-4.5
WC-Co	~ 98.6	13	1436	13.36	9-14
TiC-NiAl	~ 97.6	5.174	1077	9.95	7-10

Table 1. Mechanical properties of samples.

5. Conclusions

TiC-NiAl composite has high hardness and fracture toughness in acceptable limitation in comparison sintering cutting tools and mechanical seal ring samples. Therefore primary evaluation shown by combustion synthesis can produce composite compound with excellent mechanical properties like mechanical seal and cutting tools. Also TiC-NiAl has good primary condition for use in mechanical seal and cutting tools.

6. References

- [1] K.L. Choy (2003). Chemical vapour deposition of coatings, *Prog in Mater Sci.*, **114**, 57-170.
- [2] D. Richerson (1992). *Modern Ceramic Engineering: Properties, Processing, and Use in Design*, 2nd, Marcel Dekker, New York, 126-131.

THE DISCRETE ELEMENT METHOD WITH APPLICATION TO SIMULATION OF GRANULAR FLOW AND DYNAMIC FRACTURE OF SOLIDS

R. Kačianauskas

Vilnius Gediminas Technical University, Vilnius, Lithuania

1. General

The discrete (sometimes referred to as distinct) element method (DEM) introduced by Cundall and Strack [1] started with its first application to simulate the dynamic behaviour of granular material. Contrary to the methods based on the continuum approach, DEM is based on the Lagrangian approach, meaning that particles of granular material are treated as contacting bodies, while dynamical parameters (position, velocity, orientation, etc.) of each body are tracked during the simulation.

Generally, the DEM concept permits numerical simulation of a wide variety of problems ranging in different scales. It comprises fundamental ideas of molecular and multi-body dynamics. On the other hand, DEM may be considered as one of the numerical methods describing the behaviour of continuum in terms of a finite number of discrete parameters. Recently, the DEM has become a powerful tool for solving many scientific and engineering problems.

2. Concept and methodology

The granular material considered in this paper presents a space filled with deformable bodies, termed here as discrete elements. The simple and most popular particle shapes in three-dimensions are the sphere and the ellipsoid. When moving, the particles as contacting bodies impact and deform each other.

Individual bodies change their position due to free rigid body motion or interactions with the neighbouring bodies or walls. The translation and rotation of each body in time t are described by the second Newton's law and expressed in terms of resulting forces acting at the centre of gravity. The most popular inter-particle contact model of frictional visco-elastic body considers a combination of elasticity, damping and friction force effects.

3. Computational aspects

Computational aspects of DEM involve [2-3] basically problem formulation, contact searching, computation of forces and time integration of equations of motion. Problem formulation involves a specific technique to set up the initial and boundary conditions. The explicit time integration technique prevails in the DEM computations.

The main disadvantages of the DEM technique, in comparison with the well-known numerical methods based on continuum approach, are related to computational capabilities limited by a huge number of particles and a relatively small time step used in time integration, therefore, much attention is also paid to software implementation. Improvement of computational efficiency by using parallel implementation is a realistic alternative.

4. Application to granular materials

Several application examples of DEM to dry non-cohesive granular material problems are considered and selected modelling results are presented. Simulation of filling and unsteady/steady discharge processes in three-dimensional hoppers of different geometry is illustrated in details [4].

The microscopic parameters of granular material composed of spherical particles are analysed in terms of their contribution to macroscopic parameters, such as time-dependent evolution of the system kinetic energy, porosity fields, discharge rates as well as wall and material stresses.

Along with spherical particles, the multi-sphere (MS) approximation approach [5] of the 3D axi-symmetric ellipsoidal particle is also illustrated. Performance of the MS approach is examined by solving a piling problem. The deviation of a multi-sphere shape from ellipsoid at the particle level is evaluated.

5. Modelling of solids

DEM is also extensively applied to the simulation of solids, mainly concerning dynamic deformation behaviour and fracture problems. Development of the continuum consistent lattice-type DE model for 2D solids is considered. The proposed DEM approach assumes that deformation behaviour of solid is described by translational motion of particles, while inter-particle forces are expressed in terms of axial forces of the axially deformed connection element.

The FEM technique was applied to the development of the DEM model. By applying a standard constant strain triangle finite element it was shown that Cartesian elastic inter-particle forces may be expressed in terms of stiffness matrices of the triangles incorporated. The developed combined DEM/BEM approach is based on the analogy between the structural and continuum variables in a triangle. The resultant normal elastic force presents the sum of individual edge forces of adjacent triangles. Additionally, each of the edge forces is composed of two components involving influences of the axial and shear stiffness. For isotropic solid, two stiffness parameters may be directly extracted from the stiffness matrix of the triangle.

The suggested approach is independent on the Poisson's ratio and the shape of the triangle lattice. From the physical point of view, conventional mutual interaction of particles is modified by the collaborative interaction of the local particle assembly. Consequently, modification of the algorithm and the DEM code is required. Multi-fracture with randomly distributed tensile strength properties of the material is considered for illustration.

6. Acknowledgements

The author is thankful to his co-workers R. Balevičius, D. Markauskas, A. Maknickas and V. Vadluga at Vilnius Gediminas Technical University, Lithuania, for providing numerical results and illustrations and to Professor Z. Mroz, Institute of Fundamental Technological Research, Warsaw, Poland, for valuable comments and discussions. Support of the Lithuanian State Science and Studies Foundation under Grant No T - 110/08 is gratefully acknowledged.

7. References

- [1] P.A. Cundall and O.D.L. Strack (1979). A discrete numerical model for granular assemblies, *Geotechnique*, **29**, 47-65.
- [2] R. Balevičius, R. Kačianauskas, A. Džiugys, A. Maknickas and K. Vislavičius (2006). Investigation of performance of programming approaches and languages used for numerical simulation of granular material by the discrete element method, *Comp. Phys. Comm.*, **175**(6), 404-415.
- [3] A. Maknickas, A. Kačeniauskas, R. Kačianauskas, R. Balevičius and A. Džiugys (2006). Parallel DEM Software for Simulation of Granular Media, *Informatica*, **17**(2), 207-224.
- [4] R. Balevičius, R. Kačianauskas, Z. Mróz and I. Sielamovicz (2007). Microscopic and macroscopic analysis of granular material behavior in 3D flat-bottomed hopper by the discrete element method, *Arch. Mech.*, **59**(3), 231-257.
- [5] D. Markauskas (2006). Discrete element modelling of complex axi-symmetrical particle flow, *Mechanika*, **6**(62), 32-38.

MODELLING OF DEFORMATION AND DAMAGE OF HETEROGENEOUS-ENGINEERING STRUCTURES: MASONRY MECHANICS

A. Bacigalupo and L. Gambarotta

*Department of Civil, Environmental and Architectural Engineering
University of Genova, Italy*

1. Introduction

Sustainability of the built-up environment requires making best use of historical and monumental constructions of the architectural heritage and of many bridges of transport systems made of masonry and designed according to empirical rules. The conservation and restoration of these masonry structures has to be supported by an exhaustive structural assessment. An awareness of the limitations of the conservative approximations commonly made in structural analysis, generally providing underestimations of the load-bearing capacity of these structures, has stimulated great interest in new approaches to the mechanical modelling of masonry structures.

Compared to conventional steel and reinforced concrete constructions, where the structure can be clearly identified, masonry constructions are very complex structural systems obtained from an assemblage of different components like walls, vaults and pillars, requiring highly statically indeterminate structural models. Moreover, masonry is a heterogeneous material consisting of units, such as bricks, blocks, ashlars, adobes, irregular stones etc. assembled with mortar or dry joints according to different patterns. As a consequence a great variety of masonry materials can be found ranging from periodic brick masonry to dry stone rubble masonry.

The mechanical response of this two-phase composite material observed in experiments is rather complex, depending on the unit and joint material, the masonry pattern and the applied loads. Moreover, experiments on units and masonry assemblages show uncertainty on the material characteristics. This behaviour can be attributed to the quasi-brittle behaviour of the components and the interfaces. Elastic, damage/crack and stress induced anisotropy, including different response to tensile versus compressive stress, hysteretic response to cyclic loads and fracture are the main observed phenomena, having a strong effect on the stress redistribution in structural components (walls and vaults) and on dynamic response to seismic actions. As a consequence modelling of deformation and damage of masonry material and structures aimed at prediction of the behaviour of masonry structures under ultimate loads, base settlements and seismic events remains a challenge.

2. Constitutive models for damaging brick/block masonry

As usual in modelling material, different approaches to the analysis of masonry structures such as pillars, walls and vaults, can be pursued in order to simulate the main features of the mechanical response. In any case, the structural model has to encompass several constitutive ingredients such as elasticity, plasticity, unilateral contact, friction-damage, localization and size effects, fracture and time dependent response. In discrete approaches the constituents are modelled individually and the actual assemblage of brick/block masonry is considered in detail. Although these models may be useful in interpreting experimental results and in the calibration of material parameters, they lead to excessive computational effort even for simple structures, thereby making continuous models more appealing for applications to large scale structures.

Apart from the case of the so-called no-tension material proposed by Heyman to formulate a theory for the limit analysis of masonry structures, the complexity of the masonry material makes the formulation of purely phenomenological models a rather difficult task, with the exception of the case of rubble or disordered masonry. On the other hand, mesomechanical approaches based on the

homogenization of a periodic cell, a representative element of brickwork, are suitable for regular brick/block masonry, frequently found in ancient and historical constructions, where the units are joined by horizontal and vertical mortar beds to obtain a periodic structure. This latter approach is interesting because it may allow consideration of different characteristic lengths in the structural system (materials, unit cell, structure).

The evaluation of the load carrying capacity of eccentrically compressed pillars, commonly based on the simplifying assumption of homogeneous material, is analyzed considering a periodic discrete model of the stack of units. In this class of problems, defined at the scale of masonry units, the mismatch of the material parameters may significantly affect the inelastic mechanisms at the lateral free edges of the pillar and at the head mortar joints and the overall strength. Theoretical evaluations of the load carrying capacity are compared to experimental results and open issues are discussed. Application to the assessment of masonry bridges are presented and discussed.

Modelling the in-plane and out-of-plane response of perforated masonry walls is a critical issue in the evaluation of the seismic vulnerability of masonry buildings. This problem is analyzed considering constitutive models at different details of description of the masonry pattern and of the inelastic frictional-damage mechanisms. Starting from the simplified assumption of a layered continuum with horizontal critical planes, where damage mechanisms are attained, the analysis encompasses more elaborate constitutive models based on the homogenization of periodic masonry cell, including micropolar and higher order constitutive equations, whose characteristic lengths are related to the unit size and to the bond pattern. Simulations of experiments on perforated masonry walls are presented. The consequences of assuming different constitutive models including friction/plastic and damage ingredients are analyzed in terms of structural response and computational implementation and comparisons with results provided by simple models (elastic-no-tensile-resistant for instance) are drawn.

6. References

- [1] Cavicchi A., Gambarotta L., Lower bound limit analysis of masonry bridges including arch-fill interaction, *Engineering Structures*, **29**, 3002-3014, 2007.
- [2] Cavicchi A., Gambarotta L., Two-dimensional Finite Element Upper Bound Limit Analysis of Masonry Bridges, *Computers and Structures*, **84**, 2316-2328, 2006.
- [3] Brencich A., Corradi C., Gambarotta L., Eccentrically loaded brickwork: theoretical and experimental results, *Engineering Structures*, 2008.
- [4] Brencich A., Gambarotta L., Mechanical response of solid clay brickwork under eccentric loading. Part I: Unreinforced Masonry, *Materials and Structures*, **38**, 257-266, 2005.
- [5] Brencich A., Gambarotta L., Mechanical response of solid clay brickwork under eccentric loading. Part II: CFRP Reinforced Masonry, *Materials and Structures*, **38**, 267-273, 2005.
- [6] Gambarotta L., Friction-Damage Coupled Models for Brittle Materials, *Engineering Fracture Mechanics*, **71**, 829-836, 2004.
- [7] Gambarotta L. and S. Lagomarsino, Damage models for the seismic response of brick masonry shear walls. Part I: the mortar joint model and its applications, *Earthquake Engineering & Structural Dynamics*, **26**, 423-439, 1997.
- [8] Gambarotta L. and S. Lagomarsino, Damage models for the seismic response of brick masonry shear walls. Part II the continuum model and its applications, *Earthquake Engineering & Structural Dynamics*, **26**, 441-462, 1997.

LONG-TERM MICRODAMAGING OF COMPOSITES WITH TRANSVERSALLY-ISOTROPIC COMPONENTS FOR LIMITED FUNCTION OF DURABILITY

L. Nazarenko¹, L. Khoroshun², W.H. Müller¹ and R. Wille¹

¹ *LKM TU Berlin, Berlin, Germany*

² *S.P. Timoshenko Institute of Mechanics of NAS of Ukraine, Kiev, Ukraine*

1. Introduction

One of the important problems of mechanics of composites is the investigation of stresses under elevated loads. Such a loading is associated with the accumulation of damage which finally leads to the fracture of the material. A survey of theoretical papers dealing with microcracked elastic materials is presented in [1]. A study of materials weakened by periodically or randomly distributed microcracks was performed in [2] by using homogenization methods. In [3] a stochastic model of short-term microdamages of the material was proposed and then applied to the case of anisotropic composites [4]. In the present paper a stochastic model is developed for investigation of long-term microdamages of discrete-fibers composites with transversally-isotropic components.

2. Mechanical model. General relation

We consider a representative volume V of a composite. Under homogeneous loading the stresses and strains appearing in the representative volume will form statistically homogeneous random fields satisfying the ergodicity condition and we can replace the operation of averaging over the representative volume by the operation of averaging over an ensemble of realizations. Then the macroscopic stresses $\langle \sigma_{ij} \rangle$ and strains $\langle \varepsilon_{kl} \rangle$ of such a material will be related by Hooke's law:

$$(1) \quad \langle \sigma_{ij} \rangle = \lambda_{ijkl}^* \langle \varepsilon_{kl} \rangle, \quad (i, j, k, l = 1, 2, 3).$$

Here, λ_{ijkl}^* is the tensor of effective elastic constants, which can be determined by the method of conditional moments [5]. The effective elastic moduli of the composite are functions depending on the elastic moduli of the components $\lambda_{ijkl}^{[1]}$, $\lambda_{ijkl}^{[2]}$, the volume contents of the inclusions c_1 , the porosity of the components p_1, p_2 , and the shape of the inclusions s

$$(2) \quad \lambda_{ijkl}^* = \lambda_{ijkl}^* (\lambda_{mnp}^{[1]}, \lambda_{mnp}^{[2]}, c_1, p_1, p_2, s), \quad s = s_1/s_2, \quad (m, n, p, r = 1, 2, 3),$$

where s_1, s_2 are semi-axes of spheroids. Knowing the effective elastic moduli and the macrostresses or macrostrains of such a composite it is possible to calculate stresses $\langle \sigma_{ij}^r \rangle$ averaged over the skeletons of components using the relations obtained in [5]. As a the fracture criterion we consider generalized Huber-von Mises criterion for a transversally-isotropic material

$$(3) \quad J_{\sigma}^r = \sqrt{\sigma_{ij}^r \sigma_{ij}^r + a_{1r} (\sigma_{33}^r)^2 + a_{2r} (\sigma_{11}^r + \sigma_{22}^r) \sigma_{33}^r + a_{3r} \left((\sigma_{13}^r)^2 + (\sigma_{23}^r)^2 \right)} = k_r, \quad (r = 1, 2),$$

where a_{1r}, a_{2r}, a_{3r} are dimensionless constants, σ_{ij}^r is the deviator of the stresses averaged over an undamaged part of the material of the r -th component, and k_r is the limiting value of the material strength, which is a random function of coordinates. If the invariant J_{σ}^r does not achieve its limiting value k_r in some microvolume, then according to the long-term failure criterion, failure will occur after some time τ_k^r , which depends on how close J_{σ}^r is to k_r . This dependence can be represented by

$$(4) \quad \tau_k^r = \varphi (J_\sigma^r, k_r).$$

The one-point distribution function $F(k_r)$ of the ultimate strength k_r in a microvolume of the undamaged part of the material can be approximated by a Weibull distribution function:

$$(5) \quad F(k_r) = \begin{cases} 0 & , k_r < k_{0r} \\ 1 - \exp(-m_r(k_r - k_{0r})^{\alpha_r}) & , k_r \geq k_{0r} \end{cases},$$

k_{0r} is the minimum value of the ultimate microstrength of the material of the r -th component, m_r and α_r are constants determined by fitting experimental microstrength scatter curves. If the stresses $\langle \sigma_{ij}^r \rangle$ are known, then the distribution function $F(k_r)$ determines the relative content of the destroyed microvolumes in the undamaged part of the material of the r -th component. If the destroyed microvolumes are modeled by pores, it is possible to write down the balance porosity equation

$$(6) \quad p_r = p_{0r} + (1 - p_{0r})F(k_r),$$

where p_{0r} denotes the initial porosity of the material of the r -th component. If the stresses or strains act for some time t , then, according to (4), microvolumes with the following values of k_r will fail in this time τ_k^r , which can be represent by a fractional power law

$$(7) \quad t \geq \tau_k^r = \varphi (J_\sigma^r, k_r), \quad \varphi (J_\sigma^r, k_r) = \tau_{0r} \left((k_r - J_\sigma^r) / (J_\sigma^r - \gamma_r k_r) \right)^{n_r}, \quad (\gamma_r k_r \leq J_\sigma^r \leq k_r, \gamma_r < 1),$$

where τ_{0r} , n_r and γ_r are determined by fitting experimental long-term strength curves.

Transforming (7) we arrive at the inequality

$$(8) \quad k_r \leq J_\sigma^r \psi(\bar{t}_r), \quad \psi(\bar{t}_r) = \left(1 + \bar{t}_r^{1/n_r} \right) / \left(1 + \gamma_r \bar{t}_r^{1/n_r} \right), \quad (\bar{t}_r = t / \tau_{0r}).$$

In this case the function $F[J_\sigma^r \psi(\bar{t}_r)]$ defines the relative fraction of destroyed microvolumes in the part of the material which is undamaged prior to loading at the time \bar{t}_r . Then for given macrostresses or macrodeformations, the equation of balance of destroyed microvolumes or porosity under long-term damage can be represented by

$$(9) \quad p_r = p_{0r} + (1 - p_{0r})F[J_\sigma^r \psi(\bar{t}_r)].$$

On the basis of the above approach we investigate the stress-strain state of transversally-isotropic composite material under matrix microdamages.

6. References

- [1] M. Kachanov. Effective elastic properties of cracked solids: critical review of some basic concepts. *Appl. Mech. Rev.* 1992. 45(8): 304-335, (1992).
- [2] B. Gambin and J.J. Telega. Effective properties of elastic solids with randomly distributed microcracks. *Mechanics Research Communications.* 27(6): 697-706, (2000).
- [3] L.P. Khoroshun. Principles of the micromechanics of material damage. 1. Short-term damage. *International Applied Mechanics.* 34(4): 1035 – 1041, (1999).
- [4] L.P. Khoroshun and L.V. Nazarenko. Deformation and microdamaging of discretely-fibrous composites with transversally-isotropic components. *International Applied Mechanics.* 39(6): 696-703, (2003).
- [5] L.P. Khoroshun, B.P. Maslov, E.N. Shikula, and L.V. Nazarenko. *Statistical mechanic and effective properties of materials [in Russian]*. Naukova Dumka, Kiev, (1993).

EIGENSPECTRA AND ORDERS OF STRESS SINGULARITY AT A MODE I CRACK IN A POWER-LAW MEDIUM

L. Stepanova

Samara State University, Samara, Russia

1. Introduction

Solutions for crack-tip fields are very important in understanding the mechanisms of crack initiation and propagation in elastic-plastic and creeping materials. The stress field in the vicinity of the crack tip in power-law materials (power-law hardening materials, power-law creeping materials) is widely discussed in literature. The stress singularity for a crack in a homogeneous power-hardening material with hardening exponent n was first studied by Hutchinson [1], Rice and Rosengren [2]. In [1] the problem of plastic stress singularity is reduced to a nonlinear eigenvalue problem and the shooting method is used to solve the homogeneous differential equation obtained in the analysis. It should be noted that for some time multi-term asymptotic solutions with the well-known HRR-field as the leading order term of the asymptotic expansion aroused considerable interest of many researchers. Nowadays the whole eigenspectrum and orders of stress singularity at the crack tip for a power-law medium are of prevailing interest. The present study offers a technique developed in the perturbation theory for analysis of nonlinear eigenvalue problems arising from fracture mechanics.

2. Mode I crack. Basic equations

Let us consider eigenspectra and orders of singularity of the stress field near a mode I crack tip in a power-law material. The power-law constitutive relations $\varepsilon_{ij} = (3/2)B\sigma_e^{n-1}s_{ij}$, where ε_{ij} is the strain, s_{ij} is the stress deviator, σ_e is the Mises equivalent stress, B , n are material constants, for the plane strain condition are described by $\varepsilon_{rr} = -\varepsilon_{\theta\theta} = 3B\sigma_e^{n-1}(\sigma_{rr} - \sigma_{\theta\theta})/4$, $\varepsilon_{r\theta} = 3B\sigma_e^{n-1}\sigma_{r\theta}/2$, where the equivalent stress is expressed by $\sigma_e^2 = 3(\sigma_{rr} - \sigma_{\theta\theta})^2/4 + 3\sigma_{r\theta}^2$.

In analyzing the asymptotic behaviour of the stress field near the crack tip the Airy stress potential can be presented in the following form $F(r, \theta) = r^{\lambda+1}f(\theta)$. Using the constitutive equations and the compatibility equation one finds

$$\begin{aligned}
 & f_e^2 f^{IV} \left\{ (n-1) [(1-\lambda^2)f + f'']^2 + f_e^2 \right\} + f_e^4 (1-\lambda^2) f'' + (n-1)(n-3) \times \\
 & \times \left\{ [(1-\lambda^2)f + f''] [(1-\lambda^2)f' + f'''] + 4\lambda^2 f' f'' \right\}^2 [(1-\lambda^2)f + f''] + \\
 & + (n-1) f_e^2 \left\{ [(1-\lambda^2)f' + f''']^2 + [(1-\lambda^2)f + f''] (1-\lambda^2) f'' + 4\lambda^2 (f''^2 + f' f''') \right\} \times \\
 (1) \quad & \times [(1-\lambda^2)f + f''] + 2(n-1) f_e^2 \left\{ [(1-\lambda^2)f + f''] [(1-\lambda^2)f' + f'''] + 4\lambda^2 f' f'' \right\} \times \\
 & \times [(1-\lambda^2)f' + f'''] + C_1(n-1) f_e^2 \left\{ [(1-\lambda^2)f + f''] [(1-\lambda^2)f' + f'''] + 4\lambda^2 f' f'' \right\} f' + \\
 & + C_1 f_e^4 f'' - C_2 f_e^4 [(1-\lambda^2)f + f''] = 0,
 \end{aligned}$$

where $f_e^2 = [(1-\lambda^2)f + f'']^2 + 4\lambda^2 f'^2$, $C_1 = 4\lambda[(\lambda-1)n+1]$, $C_2 = (\lambda-1)n[(\lambda-1)n+2]$.

The fourth order nonlinear ordinary differential equation (1) with the boundary conditions $f(\theta = \pm\pi) = 0$, $f'(\theta = \pm\pi) = 0$ defines a nonlinear eigenvalue problem in which the constant λ is the eigenvalue and $f(\theta)$ is the corresponding eigenfunction. The direct integration of the differential equation (1) is generally realized by the Runge-Kutta method in conjunction with the shooting method. Obviously, the eigenvalue λ and the initial value $f''(\theta = -\pi)$ are coupled with each other in general, and they have to be searched simultaneously. Only in some special cases one can assign a

certain λ a priori through additional physical presumptions. Now the whole eigenspectrum and orders of stress singularity at the crack tip are of interest. The whole eigenspectrum stipulates the possible stress distributions in the neighbourhood of the crack tip. The purpose of this study is to obtain the whole eigenspectrum for the stress field near a mode I crack in a power-law material.

3. The perturbation theory approach

The underlying idea of the method is to consider the expansion representing the eigenvalue λ of the nonlinear eigenvalue problem formulated for an arbitrary exponent n to be a sum of the eigenvalue λ_0 corresponding to the "undisturbed" linear problem ($n = 1$) and a small parameter ε which quantitatively describes the nearness of the eigenvalues: $\lambda = \lambda_0 + \varepsilon$. The exponent n and the stress function $f(\theta)$ can be presented as formal series with respect to ε : $n = 1 + \varepsilon n_1 + \varepsilon^2 n_2 + \dots$, $f(\theta) = f_0(\theta) + \varepsilon f_1(\theta) + \varepsilon^2 f_2(\theta) + \dots$, where $f_0(\theta)$ denotes the solution of the linear problem ($n = 1$). Introducing the asymptotic expansions for λ , n and $f(\theta)$ into (1) and collecting terms of equal power in ε , the set of linear differential equations is obtained. Thus, the boundary value problems for the nonhomogeneous fourth order linear differential equations with respect to $f_i(\theta)$ are formulated. It is known that if the boundary value problem for the homogeneous differential equation has a nontrivial solution then there can exist no solution of the corresponding nonhomogeneous differential equation unless the solvability condition is realized.

Analysis of the solvability condition for the boundary value problems obtained results in the three-term asymptotic expansions of the exponent n : $n = 1 - 2\varepsilon/(\lambda_0 - 1) + \varepsilon^2 n_2 + O(\varepsilon^3)$, where for $\lambda_0 \leq -\frac{3}{2}$ and for $\lambda_0 \geq \frac{3}{2}$ $n_2 = -\frac{\lambda_0^5 - 2\lambda_0^4 - 7\lambda_0^3 + 11\lambda_0^2 + 4\lambda_0 - 5 - (\lambda_0^2 - 1)\text{sgn}(\lambda_0)}{(\lambda_0 + 1)(\lambda_0 - 1)^4}$.

For $\lambda_0 = 1/2$ corresponding to the classical HRR-problem the following closed form solution

$$(2) \quad n_k = -\frac{(-1)^k}{(\lambda_0 - 1)^{k+1}}, \quad n = 1 - \frac{1}{\lambda_0 - 1} \sum_{k=1}^{\infty} \left(-\frac{\varepsilon}{\lambda_0 - 1}\right)^k = -\frac{\lambda}{\lambda - 1}, \quad \lambda = \frac{n}{n + 1}$$

is found. Hence, the well-known formula (2) connecting the hardening exponent n and the eigenvalue λ for the HRR-problem is derived.

4. Conclusions

Using the perturbation method the whole set of eigenvalues for a mode I crack tip in a power-law material is determined. The three-term asymptotic expansion for the exponent n allowing to find the eigenvalue via $\lambda = \lambda_0 + \varepsilon$ for the nonlinear eigenvalue problem is obtained.

The relative error of the three-term asymptotic expansion for a crack in the power-law material with $n = 2$ to the exact HRR-solution is 2%. The results obtained for $\lambda_0 = -1/2$ were compared with those found for the same problem by the Runge-Kutta method in conjunction with the shooting method. The comparison of the eigenvalues for $n = 2$ calculated by the three-term asymptotic expansion and by the numerical scheme $\lambda = -0.9801$ and $\lambda = -1.000$ shows the good agreement. The eigenvalues for $n = 3$ given by the four-term asymptotic expansion for $\lambda_0 = -1/2$ and by the Runge-Kutta method are $\lambda = -0.7716$ and $\lambda = -0.7755$. Consequently, a quite satisfactory solution is obtained by taking the asymptotic expansion achieved.

5. References

- [1] J. W. Hutchinson (1968). Singular behavior at the end of tensile crack in a hardening material, *J. Mech. Phys. Solids* **16**, 13-31.
- [2] J. R. Rice and G. F. Rosengren (1968). Plane strain deformation near a crack tip in a power-law hardening material, *J. Mech. Phys. Solids.*, **16**, 1-12.

THERMODYNAMICS OF PLASTIC DEFORMATION OF NANOCRYSTALLINE TITANIUM

O. Plekhov¹, N. Saintier², O.Naimark¹, T. Palin-Luc², R. Valiev³, I.Semenova³

¹*Institute of continuous media mechanics of Russian Academy of Sciences, Perm, Russia.*

²*Laboratoire Matériaux Endommagement Fiabilité et Ingénierie des Procédés (LAMEFIP), Bordeaux, France.*

³*Institute of physics of perspective materials УГАТУ, Ufa, Russia*

1. Introduction

Recent discoveries of unique properties of bulk nanostructural materials (BNM) (unusual mechanisms of deformation, anomalies of conductivity, magnetic and optical properties) have given an impact to new scientific direction related to nanotechnology. At present time, two general approaches to the development of BNM are considered. The first approach, the so-called «bottom-up approach», involves compaction of the nano-size powders (ultra disperse powders can be obtained by gas condensation in the inertial atmosphere or by plasma-chemical method, aerosol and chemical synthesis, and also by grinding of powders in a spherical mill, etc.). The second method is the intensive plastic deformation leading to the grain refining that provides a unique mechanical behavior of bulk nanostructural materials. Physical properties of BNM are defined by the length and intensity of the grain boundaries, which for the grain sizes of about 10-100 nm contain 10-50% of atoms of the material. Hence, the transition to bulk nanocrystalline state is characterized by pronounced scaling effects the increasingly growing role of grain boundary defects is the crucial for the explanation of unique properties of BNM.

An effective method for studying material properties under transition to nanocrystalline state is the analysis of energy absorption mechanisms, which by analogy with phase transitions can lead to qualitative changes in materials with fine-grain structure related to the specific interaction between the grain boundary defects. This work is concerned with investigation of the energy absorption process in coarse grain and fine grain titanium under plastic loading. It has been found that BNM exhibit energy dissipation anomaly, which can be treated as a result of specific structural evolution in this material.

2. Material and experimental conditions

The samples of titanium Grade 2 in submicrocrystalline state were manufactured by the method of intensive plastic deformation [1] and had the grain size of about 150 nanometers. The mechanical properties of titanium Grade 2 in polycrystalline and submicrocrystalline state are presented in Table 1. The quasistatic tension was carried out using Zwick 100 testing machine. The temperature field was recorded with the infra-red camera CEDIP Jade III. Sensitivity of the camera is higher than 25 mK at 300°K, a spectral range is 3-5 microns, and the maximal size of the frame is 320x240 points.

Type of treatment	tensile strength, σ_B , (MPa)	yield stress, $\sigma_{0.2}$, (MPa)	ultimate elongation, (δ ,%)
Initial coarse grain state (grain size 25 μm)	440	370	38
IPD + hot rolling (grain size 0.3 μm)	1090 \pm 20	980 \pm 20	13 \pm 1

3. Experimental results

Figure 2 presents the results of experiments. The nanotitanium shows high increasing of mechanical properties. The yield stress increases in 2.6 times. The deformation process of nanotitanium is characterized by long softening and long elastic part. The initial stage of nanotitanium deformation is accompanied by pronounced thermo-elastic effect. This fact proves that the deformation is “pure” elastic and material defects don’t initiate and move. The second part of temperature-time curve is more sharp. This fact allows us to conclude that defect evolution under plastic deformation of nanotitanium is more intensive than in coarse grain titanium. But, relative energy storage rate in nanotitanium is higher than in coarse grain specimen. The deformation localization in nanotitanium is more pronounced than in coarse grain one. A fracture of nanotitanium has brittle character and emergence at 15 percent of elongation. The final elongation of coarse grain titanium was 25 percent.

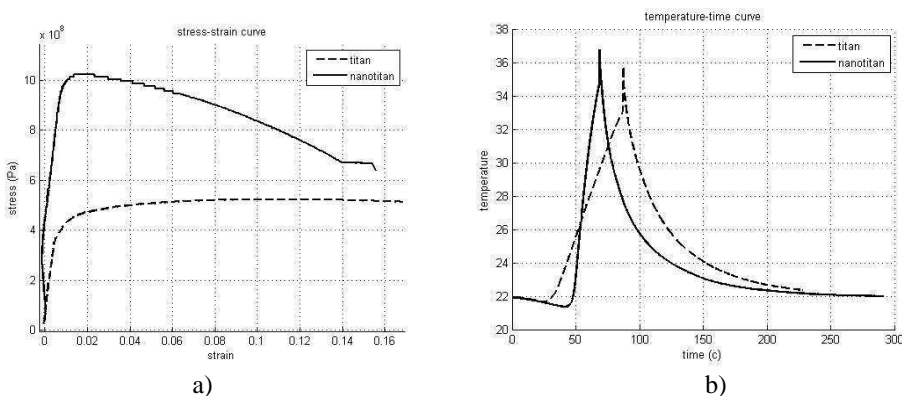


Fig. 1. The stress-strain curve (a) for coarse grain and nanotitanium. Temperature evolution (b) during the experiments for coarse grain and nanotitanium

The peculiarities of defect evolution can be investigated by calculation of energy balance in materials under deformation process. The procedure of energy balance estimation was presented in [2]. The specimen necking and strain rate fluctuation don’t allow us to exactly calculate the energy expended for specimen deformation. The curve can be analyzed on hardening part only. The conclusion can be formulated as follow. The nanotitanium stores more energy than coarse grain one. The evolutions of energy storage in both titanium are similar.

5. Acknowledgement

Work is partially supported by grants of the Russian Fund for Basic Research 07-08-96001, 07-01-91100.

6. References

- [1] V. Latysh, I. Semenova, G. Salimgareeva, I. Kandarov, Y. Zhu, T. Lowe, R. Valiev, (2006) *Mater. Sci. Forum*, **503-504**, 763-768.
- [2] O.A.Plekhov, N.Santier and O.Naimark. (2007) Experimental study of energy accumulation and dissipation in iron in an elastic-plastic transition. *Technical Physics* –**52.**, 9, 1236-1238.

STUDY OF HIGH STRAIN RATE BEHAVIOUR OF MICRO-CONCRETE

B. Erzar, P. Forquin, J.R. Klepaczko

Laboratory of Physics and Mechanics of Materials, Metz, France

Abstract:

Concrete materials are widely used in structures as buildings, nuclear power stations, shelters, bridges... These structures have to be optimized regarding extreme conditions as blast or impact loadings. Consequently, the knowledge and understanding of the tensile behaviour of concretes at high strain rates need to be improved.

When concrete is subjected to high strain rates in tension (beyond s^{-1}), its tensile strength increases significantly. Phenomenon of spalling has been applied for approximately one decade to characterise the dynamic strength of concrete materials [1, 2, 3]. During such test, a cylindrical specimen of concrete is placed at the end of a Hopkinson bar, Fig. 1. A compressive pulse is generated by impact of a striker at the opposite end. A large part of this pulse is transmitted to the specimen and the other small part is reflected into the Hopkinson bar. When the transmitted pulse (negative) reaches the free end of the specimen, it is reflected as a tension pulse (positive). Superposition of both waves induces a tensile loading at a specific distance in the specimen that leads to its failure.



Fig.1 Principle of a modified experimental arrangement used for estimation of dynamic strength in tension

In this work, spalling tests are performed to investigate the tensile behaviour of a micro-concrete (maximum aggregate size: 5 mm) in the range of $10 s^{-1}$ to $100 s^{-1}$. A specific methodology was applied to process experimental data. First, a laser displacement gage was used to measure the axial velocity on the rear face of the specimen, Fig.1. An example of the record is shown in Fig. 2. The spalling strength is deduced from Eq. (1) in which ρ and C_0 are respectively the density and the speed wave of the concrete and ΔV corresponds to the difference between the maximum and the rebound velocities. This equation was checked by numerical simulation of the tests in which an arbitrary failure criterion was used.

$$(1) \quad \sigma_{spall} = \frac{1}{2} \rho C_0 \Delta V$$

The transmitted pulse is reconstructed using incident and reflected pulses recorded from gages located on the Hopkinson bar, [1]. This pulse is implemented in a numerical simulation that involves the specimen alone assuming a purely elastic behaviour of the concrete. This calculation allows deducing the state of stress and strain rate before failure. Because failure is signalled by an increase of the mass velocity on the rear specimen face, Fig. 2, the failure time is also obtained. Thus, the strain rate at failure is also extracted from the numerical analysis. Finally, several tests

performed with dry and wet specimens are compared with data available in the literature.

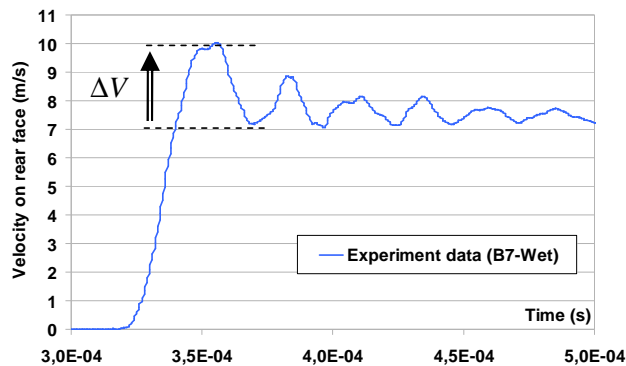


Fig.2. Velocity on the rear face measured by laser gage during test

Several Edge-On Impact (EOI) tests have been also performed to characterise the multiple fragmentation of dry and wet concrete tiles. This setup allows studying damage mechanisms in brittle materials like ceramics [4], rocks [5], and ultra-high strength concrete [6], under impact loadings. Post-mortem observations were performed after infiltration with a coloured hyperfluid resin. The cracking pattern is compared to those revealed in spalled specimens.

An anisotropic damage model was developed based on a micromechanical description of dynamic fragmentation process [7, 6]. In this work, this model is used to simulate the damage process of concrete specimens during spalling tests and EOI tests. The model allows explaining the increase of strength with loading rate. Moreover, different experimental data like velocity measured on rear face of specimens by the laser and the damage patterns are crosschecked with data obtained from the numerical simulations. Finally, the modelling is used to highlight the possible roles played by microstructure on the dynamic response of concrete materials under such high loading rates.

References

- [1] J.R. Klepaczko and A. Brara (2001). An experimental method for dynamic tensile testing of concrete by spalling, *Int. J. Impact Eng.*, **25**, 387-409.
- [2] H. Schuler, C. Mayrhofer, K. Thoma (2006). Spall experiments for the measurement of the tensile strength and fracture energy of concrete at high strain rates, *Int. J. Impact Eng.*, **32**, 1635–1650.
- [3] J. Weerheijm and J.C.A.M. Van Doormaal (2007). Tensile failure of concrete at high loading rates: New test data on strength and fracture energy from instrumented spalling tests, *Int. J. Impact Eng.*, **34**, 609-626.
- [4] P. Riou, C. Denoual, C.E. Cottenot (1998). Visualization of the damage evolution in impacted silicon carbide ceramics, *Int. J. Impact Eng.*, **21**, 225-235.
- [5] S. Grange, P. Forquin, S. Menacci, F. Hild (2008). On the dynamic fragmentation of two limestones using edge-on impact tests, *Int. J. Impact Eng.*, in press.
- [6] P. Forquin and F. Hild (2007). Dynamic Fragmentation of an Ultra-High Strength Concrete during Edge-On Impact Tests, *ASCE J. of Eng. Mechanics*, accepted manuscript.
- [7] C. Denoual and F. Hild (2000). A Damage Model for the Dynamic Fragmentation of Brittle Solids, *Comp. Meth. Appl. Mech. Eng.*, **183**, 247-258.

DIRECT NUMERICAL COMPUTATION OF THE EFFECTIVE MATERIAL PROPERTIES OF THE MATERIAL WITH RANDOM DISTRIBUTION OF THE MICROCRACKS

G. Mejak

University of Ljubljana, Ljubljana, Slovenia

1. Introduction

In the paper direct numerical computation of the effective material properties of the material with random distribution of the frictionless microcracks is presented. To this end a new numerical method, three level finite element method is introduced. Using it problems with very fine discretization can be solved in real time. This allows computing a large population of effective material properties of materials with random distribution of microcracks. Its statistical quantities then describe probabilistic distribution of effective material properties.

2. Three level finite element method

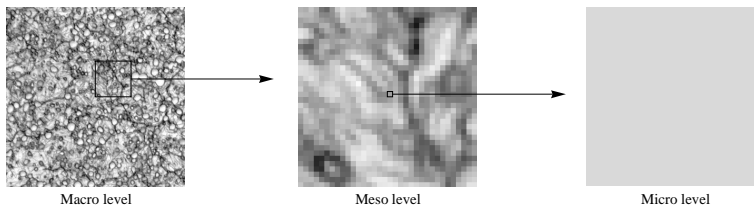


Figure 1. Three level discretization.

The method is described within the context of a linear problem although it works equally fine for nonlinear problems which are solved by iteration of linear subproblems. Figure 1 shows three discretization levels. The macro level is the size of the specimen of the material under consideration and the micro level is the size where the material becomes homogeneous. Between them is a meso level which has already complex structure but is too small for a representative volume. After standard FEM discretization the micro level degrees of freedom are statically condensed to the meso level degrees of freedom which are further condensed to the macro level. Thus at the micro level the basis functions are standard finite element functions, at the meso level the basis functions are linear combinations of the micro level basis functions and at the macro level the basis functions are linear combinations of the meso level basis functions.

Efficiency η of the three level FEM is estimated by the ratio of the number of the floating point operations of the linear solver of the standard FEM and three level FEM. For example, we consider a plane problem which has p^2 micro cells. We group m^2 micro cells into one meso cell and M^2 meso cells into one macro cell which is just the macro structure. Then $p = Mm$. The micro cell is discretized into μ^2 quadrilateral bilinear elements. It turns out that for the optimal number of the meso cells $M = (1 - 1/2\mu)^{2/3}(6 - 1/\mu)p^{1/3}$ the efficiency ratio is of order $\eta = O(p^{2/3})$ for large values of p . For example, for $p = 64$ the three level FEM is 16 times more efficient as the standard FEM. Generalization to multilevel FEM is possible. However, we note that on a single processor computer the optimal number of levels is three.

3. Numerical example

Although a real problem with random distribution of heterogeneities such as in Figure 1 and with random distribution of microcracks can be considered, we restrict ourselves to the plane stress problem for homogeneous isotropic material ($\mu/E = 2/5$) with random distribution of frictionless microcracks, see Figure 2, as this enables comparison with a dilute distribution model [1]. The length of the individual microcracks is $a = 1/64$. Individual microcracks are only in x and y directions but they can be combined into more complex patterns. At the right a bar chart of the tallies of the effective material parameters between their minimal and maximal values for population of 4000 distributions of the microcracks is shown. In particular, the normalized effective Young modulus E_1 varies between 0.857 and 0.902 with the mean 0.881 and standard deviation 0.0061.

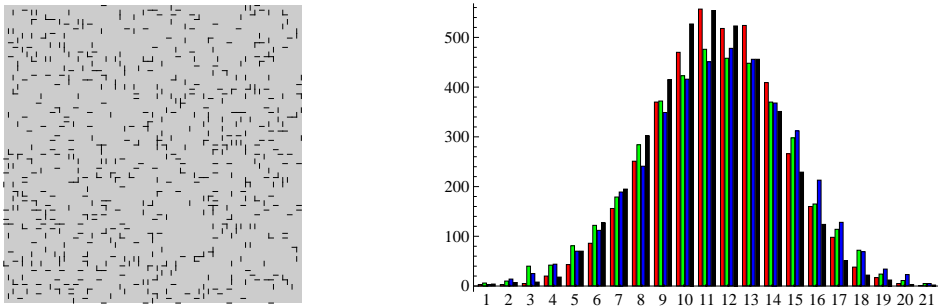


Figure 2. Left: a square domain with random distribution of 640 cracks aligned with the sides of the square. Right: a bar chart of tallies of material parameters E_1 (red), E_2 (green), μ (blue) and ν_{12} (black).

Comparison with the dilute distribution model is shown in Figure 3. Now all micro cracks are aligned with the y axis. Denoting by $f = Na^2$ the crack density parameter, N is the number of microcracks, the model predicts that for the prescribed unit tensile macrostress in x direction the normalized effective Young and shear moduli are $\bar{E}_1 = (1 + 2\pi f)^{-1}$ and $\bar{\mu} = (1 + 2\pi f\mu/E)^{-1}$. It can be seen that the dilute distribution model is valid up to $f = 0.04$. For the prescribed macrostrain the match is even better. The comparison validates our approach and opens the way to approach many other interesting problems with microcracks.

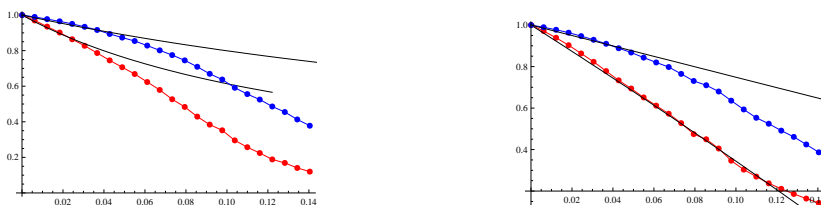


Figure 3. Computed (dotted line) effective moduli and moduli predicted by the dilute model (solid line). Lower/upper curve: normalized Young/shear modulus, prescribed macrostress/macrostrain at right/left.

4. References

- [1] M. Hori and S. Nemat-Nasser (1999). *Micromechanics: Overall Properties of Heterogeneous Materials*, 2nd ed. North-Holland, Amsterdam, 73-206.

THE NEW FRACTURE CRITERION FOR MIXED-MODE CRACK. THE MK CRITERION.

K.P. Mróz and K.Doliński

Institute of Fundamental Technological Research, Warsaw, Poland

1. Introduction

In formulating the fracture criteria an effort is usually made to refer to the physical phenomena associated with the damage processes of the material in front of the crack tip. The complexity of the damage mechanisms involved makes it necessary to introduce some assumptions that take into account the most important features of the damage process and make the analysis viable. There are many approaches based on the linear elastic fracture mechanics (LEFM). Some of them use the stress or strain energy calculated at a finite distance from the notch tip. In the case of the S -criterion [1] the strain energy density factor is assumed as a fracture criterion and calculated at a point located at a certain constant radius $r = r^C$ from the crack tip being independent of the geometry and loading conditions. A strain energy density parameter is also the basis in formulation of the T -criterion [2], but, opposite to the S -criterion, this parameter consists of two energy components: distortional, T_D , and dilatation, T_V , ones. The T -criterion postulates that the crack propagates along the direction determined by the maximum of total energy density, which is also the maximum of the dilatational strain-energy density evaluated on the locus of constant distortional strain energy density what corresponds to Mises elastic-plastic boundary. This criterion uses the variable radius of the elastic-plastic boundary but in the case of brittle materials it tends to S -criterion since the size of plastic zone is then very small and the boundary can be assume as a circle with a constant radius. However, in the vicinity of the crack tip other damage processes may exist, e.g. microcracks, especially, in the case of brittle materials. They may be accompanied by a small plastic region [3]. Then the LEFM solutions used in T - and S -criteria are not fully correct because the stress or strain energy are calculated at some finite distance from the crack tip. In many cases this distance appears to be too small for the LEFM to be used properly to formulate some fracture criteria because it is not located on the boundary of the damage zone.

2. The formulation of the new criterion

Let's assume the strain energy density components, T_D and T_V , and a condition $T_V/T_D|_{\max} \rightarrow \theta_{pr}$, cf. [2], to determine the plane of the fracture. This condition means that the fracture appears in the direction where the ratio between the dilatation, T_V (corresponding to the decohesion mechanism of the fracture process), and distortional, T_D (corresponding to the plastic deformations) components of the strain energy density achieves its maximum value. It means that the crack will propagate in direction where the dissipation energy is the smallest corresponding to decohesion. Now, we can assume that the angle of the crack fracture, θ_{pr} , will follow the minimum value the distortional component of the strain energy density, T_D , calculated on the locus $T_V(r, \theta) = T_V^C = \text{const.}$, cf. [4], associated with the maximum fracture toughness, σ_C :

$$(1) \quad \left. \frac{T_V}{T_D} \right|_{\max} \rightarrow \theta_{pr} \quad \text{at} \quad T_V = T_V^C = \text{const.} \quad \rightarrow \quad \left. T_D(r(T_V^C, \theta)) \right|_{\min} \rightarrow \theta_{pr},$$

where

$$(2) \quad r = r_v \Big|_{T_v = \text{const}} = \frac{1}{2\pi} \left(\frac{2K_I \cos \frac{\theta}{2} - 2K_{II} \sin \frac{\theta}{2}}{\sqrt{T_v^c \frac{6E}{(1-2\nu)(1+f)^2} - T}} \right)^2,$$

T -term is the second (constant) term of the series representations of the local stress and displacement, while $f=0$ for the plane stress and $f=\nu$ for the plane strain. The critical value which determines the crack initiation assumes the radius of the decohesion zone along the fracture direction to be derived from Eq. (2) as:

$$(3) \quad r \Big|_{\theta=\theta_{pr}} \geq r_{cr} \rightarrow K_I \cos \frac{\theta}{2} - K_{II} \sin \frac{\theta}{2} \geq K_{cr},$$

where r_{cr} corresponds to an uniaxial test.

3. The results

In Table 1 the angles of crack propagation θ_{pr} for various inclinations of the main crack, α , in the uniaxial tension test and various relations between the loading and maximum fracture toughness are shown. It is interesting to point out the difference between the angles of the crack propagation for the same α and different loading values. It results from the effect of the T -term included into the solution that simultaneously introduces a correction of the contour r , cf. Eq. 2, on which the components of the stress tensor are calculated. In the case of a singular solution when $T=0$ the relationship σ/σ_c appears to be unimportant for the fracture direction because the components of the stress tensor are always proportional. Accounting for the T -term causes, however, that any change of the ratio σ/σ_c affects the resulting angle of the crack propagation and, the stress tensor components are not proportional any more. There is also important to point out that the assumption that the radius defining the decohesion zone is a constant value causes the relationship σ/σ_c to be meaningless.

σ/σ_c	$\alpha [^\circ]$				
	15	30	45	60	80
Singular solut.	-85.7	-72.7	-59.6	-45.1	-19.3
0.1	-86.7	-73.7	-59.6	-43.1	-15.5
0.2	-87.7	-74.7	-59.6	-40.6	-13.5
0.4	-89.7	-76.7	-59.6	-37.6	-11.5
0.6	-91.2	-78.7	-59.6	-35.6	-11.0
0.8	-92.7	-80.2	-59.6	-34.1	-10.5
1	-93.7	-81.2	-59.6	-33.1	-10.0

Table 1. The angle of the crack propagation based on the **MK** – criterion.

4. References

- [1] G.C Sih (1973). Some basic problems in fracture mechanics and new concepts, *Engng Fracture Mechanics*, **5**, 365–377.
- [2] P.S. Theocaris and N.P. Andrianopoulos (1982). The Mises elastic-plastic boundary as the core region in fracture criteria, *Engineering Fracture Mechanics*, **16**, 425–432.
- [3] J.G. Williams (1984). Fracture mechanics of polymers, Ellis Horwood, Chichester.
- [4] K.P. Mróz (2008). Fatigue cracks growth in the bimaterial system. The mathematical model and numerical solution, Ph.D. thesis IPPT PAN (IFTR PAS), Warsaw, (in Polish).

THE ENERGY APPROACH IN THE CALCULATION OF LIVES FOR HIGH CYCLE FATIGUE

Z. Marciniak, D. Rozumek, C.T. Lachowicz
Opole University of Technology, Opole, Poland

In the paper an energy based method of fatigue life calculation under non-proportional random bending with torsion loading is presented and experimentally verified. The method identifies strain energy density parameter in the critical fracture plane through integration of the chosen fragments of power history according to the distinguished ranges of stresses. Round specimens made of steel 10HNAP (S355J2G1W) included in the standard PN-EN 10155 of 1997 were tested. The material is a low-alloy of higher resistance to atmospheric corrosion structural steel. The tests performed in the high cycle fatigue regime (HCF) under variable-amplitude and pseudo-random combined bending and torsion loading, were held at Opole University of Technology [1]. The tests were carried out under narrow-band loading with the dominating frequency 20 Hz and 28.8 Hz the coefficient of irregularity $I = 1$ and 0.99. The equivalent instantaneous power, $p_{eq}(t)$, understood as a scalar product of instantaneous values of suitable components of the stress tensor $\sigma_{ij}(t)$ and the strain rate tensor $\dot{\epsilon}_{ij}(t)$, is calculated according to the following relation [2]

$$(1) \quad p_{eq}(t) = \sigma_{ij}(t) \bullet \dot{\epsilon}_{ij}(t)$$

where $i, j = 1, 2, 3$.

Eq. (1) is integrated in the time interval $t_{k+1} - t_k$ for each distinguished stress range $\sigma_{ij}(t_{k+1}) - \sigma_{ij}(t_k)$, and increment of the strain energy density is calculated

$$(2) \quad \Delta E_{eq[(k+1)-k]} = \int_{t_k}^{t_{k+1}} p_{eq}(t) dt = \int_{t_k}^{t_{k+1}} \sigma_{ij}(t) \dot{\epsilon}_{ij}(t) dt$$

The procedure of calculation of strain energy density for one stress range includes observation of changes of stress history and integration of suitable fragments of instantaneous power histories (Fig. 1). Energy changes, determined in the moments corresponding to the distinguished ranges in the stress history, correspond to work of external forces on suitable displacements. They are identified with elastic energy temporarily accumulated in the material. In the assumed algorithm of calculations there is a possibility of precise distinction of work under both compression and tension [2].

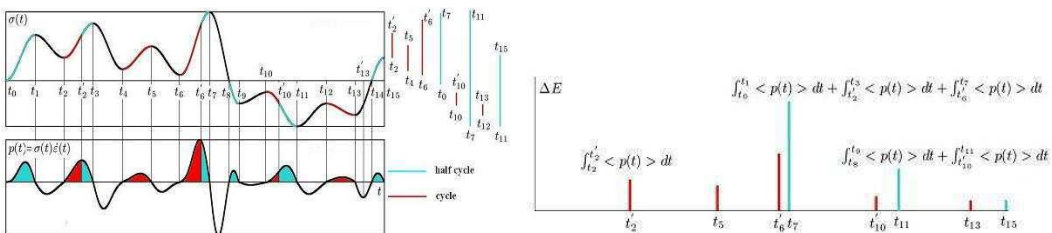


Fig 1. Exemplary histories of stress and power with distinguished of stress $\sigma(t)$, where the power history $p(t)$ is integrated.

Calculated fatigue lives obtained from evaluation according to the strain energy density criterion from Eq. (2). Fig. 2 presents comparison of calculated and experimental fatigue lives for 10 combinations of variable-amplitudes and 13 combinations of bending and torsion pseudo-random loading.

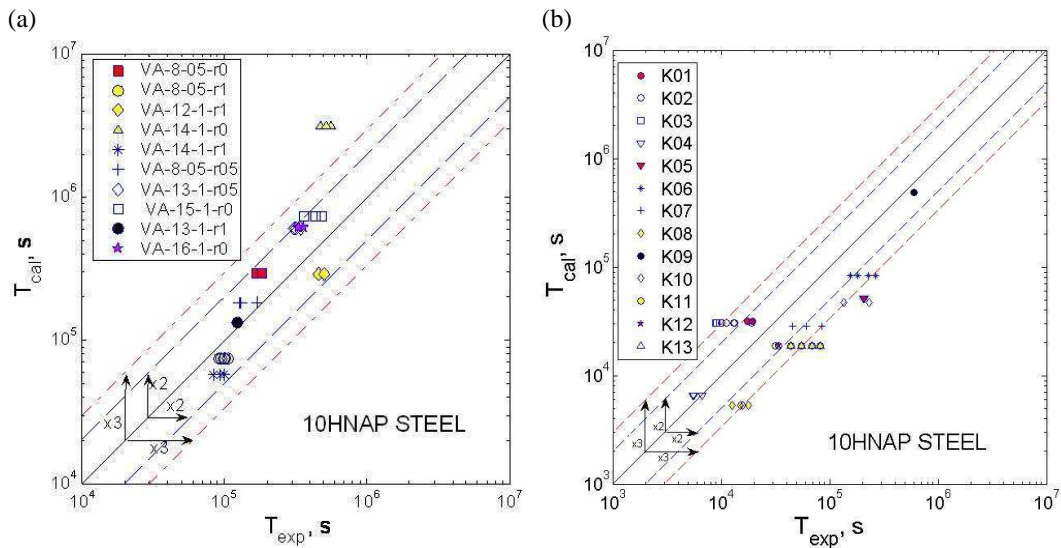


Fig 2. Comparison of fatigue lives obtained from calculations T_{cal} and experimental T_{exp} for: (a) variable-amplitudes loading, (b) pseudo-random loading.

The greatest part of compared results for variable-amplitudes loading is included in the scatter band of the factor 2 and for pseudo-random loading is included in the scatter band of the factor 3. The test results for pseudo-random loading exceeding the scatter band of coefficient 3 occurred at the safe side.

After averaging of life and taking the confidence intervals into account, all the test results were included into the scatter band equal to 3 (1/3).

References

- [1] Z. Marciniak, C.T. Lachowicz, D. Rozumek & E. Macha (2007). The strain energy density in the description of fatigue lives under non-proportional bending and torsion. *Proc. of the 8th International Conference on Multiaxial Fatigue and Fracture (ICMFF8-2007)*, Sheffield Hallam University, Sheffield, UK, 88-89 and CD, ps 9.
- [2] C.T. Lachowicz (2001). Calculation of the elastic-plastic strain energy density under cyclic and random loading. *Int. J. of Fatigue.*, **23**, 643-652.

MODEL OF DEFORMABLE RIGID BODY WITH DANGEROUS VOLUME

L. Sosnovskiy¹, S. Sherbakov²

¹ S&P Group TRIBOFATIGUE Ltd., Gomel, Belarus

² Department of Mechanics and Mathematics, Belarusian State University, Minsk, Belarus

Variety of practically important systems such as toothings, wheel/ rail etc. work in conditions of complex stress-strain state conditioned by local contact and general non-contact volume deformation. Such mechanical systems are called active systems [1] and for them special analysis of surface and subsurface deformation and damage is needed.

Generally the analysis of interaction and damage of elements of active systems is based on statistical model of deformable rigid body with dangerous volume that contains the criteria for limitation of dangerous volumes and the general procedure of their calculation [1].

Definition of forms and sizes of dangerous volumes requires the knowledge of function of distribution of fatigue limits for corresponding element of a system and the stress state in considered areas of interacting bodies. Dangerous volumes are finite three-dimensional areas where the stresses exceeding the minimum values of fatigue limit ($\sigma_{-1\min}$) distribution are present (figure 1).

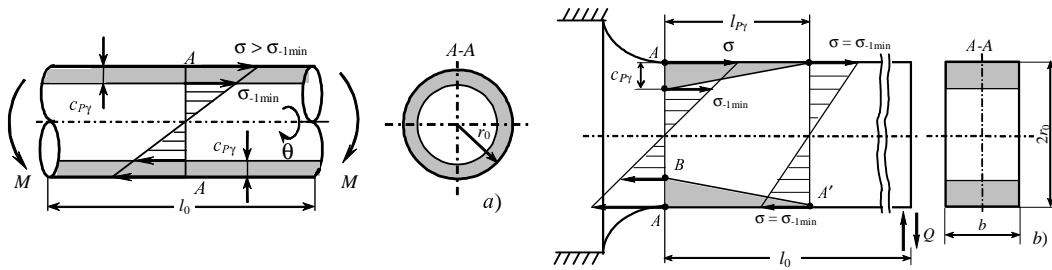


Figure 1. Scheme of formation of dangerous volume for pure bending of a shaft (a) and console bending of a thick plate (b).

Active system differs from a bent shaft because all six independent components stress tensor are usually nonzero. Generally the limiting state according to the criterion of contact fatigue (formation of microcracks) in some point of an active system may be reached by several various tensor components. Thus fatigue limit for an active system is defined for every independent tensor component as an extreme value of its distribution under the action of limiting load F_{*lim} . For a homogeneous isotropic deformable rigid body limiting normal and tangential stresses $\sigma_n^{(*lim)}$ and $\sigma_\tau^{(*lim)}$ and also limiting main stress $\sigma_1^{(*lim)}$ and limiting intensity of stresses $\sigma_{int}^{(*lim)}$ are defined in the following way [2]:

$$(1) \quad \sigma_n^{(*lim)} = \max_{dV, i} \left(\left| \sigma_{ii}(F_{*lim}, dV) \right| \right), \quad i=x, y, z, \quad \sigma_\tau^{(*lim)} = \max_{dV, i, j} \left(\left| \sigma_{ij}(F_{*lim}, dV) \right| \right), \quad i, j=x, y, z, \quad i \neq j, \\ \sigma_1^{(*lim)} = \max_{dV} \left(\left| \sigma_1(F_{*lim}, dV) \right| \right), \quad \sigma_{int}^{(*lim)} = \max_{dV} \left(\sigma_{int}(F_{*lim}, dV) \right),$$

where dV - elementary volume of the loaded body.

Limiting stresses $\sigma_{ij}^{(\pm*lim)}$, $i, j = x, y, z$, $\sigma_i^{(\pm*lim)}$, $i = 1, 2, 3$, $\sigma_{int}^{(*lim)}$ are defined similarly for the general case of rigid body.

Then the conditions for limitation of dangerous volumes are

$$(2) \quad V_{(ij)} = \left\{ dV / \sigma_{ij} \geq \sigma_k^{(*lim)}, dV \subset V_k \right\}, \quad i, j = x, y, z, \quad k = \begin{cases} n, & \text{при } i = j, \\ \tau, & \text{при } i \neq j, \end{cases}$$

$$(3) V_{(i)} = \{dV / \sigma_i \geq \sigma_i^{(*\text{lim})}, dV \subset V_k\}, i = 1, 2, 3, V_{\text{int}} = \{dV / \sigma_{\text{int}} \geq \sigma_{\text{int}}^{(*\text{lim})}, dV \subset V_k\}, V_T = \bigcup_{i,j} V_{ij}$$

where V_k - working volume of a deformable rigid body.

Corresponding measures of damage are

$$(4) \omega_{ij} = V_{ij} / V_k, \omega_T = V_T / V_k.$$

Since dangerous volumes may have arbitrary and complex form and their analytical definition is difficult then they are calculated using Monte-Carlo method.

Figure 5 shows the example of calculation of dangerous volumes for the case of non-conforming elliptical Hertzian contact for the following initial data: $\sigma_n^{(*\text{lim})} = 0.3p_0$, $\sigma_\tau^{(*\text{lim})} = 0.09p_0$ (p_0 is the maximum contact pressure in the center of contact), friction coefficient $f = 0,05$, ratio between smaller b and bigger a semi-axes of contact ellipse $b/a = 0.813$ [2]. It is visible from the given figures that the greatest by size are $V_{(zz)}$, $V_{(xz)}$ and $V_{(yz)}$ dangerous volumes correspond to the greatest stresses $\sigma_{zz}^{(n)}$, $\sigma_{xz}^{(n)}$ and $\sigma_{yz}^{(n)}$.

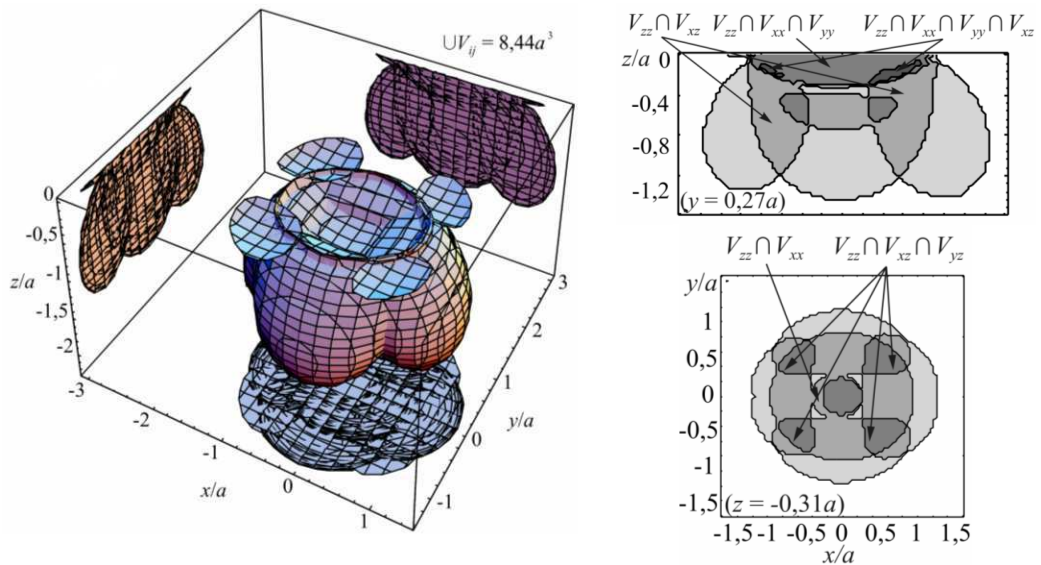


Figure 2. Union of dangerous volumes and its sections

Since dangerous volumes are the measures of damage of deformable bodies then while analyzing figure 2 it is possible to specify concrete areas where the origin and development of both surface and internal cracks is possible. It is obvious, that occurrence of irreversible damages (primary cracks) have higher probability where corresponding dangerous volumes intersect.

References

- [1]. L.A. Sosnovskiy (2004). Tribo-Fatigue. Wear-fatigue damage and its prediction (Foundations of engineering mechanics), Springer.
- [2]. L. A. Sosnovskiy, S.S. Sherbakov (2007). Vibro-impact in rolling contact, J. of Sound and Vibration, 308, 489–503.

INTERFACIAL THERMAL STRESS ANALYSIS OF AN ELLIPTICAL INCLUSION WITH AN IMPERFECT INTERFACE IN ANISOTROPIC PLANE

C.H. Wang

Dept. of Aeronautical Engineering, National Formosa University, Yunlin County, Taiwan

1. General introduction

At the early stage on developing the analysis of inclusion problems, the bonding condition between the inclusion and the matrix is always considered perfectly bonded. However in the most real situation, the inclusion interfaces are not perfectly bonded at all especially as the temperature of the composite is in relatively higher level. This study provides the interfacial thermal stress analysis for the problems of an elliptical inclusion embedded in an anisotropic plane with imperfect interface. The thermal load we consider here is that the inclusion is subjected to a uniform temperature change. The analytical results which give the distributions of interfacial stresses are derived base on Stroh formalism [1] in conjunction with the techniques of using mapping functions. As to the imperfect interface, a spring-type model with vanishing thickness is applied such that we consider the interfacial tractions are continuous and the displacement jumps across the interface layer are in proportion to the traction components in their respective direction [2]. The non-negative interfacial parameter h_j , n , t or z , which is the ratio of the interfacial stress and the interfacial displacement jump in the normal, tangential or anti-plane direction, varies from zero to infinite value. The limiting value of interfacial parameters, i.e. $h_j=0$ or $h_j=\infty$, imply a particular case which represents a completely debonded interface or a perfectly bonded interface, respectively. Therefore, our results can be applied to the most problems of all possible kinds of interfaces. Among the derivations of this study, due to the fact that the interfacial displacement jumps proportionally relate to the corresponding interfacial stresses, only using analytical continuation could lead to an unsolvable situation with expanding the solution on the inclusion domain into a complex Fourier series. To overcome this awkward situation, an idea of semi-inverse manipulation is introduced by virtue of applying the exact expression for a Fourier series, which is the multiplication of two different Fourier series [3]. According to the obtained distribution curves for the interfacial thermal stresses of an elliptical inclusion problem with an imperfect interface, the results of this research indicate that the extreme values and distributions of the interfacial stresses strongly depend on the values of interfacial parameters.

2. Basic formulations

In a coordinate system x_i , $i=1, 2, 3$, the temperature, displacement vector $\mathbf{u} = [u_1, u_2, u_3]^T$ and stress function vector $\phi = [\phi_1, \phi_2, \phi_3]^T$ on an anisotropic plane can be expressed as follows [1]

$$(1) \quad T = 2\text{Re}\{g'(z_\tau)\}$$

$$(2) \quad \mathbf{u} = 2\text{Re}\{\mathbf{A}\mathbf{f}(z_\alpha) + \mathbf{c}g(z_\tau)\}$$

$$(3) \quad \phi = 2\text{Re}\{\mathbf{B}\mathbf{f}(z_\alpha) + \mathbf{d}g(z_\tau)\}$$

where \mathbf{A} and \mathbf{B} are Stroh matrices, \mathbf{c} and \mathbf{d} are heat eigenvectors, and $g(z_\tau)$ and $\mathbf{f}(z_\alpha)$ are arbitrary functions of their arguments. According to the assumptions for a spring-type model for an imperfect interface, the interfacial conditions at the elliptical interface are given by

$$(4) \quad \|\sigma_{mi}(a_0, \theta)\| = 0,$$

$$(5) \quad \sigma_{ij}(a_0, \theta) = h_j (\|u_i(a_0, \theta)\| - u_i^*); i, j = n, t, z.$$

where the notation $\|*\| = (*)_2 - (*)_1$ denotes for the function value jump across the interface layer and u_i^* represents the displacements in direction i associated with the eigenstrain. The subscript indices “1” and “2” stand for the associate quantities on the matrix and the inclusion domains, respectively. The values of the three non-negative interfacial parameters h_n, h_t, h_z , in Eq. (5) can represent the bonding condition at the interface. By using Eqs. (1)–(3) Eqs. (4) and (5) lead to a set of simultaneous equations in terms of $\mathbf{f}_1(z_\alpha)$ and $\mathbf{f}_2(z_\alpha)$ pertaining to the exact solutions on the domains of matrix and inclusion, respectively. After mapping the elliptical interface into a unit circle and then expanding $\mathbf{f}_2(z_\alpha)$ into a Laurent series, the exact forms are successfully solved by virtue of introducing a semi-inverse approach in conjunction with the analytical continuation method.

3. Numerical results

The results of this research are presented by the interfacial shear stress curve for an orthotropic inclusion problem. Consider a temperature change of 100°C on the inclusion and the half length of the axes $a=1.5, b=1$ and that the material properties of the composite system are as

$$\begin{aligned} (E_1)_1 &= 10 \text{ GPa}, (E_2)_1 = 5 \text{ GPa}, (E_3)_1 = 5 \text{ GPa}, (\nu_{ij})_1 = 0.4, i, j = 1 \sim 3, i \neq j, (G_{12})_1 = 1 \text{ GPa}, \\ (G_{13})_1 &= 2 \text{ GPa}, (G_{23})_1 = 1 \text{ GPa}, (\alpha_{11})_1 = 70 \times 10^{-6} (1/^\circ\text{C}), (\alpha_{22})_1 = 50 \times 10^{-6} (1/^\circ\text{C}), \\ (\alpha_{33})_1 &= 50 \times 10^{-6} (1/^\circ\text{C}), (k_{11})_1 = 1 \text{ W/m}^\circ\text{C}, (k_{22})_1 = 0 \text{ W/m}^\circ\text{C}, (k_{12})_1 = 0 \text{ W/m}^\circ\text{C}, \\ (E_1)_2 &= 17 \text{ GPa}, (E_2)_2 = 7 \text{ GPa}, (E_3)_2 = 5 \text{ GPa}, (\nu_{ij})_2 = 0.3, i, j = 1 \sim 3, i \neq j, (G_{12})_2 = 3 \text{ GPa}, \\ (G_{13})_2 &= 2 \text{ GPa}, (G_{23})_2 = 1 \text{ GPa}, (\alpha_{11})_2 = 70 \times 10^{-6} (1/^\circ\text{C}), (\alpha_{22})_2 = 50 \times 10^{-6} (1/^\circ\text{C}), \\ (\alpha_{33})_2 &= 60 \times 10^{-6} (1/^\circ\text{C}), (k_{11})_2 = 1 \text{ W/m}^\circ\text{C}, (k_{22})_2 = 0 \text{ W/m}^\circ\text{C}, (k_{12})_2 = 0 \text{ W/m}^\circ\text{C}, \end{aligned}$$

Figure 1 shows the comparison of the interfacial shear stress distribution curves for two different cases: the perfectly bonded interface and the frictional sliding interface. It is obvious that the interfacial shear stress distribution can change evidently and the extreme value of shear stress notably magnifies as the interface changes from perfectly bonded to frictional sliding.

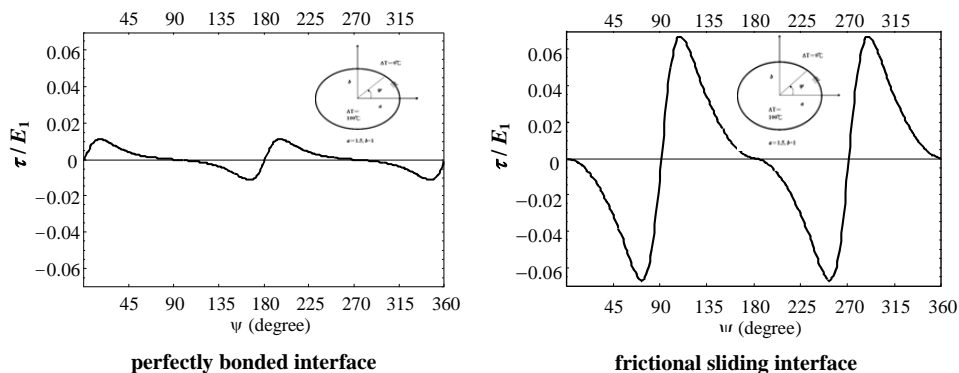


Fig. 1. The distribution curves of the interfacial shear stress along the elliptical interface.

4. References

- [1] T. C. T. Ting (1991). *Anisotropic Elasticity—Theory and Applications*, Oxford University Press, New York, 506-511.
- [2] Y. Benvensite (1985). The effective mechanical behavior of composite materials with imperfect contact between the constituents, *Mech. Mater.*, **4**, 197-208.
- [3] T. Chen (2001). Thermal conduction of a circular inclusion with variable interface parameter, *Int. J Solids Struc.*, **38**, 3081-3097.

SIMULATION OF FRACTURE PROCESS IN CONCRETE ELEMENTS WITH STEEL FIBRES USING DISCRETE LATTICE MODEL

J. Kozicki and J. Tejchman

Gdańsk University of Technology, Gdańsk, Poland

1. Introduction

The fibre reinforced concrete is commonly used for industrial floors. The determination of its strength and ductility is of a major importance for the design of floors. This paper deals with simulations of a fracture process in concrete including steel fibres with our novel discrete lattice model [1], [2]. Concrete is described at a meso-scale as a four-phase material composed of aggregate, cement matrix, interfacial zones and steel fibres. The elements are stochastically distributed in the form of a lattice mesh using a Delaunay's construction scheme. The calculations are carried out for concrete specimens including steel fibres subject to uniaxial extension and three point bending.

2. Discrete lattice model

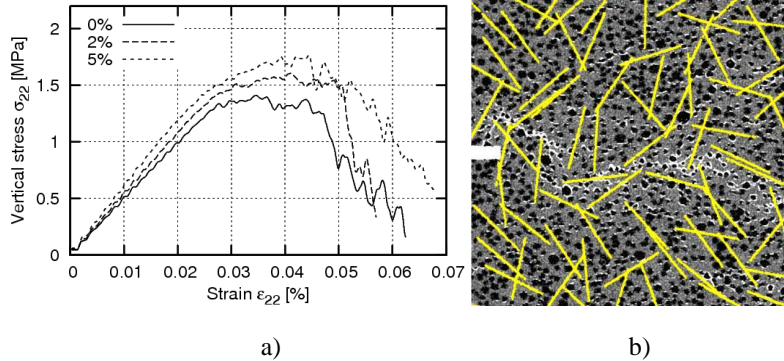
Our lattice model [1], [2] differs from classical lattice beam models [3] composed of beams connected by non-flexible nodes in that it consists of rods with flexible nodes subject to longitudinal deformability and rigid body rotation. Thus, shearing, bending and torsion are represented by a change of the angle between rod elements connected by angular springs. This quasi-static model is of a kinematic type. The calculations of element displacements are carried out on the basis of the consideration of successive geometrical changes of rods due to translation, rotation and normal and bending deformation. Thus, the global stiffness matrix is not built and the calculation method had a purely explicit character. Owing to that, the computation time is significantly reduced. In addition, torsion in three-dimensional simulations is included. Each rod element is removed from the lattice if the local critical tensile strain is exceeded. The lattice elements possess a longitudinal stiffness k_l (controls the changes of the element length), bending stiffness k_b (controls the changes of the angle between elements) and torsional stiffness k_t (controls the changes of the torsional angle between elements). The quasi-brittle material is discretized in the form of a 3D tetrahedral grid or a 2D triangular grid including lines. The distribution of elements is assumed to be completely random using a Delaunay's construction scheme. First, a tetrahedral grid of nodes is created in the material with the side dimensions g . Then each node is randomly displaced by a 3D vector of the magnitude s . Then each edge in the Delaunay mesh connecting those nodes forms a lattice rod. The model needs 2 parameters to randomly distribute elements in the lattice. The material heterogeneity is implemented by projecting it on the lattice and corresponding properties are assigned to relevant lattice elements with steel fibres distributed in the whole specimen. The material parameters have been determined empirically to match the experimental results at the macro-scale with the numerical ones on the basis of a uniaxial tension and compression test [2].

3. Numerical results

Figure 1 presents results with plane concrete specimens composed of 200000 rod elements subject to uniaxial extension (Fig.1A) and three-point bending (Fig.1B). The average rod length was $g=1$ mm (the rod length changed between 0.3 mm and 2 mm). One assumed following material parameters for the cement matrix, aggregate and bond: $k_b/k_l=0.6$ (with $k_t=20$), local $\epsilon_{min}=0.2\%$

(cement matrix), $k_b/k_l=0.6$ (with $k_l=60$), local $\varepsilon_{min}=0.133\%$ (aggregate), $k_b/k_l=0.6$ (with $k_l=14$), local $\varepsilon_{min}=0.05\%$ (bond) and $k_b/k_l=1$ (with $k_l=160$), local $\varepsilon_{min}=3\%$ (steel fibres). The aggregate density was assumed to be 25%. The mean aggregate diameter was $d_{50}=3.5$ mm (the aggregate diameter changed between 2 mm and 16 mm). Five simulations were performed. The steel fibres content was 0%, 2% and 5% respectively (with respect to the total amount of rods). The moduli of elasticity were: 60 GPa (aggregate), 20 GPa (matrix), 14 GPa (bond) and 160 GPa (fibres), respectively. The interface had, thus, the lowest strength.

A)



B)

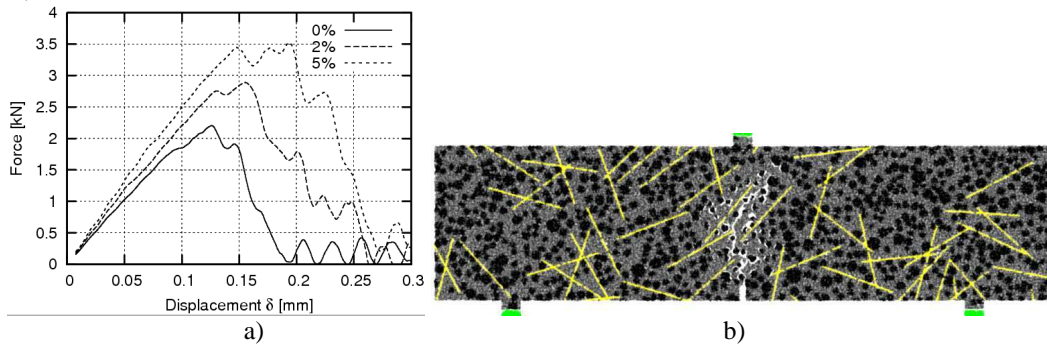


Figure 1: Notched concrete specimens with a different steel fibre amount subject to uniaxial extension (A) (a) vertical normal stress versus vertical normal strain, b) crack propagation) and three-point bending (B) (vertical force versus vertical displacement, b) crack propagation)

The results show that the presence of fibres increases both the strength and ductility of concrete elements due to a longer propagation way of cracks.

4. References

- [1] J. Kozicki and J. Tejchman (2006). 2D lattice model for fracture in brittle materials, *Archives of Hydro-Engineering and Environmental Mechanics*, **53**, 2, 71-88.
- [2] J. Kozicki and J. Tejchman (2007). Effect of aggregate structure on fracture process in concrete using 2D lattice model, *Archives of Mechanics*, **59**, 4-5, 365-384.
- [3] J.G.M. van Mier, E. Schlangen and A. Vervuurt (1995). Lattice type fracture models for concrete, *Continuum Models for Materials with Microstructure*, H.-B. Muehlhaus, ed., John Wiley & Sons, 341-377.

Modelling of chemo-damage in concrete due to sulfate corrosion

W. Węglewski, M. Basista

Institute of Fundamental Technological Research, Warsaw, Poland

e-mail: wweglew@ippt.gov.pl; mbasista@ippt.gov.pl

1. Introduction

The sulfate corrosion of concrete is a process in which a series of chemical reactions between migrated sulfate ions and active concrete particles lead to the degradation of concrete structure [1]. The product of this reaction, a strongly expansive crystal – ettringite, exerts a pressure on the surrounding concrete walls, which leads to propagation of pre-existing microcracks. The ettringite may crystallize in two type of reactions: through-solution reaction and topochemical reaction. Despite long lasting discussion in specialized literature there's still no agreement between researchers which type of reaction leads to expansive ettringite creation. In this paper a micromechanical model is proposed of sulfate attack in concrete element with and without external load. The model involves coupled processes of nonsteady diffusion of sulfate ions (second Fick's law), expansion of ettringite inclusions calculated from micromechanical solutions and microcracking induced by this expansion. The difference between expansions calculated from the model assuming a topochemical reaction and the one with a through-solution reaction of the ettringite crystallization will be presented. The obtained solutions will be compared with the experimental data in order to find out which type of reaction leads to harmful ettringite crystallization.

2. Expansion of ettringite crystal

The crystallizing ettringite exerts pressure on the surrounding concrete walls. Depending on the form of the ettringite crystallizing reaction, the pressure will be calculated from chemical thermodynamics (through-solution reaction) Equation (1), or from micromechanics (topochemical reaction) Equation (2).

$$(1) \quad P_{tsr} = \frac{RT}{v_s} \ln \frac{c_e}{c_{e0}} \quad (2) \quad P_{tch} = \frac{2}{9} \frac{E}{(\nu - 1)} \varepsilon_{kk}^{**}$$

where R is the universal gas constant, T is the temperature, v_s is the stoichiometric coefficient of ettringite, c_e and c_{e0} are actual and "in referred state" concentrations of ettringite, respectively, E is the Young's modulus, ν is the Poisson's ratio, ε_{kk}^{**} is the inclusion eigenstrain calculated using the equivalent inclusion method. When the external stress is applied, the stress caused crack propagation is calculated from

$$(3) \quad \sigma_{ij}^0 + \sigma_{ij} = 2\mu(\varepsilon_{ij}^0 + S_{ijmn}\varepsilon_{mn}^{**} - \varepsilon_{ij}^{**}) + \lambda\delta_{ij}(\varepsilon_{kk}^0 + S_{kkmn}\varepsilon_{mn}^{**} - \varepsilon_{kk}^{**}),$$

where σ_{ij} is the stress field generated by the ettringite, σ_{ij}^0 is the external stress, S_{ijkl} is the Eshelby's tensor.

3. Damage induced by ettringite formation

Assuming that the growing spherical ettringite crystal generates a penny-shaped microcrack, the stress intensity factor at the crack perimeter was derived as [2]

$$(4) \quad K_I = \frac{p}{\sqrt{\pi a}} \left(a - \sqrt{a^2 - r^2} \right),$$

where p is the pressure calculated from Equation (1) or (2) or (3) depending on type of reaction and on the applied external stress. Once the sulfate concentration was known from the solution of

second Fick's law [2] and the microcrack radius from the Griffith criterion $K_I = K_{IC}$, it was possible to determine Walsh-Budiansky-O'Connell crack density parameter ω ($\omega = N \langle a^3 \rangle$; N -number of cracks per unit volume, a -crack radius) and, thus, the effective diffusivity and stiffness from the self-consistent model and percolation theory. The microscale model was then volume averaged to arrive at the macroscopic constitutive stress-strain relation.

4. Application

The proposed model was implemented numerically to compute the expansion of a slender mortar prism (ASTM C490) specimen immersed in sodium sulfate solution of concentration 0.352 mol/l. Calculations were carried out for ettringite formation in through-solution (Fig. 1) and topochemical (Fig 2) reaction and when specimen was under external compressive load. The axial strain due to plane diffusion in x, y directions in the region with low-to-moderate microcracking is:

$$(5) \quad \varepsilon_z = \frac{\sigma_{33}^0}{E_{(x,y,t)}} + \frac{1}{E_{(x,y,t)} w_0} \int_0^1 \int_0^1 E_{(x,y,t)} f_{(x,y,t)}^I \varepsilon_{(x,y,t)}^{**} dx dy \quad \text{for } \omega < \omega_c$$

and for heavily damaged region:

$$(6) \quad \varepsilon(\tilde{x}, \tilde{y}, \tilde{t}) = f^I \varepsilon^{**} \quad \text{for } \omega > \omega_c$$

where f^I is volume density of ettringite inclusions and σ_{33}^0 is the external load. The problem was solved numerically using *FEM* program coded for the present case.

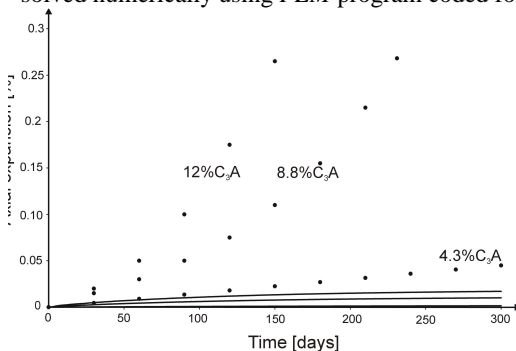


Fig. 1. Expansion of mortar specimen (through-solution reaction). Solid lines - predictions of the present model, circles - test data [3]

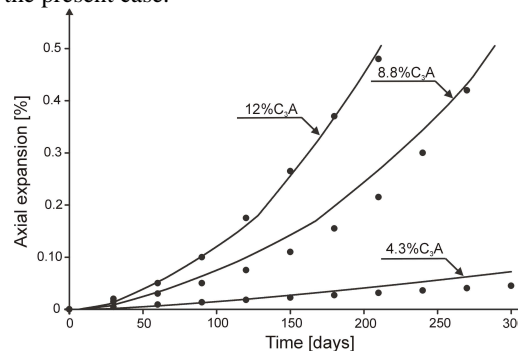


Fig. 2. Expansion of mortar specimen (topochemical reaction). Solid lines - predictions of the present model, circles - test data [3]

5. Conclusions

A micromechanical model has been proposed for the progressive damage in hardened concrete induced by the external sulfate attack. Expansions induced by two different types of ettringite formation have been studied. For the model with topochemical reaction of ettringite formation (Fig. 2) a good agreement with experiment data has been obtained. This supports the view of a number of researchers that expansive ettringite crystallizes in a topochemical reaction. The influence of external load on microcracking, diffusion and axial expansion have also been considered.

6. References

- [1] Skalny, J., Marchand, J., and Odler, I. (2002). *Sulfate Attack on Concrete*, Spon Press, London.
- [2] Basista, M., Weglewski, W. (2008). Chemically-assisted damage of concrete: a model of expansion under external sulfate attack, *International Journal of Damage Mechanics*, in press.
- [3] Ouyang, C., Nanni, A. and Chang, W.F. (1988). Internal and external sources of sulphate ions in portland cement mortar: two types of chemical attack, *Cement and Concrete Research*, **18**: 699-709.

FE-MODELLING OF CONCRETE BEHAVIOUR UNDER MIXED MODE CONDITIONS WITH NON-LOCAL AND COHESIVE CONSTITUTIVE MODELS

J. Bobiński and J. Tejchman
Gdansk University of Technology, Gdansk, Poland

1. Introduction

The behaviour of concrete is very complex due to its heterogeneity, anisotropy, non-linearity and localisation of deformation in the form of cracks (failure mode I) and shear zones (failure mode II). An understanding of the mechanism of the formation of strain localisation is very important, since it acts as a precursor to the ultimate fracture and failure. Classical FE-simulations with material with softening are not able to model localisation properly. The obtained results suffer from the mesh sensitivity. The reason is that differential equations of motion change their type and the boundary value problem is ill-posed. To capture properly strain localisation within continuum mechanics, a characteristic length of the microstructure has to be included. It restores a well-posedness of a boundary value problem and enables one to obtain an objective numerical solution. In addition, a deterministic size effect can be captured.

The aim of the paper is to show results of realistic FE-simulations of concrete elements under mixed mode conditions (simultaneous occurrence of the failure mode I and II) [1]. To describe strain localization in concrete, three constitutive models defined within continuum mechanics were enriched by a characteristic length of micro-structure using a non-local theory. Alternatively, FE-simulations of strain localizaion were also performed using cohesive elements.

2. Constitutive models

First, an elasto-plastic model with isotropic hardening and softening was assumed. In a compression regime, a linear Drucker-Prager criterion with a non-associated flow rule was used. In a tensile regime, a Rankine criterion wit an associated flow rule was adopted. Second, a strain formulation of the damage model was used with a single scalar damage parameter. Different definitions of the equivalent strain measure were tested. Alternatively, a multi-fixed orthogonal smeared crack model was assumed. In this approach the crack was created, when the maximum tensile stress exceeded the material tensile strength. The orientation of the crack was described by its primary inclination at the formation time, i.e. the crack did not rotate during loading. To define softening of the material in a normal direction under tension, a Hordijk curve was assumed. After cracking, the shear modulus was reduced by a shear retention factor. All constitutive laws were enriched in a softening regime by a characteristic length of micro-structure by means of a non-local theory to capture properly strain localisation [2].

As an alternative, a discrete approach using cohesive elements was adopted [3]. These elements were defined at the interface between standard elements to nucleate cracks and propagate them following the deformation process. They governed the separation of crack flanks in accordance with irreversible cohesive laws. A simple class of mixed-mode cohesive laws was used accounting for tension-shear coupling obtained by introduction of an effective opening displacement (including both the normal opening displacement and sliding displacement).

3. Benchmark problems for concrete elements

Two benchmark problems with curved cracks under mixed mode conditions were carefully analysed. First, a double-edge notched concrete specimen under various different loading paths of combined shear and tension was analysed [4]. The dimensions of the largest specimen and

boundary conditions are presented in Fig.1. The loading was prescribed by rigid steel frames glued to concrete. In one of the loading paths [4], first a shear force P_s was applied until it reached a specified value, while the horizontal edges were free. At the second stage, the shear force remained constant and the vertical tensile displacement was prescribed. Two curved cracks with an inclination depending of the value of the shear force (for small value of P_s – almost horizontal, for large value of P_s – highly curved) were obtained.

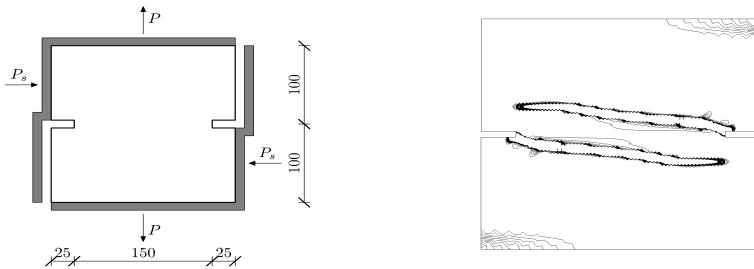


Fig. 1. Test [4]: geometry and FE-results within elasto-plasticity with non-local softening

Next, the single-edge notched (SEN) concrete beam under four-point shear loading (anti-symmetric loading) was analysed [5]. The dimensions and boundary conditions are shown in Fig. 2. A curved crack starting from the lower-right part of the notch towards a point to the right of the lower right support was obtained both in the experiment and FE-calculations.

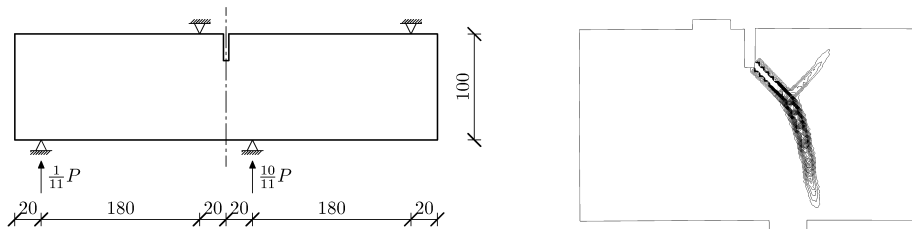


Fig. 2. Test [5]: geometry and FE-results within elasto-plasticity with non-local softening

4. References

- [1] J. Bobinski and J. Tejchman (2007). Simulation of concrete behaviour under mixed mode failure conditions with two different non-local models. *Proc. Int. Conf. on Computational Fracture and Failure of Materials and Structures CFRAC 2007*, Nantes, France, June 11-13.
- [2] T. Malecki, I. Marzec, J. Bobinski and J. Tejchman (2007). Effect of a characteristic length on crack spacing in a reinforced concrete bar under tension. *Mechanics Research Communications*, **34**, 5-6, 460-465.
- [3] M. Ortiz and J. Pandolfi. (1999). Finite deformation irreversible cohesive elements for three dimensional crack propagation analysis, *Int. J. Num. Meth. Eng.*, **44**, 1267–1282.
- [4] M.B. Nooru-Mohamed (1992). *Mixed mode fracture of concrete: an experimental approach*, PhD Thesis, Delft University of Technology.
- [5] H.E.J. Schlangen (1993). *Experimental and numerical analysis of fracture processes in concrete*, PhD Thesis, Delft University of Technology.

SLIGHT IN-PLANE PERTURBATION OF A SYSTEM OF TWO COPLANAR PARALLEL TENSILE SLIT-CRACKS

N. Pindra, V. Lazarus and J.B. Leblond

Institut Jean Le Rond d'Alembert, Université Pierre et Marie Curie (Paris VI), Tour 65-55, 4 place Jussieu, 75252 Paris Cedex 05, France

1. Introduction

A number of recent papers have studied the evolution in time of the shape of the front of planar cracks propagating in brittle materials with heterogeneous fracture properties. The ultimate goal of such studies is to get a better understanding of the path of propagation of cracks in composite materials and geological faults. Favier *et al.* [1] considered for instance the case of a tensile slit-crack propagating in fatigue in an infinite body with spatially varying Paris constant.

The aim of the present work is to lay the grounds for an extension of Favier *et al.*'s [1] work to a system of *two coplanar parallel slit-cracks*. The aim of this extension will be to study the evolution in time of the shape of the fronts of the cracks during their coalescence.

2. Presentation of the problem

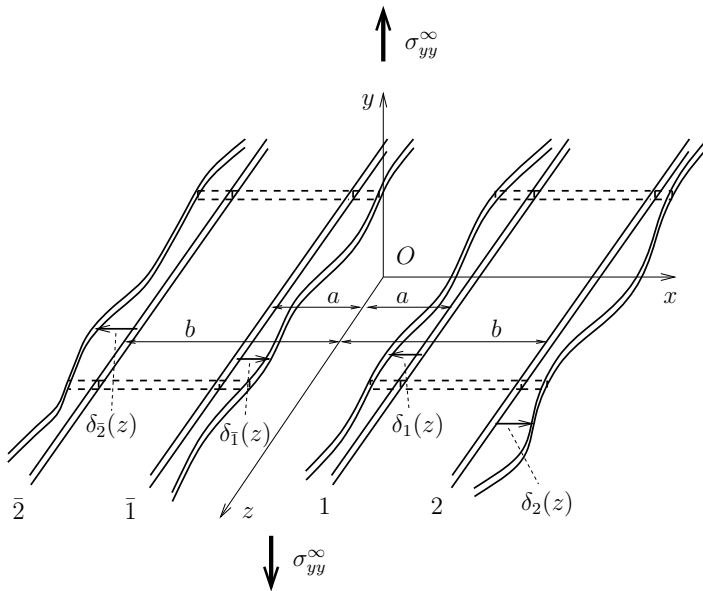


Figure 1. A system of two coplanar parallel slit-cracks with slightly perturbed crack fronts

The geometry of the problem is represented in Figure 1. The two slit-cracks lie in the plane Oxz . The unperturbed fronts 1 and 2 of the first crack are located at $x = a$ and $x = b$ respectively, and the fronts $\bar{1}$ and $\bar{2}$ of the symmetric crack at $x = -a$ and $x = -b$. All fronts are slightly perturbed within the plane Oxz ; the local perpendicular distance between the unperturbed and perturbed positions of

the front α ($\alpha = 1, 2, \bar{1}, \bar{2}$) is denoted $\delta_\alpha(z)$. The cracks are loaded through some uniform tensile stress σ_{yy}^∞ exerted at infinity.

The discussion of crack propagation of course demands detailed knowledge of the distribution of the (mode I) stress intensity factors $K_\alpha(z)$ along the perturbed crack fronts. The variations $\delta K_\alpha(z)$ of the $K_\alpha(z)$ are given, to first order in the perturbation, by the following formula (Rice [2]):

$$(1) \quad \begin{aligned} \delta K_\alpha(z) = & C_\alpha(z)\delta_\alpha(z) + PV \int_{-\infty}^{+\infty} f_\alpha \left(\frac{z-z'}{b} \right) K_\alpha(z') \frac{\delta_\alpha(z') - \delta_\alpha(z)}{(z-z')^2} dz' \\ & + \sum_{\beta \neq \alpha} \int_{-\infty}^{+\infty} g_{\alpha\beta} \left(\frac{z-z'}{b} \right) K_\beta(z') \frac{\delta_\beta(z')}{b^2} dz'. \end{aligned}$$

In this expression the functions C_α depend on both the unperturbed geometry and the loading, but the functions f_α and $g_{\alpha\beta}$, which are tied to Bueckner-Rice's fundamental weight functions, depend only on the unperturbed geometry, that is on the ratio $k \equiv a/b$.

Although the work of Rice [2] does establish the *existence* of the functions $f_\alpha, g_{\alpha\beta}$, it does not provide their *actual values* for the specific geometry considered, which are of course required for the discussion of crack propagation. The present paper is therefore devoted to the calculation of these functions.

3. Method of analysis

The method of calculation of the functions $f_\alpha, g_{\alpha\beta}$ is similar to that already used by Leblond *et al.* [3] in the case of a single slit-crack. Another formula of Rice [2] provides the variation of the functions $f_\alpha, g_{\alpha\beta}$ arising from an arbitrary perturbation of the fronts. This equation is applied to special perturbations preserving the shape and relative dimensions of the cracks while modifying their size and orientation. Since for such perturbations, the unperturbed and perturbed geometries are identical up to a change of scale combined with a rotation, the variations of the functions $f_\alpha, g_{\alpha\beta}$ are tied to these functions themselves. Rice's formula then yields a system of nonlinear integrodifferential equations on the functions $f_\alpha, g_{\alpha\beta}$, which are transformed *via* Fourier transform in the direction z of the crack fronts into nonlinear ordinary differential equations on the Fourier transforms $\bar{f}_\alpha, \bar{g}_{\alpha\beta}$. These differential equations are solved numerically once and for all for all values of the parameter k .

The case $a \rightarrow 0$ or equivalently $k \rightarrow 0$ is of special interest for the future study of the coalescence of the cracks. Taking this limit is a non-trivial task because it raises a problem of singular perturbation in Fourier's space, implying the presence of a boundary layer for small values of the wavenumber (large values of the wavelength). This problem is solved through matched asymptotic expansions. The output consists of a system of two nonlinear differential equations on the sole functions $\bar{f}_1, \bar{g}_{1\bar{1}}$, which is again solved numerically.

It is thus possible to obtain the functions $f_\alpha, g_{\alpha\beta}$, at least numerically, for both finite and infinitesimal values of the parameter k , and this opens the way to the study of the evolution in time of the shape of the fronts during the propagation of the cracks, including their coalescence.

4. References

- [1] E. Favier, V. Lazarus and J.B. Leblond (2006). Statistics of the deformation of the front of a tunnel-crack propagating in some inhomogeneous medium, *J. Mech. Phys. Solids*, **54**, 1449-1478.
- [2] J.R. Rice (1989). Weight function theory for three-dimensional elastic crack analysis, in: *Fracture Mechanics: Perspectives and Directions (Twentieth Symposium)*, ASTM STP 1020, Philadelphia, USA, pp. 29-57.
- [3] J.B. Leblond, S.E. Mouchrif, G. Perrin (1996). The tensile tunnel-crack with a slightly wavy front, *Int. J. Solids Structures*, **33**, 1995-2022.

STRENGTH ANALYSIS OF A SQUARE-FORM PERFORATED MICROFILTER

Ádám Kovács¹, Zsolt Vízváry¹ and András Kovács²

¹*Budapest University of Technology and Economics, Budapest, Hungary*

²*Hochschule Furtwangen University of Applied Sciences, Furtwangen, Germany*

1. Introduction

Perforated membranes are often used in various engineering applications. As an example, they can serve for microfiltering purposes in micro-electromechanical systems (MEMS). The investigated square-form membrane is very thin and is made from silicon-nitride (SiN), a brittle ceramic material showing very good material properties concerning load-capacity, high temperature and chemical stability. The membrane is produced from a wafer by wet etching technology. Its simplified mechanical model can be seen in Figure 1.

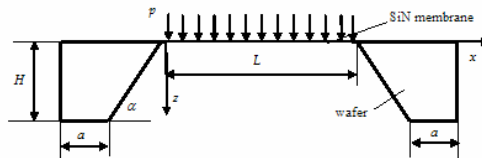


Figure 1: Simplified model of the structure

The performance of the filter highly depends on the perforation rate. In order to obtain better filtration the perforation rate should be as high as possible [1] which diminishes the strength, and consequently, the load capacity of the microfilter. Adequate methods should be used in the design to estimate the critical pressure. In microfiltration the side-length of plates are some order greater than the thickness, therefore classical thin plate theories can not be applied effectively to perform strength analysis. A challenging mechanical problem is the treatment of the very large deflection of the membrane due to even small pressure. Exact solution for this problem is not known.

Van Rijn et al. [2] worked out an analytical approximation for the maximum deflection and maximum load by combining a fixed-edge beam problem with a simply-supported thin plate. Unfortunately, their estimates do not fit well to the results of experiments. We show a simple method to predict the critical pressure semi-analytically from the normal stress at the middle point of the plate using stress coefficients obtained from finite element calculation.

2. Analysis

Because of the simple geometry analytical estimates based on the von Kármán plate theory using Ritz-method can be given for the deflection and the normal stress at the middle point of the fully closed membrane [3] as follows:

$$(1) \quad w_0 = 0.319L \sqrt{\left(\frac{p}{E}\right) \left(\frac{L}{h}\right)},$$

$$(2) \quad \sigma_0 = 0.319E \sqrt[3]{\left(\frac{p}{E}\right)^2 \left(\frac{L}{h}\right)^2}.$$

Although displacement could be determined relative good with Ritz' method, it is not suitable to predict the maximum normal stress, which is proportional to the critical pressure. Some thousands of linear thin shell elements were used to mesh the membrane and a nonlinear finite element procedure using total Lagrange description was performed to calculate the stress distribution in the membrane. It was proved that maximum normal stress is proportional to the normal stress in the middle point, so that

$$(3) \quad \sigma_{1\max} = C_{\sigma} K_{\sigma} \sigma_0,$$

where where C_{σ} and K_{σ} are constant factors. Material properties were measured by experiments.

3. Results and discussion

In order to show the applicability of our method a physically realized structure was analyzed and compared with experimental results (Fig. 2).

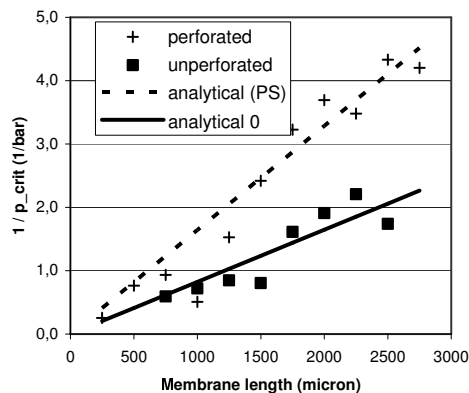


Figure 2 Measured and calculated load-capacity

The theoretical prediction of load capacity of perforated thin membranes requires numerical simulations in order to find appropriate mathematical relation between the maximum principal stress and the normal stress risen in the midpoint of the membrane. Once this relationship has been established, the load capacity can be estimated from measured or simulated mechanical response of an unperforated membrane.

4. Acknowledgment

This work has been financially supported by the National Scientific Research Fund (OTKA) under contract no. T49848, which is highly appreciated.

5. References

- [1] C.J.M. Van Rijn, *Nano and Micro Engineered Membrane Technology*, Elsevier, 2004.
- [2] C.J.M. Van Rijn, M. Van der Wekken, W. Nijdam & M. Elwenspook, "Deflection and maximum load of microfiltration membrane sieves made with silicon micromachining," *J. of Microelectromechanical Systems* 6, 48-54, (1997).
- [3] A.C. Ugural, *Stresses in Plates and Shells*, McGraw-Hill, Boston, 1999.

ADVANCED CONSTITUTIVE RELATION FOR NUMERICAL APPLICATIONS: MODELING OF STEELS IN A WIDE RANGE OF STRAIN RATES AND TEMPERATURES

A. Rusinek¹, J. A. Rodríguez-Martínez², J.R. Klepaczko¹

¹Laboratory of Physics and Mechanics of Materials, UMR CNRS 7554, University Paul Verlaine of Metz, Ile du Saucy, 57000 Metz, France

²Department of Continuum Mechanics and Structural Analysis, University Carlos III of Madrid, Avda. de la Universidad 30, 28911 Leganés, Madrid, Spain

Abstract

Among many constitutive relations implemented so far in a number of commercial computer codes, the most advanced are those that include strain hardening and also strain rate and temperature sensitivities of flow stress. Almost all of them are based on the concept of the Mechanical Equation of State (MES). One of such modern constitutive relations that have been proposed by Rusinek and Klepaczko (RK), [1], include an extended flexibility in an accurate approximation of materials behavior over wide range of plastic strain, strain rates and temperatures. The RK constitutive relation has only eight fundamental constants and the meaning of each constant is analyzed in detail in this paper. The main goal of this contribution is to demonstrate some recent applications of the RK constitutive relation in solving a wide variety of complex dynamic boundary value problems, for example perforation and many others, using the Finite Element (FE) method.

1. Introduction

Metals and alloys used in engineering fields show different mechanical behavior depending on the strain rate and temperature which they are subjected to. The implementation of advanced structural materials in the automotive, aeronautical, metalworking and other industries created the need to introduce more advanced constitutive relations for engineering applications. Thus, the constants required to define the material behavior must be easily identifiable, but at the same time the material response under complex stress states must be correctly predicted. For example, in the case of high strength steels as Weldox, DH-36 or TRIP, that are widely used in civil, naval and automotive industries, the thermal coupling in form of adiabatic heating cannot be neglected, especially at high strain rates and large deformations, Fig. 1. The adiabatic increase of temperature leads to thermal softening and plastic instabilities as precursors of failure.

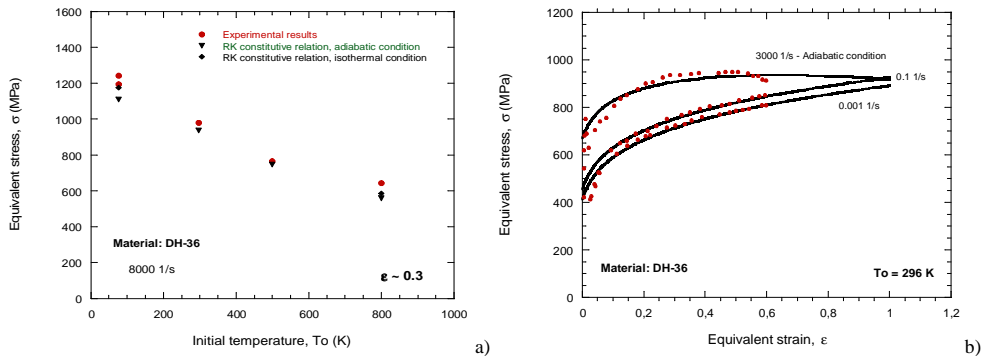


Fig. 1. Comparison between experimental results [2] and RK model; a- Temperature sensitivity, b- Strain rate sensitivity

It can be concluded that a sophisticated constitutive relation must cover large strains, $0 \leq \bar{\epsilon}_p \leq 1.0$, a wide range of strain rates, $10^{-4} \text{ s}^{-1} \leq \dot{\bar{\epsilon}}_p \leq 10^4 \text{ s}^{-1}$, and an adequate range of absolute temperatures, $200 \text{ K} \leq T \leq 0.5T_m$, where T_m is the melting temperature. However, to cover such ranges of the variables $(\bar{\epsilon}_p, \dot{\bar{\epsilon}}_p, T)$ using experimental techniques is not an easy task. Thus, many experimental results in the form $\bar{\sigma} = f(\bar{\epsilon}_p, \dot{\bar{\epsilon}}_p, T)$, where $\bar{\sigma}$ is the true stress in tension/compression, are frequently different for the same material. Therefore, the first step is evaluation of material constants which define adequate constitutive relation is an analysis of the mean experimental data.

2. Constitutive relation with strain rate and temperature dependence of strain hardening

An advantage to predict the material behavior when subjected to high temperature and high strain rate is an assumption of strain hardening exponent n in general form $n = n_0 f(\dot{\epsilon}_p, T)$, where f is the weigh function. The rate and temperature sensitive strain hardening was introduced into constitutive modeling for the first time in an open publication by Rusinek and Klepaczko in 2001, [1]. It was assumed in addition that the flow stress has two components called the internal and the effective stress. This concept due to Seeger is based on the theory of dislocations. The internal stress component accounts for the multiplication and storage of the immobile dislocations producing strain hardening. The total stress is therefore the sum of these two components, the internal stress σ_μ and the effective stress σ^* respectively

$$\sigma(\dot{\epsilon}_p, \dot{\epsilon}_p, T) = \frac{E(T)}{E_0} [\sigma_\mu(\dot{\epsilon}_p, \dot{\epsilon}_p, T) + \sigma^*(\dot{\epsilon}_p, T)] \quad (1)$$

Where $E(T)$ is the temperature-dependent Young's modulus, E_0 is the Young's modulus at $T = 0$ K. The effective stress component is related to the evolution of the mobile dislocation density leading to rate and temperature sensitivity of flow stress. Within the framework of the MES the RK constitutive relation, [1], is given by

$$\sigma = B(\dot{\epsilon}, T)(\epsilon_0 + \epsilon_p)^{n(\dot{\epsilon}, T)} + \sigma_0^* \left\langle 1 - D_1 \left(\frac{T}{T_m} \right) \log \left(\frac{\dot{\epsilon}_{\max}}{\dot{\epsilon}} \right) \right\rangle^{m^*} \quad (2)$$

Where $B(\dot{\epsilon}_p, T)$ is the modulus of plasticity, $n(\dot{\epsilon}_p, T)$ is the rate and temperature dependent strain hardening exponent, σ_0^* is the threshold of the effective stress at $T = 0$ K, D_1 and T_m are respectively the material constant and the melting temperature. Typical value for the strain rate upper limit is $\dot{\epsilon}_{\max} \approx 10^7 \text{ s}^{-1}$. Because the set of those constitutive equations is assumed to be applied also within a wide range of temperatures, assumed temperature values vary in the range $50\text{K} \leq T \leq T_m/2$. Two limits in Eq.(2) are imposed: if $\langle \cdot \rangle < 0$ then $\langle \cdot \rangle = 0$, also if $n < 0$ then $n = 0$. The two stress components are corrected for the temperature-dependent rigidity of the crystalline lattice via the temperature variations of Young's modulus $E(T)$ as reported originally by Klepaczko, [3]. Moreover, a stress correction for the adiabatic increase of temperature is described using the equation of energy balance. Theory of J_2 plasticity for isotropic behavior combined with the implicit integration scheme for finite element simulation is the base for a wide range of applications, as shown in Fig.2. An original implicit algorithm developed by Zaera and Fernández-Sáez, and reported in [4], is used to solve incrementally the set of RK constitutive equations defined above. With this algorithm many dynamic problems can be simulated by finite element codes. The material constants of the RK constitutive relation are identified so far for more than twenty materials, mostly steels used in the aeronautical and automotive industries.

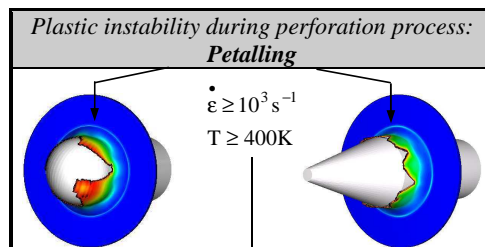


Fig. 2. Numerical simulation of perforation process using RK model to describe behavior of DH-36 steel

References

- [1] Rusinek A., Klepaczko J. R. Shear testing of sheet steel at wide range of strain rates and a constitutive relation with strain-rate and temperature dependence of the flow stress, *Int. J. Plasticity*, 17 (2001), 87.
- [2] Nemat-Nasser S, Guo W.G. Thermomechanical response of DH-36 structural steel over a wide range of strain rates and temperatures. *Mech. Mat.* 35 (2003) 1023–1047
- [3] Klepaczko J. R. A general approach to rate sensitivity and constitutive modeling of FCC and BCC metals, in: *Impact – Effects of Fast Transient Loading*, A.A. Balkema, Rotterdam (1988), 3.
- [4] Zaera R., Fernández-Sáez J. An implicit consistent algorithm for the integration of thermo-visco-plastic constitutive equations in adiabatic conditions and finite deformations, *Int. J. Solids and Structures*, 43, (2006), 1594.

DAMAGE ACCUMULATION MODEL FOR LOW CYCLE FATIGUE UNDER MULTIAXIAL SEQUENTIAL LOADING

S. Shukayev, M. Gladskiy, K. Panasovskyi and A. Movaggar

National Technical University of Ukraine "Kyiv Polytechnic Institute", Kyiv, Ukraine

1. Introduction

Machine and constructions elements often undergo multiaxial sequential cycle loading. Though fatigue life of materials has been studied for a long time and enough of experimental data has been accumulated, problem of multiaxial irregular loading low-cycle fatigue is still actual. Many attempts to describe fatigue damage process were made, which resulted in many developed models of damage accumulation. The most wide-spread is the conception of linear damage accumulation, offered by Miner. This approach is easy to use but it does not give adequate estimation of life in many cases. It is studied influence of sequential loading effects on the titanium alloys BT9 and BT1-0 fatigue damage and under tension-compression, torsion and 90° out-of-phase non-proportional loading.

2. Extend

The test results on low-cycle fatigue of titanium alloy BT9 and technically pure titan BT1-0 under biaxial loading are given. It is also determined that damage accumulation process for fully reversed pure torsional fatigue experiment is described in the best way by linear damage accumulation rule and has a nonlinear character for tension - compression. The paper shows that a deviation from linear damage accumulation law for tension - compression of both materials under «low - high» sequence loading is bigger in comparison with «high - low» sequence loading. It is obtained that a damage accumulation under «non-proportional - proportional» sequence loading is more intensive in comparison with «proportional – non-proportional» sequence loading.

Earlier in the paper [1] the criterion for multiaxial regular cycle loading was proposed. This criterion is based on the non-proportional strain parameter [2]. Analyzing calculation data one can see that during the application of the criterion [1] and the linear damage accumulation hypothesis the best correlation of the predicted and test data is obtained for alternating torsion. As a result, one can come to a conclusion about the linearity of damage accumulation process for a given loading type. The combined application of this criterion and damage curve approach by Manson and Halford [3] showed the high level of predicted and test data correlation for all the loading programmes except the alternating torsion. So the following modification of the Manson and Halford approach is proposed:

$$D_i = (n_i/N_i)^{\beta(\omega)},$$

where $\beta(\omega) = \left(\frac{N}{N_r}\right)^\alpha + \frac{2\omega}{\pi} \left[1 - \left(\frac{N}{N_r}\right)^\alpha\right]$; $\omega = \arctg\left(\frac{\gamma_a \cdot \varepsilon_{fs}}{\varepsilon_a \cdot \gamma_{fs}}\right)$ – strain path orientation angle, which

determines the dominating type of the strain state.

3. Conclusion

Suggested method for metal alloys fatigue life estimation under irregular multiaxial low-cycle loading is based on damage curve approach.

Application boundaries of the proposed method for different deformation path have been analyzed. It is shown that the suggested method can be successfully used for fatigue life estimation of materials with different sensitivity to non-proportionality loading.

4. References

- [1] Shukayev S., Zakhovayko O., Gladnyi M., Panasovsky K. *Estimation of low-cycle fatigue criteria under multiaxial loading* // Int. J. Reliability and life of machines and structures. – 2004, vol.2, pp. 127-135.
- [2] Itoh T., Sakane M., Ohnami M., Kida S., Sosie D. F. *Dislocation Structure and Non-Proportional Hardening of Type 304 Stainless Steel* // In: Proceeding of the 5th International Conference Biaxial-Multiaxial Fatigue and Fracture, Cracow. – 1997, vol. 1, pp. 189-206.
- [3] Manson S.S., Halford G.R. *Practical implementation of the double linear damage rule and damage curve approach for treating cumulative fatigue damage* // Int. J. of Fracture. – 1981, vol. 17, pp. 169-192.

SIMULATIONS OF CRACK GROWTH IN PIEZOELECTRIC STRUCTURES WITH MODERN, AUTOMATIC AND EFFICIENT FINITE ELEMENT SOFTWARE

Ł. Jański, M. Kuna and M. Scherzer

Institute of Mechanics and Fluid Dynamics, TU Bergakademie Freiberg, Germany

1. Motivation

Sensors and actuators are nowadays standard components of many modern adaptive mechanical systems. The role of these components implies frequently the application of piezoelectric and ferroelectric materials by their construction. The implementation of these sensors and actuators into mechanical systems leads to common problems associated with mechanical loading e.g.: providing of a satisfactory strength, durability and fracture resistance. Electromechanical sensors and actuators, however, are loaded not only mechanically but also electrically. This means also the case when the external force has a purely mechanical character and their internal response is electromechanical. Such behaviour can be observed due to the electromechanical coupling property of piezoelectric and ferroelectric materials. To assure a satisfactory fracture resistance of sensors and actuators, the knowledge of electrical as well as mechanical fields in the vicinity of cracks is necessary. This information makes the evaluation of the cracks behaviour under electromechanical static or cyclic loads possible. Electrical and mechanical fields in the vicinity of cracks can be obtained with classical solution strategy of complex functions theory. This strategy, however, can be in general used only for infinite domains. On the other hand, real engineering tasks always refer to finite domains with special electromechanical boundary conditions. The finite element method is usually used to obtain electrical and mechanical fields in the vicinity of cracks for real problems. Various variants of this method have already been tested for stationary cracks in homogeneous piezoelectric structures [1]. There are still many open questions concerning fatigue crack growth under electromechanical alternating loads. The present work should give at least some answers to these questions. To reach this aim, a special finite element tool is developed for modelling of a crack growth in piezoelectric structures and simulations of the crack growth are realised. The structure of this tool, shortly described in the following part of this abstract, is crucial for the effectivity of the simulations.

2. FE-program structure

The developed finite element tool is composed of four modules. The piezoelectric boundary value problem is solved with the finite element method in an adaptive manner in the main module. The finite element discretisation of the piezoelectric boundary value problem leads to an indefinite formulation. The Bramble-Pasciak preconditioner [2] is used to avoid complications arising from this fact. The preconditioned linear system of equations is solved with the conjugate gradient method. Because high gradients of the stress and the dielectric displacement associated with a crack tip are expected in the solution, an automatic, adaptive algorithm for the finite element mesh density optimisation is implemented. Information associated with the edge hierarchy established in the adaptive process is used for the construction of a very efficient hierarchic preconditioner.

Fracture parameters, e.g. mechanical and electrical intensity factors, are calculated in the second module. The implementation necessity of the crack tip finite elements in each adaptive step is avoided with the application of the interaction integral technique [3]. The asymptotic solution [4] is chosen as the auxiliary field in the interaction integral technique and also utilised by the construction of the Irwin's matrix [5].

Fracture criteria are evaluated and the decision undertaken whether the crack propagates or not in the third module. If the decision is positive, the parameters such as the length and the orientation of an incremental crack advance are calculated. At this juncture, classical fracture criteria of the linear piezoelectric fracture mechanics e.g. based on the circumferential stress or the mechanical energy release rate can be used in the first approximation.

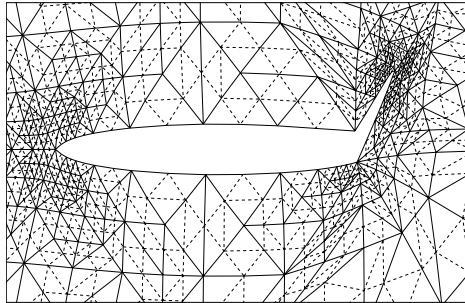


Figure 1. Finite element mesh around a crack with a kink.

The crack propagation is automatically realised in the finite element mesh in the fourth module. On one hand the length and the orientation of the incremental crack advance obtained in the former module are physically determined, on the other the crack propagation can be only realised along finite element edges which depend strictly on a meshing strategy. Consequently, new finite element nodes and edges must be constructed to let the crack grow. In Figure 1, an example of a finite element mesh around a crack with a kink which automatically propagated from the crack is presented.

3. Simulation results

Mechanical and electrical intensity factors are calculated for configurations, e.g. kinked crack, Griffith's crack, for which analytical solutions are known and appropriate factors compared to prove the efficiency of the first and the second module. Kinks are automatically generated for various orientations to test the fourth module. Crack propagation simulations are carried to check the third module and the whole finite element software. The results are analysed and discussed.

4. References

- [1] M. Kuna (2006). Finite element analyses of cracks in piezoelectric structures: a survey, *Archive of Applied Mechanics*, **76**, 725-745.
- [2] A. Meyer and T. Steidten (2001). Improvements and Experiments on the Bramble-Pasciak Type CG for Mixed Problems in Elasticity, *Preprint-Reihe des Chemnitzer Sonderforschungsbereiches 393*, **Nr.:01-13**.
- [3] M. Stern and E.B. Becker (1976). A contour integral computation of mixed-mode stress intensity factors, *International Journal of Fracture*, **12**, 359-367.
- [4] M. Scherzer and M. Kuna (2004). Combined analytical and numerical solution of 2D interface corner configurations between dissimilar piezoelectric materials, *International Journal of Fracture*, **127**, 61-99.
- [5] L. Janski and P. Steinhorst (2007). Modellierung von Risswachstum in piezoelektrischen Materialien mittels moderner adaptiver FEM-Lösungsstrategien, *DVM-Bericht*, **239**, 153-162.

THERMAL STRESSES AROUND AN INTERFACE RIGID CIRCULAR INCLUSION IN A BIMATERIAL PERIODICALLY LAYERED SPACE

A. Kaczyński¹, B. Monastyrskyy²

¹*Warsaw University of Technology, Warsaw, Poland*

²*Pidstryhach Institute for Applied Problems of Mechanics and Mathematics, Lviv, Ukraine*

It is the intention of this paper to calculate the distribution of thermal stresses in a periodic two-layer space containing an interface absolutely rigid circular inclusion under a vertically uniform heat flow (see Fig. 1). The corresponding problem involving thermal stresses induced by an interface crack was analyzed in [1].

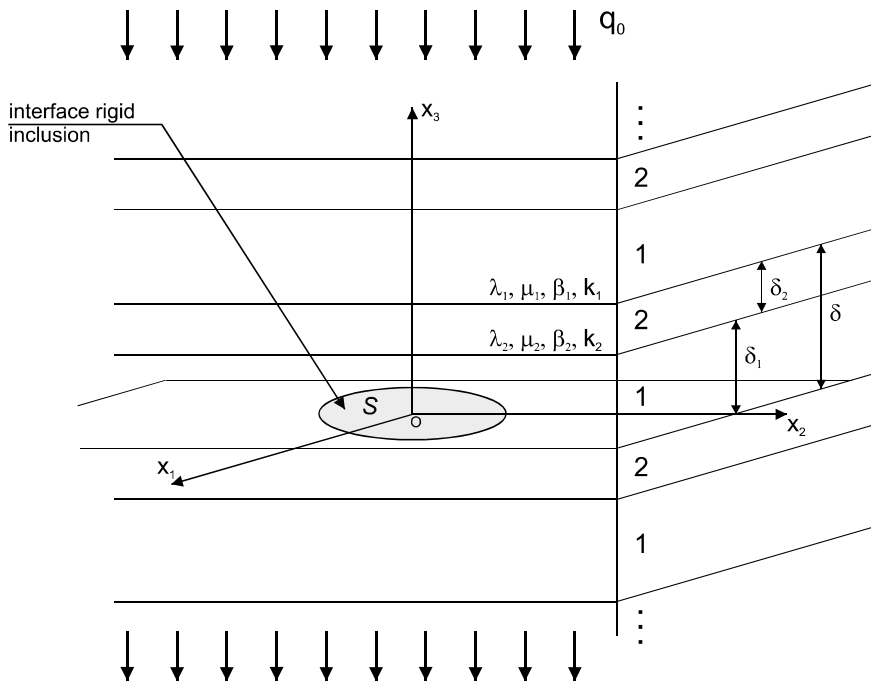


Fig. 1. An interface rigid sheet-like inclusion in a two-layered periodic space with heat flow.

An approximate analysis is carried out within the framework of linear stationary thermoelasticity with microlocal parameters [2]. The advantage of this approach is a relatively simple form of the governing equations appearing similar to the thermoelasticity for transverse isotropy, which makes it possible to construct the appropriate potentials and establish an analogy between the thermal crack problems and their mechanical counterparts.

A two-staged method for obtaining the solution is used. The steady-state temperature field is first determined taking into account the thermal resistance of the inclusion. Next, the associated induced thermal stresses perturbed problem is solved by using the potential method, developed in [3], and by reducing to one in the classical potential theory. A complete solution in elementary

functions is given due to the results achieved in [4]. Exact expressions for the thermoelastic field at the plane of inclusion surface are explicitly derived. It is observed [5] that the thermal stress fields near the inclusion front at the inclusion surfaces have the typical (nonoscillating) inverse square root singularities. From the standpoint of classical fracture mechanics the results obtained suggest that failure of the material surrounding the inclusion border is described by two mechanisms: Mode II (shear) and separation of the material from the inclusion.

References

- [1] A. Kaczyński and S.J. Matysiak (2003). On the three-dimensional problem of an interface crack under uniform heat flow in a bimaterial periodically-layered space, *Int. J. Fract.*, **123**, 127-138.
- [2] Cz. Woźniak (1987). A nonstandard method of modelling of thermoelastic periodic composites, *Int. J. Eng. Sci.*, **25**, 483-499.
- [3] A. Kaczyński (1994). Three-dimensional thermoelastic problems of interface cracks in periodic two-layered composites, *Eng. Fract. Mech.*, **48**, 783-800.
- [4] V. I. Fabrikant (1991). *Mixed boundary value problems of potential theory and their applications in engineering*, Dordrecht, Kluwer Academic Publishers.
- [5] A. Kaczyński and B. Monastyrskyy (2008). Thermal stresses in a periodic two-layer space with an interface rigid inclusion under uniform heat flow, *Acta Mech.* (in print)

FE-ANALYSIS OF THE BEHAVIOUR OF CONCRETE ELEMENTS WITH COUPLED ELASTO-PLASTIC-DAMAGE MODELS WITH NON-LOCAL SOFTENING

I. Marzec and J. Tejchman

*Faculty of Civil and Environmental Engineering,
Gdańsk University of Technology, Gdańsk, Poland*

1. General

The analysis of concrete elements is complex due to their stiffness degradation during cyclic loading caused by strain localization in the form of cracks and shear zones. The determination of the width and spacing of strain localization is crucial to evaluate the material strength at peak and in the post-peak regime.

The aim of the present paper is to show the capability of two different coupled elasto-plastic-damage continuum models to describe strain localization and stiffness degradation in concrete elements subject cyclic loading during bending, uniaxial compression and extension. First, a coupled elasto-plastic-damage model based on the idea by Pamin and de Borst [1] was used [2]. Second, a coupled elasto-plastic-damage model using the formulation proposed by Carol et al. [3] and Hansen and Willam [4] was taken into account.

To describe properly strain localization, to preserve the well-posedness of the boundary value problem, to obtain FE-results free from spurious discretization sensitivity and to capture a deterministic size effect, a integral-type non-local theory was used as a regularization technique in a softening regime [5]. It was achieved by weighted spatial averaging over a neighborhood of each material point of a suitable state variable. Thus, the stress at a certain material point depended not only on the state variable at that point but also on the distribution of the state variable in a finite neighborhood of the point considered.

2. Coupled models for concrete

The first coupled model [1], [2] combines non-local damage with hardening plasticity and assumes that total strains are equal to strains in a undamaged skeleton. Plastic flow can occur only in a undamaged specimen, thus an elasto-plastic model is defined in terms of effective stresses. As a consequence, the damage degradation does not affect plasticity.

In the second coupled model [3], [4], plasticity and damage are connected by two loading functions describing the behaviour of concrete in compression and tension. The model assumes that the damage approach simulates the behaviour of concrete under tension while plasticity describes the concrete behaviour under compression. According to this assumption, a failure envelope is created by combining a Drucker Prager formulation in compression with a damage formulation based on a conjugate force tensor and pseudo-log damage rate in tension. Both models require only few material parameters. Except of the Young modulus and Poison's ratio, the following parameters need to be defined: initial value of strain when damage starts, two parameters describing the damage growth and ratio between the compression and tensile strength to define the equivalent strain measure (when using a modified von Mises definition) in the first model, and the internal friction angle, dilatancy angle, softening function in compression and fracture energy with its elastic part to describe the resistant function in tension in the second model.

3. FE-simulations

The mesh-independent FE-results for concrete beams under cyclic loading were compared with corresponding laboratory tests [6], [7]. They show that the both models were able to proper describe

the behaviour of concrete under cyclic loading. Fig.1 shows a comparison with experiments on concrete beams under bending subjected to cyclic loading [6] using the first coupled elasto-plastic–damage model. The numerical result fits the experimental data quite well.

However, both models have also some disadvantages. In the first model is hard to properly define all parameters to control both plasticity and damage at the same time. In addition, there is no clear distinction between elastic, plastic and damage strains. In turn, the second model is not able to reproduce plastic strains in compression during cycling loading. So it implies a necessity to improve the models to couple damage and plasticity more realistically in one formulation.

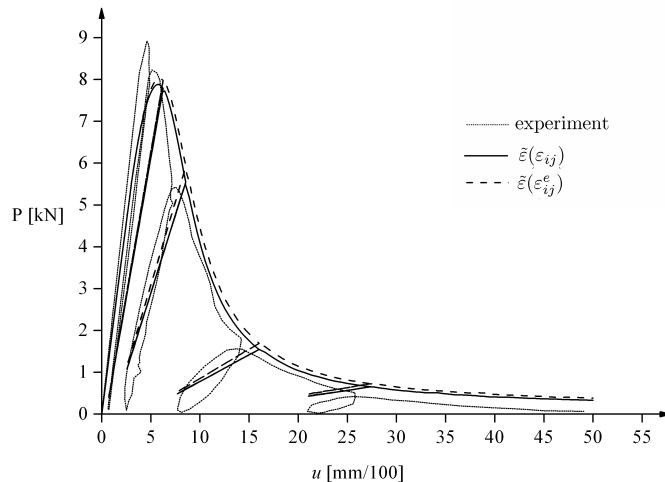


Fig. 1: Calculated load-displacement curves for a coupled elasto-plastic-damage model with non local softening during cycling loading compared with experimental data [6]

4. References

- [1] J. Pamin and R. de Borst (1999). Stiffness degradation in gradient-dependent coupled damage-plasticity, *Arch. Mech.*, **51**, 3-4, 419-446.
- [2] J. Bobinski and J. Tejchman (2006). Modeling of strain localization in quasi-brittle materials with coupled elasto-plastic-damage model, *Journal of Theoretical and Applied Mechanics*, **44**, 4, 767-782.
- [3] I. Carol, E. Rizzi and K. Willam (2001). On the formulation of anisotropic elastic degradation, *Int. J. of Solids and Structures*, **38**, 491-518.
- [4] E. Hansen and K. Willam (2001). A two-surface anisotropic damage-plasticity model for plane concrete, *Proc. Int. Conf. Fracture Mechanics of Concrete Materials (R. de Borst, ed.)*, Paris, Balkema, 549-556.
- [5] T. Majewski, J. Bobinski and J. Tejchman (2008). FE-analysis of failure behaviour of reinforced concrete columns under eccentric compression, *Engineering Structures*, doi:10.1016/j.engstruct.2007.03.024.
- [6] D.A. Hordijk (1991). Local approach to fatigue of concrete, *PhD Thesis*, Delft University of Technology.
- [7] P.C. Perdikaris and A. Romeo (1995). Size effect on fracture energy of concrete and stability issues in three-point bending fracture toughness testing, *ACI Mater. J.* **92**, 5, 483-496.

IDENTIFICATION AND VALIDATION OF MATERIAL PARAMETERS FOR ISOTROPIC DAMAGE MODEL IN VISCOPLASTIC FLOW CONDITIONS

P. Kłosowski, Ł. Pyrzowski

Gdansk University of Technology, Gdansk, Poland

1. General

Identification of damage material parameters is one of the most important and most contentious aspects of the continuum damage mechanics. The incorrect identification may leads to wrong results, even if a good model is applied.

In this communication, the Lemaitre's isotropic damage model [1], regarding the concept of the damage variable proposed by Kachanov in 1958 [2], is concerned. In the literature different methods of damage material parameters identification for assumed model are applied. The identifications are based on different foundations and use results of different experiments: the uniaxial tensile tests or the uniaxial reversed cyclic tests. In their approaches authors calibrate both S and s damage coefficients or assume s calibrating only S . Each of them is applied for different material type, and very seldom researchers tried to conduct these identifications for one material and compare the results with experiment to give the answer which of them is the most suitable.

The authors of this paper have applied all presented identification methods for calibration the damage coefficients for the Al2017 aluminum. Then the results have been compared with the real experiment by numerical modeling, using the elasto-viscoplastic Chaboche [3] model with damage.

2. Damage model formulation

The isotropic damage is expressed by the scalar parameter D , which is the surface density of the discontinuities in the material. Its evolution, according to Lemaitre [1], is defined by equation:

$$(1) \quad \dot{D} = \left(-\frac{Y}{S} \right)^s \cdot \dot{p},$$

where s and S are the damage material parameters, \dot{p} is the accumulated plastic strain rate and Y is the damage strain energy release rate, given by:

$$(2) \quad -Y = \frac{\sigma_{eq}^2}{2(1-D)^2 E} \left[\frac{2}{3}(1+\nu) + 3(1-2\nu) \left(\frac{\sigma_H}{\sigma_{eq}} \right)^2 \right],$$

where ν is the Poisson's ratio, E is the Young's modulus of undamaged material, σ_{eq} is the Huber-Misses equivalent stress and σ_H is the hydrostatic stress.

3. Methods of the material parameters identification

The first presented method of the material parameters identification for isotropic damage is proposed by Mashayekhi and Ziaei-Rad [4]. This identification is conducted on the basis of the uniaxial reversed cyclic test and based on the foundation that the damage exponent s is arbitrary assumed. When the damage exponent s is known at the beginning, the damage strength parameter S can be calibrate directly from the equation:

$$(3) \quad S = \frac{\sigma^2}{2E(1-D)^2 dD/d\varepsilon_{pl}},$$

where σ is the stress and ε_{pl} is the inelastic strain, both in uniaxial loading conditions.

The second method is proposed by Daudonnet [5]. It is conducted on the basis of the same experimental tests, but does not introduce the material parameter assumptions, both s and S parameters are calibrated (the last square method approximation):

$$(4) \quad \frac{dD}{d\varepsilon_{pl}} = \left(\frac{\sigma^2}{2E(1-D)^2 S} \right)^s.$$

The last method is proposed by Ambroziak [6]. This identification does not need to conduct the reversed cyclic tests, it is based on the simple uniaxial tensile test with the constant strain rate but has two disadvantages. The first is, similar to Mashayekhi and Ziaei-Rad approach: the assumption of the damage exponent s at the beginning, the second is the assumption that rupture of the specimen is specified while the damage parameter $D = 1$ (performing the tensile test instead of the reversed cyclic does not allow to identify D). The damage strength parameter S , in this method, is calibrated from the equation:

$$(5) \quad S = \frac{(2 \cdot s + 1)^{1/s}}{2 \cdot E} \cdot \left(\int_0^{t_r} (\sigma^{2s} \cdot \dot{p}) dt \right)^{1/s}.$$

4. Identification and validation of material parameters for Al2017 aluminum

The best method to certify, which identification is the most suitable, is to conduct all of them for one material type and compare the results with the real experiment. The authors decided to choose Al2017 aluminum, the selected results are presented in Table 1. For the methods comparison, the numerical simulation of the uniaxial tensile tests with the constant strain rate, has been applied. The detail results and final conclusions will be presented during the conference.

Method	Exponent s [-]	Strength parameter S [MPa]
Mashayekhi and Ziaei-Rad	$s = -1$ (assumed)	$S = 2,67$
Daudonnet	$s = -0,88$	$S = 2,92$
Ambroziak	$s = 1$ (assumed)	$S = 0,23$

Table 1. Results of the damage material parameters identification

6. References

- [1] J. Lemaitre (1985). A continuous damage mechanics, *J. Eng. Mater. Technol.*, **107**, 83-89.
- [2] L.M. Kachanov (1958). Time of rupture process under creep conditions, *Otd. Tech. Nauk.*, **8**, TVZ Akad. Nauk. S.S.R., 26-31.
- [3] J. L. Chaboche and J. Lemaitre (1990). *Mechanics of solid materials*, Cambridge University Press, Cambridge, 253-345.
- [4] M. Mashayekhi and S. Ziaei-Rad (2006). Identification and validation of a ductile damage model for A533 steel, *J. Mater. Proces. Techn.*, **177**, 291-295.
- [5] B. Daudonnet (2006). *Etude numerique de la rupture d'elements de structures constituant des reservoirs sous chargement dynamique*, PhD Thesis, Universite d'Orleans, Bourges, 60-63.
- [6] A. Ambroziak (2007). Identification and validation of damage parameters for elasto-viscoplastic Chaboche model, *Engng. Trans.*, **55**, 1-28.

EXTENSION OF ISOTROPIC MULLINS MODELS TO ANISOTROPIC STRESS-SOFTENING MODELS

M.H.B.M. Shariff

Khalifa University of Science, Technology and Research

1. Abstract

The Mullins effect in rubber-like materials is inherently anisotropic. For example, in Pawel-ski [1] homogeneous plain strain compression experiment, after loading from a virgin state and un-loading, the block is rotated by 90 degrees and compressed; it was found that the non-virgin material behaves almost like a virgin one, which indicates that stress softening in the first direction has hardly any influence on stress softening in the direction orthogonal to the first. This anisotropic behaviour can also be found in other experiments [2] [3]. However, most models developed in the past, for Mullins effect, are isotropic. Nevertheless, recently, Shariff [4] developed a constitutive equation that char-acterizes anisotropic stress softening. Shariff's [4] theory compares well with several anisotropic experimental data and is consistent with expected behaviour. In this paper, based on Shariff's [4] theory, we proposed a model that can easily extend some well known isotropic models [5] [6] to describe incompressible anisotropic behaviour of Mullins phenomenon; hence indicating the gener-ality of the proposed model. The quasi-static constitutive equation is purely phenomenological and does not take account the underlying physical structure of the material; hence it can be applied to any incompressible material exhibiting anisotropic stress softening induced by strain. We treat the virgin undeformed material as isotropic and are not concerned with hysteresis, residual strain and, thermal and viscoelastic effects.

We use a principal axes technique to facilitate our anisotropic modelling. This type of technique is also used by Shariff [7] to derive a novel constitutive equation for an incompressible transversely isotropic hyperelastic solid. In the proposed model, a set of damage parameters which depend on the history of the principal-direction line elements is proposed. Together with this, we introduce a general concept of damage function to facilitate the analysis of anisotropic stress softening. The ef-fect of shearing on stress softening materials is described via shear-history parameters; they are the maximum and minimum values of the cosine of the angle between two principal-direction line ele-ments throughout the history of the deformation. The damage and shear-history parameters are intro-duced into the constitutive equation via symmetric, second order, damage and shear-history structural tensors, respectively. The damage tensor is positive definite. The "free" energy is expressed as a function of principal stretches and invariants of the dyadic products of the principal directions of the right stretch tensor and the two structural tensors. In this communication, we only consider a class of free energy functions that is a subset of a wider class of free energy functions proposed in this paper. Energy dissipation is shown via the Clausius-Duhem inequality.

The generality of the proposed damage function allows us to easily extend some existing well known isotropic models to model anisotropic behaviour of Mullins effect. In order to demonstrate the capabilities of the proposed theory, results are given for several types of homogeneous deforma-tions. For some of these deformations, we show that the non-virgin stress free configurations have certain types of anisotropy which are consistent with previous conjectures [8]. We also show that our theoretical results compare well, qualitatively and quantitatively, with published experimental data.

2. References

- [1] H. Pawelski (2001). Softening behaviour of elastomeric media after loading in changing directions. In: D. Besdo, R.H. Schuster & J. Ihlemann (eds), *Constitutive Models for Rubber II*. Lisse: A.A. Balkema, 27-36.
- [2] A.H. Muhr, J. Gough and I.H. Gregory (1999). Experimental determination of model for liquid silicone rubber. In: A. Muhr & A. Dorfmann (eds), *Constitutive Models for Rubber*. Rotterdam: A.A. Balkema, 181-187.
- [3] J. Gough (2000). Stress-strain behaviour of rubber, *PhD Thesis Queen Mary and Westfield College, University of London* 255pp.
- [4] M.H.B.M. Shariff (2006). An anisotropic model of the Mullins effect, *J. of Engng. Maths.*, **56**, 415-435.
- [5] R.W. Ogden and D.G. Roxburgh (1999). A pseudo-elastic model for the Mullins effect in filled rubber, *Proc. R. Soc. Lond.*, **A 455**, 2861-2877.
- [6] M.F. Beatty and S. Krishnaswamy (2000). A theory of stress-softening in incompressible isotropic materials, *J. Mech. Phys. Solids*, **48**, 1931-1965.
- [7] M.H.B.M. Shariff (2008). Nonlinear transversely isotropic elastic solids: an alternative representation, *Q. J. Mech. Appl. Math.*, DOI:10.1093/qjmam/hbm028, 1-21.
- [8] C.O. Horgan, R.W. Ogden and G.Saccomandi (2004). A theory of stress softening of elastomers based on finite chain extensibility, *Proc. R. Soc. London*, **A 460**, 1737-1754.

COMPUTATIONS OF EFFECTIVE ELASTIC PROPERTIES OF SOLIDS WITH MICROCRACKS USING THE BOUNDARY ELEMENT METHOD

P. Fedelinski

*Department of Strength of Materials and Computational Mechanics,
Silesian University of Technology, Gliwice, Poland*

1. Introduction

One of the most important aims of micromechanical modeling is the determination of effective material properties of bodies containing microcracks [1, 2]. There are several theoretical approaches to analyze these problems. In the *non-interacting method*, it is assumed that the microcracks are isolated in the initial undamaged material. In the *self-consistent method*, the microcracks are embedded in the effective medium. The influence of interactions is simulated by reducing stiffness of the surrounding material. In the *differential method*, similar to the self-consistent method, one isolated crack is considered in the effective material. The interactions are taken into account through an incremental increase of crack densities and the effective modulus of the matrix is recalculated at each iteration. The interactions cause softening and effective moduli are lower than predicted by the non-interacting method. These theoretical methods usually give accurate results for low crack densities.

More general cases can be considered using numerical methods. Renaud et. al. [3] applied the indirect boundary element method (BEM) – the displacement discontinuity method to compute effective moduli of brittle materials weakened by microcracks. Structures with microcracks of different size, location and orientation were investigated. The structures were subjected to tensile and compressive loadings. In the last case an iterative algorithm was used to analyze cracks in contact with friction. The numerical results were compared with theoretical approximations. For microcracks in finite bodies good agreement with the differential method was obtained. Contact with friction decreases the effect of randomly distributed cracks on effective compliance. Huang et. al. [4] used the boundary element method and the unit cell method to calculate effective properties of solids with randomly distributed and parallel microcracks. In the BEM the modified fundamental solutions were used. The method does not require integration along the crack surfaces. Traction free cracks were considered. The results agree well with the differential method for low crack densities and with the generalized self-consistent method for high crack densities. Zhan et. al. [5] applied a series expansions of complex potentials and the superposition technique. The governing equations were solved numerically using the boundary collocation procedure. The effective Young moduli were calculated for randomly distributed and parallel cracks. The results were compared with various micromechanical models and experimental results. For randomly oriented cracks the results agree with differential method and for parallel cracks the moduli are below non-interacting solution and above the differential results.

The effective moduli were also determined experimentally by Carvalho and Labuz [6]. Artificially cracked aluminum plates with randomly distributed slots were subjected to tension. The experimental results agree well with the non-interacting approximation even for high density of cracks, where interactions are expected to occur. The authors found that the number of slots should be about 20 to guarantee the randomness of distribution.

Structures with high density of cracks have small Young moduli, however there is no direct quantitative correlation between the stiffness and damage [1]. Local positions of microcracks have strong influence on stress intensity factors while the effective modulus, which is a volume average quantity, is insensitive to such distributions.

2. The boundary element method for static and dynamic crack problems

In the present work microcracks in two-dimensional, linear-elastic, isotropic and homogenous solids will be analyzed using the dual boundary element method (DBEM) [7]. In this approach only boundaries of the body and crack surfaces are divided into boundary elements. The variations of boundary coordinates, displacements and tractions are interpolated using shape functions and nodal values. In the DBEM the relations between boundary displacements and tractions are expressed by the displacement and traction boundary integral equations. The displacement equation is applied for boundary nodes and both equations for nodes on crack surfaces. For dynamic problems, additionally the time of analysis is divided into time steps [8]. In this method boundary displacements and tractions are computed directly. For crack problems stress intensity factors (SIF) can be calculated very accurately using crack opening displacements or path independent integrals.

3. Numerical computations of effective elastic properties of solids with microcracks

The DBEM is very efficient method for analysis of effective properties of solids with multiple microcracks. It is very easy to generate solids with randomly distributed microcracks because in this approach only crack surfaces are discretized.

The method will be used to compute effective Young modulus and Poisson ratio for randomly distributed and parallel microcracks in bodies subjected to static loadings. The influence of crack density on effective properties of cracked materials will be investigated. The numerical results will be compared with available theoretical and experimental results. Additionally, stress intensity factors will be analyzed for various structures. The influence of microcracks densities on velocities of waves will be investigated for cracked bodies subjected to dynamic loadings.

4. Conclusions

Computations of effective material properties of damaged structures require analysis of many structures having different configurations of defects. The boundary element method is very efficient for such problems because modification of defects is simpler than in methods, which need discretization of the whole domain of the body. Contrary to analytical methods, solids with high density of cracks, curved and intersecting cracks can be considered.

5. References

- [1] M. Kachanov (1992). Effective elastic properties of cracked solids: critical review of some basic concepts, *Appl. Mech. Rev.*, **45**, 304-335.
- [2] M. Kachanov (1993). On the effective moduli of solids with cavities and cracks, *Int. J. Frac.*, **59**, R17-R21.
- [3] V. Renaud, D. Kondo and J.P. Henry (1996). Computations of effective moduli for microcracked materials: a boundary element approach, *Comp. Materials Science*, **5**, 227-237.
- [4] Y. Huang, A. Chandra, Z.Q. Jiang, X. Wei and K.X. Hu (1996). The numerical calculation of two-dimensional effective moduli for microcracked solids, *Int. J. Solids Structures*, **33**, 1575-1586.
- [5] S. Zhan, T. Wang and X. Han (1999). Analysis of two-dimensional finite solids with microcracks, *Int. J. Solids Structures*, **36**, 3735-3753.
- [6] F.C.S. Carvalho and J.F. Labuz (1996). Experiments on effective elastic modulus of two-dimensional solids with cracks and holes, *Int. J. Solids Structures*, **33**, 4119-4130.
- [7] A. Portela, M.H. Aliabadi and D.P. Rooke (1992). The dual boundary element method: effective implementation for crack problems, *Int. J. Num. Meth. Eng.*, **33**, 1269-1287.
- [8] P. Fedelinski, M.H. Aliabadi and D.P. Rooke (1995). A single-region time-domain BEM for dynamic crack problems, *Int. J. Solids Structures*, **33**, 3555-3571.

NONLOCAL CONDITIONS FOR THE TRANSITION DAMAGE TO A LOCALIZED FAILURE IN GRANULAR AND FIBRE-REINFORCED COMPOSITES UNDER QUASISTATIC LOADING

A. V. Zaitsev

Perm State Technical University, Perm, Russia

1. Introduction

The investigation of inelastic deformation and failure of composites is associated with the necessity to develop mechanical models for the correct description of the behaviour of damaged heterogeneous materials in elements of structure. Besides, there is a need to improve the procedures of strength analysis in order to take into account actual loading conditions and the evolution and character of the collective interaction in a system of defects which determines the instant of macrofailure, when the damage accumulation becomes unstable. Without understanding the regularities and mechanisms of damage accumulation, without evaluating its stability and determining the conditions of localization beginning, the macrofracture of composites will remain latent and poorly predictable phenomenon of internal structure evolution of the material.

2. Regularities of damage evolution in granular composites

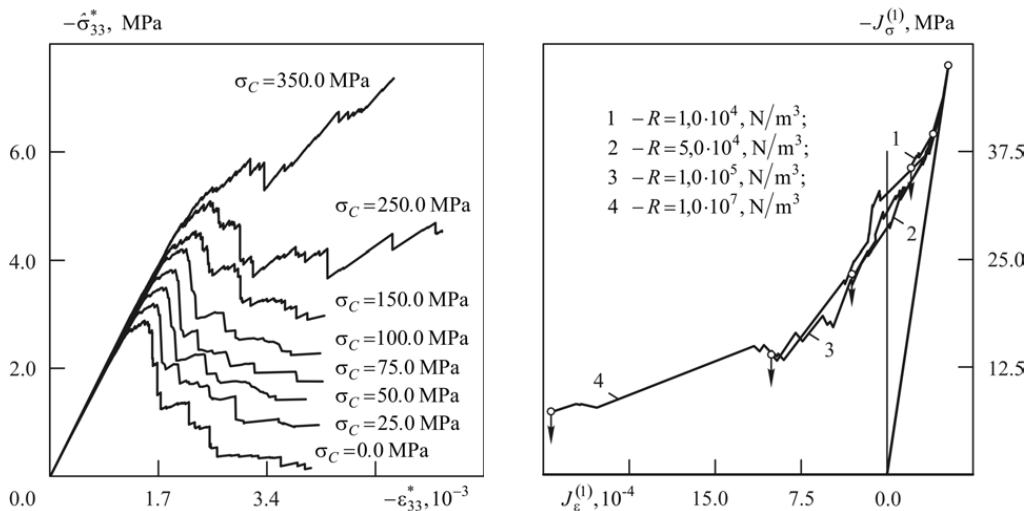


Figure 1. Uniaxial compression stress-strain diagrams under different lateral pressure σ_C (a).

Dilatation under uniaxial compression with different stiffness of the loading system R (b). Stable stress-strain states corresponding to the instant of macrofailure are marked by arrows

The two-level-phenomenological structural model for granular composite was developed with the aim to study the character of collective multi-particle interaction in the defect ensemble, the general laws and the change in failure mechanisms and scale levels of damage evolution under combined triaxial quasistatic loading. A partial or complete loss of load-carrying capacity by structure elements is connected with violation of strength conditions and, as consequence, with jump-like changes of deformational characteristics. The model allowed us to describe the inelastic deformation accompanied by inclination and coarsening of defects as a multistage process of damage accumulation and to determine the instant of composite macrofailure as a result of loss of

stability of this process. In the course of computational experiments, we found and analyzed such regularities of mechanical behaviour of granular composites as the strains corresponding to the instant of macrofailure and the character of damage evolution in relation to the stiffness of the loading system, the effect of lateral pressure on strain-softening (Fig. 1, a), the dilatation under uniaxial compression (Fig. 1, b), the unequal resistance of heterogeneous bodies, and the self-supported accumulation of defects. A nonlocal critical dimensional lengths constant for damaged solids is found to exist, which does not depend on the type of stress-strain state and quasistatic proportional and nonproportional loading modes. The constant determines the instant of transition from the stage of accumulation of disperse damage to a localized failure and to the strain-softening. The new nonlocal criterion allow one to determine a unique quantitative relation between the connection of damaged domains and the regularities in the behaviour of isotropic and anisotropic media.

3. Micro- and macrofailure of fibre-reinforced composites

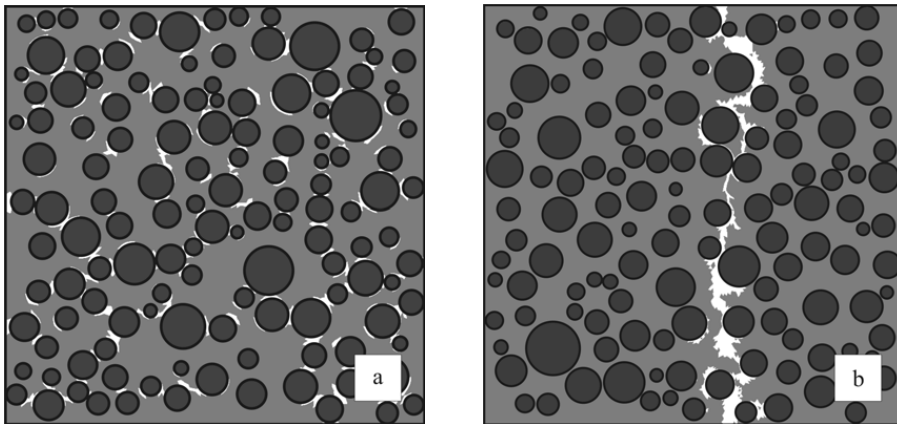


Figure 2. Effect of 'quantum' damage evolution under hydrostatic displacement-controlled compression $\varepsilon_{11}^* = \varepsilon_{22}^* = -\varepsilon_{33}^*$, $\varepsilon_{33}^* > 0$ (a) and macrofailure of glass-epoxy plastic with fibre void fraction $v_f = 0.4$ under antiplane shear $\varepsilon_{13}^* > 0$ (b)

The structural stochasticity of unidirectional composites is caused by randomness of the shape, relative arrangement and orientation of fibres and the scatter of fibre diameters. Computational experiments in transverse shear and tension, uniform tension in the reinforcement direction, and antiplane shear showed that the effective elastic moduli, which were determined for the representative volume element of composites with account of multiparticle interaction in the system of reinforcement elements, did not depend on the symmetry and asymmetry aspects of the distribution laws. But the asymmetry aspect was influenced significantly by the fractional structure of the materials, as well as by the character of multiparticle interaction at distances from half to two averaged fibre diameters. These length scales predetermined the character of strain and stress inhomogeneities in undamaged composites and significantly influenced the damage evolution scenario at the initial stage of quasistatic loading. The effect of 'quantum' damage evolution under hydrostatic compression (Fig. 2, a), which not depends on the type of statistical distribution law of fibre diameters, was found out and investigated. Qualitative coincidence of macrofailure in computational experiments (Fig. 2, b) with results of mechanical tests in antipain shear of glass-epoxy plastics is shown.

4. Acknowledgements

The author acknowledge the support of the Russian Foundation for Basic Research (Grant RFBR-Urals No 07-01-96056).

Failure and fracture of concrete and brick walls imposed by explosion

T. Jankowiak, T. Łodygowski, P. Sielicki

Poznan University of Technology, Institute of Structural Engineering, Poznan, Poland

Abstract

The structures like concrete or bricks wall are often subjected of unique loadings. For example the blast wave as well as impact belongs to this type of loadings. The paper presents only the first class of structural external forces, that comes from an explosion of the material as TNT. To describe properly the pressure wave propagation in the air, produced by detonation, which acts on the structure, it is necessary to simulate the explosion and the waves' motion. In the numerical simulation of the explosion process, we accept the Jones-Wilkens-Lee (or JWL) equation of state for TNT and typical equation of state for air [1]. The data of TNT and the air are in Tab. 1. Using these values of material parameters and ALE description of deformations guarantee the proper solution of explosion simulation and finally the distribution of pressure loading on structure. There are many analytical functions in literature [1], which describe the influence of time and distance from the ignition on the pressure distribution. The numerical simulation results [2] are compared with analytical functions of the blast to validate the accepted models. The results of the pressure distribution change depends on time after explosion and the distance from the ignition point are presented in Fig. 1.

The interaction of the fluid (air) with both walls is performed using sub-modeling. There are two kinds of models for both cases, the global and local. The global model consists the cubic explosive material, surrounded air and the structure wall. The local models include only structural parts (the concrete and masonry walls). Sub-modeling technique is accepted if the coupling exist in one way between the global to local models, but not in opposite. It is sufficient assumption for blast simulation. The idea of global and local models is presented in Fig. 2. When modeling 1/8 part of the space three planes of symmetry are assumed. The global model is extended up to 5 meters from the model center. It is possible to obtain the positive and negative overpressure phase on the surface of the structure like in experiments [1, 2]. The first kind of structure under consideration is concrete wall and the second is periodic composite masonry wall created of mortar and bricks. Both form the local models. Cumulative Fracture Criterion (CFC) introduced in [3, 4] and discussed before [5, 6] is used and has been added to Abaqus/Explicit environment by VUMAT procedure. This criterion in integral form is as following:

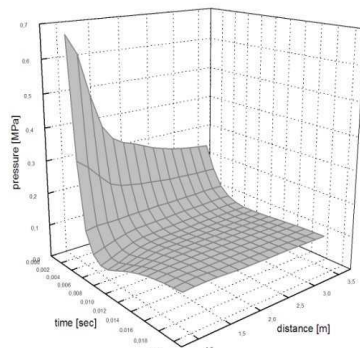


Fig. 1 The positive and negative overpressure (above or below atmospheric pressure)

Tab.1 EOS parameters

AIR
$R=287(\text{J}/(\text{kgK})),$
$\rho=1.293(\text{kg}/\text{m}^3),$
$p_A=101325(\text{Pa}),$
$E_{m0}=0.193\text{e}6(\text{J}/\text{kg}), T^Z=0(\text{K}),$
$T_0=288.4(\text{K}),$
$c_v=1003.5(\text{J}/(\text{kg K}))$
TNT
$A=3.73\text{e}11(\text{Pa}),$
$B=3.74\text{e}9(\text{Pa}), R1=4.15(-),$
$R2=0.9(-), E_{m0}(\text{J}/\text{kg}),$
$\omega=0.35(-), v_d=6930(\text{m}/\text{s}),$
$\rho_0=1630(\text{kg}/\text{m}^3)$

$$t_{c0} = \int_0^{t_c} \left(\frac{\sigma_F^{eq}(t)}{\sigma_{F0}^{eq}} \right)^{\alpha(r)} dt \quad \text{if} \quad \sigma_F^{eq}(t) > \sigma_{F0}^{eq}, \tag{1}$$

where t_{c0} is the longest critical time, $\alpha(T)$ is the parameter connected with energy activated during the separation process and σ_{F0}^{eq} is quasi-static equivalent tensile strength of concrete. This measure is introduced to describe better the deformation in advanced triaxial state of stress [6]:

$$\sigma_F^{eq} = \frac{k-1}{2k(1-2\nu)} I_1 + \frac{1}{2k} \sqrt{\left(\frac{k-1}{1-2\nu} I_1\right)^2 + \frac{6k}{(1-\nu)^2} J_2}, \quad (2)$$

where

$$I_1 = \sigma_1 + \sigma_2 + \sigma_3 \quad \text{and} \quad J_2 = \frac{1}{3} [(\sigma_1 - \sigma_2)^2 + (\sigma_1 - \sigma_3)^2 + (\sigma_2 - \sigma_3)^2] \quad (3)$$

σ_F^{eq} is the generalization of the Huber-Mises equivalent stresses [6]. I_1 and J_2 are the first and the second invariants of the stress tensor and deviatoric part of the stress tensor, respectively. The k influences the shape of the critical failure surface in the space of principal stresses. The criterion

describes generally the time up to failure under the stress impulse. In both, concrete and masonry structures this criterion is used. In the second one only for the mortar CFC is accepted. It means that we assumed elastic-visco-brittle material, see Tab. 2. This criterion results in strain rate sensitivity of the material behavior. In the presentation the sensitivity of structure failure patterns to the constitutive parameters, the boundary conditions and the geometry of the global and local models is considered. Particularly, important is the distance between the explosive material and the wall obstacle. Instructive numerical examples will be presented and discussed during the conference.

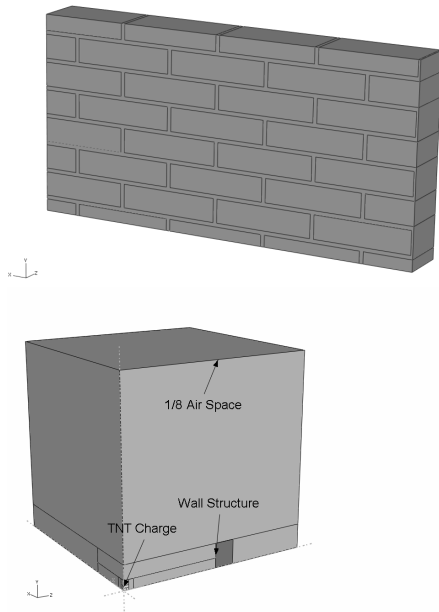


Fig. 2 Analyzed models: a) Local b) Global

Tab. 2 The parameters of concrete

E	35e9 [Pa]
v	0.2
ρ	2395 [kg/m ³]
k	10
t_{c0}	0.000049 [s]
$\alpha(T)$	0.95
σ_{F0}^{eq}	4.2e6 [Pa]

References

- [1] P.D. Smith and J.G. Hetherington, *Blast and Ballistic Loading of Structures*, Butterworth-Heinemann, Oxford 1994.
- [2] Jankowiak T., Łodygowski T., Sielicki P.W., *Modeling of pressure distribution after explosion*, Computer Methods in Mechanics, 2007
- [3] J.R. Klepaczko, *Behavior of rock like materials at high strain rates in compression*, Int. J. Plasticity 6, (pp. 415-432) 1990.
- [4] J.R. Klepaczko and A. Brara, *An experimental method for dynamic tensile testing of concrete spalling*, Int. J. Imp. Eng. 25, (387-409) 2001.
- [5] T. Jankowiak and T. Łodygowski, *Numerical modeling of fracture in brittle material under impact loading*, Vibrations in Physical Systems 22, (pp. 143-148) 2006.
- [6] T. Jankowiak, J.R. Klepaczko, and T. Łodygowski, *Numerical modeling of wave propagation and interaction in bars*, Found. Civ. Env. Eng. 7, (pp. 187-199) 2006.

EFFECT OF STRAIN PATH CHANGE ON MICROSTRUCTURE AND PROPERTIES OF HOT-ROLLED Q235 STEEL

W. P. Jia¹, J. G. Wang² and D.Y. Ju³

¹ University of Science and Technology Liaoning, China

² Saitama Institute of Technology Graduate school, Japan

³ Saitama Institute of Technology, Japan, email: dyju@sit.ac.jp

1. Introduction

Cyclic deformation, fatigue crack initiation and fatigue crack growth, as the basic fatigue properties of materials, have been widely studied by many researchers and many achievements have been reached^[1]. In fact, nearly 90% of total fatigue of most materials is at the stage of cyclic deformation and crack initiation, so trying to clarify cyclic deformation behaviour of materials is of much importance not only in theory research, but also in engineering application^[2]. Up to date, most research works in literature about this are on the cyclic deformation behaviour of annealed materials. Recently, the cyclic deformation behaviour of materials with prestrained history has also been studied because of its industrial application background. However, some aspects about it are not very clear yet, further system study is necessary. The present work is mainly about the cyclic deformation behaviour of low-carbon steel prestrained, the mechanical properties, the dislocation structures as well as the relationship between them are emphasized in this paper. In addition, the tensile deformation behaviour of low-carbon steel prestrained in fatigue is studied.

2. Experimental Procedure

The material used in this investigation was Q235 hot-rolled steel plate with chemical compositions of (in wt%): 0.14C, 0.17Si, 0.40Mn, 0.012P, 0.006S. For the mechanical tests, two angle value (namely $\varphi=0^\circ$ and $\varphi=45^\circ$, φ is the angle between the loading direction and the rolling direction) were chosen in each case. The dimensions for the specimens are shown in Fig.1.

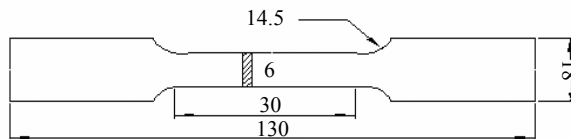


Fig.1 Dimensions of specimens (mm)

Tension-fatigue: For the preloading in tension, tests were performed until strain amount reached these value: 2%, 5%, 10%, the subsequent fatigue tests were performed under three different constant plastic strain amplitudes: 0.6×10^{-3} , 1.5×10^{-3} , 2.5×10^{-3} . All the fatigue tests were conducted until the specimens were saturated. **Fatigue-tension:** The preloading in fatigue as well as the subsequent fatigue of the tension-fatigue tests, the subsequent tension tests were conducted until the specimens were rupture.

3. Result and Discussion

Tension-fatigue: In the tests, the cyclic softening phenomenon happened at both case. In general, at both cases, a higher tension prestraining amount leads to a higher axial stress at the beginning of cyclic deformation under same applied plastic strain amplitude. The axial stress of all specimens in present study remains constant during the major part of cyclic deformation, which means stress saturation. With the amplitude increasing, the saturate stress of higher tension prestraining amount is lower than that of lower tension prestraining amount.

In $\varphi=45^\circ$ case, the axial stress at the beginning of reloading and the saturation stress at the end of fatigue tests is a little higher than that of $\varphi=0^\circ$ case under the lower tension prestraining amount and the same applied reloading plastic strain amplitude. However, the tendency of cyclic softening curves is independent of the amplitude of strain path change under the higher tension prestraining amount, i.e. φ value.

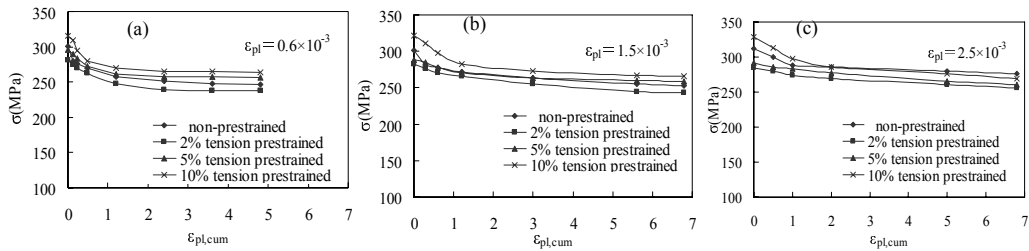


Fig.3 Cyclic softening curve of specimen with different tension prestraining amounts at various plastic strain amplitude, $\varphi=0^\circ$

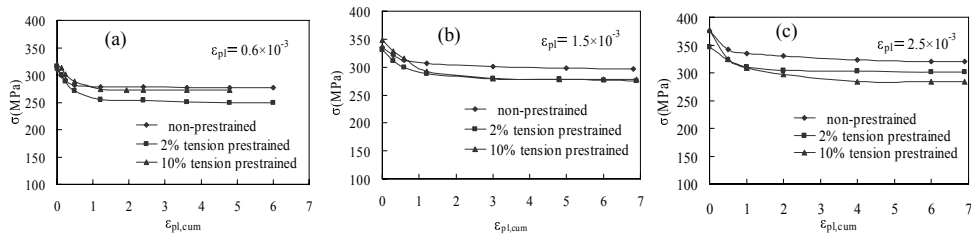


Fig.4 Cyclic softening curve of specimen with different tension prestraining amounts at various plastic strain amplitude, $\varphi=45^\circ$

Fatigue-tension: For both case ($\varphi=0^\circ$ and $\varphi=45^\circ$), the yield phenomenon graduate away with the applied plastic strain amplitude increasing. A higher fatigue prestraining leads to a higher tensile strength, yield strength and a lower elongation ratio at tensile tests. In $\varphi=45^\circ$ case, the stress level is a little higher than that of $\varphi=0^\circ$ case at tensile tests. However, the tendency of tensile curves is independent of the strain path.

4. Conclusion

- (1) In the subsequent cyclic deformation, with the cyclic number increasing, the dislocation structure formed in preloading is resolved gradually, at the end of fatigue tests, for most specimens, the dislocation structures are almost the same as that of specimens as if the tension preloading did not happen.
- (2) Tensile deformation behaviour of Q235 steel with fatigue prestraining at two amplitudes of strain path change was studied. It was found that for both case ($\varphi=0^\circ$ and $\varphi=45^\circ$), the yield phenomenon graduated away with the applied plastic strain amplitude increasing. A higher fatigue prestraining leads to a higher tensile strength, yield strength and a lower elongation ratio at tensile tests. In $\varphi=45^\circ$ case, the stress level is a little higher than that of $\varphi=0^\circ$ case at tensile tests.

References:

- [1] J. H. Schmitt. A parameter for measuring the magnitude of a change of strain path: validation and comparison with experiments on low carbon steel. *Int. J. Plasticity*, 10 (1994):535
- [2] W.P. Jia, J.V. Fernandes, Mechanical behaviour and the evolution of the dislocation structure of copper polycrystal deformed under fatigue-tension and tension-fatigue sequential strain paths, *Mater. Sci. and Eng.*, A348(2003):133~144

CONTACT STATE ANALYSIS BY RST, NFIS, AND SOM SYSTEMS

H. O. Ghaffari

*Department of mining & metallurgical engineering, Amirkabir University of Technology,
Tehran, Iran*

1. An overview

This paper reports application of Neuro- fuzzy inference system (NFIS), self organizing feature map- neural networks - (SOM) and rough set theory (RST), on detection of contact state in a block system. In this manner, on a simple system, evolutions of contact states, by parallelization of Discontinuous Deformation Analysis (DDA) method, have been investigated. So, a comparison between NFIS and RST results has been presented. The results show applicability of the proposed methods, by different accuracy, on detection of contact's distribution. Other benefit of our method is how one can insert the role of approximate analysis in the most consuming time part of the discrete mechanics analysis, contact detection.

2. The proposed algorithms

This part of paper, proposes three different flowcharts, which comprises the varying combinations of DDA, NFIS, SOM and RST, upon the information granulation theory and balancing between the successive granules (1, 2). Information granules are collections of entities that are arranged due to their similarity, functional adjacency, or indiscernibility relation. The process of forming information granules (2) is referred to as IG. There are many approaches to construction of IG, for example SOM, Fuzzy C-Means (FCM), and RST. The granulation level depends on the requirements of the project. The smaller IGs come from more detailed processing. On the other hand, because of complex innate feature of information in real world and to deal with vagueness, adopting of fuzzy and rough analysis or the combination form of them is necessary. In this study, the main aim is to develop a hierarchical extraction of IGs using three main steps:

1-Random selection of initial crisp granules: this step can be set as "Close World" Assumption. But in many applications, the assumption of complete information is not feasible (CWA), and only cannot be used. In such cases, an Open World Assumption (OWA), where information not known by an agent is assumed to be unknown, is often accepted.

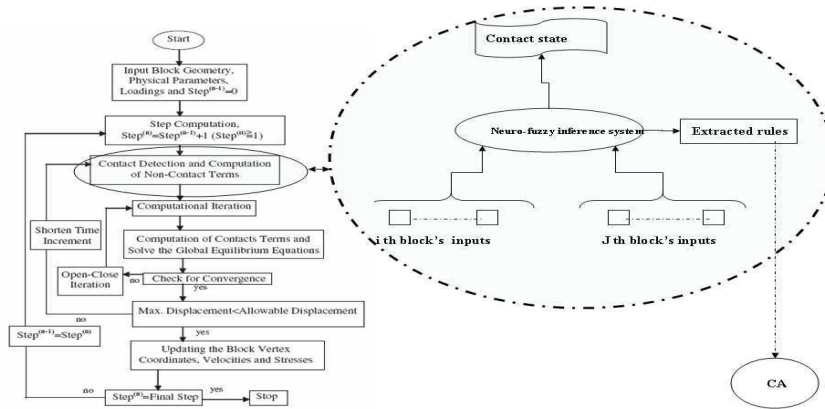
2- Fuzzy granulation of initial granules: sub fuzzy granules inside precise granules and extraction of if-then rules.

3- The close-open iteration: this process is a guideline to balancing of crisp and sub fuzzy granules by some random selection of initial granules or other optimal structures and increment of supporting rules, gradually.

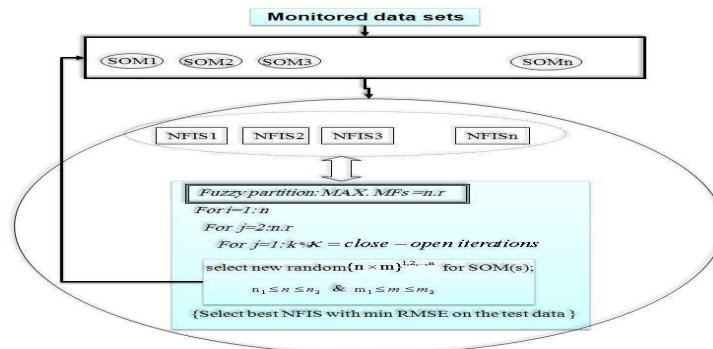
3. Results

The Contact State (C.S) in 2-D on block system has four components: "no contact: 0; V-V: 1; V-E: 2; E-E: 3", where numbers are the attributed codes. All of training and checking data set were 100 and 50, respectively, which were revealed from DDA. Inputs for any block were vertex positions and area (total inputs: 18). The extraction of rules by NFIS and RST, under eliciting of best granules (rules and clusters) get an acceptable approximation of the distribution of contact's state (so, resulted from SOM), can deployed

in the core of contact detection part of DDA or other discrete element methods (so in some lattice mechanics based methods).



1-Contact state detection by NFIS



2-SOM-NFIS based on two forms: random and regular neuron growth (SONFIS)

4. References

1. Jang J.S.R., Sun C.T. & Mizutani E. *Neuro-Fuzzy and Soft Computing*, New Jersey. Prentice Hall, 1997
2. Nauk D, Klawoon F, & Kruse R. *Foundations of Neuro-Fuzzy Systems*, John Wiley & Sons, 1997
3. Owladeghaffari, H., Shahrair, K. & Pedrycz, W. 2008. *Graphical Estimation of Permeability Using RST&NFIS, NAFIPS*; New York, May 19-22, 2008, available at: <http://arxiv.org/>
4. Shi GH. *Block System Modeling by Discontinuous Deformation Analysis*, Computational mechanics publications, England, 1993.
5. Kohonen, T. *Self-Organization, and Associate Memory*, 2nd, Springer – Verlag, Berlin, 1987
6. Zadeh LA. *Towards a theory of fuzzy information granulation and its centrality in human reasoning and fuzzy logic*, *Fuzzy Sets and Systems*; 19:111:127. 1997
7. Pawlak, Z., *Rough sets: theoretical aspects reasoning about data*, Kluwer academic, Boston. 1991

SHEAR BAND ANALYSIS OF WEATHERED BROKEN ROCK IN DRY AND WET STATES

E. Bauer, S.F. Tanton

Institute of Applied Mechanics, Graz University of Technology, Graz, Austria

1. Mechanical properties of weathered broken rock

The degree of geological disintegration, i.e. by chemical weathering or by the intensity and the orientation of micro-cracks, has a significant influence on the granular hardness and as a consequence on the resistance to compaction and shearing, which leads to phenomena such as rockfill creep and collapse. It is experimentally evident that the mechanical properties of weathered broken rock are different for dry and wet states of the material [1]. Furthermore for rockfills with coarse-grained and uniform particles under stress the forces at the contact areas are much higher than in a well graded granular material. Thus grain abrasion and grain crushing caused by the plastification of contact zones and the progressive development of micro-cracks are usually more pronounced in rockfills. When water penetrates the micro-cracks, the disintegration of the granular hardness of the grain ensemble can be accelerated. Grain abrasion and grain crushing change the grain size distribution and consequently the value of the limit void ratios of the material.

Recently the essential mechanical properties of coarse-grained weathered broken rock were modeled within the framework of hypoplasticity by extending the model for unweathered stable grains and simple grain skeletons with a granular hardness depending on the degree of weathering and the moisture content [2]. In particular the granular hardness is defined as the pressure at which the isotropic compression curve in a semi-logarithmic representation shows the point of inflection (Figure 1.a). It was found by experiments that the point of inflection is related to the state where grain crushing becomes dominant. For the wet material the granular hardness is lower (Figure 1.b). The constitutive equation for the evolution of the stress is based on nonlinear tensor-valued functions depending on the current void ratio, the stress, granular hardness and the rate of deformation. The model also includes inelastic material properties, a pressure and density dependent stiffness and peak friction angle, strain softening and critical states. Creep and stress relaxation during the time-dependent process of degradation of the granular hardness are taken into account with an additional term added to the constitutive relation [3]. As the hypoplastic concept does not need to distinguish between elastic and plastic deformation the calibration of the constitutive constants is rather easy. It is demonstrated that for weathered broken granite the model captures the essential mechanical properties within a wide range of pressures and densities both for dry and wet states.

2. Shear band analysis for plane strain element compression

While for unweathered granular materials modeled with hypoplasticity shear banding has already been extensively investigated in earlier publications [4], the results obtained for a weathered broken rock [2] will be discussed in the present paper. Based on the general bifurcation theory the possibility of a spontaneous formation of a shear band in plane strain biaxial compression under a constant lateral stress is studied for the dry state and the water saturated state of weathered granite. Figure 1.c shows the evolution of the stress ratio and the volume strain under a homogeneous and drained element deformation starting from an initial isotropic stress state. It is obvious that for the dry material the incremental stiffness at the beginning of compression and also the maximum stress ratio is higher than for the water saturated material. Densification is more pronounced for the saturated material and dilatancy can only be observed for the dry material after the peak. The

bifurcation analysis show that the first possibility of a shear band (marked with a dot) may appear before the peak. States above the first bifurcation point (dotted curves) again fulfill the bifurcation criterion. It can clearly be seen that the smallest stress ratio and shear band inclination for a possible shear band bifurcation is a little higher for the dry state of the material.

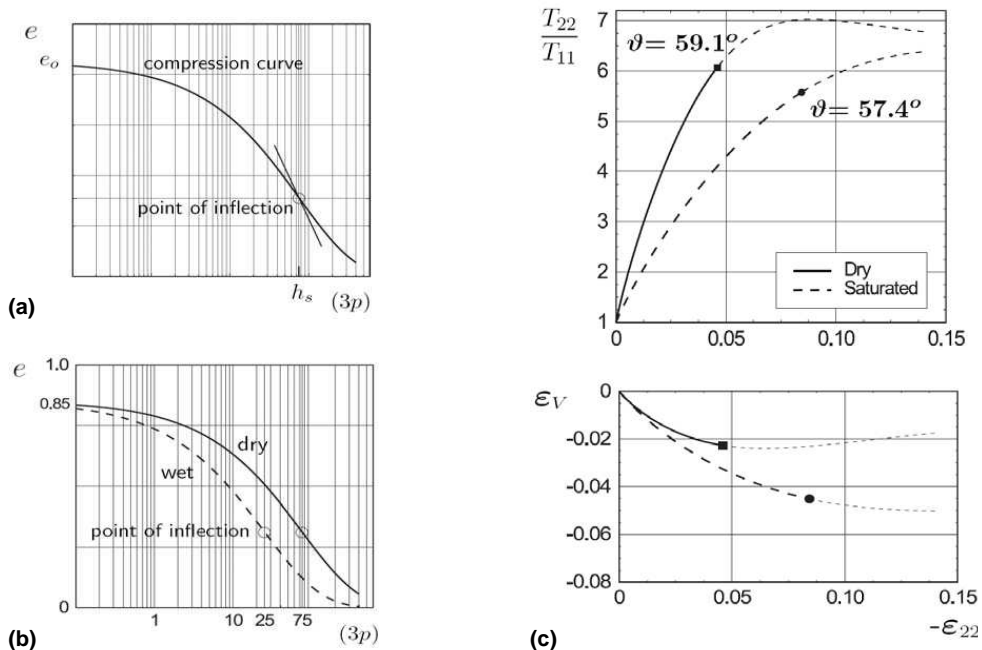


Figure 1. (a) Compression curve; (b) reduction of the granular hardness for the wet material; (c) Plane strain compression under constant lateral stress $T_{11} = -0.8$ MPa: stress ratio T_{22}/T_{11} against the vertical strain ϵ_{22} , volume strain ϵ_V against the compression strain ϵ_{22} . (solid curves: dry state; dashed curves: saturated state; ϑ = shear band inclination)

3. References

- [1] A. Oldecop and E.E. Alonso (2001). A model for rockfill compressibility, *Géotechnique*, **51**, No. 2, 127-139.
- [2] E. Bauer, K. Kast, S.F. Tanton and W. Cen (2007). Modeling the influence of pressure and moisture content on the disintegration of weathered rockfill materials, *Bifurcations, Instabilities, Degradation in Geomechanics*, eds. G. Exadaktylos and I. Vardoulakis, Springer Publication, 277-299.
- [3] E. Bauer, S.F. Tanton, A. Niemunis, K. Kast, W. Cen, S. Liu and Y. Zhu (2007). Modelling the disintegration of weathered and partly saturated grains of rockfill material, *Proc. of the 3rd Asian Conference on Unsaturated Soils*, eds. Y. Zongze, Y. Junping and A.C.F. Chiu, Science Press, 335-340.
- [4] C. Tamagnini, G. Viggiani and R. Chambon (2001). Some remarks on shear band analysis in hypoplasticity, *5th Int. Workshop on Localisation and Bifurcation Theory in Geomechanics*, eds. Muehlhaus, Dyskin and Pasternak, Balkema Publisher, 85-93.

THE INFLUENCE OF SOIL PLUGGING ON THE DRIVING RESISTANCE AND BEARING CAPACITY OF OPEN-ENDED STEEL PILES

C. Slominski, R. Cudmani

Bilfinger Berger Civil, Structural Design Geotechnics, Wiesbaden, Germany

1. General

During the installation of open-ended piles two mechanisms of penetration can occur depending on the ground conditions, load type and the dimensions of the pipe: 1) The soil enters continuously into the pipe, 2) a soil plug develop, which impedes subsequent entry of soil. From the practical point of view, soil plugging have the positive effect of increasing the bearing capacity of the pipe towards that of a closed-ended pile. At the same time, the driving resistance can become considerably larger than that expected for unplugged conditions.

At the present, the calculation of the driving resistance and bearing capacity of open-ended piles are based on empirical assumptions and does not consider the effect of soil plugging properly. The common procedure for geotechnical design consists in assuming plugged conditions for driveability analysis and unplugged conditions for the determination of bearing capacity. Obviously, this approach is conservative and may lead to heavier driving equipment and too long piles and thus, may result in uneconomical design. Methods which apply empirical reduction factors to the equivalent capacity of a closed-ended pile are questionable and unsafe, as ground conditions, pile dimensions and load conditions of the pile cannot be rationally accounted for.

In this contribution a model is proposed for both the prediction of soil plugging during driving and the evaluation of the bearing capacity depending on plugging conditions. The model is validated using experimental data from the literature. The application of the proposed approach is shown exemplarily by means of a case study.

**AGE-DEPTH CORRELATION, GRAIN GROWTH AND DISLOCATION ENERGY
EVOLUTION, FOR THREE ICE CORES**

L. W. Morland

*School of Mathematics, University of East Anglia
Norwich NR4 7TJ, United Kingdom*

Two previous theoretical analyses of data from the GRIP, Vostock and Byrd ice cores, presenting age-depth correlations, grain growth and dislocation energy evolution, are re-examined. It is found that the age-depth correlations are inconsistent with the idealised flow with unchanging history adopted, but that good correlations can be obtained by relaxing those restrictions. A modified grain growth relation is proposed consistent with the distinct growth profiles of the Vostock and the other two cores, which can be solved simultaneously with the given dislocation density evolution equation. These are solved for all three cores with the given parameters, and the depth profiles of grain diameter and dislocation density at the present time determined with the new age-depth correlation and with that shown empirically in the papers. The varying flow history influences the age-depth correlation, and hence the depth profiles, which is important both for the interpretation of core data, and for the determination of constitutive variables at each depth at the present time.

EXPERIMENTAL AND THEORETICAL INVESTIAGTIONS OF SILO MUSIC DURING GRANULAR FLOW

K. Wilde, M. Rucka and J. Tejchman

*Faculty of Civil and Environmental Engineering,
Gdańsk University of Technology, Gdańsk, Poland*

1. Introduction

Dynamic effects can occur in granular bodies during confined flow in silos. Strong vibrations are accompanied by a booming sound, sometimes called silo music or by repeated shocks called silo quake. In dry cohesionless granular silo fills, only silo music has been observed. In cohesive silo fills, silo music and silo quake can take place. These strong dynamic effects have been recorded in various conditions, e.g., in large full scale silos, small experimental models, during mass, funnel or expanded flow, and during controlled or free outlet. The strong dynamic effects create noise pollution that disturbs the neighborhood (e.g. local population residing close to industrial plants) or can cause hearing damage of plant workers. They may cause earthquake type movements which endanger surrounding structures and contribute to fatigue of joints and connections. In the most extreme cases, rapid vibrations can cause silo failures. In spite of many experimental studies, the phenomenon of the silo music is still not well understood.

On the basis of experiments, several sources of extensive dynamic effects in silos have been proposed which include: slip-stick behavior between stored solids and silo walls, grain collisions and a frozen disorder of the bulk solid, insufficient flow ability of the silo fill, energy release by the fall of the bulk solid from the region of mass flow into the region of channel flow, propagating longitudinal stress waves due to a resonant interaction between the granular material and the silo structure which were induced at the outlet, alternating flow patterns during flow, non-linear change of the wall friction with flow velocity, acceleration and deceleration of the granular material at the transition between bin and hopper, internal slip-stick and solid dilation during flow.

The aim of these investigations is development of the mechanism of the phenomenon of the silo music understood as pronounced vibrations connected with loud sound [1]. The study is limited to dry cohesionless sand during gravitational outflow from a cylindrical model silo.

2. Silo model tests

First, silo experiments with dry cohesionless sand during gravitational outflow were performed in a cylindrical perspex model silo. Wall accelerations and acoustic signals were recorded and the evolution of mode shapes for different levels of the granular material in a silo were determined. In addition, both pressures along the wall and inside the material above the outlet were registered. The Perspex silo model had a height of 2.00 m, an outside diameter of 0.2 m and a thickness of the wall of 40 mm. A symmetric outlet with a diameter of 0.08 m in the flat bottom induced a discharging process due to gravity. The silo was fixed at the bottom (it was supported by a steel rigid frame structure) and free at the top. As a filling substance, initially medium dense dry sand with rough grains was used. The silo was excited by modal hammer, linear motor actuator and flowing sand during emptying (when the silo music was created). In the case of an empty silo, 9 mode shapes were identified. Three lowest modes were bending ones and for higher modes - ovalling ones (i.e. the radial displacements dominated the shape of the modes). In turn, for the silo containing sand up to 1.90 m, only 3 bending modes were identified since the inertia of the filling was very large and the energy transmitted to the structure through the modal hammer and actuator was not sufficient to excite higher modes. During silo discharge, in the case of the sound signal, the dominant frequency was about 100 Hz and it corresponded to the 1st ovalling silo mode shape. For

the radial acceleration signal, the dominant frequency was also about 100 Hz. The dominant frequency of the vertical signal was found to be 50 Hz (it corresponded to the 2nd bending mode).

3. Theoretical model

It is proposed that there are some similarities between the origin of the sound in the silo and the music of bells. The mode shapes of the silo are very similar to the modes of bells. In bells, the clapper striking the shell causes that bell walls undergo radial vibrations that are associated with vertical ones. In the case of the silo, the role of the clapper is taken on by radial forces generated by the silo fill hitting the hopper at the outlet. The dominant frequency of the sound signal during flow equals to 100 Hz and it corresponds to the 1st ovaling silo mode shape which is very similar to the first bell mode.

To qualitatively explain the presence of pulsations of radial stresses during silo flow at the hopper due to the change of the shearing direction, simple plane strain FE-simulations have been conducted. The behavior of the granular body subjected to the varying shearing force along silo walls at the outlet was approximately described by a cyclic quasi-static direct shearing along wall under a constant normal stiffness (CNS) condition (which simulates the surrounding material) [2]. The FE-calculations were carried out with a micropolar isotropic hypoplastic constitutive model which describes the evolution of effective stresses and couple stresses depending on the current void ratio, stress and couple stress state, rate of deformation and rate of curvature and a mean grain diameter by isotropic linear and non-linear tensorial functions. The obtained numerical results were qualitatively the same as those obtained in the experiment with different cohesionless sand [3].

4. Conclusions

The silo music phenomenon in tall narrow silos containing granular fills occurs during gravitational outflow in the form of strong vibrations of the structure connected with a loud booming sound. The silo music requires a dynamic interaction between the silo structure and moving granular fill (i.e. frequency accordance). It is produced mainly by the change of the shearing direction in the silo fill at the outlet. Vibrations of silo walls and moving granular body cause air oscillations with frequencies audible by human beings.

The dominant frequency of the oscillating sand is 50 Hz. The exciting force transmitted mainly through sand has both vertical and radial components. The dominant frequency of the sound signal during flow equals to 100 Hz and it corresponds to the 1st ovaling silo mode shape.

The silo music is not generated by the slip-stick phenomenon understood as the variable friction between the smooth wall and granular material subjected to constant normal force.

The silo music can be significantly reduced avoiding the change of the shearing direction at the silo outlet or a decrease of a pulsating material column by additional inserts.

5. References

- [1] K. Wilde, M. Rucka and J. Tejchman (2008). Silo music—mechanism of dynamic flow and structure interaction. *Powder Technology*, <http://dx.doi.org/10.1016/j.powtec.2007.11.008>
- [2] J. Tejchman and E. Bauer (2008). FE-investigations of granular material behaviour during cyclic wall shearing under CNS condition, *Computers and Geotechnics* (accepted for publication).
- [3] J.T. DeJong, D.J. White, M. F. Randolph (2006). Microscale observation and modeling of soil-structure interface behavior using particle image velocimetry. *Soils and Foundations*, **46**, 1, 15–28.

FE-CALCULATIONS OF STRESS DISTRIBUTION UNDER PRISMATIC AND CONICAL SANDPILES WITHIN HYPOPLASTICITY

J. Tejchman¹ and W. Wu²

*¹Gdańsk University of Technology,
Gdańsk, Poland*

*²Institut für Geotechnik, Universität für Bodenkultur,
Vienna, Austria*

1. Introduction

The static and dynamic behaviour of sandpiles has attracted much attention. Simple experiments with prismatic and conical piles of granular materials indicate, contrary to intuition that the maximum vertical normal stress does not always appear directly beneath the pile vertex but at a certain distance from the apex. It was found later that the occurrence of the stress dip at the heap centre strongly depends on the method of pile construction [1]. In the case of the raining procedure by means of a sieve located above the heap, the pressure maximum occurs at the centre of the sandpile. However, when a funnel procedure (centric flow out of a hopper) is used, a pressure peak is obtained away from the centre, where a significant pressure dip appears. The pressure dip is usually more pronounced in conical heaps than in prismatic ones.

In the present paper, the stress distribution under sandpiles is studied with the FEM and micro-hypoplasticity without imposing any additional condition [2]. The analyses were performed with a micro-polar hypoplastic model which is suitable to investigate the phenomenon of the granular heap construction since it takes into account the effect of the direction of deformation rate. The calculations were carried out with prismatic and conical heaps composed mainly of an initially dense cohesionless sand.

2. Micro-polar hypoplastic model

Granular materials consist of grains in contact and surrounding voids. Thus, their micromechanical behaviour is inherently discontinuous, heterogeneous and non-linear. Despite their discrete nature, the mechanical behaviour of granular materials can be reasonably described by the principles of continuum mechanics. Non-polar hypoplastic constitutive models have been developed at Karlsruhe University, where the stress rate tensor is assumed to depend on the stress tensor, strain rate tensor and the void ratio via isotropic non-linear tensorial functions based on the representation theorem. The constitutive models were formulated by a heuristic process considering the essential mechanical properties of granular materials undergoing homogeneous deformation. A striking feature of hypoplasticity is that the constitutive equation is incrementally nonlinear in deformation rate. The hypoplastic models are capable of describing some salient properties of granular materials, e.g. non-linear stress-strain relationship, dilatant and contractant volumetric change, stress level dependence, density dependence and strain softening. A further feature of hypoplastic models is the inclusion of the critical states, i.e. states in which a grain aggregate can deform continuously at constant stress and volume (void ratio). In contrast to elasto-plastic models, a decomposition of deformation into elastic and plastic parts, the formulation of a yield surface, plastic potential, flow rule and hardening rule are not needed. The hypoplastic models were initially proposed for cohesionless soil. The hallmarks of these models are their simple formulation and procedure for determining material parameters with standard laboratory experiments. The material parameters can be related to the granulometric properties of granular materials, such as grain size distribution curve, shape, angularity and hardness of grains. A further advantage lies in the fact that one single set of material parameters is valid for a wide range of pressures and densities. Hypoplastic constitutive models without a characteristic

length cannot describe the scale effects associated with shear bands such as thickness and spacing of shear bands. A characteristic length can be introduced into hypoplasticity by means of the micro-polar, non-local and second-gradient theory. In this paper, a micro-polar theory is adopted [3], [4]. A micro-polar model makes use of rotations and couple stresses, which have clear physical meaning for granular materials.

3. FE-results

The analyses were carried out for a plane strain case and an axi-symmetric case. In the calculations, the symmetry axis was assumed. The pile was discretized with 200 triangular elements. The heap inclination to the bottom was assumed to be $\alpha=30^\circ$, which was equal to the critical internal friction angle of sand. The size of elements was not larger than $5 \times d_{50}$, which was sufficient to obtain mesh-independent numerical results.

The construction of the heap was simulated in 10 stages using two different methods, viz. the raining procedure and the funnel procedure. The sandpile was subject only to gravitational load in the vertical direction. The effect of the following parameters was investigated: a) construction method, b) mean grain diameter, c) base roughness, d) heap inclination and d) initial void ratio of sand.

4. Conclusions

A micro-polar hypoplastic constitutive model was used to study the stress distribution der the sandpile. The vertical stress distribution was dependent on the method of the heap construction, The stress increases monotonically up to the apex of the sandpile for the raining procedure. In turn, the stress showed a maximum beyond the heap mid-point for the funnel procedure. The stress distribution did not depend upon the initial void ratio, mean grain diameter, heap inclination and base roughness. The results were similar for prismatic and conical sandpiles.

The FE-results confirm the experimental results by Vanel et al. [1] and numerical results by Al Hattamleh et al. [5]. However, in contrast to the numerical results by Hattamleh et al. [5], no any additional condition (as orientation of initial slip lines) was imposed. The non-uniform distribution of the vertical normal stress beneath the sandpile during a funnel procedure was a natural numerical outcome.

5. References

- [1] L. Vanel, D. Howell, D. Clarck, R.P. Behringer and E. Clement (1999). Memories in sand: experimental test of construction history on stress distribution under sandpiles. *Physical Review E*, **60**, 5, R5040-R5043.
- [2] J. Tejchman and W. Wu (2008). FE-calculations of stress distribution under prismatic and conical sandpiles within hypoplasticity. *Granular Matter* (accepted for publication).
- [3] J. Tejchman and A. Niemunis (2006). FE-studies on shear localization in an anisotropic micro-polar hypoplastic granular material, *Granular Matter*, **8**, 3-4, 205-220.
- [4] J. Tejchman and W. Wu (2007). Modeling of textural anisotropy in granular materials with stochastic micro-polar hypoplasticity. *International Journal of Non-Linear Mechanics* **42**, 882–894.
- [5] O. Al Hattamleh, B. Muhunthan and H.M. Zbib (2005). Stress distribution in granular heaps using multi-slip formulation. *Int. Journal for Numerical and Analytical Methods in Geomechanics*, **29**, 713-727.

COMPARATIVE MODELING OF SHEAR LOCALIZATION IN GRANULAR BODIES USING A DISCRETE AND CONTINUUM APPROACH

J. Kozicki and J. Tejchman

Gdańsk University of Technology, Gdańsk, Poland

1. Introduction

The intention of this paper is to compare the calculation of shear localization in granular material by a discrete (DEM [1, 2]) and a continuum approach on the basis of the FEM and a micro-polar hypoplastic law [3].

The discrete element method [1, 2] treats a granular material as a system of particles which may be (or not) in many contacts. In this study, we used a so-called soft sphere approach with particles virtually overlapping when a contact occurs (Fig.1a). The contact force between two particles is decomposed into its normal and tangential part. The normal part takes into account an expression for the repulsive force. The tangential force involves dissipation due to different mechanisms of friction, i.e. from static friction through sliding to rolling friction. If all forces acting on a selected particle are known, the problem is reduced to the integration of the Newton's equations of motion for both translational and rotational degrees of freedom. To simulate grain roughness, the model takes into account a contact moment [2].

The DEM-calculations were carried out in co-operation with University of Grenoble, where the first author took part in the implementation of the Yade-Open DEM software [2].

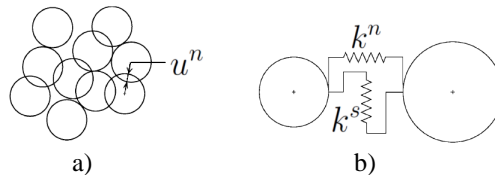


Figure 1: DEM: a) interaction between spherical discrete elements (u^n – overlap, shown bigger for clarity); b) elastic interaction between normal and shear springs (k_n, k_s - spring stiffness) [1]

In turn, the micro-polar constitutive law takes into account the effect of density, pressure, direction of deformation rate, mean grain size and grain roughness on the material behaviour [2]. Due to the presence of a characteristic length in the form of a mean grain diameter, the law can describe the formation of shear zones: their thickness and spacing, and the related size effect.

The comparative calculations of shear localization in granular bodies between DEM and FEM were performed for shearing in a direct shear tester [3], [4]. This tester is very popular in soil mechanics, used to determine important properties of granular and cohesive materials such as: drained strength envelope, angle of internal friction, wall friction angle and cohesion.

2. Discrete model DEM

The DEM method uses an explicit numerical scheme in which the interaction of particles is monitored ‘contact by contact’ with states of equilibrium. The resultant forces on any sphere are determined exclusively by its interaction with the spheres with which it is in contact. It is possible to follow a non-linear interaction of a large number of particles without excessive memory requirements or the need for an iterative procedure. The interaction force vector \vec{F} between two

spheres may be decomposed into a normal and a shear vector \bar{F}_i^n and $\Delta\bar{F}^s$ respectively, which may be classically linked to relative displacements through normal and tangential stiffness, k^n and k^s (Fig.1b). The normal contact force between two particles is governed by the normal contact overlap (Fig.1a), and the tangential contact force is related to the tangential displacement:

$$(1) \quad \bar{F}_i^n = k^n u^n \bar{n}_i, \quad \Delta\bar{F}^s = -k^s \Delta\bar{u}^s,$$

where u^n is the relative normal displacement between two elements, \bar{n}_i is the normal contact vector and $\Delta\bar{u}^s$ denotes the incremental tangential displacement. The shear force \bar{F}^s is obtained by summing the $\Delta\bar{F}^s$ - increments. The elastic moment M^L is created by the rolling part in a local set of axes L as (k^r - rolling stiffness):

$$(2) \quad \bar{M}^L = k^r \Theta_r^L,$$

where Θ_r^L is the angular vector of the rolling part. The tangential contact displacement depends on both the translations and rotations of contacting particles. A Mohr-Coulomb friction law determines the maximum value of the tangential contact force and the maximum tensile strength that a cohesive link can sustain [1].

Fig.2 shows the force distribution between spherical elements during a direct shear test under vertical pressure of 100 kPa. The granular specimen $20 \times 100 \text{ mm}^2$ included 10000 spherical elements with an average radius of 2 mm (the inter-particle friction coefficient was 0.5).

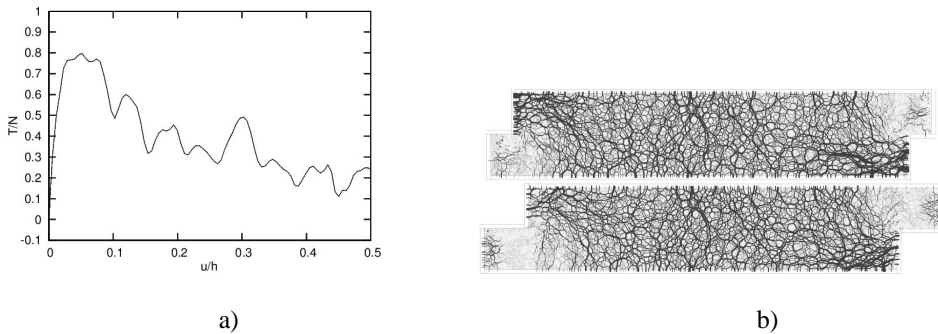


Fig. 2: DEM-results of direct shearing: a) ratio between shear and normal force versus normalized horizontal displacement, b) force distribution between spherical elements during shearing

3. References

- [1] F. V. Donze, S. A. Magnier, L. Daudeville, C. Mariotti and L. Davenne (1999). Study of the behavior of concrete at high strain rate compressions by a discrete element method, *Journal of Engineering Mechanics*, **125**, 10, 1154-1163.
- [2] J. Kozicki and F.V. Donzé (2008). Applying an open-source software for numerical simulations using finite element or discrete modelling methods, *Computer Methods in Applied Mechanics and Engineering* (submitted).
- [3] J. Tejchman and E. Bauer (2005). FE-simulations of a direct and a true simple shear test within a polar hypoplasticity. *Computers and Geotechnics* **21**,1, 1-16.
- [4] J. Kozicki and J. Tejchman (2007). Modelling of a direct shear test in granular bodies with a continuum and a discrete approach. *Proc. Int. Conf. Computer Methods in Mechanics CMM 2007*, Łódź.

SCALING LAWS OF DAMAGE-FAILURE TRANSITION IN ROCKS: FROM LABORATORY TESTS TO EARTHQUAKES

I. Panteleev¹, O. Plekhov¹, I. Pankov², A. Evseev², O. Naimark¹, V. Asanov²

¹*Institute of Continuous Media Mechanics of Russian Academy of Sciences, Perm, Russia.*

²*Mining Institute of Russian Academy of Sciences, Perm, Russia.*

1. General

Empirical observations showed that the earthquake events can be linked with dynamics of triggered slips at the top layer of the Earth crust on a wide range of spatial and temporal scales. These phenomena are characterized by the interaction of different mechanisms related to crack nucleation and propagation along numerous faults with pronounced friction properties of fault interfaces. The threshold character of earthquake events occurs due to the complexity of phenomena that have the features of self-organized criticality in the defect ensembles of different scales and can be analyzed under laboratory tests for damage-failure transitions in rocks. Statistical mechanics of mesodeflects and statistically based phenomenology allowed the consideration of dynamics of slip-block systems in the presence of noise for the interpretation of scaling laws in seismicity – the Gutenberg-Richter, Omori, Bath laws and the links of scaling laws in seismicity with new type of critical phenomena – structural-scaling transition.

The explanation of the self-criticality nature of seismic events (pre-shocks, main-shocks and aftershocks) is related to the self-similarity of scenario of damage-failure transition due to the subjection to dynamics of mesodect collective modes. It was shown that the evolution of characteristic types of collective modes (triggering waves and dissipative blow-up structures) reflect different scenario of the spinodal decomposition for qualitative different metastability of thermodynamic potential under transition of critical value of structural-scaling parameter. Since the problem concerning the representative volume for the study of scaling laws related to the earthquakes is one of the key questions the laboratory compression tests for the rocks combined with the analysis of acoustic emission data were performed.

The laboratory compression tests for gypsum and carnallite blocks combined with the acoustic emission data recording was realized and the correspondence of acoustic emission sequences to the Gutenberg and Omori laws was found.

2. Experimental conditions

Experimental study of scaling laws under damage-failure transition in salt rocks (Verchnekamskoe potash deposit) and gypsum rocks (the Novomoskovsk deposit) was carried in laboratory conditions. The cube specimens had characteristic sizes about 60 mm. The acoustic sequences in loaded salt rocks (silvinite, carnallite) and gypsum rocks were recorded under quasi-static uni-axial compression tests for relaxation and creep at room temperature using electromechanical testing machine Zwick 250. Vallen Amsy 5 system was used for the registration of acoustic emission signals using high-frequency VS2MP (350-2000 кГц) and low-frequency AE104A (50-400 KHz) gauges.

Sequences of acoustic events (AE) in laboratory test were identified as the sequences of seismic events under earthquakes. The magnitude was determined as amplitude of AE signal divided by its duration.

3. Experimental results

The correspondence of acoustic events in the laboratory test to the scaling laws under earthquakes was found according to the Gutenberg - Richter law for all investigated rocks in the frequency range 50-2000 kHz. Fig. 1.a represents the distribution of AE magnitudes under carnallite relaxation. The exponent value for different thresholds of recording equals 1.2. Fig.1.b reflects the data for AE amplitudes that is linear. Similar distributions were obtained for creep conditions.

The AE sequences during rock relaxation were considered as aftershock events. The distribution of AE obeys Omori law with exponent equals one.

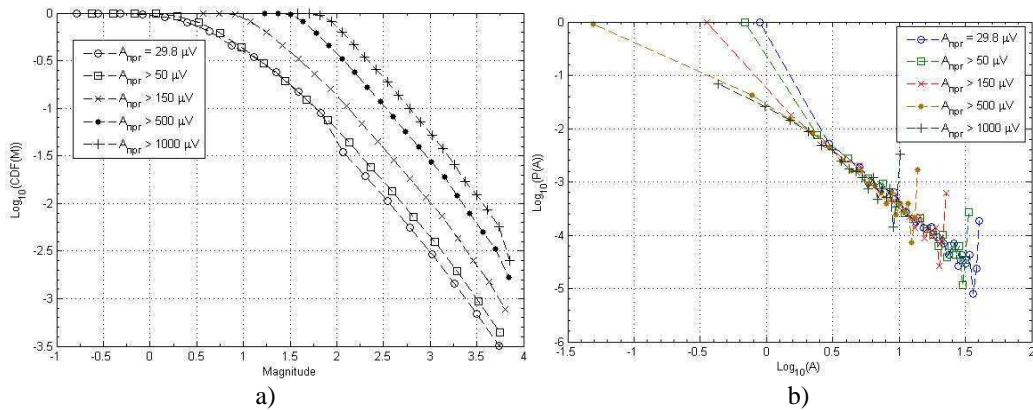


Fig.1. Gutenberg - Richter's law at 50-400 kHz spectral range under relaxation of carnallite. The curves correspond to different thresholds of recording (a). AE amplitude distribution for different thresholds of recording (b)

5. Acknowledgments

Work is executed at support of the Russian Foundation of Basic Research (grant № 07-05-96019 p_урал_a, № 07-01-91100-АФГИР_a).

PARAMETRIC STUDY OF GRADIENT-ENHANCED CAM-CLAY MODEL

A. Stankiewicz, J. Pamin

Cracow University of Technology, Cracow, Poland

1. General

In the paper the problem of instability and localization phenomena in two-phase granular medium (including the limiting cases of drained and undrained conditions) is considered. In the analysis the modified Cam-clay plasticity model in a gradient-enhanced version is used in order to avoid the spurious discretization sensitivity of finite element solutions. The main goal of the research is a parameter study of numerical solutions for selected problems. The sensitivity of the numerical results to the gradient influence parameter, to various drainage conditions, preconsolidation pressure and initial void ratio is focused on. The calculations are performed using the development version of the FEAP finite element package.

2. Material model

The yield function for the gradient-dependent modified Cam-clay model is written as [2]:

$$(1) \quad f(\boldsymbol{\sigma}, \Lambda, \nabla^2 \Lambda) = q^2 + M^2 p [p - p_c + g \nabla^2 \Lambda],$$

where $\boldsymbol{\sigma}$ is the effective stress tensor, Λ is the plastic multiplier, q is the equivalent deviatoric stress defined as $q = \sqrt{3J_2}$, M is a function of the internal friction angle ϕ : $M = \frac{6 \sin \phi}{3 - \sin \phi}$, p is the effective pressure acting on the soil skeleton, p_c is the current preconsolidation pressure. Finally, g is a positive gradient influence factor and the Laplacian $\nabla^2 \Lambda$ represents the nonlocal character of the model.

The attention is focused on fully saturated soil. The problem variables are the solid displacement vector \mathbf{u} and the water pore pressure p_f . Such a two-phase medium, with the assumption of incompressibility of solid grains, is governed by the following two equations [3, 4]:

$$(2) \quad \mathbf{L}^T \boldsymbol{\sigma}_t + \hat{\rho} \mathbf{g} = \mathbf{0},$$

$$(3) \quad \nabla^T \dot{\mathbf{u}} + \nabla^T \mathbf{v}_d + n \frac{\dot{p}_f}{K_f} = 0.$$

In eq. (2) \mathbf{L} is the differential operator matrix, $\boldsymbol{\sigma}_t = \boldsymbol{\sigma} - \boldsymbol{\Pi} p_f$ is the total stress, $\boldsymbol{\Pi} = [1, 1, 1, 0, 0, 0]^T$, $\hat{\rho} = (1 - n)\rho_s + n\rho_f$ is the saturated density of the solid-fluid mixture, n is the porosity, ρ_s - density of the solid phase, ρ_f - density of the fluid phase, \mathbf{g} - gravitation vector. In eq. (3) \mathbf{v}_d is the Darcy's fluid flow velocity given by $\mathbf{v}_d = -\mathbf{k} \nabla \frac{p_f}{\gamma_f}$, where \mathbf{k} is the permeability matrix, γ_f is the specific weight and K_f is the fluid bulk modulus. Porosity n and void ratio e are related by: $n = e/(1 + e)$.

The details of the formulation of the gradient model can be found in [2], including a discussion of other possible variants of the gradient-enhancement of the model. The finite element formulation for the gradient-enhanced two-phase material can be found in [1].

3. Numerical results

The aim of the paper is to analyse the sensitivity of the results to some material model parameters. In particular, different values of preconsolidation pressure p_c , gradient scaling factor g , initial void ratio e_0 or permeability coefficient k are taken into account.

The following example allows us to investigate the influence of the gradient scaling factor on the

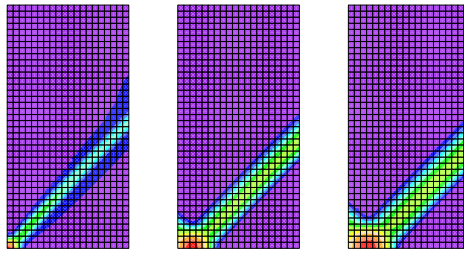


Figure 1. Equivalent plastic strain distribution for gradient scaling factor $g = 0.025 \text{ kN}^2/\text{m}^2$

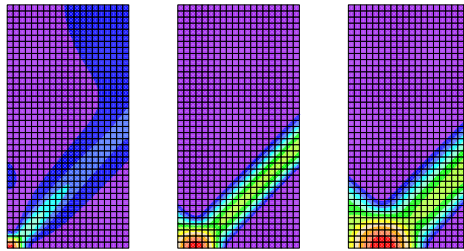


Figure 2. Equivalent plastic strain distribution for gradient scaling factor $g = 0.05 \text{ kN}^2/\text{m}^2$

results obtained in a biaxial compression test. The size of the specimen is $1\text{ m} \times 2\text{ m}$. The model is discretized with 20×40 finite elements. The following material data are adopted: Poisson's ratio $\nu = 0.2$, swelling index $\kappa = 0.013$, initial void ratio $e_0 = 1.0$, initial overconsolidation measure $p_{c0} = 1.0 \text{ MPa}$, compression index $\lambda = 0.032$, inclination of the critical state line $M = 1.1$. Two values of gradient constant g are considered: $g = 0.025 \text{ kN}^2/\text{m}^2$ and $g = 0.05 \text{ kN}^2/\text{m}^2$. Drained state is here assumed.

The diagram of the load-deformation relation (not included) shows that the solution for a larger value of g is a bit more ductile. In Figs 1- 2 the distribution of the equivalent plastic strain at various stages of numerical calculations is presented for the two values of g . We can observe that the shear bands evolve during the loading process. The width of the localization zone is different for the two considered cases and determined by the value of g . Finally, as the critical state is approached, the band width increases in both cases. This seems to be an unphysical outcome of the adopted form of regularization. To overcome this problem, the gradient factor g would must be made a (decreasing) function of a plastic strain measure (which physically means a reduction of non-locality as the critical state is approached). This option is now verified and the results will be presented at the conference together with the influence of the other mentioned material model parameters.

- [1] A. Stankiewicz and J. Pamin. Finite element analysis of fluid influence on instabilities in two-phase cam-clay plasticity model. *Computer Assisted Mechanics and Engineering Sciences*, 13(4):669–682, 2006.
- [2] A. Stankiewicz and J. Pamin. Gradient-enhanced Cam-clay model for strain localization in soil. *Foundations of Civil and Environmental Engineering*, 7:293–318, 2006.
- [3] A. Truty. On certain class of mixed and stabilized mixed finite element formulations for single and two-phase geomaterials. Technical Report Monograph 48, Cracow University of Technology, Cracow, 2002.
- [4] O.C. Zienkiewicz, A.H.C. Chan, M. Pastor, B.A. Schrefler, and T. Shiomi. *Computational Geomechanics*. John Wiley & Sons, Chichester, 2000.

UPDATE A SIMPLE HYPOPLASTIC CONSTITUTIVE MODEL

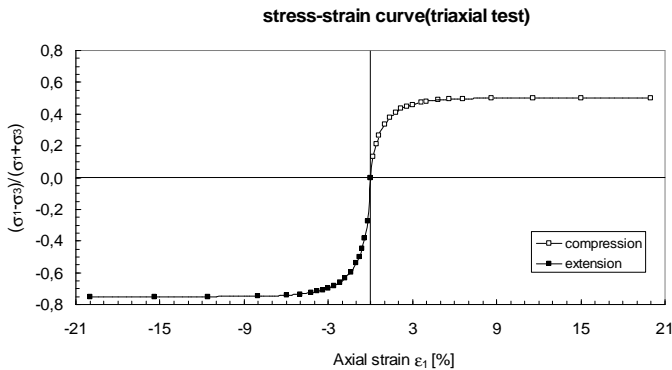
X.T.Wang¹, W. Wu¹, J. Tejchman²

¹ *Institute of Geotechnical Engineering, Universität für Bodenkultur, 1180 Vienna, Austria*

² *Civil and Environmental Engineering Department, Gdansk University of Technology, Gdansk, Poland*

Granular materials possess some fascinating properties such as strong nonlinearity, dilatancy and pressure dependence. The mechanical behaviour of granular materials is usually modeled by plasticity theory. Recently, hypoplastic constitutive models have emerged as an attractive alternative to the prevailing plasticity theory for granular materials. Compared to plasticity hypoplastic models have some distinct advantages, e.g. simple formulation and easy calibration. Some recent developments in hypoplastic models include the critical state and internal state variables.

The critical state is characterized by simultaneously vanishing stress rate and volume change. Most hypoplastic models contain four parameters, which are to be calibrated based on triaxial tests. Usually, the parameters are identified for critical state in triaxial compression. The behaviour for triaxial extension remains untouched. The model proposed by Wu and Bauer (1994) shows excessive contraction (volume reduction). In the present paper, this model is updated by including a new term into the constitutive model. In the updated model, critical state can be reached for all stress paths other than hydrostatic stress. Some well known failure surfaces, e.g. Matsuoka/Nakai and Lade, can be integrated into this model. The model performance is compared to some laboratory tests. Figure 1 shows the numerical simulation of triaxial compression and extension tests (with different dilatancy angles).



(a)

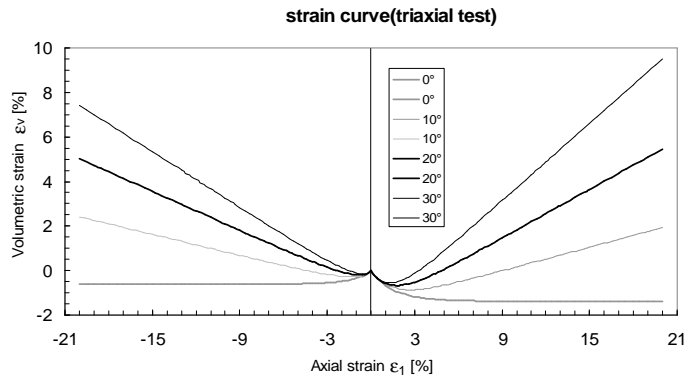


Figure 1. Numerical simulation of triaxial tests (with different dilatancy angles)

(a) stress ratio vs. axial strain; (b) volumetric strain vs. axial strain

- [1] Wu, W. and Bauer, E. (1994). A simple hypoplastic constitutive model for sand, *Int. J. Numer. Anal. Methods Geomech.*, 18: 833-862.
- [2] Wu, W. (1999). On a simple critical state model for sand, Proc. of the seventh Int. Symp. on Numerical Models in Geomechanics—NUMOG , Graz, Austria, Balkema, 47-52, 1999.
- [3] Wu, W., and Niemunis, A. (1996). Failure criterion, flow rule and dissipation function derived from hypoplasticity, *Mech. Cohesive-Frictional Mater.*, 1:145-163.

INCREMENTAL PLASTIC RESPONSE AND FLOW RULE POSTULATE UNDER GENERAL THREE-DIMENSIONAL CONDITIONS

M. Pinheiro and R. Wan

University of Calgary, Dept. of Civil Engineering, Calgary, Canada

1. Introduction

In this contribution we examine the flow rule postulate, a pillar assumption in the framework of the theory of plasticity that regards the direction of plastic strain increment as being independent of loading direction. Recent discrete element method and analytical calculations have pointed out that under three-dimensional (3D) stress conditions the direction of plastic strain increment does depend on the loading direction (Kishino, 2003, Darve and Nicot, 2005). These findings, which have not received much attention, question the validity of flow rule premise. In this respect, classic elastoplastic models based on this postulate will necessarily have shortcomings, especially in 'true' triaxial conditions. Through extensive numerical simulations using a particle flow model we verify that the incremental plastic strain response not only depends on the loading direction but also on stress history.

2. Methodology

Firstly, we analyze the incremental behaviour of a cubic assembly of polydispersed spherical particles subject to a series of 3D spherical stress probes ($\Delta\sigma_x, \Delta\sigma_y, \Delta\sigma_z$) with constant Euclidian norm of 0.1 kPa, see Figure 1a. Prior to the stress probing stage, the specimen was consolidated to 100 kPa, and then sheared along the triaxial extension stress path until the final state, corresponding to a mean stress (p) equal to 100 kPa and deviatoric stress (q) equal to 60 kPa, was achieved.

The plastic strain response under other stress state conditions reached from different stress histories (Figure 2a) prior to probe tests was subsequently investigated. One series of tests comprised of paths moving along the hydrostatic axis to $p = 100$ kPa, then radiating at various angles in the π -plane at constant value $q = 60$ kPa. Hence working within a sextant of the π -plane, various radial paths can be obtained starting from triaxial compression (TC) to triaxial extension (TE) passing through various Lode angles. Another series of tests refer to the classical conventional triaxial compression (CTC) and conventional triaxial extension (CTE) tests. In the former, the confining pressure is maintained constant with increasing axial stresses, whereas in the latter, the confining pressure is increased with constant axial stress.

3. Results

A typical strain envelope response generated from the stress probe introduced above is illustrated in Figures 1b-c. The outer (yellow) surface represents the 'total' strain incremental response, whereas the inner (orange) surface represents the elastic strain response. The (blue) dots inside are the increments of plastic strains. Differently from what the postulate of plastic flow rule assumes, the increments of plastic strain points do not fall on a single line. In fact, these increments turn out to be a function of both stress increment (probe) direction and stress state. As such, they plot as a series of points which clearly define an oval shaped envelope. Another intriguing fact is that all points fall on a plane very close to π -plane and perpendicular to the Rendulic plane (Figure 1c). Should the plane of plastic strain response coincide with π -plane in the incremental strain space, this would imply null plastic incremental volume change, that is, no dilatancy.

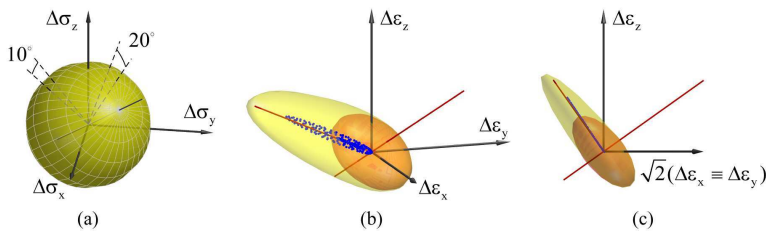


Figure 1. Spherical stress probe (a) Isometric view; (b) Total, elastic, and plastic strain envelope responses; (c) Rendulic plane view. Note: $\max(\Delta\varepsilon) = 1.24 \times 10^{-6}$.

The results from the series of probe tests under distinct loading histories given in Figure 2a are presented in Figures 2b-c. We found that the incremental plastic strain envelope is symmetric about the direction of the stress path prior to probe only in the TC, TE, CTC and CTE cases. For stress paths along Lode angles equal to 20° and 40° , there is a pronounced deviation of the plastic envelope with respect to the direction of previous stress history. This deviation is dictated by the proximity of the stress probes to the failure surface. As such, along the axisymmetric stress branches, the plastic strain response envelope is bound to be symmetrical about the radial or previous stress path direction as long as the failure envelope is symmetric or no inherent or induced anisotropy exists.

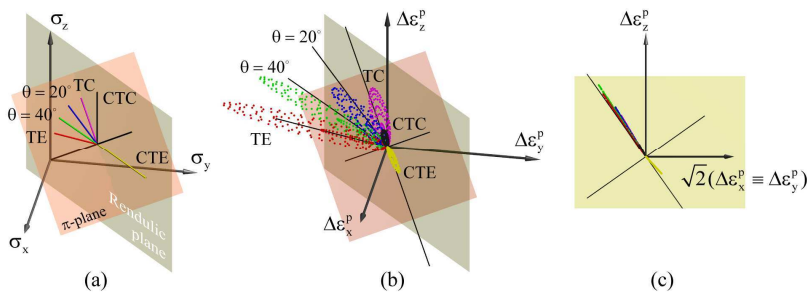


Figure 2. Stress histories prior to stress probe tests (a) Isometric view; (b) Plastic strain envelopes for different stress histories (b) Rendulic plane view.

3. Conclusion

Through discrete element analysis, we showed that plastic strain incremental response is a function of stress probing (loading) direction, as opposed to what the flow rule postulate presumes. For axisymmetric loading cases, the plastic strain envelope was found to be symmetrical about the direction of the stress path prior to probe. For ‘true’ triaxial stress paths a deviation apparently dictated by the proximity of the stress probes to the failure surface was noticed. Intriguingly, for a given spherical stress probe, all plastic response points fell on a unique plane, presumably associated with the zero eigenvector of the tangent constitutive matrix describing the stress increment/plastic strain increment map under plastic flow conditions.

4. References

- [1] Y. Kishino (2003). On the incremental non-linearity observed in a numerical model for granular media. *Italian Geotechnical J.*, **3**, 30-38.
- [2] F. Darve and F. Nicot (2005). On the flow rule in granular media: phenomenological and multi-scale views (Part II). *Intl. J. Num. Anal. Methods in Geomech.*, **29**, 1411-1432.

THREE-DIMENSIONAL DISCONTINUOUS DEFORMATION ANALYSIS (3-D DDA) COUPLED WITH FINITE ELEMENT METHOD

Q.H. Jiang¹, C.B. Zhou¹ and M.R. Yeung²

¹ *State Key Laboratory of Water Resources and Hydropower Engineering Science, Wuhan, China*

² *Civil Engineering Department, California State Polytechnic University, Pomona, CA, U.S.A.*

Discontinuous Deformation Analysis (DDA) originally proposed by Shi [1] is a two-dimensional numerical model for the statics and dynamics of discontinuous block system. DDA method is regarded as an alternative to the distinct element method (DEM) for the analysis of jointed rock masses. As one of the members of discrete numerical method families, DDA method is similar to DEM in the aspects of model-establishment for pre-processing and description of discrete blocks' contact. However, DDA method more closely parallels with FEM in solution techniques: (1) DDA method employs the displacement model similar to that of FEM, using one order polynomial or higher polynomial approximations; (2) it establishes the global equilibrium equation by minimizing the total potential energy; and (3) it uses the penalty functional method to force block elements to meet the restraint conditions of no-penetration and no-tension at the block contact interfaces.

With many people contributing to its development and applications, the original 2-D DDA has been well developed in terms of both theory and computer coding, e.g. [2]. In recent years, DDA has been also extended to three-dimensional. However, only some preliminary work on this subject has been published. Using complete one order polynomial approximations, Shi [3] presented some basic formulae of 3-D DDA. Jiang and Yeung [4] developed a model of point-to-face contact as a part of the contact theory for 3-D DDA. Because one order polynomial displacement functions are assumed, so the stresses and strains within a block element in the model are constant. The approximations preclude the application of this algorithm to the problems with significant stress variations within the block.

In this paper, a numerical model that coupled 3-D DDA with finite element method is developed. The displacement field and the stress field are solved by proper internal discretization of deformable blocks using finite element meshes. The contacts between the deformable blocks are modelling by DDA algorithm. By minimizing the total potential energy, the global equilibrium equations of the coupling method are established. The stiffness matrix, the initial stress matrix, the loading matrix, the inertia matrix, displacement resistance matrix, the contact matrix and friction force matrix are derived and added to the global equations. The coupling model can not only describe the deformability of generally shaped polyhedral blocks but also solve such movement forms as sliding and opening along block boundaries, having the advantages of both DEM and FEM.

This coupling model has also been implemented into a DDA-FEM computer program. The program can divided the distinct blocks into tetrahedral elements automatically and the users can also adjust the mesh density to satisfy demand. The problem of interaction of the concrete foundation and the elastic base is analyzed to illustrate the application of the proposed method. As shown in Figure 1, the calculational model is consist of two blocks. The material constants for the concrete foundation are: Young's modulus $E=300MPa$, Poisson's ratio $\nu=0.17$ and density $\rho=2800kg/m^3$. The material constants for the elastic base are: Young's modulus $E=2MPa$, Poisson's ratio $\nu=0.25$ and density $\rho=2000kg/m^3$. The properties for contact interface between the concrete foundation and the base are: friction angle $\phi=30^\circ$, cohesion $C=1KPa$, tensile strength $T=5KPa$. The bottom boundary and four side boundaries of the base are fixed in their respective normal directions. Besides the self-weight loading, a uniformly distributed loading $q=100KPa$ is acted on the top boundary of the concrete foundation. Figure 2 shows the settlement deformation of the elastic base (the displacements are magnified to 10 times), and Figure 3 shows the normal contact forces distribution on the interface

between the concrete foundation and the base. Obviously, the normal contact forces are concentrated at the corner of the interface.

In conclusion, the coupling method which incorporates a finite element mesh into the distinct blocks is a significant development in DDA. It not only overcomes the difficulties of using a simple constant strain concept to represent deformations of geometrically complex blocks, but also provides a platform for developing algorithms for progressive failure of rockmass structures.

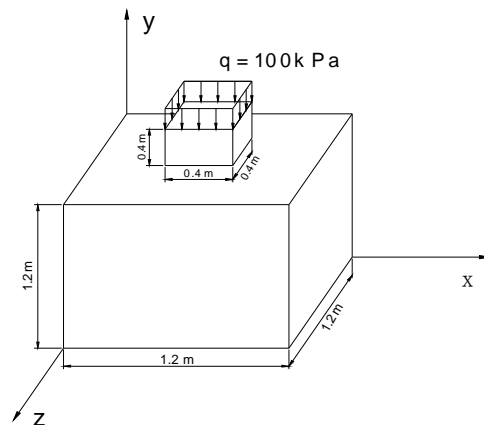


Fig.1. Interaction of the concrete foundation and the elastic base

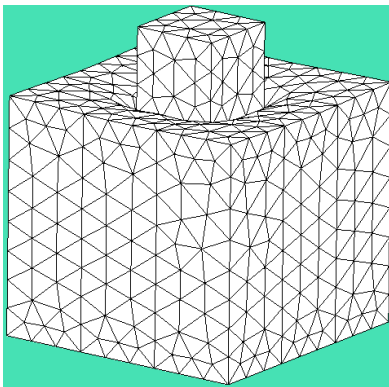


Fig.2. Settlement deformation of the base

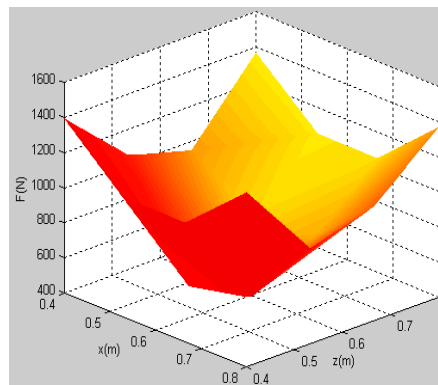


Fig.3. Normal contact forces distribution

References

- [1] G.H. Shi (1988). *Discontinuous deformation analysis-a new numerical model for the statics and dynamics of block system*, Ph.D. Thesis, Department of civil Engineering, University of California, Berkeley
- [2] C.T. Lin, B. Amadei, J. Jung, J.Dwyer (1996). Extensions of discontinuous deformation analysis for jointed rock masses, *Int J Rock Mech Min Sci*; 33, 671-694.
- [3] G.H. Shi (2001). Theory and examples of three dimensional discontinuous deformation analyses, *Proceedings of the 2nd Asian Rock Mechanics Symposium*, Beijing, China, p. 27-32.
- [4] Q.H. Jiang and M.R. Yeung (2004). A model of point-to-face contact for three-dimensional discontinuous deformation analysis, *Rock Mech and Rock Eng.*, 37, 95-116.

PRE-FAILURE BEHAVIOUR OF GRANULAR SOILS

A. Sawicki and W. Świdziński

Institute of Hydro-Engineering, Gdańsk, Poland

The aim of this presentation is to study the pre-failure behaviour of granular soils, both dry and water saturated in undrained conditions. The starting point to the analysis is extensive set of experimental data obtained from triaxial compression tests, performed in a modern apparatus that enables measurement of lateral strains. The experiments were performed for various initial states of samples, i.e. loose or dense and contractive or dilative, and for various loading paths. The results of experiments are presented in the form of stress-strain curves or the effective stress paths in the case of saturated soils, tested in undrained conditions. The experiments have confirmed that there exists, in the effective stress space, the object designated as the instability line which has interesting properties. For example, in the case of initially dilative dry soils or saturated, but tested in drained conditions, the sample first compacts when sheared and after approaching the instability line the process of dilation begins. The behaviour of initially contractive samples is different as the shearing causes only compaction, so the instability line cannot be detected during such experiments. More interesting behaviour can be seen during the undrained tests, because the instability line corresponds to the maximum shear stress that can be supported by initially contractive soil. After reaching this line by the effective stress paths, the shearing stress rapidly decreases and the sample liquefies, i.e. it behaves macroscopically as a liquid. This process is accompanied by the increase of pore pressure and reduction of the mean effective stress. The undrained behaviour of initially dilative samples is similar before the effective stress paths approaches the instability line, and then becomes different as the pore pressure begins to decrease and subsequently the mean effective stress begins to increase. As a result of this behaviour, the dilative samples can support higher shear stresses, and eventually may fail if the effective stress path reaches the Coulomb-Mohr surface.

The important aspect of the analysis presented is the distinction between the initially contractive and dilative states of granular soils, which is different from traditional classification on the initially loose and dense samples. The combination of two following parameters decides whether this initial state is dilative or contractive, namely: e = void ratio and p' = mean effective stress. These parameters define the point in the space $\log p' - e$, where is also defined the object designated as instability line. The contractive soils correspond to the points lying above the instability line, and the dilative to those below. At present, the only method of determination of the instability line is based on many experiments, which unfortunately cannot be performed easily in a standard geotechnical laboratory. We show such results obtained for the model "Skarpa" sand.

The second part of presentation deals with theoretical description of the experimental results obtained. The first attempts dealt with application of some elasto-plastic and hypoplastic models of soils, but the results were not promising. Therefore, it was decided to apply the most straightforward approach, that is based on empirical description of the soil behaviour for some simple stress paths, and then on generalization of the obtained equations for arbitrary stress paths. Obviously, the basic constitutive equations should be formulated in the incremental form, as the soil behaviour is path dependent. For the triaxial configuration considered, the following shape of these equations is proposed:

$$d\varepsilon_v = Mdp' + Ndq,$$

$$d\varepsilon_q = Pdp' + Qdq,$$

where: p' = mean effective stress; q = stress deviator; ε_v = volumetric strain; ε_q = deviatoric strain;

M , N , P and Q = some functions depending on the effective stress invariants, and perhaps on some other variables.

The functions M , N , P and Q appearing in these equations were determined experimentally for some simple stress paths, as isotropic loading and pure shearing at constant mean effective stress. The shape of these functions is different for loading and unloading, and in some cases different for initially contractive and dilative soils. These processes have been defined separately for the spherical and deviatoric parts of the stress and strain tensors, and this definition is different from that widely applied in elasto-plastic modeling of materials, not to mention hypoplasticity. The important problem of loading and unloading is also discussed in this presentation.

The functions M , N , P and Q were determined for dry soils or saturated but in free draining conditions. The empirical model was verified using the data for the stress paths, in drained conditions, different from those used in the calibration of the model. We have also used the data obtained from undrained tests in order to verify the model. The comparison of the model predictions with experimental data seems to be quite good.

The approach presented is an alternative to commonly applied elasto-plastic models of soils, which are often distant from the behaviour of real materials. We have been trying to find the way to describe the real behaviour of granular soils, which could be useful in practical applications, and which is consistent with the experimentally observed behaviour of these materials.

References

- [1] A. Sawicki (2003). Cam-clay approach to modeling pre-failure behaviour of sand against experimental data, *Archives of Hydro-Engineering and Environmental Mechanics*, **50**, 3, 239-249.
- [2] A. Sawicki (2007). A study on pre-failure deformations of granular soils, *Archives of Hydro-Engineering and Environmental Mechanics*, **54**, 3, 183-206.
- [3] A. Sawicki & W. Świdziński (2007). Drained against undrained behaviour of sand, *Archives of Hydro-Engineering and Environmental Mechanics*, **54**, 3, 207-222.
- [4] W. Świdziński (2006): *Mechanisms of Compaction and Liquefaction of Granular Soils (in Polish)*, IBW PAN Editorial House, Gdańsk, pp. 265.

SIMULATION OF ROCK CUTTING WITH EVALUATION OF TOOL WEAR

J. Rojek

Institute of Fundamental Technological Research, Warsaw, Poland

1. Introduction

High tool wear can be one of the main problems in rock cutting works [3]. Changes of tool geometry due to wear lead to difficulties in the tool penetration reducing thus cutting performance. Practical observations show that Different wear mechanisms can occur in rock cutting. Abrasive wear is one of the most important mechanisms in cutting of hard rocks especially in the presence of quartzite. Scraping of the rock surface leads to high temperatures, which softens the tool tip, resulting in increasing wear of adhesive character. Different wear mechanisms can act in parallel.

The main motivation of the research work presented in this paper is development of the numerical model increasing possibilities to predict abrasive and adhesive wear of rock cutting tools under different process conditions.

2. Numerical model of rock cutting with wear evaluation

In the approach adopted the wear is evaluated based on the simulation of rock cutting process. Evaluation of wear requires determination of forces of cutting as well as temperature distribution. This means necessity to analyse rock cutting as a thermo-mechanical process.

A numerical model of the tool-rock system allowing us to simulate a process of rock cutting has been developed within the framework of the discrete element method (DEM) [2]. In this model the tool is considered rigid and a rock material is represented as a collection of rigid spherical (in 3D) or cylindrical (in 2D) particles interacting among themselves with contact forces. The cohesive elastic perfectly brittle model is assumed for the contact interaction.

The translational and rotational motion of rigid spherical or cylindrical elements (particles) is governed by the standard equations of rigid body dynamics. For the i -th element we have

$$(1) \quad m_i \ddot{\mathbf{u}}_i = \mathbf{F}_i, \quad I_i \dot{\boldsymbol{\omega}}_i = \mathbf{M}_i,$$

where \mathbf{u} is the element centroid displacement in a fixed (inertial) coordinate frame \mathbf{X} , $\boldsymbol{\omega}$ – the angular velocity, m – the element mass, I – the moment of inertia, \mathbf{F} – the resultant force, and \mathbf{M} – the resultant moment about the central axes.

Thermal phenomena during rock cutting (heat absorption and conduction) are described by the heat balance equation, which for a single particle can be written in the following form:

$$(2) \quad m_i c \dot{T}_i = Q_i,$$

where: m_i – particle mass, c – specific heat, T_i – particle temperature, Q_i – heat flux.

Thermo-mechanical coupled problem defined by Eqs. (1) and (2) is solved using the staggered solution scheme. The two problems are coupled by heat generation process – heat generated by friction is evaluated in the solution of mechanical problem and passed to the solution of thermal problem.

The tool-rock interaction is modelled assuming Coulomb friction model extended on frictional heat generation and wear accumulation on the tool surface. Wear is considered using the classical formula of Archard [1]:

$$(3) \quad \dot{w} = k \frac{p_n v_T}{H},$$

where \dot{w} is the wear rate, p_n – the contact pressure, v_T – the slip velocity, H – the hardness of worn surface and k is a dimensionless wear parameter. The influence of temperature on wear is accounted for by taking the hardness as a function of temperature $H = H(T)$. The tool shape can be modified according to the accumulated wear obtained by integration of Eq. (3).

Values of wear constants k for different combinations of materials can be determined in laboratory tests. Wear is a relatively slow process and it can be observed after many work cycles. In the numerical algorithm developed wear is accelerated using scaled wear constants.

3. Numerical results

Simulation of rock cutting with one pick of a roadheader has been analysed using a model shown in Fig. 1a. Material sample is represented by an assembly of randomly compacted 92000 discs of radii 1–1.5 mm. Model parameters for sandstone have been determined for the discrete element model [2]. Thermomechanical analysis with wear evaluation has been carried out. Results of the analysis are shown in Figs. 1b-c. Failure of rock during cutting is shown in Fig. 1b. Temperature distribution in the tool and rock is shown in Fig. 1c, the highest temperature is observed in the contact zones, where the frictional heat is generated. The same area has maximum wear amounts as it is shown in Fig. 1d.

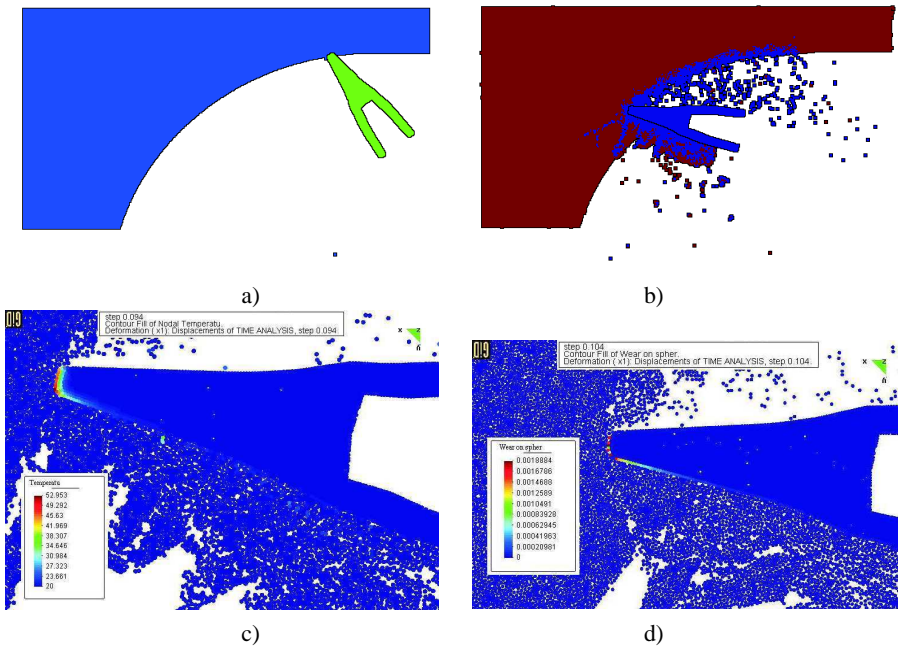


Figure 1. Simulation of rock cutting by a pick of a road header: a) numerical model, b) failure mode, c) map of temperature, d) accumulated wear on the tool surface

References

- [1] J.F. Archard. Contact and rubbing of flat surfaces. *J. Appl. Phys.*, 24(8):981–988, 1953.
- [2] J. Rojek. *Modelling and simulation of complex problems of nonlinear mechanics using the finite and discrete element methods* (in Polish). Habilitation Thesis, Institute of Fundamental Technological Research Polish Academy of Sciences, Warsaw, 2007.
- [3] P.N.W. Verhoef. *Wear of rock cutting tools*. Balkema, Rotterdam, 1997.

FE-SIMULATIONS OF SIZE EFFECTS IN GRANULAR AND QUASI-BRITTLE MATERIALS

J. Górski, J. Bobiński and J. Tejchman
Gdańsk University of Technology,
Gdańsk, Poland

1. Introduction

One of the most important properties of the behaviour of many engineering materials is a size effect phenomenon, i.e. experimental results vary with the size of the specimen [1]. Thus, the results from laboratory tests which are scaled versions of the actual structures cannot be directly transferred to them. Two main size effects can be defined: deterministic (energetic) and statistical. The first one is caused by strain localization which cannot be appropriately scaled during laboratory tests. Thus, the specimen strength increases with increasing ratio l_0/L (l_0 – characteristic length of microstructure influencing both the thickness and spacing of strain localization, L – specimen size). This feature is strongly influenced by the pressure level in granular bodies; i.e. shear resistance and dilatancy decrease with increasing pressure. A statistical effect (called also a stochastic effect) is caused by the spatial variability/randomness of local material strength. According to the Weibull's theory (Weibull 1951), this effect is caused by weak spots whose amount usually grows with increasing specimen size. Thus, the specimen strength diminishes with increasing specimen size. Up to now, the size effects are still not taken into account in the specifications of most of design codes for engineering structures. The understanding of the physical mechanism of a size effects is of a major importance for civil engineers who are forced to extrapolate experimental outcomes at the laboratory scale to results which can be used in real situations. Since large specimens or structures are far beyond the range of testing in laboratories, their design has to rely on a realistic extrapolation of testing results with small specimens or structures.

2. Size effects in granular bodies

The size effects in granular bodies were investigated with plane strain footings on sand. To describe a mechanical behaviour of a cohesionless granular material during a monotonous deformation path, a micro-polar hypoplastic constitutive model was used. Non-polar hypoplastic constitutive models formulated at the Karlsruhe University describe the evolution of the effective stress tensor depending on the current void ratio, stress state and rate of deformation by isotropic non-linear tensorial functions obtained according to the representation theorem. The constitutive models were formulated by a heuristic process considering the essential mechanical properties of granular materials undergoing homogeneous deformation. A striking feature of hypoplasticity is that the constitutive equation is incrementally linear in deformation rate. The hypoplastic models are capable of describing a number of significant properties of granular materials: non-linear stress-strain relationship, dilatant and contractant volumetric change, stress level dependence, density dependence and material softening. A further feature of hypoplastic models is the inclusion of critical states, i.e. states in which a grain aggregate can deform continuously be deformed at constant stress and a constant volume. In contrast to elasto-plastic models, a decomposition of deformation components into elastic and plastic parts, the formulation of a yield surface, plastic potential, flow rule and hardening rule are not needed. The hallmark of these models are their simple formulation and procedure for determining material parameters with standard laboratory experiments. A further advantage lies in the fact that one single set of material parameters is valid for a wide range of pressures and densities. Hypoplastic constitutive models without a characteristic length can describe only realistically the onset of shear localization, but not its formation. A characteristic length can be introduced into hypoplasticity by

means of a micro-polar, non-local and second-gradient theory. In this paper, a micro-polar theory was adopted [2]. A micro-polar model makes use of rotations and couple stresses which have clear physical meaning for granular materials. The rotations can be observed during shearing and but remain negligible during homogeneous deformation. The presence of the couple stresses gives rise to a non-symmetry of the stress tensor and a presence of a characteristic length.

In the paper, a deterministic (energetic) and statistical size effect were carefully analysed [2], [3]. The deterministic calculations were carried out with an uniform distribution of the initial void ratio for 3 different footing's widths. The numerical results with respect to the load-displacement curve and strain localization were compared with corresponding laboratory tests at Tokyo University [5]. Various properties of granular bodies may be considered as random. In the present work, only the initial void ratio was of primary interest. To investigate a statistical size effect, the distribution of the initial void ratio was assumed to be spatially correlated. In order to reduce the number of realizations without losing the accuracy of the calculations, a Latin hypercube method was applied. Initially, truncated Gaussian random fields were generated in a granular specimen using a conditional rejection method [3] for a weakly and strongly correlated random fields and a large and low standard deviation.

3. Size effects in brittle materials

The size effects were investigated in concrete elements subject to uniaxial tension or bending. The analysis was carried out with a finite element method based on an elasto-plastic crack model with non-local softening [6]. A linear Drucker-Prager criterion with an isotropic hardening and softening and a non-associated flow rule was defined in a compressive regime, and a Rankine criterion with an isotropic softening and an associated flow rule was adopted in a tensile regime. To ensure the mesh-independence, to capture properly localized zones and to investigate a deterministic size effect, both criteria were enhanced in a softening regime by a characteristic length of micro-structure with the aid of a non-local theory [6]. The deterministic calculations were carried out with different specimen sizes. They were confronted with corresponding experimental results (e.g. [7]). In the statistical calculations, the tensile strength of concrete was assumed to be random (spatially correlated). In order to reduce the number of realizations without losing the accuracy of the calculations, a Latin hypercube method was again applied.

4. References

- [1] Z. Bazant and J. Planas (1998). *Fracture and size effect in concrete and other quasi-brittle materials*. CRC Press LLC.
- [2] J. Tejchman and W. Wu (2007). Modeling of textural anisotropy in granular materials with micro-polar hypoplasticity. *International Journal of Non-Linear Mechanics* **42**, 882–894.
- [3] J. Tejchman and J. Górski (2008). Deterministic and statistical size effect during shearing of granular layer within a micro-polar hypoplasticity. *Int. Journal for Numerical and Analytical Methods in Geomechanics*, doi: 10.1002/nag.617.
- [4] J. Tejchman and J. Górski, J. (2008). Computations of size effects in granular bodies within micro-polar hypoplasticity during plane strain compression. *Int. Journal for Solids and Structures*, doi: 10.1016/j.ijsolstr.2007.10.007.
- [5] F. Tatsuoaka, S. Goto, T. Tanaka, K. Tani and Y. Kimura (1997). Particle size effects on bearing capacity of footing on granular materials. *Deformation and Progressive Failure in Geomechanics* (eds.: A. Asaoka, T. Adachi, F. Oka), 133-138.
- [6] T. Majewski, J. Bobinski and J. Tejchman (2008). FE-analysis of failure behaviour of reinforced concrete columns under eccentric compression. *Engineering Structures*, doi: 10.1016/j.engstruct.2007.03.024.
- [7] C. Le Bellego, J.F. Dube, G. Pijaudier-Cabot and B. Gerard (2003). Calibration of nonlocal damage model from size effect tests. *E. J. Mechanics A/Solids* **22**, 33-46.

IDENTIFICATION OF DAMPING IN SOIL BY MEANS OF MORLET WAVELETS

B. Wrana

Institute of Structural Mechanics, Faculty of Civil Engineering, Cracow University of Technology, Warszawska 24, 31-155 Kraków

1. Introduction

Most of the common methods for experimental determination of the damping parameters use the proportional damping assumption. The equations of motion for free vibration of a viscously damped linear discrete system with N degrees of freedom can be written as

$$\mathbf{M}\mathbf{y}(t) + \mathbf{C}\mathbf{y}(t) + \mathbf{K}\mathbf{y}(t) = \mathbf{0}, \quad (1)$$

where \mathbf{M} , \mathbf{C} and \mathbf{K} are $N \times N$ mass, damping and stiffness matrices, respectively, and $\mathbf{y}(t)$ is the $N \times 1$ vector of the generalized co-ordinates.

A typical procedure can be described to determination of damping by used modal method [1]:

1. Measure a set of transfer functions $H_{ij}(\omega)$ at a set of grid points on the structure.
2. Obtain the natural frequencies ω_k by a pole-fitting method.
3. Evaluate the modal half-power bandwidth $\Delta\omega_k$ from the frequency response functions, then the Q -factor $Q_k = \omega_k / \Delta\omega_k$ and the modal damping factor $\xi_k = 1/2Q_k$.
4. Determine the modal amplitude factors a_k to obtain the mode shapes, \mathbf{z}_k .
5. Finally, reconstruct some transfer functions to verify the accuracy of the evaluated parameters.

Such a procedure does not provide reliable information about the nature or spatial distribution of the damping, though the reconstructed transfer functions may match the measured ones well.

Methods to attempt to obtain the viscous damping matrix from the experimental measurements can be divided into two basic categories: (a) damping identification from modal testing and analysis [2], and (b) direct damping identification from the forced response measurements [3]. All these methods are based on the assumption that the damping mechanism of the structure is viscous, and their efficiency when the damping mechanism is not viscous is largely unexplored. In a soil damping depends on a strain values, and is proportional for a small strain and non-proportional for a large strain (see Fig. 1).

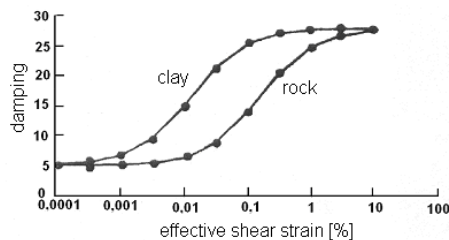


Fig. 1. Damping in a soil

2. Damping calculation by wavelet transformation

As a consequence of the windowing applied by the Gaussian function in the Morlet wavelet, the bandwidth of the resulting wavelet instantaneous spectra are larger than their Fourier equivalent. This gives the appearance of a larger value of effective damping in the signal, the extent of which depends on the scale analyzed. Consider the Morlet wavelet expression the half-power bandwidth

can be used to provide a simple measure of the bandwidth of wavelet spectra [4,5]. Assuming symmetry of the spectral peak, the HPBW is then defined as the difference between these two frequencies: $B_r = f_2 - f_1$, with the frequency corresponding to the spectral peak taken as the natural frequency of the system. Due to the multi-resolution nature of wavelets, wavelet spectra broaden toward the higher frequencies, but for a narrowbanded spectrum, the assumption of symmetry can be retained. Therefore, the scale at which this half-power bandwidth is evaluated should be the scale defining the ridge of the transform, at which the signal energy is focused. Damping coefficient in HPBW method is defined as:

$$\xi = \frac{B_r}{f_1 + f_2} \cdot 100. \quad (2)$$

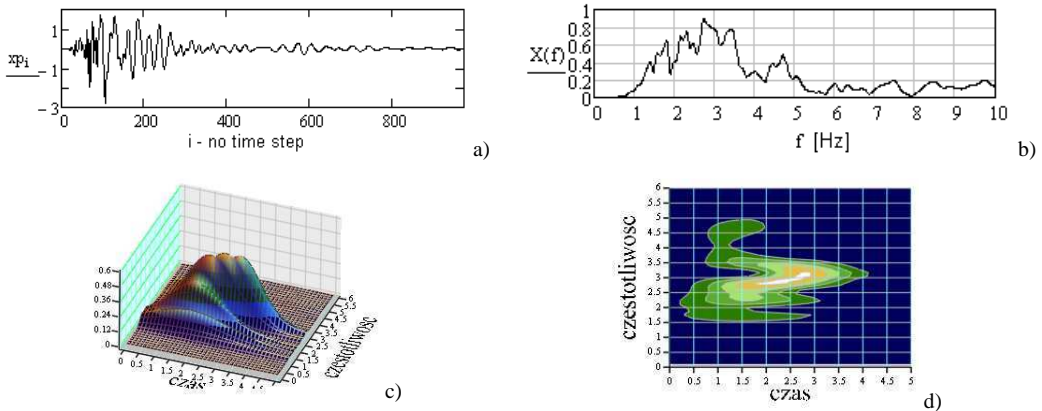


Fig. 2. Damping calculation by HPBW method: a) acceleration in time in horizontal direction, b) Fourier transformation, c), d) wavelet map with Morlet wavelets function,

3. Example of damping calculation by wavelet transformation

We consider a problem of damping calculation base on the measurement date of the Szombierki mine crump. Fig. 2a shows the measurement data in time. Damping according to eq. (2) are shown in table 1.

Table 1.

f [Hz]	1.7	2.2	2.7	3.0	3.2
ξ [%]	27.7	9.8	11.2	9.1	8.6

4. References

- [1] Adhikari S., Woodhouse J.: Identification of damping: Part 1, Viscous damping, *Journal of Sound and Vibration*, Vol. 243(1), 2001, pp. 43-61.
- [2] Alvin K. F., Peterson L. D., Park K. C.: Extraction of normal modes and full modal damping from complex modal parameters. *American Institute of Aeronautics and Astronautics Journal*, Vol. 35, 1997, pp. 1187-1194.
- [3] Baruch M.: Identification of the damping matrix. Technical Report 1AE No. 803, Technion, *Israel Faculty of Aerospace Engineering, Israel Institute of Technology*, Haifa, 1997.
- [4] Wrana B., Ruchała P.: Identification of Damping by Means of Wavelets in Intelligent Structures, *3rd International Congress on Intelligent Building Systems InBus 2004*, Cracow University of Technology, 2004, pp. 249-254.
- [5] Wrana B., Ruchała P.: Application of Wavelets to Identification of Damping of Structures, *Proceeding of CMM-2005 Computer Methods in Mechanics*, Częstochowa 2005.

COMPARISON OF WALL PRESSURES MEASURED IN THE MODEL SILO WITH DEM SIMULATION

R. Balevičius¹, R. Kačianauskas¹, Z. Mróz² and I. Sielamowicz³

¹*Technical University, Vilnius, Lithuania*

²*Institute of Fundamental Technological Research, Warsaw, Poland*

³*Technical University, Białystok, Poland*

1. Introduction

Wall stresses are very important parameter in processes run in silos and tanks. DEM method appeared to be a very useful numerical tool in simulation of granular materials [1]. The paper presents the comparison of measured wall stresses exerted by 20,400 pea grains with DEM simulation in the model of silo by the DEMMAT code [2]. Two sensors of 55 mm in diameter were placed on the lateral wall and wall stresses were registered.

2. Filling process

Figure 1 shows the initial state of the experiment before filling the model. The measurements were registered by two sensors – one placed 5.5 cm above the bottom and the second placed 11.5 cm above the bottom.

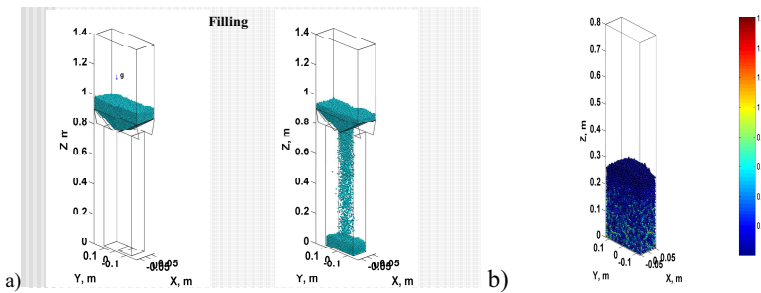


Figure 1. Initial state, a) filling the model, b) after filling.

3. Experimental measurements of wall stresses.

Figure 2 presents the registered wall stresses in the model by sensor 1 and sensor 2.

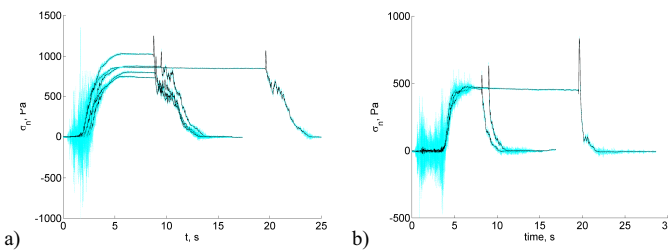


Figure.2 Experimental measurements of wall stresses during filling, storage, discharge by, a) sensor 1, b) sensor 2.

Figure 3 presents the comparison of experimental results of wall stresses with the numerical model for the filling state.

4. Wall stresses. Filling state.

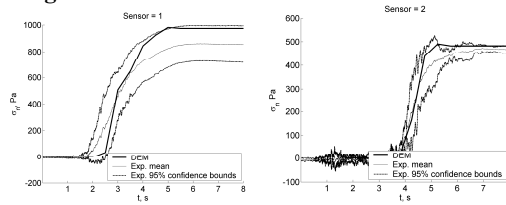


Figure 3. Comparison of the measured wall stresses with DEM for, a) sensor 1, b) sensor 2. Filling state. DEM simulation of wall stresses in filling state is presented in Figure 4.

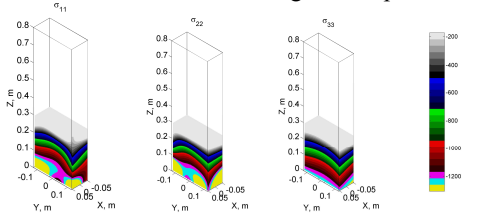


Figure 4. DEM simulation of wall stresses in the model.

5. Wall stresses. Discharge state.

Comparison of the experimental results registered by two sensors during the discharge state with DEM simulation is presented in Figure 5.

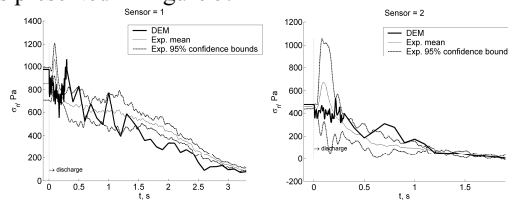


Figure 5. Discharge state of the grains. DEM simulation compared with the experiments.

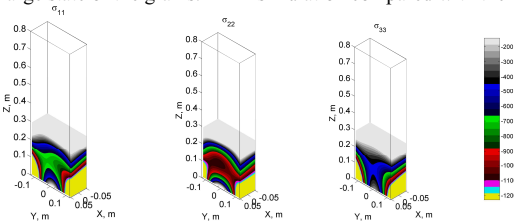


Figure 6. Wall stresses by DEM simulation.

6. Conclusions

The numerical model of DEM gave a good fit to the experimental results. Numerical model does not exceed the confidence bounds that means that the numerical model predicts the values of wall stresses in a proper way.

7. References

- [1] P.A. Cundall, O.D.L. Strack (1979) *A discrete numerical model for granular assemblies*. Geotechnique, 29, 47-65
- [2] R. Balevičius, R. Kačianauskas, R. Džiugys, A. Maknickas, A. Vislavičius (2005) *DEMMAAT code for numerical simulation of multi-particle dynamics*. Information Technology and Control 34(1): 71-78

THEORY OF ELASTICITY AT THE NANO-SCALE

H.L. Duan^{1,2}, J. Wang² and B.L. Karihaloo³

¹*Institut für Nanotechnologie, Forschungszentrum Karlsruhe GmbH, 76021 Karlsruhe, Germany*

²*LTCS and College of Engineering, Peking University, Beijing 100871, P. R. China*

³*School of Engineering, Cardiff University, Queen's Buildings, The Parade, Cardiff CF24 3AA, UK*

1. Abstract

We have shown in a series of recent papers that the classical theory of thermo-elasticity can be extended to the nano-scale by supplementing the equations of thermo-elasticity for the bulk material with the generalised Young-Laplace equations of surface elasticity. This talk will describe how this has been done in order to capture the often unusual thermo-mechanical and physical properties of nano-structured particulate and porous materials.

It will begin with a description of the generalised Young-Laplace equations for surface elasticity. We will then describe how the classical Eshelby formalism can be generalised to nano-inhomogeneities; unlike its classical counterpart the Eshelby tensor now depends on the size of the nano-inhomogeneity and the location of the material point in it. We will demonstrate its application on the calculation of the stress concentration factor of a spherical nano-void. We will next derive the Eshelby tensor for nano-particles consisting of a core surrounded by multiple outer shells. These multi-shell particles are used as novel functional materials as well as stiffeners/tougheners in conventional composites and nano-composites. In these nano-heterogeneous particles, the mismatch of thermal expansion coefficients and lattice constants between neighbouring shells induces stress/strain fields in the core and shells, which in turn affect the physical/mechanical properties of the particles themselves and/or of the composites containing them. We will apply this solution to obtain the strain fields in quantum dots (QDs) with multi-shell structures and in alloyed QDs induced by the mismatch in the lattice constants of the atomic species.

The next part of the talk will address the generalisation of the micro-mechanical framework for determining the effective elastic properties and effective coefficients of thermal expansion of heterogeneous solids containing nano-inhomogeneities. We will use this generalised framework to calculate the effective elastic constants of nano-porous/cellular materials. It will be shown, in particular that these can be made to exceed those of the parent materials provided the pore surface elastic parameters satisfy certain conditions. These stiff nano-porous materials herald a radical breakthrough in sandwich-type construction. We will also use the generalised framework to study the thermo-elastic properties of heterogeneous materials containing spherical particles or cylindrical fibres. The interface between the matrix and second phase inhomogeneity is imperfect with either the displacement or the stress experiencing a jump across it. We will relate the effective coefficient of thermal expansion (CTE) to the effective elastic moduli and thereby generalise Levin's formula, and reveal two connections among the effective elastic moduli, thereby generalising Hill's connections. In contrast to the classical results, the effective CTE in the presence of an imperfect interface will be shown to be strongly dependent on the size of the inhomogeneity, besides the interface elastic and thermo-elastic properties.

The talk will end with the introduction of scaling laws governing the properties of nano-structured materials. The underlying cause of the size-dependence of these properties at the nano-scale is the competition between surface and bulk energies. These laws provide a yardstick for checking the accuracy of experimentally measured or numerically computed properties of nano-structured materials

over a broad size range and can thus help replace repeated and exhaustive testing by one or a few tests.

2. References

- [1] H.L. Duan and B.L. Karihaloo (2007). Thermo-elastic properties of heterogeneous materials with imperfect interfaces: Generalized Levin's formula and Hill's connections, *J. Mech. Phys. Solids*, **55**, 1036-1052.
- [2] H.L. Duan, B.L. Karihaloo, J. Wang and X. Yi (2006a). Strain distributions in nano-onions with uniform and non-uniform compositions, *Nanotech.*, **17**, 3380-3387.
- [3] H.L. Duan, B.L. Karihaloo, J. Wang and X. Yi (2006b). Compatible composition profiles and critical sizes of alloyed quantum dots, *Phys. Rev. B*, **74**, 195328-1-4.
- [4] H.L. Duan, J. Wang, Z.P. Huang and B.L. Karihaloo (2005a). Eshelby formalism for nano-inhomogeneities, *Proc. Roy. Soc. Lond. A*, **461**, 3335-3353.
- [5] H.L. Duan, J. Wang, Z.P. Huang and B.L. Karihaloo (2005b). Size-dependent effective elastic constants of solids containing nano-inhomogeneities with interface stress, *J. Mech. Phys. Solids*, **53**, 1574-1596.
- [6] H.L. Duan, J. Wang, B.L. Karihaloo and Z.P. Huang (2006c). Nanoporous materials can be made stiffer than non-porous counterparts by surface modification, *Acta Mater.*, **54**, 2983-2990.
- [7] J. Wang, H.L. Duan, Z.P. Huang and B.L. Karihaloo (2006). A scaling law for properties of nano-structured materials, *Proc. Roy. Soc. Lond. A*, **462**, 1355-1363.
- [8] J. Wang, H.L. Duan and B.L. Karihaloo (2007). Nano-mechanics or how to extend continuum mechanics to nanoscale, *Bull. Pol. Acad. Sci.*, **55**, 133-140.
- [9] X. Yi, H.L. Duan, B.L. Karihaloo and J. Wang (2007). Eshelby formalism for multi-shell nano-inhomogeneities, *Archives of Mech.*, **59**, 259-282.
- [10] H.L. Duan, J. Wang and B.L. Karihaloo, Theory of elasticity at the nano-scale, *Adv. Appl. Mech.*, (in press).

DISLOCATIONS IN ATOMISTIC/CONTINUUM MODELLING OF SEMICONDUCTOR STRUCTURES

Paweł Dłużewski

Instytut Podstawowych Problemów Techniki PAN, Warszawa

Dislocations and interfacial structures formed by different chemical components of crystal lattice result the residual stresses and coupled physical fields. The fields are crucial for understanding the conditions in which the semiconductor devices grow up and work. The question is: why, in some cases, the growth results the flat layers while in others the channels, clusters, quantum dots, nanowires and other geometric objects nucleate. Such complex technological problems of crystal growth compose a new challenge for computer modelling.

In the present paper, the atomistic model with dislocations and interfacial layers of crystal lattice is embedded in a 3D finite element mesh. Thanks to such a multiscale approach the tensor fields (residual stresses, electric fields, concentration gradients of chemical and electronic elements) sharing the model of crystal lattice can be considered both in the FE and molecular methods. The advantages of such approach is shown in examples.

In the first example, we consider the GaN/AlN Quantum Dots (QDs) nucleated at the edge of threading dislocations (TDs), see Fig. 1. This phenomenon was observed first by Rouviere et al. [1]. It was caused by the fact that TDs induce local tension in certain regions of crystal lattice. This, in turn, gives the preferable geometric condition for nucleation of QDs.

Concerning the FE part, as an example, we consider the interdiffusion induced by the residual stresses and chemical potential force in semiconductor layers. The constitutive equations are based on the transport of chemical components induced by the gradient of residual stresses [GPa/nm] and chemical potentials [2,3].

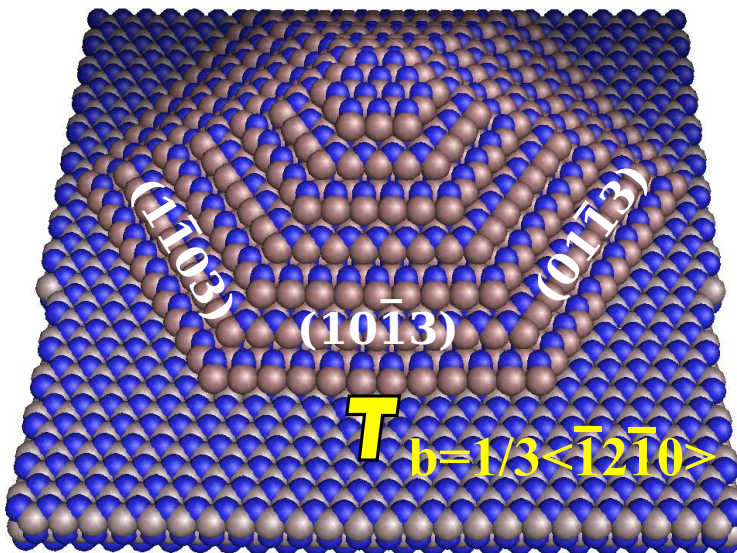


Figure 1. Atomistic model of GaN quantum dot formed on the border of edge dislocation piercing AlN layer.

Concerning the atomistic part, a 3D atomic model of a system of QDs situated on the edges of threading dislocations is considered. The resultant chemical segregation obtained from our FE simulation is next reconstructed at the atomic scale.

In the next example, the residual stresses, piezoelectric field and optoelectronic properties of QDs are considered by using the nonlinear FE method. As the input data we assume the geometry of the observed hexagonal pyramid-shape QDs [1]. Our finite element constitutive equations are based on the nonlinear anisotropic hyperelasticity [5] where the interaction with electric field is incorporated. The composition and pressure dependence of the elastic constants of AlGaIn alloys have been determined from ab-initio calculations.

At the first step the piezoelectric FE problem for QDs situated at the edge of TDs is solved. The different piezoelectric coefficients and spontaneous polarization are used for the QD and the host matrix. Finally, using the such derived electrostatic potential and stress distribution, the optical matrix elements of the QDs are calculated within the framework of k·p perturbation theory. The influence of dislocation on the properties of QDs are discussed [6].

REFERENCES

- [1] P. J. L. Rouviere, J. Simon, N. Pelekanos, B. Daudin, and G. Feuillet, Preferential nucleation of GaN quantum dots at the edge of AlN threading dislocations”. *Appl. Phys. Letters* **75**, 2632, 1999.
- [2] P. Dłużewski, Nonlinear field theory of stress induced diffusion and mass transport. *Defect and Diffusion Forum* **264**, 63-70, 2007.
- [3] P. Dłużewski, A. Belkadi, J. Chen, P. Ruterana and G. Nouet, “FE simulation of InGaIn QD formation at the edge of threading dislocation in GaN”. *Phys. Stat. Sol. (c)* **7**, 2403-2406, 2007.
- [5] P. Dłużewski, *J. Elasticity* **60**, Nr. 2, 2000, pp. 119-129.
- [6] S. P. Łepkowski, G. Jurczak, J. Majewski, *Phys. Rev. B* **72** 245201 (2005).

A SUBSTRATE EFFECT OF HARDNESS IN FILM/SUBSTRATE INDENTATION: FINITE ELEMENT STUDY ON ‘OVERSHOOT’ PHENOMENON OF HARDNESS

N. Chiba¹, N. Ogasawara¹, C.R. Anghel¹ and X. Chen²

¹ National Defense Academy, Yokosuka, Japan

² Columbia University, New York, USA

1. Introduction

Nanoindentation tests are used as a means to determine the mechanical properties of small sized materials from the measured force-depth curves, specifically to extract the elastoplastic properties of thin film deposited on the substrate. For this purpose, the quantities of the thin film must be decoupled from those of the substrate, and it is important to understand how the substrate influences the entire indentation process. We have carried out extensive finite element (FE) simulations on this indentation problem and found a new phenomenon. The measured hardness *overshot* the substrate hardness in a certain combination of the elastoplastic properties of the film and the substrate materials.

2. Computational method

The specimen, consisting of a semi-infinite substrate with a thin film deposited on it, is indented by a sharp conical indenter, as shown in Fig. 1. The thickness of the film is denoted by d , and half apex angle of the conical indenter, θ ($\theta = 70.3^\circ$). We assume that those two materials are homogeneous and their uniaxial stress-strain (σ - ε) relations obey a power-law form:

$$(1) \quad \sigma = E\varepsilon \quad \text{for} \quad \varepsilon \leq Y/E \quad \text{and} \quad \sigma = R\varepsilon^n \quad \text{for} \quad \varepsilon \geq Y/E,$$

where E and Y are Young's modulus and yield strength, respectively, and n is the work-hardening exponent with $R = Y(E/Y)^n$.

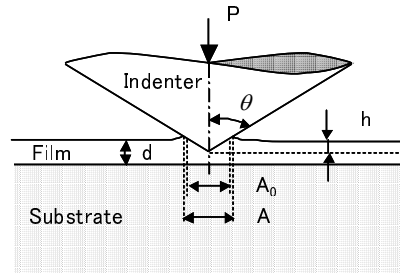


Fig. 1. Schematic of conical indentation on film/substrate specimen.

When the specimen is of a homogeneous bulk, i.e., both the film and substrate materials are identical, the relation between the force P and the indentation depth h is described by a quadratic law: $P = Ch^2$. Here the loading curvature C is a constant during the indentation, which is determined by the material properties and the indentation angle θ . When the specimen is made of two layers (Fig. 1), however, C no longer remains constant, and varies as a function of depth h , namely $C(h)$. The modified loading curvature $C(h)$ is then defined by the following relation and satisfies latter two conditions:

$$(2) \quad C(h) = P/h^2, \quad C(h) \rightarrow C_f \quad \text{when} \quad h/d \rightarrow 0, \quad \text{and} \quad C(h) \rightarrow C_s \quad \text{when} \quad h/d \gg 1.$$

Here, subscripts f and s mean that the specimen is made of bulk film material and of bulk substrate material, respectively. Indentation hardness H is given by the definition:

$$(3) \quad H = P/A, \quad A = A_0 = 24.5 h^2,$$

where A and A_0 represent true projected contact area and nominal contact area, respectively. In this study A_0 is used in place of A to calculate the hardness. This means that both pile-up and sink-in effects of the indented material are ignored.

3. Combination of material properties and calculated results

We have carried out elastoplastic axisymmetric FE calculations with ANSYS, for the material properties and their combinations, shown in Table 1, where ν means Poisson's ratio of the material.

Table 1. Material properties used in the analysis.

Case	Film				Substrate				H_f/H_s
	E (GPa)	ν	Y (GPa)	n	E (GPa)	ν	Y (GPa)	n	
A	410	0.25	4.0	0.0					0.675
B	410	0.25	4.0	0.2	470	0.25	7.0	0.0	0.838
C	410	0.25	2.0	0.5					0.931
D	410	0.25	2.5	0.5					1.008

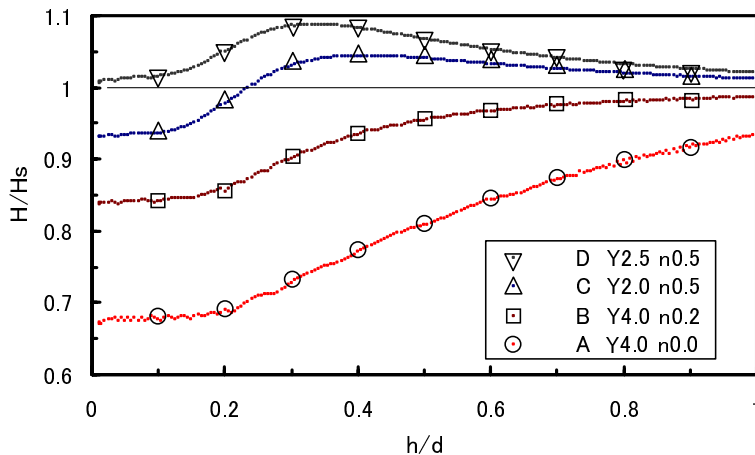


Fig. 2. Relative hardness H/H_s as a function of relative indentation depth h/d .

Calculated results are shown in Fig. 2 for the four cases shown in Table 1. In the cases of A and B, the relative hardness H/H_s remains almost constant at their own hardness of film H_f , in a relatively small depth range ($h/d < 0.2$). It then monotonically increases with increasing depth, and finally converges to H_s ($H/H_s \rightarrow 1$). The behavior is very different in cases C and D, where $H_f \approx H_s$. In these two cases, starting from H_f , the hardness is observed to overshoot both values of H_f and H_s with increasing depth before converging to H_s . Then, a question arises: why has this overshoot phenomenon not been observed or reported previously? We can think of the following two reasons: (1) The combination of material properties of C or D has not been tried in hardness tests yet, or (2) the overshoot quantity is no greater than 10 % of the hardness (H_s), and therefore, easy to be overlooked.

ATOMIC-CONTINUUM EQUIVALENCE: ATOMIC STRAIN TENSOR

R. Pyrz¹ and B. Bochenek²

¹ *Aalborg University, Aalborg, Denmark*

² *Cracow University of Technology, Cracow, Poland*

1. Introduction

The most frequently used form for the stress at atomic level is based upon the Clausius virial theorem, which determines the stress field applied to the surface of a fixed volume containing interacting particles (atoms). The virial stress includes the mass and velocity of atoms, which describes the fact that mass transfer causes mechanical stress to be applied on the surfaces external to an atomic system, as well as it includes pair-wise interatomic forces and atomic positions. It has been shown that the virial stress cannot be directly related to the classical Cauchy stress and several modifications have been proposed [1, 2]. It is essential to recognize that the stress at the location of an atom depends on the details of the interatomic interactions and the positions of interacting neighbours. Hence, the atomic stress is a non-local function of the state of the matter at all points in some vicinity of the reference atom, in contrast to the local stress field used in classical continuum theories.

It seems that the relationship between local displacements of atoms and the strain tensor is not as ambiguous as the concept of atomic stress. Position of atoms is readily available from almost all molecular simulation algorithms and the atom displacement can be easily assessed. Strain measure is a relative quantity and one needs two configurations, the reference and the present, in order to define the local atomic strain. The atomic strain should provide detailed local information about kinematics of the atom in relation to its neighbours and the true test of the atomic strain concept is how well it approximates total strain of the simulation cell by summing local atomic strains over all atoms present in the system. In the best case this sum should be equal or very close to the total strain calculated from boundary conditions of the simulation cell. The atomic strain tensor was calculated in [3] to better understand changes in local structure. However, it has not been determined whether or not the sum of local atomic strains corresponds to the total deformation of the simulation cell when loaded by external forces.

In this work we describe an atomic strain measure related to the transformation matrix between two deformation states. This measure is further modified in order to take into account nonaffine deformations taking place in molecular disordered systems. Localized areas of nonaffine deformations indicate non-elastic response which evolves during loading [4].

2. Atomic strain measure and analysis

The atomic strain will be defined in terms of Voronoi tessellation. The atoms are assumed to be in their equilibrium positions, and thermal vibrations are averaged. The Voronoi polyhedron around central atom is composed of a set of sub-polyhedrons (interaction cells) whose number is determined by a number of neighbours to the central atom. During motion, the Voronoi polyhedron associated with the atom changes its shape. The interaction cell is defined for each pair consisted of a central atom and its neighbors. It is a part of Voronoi polyhedron that contains points situated closer to this pair of points than to any other. It is build of two sub-polyhedrons (parts of polyhedron surrounding a central point and a neighboring point) having common face. This is a unique region for which it can be assumed that it is influenced only by these points.

The atomic strain is defined through the deformation gradient that is calculated by minimizing the sum of squared separation distances between neighbouring atoms and subsequently weighted by corresponding polyhedra [5].

As an example, molecular modeling and strain calculations has been performed on CNT-polypropylene nanocomposite. At first, the system is constructed and subject to energy minimization using Polak-Ribiere conjugate gradient method. Molecular dynamics simulation is performed next using NTP ensemble in order to obtain an equilibrium state, which simultaneously serves as a reference state. The nanocomposite has been subject to uniaxial tension along the nanotube axis and the analysis has been performed for nine deformation steps with equilibration runs after each step. The total atomic strain of the system resembles very closely the strain of the simulation cell calculated from boundary conditions. For instance, the strain from boundary conditions is 0.0185 at third loading step whereas atomic strain gives 0.0179.

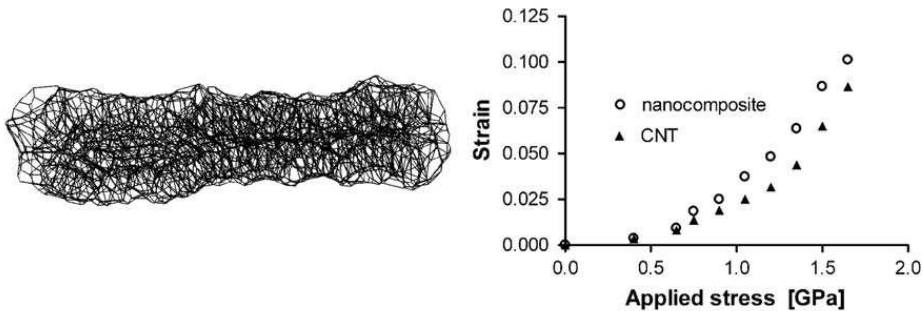


Figure 1. Voronoi tessellation of CNT at third step of deformation and evolution of the total CNT strain as compared to the total nanocomposite strain.

Figure 1 shows Voronoi tessellation only for atoms belonging to carbon nanotube at third loading step and the evolution of CNT total strain during loading history. The nanotube strain follows the strain of nanocomposite to a certain loading level and then lags after it as loading of the nanocomposite increases. This is clear evidence that we need to deal with an interfacial sliding. A detailed analysis atom by atom would be necessary to disclose and characterize an atomic nature of interfacial debonding.

3. Conclusion

The most important conclusion to emerge from present investigation is that atomic strain concept based on the construction of Voronoi cells provides means to bridge molecular and continuum length scales. This concept will be illustrated further with other examples comprising slippage of functional nanowires at interfaces in polymer based nanocomposites and cohesive fracture phenomena at interfaces.

References

- [1] M. Zhou (2003), A new look at the atomic level virial stress: on continuum-molecular system equivalence, *Proc. R. Soc. Lond. A* **459**, 2347-2392.
- [2] J.A. Zimmerman, E.B. Webb III, J.J. Hoyt, R.E. Jones, P.A. Klein and D.J. Baumann (2004), Calculation of stress in atomic simulation, *Modelling Simul. Mater.Sci. Eng.* **12**, 319-332.
- [3] P.H. Mott, A.S. Argon and U.W. Suter (1992), The atomic strain tensor, *J. Comp. Phys.*, **101**, 140-150.
- [4] D.A. Head, A.J. Levine and F.C. Macintosh (2005), Mechanical response of semiflexible networks to localized perturbations, *Phys. Rev. E*, **72**, 061914-1.
- [5] R. Pyrz and B. Bochenek (2007), Discrete-continuum transition at interfaces of nanocomposites, *Bull. Pol. Ac.: Tech.*, **55**, 1-10.

BRIDGING LENGTH-SCALE IN CONTINUUM DISLOCATION THEORY

K.C. Le, D. Kochmann and P. Sembiring

*Lehrstuhl für Allgemeine Mechanik, Ruhr-Universität Bochum,
D-44780 Bochum, Germany*

Within the framework of continuum dislocation theory the plane-strain constrained shear of a single and bicrystal strip is analyzed. For the single crystal strip we consider the single and double slip systems oriented at different angles to the direction of shear. For bicrystal strip the main assumption is that each crystal layer has only one active slip system. These slip systems are oriented differently with respect to the direction of shear. We also assume that both crystal layers are elastically isotropic and have the same elastic moduli. At the grain boundary the displacements and the tractions must be continuous. Besides, the dislocations cannot penetrate the grain boundary. The problem is to determine the displacements and the plastic distortion as functions of the given overall shear strain.

Our aim is twofold. First, we are going to find the solution in closed analytical form for the single crystal with one active slip system and with symmetric double slip systems, and for the bicrystal in the symmetric case (twins). If the dissipation can be neglected, then dislocations appear to minimize the total energy of crystal. Due to the specific form of the energy of dislocation network which is proportional to the dislocation density for small densities, we show that there is an energetic threshold for the dislocation nucleation. If the shear strain exceeds this threshold, geometrically necessary dislocations appear and pile up near the grain and phase boundaries leading to the material hardening. From the obtained solution we can compute the contribution of the geometrically necessary dislocations to the energy of grain and phase boundaries. If, in contrary, the dissipation due to the resistance to the dislocation motion is essential, the energy minimization should be replaced by the flow rule. The solution exhibits the dissipative threshold for dislocation nucleation, the Bauschinger translational work hardening, and the size effect. Our second aim is to develop the numerical procedure for the solution of this problem in the case where the active slip systems are not symmetric. The agreement between the numerical and analytical solution for the special case of symmetry will justify the correctness of developed numerical procedure.

A MIGRATION RECRYSTALLIZATION MODEL FOR POLAR ICE

R.Staroszczyk

Institute of Hydro-Engineering, Polish Academy of Sciences, Gdańsk, Poland

Ice core samples drilled from depth in a polar ice sheet reveal strong anisotropic fabrics, shown by significant re-alignment of initially randomly oriented individual ice crystals (Gow *et al.* [1], Thorsteinsson *et al.* [2]). Progressive re-orientation of crystal *c*-axes (the axes of crystal hexagonal symmetry), taking place in the material in its response to current local strain and stress situations as ice particles descend from the free surface to depth, gives rise to considerable changes in ice macroscopic viscosities on different shear planes. The main micro-process that is responsible for the development of the oriented structure of the polar ice is the crystal lattice rotation due to the dislocation glide on the crystal basal planes. This process, present throughout the whole descent of the ice from the free surface to depth, but the effects of which are most pronounced in the upper half of a glacier, leads—in the absence of other micro-mechanisms—to very strong fabrics, with the majority of the crystal *c*-axes clustered along the vertical.

Beside the above lattice rotation mechanism, polar ice is also subject to recrystallization processes which have, or may have, effect on the directional properties of the material. One such a mechanism, the so-called normal crystal growth process, has no influence on the macroscopic anisotropy of ice. The other mechanism, known as the *rotational recrystallization* (or polygonization), is most active in the middle part of an ice sheet, and leads to the nucleation of new grains, the orientations of which are very close to those of existing grains (the latter do not disappear). Therefore, the macroscopic result of this mechanism is only a slight modification of the anisotropic properties of ice. As ice particles, during their descent, enter the bottom part of a glacier and approach its base, another recrystallization process becomes increasingly active, due to which the structure of ice changes dramatically, as evidenced by multi-maxima fabrics, with very coarse and interlocking grains, found near the glacier base (Duval and Castelnau [3], De La Chapelle [4]). Such a process, known as the *migration recrystallization*, is caused by rapid migration of grain boundaries between deformed and dislocation-free crystals, and leads to the nucleation of new grains at the expense of old ones (which ultimately disappear). Not all the factors which initiate and control the migration recrystallization mechanism have been identified yet, but it seems that the most important among them are: high, i.e. near-melting temperature, high strains, strain-rates and stresses, with some role also played by the bed topography. The macroscopic outcome of the above process is a significant weakening, and sometimes a complete destruction, of the strong anisotropy that has developed at earlier stages of the ice descent through a glacier. Thus, this process has a crucial effect on the overall flow of polar ice sheets, since the latter deform mainly by shearing in near-base regions.

To date only few theoretical attempts have been made to describe the process of migration recrystallization. These include a discrete-grain model by Van der Veen and Whillans [5], a cellular automata model by Křitárev *et al.* [6], a phenomenological model by Staroszczyk and Morland [7], and a formulation by Morland [8] in which the process is described by means of a temperature-dependent critical lattice-distortion parameter.

In this paper a discrete-grain model is constructed, in which the phenomenon of migration recrystallization is modelled by extending an earlier theory by Staroszczyk [9]. In that theory, based on the Taylor-Voigt approximation of a uniform velocity gradient within a polycrystalline aggregate, the macroscopic behaviour of ice is derived by a simple average of the responses of a finite number of discrete grains representing the polycrystal. A single crystal of ice is treated as a transversely isotropic and incompressible body, the behaviour of which is assumed to be viscous. The response of

a crystal is described by a constitutive law that involves three viscosity parameters defining different shear resistances in different glide directions.

Now the model is extended by incorporating into it the migration recrystallization mechanism. It is assumed that recrystallized are those crystals in an aggregate which are most stressed. Hence, a parameter is introduced to define a critical level of the deviatoric stress invariant, and it is supposed that a given crystal starts to recrystallize once the critical magnitude of this invariant has been reached in the crystal. A new grain is nucleated from that undergoing recrystallization in a smooth manner (in existing models it is usually assumed that the process occurs abruptly), and the orientation of this new grain is chosen in a way that is most favourable for its microscopic deformation by creep (that is, a newly formed grain is least stressed in a current macroscopic stress/strain configuration).

The model predictions are illustrated by the results of numerical simulations carried out for sustained uniaxial compression and simple shear, showing the evolution of the oriented structure of the material. Further, the variation of instantaneous macroscopic viscosities with increasing strains for different magnitudes of the critical stresses triggering the process of migration recrystallization is illustrated, displaying such features as the occurrence of *recrystallization waves*, or showing an example in which the viscosity in uni-axial compression becomes, due to the recrystallization, less than that of an isotropic sample (without the recrystallization involved the axial viscosity increases with the deformation). The latter feature has been known from experiments, but has not been predicted yet by any of the theoretical recrystallization models available so far.

References

- [1] A. J. Gow, D. A. Meese, R. B. Alley, J. J. Fitzpatrick, S. Anandakrishnan, G. A. Woods, and B. C Elder (1997). Physical and structural properties of the Greenland Ice Sheet Project 2 ice core: A review. *J. Geophys. Res.*, **102** (C12), 26,559–26,575.
- [2] T. Thorsteinsson, J. Kipfstuhl, and H. Miller (1997). Textures and fabrics in the GRIP ice core. *J. Geophys. Res.*, **102** (C12), 26,583–26,599.
- [3] P. Duval and O. Castelnau (1995). Dynamic recrystallization of ice in polar ice sheets. *J. Phys. IV*, **5** (C3), 197–205.
- [4] S. De La Chapelle, O. Castelnau, V. Lipenkov, and P. Duval (1998). Dynamic recrystallization and texture development in ice as revealed by the study of deep ice cores in Antarctica and Greenland. *J. Geophys. Res.*, **103** (B3), 5091–5105.
- [5] C. J. Van der Veen and I. M. Whillans (1994). Development of fabric in ice. *Cold Reg. Sci. Technol.*, **22** (2), 171–195.
- [6] D. Kitiarev, G. Gödert, and K. Hutter (2002). Cellular automaton model for recrystallization, fabric, and texture development in polar ice. *J. Geophys. Res.*, **107** (B8), EPM 5.
- [7] R. Staroszczyk and L. W. Morland (2001). Strengthening and weakening of induced anisotropy in polar ice. *Proc. R. Soc. Lond., A* **457** (2014), 2419–2440.
- [8] L. W. Morland (2002). Influence of lattice distortion on fabric evolution in polar ice. *Continuum Mech. Thermodyn.*, **14** (1), 9–24.
- [9] R. Staroszczyk (2002). A uniform strain, discrete-grain model for evolving anisotropy of polycrystalline ice. *Arch. Mech.*, **54** (2), 103–126.

THE ENERGY APPROACH TO DETERMINING PLASTIC DEFORMATION OF METAL CRYSTALS

M. Kurza and H. Petryk

Institute of Fundamental Technological Research, Warsaw, Poland

1. Introduction

Non-uniqueness of active slip systems selection in the rate-independent theory of single crystal plasticity represents a well-known difficulty, and different methods have been proposed in the literature to overcome it. The method used in this paper is based on the energy criterion of path stability. The main concept is that a stable deformation path corresponds to step-by-step minimization of the incremental energy supply under prescribed kinematic constraints and under certain symmetry restrictions imposed on the constitutive law. A novel feature of the present approach is that the minimization is simultaneously performed with respect to shear increments on all slip systems and to the deformation gradient components that are left unconstrained. In particular, if only the overall deformation gradient is prescribed, either fully or partially, then the energetically preferable deformation pattern in a crystal can be nonuniform and lead to deformation banding and microstructure formation. A respective computational algorithm for large elastoplastic deformations of metal single crystals has been developed and used to simulate typical tests like uniaxial tension and channel-die compression.

2. Minimization of incremental energy supply

A general description of the incremental energy minimization approach can be found in [1]. The following minimization problem is examined

$$(1) \quad \Delta E \rightarrow \min \quad \text{subject to kinematical constraints}$$

where ΔE is the increment in energy to be supplied from external sources to the mechanical system, consisting of the deformed body and the loading device, in order to produce quasi-statically a deformation increment. In this paper we consider either kinematic control or zero external loads, so that ΔE reduces to the increment of deformation work ΔW split into the sum of the increments in the Helmholtz free energy and virtual dissipation. For each slip system the Schmid yield condition $\tau_k = \tau_k^c$ is adopted, where τ_k is the resolved stress (projection of Kirchhoff stress $\boldsymbol{\tau}$ on k -th slip-system dyad \mathbf{s}_k) and τ_k^c is its current critical value. It is shown that the symmetry restriction imposed by intrinsic consistency between minimization (1) performed with accuracy to the first- and second-order terms [1] is reduced to the requirement $g_{kj} = g_{jk}$ examined below.

3. The hardening moduli and symmetry restriction

The evolution equations for critical shear stresses τ_k^c and yield functions $f_k = \tau_k - \tau_k^c$ are

$$(2) \quad \dot{\tau}_k^c = \sum_j h_{kj}^* \dot{\gamma}_j, \quad \dot{f}_k = \boldsymbol{\Lambda}_k \cdot \dot{\mathbf{F}} - \sum_j g_{kj} \dot{\gamma}_j,$$

where $\dot{\gamma}_j \geq 0$ is the shear-rate on j -th slip-system, h_{kj}^* are slip-system hardening moduli, g_{kj} are slip-system interaction moduli at prescribed strain-rate, \mathbf{F} is the deformation gradient, and $\boldsymbol{\Lambda}_k$ is a tensor orthogonal to the yield surface $f_k = 0$ in \mathbf{F} -space. Taking into account the plastic flow of the material relative to the crystallographic lattice, it is shown that

$$(3) \quad g_{kj} - g_{jk} = h_{kj}^* - h_{jk}^* + \boldsymbol{\tau} \cdot (\mathbf{s}_k \mathbf{s}_j - \mathbf{s}_j \mathbf{s}_k).$$

Different ways of ensuring the required symmetry $g_{kj} = g_{jk}$ by reducing to zero the right-hand expression in (3) are considered, and their quantitative effect on the material behaviour is studied.

4. Example

As an example, the channel-die compression of an Al-alloy single crystal is considered. Idealized geometry of the specimen before and after deformation is shown in Fig. 1, the latter determined for two different initial orientations of the crystal. Compressive stress-strain diagrams calculated for five different crystal orientations are shown in Fig. 2a which can be compared to respective experimental data taken from reference [2] and shown in Fig. 2b. The effect of formation of deformation bands is also investigated.

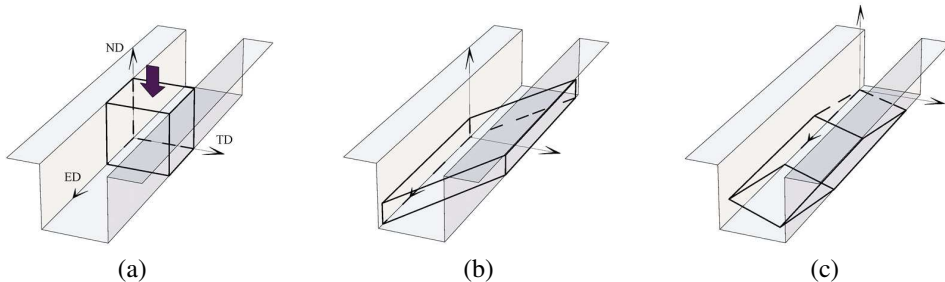


Figure 1. Initial configuration of a single crystal in a channel die (a) and calculated configurations after compression to $\varepsilon_{in} = 1.25$ for Cube (b) and Copper (c) initial crystallographic orientations.

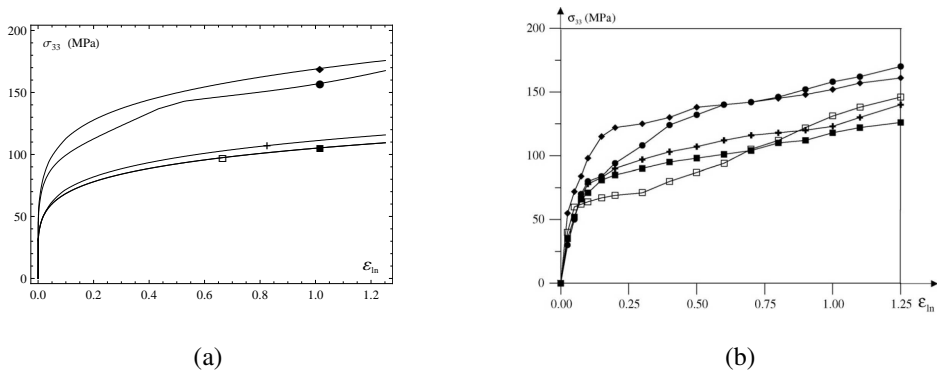


Figure 2. Compressive stress-strain diagrams for channel-die compression of a single crystal of five different crystallographic orientations: calculated curves (a) and experimental results from ref. [2] (b).

Acknowledgement This work was partially supported by the KMM NoE project.

5. References

- [1] H. Petryk (2003). Incremental energy minimization in dissipative solids, *C.R. Mecanique*, **331**, 469–474.
- [2] M. Darrieulat, J.-Y. Poussardin, R.-Y. Fillit and Ch. Desrayaud (2007). Homogeneity and heterogeneity in channel-die compressed Al-1%Mn single crystals: Considerations on the activity of the slip systems, *Mat. Sci. Engng A*, **445–446**, 641–651.

MICROMECHANICAL MODELLING OF METALLIC MATERIALS OF HIGH SPECIFIC STRENGTH ACCOUNTING FOR SLIP-TWIN INTERACTIONS

K. Kowalczyk-Gajewska

Institute of Fundamental Technological Research, Warsaw, Poland

1. Introduction

The aim of the study is development and a preliminary validation of micromechanical model of large plastic deformations of polycrystalline materials characterized by high specific strength and low ductility (eg. Mg alloys or intermetallics). Due to lattice symmetry the number of slip systems in these materials is limited. Disadvantageous effect of this fact on ductility may be partially balanced by the initiation of other mechanism of plastic deformation - twinning. In modelling of twinning, as compared to modelling of crystallographic slip, one should account for its polarized character (uni-directionality) and appearance of new twin related orientation within the grain [1]. Nowadays growing interest in hcp metals such as magnesium or titanium alloys and intermetallics resulted in development of models of crystal plasticity accounting for twinning, e.g. [2–4]. In the paper the single grain model proposed by Gambin (cf. [5]) reformulated to incorporate twinning is used. In order to account for appearance of twin related orientations a new reorientation scheme, called Probabilistic Twin Volume Consistent (PTVC) scheme, is developed. Experiments indicate couplings between evolution of activity of slip and twin mechanisms. The hardening rule describing slip-twin interactions is proposed. Model predictions will be analyzed for hcp materials and intermetallics.

2. Model description

Twinning, similarly to slip, is realized by simple shear, however, in this case only some volume fraction of a matrix grain is sheared on the specified twin plane in the specified twin direction with the specified amount of shear γ^T . As a result the twinned sub-grain is formed. Contrary to slip mechanism twin is unidirectional. The twinned part has different, but specified lattice orientation with respect to the matrix grain, though the lattice orientation in the matrix grain is also unaltered, cf. [1]. In order to account for twinning in the proposed model we follow the standard procedure, eg. [2; 4]. Twinning is described as uni-directional slip mode. The rate of pseudo-slip $\dot{\gamma}^r$ is connected to the rate of volume fraction \dot{f}^r of twinned part created by the twin system r according to the formula $\dot{\gamma}^r = \gamma^T \dot{f}^r$. Modelling of twinning in the context of texture evolution requires taking into account the appearance of new twin-related orientation. A new method, the PTVC scheme, which originates in Van Houtte reorientation condition is developed. It takes into account the history of the deformation process and maintains the volume fraction of reoriented grains at a level that is consistent with shear activity of twins contributing to the deformation. On the other hand, contrary to Predominant Twin Reorientation scheme, cf. [3], the PTVC scheme does not require the analysis of the whole polycrystalline aggregate and the identification of any additional constants or parameters [6].

Crystal plasticity with single yield surface modified in order to incorporate twinning is used, cf. [5],[7]. The evolution of slip and twin activity is captured by the hardening rule. Following the reasoning presented in [3] the hardening rule is proposed in the form (M, N - number of slip and twin systems, respectively)

$$(1) \quad \dot{\tau}_c^r = H_{(ss)}^r \sum_{q=1}^M h_{rq}^{(ss)} \dot{\gamma}^q + H_{(st)}^r \sum_{q=2M+1}^{2M+N} h_{rq}^{(st)} \dot{\gamma}^q, \quad \dot{\tau}_c^{r+M} = \dot{\tau}_c^r, \quad r \leq M$$

$$(2) \quad \dot{\tau}_c^r = H_{(ts)}^r \sum_{q=1}^M h_{rq}^{(ts)} \dot{\gamma}^q + H_{(tt)}^r \sum_{q=2M+1}^{2M+N} h_{rq}^{(tt)} \dot{\gamma}^q, \quad r > 2M$$

and $\dot{\gamma}^q = \dot{\gamma}^q + \dot{\gamma}^{q+M}$. Hardening sub-matrices $h_{rq}^{(\alpha\beta)}$ account for the mutual interactions of the deformation mechanisms of the slip-slip, slip-twin, twin-slip and twin-twin types. These matrices have the form which distinguishes between the hardening due to slip or twinning on coplanar and non-coplanar systems. The functions $H_{(\alpha\beta)}^r$ describe the hardening of r -th slip system or r -th twin system due to activity of other slip or other twin systems. For hardening of the slip system r due to activity of slip systems the Voce-type law with saturation is prescribed in the form used in [4]. This law accounts for the athermal statistical storage of moving dislocations and dynamic recovery. For the hardening of slip system r due to twin activity the following rule is used

$$(3) \quad H_{(st)}^r = h_0^{st} \setminus \tau^r \left(f^T \setminus (f_{sat}^{st} - f^T) \right)$$

that accounts for geometrical effects of twin boundaries in reducing main free path distance and h_0^{st} and $f_{sat}^{st} \leq 1$ are the material parameters. The hardening of twin system due to slip activity is neglected or governed by the simplified linear law while the hardening of twin system due to activity of twinning is assumed similarly as in (3). The corresponding parameter $f_{sat}^{tt} < 1$ enables one to describe the saturation of the volume fraction of twins below one. In the model twinning and slip in reoriented grains is more difficult than before reorientation or even impossible. Moreover, slip in reoriented grains is severely restricted to the planes that are coplanar with the matrix-twin boundary.

3. Results

The presented model will be applied to study the material response and texture evolution for hcp materials and γ -TiAl intermetallics of equiaxed and lamellar microstructure. The performance of the developed reorientation scheme will be compared to the existing approaches and available experimental results. It should be noted that both, PTVC scheme and description of slip-twin interactions with use of the hardening rule (1-2), may be applied for different averaging schemes for polycrystal as well as other models of crystal plasticity, for example the rate-dependent model.

4. References

- [1] J. W. Christian and S. Mahajan. Deformation twinning. *Prog. Mater. Sci.*, 39:1–157, 1995.
- [2] S. R. Kalidindi. Incorporation of twinning in crystal plasticity models. *J. Mech. Phys. Solids*, 46:267–290, 1998.
- [3] I. Karaman, H. Sehitoglu, A. J. Beaudoin, Y. I. Chumlyakov, H. J. Maier, and C. N. Tome. Modeling the deformation behavior of Hadfield steel single and polycrystals due to twinning and slip. *Acta Mater.*, 48:2031–2047, 2000.
- [4] A. Staroselsky and L. Anand. Inelastic deformation of polycrystalline face centered cubic materials by slip and twinning. *J. Mech. Phys. Solids*, 46:671–696, 1998.
- [5] K. Kowalczyk and W. Gambin. Model of plastic anisotropy evolution with texture-dependent yield surface. *Int. J. Plasticity*, 20:19–54, 2004.
- [6] K. Kowalczyk-Gajewska. Crystal plasticity model with regularized Schmid law for metals deforming by slip and twinning at large strains. *Mech. Mater.*, 2008, [submitted].
- [7] K. Kowalczyk-Gajewska. Micromechanical modelling of polycrystalline materials at large plastic deformations. *CD Proceedings of I Congress of Polish Mechanics*, 2007. In Polish.

Acknowledgements. Results are partly obtained in the framework of EU NoE Knowledge-based Multicomponent Materials for Durable and Safe Performance (KMM-NoE, NMP3-CT- 2004-502243).

MODELLING OF EFFECTIVE ELASTIC PROPERTIES OF INTERPENETRATING METAL-CERAMIC NETWORKS

Z. Poniznik¹, V. Salit², M. Basista¹ and D. Gross²

¹ *Institute of Fundamental Technological Research, Warsaw, Poland*

² *Darmstadt University of Technology, Darmstadt, Germany*

1. Introduction

The interpenetrating phase composites (IPC), or interpenetrating metal-ceramic networks, are advanced engineering materials which consist of entirely interconnected networks of solid phases. The rationale behind designing the IPC is to achieve a highly durable material that would combine the most desirable properties of the constituent phases. The detailed description of IPC and their applicability is given e.g. in [1]. The methods of estimation of the effective elastic properties of the IPC's are presented and compared ([2], [3], [4]). A numerical method for calculating random composite structure model was developed. Numerical methods for calculating real composite microstructures were developed and used for Al₂O₃-Cu IPC microstructure acquired from the computer micro-tomography (CT). The results of measurements of Young's modulus for different types of Al₂O₃-Cu interpenetrating composites are also presented and compared with the analytical approximations and numerical calculations.

2. FEM modeling of the interpenetrating structure

The calculations were made for the 3D interpenetrating cross structure, shown in Fig. 1, for the random voxel structure, and for the real structure obtained from computer tomography. There were three effective elastic constants calculated: Young's modulus, Poisson's ratio and shear modulus. To model Young's modulus and Poisson's ratio, tensile load was applied as the uniform displacement field applied to one side of the cube, with fixing boundary conditions on the opposite side. To model shear modulus, tangent displacements were applied together with antisymmetric boundary conditions.

There were convergence studies made to compare the results for different mesh densities for the calculations of Young's modulus, Poisson's ratio and shear modulus. The method of extrapolation to other composite components was proposed. The effect of porosity of the porous ceramics on the effective properties was also investigated.

The calculations for the real structure of the Al₂O₃-Cu interpenetrating composite obtained from computer tomography were made. The inner part of the image, with the shape of the cube of the dimensions 400×400×400 voxels, was extracted to be used for calculations. The real structure of the material was represented as cubic voxels, where each voxel was made of only one material. Each voxel was modeled as 8-node brick element. Due to complexity of such a big model the whole structure was divided into 512 equal in size cubic parts and then each part was calculated separately. The applied loads and boundary conditions were analogous to the applied for the cross structure.

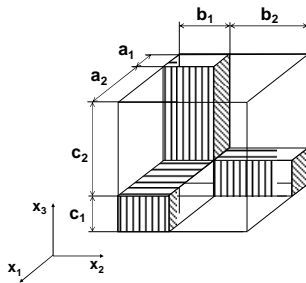


Fig. 1. Unit cubic cell of the IPC model according to [2]

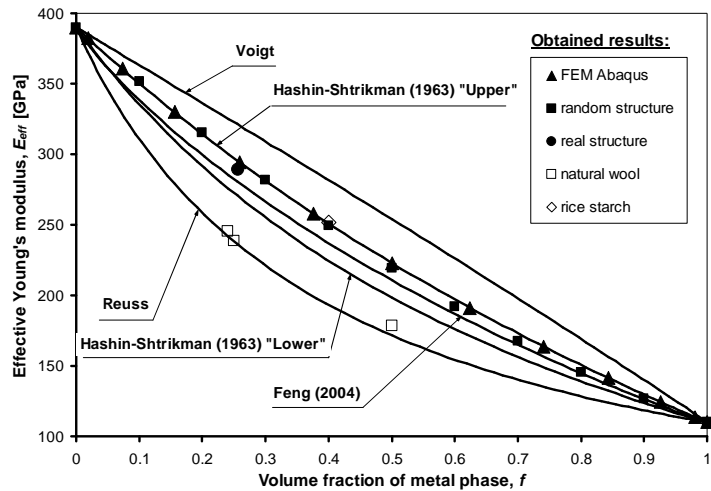


Fig. 2. Effective Young's modulus of $\text{Al}_2\text{O}_3\text{-Cu}$ IPC – analytical and numerical models and CT measurements results.

The numerical results for the effective Young's moduli are presented in Fig. 2, compared with theoretical predictions and results of measurements of the $\text{Al}_2\text{O}_3\text{-Cu}$ interpenetrating composites. It can be seen that these numerical results fit between Hashin-Shtrikman bounds [4] and are closer to the upper bound. The influence of the composite microstructure on the effective properties can be also seen.

3. Conclusions

The numerical methods of estimating the effective properties of interpenetrating phase composites were presented and compared with existing theoretical models and results of measurements of IPC's of different microstructures. The developed numerical methods are in accordance with the existing theoretical models applicable to the IPC's.

From the presented results it could also be seen that computational methods offer the best possibilities for modeling the features of the real material, such as porosity, microcracking, debonding between phases and thermal stresses. Further investigation of these methods should then be made.

4. References

- [1] Basista M. and Weglewski W. (2006). Modelling of damage and fracture in ceramic-matrix composites - an overview, *J. Theor. Appl. Mech.*, **44**, 455-484.
- [2] Feng X., Tian Z., Liu Y. and Yu S. (2004). Effective elastic and plastic properties of interpenetrating multiphase composites, *Appl. Comp. Mater.*, **11**, 33-55.
- [3] Gross D. and Seelig T. (2006). *Fracture Mechanics with an Introduction to Micromechanics*, Springer.
- [4] Hashin Z. and Shtrikman S. (1963). A variational approach to the theory of the elastic behaviour of multiphase materials, *J. Mech. Phys. Sol.*, **11**, 127-140.

MODELLING OF MICROSTRUCTURE FORMATION BY MINIMIZATION OF INCREMENTAL ENERGY SUPPLY

H. Petryk

Institute of Fundamental Technological Research, Warsaw, Poland

1. Microstructures and material instability

It is well documented experimentally that microstructures can form in initially homogeneous solids during plastic deformation or phase transition. This paper is concerned with the modelling of this phenomenon in rate-independent inelastic solids under quasi-static loading, with particular reference to plasticity of metal crystals and polycrystals and to martensitic phase transformation in shape memory alloys. Formation of dislocation cells, cell blocks, deformation bands and shear bands within single grains of plastically deformed metals and alloys, of networks of macroscopic shear bands in metal polycrystals, and of twinned martensite and austenite-martensite laminates in shape memory alloys, are viewed as basic examples. A unifying feature of these seemingly distinct microstructures is that non-uniformity of deformation associated with the microstructure formation is not enforced by external conditions but is due to intrinsic instability in the deformed material.

In elastic or pseudo-elastic solids, the well-known notions of ellipticity, rank-one convexity and quasi-convexity of a nonlinear elastic energy function are related to material stability whose loss leads to formation of fine microstructures. When the evolution of a microstructure is associated with intrinsic dissipation, the stability analysis becomes more complex. An extended condition of thermodynamic stability is developed which in general is less restrictive than the classical one on account of a rate-independent dissipation term in the respective Lyapunov functional. To describe microstructure formation, the total incremental energy supplied to a material element is minimized according to the energy criterion of stability of deformation paths [1, 2].

2. Minimization of incremental energy supply

This may be regarded as an extension of the standard approach based on minimization of the elastic or free energy to inelastic materials with rate-independent dissipation. The variational approach to determining microstructure formation in a homogeneous and uniformly strained inelastic material follows the basic rule:

$$(1) \quad \Delta E \rightarrow \min \quad \text{subject to kinematical constraints}$$

where ΔE is the increment in energy to be supplied from external sources to the thermodynamic system under consideration to produce a virtual deformation increment. The analysis is restricted to isothermal quasi-static transformations. The prefix Δ denotes a virtual increment from a given state, corresponding to an increment of an external control parameter. ΔE is generally split into the sum $\Delta E = \Delta W + \Delta \Omega$ of the deformation work increment ΔW and the increment $\Delta \Omega$ in the potential energy of external loads. If the (virtual) dissipation \mathcal{D} associated with a local deformation increment is defined then the further split $\Delta W = \Delta \bar{\phi} + \Delta \bar{\mathcal{D}}$ can be used involving the averaged increments $\Delta \bar{\phi}$ in the Helmholtz free energy and $\Delta \bar{\mathcal{D}}$ in the dissipated energy.

In applications, the energy functional in the minimization rule (1) is evaluated at least to the second-order terms since its first-order representation leaves the incremental deformation indeterminate. Accordingly, a symmetry restriction is imposed on the incremental stiffness moduli [1, 2] and dissipation function [3].

3. Examples

The microstructure formation is calculated by repetitive solving the incremental energy minimization problem (1) along a deformation path. This is illustrated below by the example of finite-element simulations of the post-critical plastic deformation of a homogeneous incrementally nonlinear material. The overall plane strain compression under periodic boundary conditions is applied, with a small amount of shearing superimposed starting from 29% compression. The deformation pattern shown in Fig. 1 emerges through a sequence of bifurcations. The advantage of using rule (1) is in automatic selection of the post-critical deformation path which is otherwise indeterminate. The rule (1) has also been applied to overcome the long-standing difficulty of non-uniqueness in crystal plasticity and to simulate the formation of banded microstructures in metal crystals.

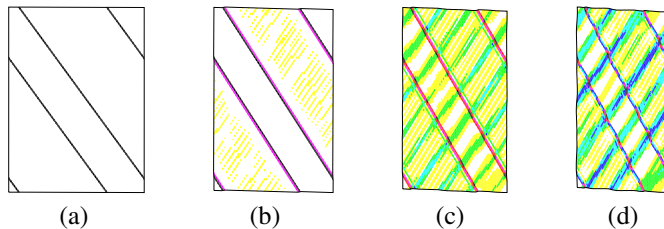


Figure 1. Calculated plane strain pattern at (a) 30% (b) 35% (c) 40% (d) 44% compression (with a small amount of shear) of a polycrystalline metal obeying the two-surface corner theory of plasticity [4].

Another area of applicability of (1) is the simulation of stress-induced martensitic microstructures in crystals of shape memory alloys, as shown schematically in Fig. 2.

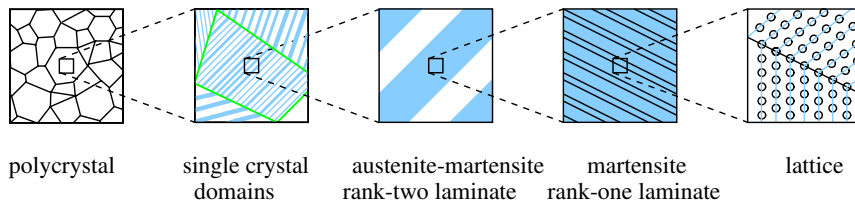


Figure 2. Schematic view of stress-induced martensitic microstructures in crystals of shape memory alloys.

4. References

- [1] H. Petryk (1992). Material instability and strain-rate discontinuities in incrementally nonlinear continua, *J. Mech. Phys. Solids*, **40**, 1227–1250.
- [2] H. Petryk (1997). Instability of plastic deformation processes, In *Proc. XIX Int. Congr. Theor. Appl. Mech.*, Kyoto 1996 (T. Tatsumi et. al, ed.), Elsevier, 497–516.
- [3] H. Petryk (2003). Incremental energy minimization in dissipative solids, *C.R. Mecanique*, **331**, 469–474.
- [4] H. Petryk and K. Thermann. Incremental energy minimization in material instability problems. *XXI Int. Congr. Theor. Appl. Mech.*, Warsaw 2004 (*unpublished*).

ON NATURAL STRAIN MEASURES OF THE NON-LINEAR MICROPOLAR CONTINUUM

V.A. Eremeyev¹ and W. Pietraszkiewicz²

¹ *South Scientific Center of RASci, Rostov-on-Don, Russia*

² *Institute of Fluid-Flow Machinery, Gdańsk, Poland*

In the micropolar (or the Cosserat type) continuum each material particle can translate and independently rotate, that is it has six degrees of freedom of a rigid body, [1,2]. The micropolar continuum is used nowadays with success to model the behaviour, for example, of granular media, composites, polycrystalline solids, liquid crystals, magnetic fluids, nano-materials as well as thin bodies: rods, plated and shells.

Two strain measures of the micropolar continuum, called usually the stretch and wryness tensors, were originally proposed by Cosserats [1] in an awkward, now hardly understandable notation. In the contemporary literature the stretch and wryness tensors are defined in different ways using, for example: a) components in two different curvilinear coordinate systems associated with the undeformed (reference) and deformed (actual) placements of the body, b) components in the convected coordinate systems, c) Lagrangian or Eulerian descriptions, d) different representations of the rotation group $SO(3)$, e) formally different definitions of gradient and divergence operators, f) different sign conventions, and f) requiring or not the measures to vanish in the undeformed placement of the body. As a result, definitions of the strain measures for the micropolar continuum used in different papers are in many cases not equivalent.

In this report we discuss three different methods of defining the strain measures of the non-linear micropolar continuum: 1) by a direct geometric approach, 2) introducing the strain measures as the fields work-conjugate to the respective internal stress and couple-stress fields, and 3) applying the principle of material frame-indifference to the polar-elastic strain energy density. All the three methods lead to the same definitions of the stretch and wryness tensors. Our strain measures expressed in the coordinate-free notation are of the relative type, for they are required to vanish in the undeformed placement of the body.

1. Geometric approach

In the undeformed placement the material particle of the micropolar body is given through the position vector $\mathbf{x} \in E$ and three orthonormal directors $\mathbf{h}_a \in E$, $a = 1, 2, 3$, where E is the 3D vector space. In the actual placement the same material particle becomes described by the position vector $\mathbf{y} \in E$ and three orthonormal directors $\mathbf{d}_a \in E$. Thus, the finite displacement of the body is described by

$$(1) \quad \mathbf{y} = \chi(\mathbf{x}) = \mathbf{x} + \mathbf{u}(\mathbf{x}), \quad \mathbf{d}_a = \varphi_a(\mathbf{h}_a) = \mathbf{Q}(\mathbf{x})\mathbf{h}_a,$$

where $\mathbf{Q} = \mathbf{d}_a \otimes \mathbf{h}_a \in SO(3)$ is the microrotation tensor.

Analysing differences between position and orientation differentials $d\mathbf{x}$, $d\mathbf{y}$, $d\mathbf{h}_a$, and $d\mathbf{d}_a$ we can define the Euclidean norms

$$(2) \quad \begin{aligned} \|d\mathbf{y} - \mathbf{Q}d\mathbf{x}\|^2 &= d\mathbf{x} \cdot \mathbf{E}^T \mathbf{E} d\mathbf{x} = d\mathbf{y} \cdot \mathbf{G}^T \mathbf{G} d\mathbf{y}, \\ \|\mathbf{C}d\mathbf{y} - \mathbf{Q}\mathbf{B}d\mathbf{x}\|^2 &= d\mathbf{x} \cdot \mathbf{\Gamma}^T \mathbf{\Gamma} d\mathbf{x} = d\mathbf{y} \cdot \mathbf{\Delta}^T \mathbf{\Delta} d\mathbf{y}. \end{aligned}$$

In (2), $\mathbf{B} = \frac{1}{2} \mathbf{h}_a \times \text{Grad } \mathbf{h}_a$ and $\mathbf{C} = \frac{1}{2} \mathbf{d}_a \times \text{grad } \mathbf{d}_a$ are the microstructure curvature tensors in the undeformed and deformed placements, respectively, with Grad and grad being the corresponding gradient operators and

$$(3) \quad \begin{aligned} \mathbf{E} &= \mathbf{Q}^T \mathbf{F} - \mathbf{I}, \quad \mathbf{G} = \mathbf{Q} \mathbf{E} \mathbf{F}^{-1} = \mathbf{I} - \mathbf{Q} \mathbf{F}^{-1}, \\ \mathbf{\Gamma} &= \mathbf{Q}^T \mathbf{C} \mathbf{F} - \mathbf{B}, \quad \mathbf{\Delta} = \mathbf{Q} \mathbf{\Gamma} \mathbf{F}^{-1} = \mathbf{C} - \mathbf{Q} \mathbf{B} \mathbf{F}^{-1}, \end{aligned}$$

where $\mathbf{F} = \text{Grad } \mathbf{y}$. The measures \mathbf{E}, \mathbf{G} are the natural stretch tensors while $\mathbf{\Gamma}, \mathbf{\Delta}$ are the natural wryness tensors of the micropolar continuum in the Lagrangian and Eulerian descriptions, respectively.

2. Work-conjugate strain and stress measures

The local equilibrium equations of the micropolar continuum in the Lagrangian description are

$$(4) \quad \text{Div } \mathbf{T} + \mathbf{f} = \mathbf{0}, \quad \text{Div } \mathbf{M} + ax(\mathbf{T} \mathbf{F}^T - \mathbf{F} \mathbf{T}^T) + \mathbf{m} = \mathbf{0},$$

where \mathbf{T} and \mathbf{M} are the stress and couple stress tensors of the 1st Piola-Kirchhoff type, and $ax(\mathbf{A})$ denotes the axial vector of the skew tensor (\mathbf{A}).

Multiplying the vector equations (4) by the kinematically admissible virtual translation $\delta \mathbf{u}$ and virtual rotation $ax(\delta \mathbf{Q} \mathbf{Q}^T)$ fields, respectively, after appropriate transformations we can formulate for the micropolar continuum the principle of virtual work in which the internal virtual power density becomes expressed as

$$(5) \quad \Sigma = \mathbf{S} \cdot \delta \mathbf{E} + \mathbf{P} \cdot \delta \mathbf{\Gamma}.$$

In (5), the virtual measures $\delta \mathbf{E}, \delta \mathbf{\Gamma}$ - the virtual changes of $\mathbf{E}, \mathbf{\Gamma}$ defined by (3) - are work-conjugate to the corresponding stress measures $\mathbf{S} = \mathbf{Q}^T \mathbf{T}$, $\mathbf{P} = \mathbf{Q}^T \mathbf{M}$ of the 2nd Piola-Kirchhoff type.

3. Principle of material frame-indifference

The elastic micropolar body is usually defined by assuming the existence of the strain energy density $W = W(\mathbf{y}, \mathbf{F}, \mathbf{Q}, \text{Grad } \mathbf{Q}; \mathbf{x})$. The function W should be invariant under transformations following from a rigid-body motion of the reference frame $\mathbf{y} \rightarrow \mathbf{O} \mathbf{y} + \mathbf{a}$, $\mathbf{Q} \rightarrow \mathbf{O} \mathbf{Q}$ for arbitrary $\mathbf{O} \in SO(3)$ and $\mathbf{a} \in E$. Then W can be reduced to $\tilde{W}(\mathbf{E}, \mathbf{Q}^T \mathbf{\Gamma}; \mathbf{x})$, that is \tilde{W} still depends on \mathbf{Q} . We bypass this inconvenience by postulating the strain energy density in the equivalent form $W = \bar{W}(\mathbf{y}, \mathbf{F}^T, \mathbf{Q}^T, \text{Grad } \mathbf{Q}^T; \mathbf{x})$ which under the transformations given above can be reduced to $\hat{W}(\mathbf{E}, \mathbf{\Gamma}; \mathbf{x})$. As a result, the density \hat{W} depending only on $\mathbf{E}, \mathbf{\Gamma}$ at each \mathbf{x} is the one which assures the principle of material frame-indifference to be identically satisfied.

We also present a review of alternative definitions of the strain measures for the micropolar continuum proposed in the literature.

4. References

- [1] E. Cosserat and F. Cosserat (1909). *Théorie des corps déformables*. Herman et Flis, Paris; English translation: *Theory of Deformable Bodies*, NASA TT F-11, 561, Washington D.C. (1968).
- [2] A.C. Eringen and C.B. Kafadar (1976). Polar field theories. In: A.C. Eringen (Ed.), *Continuum Physics*, 4, 1-75; Academic Press, New York.

BOUNDARY VALUE PROBLEMS IN THE TWO-TEMPERATURE THEORY OF THERMOELASTICITY OF BINARY MIXTURES

M. Svanadze

Ilia Chavchavadze State University, Tbilisi, Georgia

1. Introduction

The nonlinear theory of thermoelasticity of mixtures of two- or many-component solids was developed by Green and Steel [1]. A linear variant of this theory (the diffusion model) was proposed by Steel [2]. The theory of thermoelasticity of binary mixtures (the shift model) was constructed by Iesan [3]. In [1-3], the mixture components are assumed to have the same temperature value.

The linear and nonlinear theory of thermoelasticity of binary mixtures with components having different temperature values were respectively constructed by Khoroshun and Soltanov [4] and Iesan [5]. Fundamental solutions of steady oscillation (vibration) equations of the two-temperature linear theory of mixtures are constructed in terms of elementary functions in [6].

In this paper, the boundary value problems (BVPs) of steady vibration of the two-temperature linear theory of thermoelasticity of binary mixtures are investigated by means of the boundary integral equation method (potential method [7, 8]). The Sommerfeld-Kupradze type radiation conditions are established. The uniqueness and existence theorems of solutions of the BVPs are proved using the potential method and the theory of multidimensional singular integral equations.

2. Basic boundary value problems

The system of equations of steady vibration in the two-temperature linear theory of thermoelasticity of binary mixtures is written as [4, 5]

$$(1) \quad \begin{aligned} a_1 \Delta u + b_1 \operatorname{grad} \operatorname{div} u + c \Delta w + d \operatorname{grad} \operatorname{div} w + \omega^2 \rho_1 u - \alpha(u-w) - \alpha_{11} \operatorname{grad} \theta_1 - \alpha_{12} \operatorname{grad} \theta_2 &= 0, \\ c \Delta u + d \operatorname{grad} \operatorname{div} u + a_2 \Delta w + b_2 \operatorname{grad} \operatorname{div} w + \omega^2 \rho_2 w + \alpha(u-w) - \alpha_{21} \operatorname{grad} \theta_1 - \alpha_{22} \operatorname{grad} \theta_2 &= 0, \\ (a_{11} \Delta + i \omega m_{11}) \theta_1 + (a_{12} \Delta + i \omega m_{12}) \theta_2 + i \omega \operatorname{div} (\beta_{11} u + \beta_{21} w) &= 0, \\ (a_{21} \Delta + i \omega m_{21}) \theta_1 + (a_{22} \Delta + i \omega m_{22}) \theta_2 + i \omega \operatorname{div} (\beta_{12} u + \beta_{22} w) &= 0, \end{aligned}$$

where $u = (u_1, u_2, u_3)$ and $w = (w_1, w_2, w_3)$ are the partial displacements, θ_1 and θ_2 are the temperature variations of each component, $a_j, b_j, c, d, a_{lj}, \alpha_{lj}, \beta_{lj}, m_{lj}$ ($l, j = 1, 2$) are thermoelastic constants of the mixture, $\alpha \geq 0$, ω is the oscillation frequency, ρ_1 and ρ_2 are the partial densities.

Let $x = (x_1, x_2, x_3)$ be the point of the Euclidean three-dimensional space E^3 . Let S be the closed surface surrounding the finite domain Ω^+ in E^3 . $S \in C^{2,\nu}$, $0 < \nu \leq 1$, $\bar{\Omega}^+ = \Omega^+ \cup S$, $\Omega^- = E^3 \setminus \bar{\Omega}^+$. A vector function U is called *regular* in Ω^- (or Ω^+) if $U_l \in C^2(\Omega^-) \cap C^1(\bar{\Omega}^-)$

(or $U_l \in C^2(\Omega^+) \cap C^1(\bar{\Omega}^+)$), $U_l(x) = \sum_{j=1}^6 U_{lj}(x)$, $U_{lj} \in C^2(\Omega^-) \cap C^1(\bar{\Omega}^-)$, $(\Delta + k_j^2)U_{lj}(x) = 0$, and

$$(2) \quad \left(\frac{\partial}{\partial |x|} - ik_j \right) U_{lj}(x) = e^{ik_j |x|} o(|x|^{-1}),$$

for $|x| \gg 1$, where k_j is the wave number, $l = 1, 2, \dots, 8$, $j = 1, 2, \dots, 6$, $|x| = (x_1^2 + x_2^2 + x_3^2)^{1/2}$. Equalities in (2) is the Sommerfeld-Kupradze type *radiation conditions* in the two-temperature theory of thermoelasticity of binary mixture.

Problem (I)_f⁺: Find a regular solution to system (1) for $x \in \Omega^+$ that satisfies the boundary

condition $\lim_{\Omega^+ \ni x \rightarrow z \in S} U(x) \equiv \{U(z)\}^+ = f(z)$.

Problem (I)_f⁻: Find a regular solution to system (1) for $x \in \Omega^-$ that satisfies the boundary condition $\lim_{\Omega^+ \ni x \rightarrow z \in S} U(x) \equiv \{U(z)\}^- = f(z)$, where f is the known vector function on S .

4. Uniqueness and Existence Theorems

Theorem 1. Exterior BVP (I)_f⁻ admits at most one regular solution.

Theorem 2. Interior homogeneous BVP (I)₀⁺ has a non-trivial solution $U = (u, w, 0, 0)$ in the class of regular vectors, where the vector $V = (u, w)$ is a solution to the system

$$(3) \quad \begin{aligned} a_1 \Delta u + b_1 \operatorname{grad} \operatorname{div} u + c \Delta w + d \operatorname{grad} \operatorname{div} w + \omega^2 \rho_1 u - \alpha(u - w) &= 0, \\ c \Delta u + d \operatorname{grad} \operatorname{div} u + a_2 \Delta w + b_2 \operatorname{grad} \operatorname{div} w + \omega^2 \rho_2 w + \alpha(u - w) &= 0, \\ \beta_{11} \operatorname{div} u + \beta_{12} \operatorname{div} w &= 0, \quad \beta_{21} \operatorname{div} u + \beta_{22} \operatorname{div} w &= 0, \quad \text{for } x \in \Omega^+ \end{aligned}$$

satisfying the boundary condition

$$(4) \quad \{V(z)\}^+ = 0;$$

the problems (I)₀⁺ and (3), (4) have the same eigenfrequencies.

Theorem 3. If $S \in C^{2,\nu}$, $f \in C^{1,\nu'}(S)$, $0 < \nu' \leq \nu \leq 1$, then a regular solution of the problem (I)_f⁻ exists, is unique, and is represented by sum $U(x) = Z^{(2)}(x, g) + a' Z^{(1)}(x, g)$ for $x \in \Omega^-$, where $Z^{(1)}(x, g)$ and $Z^{(2)}(x, g)$ are the single-layer and double-layer potentials, respectively, $a' = a'_1 + ia'_2$; a'_1 and a'_2 are the real numbers, $a'_1 > 0$, $a'_2 < 0$, and g is a solution of the singular integral equation $-\frac{1}{2}g(z) + Z^{(2)}(z, g) + a' Z^{(1)}(z, g) = f(z)$ for $z \in S$, which is always solvable for an arbitrary vector f .

5. Acknowledgments

The designated project has been fulfilled by financial support of Georgian National Science Foundation (Grant # GNSF/ST06/3-033). Any idea in this publication is possessed by the author and may not represent the opinion of Georgian National Science Foundation itself.

6. References

- [1] A.E. Green and T.R. Steel (1966). Constitutive equations for interacting continua, *Int. J. Engng. Sci.*, **4**, 483-500.
- [2] T.R. Steel (1967). Applications of a theory of interacting continua, *Quart. J. Mech. Appl. Math.*, **20**, 57-72.
- [3] D. Iesan (1991). On the theory of mixtures of thermoelastic solids, *J. Thermal Stresses*, **14**, 389-408.
- [4] L.P. Khoroshun and N.S. Soltanov (1984). *Thermoelasticity of Two Component Mixtures*, Naukova Dumka, Kiev.
- [5] D. Iesan (1997). A theory of mixtures with different constituent temperatures, *J. Thermal Stresses*, **20**, 147-167.
- [6] M. Svanadze (1996). The fundamental solution of the equations of the steady oscillations for thermoelastic mixtures, *Int. Appl. Mech.*, **31**, 558-566.
- [7] V.D. Kupradze, T.G. Gegelia, M.O. Bacheleishvili and T.V. Burchuladze (1979). *Three-Dimensional Problems of the Mathematical Theory of Elasticity and Thermoelasticity*, North-Holland Publ. Comp., Amsterdam, New York, Oxford.
- [8] T. Burchuladze and M. Svanadze (2000). Potential method in the linear theory of binary mixtures of thermoelastic solids, *J. Thermal Stresses*, **23**, 601-626.

PIEZOELECTRIC SWITCHING TECHNIQUE FOR VIBRATION DAMPING

R. Oleśkiewicz¹, M. Neubauer² and T. Krzyżynski¹

¹ *Koszalin University of Technology,
Institute of Mechatronics, Nanotechnology and Vacuum Technique,
Koszalin, Poland*

1. Introduction

Piezoceramics are widely used as actors and sensors in many technical applications. They offer very precise positioning and high dynamics. It makes them suitable for vibration damping especially at high frequencies. However, they need comprehensive amplifiers and power supply when used as actors. An alternative approach for vibration control and damping is piezoelectric shunt damping cp. Fig.1.

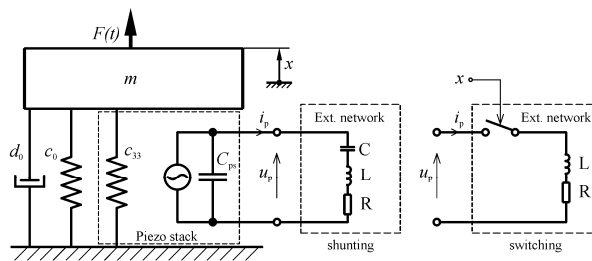


Figure 1. Mechanical structure with piezo element. Shunting and switching principles.

It features an electrical network which is connected to the electrodes of the piezoceramics. The piezoelectric transducer is embedded into the mechanical structure and couples the mechanical and the electrical systems by energy conversion by the piezoelectric effect. The aim of the network design is to cause a dynamical behavior of the piezoceramics which influences the mechanical vibration in the desired way. Typically, a resonant LR shunts are used for vibration damping, which for maximum efficiency, must be tuned to the natural frequency of the mechanical system or to the frequency of excitation [1]. The drawback of this passive solution is the small frequency bandwidth. Therefore, this technique is appropriate for vibration problems with only one dominant invariant frequency known in advance. A negative capacitance network has been proposed to increase the damping performance and the frequency bandwidth. However, a negative capacitance cannot be realized in a passive way and requires power supply for operation [2]. Another solution for vibration damping is switched LR shunt [3]. In this technique, the electrical network is connected and disconnected periodically to the electrodes of the piezoceramics. An electronic switch circuit is needed to connect and disconnect the network at appropriate times. Typically, the switching is triggered by the mechanical vibration itself. It has been shown that these switching shunts are very robust against changes of the system parameters and the excitation frequency.

2. Piezoelectric model

For the calculations, a linear, one dimensional model of the piezoceramics is used, cp. Fig.1. The mathematical model is derived from the constitutive equations [1]. In case of the switching it is necessary to establish the energy amount that may be extracted from the mechanical structure in the quasi steady state by integration of the product of the momentary voltage u_p at the piezo element

and the piezo current i_p over one mechanical vibration period: $\Delta E = \int_t^{t+\Delta t} u_p(t) i_p(t) dt$. The calculations in

Laplace domain ($s=j\omega$) are divided into two parts where the switch is open: voltage at the piezo $U_{p,open}$ Eq(1) and closed: voltage at the piezo $U_{p,close}$, and the piezo current $I_{p,close}$ Eq(2).

$$(1) \quad U_{p,open} = E(s) - \frac{U_{p,0^-}}{s};$$

$$(2) \quad I_{p,close} = \left(E(s) - \frac{U_{p,0^-}}{s} \right) \frac{1}{\frac{1}{sC_{ps}} + Z(s)}; \quad U_{p,close} = \left(E(s) - \frac{U_{p,0^-}}{s} \right) - I_{p,close} \frac{1}{sC_{ps}}$$

where: $E(s) = -X_m(s) \frac{c_{33}d_{33}}{C_{ps}}$ is the internal voltage source of the piezo, $Z(s) = R + sL$ is the switched impedance shunt, the parameters of the piezo are: C_{ps} - piezo capacitance, c_{33} - mechanical stiffness of the piezo d_{33} - piezo sensitivity, X_m - external deformation. The variation of the open and close time of the switch influences the amount of the energy being transferred to the shunt.

3. Measurements and the conclusions

The measurements are performed on the single supported beam with a piezo path attached to the structure. The energy dissipated in the system is plotted over a normalized close and open switch time cp. Fig.2.

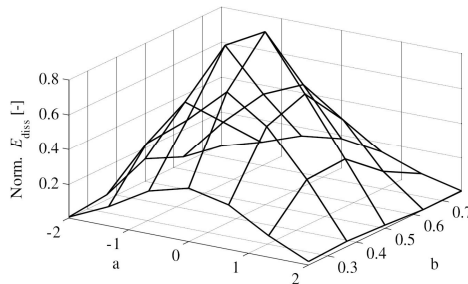


Figure 2. Measured dissipated energy.

It is proven that contrary to the heuristic control law proposed in [3], the switching times should be adjusted to the time constant of the external branch in order to achieve the maximum possible energy extraction.

5. References

- [1] N. W. Hagood, A. H. von Flotow, *Damping of structural vibrations with piezoelectric materials and passive electrical networks*, Journal of Sound and Vibration 146 (2), 1991, pp. 243-268
- [2] M. Neubauer, R. Oleskiewicz, K. Popp, T. Krzyzynski, *Optimization of damping and absorbing performance of shunted piezo elements utilizing negative capacitance*, Journal of Sound and Vibration 298, 2006, pp. 84-107
- [3] D. Niederberger, M. Morari, *An autonomous shunt circuit for vibration damping*, Smart Materials and Structures 15, 2006, pp. 359-364

CONFORMAL CONTACT BETWEEN A PUNCH AND A LAYER WITH THIN COATING

A.V. Manzhirov and K.E. Kazakov

Institute for Problems in Mechanics of the Russian Academy of Sciences, Moscow, Russia

Consider conformal contact between a double layered foundation and a rigid punch in the case of plane strain. The foundation consists of a viscoelastic aging layer of arbitrary thickness H and a thin viscoelastic aging coating of variable thickness $h(x)$ whose surface follows a complex surface of the punch. The lower border of the foundation is in the state of smooth or ideal contact with the underlying rigid base (smooth or ideal contact is achieved between the layers). Suppose that, starting from an instant τ_0 , the smooth rigid punch with a complex shape of its surface is indented into the conformal surface of the coated viscoelastic layer with force $P(t)$ applied with eccentricity $e(t)$. The contact region is independent of time, and the contact line length is $2a$. The viscoelastic coating of variable thickness is produced at an instant $\tau_1 \leq \tau_0$ and homogeneously ages thenceforth. The lower viscoelastic layer of arbitrary thickness is produced at an instant $\tau_2 \leq \tau_0$ and also ages homogeneously.

For the problem stated above, the mixed integral equation and the additional conditions in the plane-strain case have the form [1] ($t \geq \tau_0$)

$$(1) \quad (\mathbf{I} - \mathbf{V}_1) \frac{\theta q(x, t) h(x)}{E_1(t - \tau_1)} + (\mathbf{I} - \mathbf{V}_2) \mathbf{F} \frac{2(1 - \nu_2^2) q(x, t)}{\pi E_2(t - \tau_2)} = \delta(t) + \alpha(t)x, \quad x \in [-a, a],$$

$$(2) \quad \int_{-a}^a q(\xi, t) d\xi = P(t), \quad \int_{-a}^a \xi q(\xi, t) d\xi = M(t).$$

Here, $q(x, t)$ is contact pressure under the punch; $M(t) = e(t)P(t)$ is the moment of the applied force $P(t)$; $E_1(t)$ and $E_2(t)$ are instant elastic strain moduli of the coating and the lower layer, respectively; τ_1 and τ_2 are the instants at which the coating and the lower layer are produced; θ is a dimensionless coefficient that depends on the properties of the contact between the coating and the lower layer; \mathbf{I} is the identity operator; \mathbf{V}_k ($k = 1, 2$) are Volterra integral operators with tensile creep kernels $K_k(t, \tau)$; \mathbf{F} is a Fredholm integral operator with a known kernel of the plane contact problem, $k_{pi}[(x - \xi)/H]$ [1, 2]; $\delta(t)$ is the punch settlement and $\alpha(t)$ is its tilt angle. Note that conformal contact is a generalization of interaction between bodies with plane surfaces.

Given the applied force and the eccentricity, it is required to determine the contact pressure under the punch, its settlement, and its tilt angle.

A solution of equation (1) with the additional conditions (2) can be found by a generalized projection method used for solving mixed integral equations [3–6]. The structure of the solution for contact pressures has the form

$$q(x, t) = \frac{1}{h(x)} [z_0(t)P_0(x) + z_1(t)P_1(x) + \dots],$$

where $z_k(t)$ is a function of time t , and $P_k(x)$ are polynomials of some special form ($k = 0, 1, \dots$). Thus, it is possible to have an explicit dependence of the solution on the coating thickness $h(x)$. This fact allows us to find effective analytical solutions for bases with coatings whose thickness is specified by functions of a complex structure, in particular, rapidly oscillating functions. In such situations, effective analytical solutions can hardly be found by other known methods. It should be noted that in the case under consideration, contact pressures, the settlement, and the tilt angle of the punch are proportional to the indenting force. This property is observed only in solutions of the conformal contact problem.

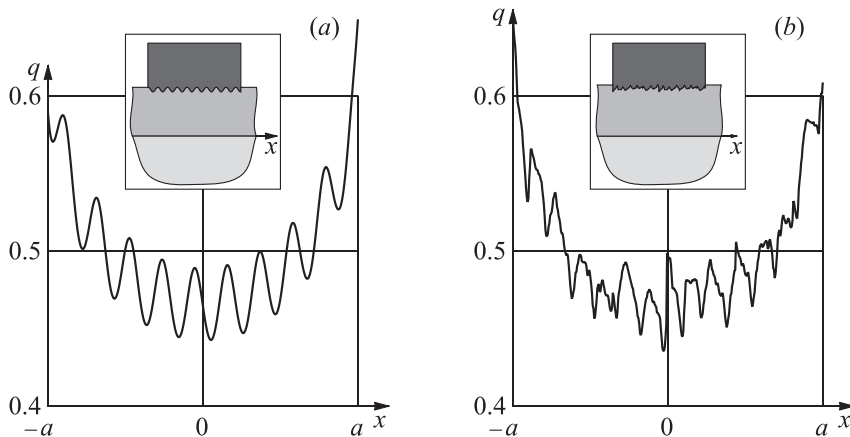


Figure. Contact pressures for $P(t)/a \equiv 1 \text{ N/m}^2$, $e(t) \equiv 0$ at the initial instant for different surface profiles.

The settlement and the tilt angle of the punch are also obtained in terms of explicit analytic formulas. Obviously, for the constant force and moment, the settlement and the tilt angle tend to some asymptotic values.

Figure represents numerical results for two cases of coated bases: (a) the coating thickness is described by an oscillating function; (b) the real surface profile is given as determined from experimental data. It can be seen that the solutions obtained above take into account all specific features of the surface profile.

A similar problem can be formulated in the axisymmetric case, and its solution can be obtained by the same method.

The authors wish to thank Dr. S. Kucharski for providing them with experimental data.

This research was financially supported by the Russian Foundation for Basic Research (projects Nos. 06-01-00521, 08-01-00003, and 08-01-00553), and by the Basic Research Program No. 13 of the Department of Power Engineering, Mechanical Engineering, Mechanics, and Control Processes of the Russian Academy of Sciences.

- [1] N.Kh. Arutyunyan and A.V. Manzhairov (1999). *Contact Problems in the Theory of Creep* [in Russian]. Izd-vo NAN RA, Yerevan.
- [2] N.Kh. Arutyunyan, A.V. Manzhairov, and V.E. Naumov (1991). *Contact Problems in Mechanics of Growing Bodies*. Nauka, Moscow.
- [3] A.V. Manzhairov (2005). Mixed integral equations of contact mechanics and tribology, in N.F. Morozov (Editor) *Mixed Problems in Solid Mechanics* [in Russian]. Izd-vo Saratov. Un-ta, Saratov, 222–226.
- [4] A.V. Manzhairov, K.E. Kazakov, and I. Fedotov (2006). Wear of elastic foundations with inhomogeneous coatings, in *35th Solid Mechanics Conference. Volume of Abstracts*. In-t of Fund. Tech. Research of the Polish Academy of Sciences, Warsaw, 279–280.
- [5] A.V. Manzhairov and K.E. Kazakov (2006). Contact problems for coated solids with real surface shape, in *Proceedings of Indo-Russian Workshop on Problems in Nonlinear Mechanics of Solids with Large Deformation*. IIT Delhi, New Delhi, 63–70.
- [6] A.D. Polyanin and A.V. Manzhairov (2008). *Handbook of Integral Equations*, 2nd Edition. Chapman & Hall/CRC Press, Boca Raton.

A COUPLED DISCRETE-HOMOGENIZED APPROACH TO STUDY THE BEHAVIOR OF BALLAST UNDER RAILWAYS

M. Hammoud, D. Duhamel and K. Sab

Université Paris-Est, Institut Navier, LAMI, Ecole des Ponts, Paris, France

1. Abstract

Modeling of granular materials is an important research area especially in civil engineering. Granular materials are strongly present in nature, and are involved in many industrial processes, such as the ballast used under the railways of a high-speed trains. Using only a discrete approach to simulate a large medium that employs an enormous number of grains of ballast seems very difficult in terms of calculations and implementation. Moreover, a homogeneous approach considered like a continuum approach, does not give the exact response in a zone where particular and localized phenomena can occur. The purpose of this paper is to present a formulation for coupling between a discrete approach at the microscopic scale and a homogenized approach deduced from the discrete approach at the macroscopic scale. Numerical methods that are enable to treat such situations where the domain can be decomposed in sub domains described by approaches on various scales, are proposed. It is at the same time a question of clarifying the bases of these approaches and of proposing numerical tools adapted to this kind of situations.

Keywords: Discrete approach, Homogenized approach, grains of ballast, static equilibrium, deflection.

2. Introduction

A primary objective of modern materials modeling, is to predict the materials response and failure governed by deformation mechanisms. Modeling the ballast all along a line at high speed (TGV) by using a Discrete Elements Method (DEM) seems very difficult in 3D. This difficulty is due to the long time of simulation and which carries out at a high cost. However, by using continuum mechanics for zones where singular phenomena occur, we can not obtain exact behavior of the studied material. It is clear that some coupled methodology must be established to combine the strengths of both discrete and continuum modeling. Although this field has acquired a substantial history, it remains an active area of research [1], [2], [3].

The majority of methods of coupling between the discrete and continuum modeling consider firstly a microscopic approach on fine scale, and deduce the coarse approach on macroscopic scale from the microscopic approach.

In the objective of basing a clear idea on the behavior of the ballast under the rails of a TGV in 2D or 3D, we propose a 1D model composed of a beam resting on springs, and on which we apply a load F .

In this work, the deflection of the beam (as well as all node parameters) that minimizes the energy of the system is calculated using two approaches; discrete approach and homogenized approach deduced from the discrete approach. A comparison between the response of the sytem obtained using these approaches will be always made in order to illustrate the cases where the homogenized approach can not replace the discrete approach. This difference will bring us to apply the coupled approach.

3. Discrete and Homogenized Approach

We note that the beam respresents a rail, under which the track tie and the grains of ballast are modelled by springs with elastic behavior. The applied load is supposed fix, so we are interested to

the static problem. The static equilibrium equation of the discrete approach is written:

$$(1) \quad EIu^{(4)}(x) + \sum_{i=1}^N h k_i u(x_i) \delta(x - x_i) = F \delta(x - D)$$

D , h and k_i means respectively the distance between the end of the beam and the point of application of the applied load, the spacing between consecutive track ties and the stiffness of springs. N is the number of track ties and x_i is the node position.

For the homogenized approach we proceed by the homogenization of the beam compared to the stiffnesses of the springs. The philosophy of this approach returns to the fact, that in the microscopic scale we started from an enormous degree of freedom (*dof*), whereas the homogenisation is used to replace the zones that have homogeneous *dof* by only one *dof*, which will have like consequence to reduce the needed computing time.

After a numerical implementation of these approaches, several test were elaborated. We tested many cases where we have heterogeneous and homogeneous stiffness. In the case of heterogeneities under the rail way, it was clear that the two approaches lead to different results, especially when the ratio between the number of the elements of two approaches increases. This difference is illustrated more particularly in the zones presenting heterogeneities. Because of this difference, a coupled approach between the homogenized and discrete approaches that is enable to produce a similar behavior of ballast like that produced by the discrete approach, is proposed.

4. Coupled Approach

The first stage in the numerical solution of the coupled approach is a homogenized approach where the ratio between the size of a homogenized element and another discrete element is very high. Firstly the mechanical parameters on the first node are calculated and the criteria of coupling is applied. This criterion can be summarized as follows: If the deflection and rotation errors calculated by two approaches is lower than 10%, the scale of computation is not changed, else the discretization is refined that it means a decreasing in the size of the homogenized element. This procedure of refinement is used as long as it is necessary in order to be placed on the scale of the discrete elements.

5. Conclusion

After applying the coupled approach in the cases where the homogenized and discrete approaches do not give an identical behavior of the ballast, we could show the efficiency of this approach and it can be summarized in two points. Firstly, the good agreement between the discrete and the coupled behavior and secondly, the reduction of the number of discrete nodes that implies a reduction in the computation time compared to the discrete approach.

6. References

- [1] E.Frangin, P.Marin, L.Daudeville (2006). *Coupled finite/discrete elements method to analyze localized impact on reinforced concrete structure*, Proceeding EURO-C.
- [2] V.B. Shenoy, R. Miller, E.B. Tadmor, D. Rodney, R. Philips, M. Ortiz (1999). *An adaptative finite element approach to atomic-scale mechanics - the quasicontinuum method*, Journal of the Mechanics and Physics of Solids 47, 611-642.
- [3] S.Kohlhoff, S.Schmauder (1989). *A new method for coupled elastic-atomistic modelling in: V. Vitek, D.J. Srolovitz (Eds), Atomistic Simulation of materials: Beyond Pair Potentials*, Plenum Press, New York, pp. 411-418.

MICROMECHANICAL MODEL OF HYPERELASTIC BEHAVIOUR OF CELLULAR MATERIALS

M. Janus-Michalska

Institute of Structural Mechanics, Cracow University of Technology, Cracow, Poland

Cellulars are an increasingly investigated class of materials solids as they reveal unique properties. Generally these materials due to their geometric structure of skeleton are characterized by high deformability and reversibility of deformation thus showing hyperelastic behaviour. Due to large pore volume fraction they can easily experience large deformations since such a deformation on the macroscopic level usually require smaller deformations of the individual walls constituting skeleton. The formulation based on micromechanical modeling [1] assumes that essential macroscopic features of mechanical behaviour on a macro scale can be inferred from the deformation response of a representative volume element. Open-cell materials with diverse regular skeleton structures as shown in Fig 1. are considered.

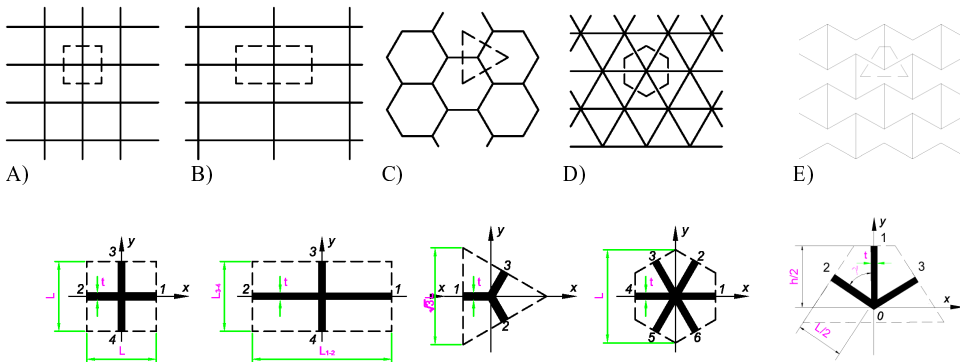


Fig. 1. Typical material structures and their representative unit cells.

Microstructure of these materials are modelled by idealized regular repeating pattern of unit cells where skeleton of a cell is modelled as elastic beam structure of unit depth with stiff joints. The idea of two-scale modelling leads to formulation of equivalent continuum, which elastic properties : elastic stiffness matrix, yield stresses and limit strains describing deformability in the elastic range depend on material properties of a solid phase of the cell and topological arrangement of it's structure.

Interest is focused on geometric nonlinearity which refers to large displacement and small strain case. The present paper extends recent effective linear anisotropic elasticity model [2,3] for cellular materials to geometric nonlinearity, which in the frame strain potential formulation [4,5] is described by constitutive relation between Green's Lagrangean strain tensor \mathbf{E} and second Piola-Kirchhoff stress tensor $\mathbf{\Pi}$, as follows:

$$(1) \quad \mathbf{\Pi}(\mathbf{E}) = \left. \frac{\partial \mathbf{\Pi}}{\partial \mathbf{E}} \right|_{\mathbf{E}=\mathbf{0}} : \mathbf{E} = \mathbf{S}_0 : \mathbf{E}$$

where: \mathbf{S}_0 is initial elasticity tensor (initial tangent operator).

Examples involving numerical test on cellular materials under homogeneous strain for uniaxial or biaxial loading in the tensile and compressive range, and under shearing are considered. The calculations are performed for cellular materials exhibiting structures specified in Table 1.

Structure type	L [mm]	h [mm]	t [mm]	γ	R_e [MPa]	E_s [GPa]
A)	20.00	-	1.00	-	200.0	20.0
C)	20.00	-	1.00	-	200.0	20.0
D)	20.00	-	1.00	-	200.0	20.0
E)	6.0	8.0	0.15	60°	100.0	10.0

Table 1. Specification of cellular microstructure.

The effect of nonlinearity is shown on example of uniaxial test. The load is applied subsequently in three chosen directions ξ with respect to x axis (shown in Fig.1) given by β angle. Due to isotropic mechanical properties the materials of structure type C) and D) are not sensitive to this load direction. The relevant plots of normal nominal stress in dependence of material stretch are given in Fig. 2.

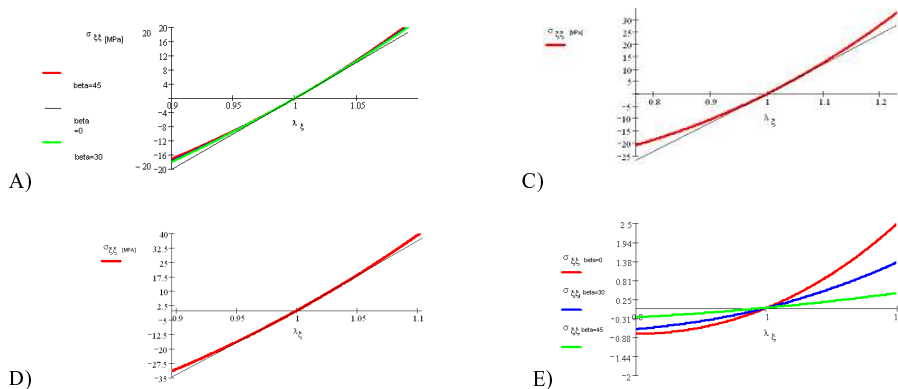


Fig2. Stress-strain curves in elastic range

The conclusion is that significant differences between infinitesimal strain behaviour and small strain regime can be observed. The influence of material structure and microstructural parameters on nonlinear effect is clearly visible and it gives the hints for material selection.

References

- [1] S.Nemat-Naser, M.Hori, (1999). *Micromechanics*, 2nd edition Elsevier.
- [2] M. Janus-Michalska, (2005). Effective Models Describing Elastic Behaviour of Cellular Materials, *Arch. Met. and Mat.*, 50, 595-608.
- [3] M. Janus-Michalska, (2007). Micromechanical Model of Auxetic Cellular Materials, *Arch. Met. and Mat.*, - submitted for publication.
- [4] M.M. Attard, (2003). Finite strain isotropic hyperelasticity, *Int. Jour. of Solids and Struct.*, **40**, 4353-4378.
- [5] A. Menzel, P.Steimann, (2003). A view on anisotropic finite hyperelasticity, *European Journal of Mechanics A/Solids*, **22**, 71-87.

MECHANICAL BEHAVIOR OF BULK METALLIC GLASSES

L. Anand

*Department of Mechanical Engineering, Massachusetts Institute of Technology
Cambridge, MA 02139, USA*

In recent years, certain amorphous metallic alloys which can be solidified in relatively large section sizes under moderate cooling rates have been developed. Such disordered metals are referred to as *bulk metallic glasses*.

When a metallic glass is deformed at ambient temperatures, well below its glass transition temperature, its inelastic deformation is characterized by strain-softening which results in the formation of intense localized shear bands; fracture typically occurs after very small inelastic strain in tension, but substantial inelastic strain levels can be achieved under states of confined compression, such as in indentation experiments. The micro-mechanisms of inelastic deformation in bulk metallic glasses are not related to dislocation-based mechanisms that characterize the plastic deformation of crystalline metals. The plastic deformation of amorphous metallic glasses is fundamentally different from that in crystalline solids because of the lack of long-range order in the atomic structure of these materials. Computer simulations in the literature show that at a micromechanical level, inelastic deformation in metallic glasses occurs by local shearing of clusters of atoms (≈ 30 to 50 atoms), this shearing is accompanied by inelastic *dilatation* that produces strain-softening, which then leads to the formation of shear bands. An important consequence of the micro-mechanism of inelastic deformation in amorphous metals is that at the macroscopic level, experimentally-determined yield criteria for inelastic deformation are found not to obey the classical pressure-insensitive forms, but show a significant pressure sensitivity of plastic flow, which may be approximated by the Coulomb-Mohr yield criterion.

In this talk I will present a complete three-dimensional constitutive model for the elastic-viscoplastic response of pressure-sensitive and plastically-dilatant isotropic materials. The flow-rule in this model is a generalization of a two-dimensional (plane-strain) “double-shearing” constitutive model (used in soil mechanics) to three-dimensions. The constitutive model has been implemented in a finite element program, and the numerical capability is used to study the deformation response of amorphous metallic glasses. Specifically, the response of an amorphous metallic glass in tension, compression, strip-bending, and indentation is studied, and it is shown that results from the numerical simulations qualitatively capture major features of corresponding results from physical experiments available in the literature.

MECHANICAL BEHAVIOUR OF TiAl ALLOYS DURING STATIC AND DYNAMIC DEFORMATIONS

H.J. Luckner, S.P. Gadaj, W.K. Nowacki

Institute of Fundamental Technological Research, Warsaw, Poland

Mechanical behavior of materials (TiAl intermetallics) applied in airplanes, helicopters and power generators subjected to compression in the range of the strain rates ($10^{-4} \text{ s}^{-1} \div 10^4 \text{ s}^{-1}$) have been investigated.

Three different TiAl alloys have been studied:

1. composition: Ti-48Al-2Cr-2 Nb - Insamet
2. composition: Ti-43Al-0.8Mo-0.8Cu-0.2 - Pol. Śl.
3. composition: Ti-6Al-4V - Stepino Titanium Company Ltd.

The stress-strain characteristics of high accuracy have been obtained in quasi-static test conducted on TiAl specimens (5 mm diameter, 5 mm height) mounted to the Instron testing machine. In order to acquire true values of mechanical parameters the laser extensometer was applied. It ensured determination of real values of strains and mechanical parameters. The smart extensometer technique enables to measure deformation of specimens directly and independently from the testing machine and the grip interaction. All experiments have been carried out at room temperature. Three tests have been done for each rate of deformation value.

Dynamic investigations were carried out on Hopkinson pressure bar apparatus, available in IPPT, according to the technique presented in [1, 2].

In each test we obtained strain-stress characteristics as well as values of Young's modulus and yield stress.

The examples of the stress-strain relations obtained during uniaxial quasi-static compression of the TiAl material, for the selected rates of deformation, are presented in the Fig. 1.

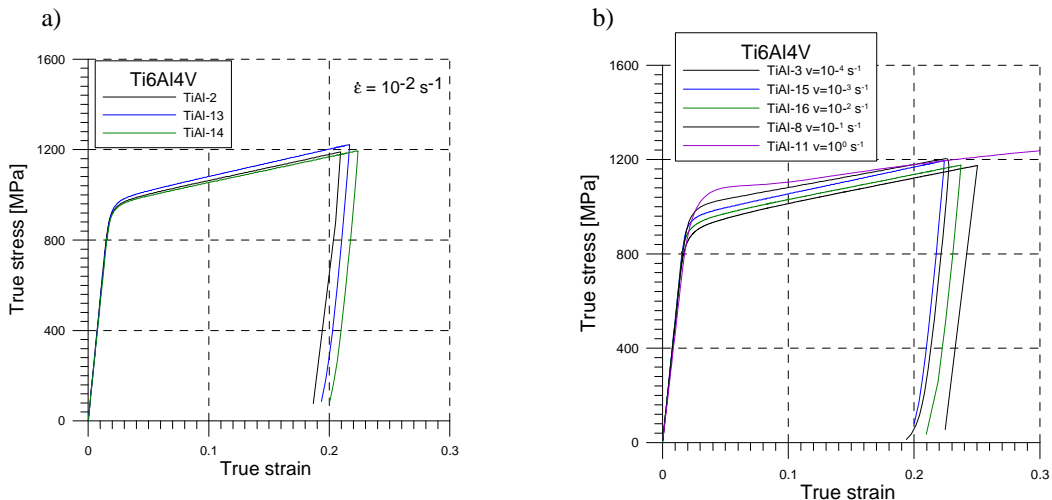


Fig. 1. Stress-strain relations obtained during quasi-static compression tests of the TiAl intermetallic: a) for the same rate of deformation, b) for different rates of deformation

The mechanical characteristics recorded for the compression tests of Ti-6Al-4V intermetallic (Fig. 1a), have pointed that the differences between results obtained for the same rate of

deformation are not significant. The results presented in the Fig. 1b have shown that for higher strain rate, the higher strain hardening is observed. Moreover, in the case of the highest strain rate being applied, namely 1 s^{-1} , the stress-strain relation has manifested a dynamic character. In the Fig. 2 examples of the same relations obtained for dynamic rates of deformation are presented.

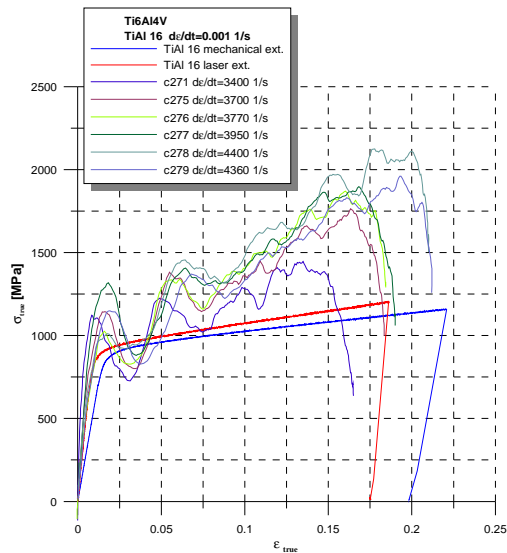


Fig. 2. Stress-strain relations obtained for dynamic compression tests of TiAl intermetallic, performed with the strain rates from the range 3400 s^{-1} - 4400 s^{-1} , and the example of quasi-static ones obtained using the mechanical and laser extensometers

The stresses recorded in the dynamic tests are higher than those observed in static tests. In the elastic range of deformation the results obtained for the dynamic rates of deformation and as well as the quasi-static ones (acquired by the laser extensometer) are comparable.

References

- [1] E.A. Pieczyska, R.B. Pęcherski, S.P. Gadaj, W.K. Nowacki, Z. Nowak, M. Matyjewski, Experimental and theoretical investigations of glass fibre reinforced composite subjected to uniaxial compression for a wide spectrum of strain rates, *Arch. Mech.* **58**, 3, 2006, pp. 273-291.
- [2] W.K. Nowacki, S.P. Gadaj, J. Luckner, Report KMM-NoE, II Part, Project TR 1.1 „Titanium aluminates for high temperature applications”, 2007.

WAVE AND DIFFUSIVE PHONON HEAT TRANSPORT IN DIELECTRICS AND SEMICONDUCTORS UNDER HIGH THERMAL LOADS

Z. Banach, W. Larecki

Polish Academy of Sciences IPPT PAN, Świątokrzyska 21, PL 00-049 Warszawa, Poland

Abstract The new types of heat transport equations for transient processes in dielectrics and semiconductors under high thermal loads are derived from the microscopic, kinetic-theory description of a phonon gas. The modified Grad expansion method is applied to the relaxation time approximation of the Boltzmann-Peierls equation in order to derive a wave hyperbolic nine-moment system. The diffusive parabolic four-moment system is obtained by means of a similar modification of the Chapman-Enskog expansion method applied to the same kinetic model. Both modifications are based on expansions of the phonon distribution function about a nonequilibrium anisotropic Planck distribution, thereby admitting arbitrarily large heat fluxes and conforming to the time scales of the phonon gas relaxation processes.

In many modern technological applications, high transient thermal loads are applied to dielectric and semiconducting materials. It is well recognized that, in those cases, neither the classical Fourier law nor the Maxwell-Cattaneo-Vernotte heat wave equation accurately predict the thermal response of the material. Since the heat transport by phonons (quanta of a crystal vibrational energy) predominates in dielectrics and semiconductors, the suitable heat transport equations should be derived in some way from the microscopic, kinetic-theory description of a phonon gas. Hence, we consider the Boltzmann-Peierls equation governing the phonon distribution function and assume the commonly used Callaway's relaxation time approximation of the collision term. The latter involves the relaxation time τ_R of resistive processes that conserve energy, and the relaxation time τ_N of normal processes that conserve additionally the quasi-momentum and lead to a nonequilibrium anisotropic Planck distribution, also called a drifting distribution. These two relaxation times determine natural time scales for the flow of a phonon gas.

Our objective is to obtain the approximate description of the phonon gas flow in the time scale of the order of τ_N , in both wave and diffusive regimes. We aim at the theory admitting arbitrarily large values of the components of the heat flux vector and taking into account the relaxation times τ_R and τ_N , since fast thermal phenomena are considered. We adopt a physically justified assumption that τ_N is much smaller than τ_R . Clearly, during the first time period, normal processes make the phonon gas approach the displaced Planck distribution, and then during the longer time period, resistive processes return it to the equilibrium Planck distribution. Hence, the use of the respective expansions of the phonon distribution function about a nonequilibrium anisotropic Planck distribution function, expressed in terms of the energy density and the heat flux [1], for the derivation of the sought hydrodynamic descriptions of the phonon gas flow suggests itself. Commonly used simplifications in the phonon kinetic model are employed. Namely, no distinction is made between longitudinal and transverse phonons, linear isotropic phonon dispersion relation $\Omega = c |\mathbf{k}|$ is assumed (c is the constant Debay speed), the components of the wave vector \mathbf{k} are assumed to range from $-\infty$ to $+\infty$ and the relaxation times τ_N and τ_R are assumed to be constant.

In order to derive the hyperbolic evolution equations for the phonon gas state variables, we generalize the method of Grad in the sense that, instead of the local equilibrium Planck distribution, we take the nonequilibrium anisotropic Planck distribution as a base for the

expansion [2,3]. Our reasoning is as follows: Firstly, we set up a weighted Hilbert space for the expansion with the aid of the formula for a kinetic entropy of the phonon gas. Secondly, we define an orthogonal basis in this Hilbert space. Then, the expansion coefficients are determined and the relations between those coefficients and the moments of the distribution function are established. Substitution of the truncated expansion into the corresponding system of moment equations leads to a system of the evolution equations for the moments. In this way, a hierarchy of closed systems is obtained. Each system contains the relaxation times τ_N and τ_R , is nonlinear in the energy density and the heat flux, and depends linearly on the higher-order moments of the distribution function. The first system of the hierarchy is the nine-moment system which includes the deviatoric part of the flux of the heat flux as a gas state variable.

A similar modification of the Chapman-Enskog method is employed for the derivation of the diffusive heat transport equations. Namely, the expansion in gradients of the energy density and the drift velocity of the phonon distribution function about a nonequilibrium displaced Planck distribution is assumed as a solution of the Boltzmann-Peierls equation. The relaxation time τ_N plays the role of the expansion parameter. The zeroth-order terms in τ_N yield the hyperbolic system for the energy density and the drift velocity, equivalent to that derived in [1]. The first-order terms result in turn in the second-order quasilinear parabolic system of equations for the same unknowns. The relaxation time τ_R appears in the production term on the right hand side of an equation for the drift velocity, whereas the relaxation time τ_N appears in the expression for the deviatoric part of the flux of the heat flux. The coefficients of the system, interpreted as the transport coefficients, are nonlinear functions of the energy density and the drift velocity. It is demonstrated that this parabolic system is consistent with the second law of thermodynamics, i.e., it enables us to define a macroscopic entropy density as a function of hydrodynamic variables which satisfies the balance equation with a non-negative production due to both resistive and normal processes. Finally, a comparison of the obtained four-moment parabolic system with the result of parabolisation of the nine-moment hyperbolic system [4] is presented. It is expected that the nine-moment quasilinear hyperbolic system and the four-moment quasilinear parabolic system can describe more adequately wave and diffusive heat transport under the rapidly varying high thermal loads than the previous theories which treat the heat flux in a perturbative manner.

Acknowledgment

This investigation was conducted within the framework of a scientific research project N N501 0074 33, financed by the Polish Ministry of Science and Higher Education during years 2007-2009, contract no.: 0074/B/T02/2007/33.

References

- [1] W. Larecki : Symmetric Conservative Form of Low-Temperature Phonon Gas Hydrodynamics. II. – Equations of Heat Transport and Thermal Waves in the Case of Linear Isotropic Approximation of Phonon Frequency spectrum. *Nuovo Cimento* **14D**:141-176, 1992.
- [2] Z. Banach and W. Larecki: Nine-moment phonon hydrodynamics based on the modified Grad-type approach: formulation, *J. Phys. A: Math. Gen.* **37**, 9885-9829, 2004
- [3] Z. Banach and W. Larecki: Nine-moment phonon hydrodynamics based on the modified Grad-type approach: hyperbolicity of the one-dimensional flow, *J. Phys. A: Math. Gen.* **37**, 11053-11072, 2004
- [4] Z. Banach and W. Larecki: Kawashima condition for a hyperbolic moment model of phonon hydrodynamics, submitted

**HEMIVARIATIONAL INEQUALITIES MODELING
DYNAMIC CONTACT PROBLEMS IN VISCOELASTICITY**

K. Bartosz

Jagiellonian University, Faculty of Mathematics and Computer Science, Institute of Computer Science, Krakow, Poland

In the paper we study a mathematical model of the dynamic process of frictional contact between a deformable body and a foundation. The unknown variables of the system are displacement vector field and stress tensor field defined on the set $\Omega \subset \mathbb{R}^d$, $d = 1, 2, 3$, which the body occupies. The body under consideration is assumed to be viscoelastic with a linear elasticity operator and a nonlinear viscosity operator. The contact is modeled with a general normal damped response condition. The quasistatic and dynamic contact problems for viscoelastic bodies have been recently investigated in many contributions, see e.g. Han and Sofonea [4], Jarusek [5], Kuttler [6], Rochdi et al. [9] and the literature therein. In this paper we consider two additional phenomena connected with the contact process.

The first of them is adhesive interaction between the body and the foundation. We refer to Frémond [2, 3] in order to introduce a surface internal bonding field having values between zero and one, which describes the fractional density of active bonds on the contact surface. An evolution of the bonding field is governed by an ordinary differential equation. In particular we consider adhesive viscoelastic bilateral contact. The main feature of this model is the fact that during the process there is no gap between the body and the foundation. From the mathematical point of view the bilateral contact condition is very convenient since it leads to a linear subspace of admissible displacements.

The second phenomenon is a wear of the material. To model the wear of the contacting surfaces we introduce (following Section 3.2 of [10]) the wear function, which measures the depth, in the normal direction, of the removed material. We treat the problem with a simplified version of the Archard law which is a rate condition for wear production. This law allows to eliminate the unknown variable, the wear function, from the model. In this manner the problem decouples and we are led to a variational formulation involving only the displacement field.

In both cases the dependence of the normal and tangential stress on the normal and tangential displacement is supposed to have nonmonotone character of the subdifferential form. Therefore, a convex analysis approach to the problem is not possible. We are lead to a mathematical model, called a hemivariational inequality, which involves the Clarke subdifferential of a locally Lipschitz functional. For instance, we formulate the system coupled with a differential equation and an evolution hemivariational inequality obtained as a variational formulation of a hyperbolic equation. The problem is following: find the displacement field u and the bonding field β such that

$$(1) \quad \begin{cases} \langle u''(t) + A(t, u'(t)) + Bu(t) - f(t), v \rangle_{V^* \times V} + \int_{\Gamma_C} j^0(x, t, \beta(x, t), \gamma u(t); \gamma v) d\sigma(x) \geq 0 \\ \text{for all } v \in V, \text{ a.e. } t \in (0, T) \\ u(0) = u_0, \quad u'(0) = u_1 \\ \beta'(t) = F(t, u(t), \beta(t)) \quad \text{on } \Gamma_C \times (0, T) \\ \beta(0) = \beta_0 \quad \text{on } \Gamma_C, \end{cases}$$

where $A: (0, T) \times V \rightarrow V^*$ is a nonlinear damping operator, $B: V \rightarrow V^*$ is a linear elasticity operator, V denotes a subspace of the Sobolev space $H^1(\Omega; \mathbb{R}^d)$, V^* is its dual, $j^0(x, t, \cdot)$ is Clarke

directional derivative of a locally Lipschitz function $j(x, t, \cdot): \mathbb{R}^d \rightarrow \mathbb{R}$, $f \in L^2(0, T; V^*)$, γ stands for a trace operator and Γ_C is the part of the boundary of the set Ω on which the contact take place. The function $\beta: \Gamma_C \times (0, T) \rightarrow [0, 1]$ measures an intensity of adhesive bonds and the function β_0 denotes the initial bonding field. The function F is prescribed.

The main result of the paper is to provide the existence of a weak solution to the adhesive frictional contact problem and to the wear contact one, respectively. It is attained by embedding the problems into a class of second order evolution inclusions and by applying a surjectivity result for multivalued operators. The novelty of the model is to consider the coupling between the viscoelastic properties of the material with the adhesive properties on the contact surface and nonmonotone possibly multivalued boundary conditions. The work is completed with a few model examples of subdifferential boundary conditions which include the functions of d.c. type (difference of convex functions) being useful in modeling of nonmonotone sawtooth contact and friction laws. These examples illustrate the applicability of our results.

- [1] K. Bartosz (2006). Hemivariational inequality approach to the dynamic viscoelastic sliding contact problem with wear, *Nonlinear Anal.* **65**, 546-566.
- [2] M. Frémond, Adhérence des solides (1987). *J. Mécanique Théorique et Appliquée*, **6**, 383-407.
- [3] M. Frémond (2002). *Non-Smooth Thermomechanics*, Springer, Berlin.
- [4] W. Han and M. Sofonea (2002). *Quasistatic Contact Problems in Viscoelasticity and Viscoplasticity*, American Mathematical Society, International Press.
- [5] J. Jarusek (1996). Dynamic contact problems with given friction for viscoelastic bodies, *Czech. Math. J.*, **46**, 475-487.
- [6] K. L. Kuttler (1997). Dynamic friction contact problem with general normal and friction laws, *Nonlinear Anal.* **28**, 559-575.
- [7] S. Migórski and A. Ochal (2006). A unified approach to dynamic contact problems in viscoelasticity, *J. Elasticity* **83**, 247-275.
- [8] S. Migórski (2005). Dynamic hemivariational inequality modeling viscoelastic contact problem with normal damped response and friction, *Appl. Anal.* **84**, 669-699.
- [9] M. Rochdi, M. Shillor and M. Sofonea (1998). A quasistatic contact problem with directional friction and damped response, *Appl. Anal.* **68**, 409-422.
- [10] M. Shillor, M. Sofonea and J.J. Telega (2004). *Models and Analysis of Quasistatic Contact*, Springer, Berlin.

ADIABATIC MICRODAMAGE ANISOTROPY IN DUCTILE MATERIALS

A. Glema¹, T. Łodygowski¹, P. Perzyna² and W. Sumelka¹

¹Poznan University of Technology, Institute of Structural Engineering, Poznan, Poland

²Institute of Fundamental Technological Research, Warsaw, Poland

1. Introduction

The main aim of the following discussion is the analysis of the adiabatic anisotropic process during fast tension test, where the rate of strains reaches nearly 10^4s^{-1} . An anisotropy is induced by the evolution of the intrinsic microstructure and affects on all stages of the analysis. The problem is defined in terms of the continuum mechanics in the framework of thermodynamics. The essential role, in the formulation, plays the definition of the temperature evolution due to the influence of the intrinsic microdamage. The microdamage introduces an additional term to the temperature evolution law, thus an identification of all of its components is needed.

The microdamage is incorporated into the constitutive structure as a component of the postulated internal state vector, and is described by the second order, symmetric tensorial field - called strictly *microdamage field* [2]. Microdamage field governs the influence of the evolution of the microvoids, microcracks etc., in micro level, on the macro material structure - what in turn can lead to the failure (the loss of the continuity in macro level).

The proposed material model is implemented in the Abaqus commercial finite element code, using the capability of the user subroutine interface.

2. Evolution of temperature

Let us assume that the free energy function ψ exists and takes the form

$$(1) \quad \psi = \varepsilon - \vartheta \eta,$$

where ε is the density of the internal energy, ϑ denotes the absolute temperature and η is an entropy. The first law of thermodynamics, after assuming that thermal energy is transferred through the surface only and keeping Eq. (1), has the local form

$$(2) \quad \frac{1}{\rho_{Ref}} \boldsymbol{\tau} : \mathbf{d} - \dot{\psi} - \dot{\vartheta} \eta - \dot{\eta} \vartheta - \frac{1}{\rho} \text{div} \mathbf{q} = 0,$$

where ρ_{Ref} is reference density, $\boldsymbol{\tau}$ is Kirchhoff stress tensor, \mathbf{d} is symmetric part of the spatial velocity gradient, ρ is actual density and \mathbf{q} denotes the vectorial heat flux.

Assuming moreover that

$$(3) \quad \psi = \hat{\psi}(\mathbf{e}, \mathbf{F}, \vartheta; \boldsymbol{\mu}),$$

where \mathbf{e} is spatial strain tensor, \mathbf{F} is deformation gradient and $\boldsymbol{\mu}$ denotes the internal state vector, one can obtain the following local form of the second law of thermodynamics

$$(4) \quad -\frac{\partial \hat{\psi}}{\partial \boldsymbol{\mu}} \cdot \mathbf{L} \boldsymbol{\mu} - \frac{1}{\rho \vartheta} \mathbf{q} \cdot \text{grad} \vartheta \geq 0,$$

and its important consequence that

$$(5) \quad \eta = -\frac{\partial \hat{\psi}}{\partial \vartheta},$$

where $L_{\mathbf{v}}$ denotes Lie derivative, where \mathbf{v} denotes velocity field. Eq. (2) can be then rewritten to the form

$$(6) \quad \rho \vartheta \dot{\eta} = -\operatorname{div} \mathbf{q} - \rho \frac{\partial \hat{\psi}}{\partial \boldsymbol{\mu}} \cdot L_{\mathbf{v}} \boldsymbol{\mu}.$$

Assuming that the internal state vector has two components, namely

$$(7) \quad \boldsymbol{\mu} = (\in^p, \boldsymbol{\xi}),$$

where \in^p is the equivalent viscoplastic deformation and $\boldsymbol{\xi}$ is microdamage tensor and taking the time derivative of the Eq. (5), we have from Eq. (6) the fundamental temperature evolution law [1]

$$(8) \quad \rho c_p \dot{\vartheta} = -\operatorname{div} \mathbf{q} + \vartheta \frac{\rho}{\rho_{Ref}} \frac{\partial \boldsymbol{\tau}}{\partial \vartheta} : \mathbf{d} + \rho \chi^* \boldsymbol{\tau} : \mathbf{d}^p + \rho \chi^{**} \mathbf{K} : L_{\mathbf{v}} \boldsymbol{\xi},$$

where the specific heat

$$(9) \quad c_p = -\vartheta \frac{\partial^2 \hat{\psi}}{\partial \vartheta^2},$$

and the irreversibility coefficients χ^* and χ^{**} are determined by

$$(10) \quad \chi^* = - \left(\frac{\partial \hat{\psi}}{\partial \in^p} - \vartheta \frac{\partial^2 \hat{\psi}}{\partial \vartheta \partial \in^p} \right) \sqrt{\frac{2}{3}} \frac{1}{\boldsymbol{\tau} : \mathbf{P}},$$

$$\chi^{**} = - \left(\frac{\partial \hat{\psi}}{\partial \boldsymbol{\xi}} - \vartheta \frac{\partial^2 \hat{\psi}}{\partial \vartheta \partial \boldsymbol{\xi}} \right) \frac{1}{\mathbf{K}}.$$

If one puts $\mathbf{q} = \mathbf{0}$, and taking the crucial assumption that $\mathbf{K} = L_{\mathbf{v}} \boldsymbol{\xi}$, the final form of the temperature evolution law in adiabatic anisotropic process is obtained

$$(11) \quad \dot{\vartheta} = \vartheta \frac{1}{c_p \rho_{Ref}} \frac{\partial \boldsymbol{\tau}}{\partial \vartheta} : \mathbf{d} + \frac{\chi^*}{c_p} \boldsymbol{\tau} : \mathbf{d}^p + \frac{\chi^{**}}{c_p} L_{\mathbf{v}} \boldsymbol{\xi} : L_{\mathbf{v}} \boldsymbol{\xi}.$$

The last term in Eq. (11) governs the influence of the anisotropy on the temperature field in material structure.

Instructive numerical examples will be presented.

3. References

- [1] P. Perzyna (2008). *Termodynamiczna teoria lepko-plastyczności*, Profesor Piotr Perzyna Doctor Honoris Causa Politechniki Poznańskiej, 20 luty 2008, Poznań, 17-54.
- [2] A. Glema, T. Łodygowski, P. Perzyna, W. Sumelka (2008). The Numerical Analysis of the Intrinsic Anisotropic Microdamage Evolution in Elasto-Viscoplastic Solids, *International Journal of Damage Mechanics*, [in print].

SIZE EFFECT OF AN ELLIPTIC INCLUSION IN ANTI-PLANE STRAIN COUPLE STRESS ELASTICITY

H.M. Shodja^{1,2} and H. Haftbaradaran¹

¹*Department of Civil Engineering, Sharif University of Technology, Tehran, Iran*

²*Institute for Nanoscience and Nanotechnology, Sharif University of Technology, Tehran, Iran*

1. Introduction

The application of higher order continuum theories, with size effect considerations, have recently been spread in the micro and nano-scale studies. One famous version of these theories, proposed by Mindlin[1], is the couple stress theory. This paper utilizes this theory to study the anti-plane problems of elliptic inclusions.

2. Solution of the governing equations

The governing field equation for the anti-plane problems of couple stress elasticity within a centrosymmetric isotropic material is given by

$$(1) \quad \nabla^2 u_3 - \ell^2 \nabla^4 u_3 = 0,$$

where ℓ is the characteristic length and u_3 is the out of plane displacement, [2]. Concerned with the problems of elliptic cylindrical inclusions, the solution of Eq.(1) is sought in elliptic coordinates, (ξ, η) with $(x_1, x_2) = c_0(\cosh \xi \cos \eta, \sinh \xi \sin \eta)$, Fig.1. Where c_0 is a positive constant.

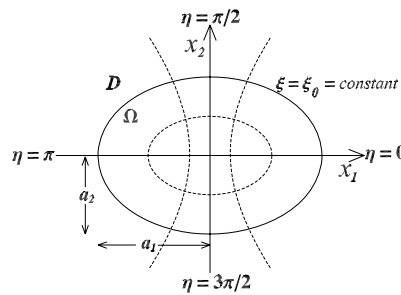


Figure 1. An elliptic domain within an infinite medium.

The general solution of this equation is taken as $\bar{u}_3 + \bar{\bar{u}}_3$, provided that

$$(2) \quad \frac{\partial^2}{\partial \xi^2} \bar{u}_3 + \frac{\partial^2}{\partial \eta^2} \bar{u}_3 = 0, \quad \frac{\partial^2}{\partial \xi^2} \bar{\bar{u}}_3 + \frac{\partial^2}{\partial \eta^2} \bar{\bar{u}}_3 - \frac{c_0^2}{2\ell^2} (\cosh 2\xi - \cos 2\eta) \bar{\bar{u}}_3 = 0.$$

Consider an elliptic domain, Ω within an infinite medium, D , as shown in Fig.1. In the elliptic coordinate system the interface between Ω and D is described by $\xi = \xi_0$. The long and short semi-axes of Ω are denoted by a_1 and a_2 , respectively. The general solution of Eq.(1), periodic in η , associated with the exterior and interior points of Ω are respectively given by $u_3^{(1)}$ and $u_3^{(2)}$ as:

$$(3) \quad u_3^{(1)}(\xi, \eta) = \sum_{k=1}^{\infty} (\bar{a}_{k1} \cos k\eta + \bar{b}_{k1} \sin k\eta) (\cosh k\xi - \sinh k\xi) + \bar{\bar{a}}_{01} c e_0(q, \eta) K e_0(q, \xi) + \sum_{k=1}^{\infty} \bar{\bar{a}}_{k1} c e_k(q, \eta) K e_k(q, \xi) + \bar{\bar{b}}_{k1} s e_k(q, \eta) K o_k(q, \xi),$$

and

$$(4) \quad u_3^{(2)}(\xi, \eta) = \sum_{k=1}^{\infty} (\bar{a}_{k2} \cos k\eta \cosh k\xi + \bar{b}_{k2} \sin k\eta \sinh k\xi) + \bar{a}_{02} c e_0(q, \eta) I e_0(q, \xi) + \sum_{k=1}^{\infty} \bar{a}_{k2} c e_k(q, \eta) I e_k(q, \xi) + \bar{b}_{k2} s e_k(q, \eta) I o_k(q, \xi),$$

where $q = -c_0^2/4\ell^2$. Here $c e_k$ and $s e_k$ are the angular Mathieu functions and $K e_k, I e_k, K o_k$ and $I o_k$ are the radial Bessel type Mathieu functions. Assume that the displacement field $u_3^* = 2e_{3i}^* x_i + e_{3ij}^* x_i x_j + \dots$ is given inside Ω , where the summation is performed on $i, j = 1, 2$ and $e_{3i}^*, e_{3ij}^*, \dots$ stand for the eigenstrains [3]. The unknown coefficients in Eqs.(3-4) are determined through satisfaction of the following conditions on $\xi = \xi_0$,

$$(5) \quad \bar{T}_3^{(1)} = \bar{T}_3^{(2)}, \quad \bar{M}_\eta^{(1)} = \bar{M}_\eta^{(2)}, \quad u_3^{(1)} = u_3^{(2)} + u_3^*, \quad \sigma_{z\xi}^{(1)} = \sigma_{z\xi}^{(2)},$$

where \bar{T}_3 and \bar{M}_η are the reduced traction components and σ_{ij} is the component of the stress tensor. The superscripts (1) and (2) over a field quantity implies that it is derived from the displacements, $u_3^{(1)}$ and $u_3^{(2)}$, respectively.

3. Numerical results and conclusion

Suppose Ω is an inclusion with uniform eigenstrain, $e_{13}^* = 1$. Ω and D are made of same material, and so they have the same shear modulus, μ and characteristic length, ℓ . To examine the size effect, various ratios for $\frac{\ell}{a_2}$ are considered. In a special case with $a_1 = a_2$, the results via the present formulation reduce to the results derived from the work of Lubarda [2]. For a case where $a_1 = 1.5a_2$, the shear stresses $\sigma_{\eta z}$ and $\sigma_{\xi z}$ just outside of the inclusion along the inclusion-matrix interface are shown in Fig.2. This figure verifies that the results of the present study approach the classical solutions as the inclusion dimensions grow. It is observed that $\sigma_{\xi z}$ attains its maximum at the end points of the long axis of the inclusion, while $\sigma_{\eta z}$ vanishes at these points.

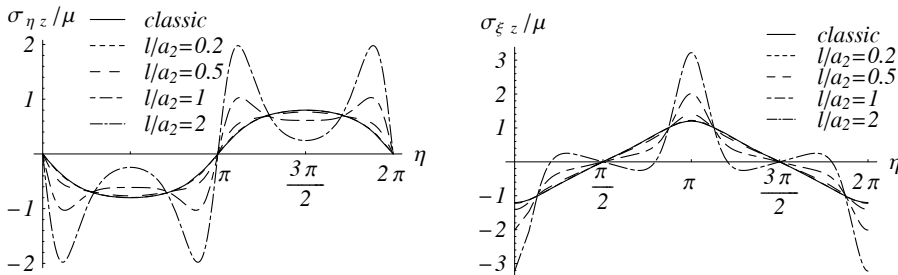


Figure 2. The stress distribution along the inclusion-matrix interface, approached from the matrix.

4. References

[1] R.D. Mindlin and H.F. Tiersten (1962). Effects of couple-stresses in linear elasticity, *Arch. Ration. Mech. Anal.*, **11**, 415-448.
 [2] V.A. Lubarda (2003). Circular inclusions in anti-plane strain couple stress elasticity, *Int. J. Solids Struct.*, **40**, 3827-51.
 [3] T. Mura (1991). *Micromechanics of Defects in Solids*, 2nd ed. Kluwer Academic Publishers, Netherlands.

ANALYSIS OF OBLIQUE PERFORATION OF CONICAL AND OGIVE PROJECTILES INTO THIN METALLIC TARGETS

M.H. Pol^{1,2}, M.A. Akbari³, G.H. Liaghat⁴, A.V. Hosseini²

1-Department of Mechanical Eng. Islamic Azad University, Ahvaz- Iran

2- Ahvaz manufacturing technology Research Center

3- Olom entezami University, Tehran-Iran

4- Department of Mechanical Eng. Tarbiat Modares University, Tehran-Iran

Keyword: Perforation, Penetration. Conical projectile, Ogive projectile, Thin Metallic target

Abstract: In this note, a theoretical and analytical model of the conical and Ogive projectile penetration into metallic targets under oblique impact is presented. The failure is assumed to be asymmetry petaling and the analysis is performed by using the energy balance and work done. The done work consist of the required work for plastic transformation W_p , the work for transferring the matter to new position W_d and the work for bending of the petals W_b .

The analytical model can be predicated the value of final and ballistic velocity of the impact by using the energy balance.

In this present study, by assuming the crater formation, the value of work done is calculated during the oblique penetration of conical projectile into thin metallic targets.

The work done consist of the required work for plastic transformation W_p , the work for transferring the matter to new position W_d and the work for bending of the petals W_b .

In several studies [3,9], it has been shown that we can neglect the loss of energy by temperature (friction). We also neglect the plastic work in dishing target plane. Although this loss of energy isn't important in speeds very higher than ballistic limit, but in speeds near to ballistic limit is considerable.

As will be shown, W_p , W_d , W_b for conical projectile are:

$$W_p = \frac{\pi}{2} b^2 Y \frac{h_o}{\cos \theta} \quad (1)$$

$$W_d = \rho h_o b^2 V_i^2 \tan^2 \alpha (1 - \tan \alpha \tan \phi)^2 \cdot \left(\int_{-\frac{\pi}{2}}^{\frac{\pi}{2}} \frac{1}{[(1 - \sin^2 \phi \sin^2 \delta)^{\frac{1}{2}} + \tan \alpha \cdot \sin \phi \sin \delta]^4} d\delta \right) \\ + 2 \rho h_o V_i^4 \tan^4 \alpha \int_{t_2}^{t_3} t \cdot \left(\int_{\delta^{***}}^{\frac{\pi}{2}} \frac{1}{[(1 - \sin^2 \phi \sin^2 \delta)^{\frac{1}{2}} + \tan \alpha \cdot \sin \phi \sin \delta]^4} d\delta \right) dt \quad (2)$$

$$W_b = \frac{Y h_o^2 b}{2} \int_{-\frac{\pi}{2}}^{\frac{\pi}{2}} \frac{[\frac{\pi}{2} + \sin^{-1}(\sin \phi \sin \delta)]}{(1 - \sin^2 \delta \sin^2 \phi)^{\frac{1}{2}}} d\delta \quad (3)$$

The total work done during penetration is equal to:

$$W = W_p + W_d + W_b \quad (4)$$

The residual speed can be obtained by using the energy balance equation.

$$\frac{1}{2}m(V_i^2 - V_r^2) = W \quad (5)$$

Therefore:

$$V_r = (V_i^2 - \frac{2W}{m})^{\frac{1}{2}} \quad (6)$$

If $V_r=0$, the ballistic limit is computable.

$$V_b = (\frac{2W}{m})^{\frac{1}{2}} \quad (7)$$

For projectiles with ogive nose W_p , W_b are the same conical projectiles, but W_d is dependent to nose shape .profile of a ogive projectile is

$$y = \sqrt{\left(d\left(C^2 + \frac{1}{4}\right)\right)^2 - x^2} - \left(d\left(C^2 - \frac{1}{4}\right)\right) \quad (8)$$

A simpler approximation formula can also be used:

$$y = \frac{d}{2} - \left[\frac{x^2}{2 \times L \times C} \right] \quad (8)$$

Where:

L = cone length, d = cone base diameter, C = the caliber of the cone ($C= L/d$).

Therefore we can calculate the work for transferring the matter to new position , W_d ,with numerical methods.

ON THE LIMIT INTERNAL PRESSURE OF HOLLOW CYLINDERS OF STRAIN HARDENING VISCOPLASTIC MATERIALS

S.-Y. Leu

Department of Aviation Mechanical Engineering, China Institute of Technology, Taiwan

1. Introduction

The paper presents the analytical and finite-element efforts of limit loads of thick-walled hollow circular cylinders. The internally pressurized structures are of strain hardening viscoplastic materials. It is appropriate to evaluate the limit loads by limit analysis sequentially to illustrate the interesting interaction between strengthening and weakening behavior reflecting the properties of strain hardening and strain-rate sensitivity during the deformation process. Particularly, the related analytical solutions are also derived for rigorous validation of the numerical results.

2. Problem Statement and numerical investigation

We consider a plane-strain viscoplastic problem of the von Mises-type material with nonlinear isotropic hardening. The problem domain D consists of the kinematic boundary ∂D_k . The problem statement leads naturally to the lower bound formulation. By duality theorems [1], the corresponding upper bound formulation can be stated in the form of a constrained minimization problem as

$$\begin{aligned} & \text{minimize } \bar{q}(\bar{u}) \\ & \text{subject to } \bar{q}(\bar{u}) = \frac{\sigma_Y}{G} \int_D \|\dot{\varepsilon}\|_{-\nu} dA \\ & \quad \nabla \cdot \bar{u} = 0 \quad \text{in } D \\ & \quad \text{kinematic boundary conditions on } \partial D_k \end{aligned} \quad (1)$$

where $\|\dot{\varepsilon}\|_{-\nu}$ is the dual norm of the primal norm $\|\sigma\|_{\nu}$ based on the flow rule associated with the von Mises yield criterion. σ_Y is a material constant denoting the yield strength. G is a constant relating to the velocity control in each step but may be of various values in a process. $\nabla \cdot \bar{u} = 0$ is the incompressibility constraint inherent in the von Mises model. On the other hand, the behavior of viscoplastic, nonlinear isotropic hardening is described in the form as

$$\sigma_Y = [\sigma_{\infty} - (\sigma_{\infty} - \sigma_0) \exp(-h\bar{\varepsilon})] (\dot{\varepsilon} / \dot{\varepsilon}_0)^m \quad (2)$$

where σ_0 is the initial yield strength, σ_{∞} is the saturation value of σ_0 and h is the hardening exponent. $\bar{\varepsilon}$ is the equivalent strain and $\dot{\varepsilon}$ is the equivalent strain rate. $\dot{\varepsilon}_0$ and m are the reference strain rate and strain-rate sensitivity, respectively. We conduct a sequence of limit analysis problems with updating the configuration of the deforming structures and the current yield strength. In each step and therefore the whole deforming process, rigorous upper bound solutions are solved iteratively by a combined smoothing and successively approximation (CSSA) algorithm [2].

3. Analytical investigation

For rigorous comparisons, we also derive the corresponding analytical solutions with the hardening exponent $h = \sqrt{3}$. The initial interior and exterior radii of the cylinder are denoted by a_0 and b_0 . Also, its current interior and exterior radii are denoted by a and b . With the boundary conditions $\sigma_r(r=a) = P_i$, $\sigma_r(r=b) = 0$, we have the limit load expressed as [3]

$$P_i / \sigma_0 = \left(1 / \sqrt{3}\right)^{m+1} \left(2\dot{a}\dot{a} / \dot{\varepsilon}_0\right)^m \left[\left(1/b^{2m} - 1/a^{2m}\right) / m + (\sigma_{\infty} / \sigma_0 - 1)(a_0^2 - a^2) \left(1/a^{2m+2} - 1/b^{2m+2}\right) / (m+1) \right] \quad (3)$$

where \dot{a} is the velocity of the innermost edge. In addition, it is interesting to reveal the interaction between strengthening and weakening behavior during the deformation process. Therefore, we come to consider the condition of stability, namely the existence of a hardening phenomenon before the weakening behavior. Mathematically, it is expressed as $\partial(P_i / \sigma_0) / \partial a > 0$. If we apply the velocity control to simulate the action of internal pressure, we get the stability condition as

$$(4) \quad \sigma_\infty / \sigma_0 > (m + 3) / 2 + [(m + 1) / 2] [(b_0 / a_0)^2 - 1] / [(b_0 / a_0)^{2m+2} - 1]$$

4. Comparison and validation

We adopt the dimensional consistently parameters: $a_0 = 5.0$, $b_0 = 10.0$, $h = \sqrt{3}$, $\dot{a} = 1.0$, $\dot{\epsilon}_0 = 1.0$, and a constant step size $\Delta t = 0.01$. Figure 1 shows the effect of the strain-rate sensitivity m on the limit internal pressure P_i / σ_0 with the yield strength ratio $R = \sigma_\infty / \sigma_0 = 2.05$. As shown, the computed upper bounds agree well with the analytical solutions. Table 1 lists the analytical results of the stability condition showing the effects of the strain-rate sensitivity m .

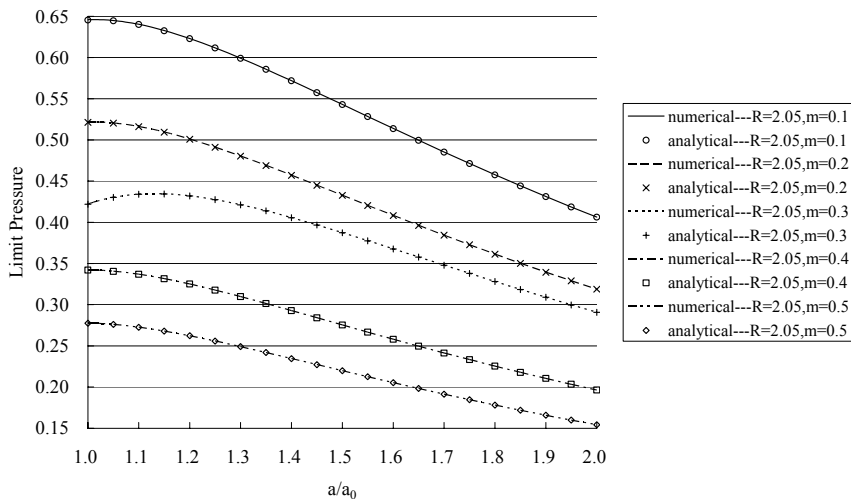


Figure 1. Effect of the strain-rate sensitivity m on the limit internal pressure P_i / σ_0

$m=0.1$	$m=0.2$	$m=0.3$	$m=0.4$	$m=0.5$
2.009	2.201	2.035	2.052	2.071

Table 1. Effect of the strain-rate sensitivity m on the stability condition in terms of the yield strength ratio σ_∞ / σ_0

5. References

- [1] W.H. Yang (1993). Large deformation of structures by sequential limit analysis, *Int. J. Num. Meth. Eng.*, **30**,1001-1013.
- [2] W.H. Yang (1982). A variational principle and an algorithm for limit analysis of beams and plates. *Comput. Meth. Appl. Mech. Eng.*, **33**, 575-582.
- [3] S.Y. Leu (2007). Analytical and numerical investigation of strain-hardening viscoplastic thick-walled cylinders under internal pressure by using sequential limit analysis. *Comput. Meth. Appl. Mech. Eng.*, **196**, 2713-2722.

THE INFLUENCE OF HISTORY OF PRECRITICAL LOADING ON BIFURCATION OF PROCESS OF DEFORMATION OF ELASTIC-PLASTIC BODIES

Yu. Chernyakov, V. Shneider and D. Teslenko

Dnepropetrovsk National University, Dnepropetrovsk, Ukraine

1. Introduction

The foundations of bifurcation theory outside elasticity were laid in works [1, 2]. Further investigations in this direction have shown that bifurcation of deformation process is closely connected with the problem of singularity of yield surface [3]. The question of systematic investigation of stability outside the limits of elasticity at complex precritical loading remains insufficiently studied. For the solving of such problems it is necessary to use theory of plasticity that adequately describes mechanical behaviour of polycrystals at arbitrary loading. In the present work the theory of micro strains [4, 5, 6] is used. This theory leads to singular yield surface and allows describing deformation of metals at complex loading. In [7] it was shown that the theory is capable to describe ratcheting – the accumulation of inelastic strain under the cyclic loading. This accumulation can cause the bifurcation in some situations.

2. Problem statement

Let's consider elastic-plastic body occupying volume V_0 in the init state. On a part of a surface Ω_u we shall specify rate of displacements v_i , and on a part of a surface Ω_σ – rate of surface pressure $\dot{p}_i(t)$. We shall assume, that during some moment of time $t = t_{cr}$, alongside with the basic solution of a boundary problem v_i^0 there is other solution v_i^b . The problem of stability for a difference of solution is reduced to following problem of optimization in a class of cinematically possible differences of velocities:

$$\int_{V_0} \Delta \dot{\mathbf{p}} : \delta(\nabla(\Delta \mathbf{v})) dV = 0, \quad \Delta \mathbf{v}(\mathbf{x}) = 0 \quad \text{при } \mathbf{x} \in \Omega_u,$$

where $\dot{\boldsymbol{\pi}}$ is rate of first Piola-Kirchhoff tensor, $\nabla \mathbf{v}$ is tensor of rate gradient and $\Delta(\cdot) = (\cdot)_b - (\cdot)_a$.

Structure of constitutive relations of theory of micro strains is such that at active pre critical loading the domain of directions of full loading, within limits of which constitutive relations are linearized, exists. At that we have following inequality

$$(\boldsymbol{\sigma}_b^J - \boldsymbol{\sigma}_a^J) : (\mathbf{d}_b - \mathbf{d}_a) \geq (\mathbf{d}_b - \mathbf{d}_a) : \mathbf{G}_0 : (\mathbf{d}_b - \mathbf{d}_a),$$

where $\boldsymbol{\sigma}^J$ - Jaumann derivative of Cauchy stress tensor, \mathbf{d} - rate deformation tensor, \mathbf{G}_0 - stiffness matrix of linearized comparison body, which coincide with stiffness matrix of theory of micro strains at full loading. It is worth to note that stiffness matrix \mathbf{G}_0 is functional of precritical loading process.

Last inequality allows reducing the problem of bifurcation of deformation process to Euler stability problem of linearized comparison body:

$$\nabla \cdot \dot{\boldsymbol{\pi}} = 0,$$

$$\dot{\boldsymbol{\pi}} = \dot{\boldsymbol{\sigma}}^J + \mathbf{R} : \nabla \mathbf{v}$$

$$\dot{\boldsymbol{\sigma}}^J = \mathbf{G}_0 : \mathbf{d},$$

with boundary conditions

$$\mathbf{v}(\mathbf{x}) = 0, \text{ при } \mathbf{x} \in \Omega_u,$$

$$\mathbf{N} \cdot \dot{\boldsymbol{\pi}} = 0 \text{ at } \mathbf{x} \in \Omega_\sigma.$$

This system of equations with homogeneous boundary conditions allows to investigate bifurcation of elastic-plastic bodies at complex loading.

3. Results

In the present work it is considered the problems of localization of plastic deformation and stability of stripe at plane strain, and also the stability of thick plate and surface of half-space at bi-axial precritical loading. The analysis of influence of type of applied loading trajectory on bifurcation of deformation process was done. Bi-axial trajectories of loading and trajectories of complex cyclic loading with ratcheting were considered. It is shown that the history of loading can essentially influence on critical parameters of problem.

6. References

- [1] F.R. Shanley (1947). Inelastic Column Theory, *J. Aeronaut. Sci.*, **V.14, N 5**, 281-287.
- [2] R. Hill (1958). A general theory of uniqueness and stability of elastic plastic solids, *J. Mech.Phys.Solids*, **6**, 236-249.
- [3] R. Hill and J.W. Hutchinson (1975). Bifurcation Phenomena in the Plane Tension Test, *J. Mech. Phys. Solids*, **23**, 239-264.
- [4] Yu.I. Kadashevich, V.V. Novozhilov and Yu.A. Chernyakov (1985). Theory of plasticity including micro strains, *Proc. of USSR AS*, **284(4)**, 821-823. (in Russian).
- [5] Yu.I. Kadashevich and Yu.A. Chernyakov (1992). Theory of plasticity taken into account micro stress, *Advances in Mechanics*, **V.15, N3-4**, 3-39.
- [6] V.P. Shneider and Yu.A. Chernyakov (2006). The development of micro deformations theory: the account of polycrystalline material grain sizes, *Proceedings of third international conference "Multiscale Material Modeling", Freiburg (Germany)*, 530-533.
- [7] Yu.A. Chernyakov and V.P. Shneider (2006). Description of complex cyclic loading in the theory of plasticity including micro strains, *Proc. of AS of Ukraine*, **6**, 56–59.

NUMERICAL INVESTIGATION OF LOCALIZED FRACTURE IN POLYCRYSTALLINE MATERIAL (DH 36 STEEL) DURING DYNAMIC DOUBLE SHEAR LOADING UNDER ADIABATIC CONDITIONS

Z. Nowak, W.K. Nowacki, P. Perzyna and R.B. Pęcherski

Institute of Fundamental Technological Research, Warsaw, Poland

The main objective of the present paper is to discuss procedure of the numerical investigation of localized fracture in polycrystalline material (particularly in DH 36 steel) generated by impact-loaded adiabatic processes. We take advantage of experimental results for DH 36 steel obtained by W.K. Nowacki and P. Gadaj. Particularly we based on the experimental observations of the double-shear specimen placed between two bars by using a Split Hopkinson Presser Bar in dynamic tests at high strain rates. Attention is focused on the proper description of a ductile mode of fracture propagating along the shear band for high impact velocities. This procedure of investigation is based on utilization the finite element method and ABAQUS system for regularized thermo-elasto-viscoplastic constitutive model of polycrystalline material.

1. Introduction

The properties of steel are strongly affected by the manufacturing process. In many processes in which large plastic deformation occurs, a large amount of heat is generated. The effect of the temperature increase on the mechanical behavior of the material can be significant and cannot be neglected in an accurate constitutive model. The understanding of high-strain-rate behavior of metals is essential for the modeling and analysis of numerous processes including high-speed machining, impact, penetration and shear localization. Recently, considerable progress has been made in understanding the role of rate controlling dislocation mechanisms on the temperature and strain rate dependence of the flow stress for metals and alloys.

In large plastic deformation that occurs in the simple shearing of sheet metal as well as in many other forming processes of polycrystalline material the microshear bands in material, resulting in a sever localized deformations, are generated.

In the present study a thermo-viscoplasticity model is used for investigating heat generation in steel with microshear banding is also studied. Special attention is directed at microshear bands generation associated with dynamic loading. In order to obtain a consistent microshear band generation and study its effects, the viscoplasticity model employed is formulated within a thermodynamic framework. In polycrystalline models, viscoplastic deformation takes place in the form of slip within a discrete slip system. A slip itself is a manifestation of dislocation motions. An increase in dislocation density results in a decrease in the mobility of the dislocations, due to pileups and to interaction with dislocation forests and other obstacles. The decrease in dislocation mobility can be seen as a plastic hardening or an increase in slip resistance. Any given dislocation is on a microscopic level surrounded by a stress field in which energy is stored. Since the viscoplastic flow is due to dislocation motion, the stored energy increases with an increase of viscoplastic deformation. The rate of stored energy is equal to the difference between the rate of plastic work and the dissipation of energy which leads to a heat generation. The heat generation is often measured by the fraction of plastic work dissipated as heat χ , which of course is also a measure of the rate of stored energy. Taylor and Quinney in 1934 made early attempts to measure this quantity. They concluded that the fraction of plastic work converted to heat is a constant lying somewhere between 0.8 and 0.95. Later experiments, on the other hand, have shown that the fraction is not a constant. Mason et al. (1994), for example, showed that for austenitic steel this fraction χ , varies between 0.6 and 1, depending upon the accumulated plastic strain. Rosakis et al. (2000) also showed that χ can be influenced by the strain rate.

2. Constitutive model

A general constitutive model of thermo-elasto-viscoplastic polycrystalline solids with a finite set of internal state variables is used. The model, formulated within a thermodynamic framework for large deformations is based on the flow rule proposed by Perzyna (2005). To obtain a thermodynamically consistent formulation here, however, account has been taken of the work of Pęcherski (1998), in which the microshear bands is incorporated on a total form in the strain rate deformation tensor. In the model that Perzyna (2005) developed the flow rule is considered to be of a power type. The set of internal state variables consists of two scalars, namely equivalent inelastic deformation and volume fraction of microshear bands. The equivalent inelastic deformation can describe the dissipation effects generated by viscoplastic flow phenomena and the volume fraction of microshear bands. The relaxation time is used as a regularization parameter. The evolution of the microshear banding related to slip resistance here is assumed to be local for each slip system and to be of a logistic function type. These assumptions turn out to be crucial for modeling the heat generation in a consistent way and also allowing it to be calibrated to experimental tests.

3. Numerical results

The capabilities of the model will be demonstrated in numerical example. The example concerns the simple shear response of polycrystalline steel, special emphasis being placed on the heat generation due to plastic work. As a numerical example we consider dynamic simple shearing and localized fracture in thin plate. We idealize the initial boundary value problem observed experimentally by assuming that the impact loading is simulated by a velocity boundary conditions which are the results of dynamic contact problem. The separation of the projectile from the specimen, resulting from wave reflections within the projectile and the specimen, occurs in the phenomenon.

A thin shear band region of finite width which undergoes significant deformation and temperature rise has been determined. Its evolution until occurrence of final fracture has been simulated. Shear band advance and the development of the temperature field as a function of time have been determined. Comparison of numerical results with experimental observation data has been presented. The numerical results obtained have proven the usefulness of the thermo-elasto-viscoplastic theory in the investigation of dynamic shear band propagations and localized fracture. The model can also be used for a fully coupled thermomechanical analysis.

4. References

- [1] J.J. Mason, J.A. Rosakis and R. Ravichandran (1994). On the strain and strain rate dependence of the fraction of plastic work converted to heat: an experimental study using high speed infrared detectors and the Kolsky bar, *Mechanics of Materials*, **17**, 135-145.
- [2] P. Rosakis, A. Rosakis, G. Ravichandran and J. Hodowany (2000). A thermodynamic internal variable model for the partition of plastic work into heat and stored energy in metals, *J. Mech. Phys. Solids*, **48**, 581-607.
- [3] P. Perzyna (2005). The thermodynamical theory of elasto-viscoplasticity, *Engineering Transactions*, **53**, 235-316.
- [4] R.B. Pęcherski (1998). Macroscopic effects of micro-shear banding in plasticity of metals, *Acta Mechanica*, **131**, 203-224.

MESODEFECT INDUCED MECHANISMS OF PLASTICITY AND FAILURE IN SHOCKED SOLIDS

Yu. Bayandin, O. Naimark

Institute of Continuous Media Mechanics, UB of RAS, Perm, Russia

Keywords: shock-waves, mesodeflects, spall

1. Abstract

Based on statistical thermodynamics the model for solids with mesodeflects (microcracks and microshears) was developed. To confirm the self-similar nature of the plastic wave front theoretical study of relaxation mechanisms was carried out using the constitutive model of solid with mesodeflects. Experimental results and numerical calculations for plane shock wave propagation and spall failure are discussed.

2. Statistical model

The developed statistical model of solid with mesoscopic defects allowed the formulation of phenomenological model in terms of two independent variables - the defect density tensor and structural scaling parameter and the simulation of shock wave propagation in the linkage with structural relaxation phenomena [1,2]. It was established the link of the Hugoniot elastic limit with kinetics of structural transition (mathematically related to the defect density tensor) in the structural metastability area, that has generally thermally-activated character. The development of plastic front is described as the consequence of self-consistent structural (orientation) transition in microshear ensemble that is realized due to the kinetics of structural scaling parameter.

Based on the statistical theory [2] the mathematical model was proposed for plane shock wave propagation in metal. The mechanisms of plasticity, induced by correlated behavior of microshear ensembles, were studied [1,3] in the of internal structural variables – the defect density tensor and the structural scaling parameter. The defect density tensor (microshear induced strain) was introduced as the mean value $p_{ik} = n \langle s_{ik} \rangle$ of “microscopic” shear tensor

$$(1) \quad s_{ik} = 1/2s(v_i l_k + l_i v_k),$$

where \vec{v} is unit vector normal to slip plane of a microscopic shear; \vec{l} is a unit vector in the direction of shear; s is the shear intensity, n is the microshear density. The statistical theory allowed us to establish the second internal variable for continuum with mesodeflects – the structural scaling parameter δ associated with two characteristic structural scales: the mesodeflect nuclei and the distance between defects. The plastic deformation is described in terms of mentioned variables as the structural-scaling transition and corresponds to the scenario of continuous orientation transition in the microshear ensemble along the structural scales.

According to statistical theory these transitions are realized as the multiply metastability of non-equilibrium free energy that for the uni-axial case ($\mathcal{E}_{xx} = \mathcal{E}, p_{xx} = p$) is given by the following nonlinear form

$$(2) \quad \Psi = F/F_m = \frac{p^2}{2\delta} - \left(\frac{p^2}{2} + 0.188p + 0.507 \text{Log}(0.385 + 0.131p + p^2) \right) + \frac{\Sigma p}{\delta},$$

where F_m is energy scale, Σ - dimensionless stress.

3. Results and discussions

Results of numerical calculations for single shock in the Armco iron are presented in papers [1,3]. It was shown that the self-similarity of the plastic shock-wave fronts in solids is the consequence of existence of two independent mechanisms defining structural relaxation. These mechanisms are related to the structural-scaling transition in terms of two independent variables (defect density tensor and structural-scaling parameter). The kinetics of these two characteristic variables (order parameters) at the steady-state plastic wave fronts is realized in the self-criticality regime with generation of auto-solitary strain modes that provides the self-similar scenario of relaxation on the large range of structural scales.

In present investigations a setup for plate impact experiment has been developed at Institute of Continuous Media Mechanics of Ural Branch of RAS to study dynamic fracture at strain rates up to 10^6 s^{-1} . Experiments were carried out at a different impactor velocity in order to investigate dependency on loading conditions.

The numerical simulation of plane shock wave propagation was carried out to establish spall conditions and to propose the mechanism of damage-failure transitions described as a specific form of self-organized criticality in the ensemble of mesoscopic defects – structural-scaling transition. Characteristic features of this transition are the generation of collective modes in mesodefekt ensemble that are responsible for damage localization and transition to failure. Collective modes have the nature of self-similar solution and describe the blow-up damage localization kinetics with characteristic time (peak-up time) on the set of spatial scales. Mechanism of spall failure can be linked with resonance excitation of blow-up collective modes and has the nature of delayed failure with the delay time corresponding to the peak-time of the self-similar solution.

4. Acknowledgments

The research was supported by the projects of the Russian Foundation of Basic Research (No. 07-01-96004, 07-08-96001 and 07-01-91100) and project of the US Civilian Research and Development Foundation (No. RUG1-2866-PE-07).

5. References

- [1] Bayandin Yu., Naimark O., 2004, Experimental and theoretical investigation of self-similar structure of shock wave plastic front in condensed matter, *Physical Mesomechanics, Sp. Is. Part I*, 7, 305-308.
- [2] Naimark O. 2003, Defect-Induced Transitions as Mechanisms of Plasticity and Failure in Multifield Continua, *Advances in Multifield Theories for Continua with Substructure*, Birkhauser Boston (Eds. G. Capriz and P. Mariano), 75-115.
- [3] Bayandin Yu., Naimark O., On self-similar nature of shock-wave propagation in metals, *Multi-phase and multi-components materials under dynamic loading: proceedings of 10th European mechanics of materials conference IFTR PAS, Warsaw, 2007*, 355 – 360.

A GRADIENT-ENHANCED COUPLED DAMAGE-PLASTICITY MODEL IN LARGE STRAIN FORMULATION

*T. Żebro*¹, *K. Kowalczyk-Gajewska*², *J. Pamin*¹

¹ *Cracow University of Technology, Cracow, Poland*

² *Institute of Fundamental Technological Research, Warsaw, Poland*

1. General

Coupled damage-plasticity models are relatively simple if isotropy is assumed, while they have all features necessary for the numerical modelling of composites: void or crack growth, irreversible deformations and stiffness degradation can be represented. However, if applied in localized failure simulations, the models require regularization which can be performed as a non-local enhancement, having either a gradient or integral form.

The aim of the paper is to present a damage-plasticity model at large strain, based on a free energy and dissipation potentials decomposed into elasto-damage and plastic parts. The model incorporates a gradient-type averaging equation for the strain energy which is a driving force of elastic damage coupled to irreversible deformations. The paper is based on the concepts presented in the paper by Liebe and Steinmann [4], extending the theory with a coupling to plasticity. An implementation in the FEAP finite element package is performed. Numerical simulations contain one-element tests and the one-dimensional tensile bar benchmark.

2. Local model

The model is based on the multiplicative split of the deformation gradient \mathbf{F} into elastic and plastic parts. We adopt the Helmholtz free energy in the form, cf. [7, 1]:

$$(1) \quad \Psi = (1 - D)\Psi^e(\mathbf{b}^e) + \Psi^p(\kappa^p),$$

where D is the scalar damage parameter growing from 0 for the intact material to 1 for complete damage, $\mathbf{b}^e = \mathbf{F}^e \mathbf{F}^{eT}$ the elastic left Cauchy-Green tensor and κ^p the internal variable (plastic strain measure).

The elastic part of the Helmholtz potential is the strain energy composed of the volumetric and deviatoric parts, respectively:

$$(2) \quad \Psi^e = W = \Psi'^e(J) + \Psi'^e(\mathbf{b}^e)$$

where $J = \det(\mathbf{F})$ and $\mathbf{b}^e = J^{-2/3} \mathbf{b}^e$ is the isochoric elastic left Cauchy-Green tensor. When the Kirchhoff stress $\boldsymbol{\tau}$ is derived from Ψ in a usual manner, the effective Kirchhoff stress tensor $\hat{\boldsymbol{\tau}}$ occurs:

$$(3) \quad \boldsymbol{\tau} = (1 - D)\hat{\boldsymbol{\tau}}$$

The definitions of Ψ'^e and Ψ''^e are based on [7] and lead to a relation between the Hencky strains (logarithmic stretches) and principal effective Kirchhoff stresses which resembles the classical linear Hooke's law. The plastic part of the Helmholtz potential is standard.

Further, the dissipation potential is postulated in a decoupled form

$$(4) \quad \Phi(\boldsymbol{\tau}, q, Y; D) = \Phi^p(\hat{\boldsymbol{\tau}}, q) + \Phi^d(Y)$$

In the associative case the first part is equal to the yield function $\Phi^p \leq 0$ that depends on the effective Kirchhoff stress $\hat{\boldsymbol{\tau}}$, while parameter q represents the yield strength with isotropic hardening. In the

simplest case linear hardening $q = \sigma_y + h\kappa^p$ and the Huber-Mises yield function are used. The second part of the dissipation potential is the damage loading function $\Phi^d = Y - \kappa^d \leq 0$, in which Y is the thermodynamic force conjugated to damage, equal to the strain energy W . Both the yield and damage conditions are subject to respective Kuhn-Tucker conditions. The damage parameter is computed as a function of the current damage history parameter κ^d :

$$D = f^d(\kappa^d), \quad \kappa^d = \max_{-\infty < s < t} (Y(s), \kappa_0^d)$$

with the initial damage threshold κ_0^d . This function can for instance be exponential [4] or based on the model of Lemaitre [7].

To integrate the nonlinear problem in time, we follow the approach pioneered by Simo in order to preserve the convenient small-strain structure of return mapping algorithm, see [2].

3. Gradient-enhancement

The introduction of gradient-enhancement requires the selection of a non-local parameter and the formulation of a corresponding averaging equation. Within elastic damage models there is an energy gradient formulation with a non-local stored energy \bar{W} serving as an independent variable, and a damage gradient formulation with damage parameter D serving as an independent variable and its gradient \mathbf{D} entering the free energy function [4]. There are also gradient enhanced theories with non-local damage parameter \bar{D} [1]. In the case of ductile damage models, a kinematic non-local variable \bar{z} is introduced, having its local kinematic counterpart, e.g. the equivalent plastic strain [3].

Here the first option is adopted, called in [4] the Energy Gradient Formulation. The damage driving force W is substituted by its non-local counterpart \bar{W} in the damage condition, cf. [6]:

$$(5) \quad \bar{W} = W - \text{Div} \mathbf{W} \quad \rightarrow \quad \Phi^d = \bar{W} - \kappa^d \leq 0, \quad \kappa^d = \max_{-\infty < s < t} (\bar{W}(s), \kappa_0^d)$$

where a damage flux \mathbf{W} is introduced. If the damage flux is derived from the non-local energy by $\mathbf{W} = -c\nabla_X \bar{W}$ with c related to the square of an internal length scale, an implicit formulation ensues which resembles the computationally convenient concept of averaging [5]. It remains to decide whether the averaging should be performed in the initial configuration as above (Lagrange averaging, cf. [6]) or in the current configuration (Euler averaging, cf. [3]). This issue is discussed and the results of one-dimensional tensile bar benchmark are presented.

- [1] P.M.A. Areias, J.M.A.C. de Sa, and C.A.C. Antonio. A gradient model for finite strain elastoplasticity coupled with damage. *Finite Elements in Analysis and Design*, 39(13):1191–1235, 2003.
- [2] F. Auricchio and R.L. Taylor. A return-map algorithm for general associative isotropic elastoplastic materials in large deformation regimes. *Int. J. Plasticity*, 15:1359–1378, 1999.
- [3] M.G.D. Geers. Finite strain logarithmic hyperelasto-plasticity with softening: a strongly non-local implicit gradient framework. *Comput. Methods Appl. Mech. Engrg.*, 193:3377–3401, 2004.
- [4] T. Liebe and P. Steinmann. Two strategies towards geometrically non-linear isotropic gradient damage. *J. Mech. Beh. Mat.*, 13:175–194, 2002.
- [5] R.H.J. Peerlings, R. de Borst, W.A.M. Brekelmans, and J.H.P. de Vree. Gradient-enhanced damage for quasi-brittle materials. *Int. J. Numer. Meth. Engng*, 39:3391–3403, 1996.
- [6] P. Steinmann. Formulation and computation of geometrically non-linear gradient damage. *Int. J. Numer. Meth. Engng*, 46(5):757–779, 1999.
- [7] P. Steinmann, C. Miehe, and E. Stein. Comparison of different finite deformation inelastic damage models within multiplicative elastoplasticity for ductile materials. *Computational Mechanics*, 13:458–474, 1994.

ON THE USE OF GURSON'S MODEL IN CONTINUUM DAMAGE MECHANICS

R. Souchet

Association Française de Mécanique

1. Introduction and statement of the problem

Originally, Gurson obtained a yield surface for porous plastic materials under some particular conditions. Here we give a generalised form of the Gurson yield surface (A), viz

$$(1) \quad f(\sigma, x, \varepsilon_M) = (\sigma_{eq} / \sigma_M)^2 + 2qx \cosh(\frac{1}{2} \text{tr} \sigma / \sigma_M) - (1 + q^2 x^2) = 0,$$

where σ denotes the Cauchy stress tensor, σ_M the flow yield strength, $q=3/2$ and x is a function of the void volume fraction v . An essential fact is the presence of the hydrostatic stress [1].

Close relations exist between stress levels in the matrix material, viewed as the effective material, and the porous material, viewed as the damaged material. By example, in CDM, the respective stress tensors (σ_r, σ) are connected by some relation [2]

$$(2) \quad \sigma_r = \sigma / y(x), \quad 0 \leq y(x) \leq 1, \quad y(0)=1, \quad y(1/q)=0,$$

where $y(x)$ is an unknown decreasing scalar operator. But the introduction of the matrix material by means of (2) leads to the explicit use of the von Mises yield surface $f_r=0$ (B) on the matrix material.

2. The yield surfaces f_r and f

As Gurson, we suppose that the matrix material is rigid-plastic. The void-function $x(v)$ is taken as a damage variable and the equivalent plastic strain ε_M as an internal variable. The yield surface (B) is given as a function of the state (σ_r, ε_M) of the matrix material. But this state (σ_r, ε_M) is connected to the state (σ, x, ε_M) of the damaged material by the formula (2); so it is equivalent to express this yield surface in function of the parameters (σ, x, ε_M), obtaining

$$(3) \quad f_r(\sigma, x, \varepsilon_M) = (\sigma_{eq} / \sigma_M)^2 - (y(x))^2 = 0.$$

Note that (3) is not a yield surface for the damaged material (except in particular cases).

Now if a mechanical process occurs in the damaged body, then from (1) we have $f \leq 0$. But the matrix material undergoes some accompanying process and from (3) we have $f_r \leq 0$. So the region $f \leq 0$ must be restricted by the region $f_r \leq 0$. This is not surprising since the Gurson surface is a necessary condition only, satisfied by the damaged material under the hypothesis $f_r=0$. If we suppose that reversible processes are possible (leaving the rigidity hypothesis), then the domains $f_r \leq 0$ and $f \leq 0$ generally intersect [2]. The particular case of the strict inclusion " $f \leq 0$ implies $f_r \leq 0$ " is possible, but not the reverse one. This last result is due to the fact that it is not possible to give an a priori evolution of the matrix material since the presence of micro-voids restricts the deformations of the matrix material. Naturally the domains $f \leq 0$ and $f_r \leq 0$ may coincide.

Due to rigidity hypothesis, it is easy to show that a damage-plasticity effect arises only when the

condition $y(x) < y_0(x) = (1 - qx)$ is satisfied. Fig 1 describes the two yield curves $f=0$ and $f_r=0$.

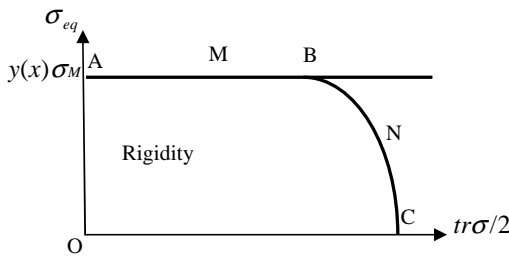


Figure 1. The three parts of the resultant yield curve: AMB, B, BNC

Along AMB, the matrix is plastically strained whereas the micro-voids do not suffer irreversible opening. Along BNC, due to very small elastic strains (rigidity hypothesis) of the matrix, micro-voids suffer opening. Finally, if the stress point rests on the intersection point B, then damage-plasticity arises.

3. Constitutive model and conclusion

We quote below the equations of *damage-plasticity process* only (arising in B, Eq (4)):

$$(4) \quad 2qx \cosh\left(\frac{1}{2} \text{tr} \sigma / \sigma_M\right) = 1 + q^2 x^2 - y^2(x) \quad , \quad (\sigma_{eq} / \sigma_M)^2 = y^2(x)$$

$$(5) \quad d_p = 3(\lambda_r + \lambda) \check{\sigma} / \sigma_M + \lambda qx \sinh\left(\frac{1}{2} \text{tr} \sigma / \sigma_M\right) I$$

$$(6) \quad \dot{\varepsilon}_M = (1 - \nu)^{-1} \sigma_M^{-1} (\sigma : d_p) \quad , \quad \dot{\nu} = (1 - \nu)(\text{tr} d_p) + a_n A(\varepsilon_M) \dot{\varepsilon}_M$$

Eq (5), for the plastic strain rate d_p , is an associative evolution law at the non-smooth point B with two multipliers (λ_r, λ) ($\check{\sigma}$ is the deviator of σ). Eq (6) are evolution laws of ε_M and ν [3,4], where the dot designs time-derivative, a_n is a material constant and A a classical Laplace-Gauss function (to be specified). In the evolution law of the void volume fraction ν , the first part represents the geometric growth ν_g and the second part the contribution of the void nucleation ν_n .

The relations (6) give $\dot{\varepsilon}_M$ and $\dot{\nu}$ through linear function of d_p , then as linear functions of the two multipliers by using (5). But the two consistency conditions give $\dot{\varepsilon}_M$ and $\dot{\nu}$ through linear functions of the stress rate $(\check{\sigma})$, so that the two multipliers may be written as linear functions of $(\check{\sigma})$. Finally we obtained an expression of d_p in function of the stress rate $(\check{\sigma})$. Simple examples show the ability of the actual scheme and so, in this work, as a new result, attention was given to the necessity of using simultaneously yield conditions of both the damaged and virgin materials.

4. References

- [1] G.Z. Voyiadjis, P.I. Kattan (1992). A plasticity-damage theory for large deformation of solids, *Int. J. Eng. Sci.*, **30**, 1089-1108.
- [2] R. Souchet (2007). On yield criteria in plasticity coupled with damage, submitted to *Int. J. Eng. Sci.*, under revision .
- [3] F. Reush. B. Svendsen, D. Klingbeil (2003). Local and non-local Gurson-based ductile damage and failure modelling at large deformation, *Eur. J. Mech. A/Sol.*, **22**, 779-792.
- [4] O.T. Bruhns, H. Xiao, A. Meyers (2001). A self-consistent Eulerian rate type model for finite deformation elastoplasticity with isotropic damage, *Int. J. Sol. Struct.*, **38**, 657-683.
- [5] R. Souchet (2005). Equivalence principles in continuum damage mechanics, *Int. J. Eng.Sci.*, **43**, 1313-1322.

THREE-DIMENSIONAL STRESS-STRAIN STATE OF ROLLER-SHAFT SYSTEM IN CONDITIONS OF CONTACT INTERACTION AND NON-CONTACT BENDING OF SHAFT

S. Sherbakov

Department of Mechanics and Mathematics, Belarusian State University, Minsk, Belarus

1. Introduction

In the mechanics of deformable rigid body a wide class of problems is devoted to the research of contact interaction of rigid bodies [1]. One of the most essential conditions accepted for the solution of contact problems is fast attenuation of stresses and strains if the distance between the considered point and contact area increases.

In addition to the solutions for contact problems mechanics of a deformable rigid body have well developed methods of studying of stress-strain state without considering local effects in the areas of load application (see for example [2]).

Mechanical systems known as active systems [3] operate in conditions of contact interaction and loaded by non-contact forces. Mechanical and mathematical model of three-dimensional stress state of typical roller-shaft active system is considered in the present work. Calculation results show significant difference between such stress state and traditional contact and non-contact stress states.

2. Stress state

Roller-shaft active system is loaded by contact F_N and non-contact Q forces (figure 1). Thus stresses caused by the action of distributed normal $p(x, y)$, tangential $q(x, y)$ contact tractions and non-contact load (figure 1) should be taken into account:

$$(1) \quad \sigma_{ij} = \sigma_{ij}^{(n)} + \sigma_{ij}^{(t)} + \sigma_{ij}^{(b)}, \quad i, j = x, y, z,$$

where $\sigma_{ij}^{(n)}$ – stresses caused by normal contact traction, $\sigma_{ij}^{(t)}$ – stresses caused by tangential contact traction (force of friction), $\sigma_{ij}^{(b)}$ – stresses caused by non-contact loads.

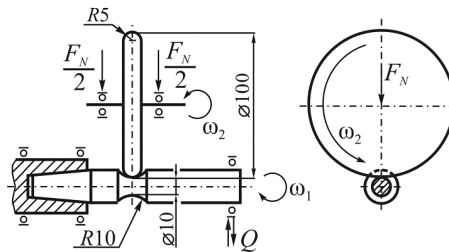


Figure 1. Loading scheme of roller-shaft system

Calculation of stresses $\sigma_{ij}^{(n)}$ in any point of the half-space under the surface when $z < 0$ caused by the action of normal contact tractions $p(x, y)$ is carried out numerically using Boussinesq problem solution $\sigma_{ij}^{(B)}$ [1] (determination of stress components in the half-space caused by unit normal force) [4,5]:

$$(2) \quad \sigma_{ij}^{(n)}(x, y, z) = \iint_{s(\xi, \eta)} p(\xi, \eta) \sigma_{ij}^{(B)}(\xi - x, \eta - y, z) d\xi d\eta,$$

Calculation of stress state $\sigma_{ij}^{(t)}$ under the action of friction force modeled by the distribution of tangential tractions $q(x, y)$ is also carried out numerically using Cerruti problem solution $\sigma_{ij}^{(C)}$ [1] (determination of stress components in the half-space caused by unit tangential force) [4,5]:

$$(3) \quad \sigma_{ij}^{(v)}(x, y, z) = \iint_{S(\xi, \eta)} q(\xi, \eta) \sigma_{ij}^{(C)}(\xi - x, \eta - y, z) d\xi d\eta,$$

Stresses caused by non-contact loads are defined applying particular approaches (for example bending theory):

$$(4) \quad \sigma_{ij}^{(b)} = \sigma_{ij}^{(M)} + \sigma_{ij}^{(N)} + \sigma_{ij}^{(Q)},$$

where indexes M , N and Q correspond to internal moment, normal and shear forces.

Since model (1) is constructed as the superposition of components $(\sigma_{ij}^{(n)}, \sigma_{ij}^{(v)}, \sigma_{ij}^{(b)})$ of stress there is a possibility of analysis of both general solution and any of special cases.

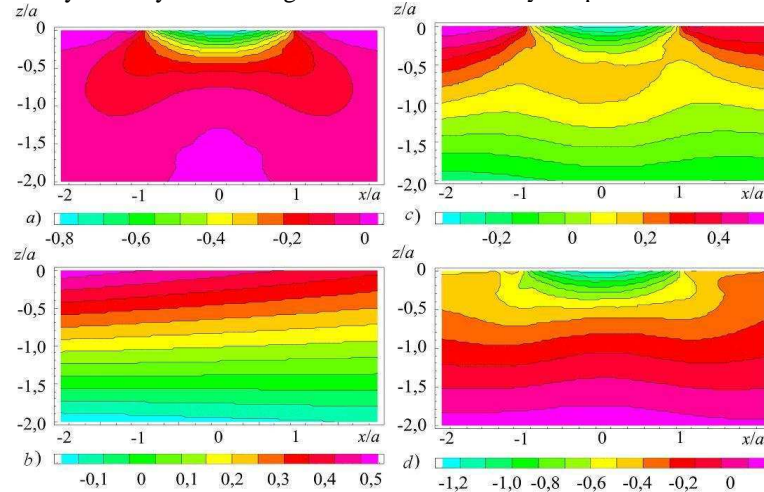


Figure 2. Distributions of stresses $\sigma_{xx}^{(n)}$ (a), $\sigma_{xx}^{(b)}$ (b), $\sigma_{xx}^{(n)} + \sigma_{xx}^{(b)}$ ($Q > 0$) (c), $\sigma_{xx}^{(n)} - \sigma_{xx}^{(b)}$ ($Q < 0$) (d), normalized by maximum Hertz stress p_0 in the neighborhood of contact area ($y = 0$, $a/b = 0.5$), (a and b are the greater and smaller semi-axes of contact ellipse)

It is easy to see from the distributions presented in figure 2 that the stress state in the active system (figures 2.c and 2.d) strongly differs (qualitatively and quantitatively) from traditionally studied stress states under contact or bending (figures 2.a and 2.b respectively). Using (1) it is possible on the one hand to investigate how the field of the stresses (strains) caused by volume deformation is disturbed in some local area where the field of contact stresses (strains) simultaneously occurs. On the other hand it is possible to investigate how the field of local stresses (strains) changes when the field of the stresses (strains) caused by volume deformation is imposed on it.

3. References

- [1]. K.L. Johnson. (1985). Contact Mechanics, Cambridge University Press, Cambridge.
- [2]. S.P. Timoshenko, J.N. Goodier (1970). Theory of Elasticity. McGraw-Hill, NY.
- [3]. L.A. Sosnovskiy Tribo-Fatigue. Wear-fatigue damage and its prediction (Foundations of engineering mechanics) (2004). Springer.
- [4]. L.A. Sosnovskiy, S.S. Shcharbakou (2005). New Class of Contact Problems. *Proceedings of the International Mechanical Engineering Congress and Exposition*, Orlando, 6 pp.
- [5]. L.A. Sosnovskiy, S.S. Sherbakov (2006). Special Class of Contact Problems and the Calculation of the Sstate of Stress of Wheel/Rail System Elements. *Proceedings of the 7th International Conference on Contact Mechanics and Wear of Rail/Wheel Systems*, Brisbane, 93–104.

ON COMPARISON OF THEORY OF MICROSTRAINS WITH THEORIES, BASED ON THE CONCEPTION OF SLIDING

Yu. Chernyakov, A. Polishchuk

Dnepropetrovsk National University, Dnepropetrovsk, Ukraine

Over the last decades a number of theories capable of describing mechanical response of different materials under a complex loading were created. These theories are usually formulated at the micro structural level and the most widely-used of them are the theories of plasticity for mono- and poly-crystalline materials which are based on the concept of sliding. The main assumption of such theories is that the plastic deformation of the representative volume is some aggregate of deformations of sliding of single-crystals on the planes of different orientation. Such direction in the theory of plasticity was developed in the works of Batdorf, Budiansky, Bazhant, Hutchinson, Hill, Leonov, Malmeister, etc. In contrast to sliding theories, in the theory of microstrains (Chernyakov, Kadashevich, Novozhilov) a representative volume is considered as an aggregate of the variously oriented grains. It is assumed that every micro-particle (grain) is characterized by an orientation tensor $\boldsymbol{\mu}$, determining the direction of micro-plastic deformation, and by the local yield limit τ . In general case the theory of microstrains assumes, that $\boldsymbol{\mu}$ is the arbitrary normed deviator i.e.

$$(1) \quad \boldsymbol{\mu} : \boldsymbol{\mu} = 1, \text{tr } \boldsymbol{\mu} = 0,$$

where ":" denotes the contraction of tensors by two indexes and "tr" means the trace of a tensor. In the papers [1-4] it was proved that other types of tensor $\boldsymbol{\mu}$ allow to obtain a number of micro structural theories of plasticity on the base of the theory of microstrains. In particular, choice of $\boldsymbol{\mu}$ like following

$$(2) \quad \boldsymbol{\mu} = \frac{1}{\sqrt{2}} (\vec{n} \otimes \vec{m} + \vec{m} \otimes \vec{n}), \quad |\vec{n}| = 1, |\vec{m}| = 1, \vec{n} \cdot \vec{m} = 0$$

allows to derive a number of sliding theories.

Results, which concern possibility of obtaining different microstructural theories, had analytical character, and only a possibility of a high-quality approximation was shown, however a quantitative side of the question was not examined due to lack of computational power.

Nowadays with intensive development of the computational engineering, a possibility of numerical implementation of integration scheme of the constitutive relations of the microstrains theory appeared. This allows us to conduct quantitative comparison of different mechanical theories which use microstructural approach.

We offer the new method of representation of the directional tensor $\boldsymbol{\mu}$ in the following form:

$$(3) \quad \boldsymbol{\mu} = \rho(\xi) \left[\left(-\frac{\cos \xi}{\sqrt{6}} - \frac{\sin \xi}{\sqrt{2}} \right) \vec{j}_1 \vec{j}_1 + \left(-\frac{\cos \xi}{\sqrt{6}} + \frac{\sin \xi}{\sqrt{2}} \right) \vec{j}_2 \vec{j}_2 + \left(\frac{\cos \xi}{\sqrt{6}} \right) \vec{j}_3 \vec{j}_3 \right],$$

where \vec{j}_k , $k = 1..3$ are three principal directions of the tensor, which are defined as arbitrary oriented orthogonal unit vectors and can be expressed through two spherical angles ϕ , ψ and one auxiliary angle θ and ξ is a type-angle parameter (measure of a third invariant) for the tensor $\boldsymbol{\mu}$.

In the case $\rho(\xi) = 1$ the representation (3) fulfils conditions (1) and leads to the known variant of the theory of microstrains [2]. Choosing $\rho(\xi) \neq 1$ allows us to obtain the variants of theory which are capable of describing materials whose mechanical response is different under the compression, tension and shear. In this case holds $\boldsymbol{\mu} : \boldsymbol{\mu} = \rho(\xi)$, i.e. the norm of $\boldsymbol{\mu}$ is not identity like in

classical variant of theory. This fact required a proper generalisation of constitutive relations which was successfully made. Also, choosing $\xi = const$, in particular $\xi = \pi/6$, makes (3) equivalent to (1). So the representation (3) of the orientation tensor $\boldsymbol{\mu}$ is rather general and can be used to obtain different cases.

A unified numerical integration algorithm for the constitutive relations of the theory of microstrains based on the new representation of the directional tensor (3) was created. This approach allows to unify numerical implementation for different theories based on the framework of the microstrains theory. It is now possible to investigate a number of different cases of microstrains theory and their connection with other microstructural theories. However an emphasise was made on comparison of theory of microstrains to the theories, based on conception of sliding. And it is shown that distinction of deformations, expected in the theory of microstrains and sliding theories in a material subjected to complex loading has an order of distinction of initial yield conditions, i.e. conditions of Huber-Mises and Treska

- [1] Yu. I. Kadashevich, V.V. Novozhilov (1968.) On the effect of micro pre-stresses in the theory of plasticity. *Eng. J.Solids Mechanics*, **3**, 81-91. (in Russian)
- [2] Yu. I. Kadashevich, V.V. Novozhilov, Yu. A. Chernyakov (1985) Theory of plasticity including micro strains. *Proc. of USSR AS*, 284 (4), 821-823. (in Russian)
- [3] Yu. I. Kadashevich, Yu. A. Chernyakov (1992) Theory of plasticity, taking into account micro stresses. *Advances in Mechanics*. **15**, N. 3-4, 3-39.
- [4] V. P. Shneider, Yu. A. Chernyakov (2006) The development of micro deformations theory: the account of polycrystalline material grain sizes. *In Proceedings of third international conference "Multiscale Material Modeling"*. Freiburg (Germany), 530-533.

INFLUENCE OF STRESS-STRAIN STATE CAUSED BY NON-CONTACT FORCES ON FORMATION OF CONTACT BOUNDARY CONDITIONS

S. Sherbakov¹, L. Sosnovskiy²

¹ *Department of Mechanics and Mathematics, Belarusian State University, Minsk, Belarus*
² *S&P Group TRIBOFATIGUE Ltd., Gomel, Belarus*

1. Introduction

Traditionally friction force is considered dependent only on one force factor that is normal contact load [1]. Research of mechanical systems named active stress-strain state of which is conditioned by action of both contact and non-contact loads showed that stresses and strains caused by not-contact loads form additional boundary conditions on contact surface [2]. It therefore leads to essential change of characteristics of friction.

2. Formation of boundary condition

Friction force F in an active system can be considered as some function of usual friction force $F^{(c)}$ [1] in sliding (or rolling) and non-contact component of friction force $F^{(b)}$ that appear due to action of non-contact (cyclic) stresses and strains. Generally friction force in active system may be considered as the vector sum of components $F^{(c)}$ and $F^{(b)}$:

$$(1) \quad \mathbf{F} = \mathbf{F}^{(c)} + \mathbf{F}^{(b)},$$

In (1) $P_b = \int_S p_b(s) ds$ is additional contact load caused by distribution of contact pressure

$$(2) \quad p_b = p_b(\sigma_{zz}|_{S(z=0)}, \mathbf{u}_b|_{S(z=0)}),$$

where $z \perp S$, S – contact area.

In formula (2) $\sigma_{zz}|_{S(z=0)}, \mathbf{u}_b|_{S(z=0)}$ are boundary conditions in the field of contact the emerge due to the action of non-contact force.

Let us consider their formation using roller-shaft active system as an example.

In the neighborhood of contact nonzero components of console shaft stress-strain state caused by bending force Q are defined according to following formulas

$$(3) \quad \sigma_{yy}^{(b)} = \frac{Q(y-l)}{4(1+\nu)I} (R+z), \quad \epsilon_{yy}^{(b)} = \frac{1}{E} \sigma_{yy}^{(b)}, \quad \epsilon_{zz}^{(b)} = \epsilon_{xx}^{(b)} = -\frac{\nu}{E} \sigma_{yy}^{(b)}$$

where $I = \pi R_2^4 / 64$, R – shaft radius, $l = l_1 - l_2$, l_1 – shaft length, l_2 – distance from a point of the fixing of the shaft to the centre of contact

Displacements corresponding to stress-strain state (3) of contact area points are

$$(4) \quad \bar{u}_i^{(b)} = \int \epsilon_{ii}^{(b)} di \Big|_{z=0} \quad (i = x, y, z)$$

Let us consider the simplest approach to definition of contact tractions p_b for the given displacements $\bar{u}_z^{(b)}$.

We will assume that contact platform and half-space underneath as a compressed cylinder with the cross-section in the form of contact platform. Cylinder's height is R because in coordinate system originating in the centre of contact area displacements $u_z^{(b)}|_{z=-R} = 0$. Then contact force P_b (compressing cylinder) corresponds to displacements $\bar{u}_z^{(b)}$ on the surface of contact (upper surface of cylinder). Force P_b is found from the equality of $\bar{u}_z^{(b)}$ and the value of displacement of upper surface of compressed cylinder:

$$(5) \quad P_b = p_b S = \frac{\bar{u}_z^{(b)} E}{R_2}.$$

In a case of Coulomb dependences between normal force and friction force friction coefficient in the active system will be

$$(6) f = F / F_N = (F^{(c)} + F^{(b)}) / F_N = (f^{(c)} F_N + f^{(c)} P_b) / F_N = f^{(c)} (1 + P_b / F_N) = f^{(c)} \left[1 + k_{\sigma/p} \left(\frac{\sigma_{yy}^{(b)}}{p_0} \right) \right].$$

In formula (6) $k_{\sigma/p} \left(\frac{\sigma_{yy}^{(b)}}{p_0} \right) = \frac{F^{(b)}}{F_N} = \frac{3p_b}{2p_0} = -3\nu \frac{\sigma_{yy}^{(b)}|_{z=0}}{p_0}$, p_0 is the maximum contact pressure in

the center of contact

Analysis of formula (6) and a figure 1.a,b shows that in active system under simultaneous action of contact and non-contact loads the resulting coefficient (force) of friction in extension zone of the shaft decreases and in a compression zone increases in comparison with coefficient (force) of pure friction.

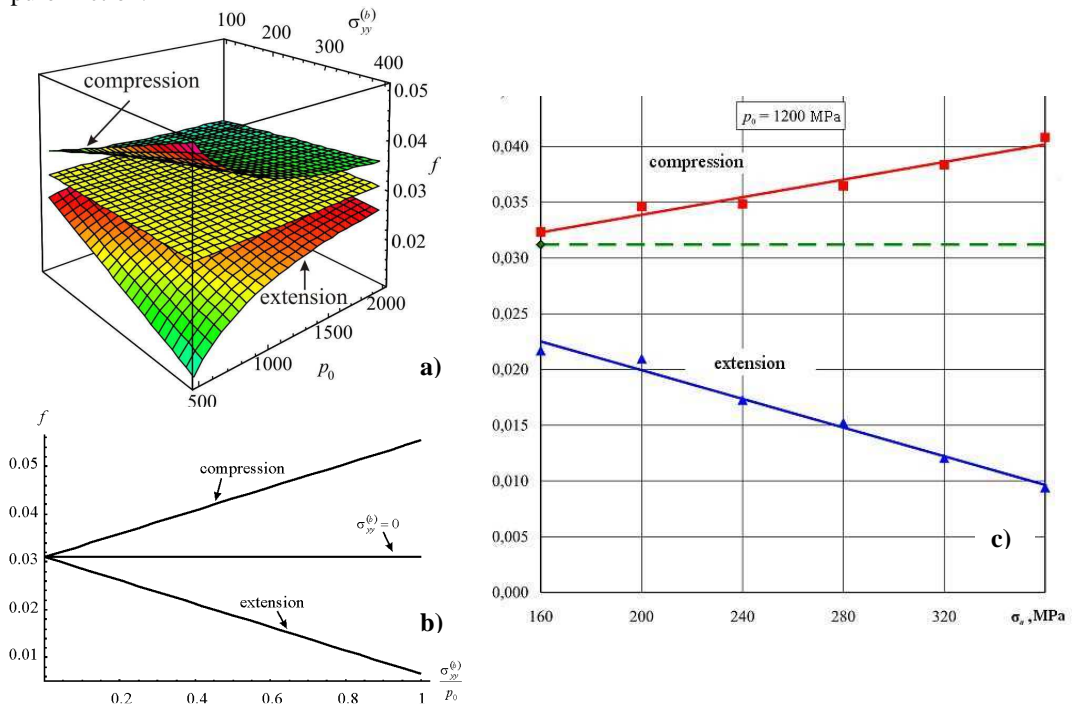


Figure 1. Analytical (a,b) and experimental (c) dependences between coefficient of friction and stresses caused by non-contact load in active system.

Figure 1 shows that analytical dependence qualitatively corresponds to the results of experiments.

The presented dependence is practically significant because it gives the possibility to control friction process by means of non-contact loading as effectively as by means of contact loading.

3. References

- [1] K.L. Johnson. (1985). Contact Mechanics, Cambridge University Press, Cambridge.
- [2] L.A. Sosnovskiy Tribo-Fatigue. Wear-fatigue damage and its prediction (Foundations of engineering mechanics) (2004). Springer.

RECOVERING THE BIPOTENTIAL OF AN IMPLICIT STANDARD MATERIAL BY FITZPATRICK'S METHOD

C. Vallée¹, C. Lerintiu¹, D. Fortuné¹, K. Atchonouglo¹, M. Ban²

¹*Université de Poitiers, LMS, SP2MI, Futuroscope-Chasseneuil Cedex, France*

²*RWTH Aachen, IAM, Templergraben 64, Aachen, Germany*

1. Implicit Standard Materials

The mechanical behavior of many materials can be modeled by a constitutive law deriving from a convex lower semi-continuous (lsc) **potential** Φ . A stress-like variable y is related to a strain-like variable x equivalently by one of the three following conditions:

- (i) $y \in \partial\Phi(x)$ i.e. y belongs to the subdifferential of Φ at x ($\forall \xi, \Phi(\xi) \geq \Phi(x) + \langle \xi - x, y \rangle$)
- (ii) $x \in \partial\Phi^*(y)$ i.e. x belongs to the subdifferential of Φ^* at y ($\forall \eta, \Phi^*(\eta) \geq \Phi^*(y) + \langle x, \eta - y \rangle$)
- (iii) $\Phi(x) + \Phi^*(y) = \langle x, y \rangle$.

The brackets enclosing x and y denote the duality product between x and y . Condition (iii) can be regarded as an extremal case of the **Fenchel-Young inequality** $\Phi(x) + \Phi^*(y) \geq \langle x, y \rangle$ derived directly from the definition of the **Legendre-Fenchel-Moreau functional transformation** [10]

$$\Phi^*(y) = \sup_x (\langle x, y \rangle - \Phi(x)).$$

Such materials are called **"Generalized Standard Materials"** [8]. However, there exist materials, clays for example [5], whose behavior cannot be modeled by a convex lsc potential. In this case, the constitutive law is called **non-associated**. Giving up the sum decomposition in (iii), Gery de Saxcé [5] succeeded in modeling the behavior of a new class of materials, the **"Implicit Standard Materials"**. These materials are characterized by a bipotential $b(x, y)$, as stated in the following section.

2. Bipotentials

A function $b(x, y)$ satisfying the conditions:

- (i) $b(x, y)$ is convex and lsc in x
 - (ii) $b(x, y)$ is convex and lsc in y
 - (iii) $b(x, y) \geq \langle x, y \rangle$
- is called **bipotential** [4]. When the constitutive law of a material can be expressed indifferently by any of the following three conditions:
- (iv) $y \in \partial_x b(x, y)$ i.e. y belongs to the subdifferential of the function $\xi \mapsto b(\xi, y)$ at $\xi = x$
 - (v) $x \in \partial_y b(x, y)$ i.e. x belongs to the subdifferential of the function $\eta \mapsto b(x, \eta)$ at $\eta = y$
 - (vi) $b(x, y) = \langle x, y \rangle$

this law is said to admit the bipotential b , and the material is referred as "Standard Implicit".

The "Generalized Standard Materials" are special "Implicit Standard Materials" with **separable bipotentials** of the type $b(x, y) = \Phi(x) + \Phi^*(y)$, for which condition (iii) is nothing else than the Fenchel-Young inequality.

3. Parallelism of two vectors

As a start point to exhibit the bipotential modeling the Coulomb dry friction ([5], [6]), let us consider the constitutive law enacting that two vectors x and y of an Hilbert space H have the same orientation. This constitutive law is not maximal monotone and therefore cannot be described by a convex lsc potential. Nevertheless, one can express this law by making equal the product of the norms with the duality product: $\|x\| \|y\| = \langle x, y \rangle$. We can remark that the function $b(x, y) = \|x\| \|y\|$

satisfies the conditions (i), (ii) and (iii) of Section 2, the last one being true thanks to the Cauchy-Schwarz-Buniakovsky inequality. The equivalence of the three conditions (iv), (v) and (vi) is due to the following property of the norm in a Hilbert space: the subdifferential of the norm at x is equal to the closed unit ball if $x = 0$ and is reduced to $\left\{ \frac{x}{\|x\|} \right\}$ if $x \neq 0$.

4. Representing a constitutive law by a function

For representing a **maximal monotone multifunction** $x \mapsto y \in Tx \subset H$, S. Fitzpatrick ([3],[7]) introduced the global convex lsc function

$$F(x, y) = \langle x, y \rangle - \inf_{y' \in Tx'} \langle x' - x, y' - y \rangle.$$

Since T is maximal monotone, the above infimum $\inf_{y' \in Tx'} \langle x' - x, y' - y \rangle$ is non-positive and its equality to 0 holds if and only if $y \in Tx$. Therefore $F(x, y)$ is bounded from below by the duality product $\langle x, y \rangle$, and we recover the conditions of Section 2 for F to be a bipotential representing T .

Thus, in case of maximal monotonicity of the constitutive law, a bipotential can be constructed as a **Fitzpatrick function** ([1],[2],[9]). But, does Fitzpatrick's method work for non monotone constitutive laws?

In this lecture we will present two examples. The first one concerns the linear monotone explicit law $y = Ax$ with $S = \frac{A+A^T}{2}$ as a positive-definite linear mapping. The second one is devoted to the non monotone implicit law discussed in Section 3.

5. References

- [1] S. Bartz, H.H. Bauschke, J.M. Borwein, S. Reich, and X. Wang (2007). Fitzpatrick functions, cyclic monotonicity and Rockafellar's antiderivative, *Nonlinear Analysis*, **66**, 1198-1223.
- [2] H.H. Bauschke (2006). Fitzpatrick functions, cyclic monotonicity and Rockafellar's antiderivative, *AARMS/ Dalhousie Atlantic Analysis Days, Session on Non-Smooth Analysis*, Halifax.
- [3] J.M. Borwein and Q.J. Zhu (2005). *Techniques of Variational Analysis*, CMS books in mathematics, Springer Science + Business Media, New York.
- [4] M. Buliga, G. de Saxcé, and C. Vallée (2008). Existence and construction of bipotentials for graphs of multivalued laws, *J. of Convex Analysis*, **15/1**, 87-104.
- [5] G. de Saxcé, and L. Bousshine (2002). *Implicit Standard Materials. In D. Weichert and G. Maier, eds: Inelastic Behaviour of Structures Under Variable Repeated Loads – Direct Analysis Methods*, CISM Courses and Lectures No. 432, Springer, Wien, New York, 59-76.
- [6] G. de Saxcé, and Z. Q. Feng (1991). New Inequation and Functional for Contact with Friction: the Implicit Standard Material Approach, *International Journal Mechanics of Structures and Machines*, **19/3**, 301-325.
- [7] S. Fitzpatrick (1988). Representing monotone operators by convex functions, *Workshop/Miniconference on Functional Analysis and Optimization, Proceedings of the Centre for Mathematical Analysis, Australian National University*, **20**, Australia, 59-65.
- [8] B. Halphen, and Q. S. Nguyen (1975). Sur les matériaux standard généralisés, *Journal de Mécanique*, **14**, 39-63, in french.
- [9] J.-E. Martinez-Legaz, and B. F. Svaiter (2005). Monotone Operators Representable by l.s.c. Convex Functions, *Set-Valued Analysis*, **13**, 21-46.
- [10] J. J. Moreau (2003). *Fonctionnelles convexes*, Istituto poligrafico e zecca dello stato S. p. A., Roma.

SHEAR BEHAVIOUR OF HYBRID STEEL GIRDERS

S. Shimizu and K. Hara

Department of Civil Engineering, Shinshu University, Nagano, Japan

1. Introduction

This paper describes the strength and the collapse mode under shear of hybrid steel girders which are considered as the combination of shell elements.

When an I-sectioned girder is subjected to the bending, higher stress arises in the flange plates of the girder. A hybrid steel girder is a girder which has flange plates made with the higher strength steel and a web plate with "normal" steel. In the discussion on a hybrid steel girder, behaviour under the bending has been mainly focused. As a member of the Subcommittee on "the design method of hybrid steel girders" organized by JSSC (Japanese Society of Steel Construction)[3], one of the authors made a series of studies[1-2] on the hybrid steel girders. As described above, a hybrid steel girder is effective for the bending. Therefore, it is natural that the bending behaviour of the hybrid girders is focused.

However, to design a hybrid steel girder, its shear behaviour such as the collapse mechanism under shear must be known. Thus, in this paper, numerical analyses are made to know the strength and the collapse mechanism of hybrid steel girders under shear. The results of the collapse mechanism and strength are compared to those of the homogeneous girders which are made of the same grade steel for their flange and web plate.

2. Numerical models and numerical method

A typical numerical model is illustrated in Figure 1. As illustrated in Figure 1, the model is fixed at its left, and is subjected a downward load at its right edge. This model has its length $l=5000$ mm, web depth $b=1200$ mm and flange width $b_f=260$ mm. The web panel with the width of a and subtended by two stiffeners is focused in this study. The stiffeners have their section of 100×8 mm. The web thickness t_w is $t_w=8$ mm or $t_w=12$ mm, and the flange thickness t_f is varied from $t_f=4$ mm to $t_f=20$ mm to investigate the effect of the flange stiffness.

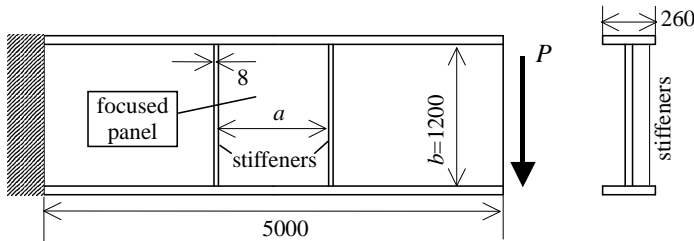


Figure 1. A typical numerical model

The aspect ratio of the focused panel, $\alpha=a/b$ is considered as one of parameters and from 0.75 to 3.0, that is, a is from 900mm to 3 600mm.

In this study, the grade SM400 steel which has the yielding stress σ_y of $\sigma_y=245$ Mpa and the grade SM570steel with $\sigma_y=460$ MPa are considered. For the hybrid girder, The SM570 steel is utilized for only the flange plates of the hybrid girder, and for the flanges of the homogeneous girder and the web plates, SM400 is considered.

The numerical analysis is made with the computer program package MSC Marc, and the model is discretized with 50×50 mm thick shell elements.

3. Numerical results

In Figure 2, a deformation pattern of the hybrid girder with $t_w=8\text{mm}$, $t_f=12\text{mm}$ and $\alpha=1.0$ at the ultimate load is illustrated. The distinct shear buckling deformation is observed in the web plate in this figure. This figure also shows that each flange plate deforms with the web deformation. However, although it is not clear in this figure, no plastic hinge is formed in the flange plate in this model.

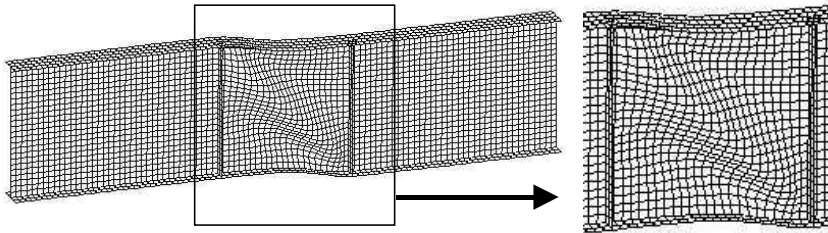


Figure 2. Shear Deformation of Hybrid Girder ($\alpha=1.0$, $t_w=8\text{mm}$, $t_f=12\text{mm}$)

The maximum load P_{\max} of this model is $P_{\max} = 1096 \text{ kN}$, and the corresponding homogeneous girder has its P_{\max} is $P_{\max} = 1091 \text{ kN}$. Thus, in this case, the hybrid girder has almost equal strength to the corresponding homogeneous girder. In the case with the aspect ratio $\alpha=3.0$ and with the same plate thickness, both the hybrid girder and the homogeneous girder also have no plastic hinge in their flange plates. However, in this aspect ratio, the hybrid girder has its $P_{\max} = 758 \text{ kN}$ and this is larger by 8% than the homogeneous girder which has the $P_{\max} = 700 \text{ kN}$. Although the detail is not shown in this abstract, with the larger aspect ratio, hybrid girders have larger P_{\max} than homogeneous girders.

In addition, on the cases with the plate thickness of $t_w=12\text{mm}$, $t_f=12\text{mm}$, or $t_w=8\text{mm}$, $t_f=8\text{mm}$, hybrid girders have no plastic hinge in the flange plates although in corresponding homogeneous plastic hinges arise in the flanges. That is, in these cases, the hybrid girder and the homogeneous girder have different collapse mode to each other.

4. Conclusion

The flange plates of a plate girder carry mainly the bending, and the shear is carried by mainly web plate. A hybrid steel girder is originally considered to carry the bending effectively. However, the results shown in this paper indicate that a hybrid girder is also effective for the shear when the girder has the larger aspect ratio. In addition, to estimate the shear strength of a girder, the collapse mode with the plastic hinges in the flange plates is often adopted. But, the collapse mode of a hybrid girder obtained in this study has, in some cases, no plastic hinge although the plastic hinges arise in the corresponding homogeneous girder. This fact suggests that a separate shear collapse mode is required for the hybrid girders other than the homogeneous girder.

5. References

- [1] S. Shimizu, J.Zhang, N.Tanaka, K.Akehashi and H.Nakai (2003). An Experimental Study on Ultimate Strength Behaviour of Hybrid Steel Plate Girders, *Steel Construction Engineering, JSSC(Japanese Society of Steel Construction)*, **10**, 51-60.(in Japanese)
- [2] S. Shimizu, J.Zhang, N.Nakada, N.Tanaka and H.Nakai (2003). Effect of Stiffeners in Hybrid Steel Plate Girders, *Steel Construction Engineering, JSSC(Japanese Society of Steel Construction)*, **10**, 43-50.(in Japanese)
- [3] Subcommittee for Design Method of Hybrid Steel Plate Girders (2002), *A Proposal for Design Method of Hybrid Steel Plate Girders using Ultimate State Design*, JSSC(Japanese Society of Steel Construction), Tokyo

ON PHASE TRANSITIONS IN THERMOELASTIC AND THERMOVISCOELASTIC SHELLS

V.A. Eremeyev¹ and W. Pietraszkiewicz²

¹ South Scientific Center of RASci and South Federal University, Rostov-on Don, Russia

² Institute of Fluid-Flow Machinery of PASci, Gdańsk, Poland

Phase transitions (PT) play an important role in different problems of continuum mechanics. Equilibrium conditions of elastic thin-walled structures (plates and shells) undergoing PT of martensitic type were formulated in [1, 2] within the dynamically and kinematically exact theory of shells presented in books [3, 4]. From experimental data we know that PT depending on strain rates and inelastic effects may considerably influence the stress state of the solid.

The aim of this contribution is to extend the results of [1, 2] by taking into account thermal and viscoelastic effects of the shell material phases under quasistatic loading.

1. Basic relations of nonlinear shell thermostatics

The 2D local *equilibrium equations* as well as the *energy balance* and the *Clausius-Duhem inequality* satisfied at any part of the undeformed base surface M of the shell are [1, 2]

$$(1) \quad \begin{aligned} Div_s \mathbf{N} + \mathbf{f} &= \mathbf{0}, \quad Div_s \mathbf{M} + ax(\mathbf{N}\mathbf{F}^T - \mathbf{F}\mathbf{N}^T) + \mathbf{c} = \mathbf{0}, \\ \rho \frac{d\varepsilon}{dt} &= \rho(q^+ + q^- + q_{\Pi}) - Div_s \mathbf{q} + \mathbf{N} \bullet \mathbf{E}^\circ + \mathbf{M} \bullet \mathbf{K}^\circ, \\ \rho \frac{d}{dt} \eta &\geq \rho \left(\frac{q^+}{T_{ext}^+} + \frac{q^-}{T_{ext}^-} + \frac{q_{\Pi}}{T} \right) - Div_s \left(\frac{1}{T} \mathbf{q} \right). \end{aligned}$$

Here \mathbf{N} and \mathbf{M} are the internal surface stress resultant and couple stress tensors of the nominal type, $\mathbf{F} = Grad_s \mathbf{y}$ is the surface gradient of shell deformation $\mathbf{y} = \boldsymbol{\chi}(\mathbf{x}) = \mathbf{x} + \mathbf{u}$, $ax(\mathbf{A})$ denotes the axial vector associated with the skew tensor \mathbf{A} , while $Grad_s$ and Div_s are the surface gradient and divergence operators on M , respectively. Additionally, ε is the surface internal energy density, η is the surface entropy density, \mathbf{q} is the surface influx vector, q^\pm are the heat influxes through the upper (+) and lower (-) shell faces, q_{Π} is the internal surface heat supply, while by T_{ext}^+ and T_{ext}^- we denote temperatures of the external media surrounding the shell from above and below.

2. Constitutive equations of thermoviscoelastic shells

The surface stress measures \mathbf{N}, \mathbf{M} depend only on prehistories of the surface natural strain and bending tensors \mathbf{E}, \mathbf{K} , [4], as well as on the temperature T . We split the surface stress measures and their constitutive equations into elastic (equilibrium) and inelastic (dissipative) parts, $\mathbf{N} = \mathbf{N}_E + \mathbf{N}_D$ and $\mathbf{M} = \mathbf{M}_E + \mathbf{M}_D$, where

$$(2) \quad \mathbf{N}_E = \rho \frac{\partial \psi}{\partial \mathbf{E}}, \quad \mathbf{M}_E = \rho \frac{\partial \psi}{\partial \mathbf{K}}, \quad \mathbf{N}_D = \mathbf{N}_D(T, \mathbf{E}, \mathbf{K}, \dot{\mathbf{E}}, \dot{\mathbf{K}}), \quad \mathbf{M}_D = \mathbf{M}_D(T, \mathbf{E}, \mathbf{K}, \dot{\mathbf{E}}, \dot{\mathbf{K}}).$$

Here $\psi = \varepsilon - T\eta = \psi(T, \mathbf{E}, \mathbf{K})$ is the surface free energy density, and $\mathbf{N}_D = \mathbf{N}_D(T, \mathbf{E}, \mathbf{K}, \mathbf{0}, \mathbf{0}) = \mathbf{0}$, $\mathbf{M}_D = \mathbf{M}_D(T, \mathbf{E}, \mathbf{K}, \mathbf{0}, \mathbf{0}) = \mathbf{0}$.

3. Continuity conditions and kinetic equation

The phase interface in the shell may be modelled by a smooth surface curve $C \subset M$. Then along C the 1D local *equilibrium and thermodynamic continuity conditions* are [5]

$$(3) \quad \begin{aligned} & [\mathbf{N}\mathbf{v}] = \mathbf{0}, \quad [\mathbf{M}\mathbf{v}] = \mathbf{0}, \\ & V[\rho\varepsilon] + [\mathbf{N}\mathbf{v} \cdot \mathbf{v}] + [\mathbf{M}\mathbf{v} \cdot \mathbf{w}] - [\mathbf{q} \cdot \mathbf{v}] = 0, \quad V[\rho\eta] - \left[\frac{1}{T} \mathbf{q} \cdot \mathbf{v} \right] \equiv -\delta^2 \leq 0. \end{aligned}$$

Here the expression $[\dots] = (\dots)^+ - (\dots)^-$ means the jump at C , $\mathbf{v} = \dot{\mathbf{u}}$ is the translational velocity vector, $V = \dot{\mathbf{x}}_C \cdot \mathbf{v}$ is the normal velocity tangent to $T_x M$ of the phase curve C with the unit outward normal \mathbf{v} and $\dot{\mathbf{x}}_C$ the velocity of C kinematically independent on \mathbf{v} , $\mathbf{w} = ax(\dot{\mathbf{Q}}\mathbf{Q}^T)$ is the angular velocity vector, and δ^2 represents creation of entropy at the interface C .

Transforming (3) it can be shown that the surface Eshelby tensor \mathbf{C} introduced in [1] satisfies the *thermodynamic continuity condition* $[\mathbf{v} \cdot \mathbf{C}\mathbf{v}] = 0$ in the case of equilibrium. For the *coherent* interface, when the independent translation \mathbf{u} and rotation \mathbf{Q} fields are supposed to be continuous at C , we obtain $\mathbf{C} \equiv \mathbf{C}_c = \rho\psi\mathbf{A} - \mathbf{N}^T\mathbf{F} - \mathbf{M}^T\mathbf{K}$. For the interface *incoherent in rotations*, when only \mathbf{u} is continuous at C and continuity of \mathbf{Q} may be violated, we have $\mathbf{C} \equiv \mathbf{C}_i = \rho\psi\mathbf{A} - \mathbf{N}^T\mathbf{F}$. From the thermodynamic point of view the expression $d[\mathbf{v} \cdot \mathbf{C}\mathbf{v}]/ds$ is the configurational force acting on the phase interface, with s the length along C .

Thermodynamically consistent *kinetic equation* along C is given by the relation

$$(4) \quad V = K(d[\mathbf{v} \cdot \mathbf{C}\mathbf{v}]/ds),$$

where K is a non-negative definite kinetic function. The equation (4) describes motion of the phase interface C under quasistatic deformations of the shell. It generalizes the balance equations on the equilibrium phase interface obtained in [1, 2].

During Solmech2008 we present solutions of some model problems for two-phase viscoelastic shells under quasistatic loading.

4. References

- [1] V. A. Eremeyev and W. Pietraszkiewicz (2004). The nonlinear theory of elastic shells with phase transitions. *J. Elasticity* **74**(1), 67–86.
- [2] W. Pietraszkiewicz, V. A. Eremeyev and V. Konopińska (2007). Extended non-linear relations of elastic shells undergoing phase transitions, *Z. angew. Math. Mech.* **87**(2), 150–159.
- [3] A. Libai and J. G. Simmonds (1998). *The Nonlinear Theory of Elastic Shells*, 2nd ed. Cambridge, UK.
- [4] J. Chrościelewski, J. Makowski and W. Pietraszkiewicz (2004). *Statics and Dynamics of Multifold Shells: Nonlinear Theory and Finite Element Method* (in Polish). Wydawnictwo IPPT PAN, Warszawa.
- [5] V. A. Eremeyev and W. Pietraszkiewicz (2007). On quasi-static propagation of the phase interface in thin-walled inelastic bodies. Proc. EMMC-10 Conference "Multi-Phase and Multi-Component Materials Under Dynamic Loading". IPPT PAN, Warsaw, 99-105.

**EXACT SOLUTIONS OF PROBLEMS OF STATICS, DYNAMICS AND STABILITY
OF NON-CLOSED CIRCULAR CYLINDRICAL SHELLS STRENGTHENED IN ONE
DIRECTION BY “ALMOST REGULARLY PLACED” RIBS**

*H. Abramovich and V. Zarutsky
Israel Institute of Technology, Haifa, Israel*

Non-closed circular cylindrical shells simply supported on longitudinal edges strengthened by “almost regular” systems of longitudinal or annular ribs are considered. Exact solutions of the problems of statics, dynamics and stability of the shells are obtained in the form of trigonometric series with respect to the coordinate orthogonal to the ribs. Previously such solutions have been found only for the closed shells strengthened by regular systems of longitudinal ribs.

At a regular placement all mechanical and geometrical parameters of ribs are equal. The distances between ribs are equal and distances from edges of shells up to the nearest ribs are equal to the distances between the ribs. At “almost regular” placement of the ribs, as opposed to regular placing, distances from the shell edges up to the nearest ribs are equal to half of the distance between the ribs. In both placing cases a shell is segmented by ribs, the number of segments is equal to the number of ribs.

The obtained solutions are convenient both for calculations and for the analysis of deformation of shells, as they lead to the sufficiently simple transcendental equations for determination of characteristic numbers, critical stresses at loss of stability, natural frequencies of vibrations and wave parameters.

The “almost regular” placement of ribs is widely used in many structural designs of elements and mechanical constructions.

These are the problems that are solved for shells strengthened by longitudinal ribs:

A. A common solution of a non-homogeneous system of equations of balance is obtained. It enables studying both the character of influence of loadings at a curvilinear edge of a semi-infinite shell on its stress-strain state and the influence of a discrete ribs placement on a zone extent in which it is essential.

B. The problem of finding critical stresses at loss of stability of the shells simply supported on all edges under joint action of a longitudinal tension or compression and external or internal pressure is reduced to the calculation of minimal roots of the transcendental equations of three types, differing by character of wave formation:

1. The wavelength in the circumferential direction is almost independent of a ribs arrangement (in this case critical stresses depend on all rigidity characteristics of the ribs).
2. The maxima of the form of deflection are on axes of ribs (in this case critical stresses depend only on ribs rigidity in bending in a radial plane and in tension - compression).
3. Nodes of the deflection curve are on the axes of the ribs (in this case critical stresses depend only on ribs rigidity in bending in the planes equally distant to tangents to the shell surfaces, and in torsion).

As a result of the analysis of the above-mentioned transcendental equations, the simple approximate formulas for calculation of the shells stability are suggested at a large sufficiently number of ribs. The condition of applicability of the structurally orthotropic shell theory is formulated.

C. The problem of determination of natural frequencies of vibration of shells which are simply supported on all edges is also reduced to calculation of the roots of the transcendental equations of the specified three types. Their analysis permits obtaining simple expressions to find low natural frequencies at a sufficiently large number of ribs and to formulate conditions of applicability of the constructively orthotropic shell theory.

D. It is found that investigation of the influence of a discrete ribs placement on wave parameters of harmonic waves propagating along shells is reduced to the determination of roots of transcendental equations of the same three types. The analysis of these equations is fulfilled.

For non-closed shells which are simply supported on all edges strengthened by “almost regular” systems of annular ribs the problem of determination of critical stresses under joint action of compression (tension) and external (internal) pressure is solved. Their calculation is reduced to the determination of the minimal roots of the transcendental equations of the three types similar to those obtained for shells strengthened by longitudinal ribs. Previously for the shells strengthened by regular systems of annular ribs only the approximate equations of two types (the first one and the third one) have been derived.

The determination of natural frequencies of vibrations of the shells strengthened by “almost regular” systems of annular ribs is also reduced to the calculation of roots of the transcendental equations of the three types. For mentioned shells the obtained approximate expressions enable calculation of the critical stresses and natural frequencies of vibrations at a sufficiently large number of ribs.

Similar exact solutions and approximate formulas are also deduced for the closed shells strengthened by “almost regular” systems of annular ribs.

EVALUATION OF THE PERTURBATION SENSITIVITY AND THE LIMIT LOADS OF SHELLS BY THE PERTURBATION ENERGY CONCEPT

J. Pontow and D. Dinkler

Institute for Structural Analysis, Braunschweig, Germany

1. General

The perturbation sensitivity and the limit loads of shells are widely discussed phenomena. Both phenomena may be classified with respect to the time and the type of a perturbation. Contrary to other methods, the perturbation energy concept enables to describe the buckling process in a very natural way and to analyse the perturbation sensitivity as well as the limit loads by a uniform approach.

2. Perturbation energy concept

Basic idea of the perturbation energy concept is the identification of a critical state belonging to a fundamental state F [1]. The difference of strain energy between both states is an indicator for the stability of the fundamental state and referred to as the perturbation energy Π_{cr} . As several critical states may exist, the identification of the critical state which is relevant for the stability of the fundamental state is interpreted as an optimisation problem,

$$(1) \quad f(\mathbf{z}_F, \Delta \mathbf{z}) = \Pi_{cr} \rightarrow \text{Min.}$$

In this problem, the fundamental state is represented by the state variables \mathbf{z}_F and the distance as well as the direction between the fundamental and the critical state are denoted by the change $\Delta \mathbf{z}$ of the state variables. The kind of the critical state depends on the distribution in time of the perturbation. For a kinetic perturbation, the state N characterised by vanishing first variation of the incremental elastic potential and by no change of the fundamental load is the critical state, compare figure 1. In case of a static perturbation, the state M of vanishing second variation of the potential is the critical state. These conditions constrain the optimisation problem (1) whose solution may be found by non-linear eigenvalue problems. Thereby, the order of nonlinearity with respect to the eigenvalue and the eigenvector, respectively, is governed by the formulation of the potential.

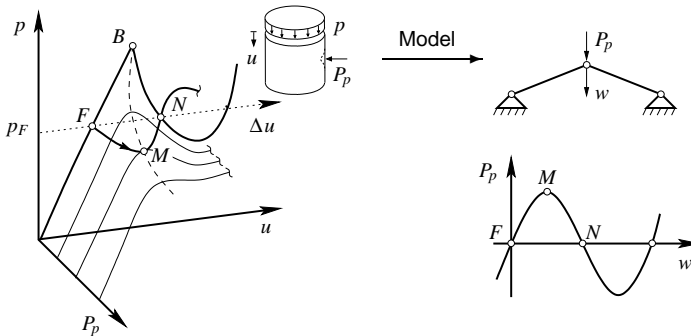


Figure 1. Load-deformation behaviour of a perturbation-sensitive shell

In general, non-initial load perturbations P_p are necessary to reach a critical state. Non-initial perturbations concerning other parameters of the model equations, such as the bedding modulus and the wall thickness, influence the topology of the energy surface and emphasise the similarity between the perturbation energy concept and the perturbation theory. The effect of initial perturbations is

measured by the associated change of the fundamental energy Π_F as well as the change of the perturbation energy. For identifying the static limit loads of different shells by one energy value, the perturbation energy is normalised by the bending stiffness of the shell continuum as bending energy is the dominating part of the perturbation energy. The reference value of the normalised perturbation energy, $\pi_{cr,M} = 2.7\%$, represents a proper indicator for realistic static limit loads. Kinetic limit loads are determined with respect to a fundamental state and by the degree of stability [2]. Furthermore, the optimisation of the perturbation sensitivity of a shell in terms of a certain load level and the design parameter x may be described by the objective function

$$(2) \quad f(x, \mathbf{z}_F(x), \Delta \mathbf{z}(x)) = \Pi_{cr} - \Pi_{cr}^{req} = 0$$

where Π_{cr}^{req} represents the required perturbation sensitivity. The computation of the solution of this load-level-specific optimisation is based on the linearisation of the objective function which is performed by the forward difference scheme. In general, the solution is found after few iterations. During the optimisation, the energy surface and so the fundamental state as well as the distance and the direction between the fundamental and the critical state are changing. Furthermore, the optimisation influences the fundamental energy and the load level of singular points in the primary load-deformation path. The advantage of the proposed optimisation procedure over a systematic change of the design parameter becomes obviously especially for high-dimensional systems and several design parameters.

3. Numerical results

For cylindrical and spherical shells, the perturbation sensitivity and static limit loads are analysed including different loadings, geometries, boundary conditions and material parameters. The results indicate that spherical shells under radial pressure are nearly as perturbation-sensitive as cylindrical shells subjected to axial pressure. For these buckling cases, limit loads according to the reference value of the normalised perturbation energy are in good agreement with those corresponding to the ECCS-Recommendations, but differ for elasto-plastic material behaviour significantly to those according to DIN 18800 [3]. The limit loads calculated for conical shells under meridional pressure are for different meridional angles similar to those corresponding to DASt-Richtlinie 013. In addition, buckling cases less intensively discussed in the design rules are analysed. But it is not possible to specify realistic limit loads of all these buckling cases by the reference value of the normalised perturbation energy due to the absence of a problem-specific scaling of the perturbation energy. Nevertheless, for fibre reinforced composites consisting of uniform UD-layers an adequate scaling is feasible.

The stability of a shell against a kinetic perturbation load depends on the energy induced into the system by the perturbation load. Therefore, the influence of the distribution in time and space of the perturbation load on the stability of a spherical shell is investigated. The results highlight the importance of the perturbation energy concept not only for the evaluation of the buckling resistance but also for the determination of an unfavourable perturbation load and the kinetic limit load, respectively.

4. References

- [1] B. Kröplin, D. Dinkler and J. Hillmann (1985). An energy perturbation applied to nonlinear structural analysis, *Comp. Meth. Appl. Mech. Eng.*, **52**, 885-897.
- [2] Dinkler, D. and Kröplin, B. (1990). Stability of dynamically loaded structures, *In W. B. Krätzig and E. Oñate (Ed.): Computational Mechanics of Nonlinear Response of Shells*, Berlin, 183-192.
- [3] O. Knoke and D. Dinkler (2003). Elasto-plastic limit loads of cylinder-cone configurations, *J. of Theor. and Appl. Mech.*, **41**, 443-457.

A NOVEL METHOD FOR STATIC ANALYSIS OF THIN CURVED SHELLS WITH VARIABLE THICKNESS

R. Attarnejad, M. Eslaminia, A. Shahba

School of Civil Engineering, University College of Engineering, University of Tehran, Tehran, Iran

Stiffness method (displacement based formulation) is a widely applicable method for analysis of structures such as beams, plates, shells and etc. Analyzing structures with variable thickness by using stiffness method, the structure is discretized into straight elements with constant mechanical properties and a constant thickness which is an average of thickness at the element's nodes. Increasing number of elements, a better approximation is obtained but on the other hand, dimensions of stiffness and mass matrices increase so that more time and memory would be required. However, this method is the proper conventional method which can be found in technical literature. In general, application of the displacement based formulations lead to violation of one of the three basic equilibrium equations due to assumption of displacement fields in that method.

Force methods (flexibility method) can be a proper substitute for stiffness method as they absolutely satisfy the three basic equilibrium equations at all points of the element. In the present paper, unit load method which is considered as force method has been applied for derivation of stiffness matrix. However, application of force method is generally more complicated than stiffness method so that a combination of these methods (stiffness and force methods) can bring in accuracy, simplicity and time and memory saving.

In this paper, a new method for static analysis of thin curved shells with variable thickness is presented. The basis of the method is employing shape functions of non-prismatic curved beams which are obtained by utilizing unit load method. This new method can be applied to any kind of shells with any variable thickness function and boundary conditions. This method could be easily extended to complex analysis of structures such as non-linear analysis in both geometric and material non-linearity cases. In fact, this method is the logical development of finite element calculations and employs mathematical computations and numerical integrals.

Comparing the results obtained by this method and those obtained by ordinary methods obviously proves its excellence in both convergence and economy. In static analysis of spherical and cylindrical shells, indeed, the results computed by using few elements with this formulation are completely comparable with the results obtained by using numerous elements with ordinary formulations. It is worth to note that this new formulation can be applied in any standard displacement based finite elements programs and algorithms.

The authors have started a new studying on extension of this method to dynamic analysis of shells with variable thickness and good results have been gained, so far.

References

- [1] Attarnejad R. (2000), On the derivation of geometric stiffness and consistent mass matrices for non-prismatic Euler-Bernoulli beam elements: ECCOMAS
- [2] Attarnejad R. (2002), Free vibration of non-prismatic beams., 15th ASCE Eng Mech Conf.

-
- [3] R. Attarnejad, Geometric nonlinear analysis of non-prismatic beams , To appear.
 - [4] R.Szilarad (2004) , Theories and Applications of Plate Analysis, John Wiley & Sons INC
 - [5] D.Zhou (2002) , Vibrations of point-supported rectangular plates with variable thickness using a set of static tapered beam functions, International Journal of Mechanical Sciences 44,149–164
 - [6] Timoshenko, S., and Woinowsky-Kieger, S. (1959), Theory of Plates and Shells, McGraw-Hill Book Co., New York
 - [7] R.Szilarad (1974), Theories and Applications of Plate Analysis, Prentice-Hall
 - [8] Dawe DJ. (1974) , Numerical studies using circular arch finite elements. Comput Struct, 4:729-40.
 - [9] Prathap G. (1985) , The curved beam/deep arch/ finite ring element revisited. Int J Num. Methods Eng, 21:389-407
 - [10] T.Y. Yang (1986) , Finite Element Structural Analysis, Prentice-Hall

AN ASYMPTOTIC APPROACH TO PROBLEMS OF SCATTERING ACOUSTIC WAVES BY ELASTIC SHELLS

V. Kovalev

Moscow University of Management of Moscow Government, Moscow, Russia

1. Scattering of stationary acoustic waves by elastic shells is considered. A procedure is proposed for constructing an approximate solution, based on matching the expansions for different asymptotic models of the interaction of the shell with the acoustic medium. In the vicinities of zero frequency the refined Kirchhoff-Love theory of fluid-structure interaction is applied [1]. This model takes into consideration transverse compression of a shell by a fluid and some other phenomena. In the vicinities thickness resonance frequency long-wave high-frequency approximations are employed [2,3]. They describe small number resonance of higher order Lamb waves. Outside the vicinities of zero frequency and thickness resonance frequency vibrations of a shell correspond to short-wave motions. Here a flat layer model is used [2,3]. It is shown for different parameters of material in a shell that the flat layer model has overlap regions both the refined Kirchhoff-Love theory and the theories associated with long-wave high-frequency approximations. A comparison of numerical data corresponding to asymptotic and exact solutions cylindrical and spherical shells shows that the proposed procedure is highly efficient.

2. Let the plane acoustic wave $p_i = p_0 \exp[-i(k\xi + \omega t)]$ be scattered either by a circular cylindrical shell or by a spherical shell. We introduce the following parameters characterizing the scattering process:

$$\kappa = \rho / \rho_1, \quad \beta_i = c_i / c \quad (i = 1, 2), \quad \gamma_0 = c_2 / c_1, \quad k = \omega / c.$$

Here c_1 and c_2 are the dilatation and distortion wave speeds in the material of the shell, respectively, ρ_1 is the mass density of the shell, c is the sound speed in the fluid, ρ is the mass density of the fluid, ω is the circular frequency, p_i is the pressure in the incident wave, p_0 is a constant. The incident pressure p_i and the scattered pressure p_s have to satisfy the Helmholtz equation. In addition, the scattered pressure p_s should obey the radiation condition at infinity.

Let (r, θ) be cylindrical or spherical coordinates (the problem do not depend upon the axial coordinate in the case of a cylindrical shell and upon the angle along parallel in the case of a spherical shell), the radius of the shell be equal R , and the half-thickness of the shell be equal h .

The incident pressure can be written as $p_i = p_0 \sum_{n=0}^{\infty} E_n (-i)^n f_n(kr) F_n(\theta)$.

Here for a cylindrical shell $E_0 = 1$, $E_n = 2$ ($n \geq 1$), $f_n = J_n$, $g_n^{(1)} = H_n^{(1)}$, $F_n(\theta) = \cos n\theta$,

$N = n$, J_n is a cylindrical Bessel function of the first kind, $H_n^{(1)}$ is a Hankel function of the first kind; for a spherical shell sphere $E_n = 2n + 1$, $f_n = j_n$, $g_n^{(1)} = h_n^{(1)}$, $F_n(\theta) = P_n(\cos \theta)$,

$N = n + 1/2$, j_n is a spherical Bessel function of the first kind, $h_n^{(1)}$ is a spherical Hankel function of the first kind, P_n is a Legendre polynomial. The solution for the scattered pressure in the case of normal incidence of the plane acoustic wave has the form

$$(1) \quad p_s = p_0 \sum_{n=0}^{\infty} E_n (-i)^n B_n g_n^{(1)}(kr) F_n(\theta)$$

The coefficients B_n have to be defined by solving the contact problems for the equations describing the motion of the shell. We introduce the relative half-thickness of the shell $\eta = h/R$. Let us consider three approximate models mentioned above.

The regions in which the refined asymptotic model and the model based on classical Kirchhoff–Love theory can be used are limited by the inequalities $\omega R/c_2 \ll \eta^{-1}$, $\omega R/c_2 \ll \eta^{-1/2}$, respectively [1]. Thus, both of these theories describe only the order Lamb-type waves S_0 and A_0 or the fluid-born wave A . The relevant mode numbers lie in the ranges $n \ll \eta^{-1}$ and $n \ll \eta^{-1/2}$ for the refined asymptotic model and the Kirchhoff–Love theory, respectively.

The first modes of higher order Lamb-type waves correspond to long-wave high-frequency vibrations of fluid-loaded shells. There are two types of the long-wave high-frequency approximations [2,3]. The transverse approximation is to use in the vicinities of the thickness stretch resonance frequencies. In the vicinities of the thickness shear resonance frequencies the tangential approximation should be used. The model formulated above is applicable only for the small values of the parameter n ($n \ll \eta^{-1}$). But series (1) only begin to converge when $n \sim x \sim \eta^{-1}$, where $x = ka$, i.e. solution contains short-wave components as well. Consequently, when calculating the scattered pressure using formula (1) the long-wave high-frequency approximations must be used together with the flat elastic layer model that will be considered below.

The flat elastic layer model is developed in references [2,3]. The equations for this model are valid under following conditions: $\partial/\partial\zeta \sim \partial/\partial\theta \sim \omega R/c_2 \sim \eta^{-1}$, i.e. for short-wave motions of the shell. In this case the equations of elasticity written in curvilinear coordinates can be replaced by those in plane problem of elasticity presented in Cartesian coordinates, in doing so the radial coordinate is “frozen” on the mid-surface of a shell.

The results of the synthesis of the form function in the far field ($r \rightarrow \infty$) in the case of backscattering ($\theta = 0$) are presented in [2,3]. Here

$$(2) \quad p = G \left| \sum_{n=0}^{\infty} E_n B_n (-1)^n \right|$$

The long-wave high-frequency approximation is applied beginning with the first thickness resonance frequency and only for $n < 10$. The rest of series (2) is evaluated by the flat layer model. A numerical analysis demonstrates advantages of the chosen scheme. The calculations for different parameters of material in a shell and value parameter η ($1/69 \leq \eta \leq 1/17$) show that there exist overlap regions, therefore, the proposed method give a possibility to describe both the resonance components of the partial modes and the scattered pressure with high accuracy.

3. References

- [1] V.A. Kovalev (2002). Application a refined asymptotic model in scattering of a plane acoustic waves by a spherical shell, *Izv. AN MTT (Mechanics of solids)*. **37** (2), 155–162.
- [2] J.D. Kaplunov, V.A. Kovalev, M.V. Wilde (2003). Matching of asymptotic models in scattering of a plane acoustic wave by an elastic cylindrical shell, *J. of Sound and Vibration*. **264** (3), 639–655.
- [3] V.A. Kovalev (2002). Synthesis of acoustic pressure scattered by an elastic cylindrical shell basis on acoustic waves by elastic spherical shell, *J. of Appl. Maths. and Mechs.* **66** (4), 581–590.

BUCKLING/COLLAPSE BEHAVIOUR OF CYLINDRICAL SHELLS IN BILGE REGION OF SHIP HULL GIRDERS UNDER INPLANE COMPRESSION

M.R. Khedmati¹, P. Edalat¹ and M. Rastani²

¹ Faculty of Marine Technology, Amirkabir University of Technology, Tehran, Iran

² Statoil-Petropars JV, Tehran, Iran

1. General

In this paper, the results of a series of elastoplastic large deflection analyses on a specific cylindrical shell part of the ship hull girders under inplane compression is reported. Nonlinear finite element method is applied in the calculations. It is revealed that the assumption of elastic-perfectly plastic behaviour for this part of the ship hulls is not realistic and may result in very optimistic predictions of the ship hull overall strength.

2. Introduction

Flat and curved stiffened plates are the key elements in the construction of ships and offshore structures. In a transition region between the bottom and side shells of the ship hull, there is a cylindrical part that is so-called *bilge*, Figure 1 (left). In most of the research works concerning with the ultimate strength of the ship hull girders under extreme sea conditions, the behaviour of this part is assumed to follow an elastic-perfectly plastic regime. No serious assessment has already been made or published on the strength and behaviour of this cylindrical shell part.

A series of full range elastoplastic large deflection analyses is performed on a parametric model of the bilge shell plating. The nonlinear finite element approach is applied for the investigations. Buckling and collapse modes are detected for the models. Also the average stress-average strain relationships of the models are summarised in a format to get a deep insight into the behaviours. Finally, it is revealed that the assumption of elastic-perfectly plastic behaviour for this part of the ship hulls is not realistic and may result in very optimistic predictions of the ship hull overall strength.

3. Model for analysis

The extent of the model for analysis is shown in the left part of the Figure 1. It is located between the two mid-span lines of the bilge brackets. Proper boundary conditions derived from real situations are applied to the edges of the model. Mechanical and geometrical characteristics of the parametric model are given in Table 1. A typical FE model for analysis with incorporated boundary conditions is shown in the Figure 1 (right). The model also is imperfect and initial deflections based on the real measurements are included in it.

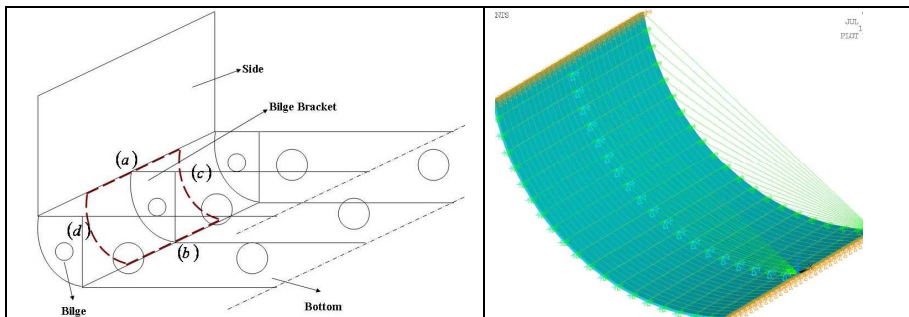


Figure 1. Extent of the bilge part for analysis (left) and its FE model (right).

Length (L) [mm]	2250
Radius (R) [mm]	1800
Thickness (t) [mm]	9,10,12,14,16
Yielding Stress (σ_Y) [MPa]	235.2,274.4,313.6
Young's Modulus (E) [MPa]	206000
Poisson's Ratio (ν)	0.3

Table 1. Mechanical and geometrical characteristics of the model.

4. Results and conclusions

A series of elastoplastic large deflection analyses is performed applying nonlinear finite element method. An extract of the results are shown in Figure 2. Some of the key results are:

The average stress-average strain relationships for the models are the same in a pre-collapse or pre-ultimate strength level, regardless of the changes for thickness or yield stress. With the increase of the shell thickness, or decrease in the yield stress, the slope of the post-ultimate strength part of the curves would be decreased. In the case of very extremely thick plates of a regular yield stress, a behaviour near to the elastic-perfectly plastic behaviour might be observed. It is finally concluded that the assumption of elastic-perfectly plastic behaviour for this part of the ship hulls is not realistic.

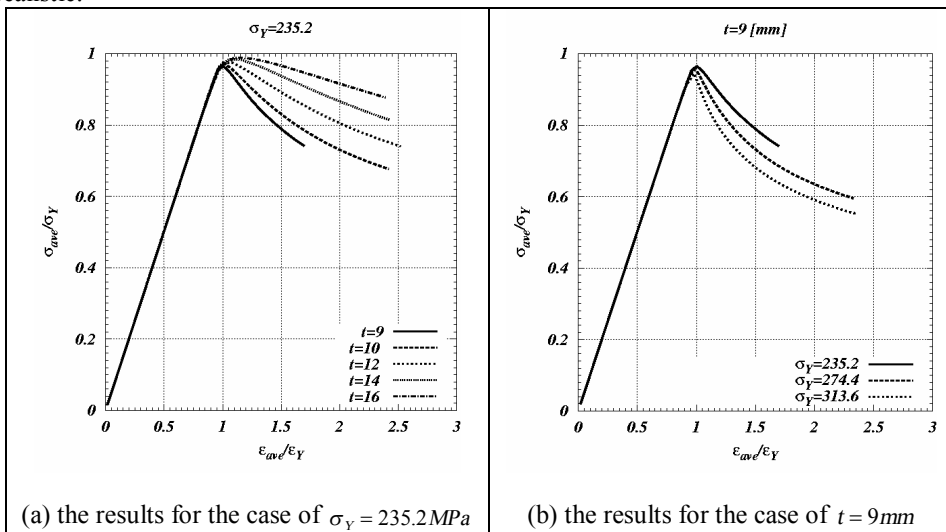


Figure 2. Average stress-average strain relationships of some analysed cases with different values of thickness or yield stress.

5. References

- [1] S. Timoshenko and S. Woinowsky-Krieger (1991). *Theory of Plates and Shells*, 2nd ed. McGraw Hill, New York, 122–131.
- [2] J.K. Paik, B.J. Kim and J.K. Seo, (2007). *Methods for ultimate Limit State Assessment of Ships and Ship-shaped Offshore Structures: Part 3 Hull girders*. Ocean Engineering.

CONTROLLABILITY FOR THIN LINEARLY ELASTIC SHELLS

G. Geymonat¹, A. Münch²

¹*Laboratoire de Mécanique et de Génie Civil, Université de Montpellier II, UMR CNRS 5508, CC 048, Place Eugène Bataillon, 34095 Montpellier cedex 5, France*

²*Laboratoire de Mathématiques, Université de Franche-Comté, UMR CNRS 6623, 16, route de Gray, 25030 Besançon, France*

Thanks to the pioneering works of J.L. Lions [1] there exists a general tool for the study of the exact controllability of a distributed system, in particular of various shell models. More precisely let us suppose that it is possible to act on (at least) a part of the boundary of a thin, linearly elastic and isotropic shell with suitable boundary conditions. Then null (or exact) controllability consists in proving that starting from an arbitrary initial state it is possible to steer the shell to rest, by a proper choice of the boundary control, in a finite time. The Hilbert Uniqueness Method (HUM) introduced by J. L. Lions allows to find a control as a minimum of a functional (continuous and convex in a suitable framework) whose coercivity is essentially reduced to the proof of a uniqueness result.

The summation convention is adopted, the greek indices take values in the set 1, 2 and the latin indices in the set 1, 2, 3.

Let ω be a bounded connected domain in \mathbb{R}^2 with boundary γ and let $y = (y_\alpha)$ denote a generic point of $\bar{\omega}$. Let $\theta \in C^\infty(\bar{\omega}; \mathbb{R}^3)$ be an injective mapping such that the vectors $\mathbf{a}_\alpha(y) := \partial_\alpha \theta(y)$ form the covariant basis of the tangent plane to the surface $S := \theta(\bar{\omega})$ at the point $\theta(y)$; let $\mathbf{a}_3(y) = \mathbf{a}^3(y) := \frac{\mathbf{a}_1(y) \wedge \mathbf{a}_2(y)}{|\mathbf{a}_1(y) \wedge \mathbf{a}_2(y)|}$ be the unit normal vector to S . For any displacement field $v_i \mathbf{a}^i$ expressed in terms of the contravariant basis the deformed surface is $\tilde{\theta}(\mathbf{v})(\bar{\omega})$ where $\tilde{\theta} : \mathbf{v} = (v_i) \rightarrow \theta + v_i \mathbf{a}^i$. In the framework of linearized theory small displacement \mathbf{v} are considered. In the Koiter model the membrane and flexural deformation energy are defined by the symmetric forms

$$(1) \quad a_M(\mathbf{u}, \mathbf{v}) = \int_{\omega} a^{\alpha\beta\lambda\mu} \gamma_{\alpha\beta}(\mathbf{u}) \gamma_{\lambda\mu}(\mathbf{v}) \sqrt{a} dy$$

$$(2) \quad a_F(\mathbf{u}, \mathbf{v}) = \int_{\omega} a^{\alpha\beta\lambda\mu} \rho_{\alpha\beta}(\mathbf{u}) \rho_{\lambda\mu}(\mathbf{v}) \sqrt{a} dy$$

where $\gamma_{\alpha\beta}(\mathbf{u})$ and $\rho_{\alpha\beta}(\mathbf{u})$ are the linearized change of metric and of curvature tensors associated to \mathbf{u} . Let $\epsilon \geq 0$ a real parameter and let be $\mathbf{A}_\epsilon = \mathbf{A}_M + \frac{\epsilon^2}{3} \mathbf{A}_F$ the operator in $\mathbf{H} = L^2(\omega)^3$ associated to the bilinear form

$$(3) \quad a_\epsilon(\mathbf{u}, \mathbf{v}) = a_M(\mathbf{u}, \mathbf{v}) + \frac{\epsilon^2}{3} a_F(\mathbf{u}, \mathbf{v})$$

defined on a suitable subspace \mathbf{V} of kinematically admissible displacements (as general references on shell theory see e.g. [2], [3], [4]). Let us consider the evolution problem :

$$(4) \quad \begin{cases} \frac{\partial \mathbf{u}}{\partial t^2}(y, t) + \mathbf{A}_\epsilon \mathbf{u}(y, t) = 0, & \text{for } y \in \omega \text{ and } t > 0 \\ \mathbf{u}(y, 0) = \mathbf{u}^0(y), \frac{\partial \mathbf{u}}{\partial t}(y, 0) = \mathbf{u}^1(y) & \text{for } y \in \omega \\ \mathbf{B}\mathbf{u}(y, t) = \mathbf{v}(y, t) & \text{for } y \in \gamma \text{ and } t \geq 0 \end{cases}$$

where \mathbf{B} is a suitable system of boundary conditions. The system is *exactly controllable in time T* if given an initial data $(\mathbf{u}^0, \mathbf{u}^1)$ it is possible to find a control \mathbf{v} that can drive the system (4) to rest at time T i.e.

$$\mathbf{u}(y, T) = \mathbf{0}, \quad \frac{\partial \mathbf{u}}{\partial t}(y, T) = \mathbf{0} \quad \text{for } y \in \omega$$

In [5] it is for instance proved the exact controllability when the middle surface of the shell satisfies a suitable condition (e.g. is not too far from a plane). It is natural to study the dependence of the controllability time T on ϵ . Let us remark that when $\epsilon \rightarrow 0$ one has a singular perturbation problem ; hence one can expect that the controllability time $T(\epsilon) \rightarrow \infty$. This can be proved in similar situations (see e.g. [7]). Moreover one can prove in the case $\epsilon = 0$ a non-controllability result [6] : there exist some in initial data $(\mathbf{u}^0, \mathbf{u}^1)$ such that the evolution system (4) is not exactly controllable.

In this paper we address the following problem :

In the case $\epsilon = 0$ find a space of controllable initial data $(\mathbf{u}^0, \mathbf{u}^1)$.

We will give some preliminary partial results obtained in a joint work with Farid Ammar-Khodja and Arnaud Münch, [8]. The characterization of the controllable initial data depends on the study of the spectral problem associated to the operator \mathbf{A}_M . This will be illustrated on the example of hemispherical shells and on the example of an arch.

- [1] Lions J.L., *Contrôlabilité exacte, perturbations et stabilisations de systèmes distribués*, 2 Tomes, Masson, Paris 1988.
- [2] P.G. Ciarlet, *Mathematical Elasticity, vol. III : Theory of shells*, Studies in mathematics and its applications, North-Holland, Amsterdam, 2000.
- [3] J. Sanchez-Hubert, E. Sanchez-Palencia, *Coques élastiques minces : propriétés asymptotiques*, Masson, Paris, 1997.
- [4] K. J. Bathe, D. Chapelle, *The finite element analysis of shells-fundamentals*, Springer, Berlin, 2003.
- [5] Miara B., Valente V., *Exact controllability of a Koiter Shell by a Boundary Action*, J. Elasticity **52** 267-287 (1999).
- [6] Geymonat G., Valente V., *A noncontrollability result for systems of mixed order*, SIAM J. Control Optim , **39** (3), 661-672 (2000).
- [7] Lagnese J.E., Lions J.L., *Modelling, Analysis and Control of Thin Plates*, Masson, Paris, 1988.
- [8] Ammar-Khodja F., Geymonat G., Münch A., In preparation

**STRESS STATE OF NONTHIN NONCIRCULAR ORTHOTROPIC
CYLINDRICAL SHELLS WITH VARIABLE THICKNESS UNDER
DIFFERENT TYPES OF BOUNDARY CONDITIONS.**

Ya. Grigorenko and S. Yaremchenko

S.P. Timoshenko Institute of mechanics of NAS of Ukraine, Kiev, Ukraine

1. Basic assumptions

The abstract addresses the static problems for nonthin noncircular orthotropic shells using re-fined Timoshenko-type model based on the hypothesis of a straight line .

Let the shell mid surface be referred to the orthogonal coordinate system s, θ , where s and θ are the coordinates along the generatrix and directrix, respectively. Let γ be normal coordinate to the surface s, θ .

The first quadratic form of the mid surface is $dS^2 = A_1^2 ds^2 + A_2^2 d\theta^2$, ($0 \leq s \leq l, \theta_1 \leq \theta \leq \theta_2$), where $A_1 = 1$ and $A_2 = A_2(\theta)$ are the Lamé coefficients.

According to the hypothesis accepted, the displacements of the shell can be represented as

$$(1) \quad u_s(s, \theta, \gamma) = u(s, \theta) + \gamma \psi_s(s, \theta), \quad u_\theta(s, \theta, \gamma) = v(s, \theta) + \gamma \psi_\theta(s, \theta), \quad u_\gamma(s, \theta, \gamma) = w(s, \theta),$$

where u, v and w are the displacements of points of the coordinate surface along the directions s, θ, γ , respectively; ψ_s and ψ_θ are the total angles of rotation of the rectilinear element.

The strains can be expressed as

$$(2) \quad e_s(s, \theta, \gamma) = \varepsilon_s(s, \theta) + \gamma \varkappa_s(s, \theta), \quad e_\theta(s, \theta, \gamma) = \varepsilon_\theta(s, \theta) + \gamma \varkappa_\theta(s, \theta), \\ e_{s\theta}(s, \theta, \gamma) = \varepsilon_{s\theta}(s, \theta) + \gamma 2\varkappa_{s\theta}(s, \theta), \quad e_{s\gamma}(s, \theta, \gamma) = \gamma_s(s, \theta), \quad e_{\theta\gamma}(s, \theta, \gamma) = \gamma_\theta(s, \theta),$$

where

$$(3) \quad \varepsilon_s = \frac{\partial u}{\partial s}; \quad \varepsilon_\theta = \frac{1}{A_2} \frac{\partial v}{\partial \theta} + kw; \quad \varepsilon_{s\theta} = \frac{1}{A_2} \frac{\partial u}{\partial \theta} + \frac{\partial v}{\partial s}; \quad \varkappa_s = \frac{\partial \psi_s}{\partial s}; \quad \varkappa_\theta = \frac{1}{A_2} \frac{\partial \psi_\theta}{\partial \theta} - k\varepsilon_\theta; \\ 2\varkappa_{s\theta} = \frac{1}{A_2} \frac{\partial \psi_s}{\partial \theta} + \frac{\partial \psi_\theta}{\partial s} - \frac{k}{A_2} \frac{\partial u}{\partial \theta}; \quad \gamma_s = \psi_s - \vartheta_s; \quad \gamma_\theta = \psi_\theta - \vartheta_\theta; \\ \vartheta_s = -\frac{\partial w}{\partial s}; \quad \vartheta_\theta = -\frac{1}{A_2} \frac{\partial w}{\partial \theta} + kv;$$

k is the directrix curvature.

The equilibrium equations are:

$$(4) \quad \frac{\partial N_s}{\partial s} + \frac{1}{A_2} \frac{\partial N_{\theta s}}{\partial \theta} + q_s = 0, \quad \frac{1}{A_2} \frac{\partial N_\theta}{\partial \theta} + \frac{\partial N_{s\theta}}{\partial s} + kQ_\theta + q_\theta = 0, \\ \frac{\partial Q_s}{\partial s} + \frac{1}{A_2} \frac{\partial Q_\theta}{\partial \theta} - kN_\theta + q_\gamma = 0, \quad \frac{\partial M_s}{\partial s} + \frac{1}{A_2} \frac{\partial M_{\theta s}}{\partial \theta} - Q_s = 0, \quad \frac{1}{A_2} \frac{\partial M_\theta}{\partial \theta} + \frac{\partial M_{s\theta}}{\partial s} - Q_\theta = 0,$$

where $N_s, N_\theta, N_{s\theta}$, and $N_{\theta s}$ are the tangential forces; Q_s, Q_θ are the shear forces; $M_s, M_\theta, M_{s\theta}$, and $M_{\theta s}$ are the bending and twisting moments; q_s, q_θ and q_γ are the components of the surface load. Elastic relations for orthotropic shells, which are symmetrical with respect to the chosen coordinate surface, have the form

$$(5) \quad N_s = C_{11}\varepsilon_s + C_{12}\varepsilon_\theta, \quad N_\theta = C_{12}\varepsilon_s + C_{22}\varepsilon_\theta, \quad N_{st} = C_{66}\varepsilon_{s\theta} + 2kD_{66}\varkappa_{s\theta}, \\ N_{\theta s} = C_{66}\varepsilon_{s\theta}, \quad M_s = D_{11}\varkappa_s + D_{12}\varkappa_\theta, \quad M_\theta = D_{12}\varkappa_s + D_{22}\varkappa_\theta, \\ M_{\theta s} = M_{s\theta} = 2D_{66}\varkappa_{s\theta}, \quad Q_s = K_1\gamma_s, \quad Q_\theta = K_2\gamma_\theta,$$

where C_{ij} , D_{ij} , K_1 , and K_2 are the parameters that depend on the material properties and shell thickness.

2. Resolving technique and its application

Choosing the displacements u , v , w , and the total angles of rotation ψ_s , ψ_θ as unknown functions and using (3)–(5) the resolving system of partial differential equation describing the stress state of orthotropic non circular cylindrical shells can be presented as follows [2]:

$$(6) \quad L\bar{y} = 0,$$

where L is the linear differential operator of the second order and $\bar{y} = \{u, v, w, \psi_s, \psi_\theta\}$ is the desired vector-function. Adding to (6) boundary conditions on ends and boundary conditions on rectilinear contours in the case of a closed shell or symmetry conditions, if a shell is open, we obtain two-dimensional boundary-value problem, whose solution can be presented in the following form:

$$(7) \quad \bar{y} = \Phi \bar{y}_*,$$

where $\bar{y}_* = \{u_0(\theta), \dots, u_N(\theta), v_0(\theta), \dots, v_N(\theta), w_0(\theta), \dots, w_N(\theta), \psi_{s0}(\theta), \dots, \psi_{sN}, \psi_{\theta 0}(\theta), \dots, \psi_{\theta N}(\theta)\}$ is unknown vector-function and components of matrix Φ , which satisfy various boundary conditions on ends, are linear combinations of cubic B-splines on a uniform mesh. Substituting (7) into (6) and boundary or symmetry conditions, we require that they would be held at the $N + 1$ points of collocation s_i along the generatrix. As a result, we obtain one-dimensional boundary-value problem

$$(8) \quad \frac{d\bar{z}}{d\theta} = A\bar{z} + \bar{f}, \quad B_1\bar{z} = \bar{b}_1 \quad (\theta = \theta_1), \quad B_2\bar{z} = \bar{b}_2 \quad (\theta = \theta_2),$$

where $\bar{z} = \{\bar{y}_*, \bar{y}'_*\}$ is the vector-function of θ ; \bar{f} is the vector of right-hand sides; A is the square matrix whose elements depend on θ ; B_1 and B_2 are the matrices of boundary conditions, \bar{b}_1 and \bar{b}_2 are the corresponding vectors. The one-dimensional boundary-value problem (8) can be solved by the discrete-orthogonalization method [1]. Substituting \bar{y}_* into (7), we obtain the solution of the two-dimensional boundary-value problem.

On the basis of the approach proposed, we have solved the set of problems related to the stress-strain state of orthotropic cylindrical shells with an elliptical and corrugated cross-section. Analysis of displacement and stress fields under different boundary condition is carried out.

- [1] R. Bellman and R. Kalaba (1965). *Quasilinearization and nonlinear boundary-value problems*, Elsevier, 218 p.
- [2] Ya.M. Grigorenko and S.N. Yaremchenko (2004). Stress Analysis of Orthotropic Noncircular Cylindrical Shells of Variable Thickness in a Refined Formulation, *Int. Appl. Mech.*, **40**, 266-274.

ON THE IMPROVED MEMBRANE PART OF MIXED SHELL ELEMENTS

K. Wisniewski¹, E. Turska²

¹*Institute of Fundamental Technological Research, Warsaw, Poland*

²*Polish Japanese Institute of Information Technology, Warsaw, Poland*

1. Introduction

Mixed finite elements exhibit a higher accuracy of displacements and stresses and a better convergence rate in non-linear problems than elements based on other formulations. Since the pioneering paper by Pian of 1964, a lot of work has been done to improve mixed methods; the elements and their theoretical foundations.

Among the mixed elements, particularly well known is the Pian-Sumihara (PS) element [1], which is slightly more accurate than the EAS4 element for coarse distorted meshes. Afterwards, several elements were developed, which perform slightly better than the PS element, including the element by Yuan, Huang and Pian [5] and by Piltner and Taylor of [2].

The objective of the current paper is to present our recently developed mixed finite elements based on the incremental Hellinger-Reissner (HR) functional and the incremental Hu-Washizu (HW) functional, see [3] and [4]. They are directly applicable to 'solid-shell' elements and to the shell elements without the drilling rotation.

2. Characteristics of the approach

The key feature of our approach is the use of the skew coordinates associated with the natural basis at the element's center $\{\mathbf{g}_k^c\}$, and defined as follows

$$(1) \quad x_S = \xi + \frac{(j,\eta)_c}{j_c} \xi \eta, \quad y_S = \eta + \frac{(j,\xi)_c}{j_c} \xi \eta,$$

where j_c , $(j,\xi)_c$ and $(j,\eta)_c$ are the parts of the expansion of the Jacobian's determinant, $\det \mathbf{J} = j_c + (j,\xi)_c \xi + (j,\eta)_c \eta$. The motivation behind the use of these coordinates will be explained in the presentation. The representations of stress and strain are assumed in terms of the skew coordinates as follows.

The contra-variant components of stress are assumed in the basis $\{\mathbf{g}_k^c\}$, i.e. $\boldsymbol{\sigma} = \sigma^{kl} \mathbf{g}_k^c \otimes \mathbf{g}_l^c$, $k, l = 1, 2$. The representation of σ^{kl} is assumed (matrix \mathbf{G}_1) and transformed to the reference basis on use of

$$(2) \quad \boldsymbol{\sigma}^{ref} = \mathbf{J}_c \mathbf{G}_1 \mathbf{J}_c^T, \quad \mathbf{G}_1 \doteq \begin{bmatrix} q_1 + q_2 y_S & q_5 \\ \text{symm.} & q_3 + q_4 x_S \end{bmatrix},$$

where \mathbf{J}_c is the Jacobian matrix evaluated at the element center. The above 5-parameter representation in \mathbf{G} is identical as in the PS element, but the skew coordinates are used.

The co-variant components of strain are assumed in the co-basis $\{\mathbf{g}_c^k\}$, i.e. $\boldsymbol{\varepsilon} = \varepsilon_{kl} \mathbf{g}_c^k \otimes \mathbf{g}_c^l$. The representation of $\varepsilon_{\alpha\beta}$ is assumed (matrix \mathbf{G}_2) and transformed to the reference basis on use of

$$(3) \quad \boldsymbol{\varepsilon}^{ref} = \mathbf{J}_c^{-T} \mathbf{G}_2 \mathbf{J}_c^{-1}, \quad \mathbf{G}_2 \doteq \begin{bmatrix} q_6 + q_7 y_S + q_8 x_S & q_{12} + q_{13} x_S + q_{14} y_S \\ \text{symm.} & q_9 + q_{10} x_S + q_{11} y_S \end{bmatrix}.$$

The applied 9-parameter representation of strain is linear for all components.

A beneficial consequence of using the above representations in skew coordinates is that, for a linear elastic case, the homogenous equilibrium equations and the compatibility condition are satisfied point-wise, regardless of the element's shape, which is an exceptional property. Note that for the representations in the natural coordinates, these equations are satisfied only for parallelograms.

3. Mixed and mixed/enhanced elements based on HR and HW functionals

Several mixed and mixed/enhanced 4-node elements are developed and tested in [3] and [4], using also the 7-parameter representation of stress, which requires an additional strain enhancement. We selected two elements, designated as HR5-S and HW14-S, as the best performers. The HR5-S is based on eq.(2), while the HW14-S on eq.(2) and eq.(3). These elements are mixed; although they use less parameters they still perform similarly as the mixed/enhanced elements.

The developed elements are based on the Green strain, and are applicable to large deformation problems and non-linear materials. They have a correct rank, and pass the patch test. They were subjected to a range of benchmark tests, to establish the coarse mesh accuracy and the sensitivity to mesh distortion. One of these tests is the Cook's membrane, see Fig.1, where $E = 1$, $\nu = 1/3$, $h = 1$, $P = 1$, which is very indicative, because the shear deformation dominates, and the elements are trapezoidal.

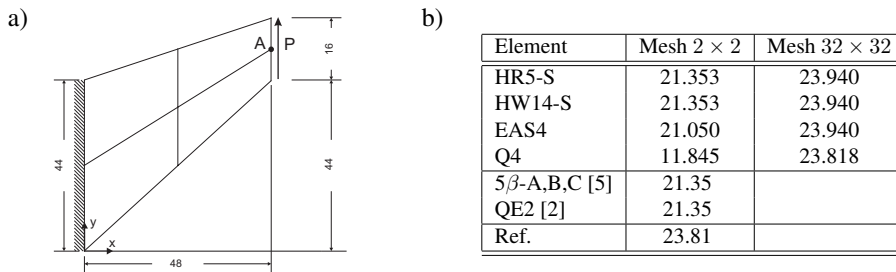


Figure 1. Cook's membrane. a) Initial geometry and load, b) Displacement u_y at point A for two meshes.

The numerical results confirm that our new HR5-S and HW14-S elements are more accurate and less sensitive to mesh distortion than the EAS4 element and the PS element. They use a smaller number of modes than the other top elements described in the literature, because the enhancement is not needed, yet they yield equally accurate results.

4. References

- [1] Pian T.H.H., Sumihara K.: *Rational approach for assumed stress finite elements*. Int. J. Num. Meth. Engng, Vol.20, 1685–1695 (1984)
- [2] Piltner R., Taylor R.L.: *A quadrilateral mixed finite element with two enhanced strain modes*. Int. J. Num. Meth. Engng, Vol.38, 1783–1808 (1995)
- [3] Wisniewski K., Turska E.: *Improved four-node Hellinger-Reissner elements based on skew coordinates*. Int. J. Num. Meth. Engng, (2008) DOI: 10.1002/nme.2343
- [4] Wisniewski K., Turska E.: *Improved four-node Hu-Washizu elements based on skew coordinates*. submitted (2008)
- [5] Yuan K-Y., Huang Y-S., Pian T.H.H.: *New strategy for assumed stress for 4-node hybrid stress membrane element*. Int. J. Num. Meth. Engng, Vol.36, 1747–1763 (1993)

A PIEZOELECTRIC SOLID SHELL ELEMENT ACCOUNTING FOR MATERIAL AND GEOMETRICAL NONLINEARITIES

S. Klinkel and W. Wagner

Institut für Baustatik, Universität Karlsruhe (TH), Germany

1. Introduction

This contribution is concerned with a piezoelectric solid shell finite element formulation. In recent years several new elements have been proposed. Some of these model a reference surface of the shell structure. Here, a surface oriented piezoelectric solid shell element is developed. With respect to the laminated structure of piezoelectric devices a more or less sophisticated laminate theory is necessary. The so-called solid shell elements circumvent laminate theories by modelling each ply with one element, see e.g. [3] and the references therein.

The most piezoelectric shell formulations assume a geometrically linear theory. In [4] it is pointed out that nonlinear characteristics can significantly influence the performance of piezoelectric systems. In particular this holds for buckling of plates. A geometrically non-linear theory allows large deformations and includes stability problems. Typical materials for the utilization of the piezoelectric effect are ferroelectric ceramics like barium titanate (BaTiO_3) and lead zirconate titanate (PbZrTiO_3) abbreviated as PZT. Ferroelectric ceramics show a strongly nonlinear behavior, which is caused by so-called domain switching effects, see e.g. [2] and the references therein. The present shell formulation incorporates a material model accounting for the physical nonlinearities. The model is thermodynamically consistent and determined by two scalar valued functions: the Gibb's free energy and a switching criterion.

Usually the electric potential inside the piezoelectric model is assumed to be linear through the shell thickness. To fulfill the electric charge conservation law exactly a quadratic electric potential through the thickness is necessary. In this paper the finite element formulation is based on a variational principle including six independent fields: displacements, electric potential, strains, electric field, mechanical stresses and dielectric displacements. To obtain correct results in bending dominated situations a linear distribution through the thickness of the independent electric field is assumed. The element has 8 nodes; the nodal degrees of freedom are displacements and the electric potential. The presented finite shell element is able to model arbitrary curved shell structures and incorporates a 3D-material law.

2. Numerical simulation

Telescopic actuators consist of concentric shells interconnected by end caps which alternate in placement between the two axial ends of the shells, see Fig. 1. The diameters in Fig. 1 refer to the outside of the cylindrical shells. The telescopic actuators are designed to accomplish for a high displacement actuation at the cost of force, see [1]. The cascading shells are polarized in radial direction. The transversal isotropic elastic material constants are given as $E_1 = E_2 = 60.61 \cdot 10^9 \text{ N/m}^2$, $E_3 = 48.31 \cdot 10^9 \text{ N/m}^2$, $\nu_{23} = \nu_{13} = 0.41$, $\nu_{12} = 0.29$, $G_{23} = G_{13} = 22.99 \cdot 10^9 \text{ N/m}^2$, $G_{12} = 23.47 \cdot 10^9 \text{ N/m}^2$. The piezoelectric modulus is described by $e_{13} = e_{23} = -29.878 \text{ C/m}^2$, $e_{33} = 10.631 \text{ C/m}^2$, $e_{51} = e_{62} = 17.034 \text{ C/m}^2$ and the permittivity is defined as $\epsilon_{11} = \epsilon_{22} = 15.09 \cdot 10^{-9} \text{ C}^2/\text{N m}^2$, $\epsilon_{33} = 14.16 \cdot 10^{-9} \text{ C}^2/\text{N m}^2$. The piezoelectric constants e_{13} and e_{33} are taken from [1] and all other quantities are assumed. The nonlinear material model is described in [2]. The orientation of the local basis system t_i is defined by t_1 in circumferential direction, t_2 in axial direction and t_3 in radial direction. With respect to symmetry only a quarter of the system is modeled by finite elements, see Fig. 1.

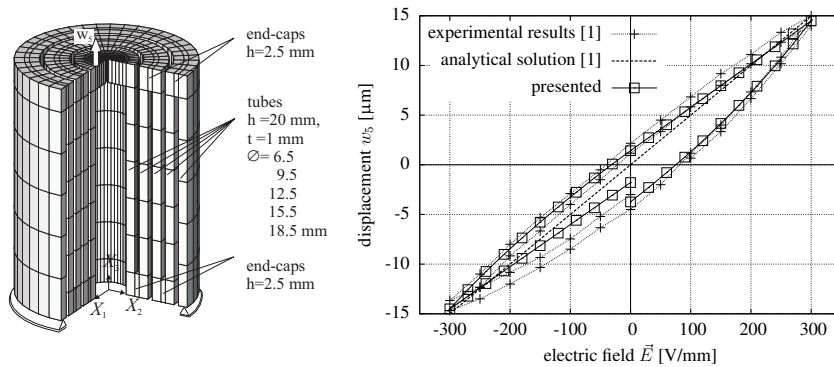


Figure 1. Left: Telescopic actuator: system, boundary conditions and finite element model. Right: axial deflection versus electric field

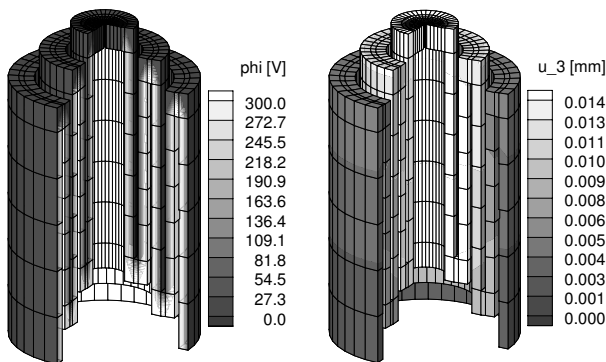


Figure 2. Telescopic actuator: deformed configuration with a plot of electric potential and axial displacement

The system is supported in X_3 -direction at the lower bottom at the outside edge and it is loaded by applying an electric potential to the piezoelectric cylindrical shells shown in Fig. 2. The load deflection behavior of the axial displacements, see Fig. 1, is highly nonlinear due to the occurring domain switching effects. A comparison to the experimental data in [1] shows good agreement, which is very promising for further calculations.

3. References

- [1] P. Alexander, D. Brei, W. Miao, J. Halloran (2001), Fabrication and experimental characterization of d_{31} telescopic piezoelectric actuators. *Journal of Material Science*, **36**, 4231–4237.
- [2] S. Klinkel (2006). A phenomenological constitutive model for ferroelastic and ferroelectric hysteresis effects in ferroelectric ceramics, *Int. Journal of Solids and Structures*, **43**, 7197–7222.
- [3] S. Klinkel and W. Wagner (2008). A piezoelectric solid shell element based on a mixed variational formulation for geometrically linear and nonlinear applications, *Comp. & Struct.*, **86**, 38–46.
- [4] H.S. Tzou HS and Y.H. Zhou (1997). Nonlinear piezothermoelasticity and multi-field actuations, part 2: Control of nonlinear deflection, buckling and dynamics. *Journal of Vibration and Acoustics*, **119**, 382–389.

FREE VIBRATIONS OF ORTHOTROPIC SHALLOW SHELLS OF VARIABLE THICKNESS ON BASIS OF SPLINE-APPROXIMATION METHOD

V.D. Budak², A.Ya. Grigorenko¹, S. V. Puzyrev²

¹ *S. P. Timoshenko Institute of Mechanics of NAS of Ukraine, Kiev, Ukraine,*

² *V.A. Suhomlinskii Nikolayev State University, Nikolayev, Ukraine*

Plates and shells with a complex shape made of inhomogeneous anisotropic materials are widely used for construction of structure elements in modern engineering. The present report proposes an efficient approach to solving the free vibrations problems of shallow shells with the variable thickness within the framework of the classic models. The object of investigation is the class of free vibration problems for orthotropic rectangular in a plane shallow shells of variable thickness in two coordinate directions. The problems are described by the system of linear partial differential equations with the variable coefficients [1]:

$$\begin{aligned}
 & C_{11} \frac{\partial^2 u}{\partial x^2} + \frac{\partial C_{11}}{\partial x} \frac{\partial u}{\partial x} + C_{66} \frac{\partial^2 u}{\partial y^2} + \frac{\partial C_{66}}{\partial y} \frac{\partial u}{\partial y} + (C_{12} + C_{66}) \frac{\partial^2 v}{\partial x \partial y} + \frac{\partial C_{66}}{\partial y} \frac{\partial v}{\partial x} + \\
 & + \frac{\partial C_{12}}{\partial x} \frac{\partial v}{\partial y} + (C_{11} k_1 + C_{12} k_2) \frac{\partial w}{\partial x} + \frac{\partial (C_{11} k_1 + C_{12} k_2)}{\partial x} w = 0, \\
 & C_{66} \frac{\partial^2 v}{\partial x^2} + \frac{\partial C_{66}}{\partial x} \frac{\partial v}{\partial x} + C_{22} \frac{\partial^2 v}{\partial y^2} + \frac{\partial C_{22}}{\partial y} \frac{\partial v}{\partial y} + (C_{12} + C_{66}) \frac{\partial^2 u}{\partial x \partial y} + \frac{\partial C_{12}}{\partial y} \frac{\partial u}{\partial x} + \\
 & + \frac{\partial C_{66}}{\partial x} \frac{\partial u}{\partial y} + (C_{12} k_1 + C_{22} k_2) \frac{\partial w}{\partial y} + \frac{\partial (C_{12} k_1 + C_{22} k_2)}{\partial y} w = 0, \\
 & D_{11} \frac{\partial^4 w}{\partial x^4} + D_{22} \frac{\partial^4 w}{\partial y^4} + 2(D_{12} + 2D_{66}) \frac{\partial^4 w}{\partial x^2 \partial y^2} + 2 \frac{\partial D_{11}}{\partial x} \frac{\partial^3 w}{\partial x^3} + 2 \frac{\partial D_{22}}{\partial y} \frac{\partial^3 w}{\partial y^3} + \\
 & + 2 \frac{\partial}{\partial y} (D_{12} + 2D_{66}) \frac{\partial^3 w}{\partial x^2 \partial y} + 2 \frac{\partial}{\partial x} (D_{12} + 2D_{66}) \frac{\partial^3 w}{\partial x \partial y^2} + \left(\frac{\partial^2 D_{11}}{\partial x^2} + \frac{\partial^2 D_{12}}{\partial y^2} \right) \frac{\partial^2 w}{\partial x^2} + \\
 & + \left(\frac{\partial^2 D_{12}}{\partial x^2} + \frac{\partial^2 D_{22}}{\partial y^2} \right) \frac{\partial^2 w}{\partial y^2} + 4 \frac{\partial^2 D_{66}}{\partial x \partial y} \frac{\partial^2 w}{\partial x \partial y} + (C_{11} k_1^2 + 2C_{12} k_1 k_2 + C_{22} k_2^2) w + \\
 & + (C_{11} k_1 + C_{12} k_2) \frac{\partial u}{\partial x} + (C_{12} k_1 + C_{22} k_2) \frac{\partial v}{\partial y} + \rho h \frac{\partial^2 w}{\partial t^2} = 0.
 \end{aligned}
 \tag{1}$$

Here u , v and w are the unknown displacements of shell midsurface points; t is the time; $h = h(x, y)$ is the shell thickness; $\rho = \rho(x, y)$ is the density of the material; $C_{ij} = B_{ij} h$, $D_{ij} = B_{ij} h^3 / 12$ ($\{i, j\} = \{1, 2, 6\}$) are the strain and bending stiffness of the shell.

The different boundary conditions (rigid fixing, hinge supporting and their combinations) for displacements are specified on the shell contours.

System (1) is solved in two steps. At the first step, we approximate the unknown displacements in one of the coordinate directions (for example OY) by the segments of series consisting the linear combinations of the B-splines of the third and fifth power [2, 3]:

$$u = e^{j\omega t} \sum_{i=0}^N u_i(x) \psi_{1,i}(y), \quad v = e^{j\omega t} \sum_{i=0}^N v_i(x) \psi_{2,i}(y), \quad w = e^{j\omega t} \sum_{i=0}^N w_i(x) \psi_{3,i}(y),
 \tag{2}$$

where, $v_i(x)$ and $w_i(x)$ ($i = \overline{0, N}$) are the unknown functions, $\psi_{1,i}(y)$ and $\psi_{2,i}(y)$ are the linear combinations of the B-splines of the third power, $\psi_{3,i}(y)$ are the linear combinations of the B-

splines of the fifth power, which exactly satisfied boundary conditions for displacements on the contours $y = const$; ω is the unknown frequency of free vibrations; $j = \sqrt{-1}$; $0 \leq y \leq b$.

Substituting (2) into (1) with allowance for the boundary conditions and requiring expansion (2) would be the coincident with the exact solution in the number of points of collocation, which are the roots of the Legendre second-order polynomial on segment $[0,1]$, we arrive at the one-dimensional eigen-value problem. This problem can be written down in the normalized Cauchy form as:

$$(3) \quad \frac{d\bar{Y}}{dx} = \mathbf{A}(x, \omega)\bar{Y} \quad (0 \leq x \leq a),$$

$$(4) \quad \mathbf{B}_1\bar{Y}(0) = \bar{0}, \mathbf{B}_2\bar{Y}(a) = \bar{0},$$

where $\bar{Y} = [\bar{u}, \bar{u}', \bar{v}, \bar{v}', \bar{w}, \bar{w}', \bar{w}'', \bar{w}''']^T$ is the vector-column of the unknown functions and their derivatives with the dimensionality $8(N+1)$; $\mathbf{A}(x, \omega)$ is the specified square matrix of the order $8(N+1)$; \mathbf{B}_1 and \mathbf{B}_2 are specified rectangular matrices with the dimensionality $4(N+1) \times 8(N+1)$.

At the second step, the one-dimensional eigen-value problem (3) – (4) is solved by the stable numerical method of discrete orthogonalization in combination with the method of incremental-step search [2, 3].

On the basis of the method proposed, the spectrum of frequencies and modes of free vibrations of orthotropic plates and shallow rectangular in a plane shells of different shapes, whose thickness varies in one or two coordinate directions, is studied. It is supposed that the shells contours are rigidly fixed or hinged supported. Their combinations are possible.

The following cases of free vibrations are considering: the orthotropic rectangular plate with linearly-variable thickness:

$$(5) \quad h = h_0[1 + \alpha(2x/a - 1)];$$

orthotropic shallow rectangular in plane cylindrical shell of the thickness varying by the law :

$$(6) \quad h = h_0[1 + \alpha(6x^2 - 6x + 1)];$$

cylindrical orthotropic panel with the thickness varying in two directions by the law:

$$(7) \quad h = h_0(1 + \alpha \cos(\pi x/a))(1 + \beta \cos(\pi y/b)).$$

Here h_0 is the thickness of plates (shallow shells) with an equivalent mass and constant thickness, $|\alpha| \leq 0.5$, $|\beta| \leq 0.5$ are the coefficients, which determine the type of the shell in the given coordinate direction.

The numerical-analytical approach proposed makes it possible to analyze frequencies and modes of free vibrations of rectangular in plane shallow anisotropic shells with different boundary conditions and the thickness varying in two directions in wide range of varying geometrical and mechanical parameters. rectangular planes rectangular planes rectangular planes rectangular planes .

References

- [1] A.Ya. Grigorenko, T.L. Efimova *Spline-Approximation Method Applied to Solve Natural-Vibration Problems for Rectangular Plates of Varying Thickness* // Int. Applied Mech. – Vol. 41, № 10 – 2005. – P. 1161–1169.
- [2] V.D. Budak, A.Ya. Grigorenko, S.V. Puzyrev *Solution describing the natural vibrations of rectangular shallow shells with varying thickness* // Int. Applied Mech. – Vol. 43, № 4 – 2007. – P. 432–441.
- [3] V.D. Budak, A.Ya. Grigorenko, S.V. Puzyrev *Free vibrations of rectangular orthotropic shallow shells with varying thickness* // Int. Applied Mech. – Vol. 43, № 6 – 2007. – P. 670 – 682.

IDENTIFICATION AND SIMULATION OF SHELLS GEOMETRIC INITIAL IMPERFECTIONS

J. Górski and T. Mikulski

Gdańsk University of Technology, Gdańsk, Poland

1. Introduction

It is well known that the effect of structural geometric imperfections can dramatically decrease the nominal load carrying capacity of shell structures. As it is difficult and expensive to measure the initial structure imperfections in situ or in laboratory a methodology of identification and description of the available data should be provided. An important part of the structural imperfection modelling in a reliability context is the representation of random fields describing the statistical variation of properties or structure parameters. The presented procedure provides an opportunity for the reproduction of the measured maps of steel cylindrical tank geometric imperfections. Generations of the nonhomogeneous random fields based on the original conditional-rejection method of simulation are applied [1, 3]. Using the measured data an envelope of the imperfections is also estimated. It allows for simulation of extreme but still realistic fields of imperfections. When nonlinear geometric and material effects are taken into consideration the shell reliability can be evaluated only numerically. Nonlinear numerical analyses of petrol tanks, silos and underground tanks with and without initial geometric imperfections are performed. Soil parameter randomness is also included in the calculations. The results indicate that the initial imperfections influence the solutions.

2. Identification of the measured geometric imperfections

The identification and simulation procedure is presented on the basis of measured in situ imperfections of nine steel cylindrical vertical tanks of $V = 5000 \div 50000 \text{ m}^3$ capacity [2]. The tank side surface imperfections can be considered in terms of a two-dimensional scalar random field described by a probability density function. The following hypotheses were formulated and proved [3]: the stochastic process is stationary and ergodic along the horizontal lines, and the random variables can be described by a Gaussian probability density function. Using the above assumption the following nonhomogeneous correlation function is introduced

$$(1) \quad K(y_1, y_2, z_1, z_2) = \alpha \frac{z_1 z_2}{h^2} \cos(\omega(y_2 - y_1)) \exp(-\beta|y_2 - y_1| - \gamma|z_2 - z_1|),$$

where: $y_1, y_2, z_1,$ and z_2 are the point coordinates, and h denotes the tank height. The correlation function parameters $\alpha, \omega, \beta,$ and γ are estimated on the basis of the measured data. The assumption that the random field of imperfections is ergodic along the horizontal lines, makes it possible to analyse not single (the measured) but hundreds of realizations. The global experimental covariance matrix \mathbf{K}_e of the measured imperfection field was obtained according to the following statistical formulas:

$$(2) \quad \mathbf{K}_e = \frac{1}{NR-1} \sum_{i=1}^{NR} (\mathbf{x}_i - \bar{\mathbf{x}})(\mathbf{x}_i - \bar{\mathbf{x}})^T, \quad \bar{\mathbf{x}} = \frac{1}{NR} \sum_{i=1}^{NR} \mathbf{x}_i,$$

where \mathbf{x}_i ($i = 1, \dots, NR$) is the measured imperfection vector, NR is the number of realizations, and $\bar{\mathbf{x}}$ represents the mean value vector. Making use of the calculated matrix \mathbf{K}_e the parameters of the correlation function (1) are determined by a standard regression analysis. The error analysis proved that the scattered pattern of imperfections was modelled accurately.

It is possible to describe the correlation function as an envelope of the extreme imperfections. Examining the calculated normalized standard deviations for all tank data it is easy to notice that the simplest solution is the approximation of the standard deviation to a parabolic function.

3. Simulation of the geometric imperfections

The field of geometric imperfections is numerically simulated taking advantage of the correlation function (1) and the estimated constants. In the process the conditional-rejection simulation method is used [1, 3]. An important role in the calculations is played by the propagation base scheme covering sequentially the mesh points and the random field envelope which allows to fulfill the geometric and boundary conditions of the structure model. Any homogeneous or non-homogeneous field of practically unlimited sizes can be generated.

The simulation process is presented using the data of tank of 5000 m³ capacity. Two cases are analysed, i.e. the simulation of the measured imperfections as precisely as possible, and the simulation of the maximal imperfection values. As the field of the initial imperfections is an example of circular data the simulation method has been appropriately modified. As many as 2000 realizations have been simulated. The calculated global and variance errors of the simulations indicate excellent convergence of the field estimators.

4. Numerical calculations and conclusions

The numerical calculations include three cases of tank of 5000 m³ capacity. The first case refers to an ideal cylindrical shell. The tank data for the second case include the measured initial geometric imperfections. The third calculation is performed for the simulated extreme imperfections.

The results of the nonlinear calculations indicate that the tank initial imperfections can cause significant variations in stress fields in comparison with the solution related to an ideal surface. The steel of the tank with imperfections has yielded at a point connecting the bottom with the side plates, and in the areas where extreme imperfections appear. It should be noted that the yielding process has occurred despite the fact that the initial field of imperfections is rather a typical one.

Additionally, the random numerical model of tanks is extended by introducing random variability of soil foundations which can have a degrading effect on the tank loading capacity. To this end the randomness of the soil parameters should be described by a correlation function which was chosen arbitrarily. The results indicate that the influence of the soil parameters variability is not significant in this case.

The numerical calculations for silos and underground tanks revealed that the initial geometric imperfections influenced their mechanical behaviour. However, because of the lack of experimental data the results are preliminary ones.

It should be stressed that formulation of a methodology of identification, classification and description of the tank imperfections can lower the laborious and high cost of experiments, and ensure a better and much safer design.

5. References

- [1] J. Górski (2006). *Non-linear models of structures with random geometric and material imperfections simulation-based approach*. Gdansk University of Technology, Monograph, Vol. 68.
- [2] G. Orlik (1976). *Deformation of shapes of cylindrical steel shells, statistical analysis and numerical simulations*. Ph.D. Thesis. Technical University of Gdańsk, Gdańsk, (in Polish).
- [3] H. Walukiewicz, E. Bielewicz and J. Górski (1997). Simulation of nonhomogeneous random fields for structural applications, *Computers and Structures*, **64**, No. 1-4, 491-498.
- [4] P. Wilde (1981). *Random fields discretization in engineering calculations*, Warsaw: PWN, (in Polish).

ON DETERMINING THE DEFORMED SHELL MIDSURFACE FROM PRESCRIBED SURFACE STRAINS AND BENDINGS

W. Pietraszkiewicz¹, M.L. Szwabowicz², and C. Vallée³

¹ *Institute of Fluid-Flow Machinery, Gdańsk, Poland*

² *Maritime University, Gdynia, Poland*

³ *Université de Poitiers, Futuroscope, France*

The intrinsic formulation of the geometrically non-linear theory of thin elastic shells, proposed in [1], allows one to find strains $\gamma_{\alpha\beta}$ and bendings $\kappa_{\alpha\beta}$ of the shell midsurface. Then the position vector \mathbf{y} of the midsurface of the deformed shell can be found from known $\gamma_{\alpha\beta}$ and $\kappa_{\alpha\beta}$ by one of two methods proposed in [2].

In this report we develop an alternative novel method of determining the vector \mathbf{y} from prescribed $\gamma_{\alpha\beta}$ and $\kappa_{\alpha\beta}$. The present approach uses the right polar decomposition of the midsurface deformation gradient $\mathbf{R} = \mathbf{R}\mathbf{U}$, where \mathbf{U} is the surface right stretch tensor and \mathbf{R} is the 3D rotation tensor. Applying the method developed here the vector \mathbf{y} is calculated in three consecutive steps described briefly below.

Let $\mathbf{x} = \mathbf{x}(\theta^\alpha)$, $\alpha = 1, 2$, be the position vector of the shell midsurface M in the reference (undeformed) configuration. At each point $x \in M$ we define the natural base vectors $\mathbf{a}_\alpha = \partial \mathbf{x} / \partial \theta^\alpha \equiv \mathbf{x}_{,\alpha}$, the unit normal vector $\mathbf{n} = \frac{1}{\sqrt{a}} \mathbf{a}_1 \times \mathbf{a}_2$, the covariant components $a_{\alpha\beta} = \mathbf{a}_\alpha \cdot \mathbf{a}_\beta$ of the surface metric tensor \mathbf{a} with $a = \det(a_{\alpha\beta})$, and the covariant components $b_{\alpha\beta} = -\mathbf{a}_\alpha \cdot \mathbf{n}_{,\beta}$ of the curvature tensor \mathbf{b} . In the deformed configuration the shell midsurface \bar{M} is parameterized by the convected coordinates $\bar{\theta}^\alpha$ so that its geometry is described by the same symbols with a bar above them: $\bar{\mathbf{a}}_\alpha, \bar{\mathbf{n}}, \bar{a}, \bar{a}_{\alpha\beta}, \bar{b}_{\alpha\beta}$, etc. Then the deformation state of the shell midsurface is described by the covariant components $\gamma_{\alpha\beta} = \frac{1}{2}(\bar{a}_{\alpha\beta} - a_{\alpha\beta})$ and $\kappa_{\alpha\beta} = -(\bar{b}_{\alpha\beta} - b_{\alpha\beta})$ of the surface strain $\boldsymbol{\gamma}$ and bending $\boldsymbol{\kappa}$ tensors, respectively.

Introducing the midsurface deformation gradient $\mathbf{F} = \mathbf{y}_{,\alpha} \otimes \mathbf{a}^\alpha$, by the theorem of Tissot we can justify the right polar decomposition $\mathbf{F} = \mathbf{R}\mathbf{U}$. Then the field $\mathbf{y} = \mathbf{y}(\theta^\alpha)$ can be found in the three steps described below.

a) From known $\gamma_{\alpha\beta}$ the stretch field $\mathbf{U} = \mathbf{U}(\theta^\alpha)$ is found by pure algebra through the explicit formula

$$(1) \quad \mathbf{U} = \frac{\left(1 + \sqrt{1 + 2 \operatorname{tr} \boldsymbol{\gamma} + 4 \det \boldsymbol{\gamma}}\right) \mathbf{a} + 2 \boldsymbol{\gamma}}{\sqrt{2 \left(1 + \operatorname{tr} \boldsymbol{\gamma} + \sqrt{1 + 2 \operatorname{tr} \boldsymbol{\gamma} + 4 \det \boldsymbol{\gamma}}\right)}}.$$

b) From known \mathbf{U} and $\kappa_{\alpha\beta}$ the rotation field $\mathbf{R} = \mathbf{R}(\theta^\alpha)$ is calculated by solving the system of two linear PDE's

$$(2) \quad \begin{aligned} \mathbf{R}_{,\alpha} &= \mathbf{R} \times \mathbf{k}_\alpha, \quad \mathbf{k}_\alpha = \varepsilon^{\lambda\kappa} \mu_{\lambda\alpha} \mathbf{a}_\kappa + k_\alpha \mathbf{n}, \\ \mu_{\alpha\beta} &= b_{\alpha\beta} - \sqrt{\frac{a}{a}} \varepsilon^{\lambda\kappa} \varepsilon_{\alpha\rho} U_\kappa^\rho (b_{\lambda\beta} - \kappa_{\lambda\beta}), \quad k_\alpha = -\sqrt{\frac{a}{a}} \varepsilon^{\kappa\rho} U_\alpha^\lambda U_{\lambda\kappa\rho}, \end{aligned}$$

where $\varepsilon_{\alpha\beta}$ and $\varepsilon^{\lambda\kappa}$ are components of the surface permutation tensor $\boldsymbol{\varepsilon}$, and $(\cdot)_{,\alpha}$ denotes the surface covariant derivative in the metric $a_{\alpha\beta}$. The integrability conditions $\varepsilon^{\alpha\beta} \mathbf{R}_{,\alpha\beta} = \mathbf{0}$ of the system (2)₁ are proved to be equivalent to the compatibility conditions of the non-linear theory of thin shells.

Using the theorem of Frobenius – Dieudonné it has been shown that the solutions to the problem (2)₁ can be converted into an infinite set of systems of ODE's along curves $C \subset M$, parameterized by the length coordinate s and covering densely the entire domain of M :

$$(3) \quad \frac{d\mathbf{R}}{ds} = \mathbf{R}\mathbf{K}, \quad \mathbf{K} = \mathbf{I} \times \mathbf{k}, \quad \mathbf{k} = \mathbf{k}_\alpha \frac{d\theta^\alpha}{ds},$$

where \mathbf{I} is the identity tensor of the 3D vector space.

Solution to the initial value problem (3)₁ may be obtained with any of the well known techniques, numerical techniques inclusive. In particular, applying the method of successive approximations the solution to (3)₁ can be given in the form

$$(4) \quad \begin{aligned} \mathbf{R} &= \mathbf{R}_0 \mathbf{R}_s, \quad \mathbf{R}_s = \sum_{i=0}^s \mathbf{O}_i, \\ \mathbf{O}_0(s) &= \mathbf{I}, \quad \mathbf{O}_i(s) = \int_{s_0}^s \mathbf{O}_{i-1}(t) \mathbf{K}(t) dt, \quad i \geq 1, \end{aligned}$$

where $\mathbf{R}_0 = \mathbf{R}(s_0)$ is the rotation tensor at $s = s_0$.

c) With \mathbf{R} and \mathbf{U} already known the system $\mathbf{y}_{,\alpha} = \mathbf{F}\mathbf{a}_\alpha$ can be integrated by quadrature

$$(5) \quad \mathbf{y} = \mathbf{y}_0 + \int_{x_0}^x \mathbf{R}\mathbf{U}\mathbf{a}_\alpha d\theta^\alpha, \quad \mathbf{y}_0 = \mathbf{y}(x_0).$$

The equation (3)₁ is identical with the one describing spherical motion of a rigid body about a fixed point. Thus, one can point out a number of special cases when the equation has the solution in closed form. This indicates that the novel method presented here might in some cases be more efficient in applications than those proposed in [2].

Details of the method will be published in [3].

A similar approach has recently been successfully applied to analyse the classical problem of differential geometry: recovery of the surface from components of its two fundamental forms.

References

- [1] S. Opoka and W. Pietraszkiewicz (2004). Intrinsic equations for non-linear deformation and stability of thin elastic shells, *Int. J. Solids Str.*, **41**, 3275-3292.
- [2] W. Pietraszkiewicz and M.L. Szwabowicz (2007). Determination of the midsurface of a deformed shell from prescribed surface strains and bendings, *Int. J. Solids Str.*, **44**, 6163-6172.
- [3] W. Pietraszkiewicz, M.L. Szwabowicz and C. Vallée (2008). Determination of the midsurface of a deformed shell from prescribed surface strains and bendings via the polar decomposition, *Int. J. Non-Linear Mech.* (in print).
- [4] W. Pietraszkiewicz and C. Vallée (2007). A method of shell theory in determining position of a surface from components of its two fundamental forms, *ZAMM*, **87**, 603-615.

MEMBRANE SHELL FINITE ELEMENT FOR TEXTILE FABRIC MODELLING NUMERICAL AND EXPERIMENTAL ASPECTS

P. Kłosowski

Gdansk University of Technology, Gdańsk, Poland

1. Introduction

Structures made from technical fabrics become more and more popular. Design of such structures is difficult as not only geometric non-linearity, but also very special constitutive modeling is necessary. Usually the finite element method is used in the design process. Typical commercial software can not be applied in this case, as typical membrane elements can not properly express behavior of fabric threads during deformation.

There is several constitutive models which can be used in such calculations (see [1], [2]), but most of them can not be applied in commercial FEM systems. Additionally, usually they can be used for only one type of constructive modeling of threads behavior: non-linear elastic, viscoelastic or viscoplastic. Proposed in [3] the dense net model of a technical fabric can be used with all three mentioned before approaches. It is also applicable for the three node triangle [4], and for four node isoparmetric membrane shell finite elements [5].

The idea of the dense net model is relatively old, but in the paper new, practical aspects of its application will be discussed.

2. Experiments for dense net model identification

To perform calculation of any structure it is necessary to know its material properties. A technical fabric is build from at least two very different materials (threads and coating) and has different properties in different directions which additionally can change in deformation process. National standards require only very simple tests [6] which are not enough to describe the fabric behavior in FEM calculations. The type of constitutive description depends also from the type of calculations which is going to be performed (e.g. nonlinear elastic formulation is enough in the initial stage of design, viscoelastic must used in long time behavior investigations, while in extreme loadings calculations the viscoplastic approach seems to be the best). The laboratory equipment for technical fabric test must enable recording of time, displacements and forces. A standard strength machine must be equipped in a special support system, and must guarantee good accuracy and frequency of recorded results. For creep and shear tests special stands which will be presented during conference are necessary. Generally for identification of warp and weft threads the uniaxial tests are the most often performed. The bi-axial tests are difficult and their results are hard in application to constitutive identification. During conference examples of such tests will be presented and their advantages and drawbacks will be discussed.

3. Numerical aspect of dense net model application

3.1. Identification

After experimental tests identification of threads and coating properties is necessary. Pure experimental data are usually not applicable as for the rheological models calculation of the time derivatives of strains is necessary. The least squares method is the most often used numerical tool on this stage of research. The author experience in identification of non-linear elastic, viscoelastic and viscoplastic models for a warp and weft will be presented. The numerical methods of verification of identification results will be also given.

3.2. Introduction of identification results into FEM calculations

In the FEM calculations of textile structures self-constructed or commercial software can be used. From that second group only systems which enable the user subroutines introduction can be selected (e.g. MSC.Marc or Abaqus). In such subroutine the dense net model describes the constitutive relations for a typical membrane shell element. The modeling by triangle elements is easier as the directions of threads families can be univocally determinate by the edges of an element. For the four node isoparametric membrane elements more complex calculations are necessary [2]. The main problem in calculations of membrane-cable structures is determination of initial balanced configuration. This process is well known as the form-finding and is supported by special software [7]. The most important type of loading for light structure like a hanging roof is the wind loading. Due to complex shape of a roof only expensive test in an aerodynamic tunnel can give proper distribution of the wind pressure and suction. In the initial stage of design the approach proposed in [8] can be used. Very often not only static but also nonlinear dynamic calculations are necessary.

5. Calculation example

In year 2009 (for the 100th anniversary of erection) reconstruction of the Forest Opera in Sopot is planned. The theatre will be covered by the new hanging, textile roof supported by two over 100 m span steel arches. The author is involved in the roof design process. Necessary experiments and most of the calculations of the cable-textile part of the roof were performed in Gdansk University of Technology. In numerical calculations of the new roof the dense net model with different types of constitutive models was used. Some problems the form-finding of climatic loadings determination will be presented during conference.

6. References

- [1] J. Argyris, J.St. Doltsinis, V. D. Silva. Constitutive modelling and computation on non-linear viscoelastic solid. Part I: Rheological models and numerical integration techniques. Part II: Application to orthotropic PVC-coated fabric. *Computer Methods in Applied Mechanics and Engineering* **88** (1991) 135–163 and **98** (1992) 159–226.
- [2] A. Ambroziak (2005). *Geometrically non-linear analysis of membranes applied for hanging roofs with respect to different types of constitutive relations*. Ph. D. thesis, Gdansk University of Technology, Faculty of Civil and Environmental Engineering.
- [3] Cz. Branicki, P. Kłosowski (1983). Static Analysis of Hanging Textile Membranes In Nonlinear Approach. *Archive of Civil Engineering* **XXIX/3** 189–220.
- [4] P. Kłosowski, A. Zagubień, K. Woznica (2004). *Investigation on rheological properties of technical fabric “Panama”*. *Archive of Applied Mechanics*, **73** 661–681.
- [5] A. Ambroziak, P. Kłosowski (2006). A four-node 3D isoparametric membrane element. *TASK Quart.*, **10/1** 35-47
- [6] EN ISO-1421/1998 *Rubber or plastic coated fabric. Determination of tensile strength and elongation break*.
- [7] B.H.T. Topping, P. Iványi (2007). *Computer Aided Design of Cable Membrane Structures*. Saxe-Coburg Publications, Kippen, Scotland.
- [8] A. Ambroziak, P. Kłosowski (2005). Aerodynamic characteristic of membrane hanging roofs. *Inż. i Bud.* **7**, 383-386.

COMPOSITE SHELLS IN 6-FIELD NONLINEAR SHELL THEORY

J. Chróścielewski, I. Kreja, A. Sabik and W. Witkowski

Gdansk University of Technology, Gdańsk, Poland

1. General

This communication addresses the application of the general nonlinear 6-field shell theory in the analysis of layered composite shells. The FEM model is constructed basing on the statically and kinematically exact theory of shells that accommodates naturally finite (unlimited) translations and rotations [1]. Kinematics of the shell is described by the field of generalized displacements composed of the translation field and the proper rotation field. Due to the presence of rotation tensor the elements have naturally six degrees of freedom at each node, including the so-called drilling dof.

A typical composite shell made of an orthotropic fiber-reinforced material can be analyzed as a layered structure, with the fibers of the reinforcement in each lamina placed in the surfaces parallel to the shell mid-surface. It is assumed that the shell is composed of a finite number of individually homogeneous layers. Each layer is made of linearly elastic and orthotropic material. The layers are perfectly bonded and no slip between them is possible. Assuming an Equivalent Single Layer (ESL) model the entire laminate is represented by a single-layer panel with macro-mechanical properties estimated as a weighed average of the mechanical properties of each lamina [2, 3].

2. Formulation

The rigorous treatment of the shell theory and its various FEM implementations for isotropic shells has been already extensively dealt with, see e.g. [4] and references given there. Since the current formulation incorporates the drilling dofs, the strain measures are generally not symmetric ($\varepsilon_{12} \neq \varepsilon_{21}$ and $\kappa_{12} \neq \kappa_{21}$). As a consequence, the constitutive relations for the layered composite panel are assumed in the following forms:

$$(1) \quad \begin{Bmatrix} n^{11} \\ n^{22} \\ n^{12} \\ n^{21} \end{Bmatrix} = \begin{bmatrix} C^{1111} & C^{1122} & C^{1112} & C^{1121} \\ C^{2211} & C^{2222} & C^{2212} & C^{2221} \\ C^{1211} & C^{1222} & C^{1212} & C^{1221} \\ C^{2111} & C^{2122} & C^{2112} & C^{2121} \end{bmatrix} \begin{Bmatrix} \varepsilon_{11} \\ \varepsilon_{22} \\ \varepsilon_{12} \\ \varepsilon_{21} \end{Bmatrix}, \quad \begin{Bmatrix} n^{23} \\ n^{13} \end{Bmatrix} = \begin{bmatrix} C^{2323} & C^{2313} \\ C^{1323} & C^{1313} \end{bmatrix} \begin{Bmatrix} \gamma_{23} \\ \gamma_{13} \end{Bmatrix}$$

$$(2) \quad \begin{Bmatrix} m^{11} \\ m^{22} \\ m^{12} \\ m^{21} \end{Bmatrix} = \begin{bmatrix} \Sigma^{1111} & \Sigma^{1122} & \Sigma^{1112} & \Sigma^{1121} \\ \Sigma^{2211} & \Sigma^{2222} & \Sigma^{2212} & \Sigma^{2221} \\ \Sigma^{1211} & \Sigma^{1222} & \Sigma^{1212} & \Sigma^{1221} \\ \Sigma^{2111} & \Sigma^{2122} & \Sigma^{2112} & \Sigma^{2121} \end{bmatrix} \begin{Bmatrix} \kappa_{11} \\ \kappa_{22} \\ \kappa_{12} \\ \kappa_{21} \end{Bmatrix}, \quad \begin{Bmatrix} m^{23} \\ m^{13} \end{Bmatrix} = \begin{bmatrix} \Sigma^{2323} & \Sigma^{2313} \\ \Sigma^{1323} & \Sigma^{1313} \end{bmatrix} \begin{Bmatrix} \kappa_{23} \\ \kappa_{13} \end{Bmatrix},$$

where the components C^{ijkl} and Σ^{ijkl} resulted from an appropriate integration of the 3-D anisotropic constitutive relations through the thickness of the whole shell (assuming zero value of the transverse normal stress components).

3. Example

To illustrate the performance of the considered model, the results for one of the most demanding benchmark tests for large rotation shell analysis, the semi-cylindrical shell under a point load are presented in Fig. 1. This example was introduced by Stander et al. [5], who, however,

considered only the case of an isotropic shell. The case of a layered composite shell was proposed by Sze et al. [6] who investigated two different cross-ply lamination schemes: [90/0/90] and [0/90/0]. Quite recently, the same composite panel was examined by Arciniega and Reddy [7]. One should notice, that none of the authors of the papers [5-7] bothered with a proper physical meaning of the applied input data; to correct that issue we assume the following dimensions: $L = 304.8$ mm, $R = 101.6$ mm and $h = 3$ mm; together with material parameters for boron-epoxy type composites: $E_a = 20.685$ kN/mm², $E_b = 5.17125$ kN/mm², $G_{ab} = G_{ac} = 7.956$ kN/mm², $G_{bc} = 1.989$ kN/mm² and $\nu_{ab} = 0.25$. For isotropic case the following material properties are used: $E = 20.685$ kN/mm², $\nu = 0.25$. The load is assumed as the proportional $P(\lambda) = \lambda P_{ref}$, where $P_{ref} = 1000$ kN. To avoid discussions about mesh convergence or spurious zero-energy forms the computations were carried out using 40×40 CAME16 elements with full integration. The discretizations in the Fig.1 are given for the whole structure.

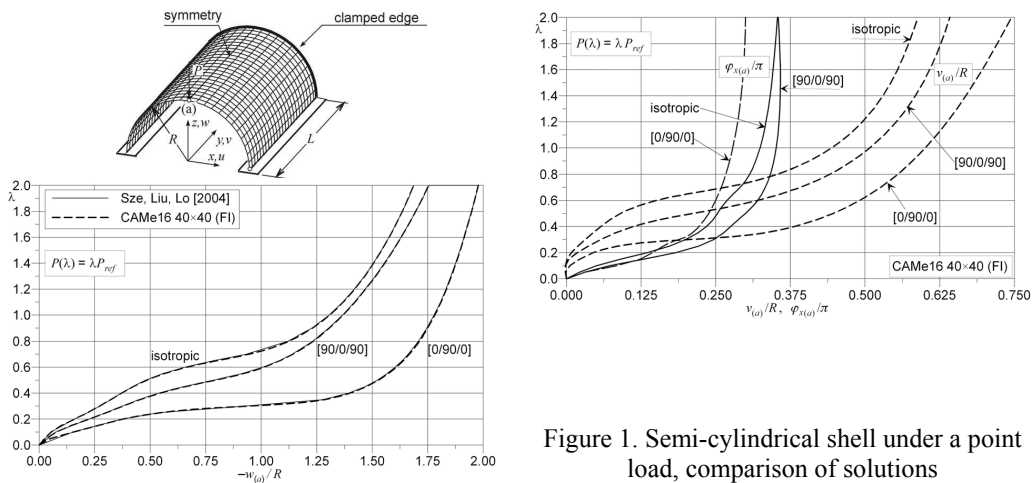


Figure 1. Semi-cylindrical shell under a point load, comparison of solutions

The obtained results, as presented in Fig. 1, show a very good agreement with the reference solutions [6], what demonstrates a big potential of the proposed formulation and encourages to further research.

5. References

- [1] J. Chróscielewski, J. Makowski and W. Pietraszkiewicz (2004). *Statics and Dynamics of Multifold Shells: Nonlinear Theory and Finite Element Method*. (in Polish). Institute of Fundamental Technological Research PASci Publisher, Warsaw.
- [2] V. V. Vasiliev and E. V. Morozov (2001). *Mechanics and Analysis of Composite Materials*, Elsevier Science Ltd, Oxford, 225-269.
- [3] I. Kreja (2007). Geometrically non-linear analysis of layered composite plates and shells. Monographs of GUT, 83, 1–176.
- [4] J. Chróscielewski, J. Makowski and H. Stumpf (1992). Genuinely resultant shell finite elements accounting for geometric and material non-linearity, *International Journal for Numerical Methods in Engineering*, **35**, 63–94.
- [5] N. Stander, A. Matzenmiller and E. Ramm (1989). An assessment of assumed strain methods in finite rotation shell analysis, *Engineering Computations* **6**, 58-66.
- [6] K. Y. Sze, X. H. Liu and S. H. Lo (2004). Popular benchmark problems for geometric nonlinear analysis of shells, *Fin. Elem. Anal. Des.* **40**, 1151–1569.
- [7] R. A. Arciniega and J. N. Reddy (2007). Tensor-based finite element formulation for geometrically nonlinear analysis of shell structures, *Comput. Methods Appl. Mech. Engrg.* **196**, 1048–1073.

VIBRATIONS OF THICK PLATE BY BOUNDARY ELEMENT METHOD

K. Myślecki and J. Oleńkiewicz

Wrocław University of Technology, Wrocław, Poland

1. Governing equations

In the theory of thick plates (differently called Reissner-Mindlin plates) is taken into account that transverse strengths and connected with them shear strains have influence on plate deformations. The thicker is the plate, the higher is the influence of transverse strengths - from here name of this theory. In the thick plate theory occurs three independent displacement parameters: deflection w and two rotations φ_α . Additional load of the plate composes moment fields m_α .

Thick plates are described by the following dynamic equilibrium equation system [1]

$$\begin{aligned}
 & -H\Delta w - H\varphi_{1,1} - H\varphi_{2,2} + c_w \dot{w} = q - \gamma h \ddot{w}, \\
 (1) \quad & Hw_{,1} + H\varphi_1 - D\varphi_{1,11} - D\frac{1-\nu}{2}\varphi_{1,22} - D\frac{1+\nu}{2}\varphi_{2,12} + c_1 \dot{\varphi}_1 = m_1 - \frac{\gamma h^3}{12} \ddot{\varphi}_1, \\
 & Hw_{,2} - D\frac{1+\nu}{2}\varphi_{1,12} + H\varphi_2 - D\varphi_{2,22} - D\frac{1-\nu}{2}\varphi_{2,11} + c_2 \dot{\varphi}_2 = m_2 - \frac{\gamma h^3}{12} \ddot{\varphi}_2
 \end{aligned}$$

Where H and D mean shear and bending stiffness of the plate, and γ is the mass density.

2. Free vibrations

We transform equations (1) into a form of free harmonic vibrations assuming

$$\begin{aligned}
 (2) \quad & q = m_\alpha = 0, \\
 & w(\mathbf{x}, t) = w(\mathbf{x}) e^{i\omega t}, \quad \varphi_\alpha(\mathbf{x}, t) = \varphi_\alpha(\mathbf{x}) e^{i\omega t}
 \end{aligned}$$

The equation system (1), written in a convenient form to calculate the fundamental solution, can be written as

$$(3) \quad L_{ij} \bar{u}_{jk} = \delta \delta_{ik}$$

The fundamental solution of the harmonic vibration equation (3) can be found using the Hörmander method. This solution is a function of the parameter ω .

Using the BEM an algebraic equation system with the parameter ω can be obtained.

$$(4) \quad \begin{bmatrix} \bar{\mathbf{A}}_q^w(\omega) & \bar{\mathbf{A}}_q^{\varphi_1}(\omega) & \bar{\mathbf{A}}_q^{\varphi_2}(\omega) & \bar{\mathbf{A}}_q^{M_1}(\omega) & \bar{\mathbf{A}}_q^{M_2}(\omega) & \bar{\mathbf{A}}_q^{Q_n}(\omega) \\ \bar{\mathbf{A}}_{m_1}^w(\omega) & \bar{\mathbf{A}}_{m_1}^{\varphi_1}(\omega) & \bar{\mathbf{A}}_{m_1}^{\varphi_2}(\omega) & \bar{\mathbf{A}}_{m_1}^{M_1}(\omega) & \bar{\mathbf{A}}_{m_1}^{M_2}(\omega) & \bar{\mathbf{A}}_{m_1}^{Q_n}(\omega) \\ \bar{\mathbf{A}}_{m_2}^w(\omega) & \bar{\mathbf{A}}_{m_2}^{\varphi_1}(\omega) & \bar{\mathbf{A}}_{m_2}^{\varphi_2}(\omega) & \bar{\mathbf{A}}_{m_2}^{M_1}(\omega) & \bar{\mathbf{A}}_{m_2}^{M_2}(\omega) & \bar{\mathbf{A}}_{m_2}^{Q_n}(\omega) \end{bmatrix} \cdot \begin{bmatrix} w \\ \varphi_1 \\ \varphi_2 \\ M_1 \\ M_2 \\ Q_n \end{bmatrix} = 0$$

Equation system (4), independent of the chosen boundary conditions, can be written in a compact form

$$(5) \quad \mathbf{A}(\omega)\mathbf{X} = 0$$

This system has a nonzero solution providing that the determinant of the matrix \mathbf{A} is equal zero:

$$(6) \quad \det \mathbf{A}(\omega) = 0 \Rightarrow \omega_i, \quad i = 1, 2, \dots$$

3. Forced vibrations

We presuppose the solution of the system (1) in a following form of eigenfunction series:

$$(7) \quad \mathbf{u} = \begin{bmatrix} w \\ \varphi_1 \\ \varphi_2 \end{bmatrix} = \sum_{n=1}^N \begin{bmatrix} w_n(\mathbf{x}) \cdot T_{wn}(t) \\ \varphi_{1n}(\mathbf{x}) \cdot T_{1n}(t) \\ \varphi_{2n}(\mathbf{x}) \cdot T_{2n}(t) \end{bmatrix}$$

Equation system (1) separates then into three independent scalar equations of time. Let's write one of them

$$(8) \quad \gamma h \ddot{T}_{wn}(t) + c_w T_{wn}(t) + \gamma h \omega_n^2 T_{wn}(t) = q_n(t)$$

The solution of this equation can be easy found in an analytical way.

A numerical example of the solution of the plate using the upper described routine will be presented during the conference.

4. References

- [1] C. M. Wang, S. Kitipornchai and Y. Xiang (1998). *Vibration of Mindlin Plates*, Elsevier Science, Oxford.
- [2] K. Myślecki (2004). *Metoda elementów brzegowych w statyce dźwigarów powierzchniowych*, Oficyna Wydawnicza Politechniki Wrocławskiej, Wrocław.
- [3] K. Myślecki and J. Oleńkiewicz (2007). Analysis of free vibration of thin plate by Boundary Element Method (in polish), *LIII Konferencja Naukowa KILiW i KN PZITB*, Krynica.

R-FUNCTIONS METHOD APPLYING TO LARGE DEFLECTION ANALYSIS OF ORTHOTROPIC SHALLOW SHELLS ON ELASTIC FOUNDATION

L. Kurpa, K. Lyubitsky

National Technical University "Kharkov Polytechnic Institute", Kharkov, Ukraine

Shallow shells are structural elements of many modern constructions, in particular case if they made from composite materials. Investigation of such shells is connected with large mathematical difficulties due to complexity of mathematical statement.

In the present work a geometric non-linear bending of orthotropic shallow shells with complex planform resting on an elastic foundation is studied. To solve the system of the governing equations the theory of R-functions [1], variational methods and step-by-step method are used. A principal advantage of this approach is the possibility to investigate the shallow shells of an arbitrary planform and consider the different boundary conditions. It should be noted that desired solution is found in analytical form.

Governing equations for large deflections of shallow shells on base of the classical theory [2] are:

$$(1) \quad \begin{aligned} L_1(D_{ij})W + \nabla_k(\Phi) - L(W, \Phi) &= q - p \\ L_2(A_{ij})\Phi + \nabla_k(W) + \frac{1}{2}L(W, W) &= 0, \end{aligned}$$

where W is the deflection function, Φ is the stress function, q is the transverse loading, p is the foundation pressure. The equilibrium system is supplied by corresponding boundary conditions.

For Winkler foundation p can be defined mathematically by

$$(2) \quad p = rW.$$

To solve nonlinear system (1) let us linearize it. One of the known method of linearization is the step-by-step method, which was proposed by Vlasov and was developed by his followers [3]. As result the given system (1) is reduced to the following linear system:

$$(3) \quad \begin{aligned} L_2(A_{ij})\delta\Phi + \nabla_k(W_i) + L(W_i, \delta W) &= 0 \\ L_1(D_{ij})\delta W + \nabla_k(\Phi_i) - L(\delta W, \Phi_i) - L(W_i, \delta\Phi) &= Q_i - r\delta W \end{aligned}$$

where δW and $\delta\Phi$ are increments of the unknown functions on the present loading step.

On every i -th step this system are solved by variational Ritz's method. Unknown functions are presented as expansions in series with help of coordinate functions satisfying the given boundary conditions. Problems of constructing such sequences for shells of an arbitrary shape have been solved by RFM (R-Functions Method). Note, that RFM allows to describe the domain boundary as uniform analytical expression, and to receive, as result, a solution in an analytical form.

The sought for solution on k -th step may be presented as

$$(4) \quad W^{(k)} = \sum_{i=1}^k \delta W_i, \quad \Phi^{(k)} = \sum_{i=1}^k \delta\Phi_i, \quad Q^{(k)} = \sum_{i=1}^k \delta Q_i$$

To exact the approximate solution method by Newton-Rafson is applied.

In the present study to find the upper and lower buckling loads the algorithm is worked out.

Proposed approach allows to build a whole deflection curve of shallow shell.

The numerical implementation of the offered approach is carried out in framework of a system POLE-RL [4]. Its reliability was checked out by test examples. To demonstrate possibilities of the proposed method there would be solved the non-linear bending problem shallow shell ($\bar{k}_1=0$, $\bar{k}_2=20$) with complex plan form (figure 1) and mixed boundary conditions. It is supported that shell is made from glass-epoxy material with following mechanical characteristics: $E_1/E_2=3$, $G_{12}/E_2=0.6$, $\nu_{12}=0.25$. Boundary conditions are assumed to be sliding simply supported on the sides $x = \pm a/2$ and sliding clamped on another parts of the boundary. Foundation modulus is $r=20$

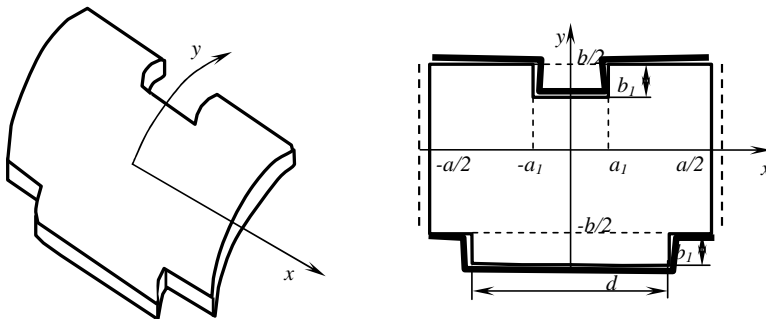


Fig. 1 Planform of a glass-epoxy shallow shell ($b/a=0.5$, $a_1/a=0.4$, $b_1/a=0.2$, $d/a=1$)

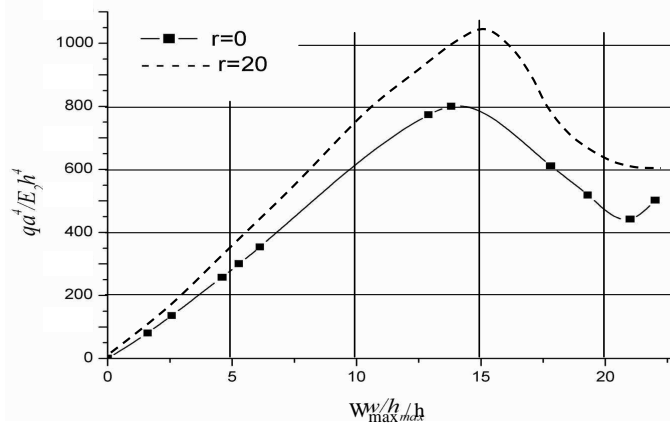


Fig. 2

On fig.2 the dependence of load-maximum deflection is presented.

References

- [1] Rvachev V.L. R-function theory and some it's applying. K., 1982. 552p (in Russian)
- [2] Ambartcumyan S.A. Total theory of anisotropic shells. M., 1974. 448 p. (in Russian)
- [3] Petrov V.V. The stage-up loadings method in nonlinear plate's and shell's theory. Saratov, 1975. 119 p. (in Russian)
- [4] Rvachev V.L., Shevchenko A.N. Problem-oriented languages and systems for engineering calculus.-K, 1988. –198p. (in Russian)

**ON A SURFACE-RELATED SHELL FORMULATION
FOR THE NUMERICAL SIMULATION OF
TEXTILE REINFORCED CONCRETE LAYERS**

R. Schlebsuch and B. Zastrau

Institute of Mechanics an Shell Structures, Dresden, Germany

1. Introduction

The numerical simulation of thin textile reinforced concrete (TRC) strengthening layers is the object of this research. Its mechanical description is implemented by a shell formulation demanding an efficient numerical solution strategy. The shell model is formulated with respect to one of the outer surfaces, i.e. the shell formulation is surface-related. The discretization and interpolation of the associated variational formulation are sources of several locking phenomena. Extensions and/or adjustments of well-known techniques to prevent or at least to reduce locking like the assumed natural strain (ANS) method and the enhanced assumed strain (EAS) method have to be made.

2. Governing Equations

Since shells are three-dimensional bodies the field equations of continuum mechanics are the starting point for the mechanical model. They can be found in many textbooks, e.g. [1]. This set of partial differential equations with pertinent boundary conditions has to be solved for the TRC strengthening layer. An efficient numerical solution of this problem becomes easier if the problem is reformulated using a background of variational calculus.

3. Variational Formulation

The weak formulation of the governing equations is gained by the standard procedure and leads for hyperelasticity to the well-known generalized HU-WASHIZU functional:

$$(1) \quad \Pi_{HW}(\mathbf{U}, \tilde{\mathbf{E}}, \mathbf{S}, \mathbf{t}_0) = \int_{\mathcal{B}_t} (\rho_t f(\mathbf{E}(\mathbf{U}) + \tilde{\mathbf{E}}) - \text{sym } \mathbf{S} : \tilde{\mathbf{E}}) dV + \int_{\mathcal{B}_t} \rho_t (\ddot{\mathbf{U}} - \mathbf{f}) \cdot \mathbf{U} dV \\ - \int_{\partial_t \mathcal{B}_t} \hat{\mathbf{t}}_0 \cdot \mathbf{U} dA + \int_{\partial_U \mathcal{B}_t} \mathbf{t}_0 \cdot (\hat{\mathbf{U}} - \mathbf{U}) dA \rightarrow \text{stat.},$$

whereby a re-parametrization following the suggestion of [5] was made:

$$(2) \quad \mathbf{E} = \mathbf{E}(\mathbf{U}) + \tilde{\mathbf{E}} \quad \Leftrightarrow \quad \mathbf{E}^U - \mathbf{E} = -\tilde{\mathbf{E}}$$

introducing the residuum of the kinematical field equation $\tilde{\mathbf{E}}$. The demand for stationarity of this functional is equivalent with the field equations and the pertinent boundary conditions. But now the residuum of the kinematical field equation: $\tilde{\mathbf{E}} = \mathbf{0}$ appears as EULER-LAGRANGE equation. Further following the suggesting of [5] a L_2 -orthogonality between the second PIOLA-KIRCHHOFF stress tensor \mathbf{S} and the residuum $\tilde{\mathbf{E}}$ of the kinematical field equation is enforced. Therefore the second term in the first integral on the right-hand side of equation (1) vanishes. This results in a modified stationarity condition that represents the following abstract variational formulation:

Find

$$(\mathbf{U}, \tilde{\mathbf{E}}) \in \mathcal{X}_1 \times \mathcal{X}_2 = \mathbb{H}^1(\mathcal{B}_t, \mathcal{E}^3) \times L_2(\mathcal{B}_t, \mathcal{E}^3 \otimes \mathcal{E}^3) \\ (\mathbf{t}_0, \mathbf{S}) \in \mathcal{M}_1 \times \mathcal{M}_2 = L_2(\mathcal{B}_t, \mathcal{E}^3) \times L_2(\mathcal{B}_t, \mathcal{E}^3 \otimes \mathcal{E}^3),$$

such that

$$\begin{aligned} a(\mathbf{U}, \tilde{\mathbf{E}}; \boldsymbol{\eta}, \delta \tilde{\mathbf{E}}) + b_1(\boldsymbol{\eta}, \mathbf{t}_0) &= \mathcal{F}(\boldsymbol{\eta}, \delta \tilde{\mathbf{E}}) \quad \forall (\boldsymbol{\eta}, \delta \tilde{\mathbf{E}}) \in \mathcal{X}_1 \times \mathcal{X}_2 \\ b_1(\mathbf{U}, \delta \mathbf{t}_0) &= \mathcal{G}_1(\delta \mathbf{t}_0) \quad \forall \delta \mathbf{t}_0 \in \mathcal{M}_1 \end{aligned}$$

and the orthogonality condition $\int_{\mathcal{B}_t} \mathbf{S} : \tilde{\mathbf{E}} \, dV = 0$ is fulfilled.

This abstract mathematical formulation allows to investigate the problem from a mathematical point of view and shows the structure of the three-dimensional problem.

4. Surface-Related Shell Formulation

The displacement field \mathbf{U} representing the motion of the shell continuum, i.e. of the TRC strengthening layer, is restricted by a kinematical assumption:

$$(3) \quad \mathbf{U} = \mathbf{V} + \Theta^3 \mathbf{W},$$

Corresponding to the particular position of the reference surface it follows for the normal coordinate $\Theta^3 \in [0, H]$. The disadvantage of this shell kinematics is that it causes POISSON thickness locking.

Starting from the kinematics (3) a surface-related shell formulation is derived, i.e. surface-related strain tensors, surface-related stress resultant tensors etc. are defined. Further details can be found in [2, 3].

5. Finite Element Formulation and Further Locking Phenomena

The discretization of the functional is one source of locking phenomena that can be reduced or even avoided by an enhancement of the strain tensor, cp. [5], or of the finite element formulation, cp. [4]. Since we are dealing with a surface-related shell formulation extensions and/or adjustments of these techniques have to be made and are presented. This procedure finally leads to a very efficient surface-related finite volume shell element that can be used in its respective framework of application, i.e. the simulation of TRC strengthening layers.

6. Acknowledgement

The authors gratefully acknowledge financial support of this research from Deutsche Forschungsgemeinschaft DFG within the Sonderforschungsbereich SFB 528 "Textile Reinforcement for Structural Strengthening and Repair" at the Technische Universität Dresden.

- [1] P. Haupt (2002). *Continuum Mechanics and Theory of Materials*, 2nd ed. Springer, Berlin.
- [2] R. Schlebusch (2005). *Theorie und Numerik einer oberflächenorientierten Schalenformulierung*, Ph.D. thesis, Institute of Mechanics and Shell Structures, Dresden.
- [3] R. Schlebusch, J. Matheas and B. Zastrau (2003). On Surface-Related Shell Theories for the Numerical Simulation of Contact Problems, *J. Theor. Appl. Mech.*, **41(3)**,623-642.
- [4] J.-C. Simo and J. C. Hughes (1986). On Variational Foundation of Assumed Strain Methods. *J. Appl. Mech.*, **53**,52-54.
- [5] J.-C. Simo and M. S. Rifai (1990). A Class of Mixed Assumed Strain Methods and the Method of Incompatible Modes. *Int. J. Num. Meth. Engng.* **29**,1595-1638.

A NUMERICAL INVESTIGATION INTO THE EFFECTS OF PARABOLIC CURVATURE ON THE BUCKLING STRENGTH OF DECK STIFFENED PLATES

M.R. Khedmati¹, P. Edalat¹ and M. Rastani²

¹ Faculty of Marine Technology, Amirkabir University of Technology, Tehran, Iran

² Statoil-Petropars JV, Tehran, Iran

1. General

A series of eigenvalue buckling analyses is performed, using the ANSYS finite element code, on the deck stiffened plates with parabolic curvature. It is revealed that the buckling strength of the deck stiffened plates with parabolic curvature is greater than that of the same panels in expanded flat situation. Besides, it is shown that the size and also the number of stiffeners would be more important parameters than the curvature in enhancing the buckling strength of such stiffened plates.

2. Introduction

Curved stiffened plates are frequently applied as the main structural elements in marine structures like ship hulls and offshore drilling platforms. The ship deck structures have a complex pattern of curvature. The curvature of the deck in the athwartships direction is so called "camber" or "round of beam", while its curvature in the longitudinal direction is so called "sheer".

Most of the research in the fields of strength and analysis of curved stiffened plates has been performed considering cylindrical curvature for them [1-2]. Therefore, the need to assess the buckling strength and behaviour of the curved stiffened plates having parabolic curvature is of prime importance when investigating the strength of the whole ship hull girders.

3. Model for analysis

The model for analysis consists of a plate that is curved in a parabolic form and stiffened with a number of stiffeners, Figure 1. Some dimensionless parameters are defined to reflect different geometries of the curved stiffened plates in the ship deck structures, Table 1. All edges of the model are assumed to be simply supported.

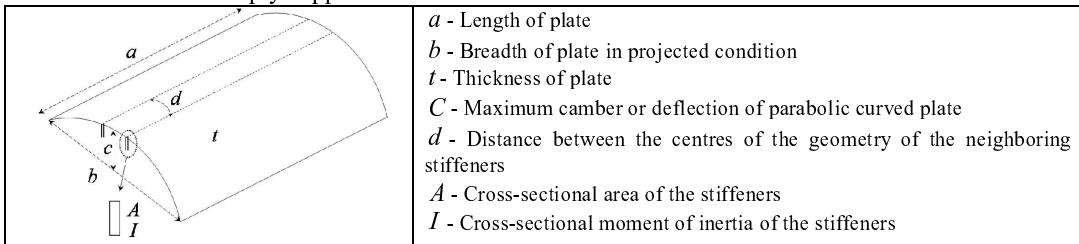


Figure 1. Geometry of the model for analysis.

Dimensionless Parameters	Value
$Z_c = a^2 C / (b^2 t) \sqrt{(1 - \nu^2)}$	10, 20, 40, ..., 10240
C / b	0.01, 0.03, 0.05, 0.1
$b^2 / 4ct$	555.56, 625, 714.29, 833.33, 1000
$\alpha = A / (dt)$	0.5, 2
$\beta = EI / (Dd)$	20, 80

Table 1. Dimensionless parameters and the ranges of their values.

4. Results and conclusions

A series of eigenvalue buckling analyses is performed applying ANSYS finite element code. An extract of the results are shown in Figures 2 and 3. The parabolic curvature in transverse direction increases the buckling strength of the stiffened plate. Stronger stiffeners cause the buckling strength to be increased more. Each of the curves in Figure 2 has an inflexion point that divides the curve into two regions. In one of the regions, the buckling strength is less sensitive to the value of curvature. While in the second region, an opposite behaviour is seen.

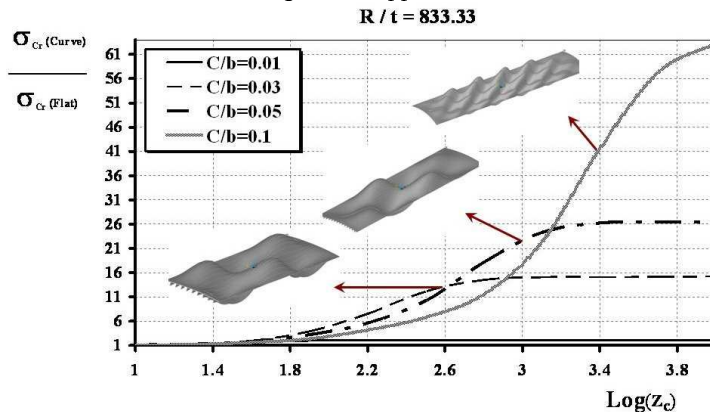


Figure 2. Relationship of $\sigma_{cr}(curved)/\sigma_{cr}(flat)$ versus Z_c for different ratios of C/b .

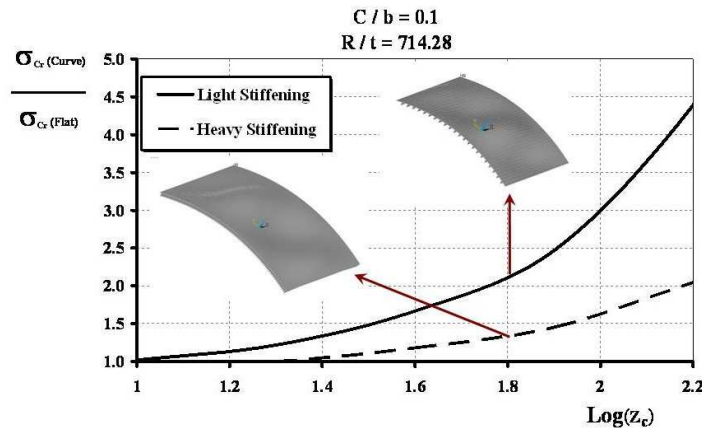


Figure 3. Relationship of $\sigma_{cr}(curved)/\sigma_{cr}(flat)$ versus Z_c for different weights of stiffening.

5. References

- [1] M.R. Khedmati, M.J. Mazaheri, and A. Karimi (2006). *Parametric Instability Analysis on Stringer Stiffened Circular Cylindrical Shells under Axial Compression/External Hydrostatic Pressure*, Eighth International Conference on Computational Structures Technology (CST2006), Canary Islands, Spain.
- [2] M.J. Mazaheri, M.R. Khedmati, and A. Bayatfar (2007). *Sensitivity Analysis on the Buckling Strength of Externally Loaded Stringer-Stiffened Cylindrical Shells*, 11th Int. Mechanical Eng. Conf. (ISME2007), Iranian Society of Mechanical Engineers, Amirkabir University of Technology, Tehran, Iran.

RECOVERY OF DISPLACEMENT FIELDS FROM STRESS TENSOR FIELDS IN SHELL THEORY

C. Mardare

Université Pierre et Marie Curie, Paris, France

The stresses and displacements arising in an elastic shell in response to applied forces are modeled by a system of partial differential equations defined over a three-dimensional domain, representing the shell in its natural state (i.e., in absence of applied forces).

In the classical theory of shells, the displacement field is the primary unknown, while the stress tensor field inside the shell is a secondary unknown, given in terms of the displacement field by the constitutive law of the elastic material; see, e.g., Ciarlet [2]. By contrast, in the intrinsic theory of shells, the stress tensor field is the primary unknown, while the displacement field is a secondary unknown; see, e.g., Antman [1], Ciarlet et al. [3], Pietraszkiewicz et al. [6, 7], and Vallée [8]. One of the principal problems arising in the intrinsic theory of shells is to show that the displacement field can be recovered from the stress tensor field inside the shell. This presentation is dedicated to this problem.

Consider an elastic shell which in absence of applied forces occupies a domain contained in a thin neighborhood of a surface $S = \boldsymbol{\theta}(\omega)$, where $\omega \subset \mathbb{R}^2$ is a domain with a sufficiently smooth boundary and $\boldsymbol{\theta} : \omega \rightarrow \mathbb{R}^3$ is a sufficiently smooth immersion. Assume that the elastic material constituting the shell is homogeneous and isotropic, hence characterized by its two Lamé constants $\lambda > 0$ and $\mu > 0$. Finally assume that the shell is subjected to applied forces and that the shell is free, i.e., the displacement is not subjected to any boundary conditions.

As a mathematical model for this problem, we select the two-dimensional Koiter equations (see Koiter [5]). According to this model, the stresses inside the shell are related to the infinitesimal change of metric and change of curvature tensor fields of the surface S by a bijective linear function. As a consequence, recovering a displacement field $\boldsymbol{\eta} : \omega \rightarrow \mathbb{R}^3$ from the stress tensor field inside the shell amounts to recovering $\boldsymbol{\eta}$ from the infinitesimal change of metric and change of curvature tensor fields of the surface S , defined in what follows by their respective covariant components $\gamma_{\alpha\beta}$ and $\rho_{\alpha\beta}$. Here and in the sequel, Greek indices and exponents vary in the set $\{1, 2\}$ and the summation convention with respect to repeated indices and exponents is used.

Our main result is as follows (for details, see [4]). Assume that ω is simply connected. Let $(\gamma_{\alpha\beta})$ and $(\rho_{\alpha\beta})$ be two symmetric matrix fields with components $\gamma_{\alpha\beta} \in L^2(\omega)$ and $\rho_{\alpha\beta} \in H^{-1}(\omega)$ that satisfy the following compatibility conditions, which we shall call the ‘‘Saint Venant equations on the surface S ’’, viz.,

$$\begin{aligned} \gamma_{\sigma\alpha|\beta\tau} + \gamma_{\tau\beta|\alpha\sigma} - \gamma_{\tau\alpha|\beta\sigma} - \gamma_{\sigma\beta\alpha\tau} + R_{\alpha\sigma\tau}^{\nu} \gamma_{\beta\nu} - R_{\beta\sigma\tau}^{\nu} \gamma_{\alpha\nu} \\ = b_{\tau\alpha} \rho_{\sigma\beta} + b_{\sigma\beta} \rho_{\tau\alpha} - b_{\sigma\alpha} \rho_{\tau\beta} - b_{\tau\beta} \rho_{\sigma\alpha}, \\ \rho_{\sigma\alpha|\tau} - \rho_{\tau\alpha|\sigma} = b_{\sigma}^{\nu} (\gamma_{\alpha\nu|\tau} + \gamma_{\tau\nu|\alpha} - \gamma_{\tau\alpha|\nu}) - b_{\tau}^{\nu} (\gamma_{\alpha\nu|\sigma} + \gamma_{\sigma\nu|\alpha} - \gamma_{\sigma\alpha|\nu}). \end{aligned}$$

Then there exists a vector field $\boldsymbol{\eta} : \omega \rightarrow \mathbb{R}^3$ of class H^1 such that the two fields $(\gamma_{\alpha\beta})$ and $(\rho_{\alpha\beta})$ are respectively the linearized change of metric and linearized change of curvature tensors associated with the displacement field $\boldsymbol{\eta}$, in the sense that

$$\begin{aligned} \gamma_{\alpha\beta} &= \frac{1}{2} (\partial_{\alpha} \boldsymbol{\eta} \cdot \partial_{\beta} \boldsymbol{\theta} + \partial_{\alpha} \boldsymbol{\theta} \cdot \partial_{\beta} \boldsymbol{\eta}) \quad \text{in } \omega, \\ \rho_{\alpha\beta} &= (\partial_{\alpha\beta} \boldsymbol{\eta} - \Gamma_{\alpha\beta}^{\nu} \partial_{\nu} \boldsymbol{\eta}) \cdot \mathbf{a}_3 \quad \text{in } \omega. \end{aligned}$$

The functions $\gamma_{\alpha\beta|\sigma}$ and $\gamma_{\alpha\beta|\sigma\tau}$ denote respectively the first and the second covariant derivatives of the field $(\gamma_{\alpha\beta})$, $R_{\alpha\sigma\tau}^\nu$ denotes the components of the Riemann curvature tensor of the surface S , $b_{\alpha\beta}$ and b_σ^τ denote respectively the mixed components of the second fundamental form of the surface $S = \boldsymbol{\theta}(\omega)$, and $\mathbf{a}_3 := \frac{1}{|\partial_1\boldsymbol{\theta} \wedge \partial_2\boldsymbol{\theta}|} \partial_1\boldsymbol{\theta} \wedge \partial_2\boldsymbol{\theta}$.

The proof of this result furnishes an explicit algorithm for recovering the vector field $\boldsymbol{\eta}$ from the matrix fields $(\gamma_{\alpha\beta})$ and $(\rho_{\alpha\beta})$: one first solves the system

$$\begin{aligned}\lambda_{\alpha\beta|\sigma} + b_{\alpha\sigma}\lambda_\beta - b_{\beta\sigma}\lambda_\alpha &= \gamma_{\sigma\beta|\alpha} - \gamma_{\sigma\alpha|\beta}, \\ \lambda_{\alpha|\sigma} + b_\sigma^\nu\lambda_{\alpha\nu} &= \rho_{\sigma\alpha} - b_\sigma^\nu\gamma_{\alpha\nu},\end{aligned}$$

where the unknowns are the antisymmetric matrix field $(\lambda_{\alpha\beta})$ and the vector field (λ_α) with components $\lambda_{\alpha\beta} \in L^2(\omega)$ and $\lambda_\alpha \in L^2(\omega)$; then one solves the system

$$\partial_\alpha\boldsymbol{\eta} = (\gamma_{\alpha\beta} + \lambda_{\alpha\beta})\mathbf{a}^\beta + \lambda_\alpha\mathbf{a}^3 \text{ in } \omega,$$

where $\{\mathbf{a}^1, \mathbf{a}^2, \mathbf{a}^3\}$ is the dual of the basis $\{\partial_1\boldsymbol{\theta}, \partial_2\boldsymbol{\theta}, \mathbf{a}_3\}$. The vector field $\boldsymbol{\eta} \in H^1(\omega; \mathbb{R}^3)$ found in this fashion has the desired properties.

Note that the first system has solutions because the matrix fields $(\gamma_{\alpha\beta})$ and $(\rho_{\alpha\beta})$ satisfy the above Saint Venant equations on a surface and that the second system has solutions because the matrix fields $(\gamma_{\alpha\beta})$ and $(\rho_{\alpha\beta})$ are symmetric.

These results may be viewed as the infinitesimal versions of the reconstruction of a surface from its fundamental forms, because the Saint Venant equations on a surface are nothing but the first order part with respect to ε of the Gauss and Codazzi-Mainardi equations associated with the immersion $(\boldsymbol{\theta} + \varepsilon\boldsymbol{\eta})$.

- [1] Antman, S.S.: Ordinary differential equations of nonlinear elasticity I: Foundations of the theories of non-linearly elastic rods and shells, *Arch. Rational Mech. Anal.* 61 (1976), 307–351.
- [2] P.G. Ciarlet (2000). *Mathematical Elasticity, Volume III: Theory of Shells*, North-Holland, Amsterdam.
- [3] Ciarlet, P.G.; Gratie, L.; Mardare, C. : Intrinsic methods in elasticity: a mathematical survey, *Discrete and Continuous Dynamical Systems*, to appear.
- [4] P.G. Ciarlet, L. Gratie, C. Mardare and M. Shen (2008). Saint Venant compatibility equations on a surface: Application to intrinsic shell theory, *Math. Models Methods Appl. Sci.*, **18**, 165-194.
- [5] Koiter, W.T.: On the foundations of the linear theory of thin elastic shells, *Proc. Kon. Ned. Akad. Wetensch B73* (1970) 169-195.
- [6] Opoka, S.; Pietraszkiewicz, W.: Intrinsic equations for non-linear deformation and stability of thin elastic shells, *Internat. J. Solids Structures* 41 (2004) 3275–3292.
- [7] Pietraszkiewicz, W.: On using rotations as primary variables in the nonlinear theory of thin irregular shells, in D. DURBAN et al. (Editors), *Advances in the Mechanics of Plates and Shells*, pp. 245-258, Kluwer, 2001.
- [8] Vallée, C.: Compatibility equations for large deformations, *Internat. J. Engrg. Sci.* 30 (1992), 1753–1757.

OPTIMAL STABILIZATION OF POSTBUCKLING PATH FOR CONICAL SHELLS UNDER EXTERNAL PRESSURE

J. Kruźelecki and D. Trybuła

Cracow University of Technology, Cracow, Poland

A postbuckling path for a conical shell under compressive radial pressure is unstable one. It means that loss of stability of a shell can be associated with a snap-through, which can lead to very large deflections and finally, to destruction of a structure

A standard problem of structural optimization under stability constraints is usually formulated as maximization of the instability load for a prescribed volume of a design element. Very often a standard optimal structure has unstable postbuckling behaviour and it is very sensitive to imperfections. That is weakness of the design and it indicates that the combination of geometrically nonlinear analysis with the design becomes necessary, especially from the practical point of view. Postbuckling constraints of a special form added to formulation of the optimization problem permit to modify the postbuckling path and the stable postbuckling path can be created, even in the case of unstable behaviour of a reference structure.

The effect of modification of the postbuckling behaviour in most cases has been obtained by changing sizing variables, which are usually dimensions of the design elements. This type of problems were considered, for example, by Bochenek [1, 2]. In this paper an alternative concept is applied, namely stabilization of the postbuckling path is obtained by application of additional loadings acting on a shell without changing of a shape and sizes of the optimized structure. These loadings can be either active forces applied to a structure or passive ones (reactions of the additional supports), or both active and passive forces acting simultaneously. Such problems, for finite-degree-of-freedom of rod system that models the behaviour of a real shell structure, was considered by Bochenek and Kruźelecki [3]. On the other hand Kruźelecki and Król [4] examined the real cylindrical shells with different geometrical parameters whereas Kruźelecki and Trybuła [5] investigated such shells under twisting moment. These papers showed that axial loadings can stabilize an initially unstable postcritical path.

In this paper stabilization of a postbuckling path for a simply supported (different variants of supports are considered) truncated conical shell under radial compressive pressure is formulated as a certain modified non-standard problem of optimization. From mentioned above types of stabilizing loadings only an active axial force is investigated here. Calculations are performed using ANSYS code for elastic shells of different length, thickness and semi-vertex angle.

The problem of optimization is stated as follows. The minimum value of the axial load N , which leads to the stable behaviour of a shell is looked for

Minimize N

$$\text{subject to } \frac{\partial p}{\partial f}(f^*, N) = \frac{\partial^2 p}{\partial f^2}(f^*, N) = 0$$

where f denotes a displacement of a wall of a shell. The displacement f^* refers to the horizontal inflexion point at the equilibrium path, Fig.1. The above conditions lead to elimination of the snap-through and finally, one obtains the stable postbuckling path even the original equilibrium path is unstable one. It is shown in Fig.1, where the thick line refers the stable equilibrium path under the minimum axial load N . This formulation of the optimization problem contains only one design variable N and two constraints, which are imposed on the postbuckling state. They ensure the stable behaviour of the cylindrical shell under external pressure. A condition of a constant volume of the structure is automatically fulfilled because that formulation does not take into account modification of the shell geometry.

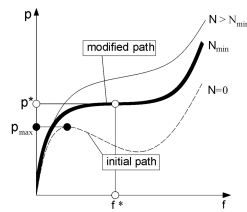


Fig.1. Equilibrium paths for $N=0$ and $N \neq 0$

Calculations were performed for a semi-vertex angle from 5 to 45 degrees, three different length and thickness of a shell assuming only elastic deformations. The numerical analysis showed that the active forces can improve the resistance of the radially compressed truncated conical shells against buckling. The critical pressure for elastic shells under additional axial loading can be much higher in comparison with a structure loaded by external pressure only. The active force can stabilize the initially unstable postbuckling path for elastic shells under external pressure. Then, the optimal shells do not lose their stability at all.

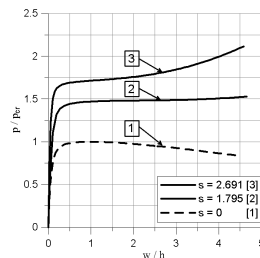


Fig.2. Equilibrium paths for the shell with semi-vertex angle equals to 15° , $R_{sr}/L=2$, $h/R_{sr}=0.005$

In Fig.2 the postbuckling paths are presented for the shell with semi-vertex angle equals to 15° , $R_{sr}/L=2$, $h/R_{sr}=0.005$, where R_{sr} means the mean value of the shell radius. The postbuckling paths are shown in dimensionless coordinates: p/p_{cr} , w/h , where p_{cr} denotes the critical pressure (maximum pressure at the equilibrium path for $N=0$) and w stands for the maximum radial displacement. As a measure of applied active force we took $s = \sigma_z / \sigma_0$, where σ_z denotes the axial stress $\sigma_z = N/A$. The dash lines (1) represent the postbuckling path for $s=0$, the line (2) corresponds to the active force, which stabilizes the postbuckling path and the line (3) is connected with the active forces, which is larger than the minimal stabilizing one.

- [1] B. Bochenek (1977). Optimization of geometrically nonlinear structures with respect to buckling and postbuckling constraints, *Engineering Optimization*, **29**, 401-415.
- [2] B. Bochenek (2001). Problems of optimal design of structures for postbuckling behaviour, *Zeszyty Naukowe Podstawowe Nauki Techniczne No.22, Politechnika Krakowska, Kraków*.
- [3] B. Bochenek, J. Kruzelecki (2001). A new concept of optimization for postbuckling behaviour. *Engineering Optimization*, **33**, 503-522
- [4] J. Kruzelecki, M. Król (2006). Optimization of postbuckling path for cylindrical shells under external pressure. In *Proc. III European Conference on Computational Mechanics; Solids, Structures and Coupled Problems in Engineering*, edited by C.A. Mota Soares, J.A.C. Martin, H.C. Rodrigues, J.A.C. Ambrosio, Springer (CD-ROM only).
- [5] J. Kruzelecki, D. Trybuła (2007). Optimal stabilization of postbuckling path for cylindrical shells under torsion, In *Proc. Seventh World Congress on Structural and Multidisciplinary Optimization* (CD-ROM only).

MULTIMATERIALS WITH SHELL-LIKE REINFORCEMENT

A.L. Bessoud^{1,2}, F. Krasucki¹ and M. Serpilli²

¹*Institut de Mathématiques et de Modélisation de Montpellier – UMR5149, Université Montpellier II
France*

²*Laboratoire de Mécanique et Génie Civil – UMR 5508, Université Montpellier II, France*

After the pioneering works of Pham Huy-Sanchez [1], and Caillerie [2], the thin inclusion of a third material between two other ones when the rigidity properties of the inclusion are highly contrasted with respect to those of the surrounding material has been deeply investigated. More recently, Chapelle-Ferent [3] in order to justify some methods used in FEM approximation have studied the asymptotic behavior of a shell-like inclusion of $\frac{1}{\varepsilon^p}$ -rigidity ($p = 1$ or $p = 3$) in a 3D domain. In a slightly different geometrical and mechanical context, Bessoud et al. [4] have studied the behavior of a ε -thin 3D layer of $\frac{1}{\varepsilon}$ -rigidity. We study a new situation where the shell-like thin layer is obtained by the translation in the normal direction of a general 2D surface. Using a system of curvilinear coordinates we deduce the formal limit problem for the two cases $p = 1$ and $p = 3$. We obtain the same limit problems as in [3], also if the kinematical assumptions for the physical problem are not the same. Indeed in [3] the authors a priori assume a shell-like energy in the thin layer. One must stress that the well-posedness of the limit problems is essentially linked to the shell inhibition phenomena [5]. For the well-posedness of the flexural and membrane shell models see e.g.[6], [5]. When ω is planar and in the isotropic case, the surface energy term can be interpreted as the membranal energy of a Kirchhoff-Love plate ($p = 1$) and as the flexural energy of a Kirchhoff-Love plate ($p = 3$).

1. Shell-like inclusion : asymptotic behavior

In the three-dimensional Euclidean space \mathcal{E}^3 referred to the Cartesian coordinate frame $(O; \mathbf{e}_1, \mathbf{e}_2, \mathbf{e}_3)$, let Ω^+ and Ω^- be two disjoint open domains with smooth boundaries $\partial\Omega^+$ and $\partial\Omega^-$. Let $\omega = \{\partial\Omega^+ \cap \partial\Omega^-\}^\circ$, which is assumed to be a domain in \mathbb{R}^2 having a positive two-dimensional measure and let $y = (y_\alpha)$ denote a generic point of $\bar{\omega}$. Let $\boldsymbol{\theta} \in \mathcal{C}^2(\bar{\omega}; \mathbb{R}^3)$ be an injective mapping such that the vectors $\mathbf{a}_\alpha(y) := \partial_\alpha \boldsymbol{\theta}(y)$ form the covariant basis of the tangent plane to the surface $S := \boldsymbol{\theta}(\bar{\omega})$ at the point $\boldsymbol{\theta}(y)$; the two vectors $\mathbf{a}^\alpha(y)$ of the tangent plane, defined by the relations $\mathbf{a}^\alpha(y) \cdot \mathbf{a}_\beta(y) = \delta_\beta^\alpha$, form its contravariant basis. Also let $\mathbf{a}_3(y) = \mathbf{a}^3(y)$ be the unit normal vector to S . Let $\Omega^{m,\varepsilon} := \omega \times]-\varepsilon, \varepsilon[$, with $\Gamma^{\pm,\varepsilon} := \omega \times \{\pm\varepsilon\}$. Let x^ε denote the generic point in the set $\bar{\Omega}^{m,\varepsilon}$, with $x_\alpha^\varepsilon = y_\alpha$. We consider a shell-like domain with middle surface $S = \boldsymbol{\theta}(\bar{\omega})$ and thickness $2\varepsilon > 0$, whose reference configuration is the image $\Theta^{m,\varepsilon}(\bar{\Omega}^{m,\varepsilon}) \subset \mathbb{R}^3$ of the set $\bar{\Omega}^{m,\varepsilon}$ through the mapping $\Theta^{m,\varepsilon} : \bar{\Omega}^{m,\varepsilon} \rightarrow \mathbb{R}^3$ given by $\Theta^{m,\varepsilon}(x^\varepsilon) := \boldsymbol{\theta}(y) + x_3^\varepsilon \mathbf{a}_3(y)$, for all $x^\varepsilon = (y, x_3^\varepsilon) = (y_1, y_2, x_3^\varepsilon) \in \bar{\Omega}^{m,\varepsilon}$. Moreover, we suppose that there exists an immersion $\Theta^\varepsilon : \bar{\Omega}^\varepsilon \rightarrow \mathbb{R}^3$ defined as follows :

$$\Theta^\varepsilon := \begin{cases} \Theta^{\pm,\varepsilon} & \text{on } \bar{\Omega}^{\pm,\varepsilon} \\ \Theta^{m,\varepsilon} & \text{on } \bar{\Omega}^{m,\varepsilon} \end{cases}, \quad \Theta^{\pm,\varepsilon}(\Gamma^{\pm,\varepsilon}) = \Theta^{m,\varepsilon}(\Gamma^{\pm,\varepsilon}),$$

with $\Theta^{\pm,\varepsilon} : \bar{\Omega}^{\pm,\varepsilon} \rightarrow \mathbb{R}^3$ immersions over $\bar{\Omega}^{\pm,\varepsilon}$ defining the curvilinear coordinates on $\bar{\Omega}^{\pm,\varepsilon}$. We insert the intermediate shell-like layer moving the image $\Theta^{+,\varepsilon}(\bar{\Omega}^{+,\varepsilon}) \subset \mathbb{R}^3$ of the set $\bar{\Omega}^{+,\varepsilon}$, (resp. $\Theta^{-,\varepsilon}(\bar{\Omega}^{-,\varepsilon})$) in the $\mathbf{a}_3(y)$ (resp. $-\mathbf{a}_3(y)$) direction of an amount equal to $\varepsilon > 0$, the small dimensionless real parameter. The structure is clamped on $\Gamma_0 \subset (\partial\Omega^\varepsilon \setminus \Gamma^{m,\varepsilon})$ and $\Gamma^{m,\varepsilon} := \partial\omega \times]-\varepsilon, \varepsilon[$ is traction free. We suppose that the materials occupying Ω^ε are linearly elastic and isotropic. Let

$$V^\varepsilon = \{(\mathbf{V}, \mathbf{v}) \in H^1(\Omega^\varepsilon; \mathbb{R}^3) \times H^1(\Omega^{m,\varepsilon}; \mathbb{R}^3); \mathbf{V}|_{\Omega^{m,\varepsilon}} = \mathbf{v}; \mathbf{V}|_{\Gamma_0} = 0\}.$$

The physical variational problem in these curvilinear coordinates on the variable domain Ω^ε is

$$(1) \quad \begin{cases} \text{Find } (\mathbf{U}^\varepsilon, \mathbf{u}^\varepsilon) \in V^\varepsilon \text{ such that for all } (\mathbf{V}^\varepsilon, \mathbf{v}^\varepsilon) \in V^\varepsilon \\ A^{-,\varepsilon}(\mathbf{U}^\varepsilon, \mathbf{V}^\varepsilon) + A^{+,\varepsilon}(\mathbf{U}^\varepsilon, \mathbf{V}^\varepsilon) + A^{m,\varepsilon}(\mathbf{u}^\varepsilon, \mathbf{v}^\varepsilon) = L(\mathbf{V}^\varepsilon), \end{cases}$$

where $A^{\pm,\varepsilon}(\mathbf{U}^\varepsilon, \mathbf{V}^\varepsilon)$ and $A^{m,\varepsilon}(\mathbf{u}^\varepsilon, \mathbf{v}^\varepsilon)$ are the bilinear form associated with the elastic behavior of the domain. In order to study the asymptotic behavior of the physical problem (1), we apply the usual change of variable, which transforms Ω^ε into a fixed domain Ω .

Now, the leading terms $(\mathbf{U}^0, \mathbf{u}^0)$ of the asymptotic expansion satisfy the following limit problems :

1. $p = 1$:

$$\begin{cases} \text{Find } (\mathbf{U}^0, \mathbf{u}^0) \in V_M \text{ such that for all } (\mathbf{V}, \mathbf{v}) \in V_M \\ A^-(\mathbf{U}^0, \mathbf{V}) + A^+(\mathbf{U}^0, \mathbf{V}) + A_M^m(\mathbf{u}^0, \mathbf{v}) = L(\mathbf{V}), \end{cases}$$

where

$$V_M = \{(\mathbf{V}, \mathbf{v}) \in H^1(\Omega; \mathbb{R}^3) \times H^1(\omega; \mathbb{R}^3); \mathbf{V}|_\omega = \mathbf{v}, \mathbf{V}|_{\Gamma_0} = 0\},$$

$A_M^m(\mathbf{u}, \mathbf{v}) = \int_\omega a^{\alpha\beta\sigma\tau} \gamma_{\sigma\tau}(\mathbf{u}) \gamma_{\alpha\beta}(\mathbf{v}) \sqrt{a} \, dy$ is the bilinear form associated with the membrane behavior of the shell, $a^{\alpha\beta\sigma\tau}$ are the contravariant components of the elasticity tensor of the shell and $\gamma_{\alpha\beta}(\mathbf{u})$ are the covariant components of the change of metric tensor.

2. $p = 3$:

$$\begin{cases} \text{Find } (\mathbf{U}^0, \mathbf{u}^0) \in V_F \text{ such that for all } (\mathbf{V}, \mathbf{v}) \in V_F \\ A^-(\mathbf{U}^0, \mathbf{V}) + A^+(\mathbf{U}^0, \mathbf{V}) + A_F^m(\mathbf{u}^0, \mathbf{v}) = L(\mathbf{V}), \end{cases}$$

where

$$V_F = \{(\mathbf{V}, \mathbf{v}) \in H^1(\Omega; \mathbb{R}^3) \times H^2(\omega; \mathbb{R}^3); \mathbf{V}|_\omega = \mathbf{v}, \mathbf{V}|_{\Gamma_0} = 0, \gamma_{\alpha\beta}(\mathbf{v}) = 0 \text{ in } \omega\},$$

$A_F^m(\mathbf{u}, \mathbf{v}) = \frac{1}{3} \int_\omega a^{\alpha\beta\sigma\tau} \rho_{\sigma\tau}(\mathbf{u}) \rho_{\alpha\beta}(\mathbf{v}) \sqrt{a} \, dy$ is the bilinear form associated with the flexural behavior of the shell and $\rho_{\alpha\beta}(\mathbf{u})$ are the covariant components of the change of curvature tensor.

- [1] H. Pham Huy, E. Sanchez-Palencia, Phénomène de transmission à travers des couches minces de conductivité élevée, *J. Math. Anal. Appl.* 47 (1974) 284–309.
- [2] D. Caillerie, The effect of a thin inclusion of high rigidity in an elastic body, *Math. Methods Appl. Sci.* 2 (1980) 251–270.
- [3] D. Chapelle, A. Ferent, Modeling of the inclusion of a reinforcing sheet within a 3D medium, *Math. Models Methods Appl. Sci.* 13 (2003) 573–595.
- [4] A.L. Bessoud, F. Krasucki, G. Michaille, Multi-materials with strong interface : variational models, (submitted).
- [5] J. Sanchez-Hubert, E. Sanchez-Palencia, *Coques élastiques minces : propriétés asymptotiques*, Masson, Paris, 1997.
- [6] P.G. Ciarlet, *Mathematical Elasticity, vol. III : Theory of shells*, Studies in mathematics and its applications, North-Holland, Amsterdam, 2000.
- [7] G. Geymonat, F. Krasucki, S. Lenci, Mathematical analysis of a bonded joint with a soft thin adhesive, *Math. Mech. Solids* 4 (1999) 201–225.

LARGE ELASTIC DEFORMATIONS OF LAMINATED CYLINDRICAL PANELS UNDER POINT LOAD

I. Kreja

Gdańsk University of Technology, Gdańsk, Poland

1. Problem statement

A series of deep cylindrical laminated panels (Fig. 1) with various stacking sequences of a laminate made of a glass-epoxy composite was considered by Tsai et al. [1] assuming the following geometrical data: $R = 12$ in, $L = 5.5$ in, $\beta = 0.5$, and $h = 0.04$ in.

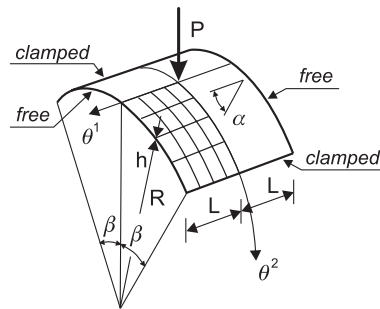


Fig. 1: Clamped cylindrical panel under point load

In the present research a more detailed study on the influence of the degree of orthotropy on the performance of the laminate is presented for selected stacking sequences of a cross-ply laminate (Fig. 2), assuming a variable degree of orthotropy $n = 1, 2, 5, 10, 15$ and 30 . The orthotropic material of a single layer characterized by $E_a = 20.46 \cdot 10^6$ psi, $E_b = E_a / n$, $G_{ab} = G_{ac} = 0.62 \cdot E_b$, $G_{bc} = 0.31 \cdot E_b$, and $\nu_{ab} = 0.313$.

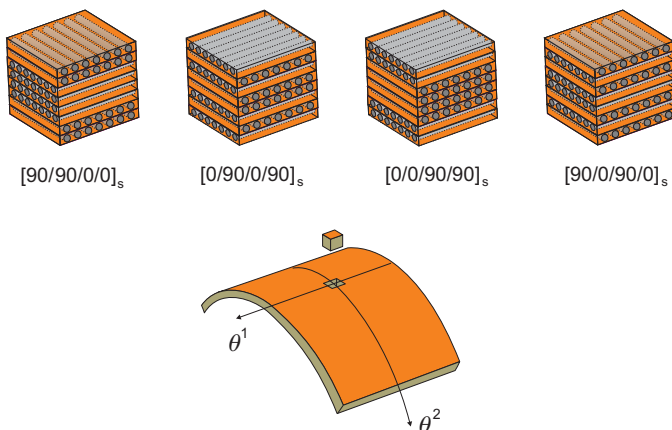


Fig. 2: Various lamination schemes considered for analyzed panel

The geometrically non-linear analysis in the present research is performed with the own FEM code SHL04 [2] based on the large rotation formulation LRT56 [3]. Constitutive relations for composite laminate are constructed assuming the *Equivalent Single Layer* (ESL) model with global constitutive relations established with enhanced *Lamination Theory* adequate for the *First Order Shear Deformation* (FOSD) theory.

2. Results examination

The results of the analysis are presented in Fig. 3 as a graph of the critical snapping load vs. the value of the degree of orthotropy, n , for all four considered cross-ply schemes: $[90/0/90/0]_s$, $[90/90/0/0]_s$, $[0/90/0/90]_s$ and $[0/0/90/90]_s$.

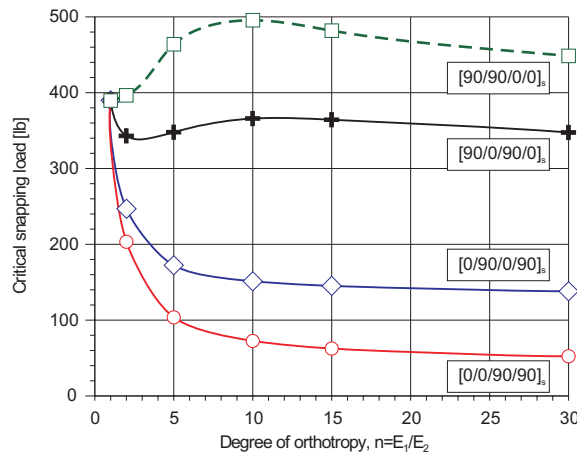


Fig. 3: Interrelation between the degree of orthotropy and the level of critical snapping load

It is quite obvious that a higher bending stiffness could be anticipated for the $[0/90/0/90]_s$ laminate than for the $[0/0/90/90]_s$ one, because in the former case the reinforcement along the θ^2 -direction is located closer to the outer surfaces. For the same reason, one can expect to obtain a higher overall bending stiffness by changing the stacking sequence from $[0/90/0/90]_s$ to $[90/0/90/0]_s$ and even a bigger increase of the stiffness can be anticipated for the $[90/90/0/0]_s$ laminate. However, with a little amazement one can observe in Fig. 3 that despite of reduction of the overall panel stiffness accompanying the increase of the degree of orthotropy, the value of the critical snapping load for the $[90/0/90/0]_s$ laminate varies in a very limited range as compared with the previous considered stacking sequences. Even more surprising observation can be made for the $[90/90/0/0]_s$ laminate, where the reduction of the overall stiffness for the increased degree of orthotropy n is accompanied quite paradoxically by the increase of the critical snapping load.

3. References

- [1] C. T. Tsai, A. N. Palazotto and S. T. Dennis (1991). Large-rotation snap-through buckling in laminated cylindrical panels, *Finite Elements in Analysis and Design* **9**, 65-75.
- [2] I. Kreja and R. Schmidt (2006). Large rotations in First Order Shear Deformation FE analysis of laminated shells, *Int. Journal Non-Linear Mechanics* **41**, 101-123.
- [3] I. Kreja (2007). *Geometrically non-linear analysis of layered composite plates and shells*, Monographs 83, Gdańsk University of Technology, Gdańsk, 1- 173.

INVESTIGATION OF OSCILLATION PROCESS OF THE SHELL ELEMENT BY METHOD OF FINITE ELEMENTS

Edgar Harutyunyan

State Engineering University of Armenia, Yerevan, Armenia

At it is well known, during the exploitation of a passenger automobile the carrying body of an automobile is under the influence of dynamic loads. Under the influence of irregularities of road an automobile body is under the forced oscillation. As the carrying body of a passenger automobile consists most of shell elements, so it is interesting to investigate the oscillation process of it. Above mentioned investigation, done by traditional analytic methods, relates with huge complexity, so this work is devoted to the investigation of mentioned process by method of finite elements. The road irregularities are exerting randomly and it is important to take into account all the cases of the oscillation in order to avoid resonances during the exploitation.

The above mentioned calculations, if they are done by traditional methods, require a lot of assumptions, which influence on the accuracy of the obtaining data. Especially, here the carrying body of an automobile is introduced as a material particle which is connected with the car suspension by the solid connection.

It doesn't make an opportunity to completely calculate and to assess the designing automobile's driving evenness.

Driving evenness is one of the operational attributes of an automobile, which describes the ability of an automobile to move on the unequal road by the given interval of velocities.

The engine generates some vibrations too. But these vibrations are too small comparison with above mentioned vibrations. Vibrations have huge influence upon not only driving evenness, but also the technique-operational attributes of an automobile.

In general, the basis of oscillation investigation is the following equation

$$(1) [M]\{\ddot{u}\} + [C]\{\dot{u}\} + [K]\{u\} = \{F(t)\} \quad \text{Where}$$

$[M]$ - Mass matrix, $[C]$ - Damping matrix, $[K]$ - Stiffness matrix, $\{\ddot{u}\}, \{\dot{u}\}, \{u\}$ are accordingly nodal acceleration, velocity and displacement vectors, (t) - time.

Above mentioned matrices are formed automatically. The density and volume have to be entered, which are the calculation starting points of the mass of each finite element.

During modal analysis the above mentioned equation has the following view.

$$(2) [M]\{\ddot{u}\} + [K]\{u\} = 0$$

During Harmonic analysis the loads are changing their influence by harmonic type. The basis equation has the same view, but in compare with the following.

$$(3) \{F(t)\} = \{F_0(\cos(\omega t + \varphi) + i \sin(\omega t + \varphi))\}$$

The modal analysis gives us an opportunity to obtain the own oscillation frequencies in the most possible directions. In this case the first five directions which are most possible are remarkable. The other ones are not actual. The results are introduced in the Table1.

Sub step	Oscillation frequency	Measure
1	12141	[Hz]
2	30593	[Hz]
3	70655	[Hz]

4	81472	[Hz]
5	87277	[Hz]

Table1. The results of calculated own oscillation frequency

These results are obtained by the calculation of the shell element, which is welded on the one side. On the other side an external force is acting by sinusoidal principle. This case is more usual in carrying body automobiles and represents more interest.

The described model is shown on the Figure1

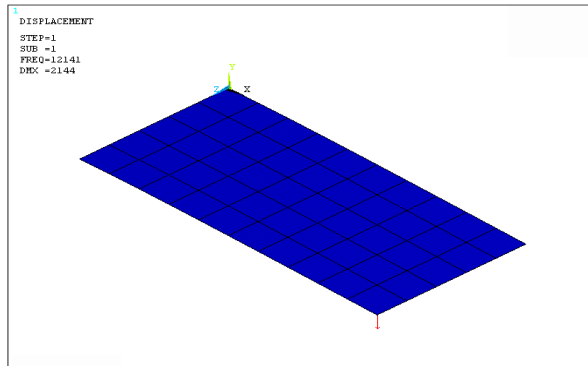


Figure1. The designed model of shell element

After above mentioned calculations, the interval of the external force frequency is given in that case, that the value of own oscillation in the according node is the mentioned interval.

The result is given the Figure2, where we can easily see the function of oscillation amplitude and frequency.

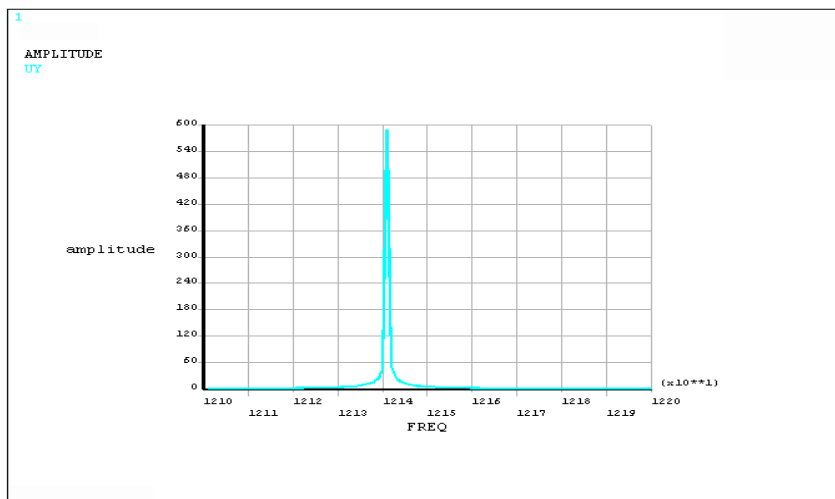


Figure2. Function of oscillation amplitude and frequency

The case of resonance is evident here.

References

- [1] G.V.Musayelyan, *Utilization of Method of Finite Elements in Transporting Systems*, SEUA, Yerevan 2003-289p.
- [2] Pippert H. *Karosserietechnik*: Vogel Verlag, 1998.- 303 s.
- [3] Müller G. *FEM für Praktiker*, Expert Verlag, 1997.- 859 s.

THE EFFECT OF PATCH LOAD ON CORRUGATED SILO WALLS

C. González-Montellano¹, E. Gallego¹, J. Morán² and F. Ayuga¹

¹ *BIPREE Research Group, Universidad Politecnica de Madrid, Spain*

² *Departamento de Ingeniería y Ciencias Agrarias, Universidad de León.*

1. Introduction

Silos are special structures widely used in industries to store all kind of agricultural products. Loads exerted by the stored material over the silo walls are critical in the silo design. Eurocode [1] specifies how to calculate the pressures due to the stored material depending on different characteristics of the silo: shape, slenderness or capacity. If filling is centric, a symmetric flow is expected and, therefore, horizontal pressures acting on the silo wall will have a constant value for the circumferential position at any height. In addition, pressures are greater for higher silo depths.

However, filling is sometimes eccentric and non-symmetric behaviours may also appear during filling and emptying. In those cases, asymmetric flow might appear and this can lead to non-symmetric pressures over the silo wall. Eurocode defines the patch-load to reproduce these non-symmetric pressures. The patch-load is an asymmetric pattern of lateral pressures applied over a part of the silo wall (Figure 1) and added to the symmetric pressures. The patch-load can be applied at any height of the silo but in a reduced length of the walls. In consequence, the design of the silo must satisfy structural safety with independence of the patch-load localisation.

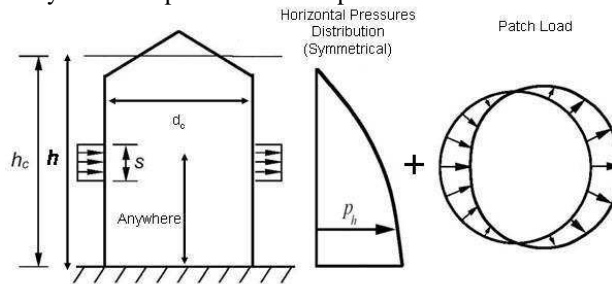


Figure 1. Requirements of patch-load according to Eurocode (EN 1991-4 2003)

For low silo capacities, Eurocode allows replacing the patch-load with a uniform increment in lateral pressures. However, this simplification is not possible for silos with large capacities. In this case, the calculation of the wall stress states due to the patch-load is more complex than for symmetric loads.

2. Methodology.

A three dimensional Finite Elements Model with ANSYS software was developed to simulate the cylindrical corrugated silo walls with flat bottoms (Figure 2). The application of unsymmetrical pressures in silo walls has been considered in some research [2] but simulating smooth walls. The possible influence of different factors in the stress state of the silo wall after the application of the patch-load was considered: the slenderness of the silo ($\lambda=h_c/d_c$), the flexibility of the wall ($t/0.5 \cdot d_c$) and the silo height, h_h , at which the patch-load is applied. By varying the silo height, h_c , the silo diameter, d_c , and the wall thickness, t , forty eight finite element models were developed as a result of considering four slenderness values ($\lambda=1.35$, $\lambda=1.62$, $\lambda=1.90$ and $\lambda=2.17$), three thicknesses of the wall ($t=2$ mm, $t=6$ mm and $t=9$ mm) and four positions for the patch-load ($h_i=0.2 \cdot h_c$, $h_i=0.4 \cdot h_c$, $h_i=0.6 \cdot h_c$, and $h_i=0.8 \cdot h_c$). Results were also obtained for different circumferential positions (0° , 45° , 90° , 135° and 180°) in the silo wall in order to detect the stresses asymmetries produced by the non-symmetric condition of the patch-load.

The purpose was the comparison of the stress states resulting after applying the patch-load and the lateral pressures due to the stored material. Firstly, lateral pressures due to the stored material were applied to the silo wall and the wall stresses in the circumferential positions were obtained. After that, the patch-load was applied to the silo wall, and the new stress state of the silo wall was obtained for the same circumferential positions. Finally both sets of results are compared, and the increment ratio of stresses, k , is obtained at every part of the silo wall.

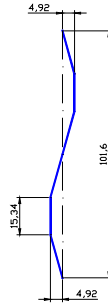


Figure 2. Geometry on an elemental undulation of the corrugated wall (Dimensions in mm).

3. Results.

The patch-load makes the silo wall suffer an inward deformation in the pressure zone and an outward deformation in the opposite part (Figure 3a). It can be clearly seen in Figure 3b that an overstress in the silo wall is detected where the patch-load is applied ($k > 1$). The patch-load does not produce any change in the stress state above the silo height where the patch-load is applied. A linear increase in k is detected for the silo wall placed below h_h . These results may be used to simplify the procedure defined in Eurocode, even for the higher capacity silos.

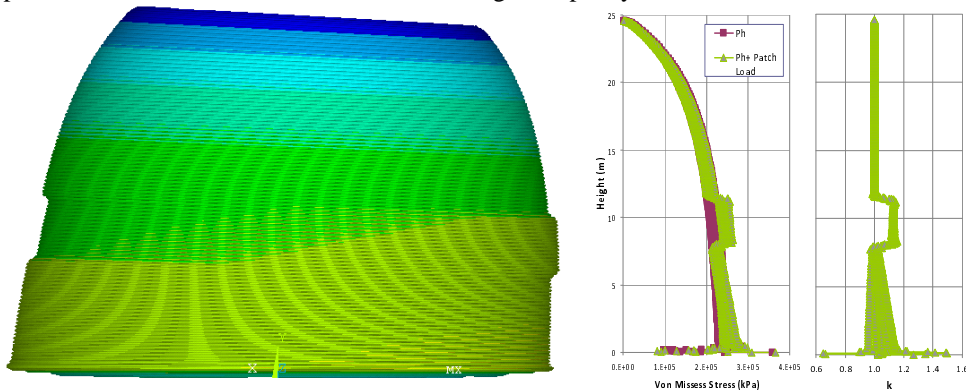


Figure 3. a) Deformation of the silo wall b) Increment ratio of stresses, k , over the silo wall.

4. References.

- [1] EN 1991:4 (2003). *Eurocode 1. Basis of design and actions on structures. Part 4: actions in silos and tanks*, CEN, Brussels.
- [2] D. Briassoulis (2000). Finite Element Analysis of a cylindrical silo shell under unsymmetrical pressure distributions, *Computers & Structures*, **78**, 271-281.

DYNAMIC CONTACT OF THE ELASTIC IMPACTOR AND SPHERICAL SHELL

A. Loktev¹ and D. Loktev²

¹ *Russian University of Innovation, Moscow, Russia*

² *Moscow State Technical University m. Bauman, Moscow, Russia*

1. General

The dynamic contact of the solid body through elastic buffer on a circular sector of spherical shell is studied. The intender is simulated by mass and the elastic cylindrical element, which strikes the target. Interaction is considered to be elastic with constant contact area. Dynamic behaviour of the shell is described by without moment moving equations taking the rotary inertia into account and, therefore, are wave equations. These equations allow to assume, that in the plate the transient longitudinal wave, because of which there is a deformation of a shell material outside of contact area, is generated with final velocity. In the present work, the procedure similar to the one proposed in [1] for the analysis of transverse impact of a solid sphere upon an elastic buffer positioned on an elastic orthotropic plate, is used to the case of shock interaction of a solid body with an elastic circular sector of spherical shell which hinge-supported on the perimeter.

During the interaction of the body with the shell, a quasilongitudinal wave representing the surfaces of strong discontinuity begin to propagate. In a spherical shell of the surface of strong discontinuity represent spherical surfaces – strip, whose generators are parallel to the normal to the median surfaces and guides locating in the median surface are circumferences extending with the normal velocity G . Behind the wave fronts, the solution is constructed in terms of ray series representing power series, whose coefficients are the different order discontinuities in the time-derivatives of the required functions, and the variable is the time passed from the moment of arrival of a wave to the given points of the shell:

$$Z(\varphi, t) = \sum_{k=0}^{\infty} \frac{1}{k!} [Z_{,(k)}]_{t=R_1\varphi/G} \left(t - \frac{R_1(\varphi - \varphi_0)}{G} \right)^k H \left(t - \frac{R_1(\varphi - \varphi_0)}{G} \right), \quad (1)$$

where $[Z_{,(k)}] = Z^+_{,(k)} - Z^-_{,(k)} = [\partial^k Z / \partial t^k]$ are the leaps of the derivatives of k -degree by the time t from the equation Z on the wave surface Σ , i.e. if $t = R_1(\varphi - \varphi_0)/G$, r_0 is the initial radius of the contact area, indexes “+” and “-” mean that the value is found directly in front of and behind the wave front respectively, $H(t)$ – the one-term Heviside’s function, R_1 – shell’s radius, φ – coordinate directed on the meridian, φ_0 – angle coordinate for boundary of contact area.

To determine the ray series coefficients for the desired functions, it is necessary to differentiate the governing equations for shell with respect to time, to take their difference on the different sides of the wave surface, and to apply the condition of compatibility [2]

$$G \left[\frac{\partial Z_{,(k)}}{\partial r} \right] = - [Z_{,(k+1)}] + \frac{\delta [Z_{,(k)}]}{\delta t}, \quad (2)$$

where $\delta/\delta t$ is the δ - derivative with respect to time.

As a result of the procedure described, we are led to the system of recurrent differential equations, which solution gives us the discontinuities in time-derivatives of the desired values within arbitrary constants

$$\left(1 - \frac{\rho(1-\sigma^2)G^2}{E}\right)U_{(k+1)} = 2\frac{\delta U_{(k)}}{\delta t} - Gctg\varphi U_{(k)} + (1+\sigma)G\sin\varphi X_{(k)} + F_{1(k-1)}, \quad (3)$$

$$X_{(k+1)} = \frac{(1+\sigma)}{G\sin\varphi}U_{(k)} + F_{2(k-1)}, \quad (4)$$

where $X_{(k)} = [w_{\gamma(k+1)}]$, $U_{(k)} = [u_{\varphi\gamma(k+1)}]$, $\varphi = \varphi_0 + R_1 Gt$,

$$F_{1(k-1)} = \frac{\delta U_{(k-1)}}{\delta t} (Gctg\varphi - 1) - G^2(1-\sigma)U_{(k-1)} - (1+\sigma)G\sin\varphi \frac{\delta X_{(k-1)}}{\delta t},$$

$$F_{2(k-1)} = -(1+\sigma) \left(\frac{1}{G\sin\varphi} \frac{\delta U_{(k-1)}}{\delta t} + 2X_{(k-1)} \right).$$

where E is the modulus of elasticity, σ is Poisson's ratio, ρ is the density shell's material, w and u_{φ} are the normal and tangential along meridian displacement respectively.

The arbitrary constants are determined at splicing on border of contact area of the solution for required function inside a contact disk and outside of it from following equations

$$m(\ddot{\alpha} + \ddot{w}) = -P(t), \quad \rho h \pi r_0^2 \ddot{w} = 2\pi r_0 (N_{\varphi} + N_{\theta}) \Big|_{\varphi=\varphi_0} \sin\varphi + P(t), \quad (5)$$

where α is the displacements of the impactor's upper end, $P(t)$ is the contact force proportional to the buffer's deformation, m is the mass of the impactor, h is the thickness of the target, r_0 is the impactor's radius, N_{φ} and N_{θ} are the longitudinal forces on the boundary of the contact region.

The compact analytical expressions for contact force and dynamical normal displacement are defined.

$$P(t) = E_1 \left[V_1 t - \frac{1}{6} E_1 V_1 \left(\frac{1}{m} + \frac{1}{\pi r_0 (\rho h r_0 - E \sin \varphi_0)} \right) t^3 - \frac{E(1+\sigma)(\sin \varphi_0)^{1/2}}{6G\rho h r_0} \times \right. \\ \left. \times \left\{ \left[\frac{ctg\varphi_0 \rho h r_0 G}{\rho h r_0 - E \sin \varphi_0} + \frac{\ln \sin \varphi_0}{4} + \frac{ctg\varphi_0 G}{4} - \varphi_0 \left[\frac{G}{4} + \frac{(1+\sigma)^2}{2G} \right] \right] c_1 + c_2 \right\} t^4 \right], \quad (6)$$

$$w(t) = \frac{1}{6\pi r_0 (\rho h r_0 - E \sin \varphi_0)} t^3 + \frac{E(1+\sigma)(\sin \varphi_0)^{1/2}}{6G\rho h r_0} \left\{ \left[\frac{ctg\varphi \rho h r_0 G}{\rho h r_0 - E \sin \varphi_0} + \right. \right. \\ \left. \left. + \frac{\ln \sin \varphi_0}{4} + \frac{ctg\varphi_0 G}{4} - \varphi_0 \left[\frac{G}{4} + \frac{(1+\sigma)^2}{2G} \right] \right] c_1 + c_2 \right\} t^4, \quad (7)$$

here E_1 is the impactor's elastic modulus, V_1 is the initial velocity of contact, c_1, c_2 are the constants.

The carried out numerical researches allow to make the conclusion about influence of parameters of a construction on dynamic characteristics of interaction.

References

- [1] A.A. Loktev (2005). Elastic Transverse Impact on an Orthotropic Plate, *Technical Physics Letters*, Vol. 31(9), 767-769.
- [2] Yu.A. Rossikhin, M.V. Shitikova (1995). The impact of a rigid sphere with an elastic layer of finite thickness, *Acta Mechanica*. Vol. 112, N 1-4. 83-93.

THEORY OF MICROPOLAR THIN ELASTIC CYLINDRICAL SHELLS

S.H. Sargsyan

*Gyumri State Pedagogical Institute, Gyumri, Armenia
National Science Academy of Armenia, Yerevan, Armenia*

1. General

Current developments of mechanics of elastic medium is closely connected with the construction of generalized mathematical models which consider material's particle as a complex object endowed with additional properties describing material's inner structure (unlike the classical theory of elasticity which considers particle as a material unit). Presently, theories of elastic mediums with micro- and nanostructure are successfully cultivated on the basis of micropolar (momental, asymmetrical) theory of elasticity, otherwise, on Cosserate's continuum.

Alongside with the development of the three-dimensional micropolar elastic model, presently, construction of applied theories for micropolar elastic plates and shells is becoming more actual.

In papers [1, 2] on the basis of the asymptotic method linear theories of micropolar thin elastic plates and shells with boundary layer are constructed. Depending on the values of sizeless physical parameters of the plate and shell theories of micropolar elastic plates and shells with independent and constraint rotation and theories with "small shift rigidity" are constructed.

In present paper on the basis of the constructed general theories of micropolar shell [2] mathematical models for micropolar elastic cylindrical shells with independent and constraint rotation and "with small shift rigidity" are studied.

2. System and boundary conditions of micropolar elastic cylindrical (axe symmetrical) shells with independent rotation

Balance equations [2]:

$$\frac{dT_{11}}{d\xi} = r(q_1^+ + q_1^-), \quad T_{22} + \frac{dN_{13}}{d\xi} = -r(q_3^+ + q_3^-), \quad \frac{dL_{12}}{d\xi} - r(N_{31} - N_{13}) = r(m_2^+ + m_2^-)$$

Elasticity correlations:

$$T_{ii} = \frac{2Eh}{1-\nu^2} [\Gamma_{ii} + \nu\Gamma_{jj}] \quad L_{12} = 2h(\gamma + \varepsilon)\chi_{12}, \quad N_{13} = -2h \frac{4\alpha\mu}{\alpha + \mu} \Gamma_{i3} - \frac{\alpha - \mu}{\alpha + \mu} N_{31}, \quad N_{31} = h(q_1^+ - q_1^-)$$

Geometrical correlations:

$$\Gamma_{11} = \frac{1}{r} \frac{du_1}{d\xi}, \quad \Gamma_{22} = -\frac{w}{r}, \quad \Gamma_{13} = -\frac{1}{r} \frac{dw}{d\xi} + \Omega_2, \quad \chi_{12} = \frac{1}{r} \frac{d\Omega_2}{d\xi}$$

where T_{11} , T_{22} , N_{13} – are forces averaged along the shell's thickness, L_{12} – is the averaged moment from momental stresses, Γ_{11} , Γ_{22} , Γ_{13} – are components of tensor deformation, χ_{12} – is the bending in shell's middle surface, u_1 , w – are the transitions, and Ω_2 – is the independent rotation of points of the shell's middle surface.

Boundary pivot conditions:

$$w|_{\Gamma} = 0, \quad T_{11}|_{\Gamma} = 0, \quad L_{12}|_{\Gamma} = 0$$

3. System and boundary conditions of micropolar elastic cylindrical (axe symmetrical) shells with constraint rotation:

Balance equations:

$$\frac{dT_{11}}{d\xi} = r(q_1^+ + q_1^-), \quad T_{22} + \frac{dN_{13}}{d\xi} = -r(q_3^+ + q_3^-), \quad \frac{d}{d\xi}(G_{11} - L_{12}) - rN_{13} = -r(m_2^+ - m_2^-) - rh(q_1^+ - q_1^-)$$

Elasticity correlations:

$$T_{ii} = \frac{2Eh}{1-\nu^2} [\Gamma_{ii} + \nu\Gamma_{jj}], \quad L_{12} = 2h(\gamma + \varepsilon)\chi_{12}, \quad G_{11} = -\frac{2Eh^3}{3(1-\nu^2)} K_{11}$$

Geometrical correlations:

$$\Gamma_{11} = \frac{1}{r} \frac{du_1}{d\xi}, \quad \Gamma_{22} = -\frac{w}{r}, \quad K_{11} = \frac{1}{r} \frac{d\beta_1}{d\xi}, \quad \beta_1 = \frac{1}{r} \frac{dw}{d\xi}, \quad \chi_{12} = \frac{1}{r} \frac{d\Omega_2}{d\xi}, \quad \Omega_2 = \beta_1$$

Boundary pivot conditions

$$T_{11}|_r = 0, \quad (L_{12} - G_{11})|_r = 0, \quad w|_r = 0$$

4. System and boundary conditions of micropolar elastic cylindrical shells (axe symmetrical) with “small shift rigidity”:

Balance equations:

$$\frac{dT_{11}}{d\xi} = r(q_1^+ + q_1^-), \quad T_{22} + \frac{dN_{13}}{d\xi} = -r(q_3^+ + q_3^-), \quad \frac{dG_{11}}{d\xi} - rN_{31} + rh(q_1^+ - q_1^-) = 0, \quad \frac{dL_{12}}{d\xi} = r(m_2^+ + m_2^-)$$

Elasticity correlations:

$$T_{ii} = \frac{2Eh}{1-\nu^2} [\Gamma_{ii} + \nu\Gamma_{jj}], \quad L_{12} = 2h(\gamma + \varepsilon)\chi_{12}, \quad G_{11} = -\frac{2Eh^3}{3(1-\nu^2)} K_{11}, \quad N_{13} = N_{31} - 8h\alpha\Gamma_{13}$$

Geometrical correlations:

$$\Gamma_{11} = \frac{1}{r} \frac{du_1}{d\xi}, \quad \Gamma_{22} = -\frac{w}{r}, \quad \Gamma_{13} = -\beta_1 + \Omega_2, \quad K_{11} = \frac{1}{r} \frac{d\beta_1}{d\xi}, \quad \beta_1 = \frac{1}{r} \frac{dw}{d\xi}, \quad \chi_{12} = \frac{1}{r} \frac{d\Omega_2}{d\xi}$$

Boundary pivot conditions:

$$w|_r = 0, \quad T_{11}|_r = 0, \quad G_{11}|_r = 0$$

On the basis of the above mentioned mathematical models of micropolar elastic cylindrical (axe symmetrical) shells, definition of stress-deformed state in them is brought to final formula and numerical results. On the basis of the numerical results, properties of the constructed applied theories of micropolar shells are analyzed, conclusions and recommendations on the application of the micropolar materials are made.

5. References

1. Sargsyan S.H (2008). Boundary problems of thin plates in asymmetrical theory of elasticity, *Applied Mathematics and Mechanics*, **72**, N 1, 129-147, (in Russian).
2. Sargsyan S.H (2008). General theory of thin elastic shells on the basis of asymmetrical theory of elasticity, *Applied Mathematics and Mechanics*, **72**, not published yet.

NINE-NODE ASSUMED STRAIN SHELL ELEMENT WITH DRILLING ROTATION

P. Panasz, K. Wisniewski

Institute of Fundamental Technological Research, Warsaw, Poland

1. Introduction

Nine-node shell elements are more complex than four-node elements, but are advantageous in some applications, involving dominant in-extensional bending.

In the current paper, we develop a finite-rotation 9-node shell element with drilling rotation, which is based on the Reissner's kinematics and the Green strain. The basic 9-node isoparametric Lagrangian shell element suffers from the transverse shear and membrane locking. Several techniques of avoiding them were proposed and tested in the literature. One of the most effective is the assumed strain (AS) method, which consists of sampling of strain components at certain points, and extrapolating these values over the element. We apply and modify this method, for details see [1].

2. Basic shell equations

Classical papers on the subject are restricted to two-parameter rotations, which have to be defined in the local basis and transformed to the reference basis. We define an *extended configuration space* in terms of the deformation function χ and rotations $\mathbf{Q} \in SO(3)$

$$(1) \quad \mathcal{C}_{\text{ext}} \doteq \{(\chi, \mathbf{Q}) : B \rightarrow R^3 \times SO(3) \mid \chi \in \mathcal{C}\},$$

which includes the drilling rotation, so, in effect, we have 3 rotational parameters per node, and the rotation vector can be directly assumed in the reference basis. The rotations are included in the formulation using the rotation constraint (RC) equation: $\text{skew}(\mathbf{Q}^T \mathbf{F}) = \mathbf{0}$, where $\mathbf{F} \doteq \nabla \chi$, see [2]. The formulation is based on the following 3D two-field functional

$$(2) \quad F_2(\chi, \mathbf{Q}) \doteq \int_B \left[\mathcal{W}(\mathbf{F}^T \mathbf{F}) + \frac{\gamma}{2} \text{skew}(\mathbf{Q}^T \mathbf{F}) \cdot \text{skew}(\mathbf{Q}^T \mathbf{F}) \right] dV + F_{\text{ext}},$$

where \mathcal{W} is the strain energy, and $\gamma \in (0, \infty)$ is the regularization parameter.

The shell kinematics is based on the Reissner's hypothesis, with the current position vector expressed as follows,

$$(3) \quad \mathbf{x}(\xi^\alpha, \zeta) = \mathbf{x}_0(\xi^\alpha) + \zeta \mathbf{Q}_0(\xi^\alpha) \mathbf{t}_3(\xi^\alpha),$$

where \mathbf{x}_0 is the current position of the reference surface, and \mathbf{Q}_0 is a rotation of the reference surface, and \mathbf{t}_3 is the shell director normal to the reference surface in the initial configuration. Besides, $\xi^\alpha \in [-1, +1]$ and $\zeta \in [-h/2, +h/2]$, where h is the initial shell thickness.

The strain energy is assumed in the Saint Venant-Kirchhoff's form, $\mathcal{W} \doteq \frac{1}{2} \lambda (\text{tr} \mathbf{E})^2 + G \text{tr}(\mathbf{E}^2)$, where $\mathbf{E} \doteq \frac{1}{2}(\mathbf{F}^T \mathbf{F} - \mathbf{I})$ is the Green strain, and λ, G are Lamé constants.

3. Features of our 9-node shell element

The developed 9-node shell element has the following features: (a) the drilling rotation is included, yielding 3 rotational dofs/node, (b) the rotations are parameterized by the canonical rotation vector, and are unrestricted, (c) the Reissner's kinematics is applied, so the transverse shear energy is included.

To eliminate the transverse shear and membrane locking, the AS method is applied. A modification of the AS method is proposed, consisting in treating the sampling and the numerical integration together, which results in 6 sampling points being replaced by two sampling lines, see Fig.1. This change facilitates the implementation and significantly improves efficiency of differentiation, for details see [1]. The two-level approximation is applied to strain components in the ortho-normal basis at the element's center.

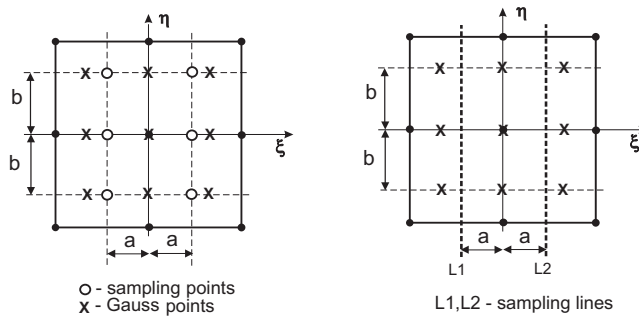


Figure 1. Location of sampling points and lines, $a = \sqrt{\frac{1}{3}}$, $b = \sqrt{\frac{3}{5}}$.

4. Numerical tests

The developed 9-AS shell element is subjected to a range of benchmark tests, to establish the sensitivity to mesh distortion, the coarse mesh accuracy, and to confirm the lack of locking. One of the tests is the analysis of deployment of a ring, with the deformation shown in Fig.2. Our results are compared with results obtained by the MITC9 element of ADINA and the S9R5 element of ABAQUS.

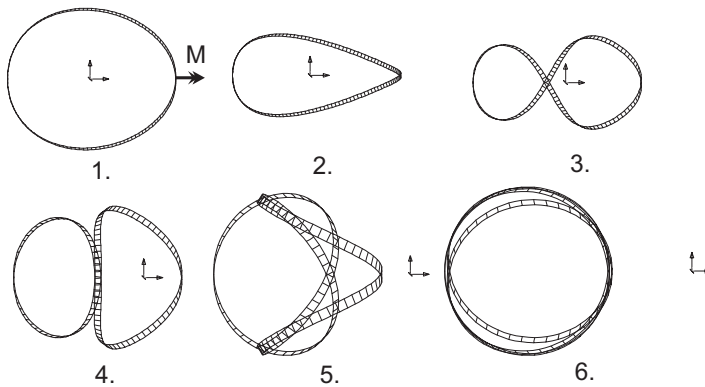


Figure 2. Deployable ring. Progressing stages of deformation.

5. References

- [1] Panasz P., Wisniewski K.: *Nine-node shell elements with 6 dofs/node based on two-level approximations*. Submitted (2007)
- [2] Wisniewski K., Turska E.: *Second order shell kinematics implied by rotation constraint equation*, J. Elasticity, Vol.67, 229–246 (2002).

FREE VIBRATIONS OF SMOOTH CYLINDRICAL SHELLS

G.D. Gavrylenko and V.I. Matsner

S.P. Timoshenko Institute of Mechanics, Ukrainian Academy of Sciences, Kiev, Ukraine

1. Theoretical results and comparison with experimental data.

The method of calculation of the problem and full notation are presented in [1]. The equations of motion are derived using the principle of stationary action.

Using the standard procedure of the energy method we obtained the analytical solution for finding the vibration frequencies of the cylindrical shell. They can be represented in the following form

$$\omega_{ij}^2 = \frac{K}{r^2 h \rho_0} \frac{A_{33}(A_{11}A_{22} - A_{12}^2) + 2A_{12}A_{13}A_{23} - A_{11}A_{23}^2 - A_{22}A_{13}^2}{(A_{11}A_{33} - A_{13}^2) + (A_{22}A_{33} - A_{23}^2) + (A_{11}A_{22} - A_{12}^2)},$$

where ω_j – frequency, $K = Eh/(1 - \mu^2)$, h, r – thickness and radius of the shell, E – modulus of elasticity, μ – Poisson's ratio, ρ_0 – the mass density of the material.

In the general case from three different values of ω^2 one can determine ω_{min} , where ω_{ij} – parameters of frequency. Shells with the following data were calculated and tested [2]: length – 450mm, diameter – 400mm, thickness – 0,5mm. The shells had boundary conditions corresponding to simple supported edges.

In Figure 1 the dependence $f_{ij} = \omega_j/2\pi$ on i is presented, where i – the number of waves in the circumferential direction, j – the number of half-waves in the longitudinal direction.

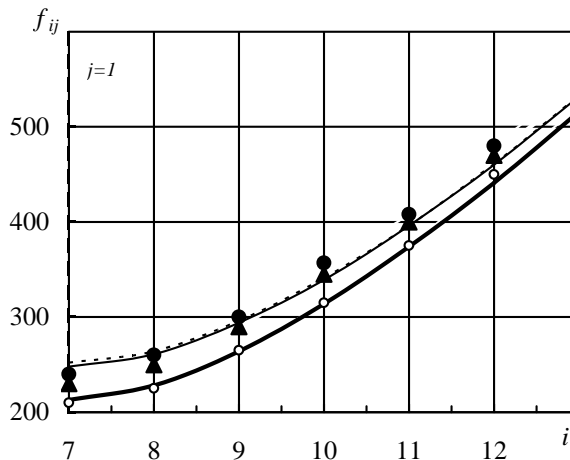


Fig. 1.

In Fig.1 the theoretical curve for an ideal shell is shown, calculated by the above method (solid dark line). The theoretical results [2] are represented by (o) while the experimental data [2] are shown by badges (●, ▲) and the theoretical results for shells having initial deflections are given by the dotted line and thin solid line. The last two shells had deflections with 3 half-waves with amplitude $w_0/h=0,5$ and the zone their placing along the length of the shell is $d/\ell=\ell_0/\ell=0,25$ (in the middle part). The first shell had two dents and one bulge, the second one had two bulges and one dent. The form of deflections was close to $w=w_0 \sin(j\pi x/\ell)$ and j equals 3. The initial imperfections increase by 15% the value of the minimal eigen frequency.

As can be seen from Figure 1 the test data (●, ▲) are close to the theoretical values (black curve). If we take in account axisymmetrical imperfections of the form, the corresponding results (dotted and thin lines) almost coincide with the test data.

From Fig. 1 is clear that regular deflections of such type increase the eigen frequencies of vibration and bring them closer to experimental ones of the defected [2].

2. Conclusions.

A new analytical approach for the analysis frequencies of vibration of the smooth cylindrical shells having initial deflections of the form is used. The analytical solution and the results of calculations are presented. At present there exists a number of methods to calculate vibrations of frequency of ideal shells. But real shells usually have nonideal forms.

The suggested method allows one to define more precisely the eigen frequencies of vibration of incomplete shells. This approach will be used to analyse ribbed cylindrical shells having axisymmetric imperfections under the compressive axial force.

The new numerical approach has been developed at last time for ribbed shells of rotation [3]. The method presented here allows to define more quickly the eigen frequencies than the numerical method [3].

3. References.

- [1] G.D. Gavrylenko & V.I. Matsner (2007). Free vibration of smooth cylindrical shells with local axisymmetrical deflections, *Reports of NAS of Ukraine*, No 12, 54 – 60.
- [2] A.I. Kukarina, V.I. Matsner and E.F. Sivak (1982). On the effect initial deflections on eigen vibrations of ribbed cylindrical shells, *Int. Appl. Mech.*, **18**, No 4, 58 – 63. (*In Russian*).
- [3] G.D. Gavrylenko & O.A. Trubitsina (2008). *Vibrations and Stability of Rotation Ribbed Shells (In Russian)*, Barviks, Dnepropetrovsk.

ON THE MECHANICS OF FUNCTIONALLY GRADED PLATES

H. Altenbach¹ and V. A. Eremeyev²

¹*Martin-Luther-Universität Halle-Wittenberg, Halle (Saale), Germany*

²*South Scientific Center of RASci & South Federal University, Rostov on Don, Russia*

Metallic and polymeric foams are more and more used as a material for lightweight structures [1]. Such structures are applied in the automotive or aerospace industries since they combine low weight, high strength and excellent possibilities to absorb energy. The foam itself can be modeled as a functionally graded material with mechanical properties changing over the thickness direction.

The aim of this contribution is a new theory based on the direct approach in the plate theory added by the effective properties concept.

1. Basic equations

Let us consider for the brevity the geometrically and physically linear theory. In addition, we assume plate-like structures. Here we use the so-called direct approach. In this case one states a two-dimensional deformable surface. On each part of this deformable surface forces and moments are acting – they are the primary variables. The next step is the introduction of the deformation measures. Finally, it is necessary to interlink the forces and the moments with the deformation variables (constitutive equations). Such a theory is formulated by a more natural way in comparison with the other approaches. But the identification of the stiffness and other parameters is a non-trivial problem and must be realized for each class of plates individually.

The motion equations and the kinematic equations are given by the relations [2–4]

$$(1) \quad \nabla \cdot \mathbf{T} + \mathbf{q} = \rho \ddot{\mathbf{u}} + \rho \Theta_1 \cdot \dot{\varphi}, \quad \nabla \cdot \mathbf{M} + \mathbf{T}_\times + \mathbf{m} = \rho \Theta_1^T \cdot \ddot{\mathbf{u}} + \rho \Theta_2 \cdot \dot{\varphi},$$

$$(2) \quad \boldsymbol{\mu} = \frac{1}{2} [\nabla \mathbf{u} \cdot \mathbf{a} + (\nabla \mathbf{u} \cdot \mathbf{a})^T], \quad \boldsymbol{\gamma} = \nabla \mathbf{u} \cdot \mathbf{n} + \mathbf{c} \cdot \varphi, \quad \boldsymbol{\kappa} = \nabla \varphi$$

Here \mathbf{T} , \mathbf{M} are the tensors of forces and moments, \mathbf{q} , \mathbf{m} are the surface loads (forces and moments), \mathbf{T}_\times is the vector invariant of the force tensor, ∇ is the nabla operator, \mathbf{u} , φ are the vectors of displacements and the rotations, Θ_1 , Θ_2 are the first and the second tensor of inertia, ρ is the density, $(\dots)^T$ denotes transposed and (\dots) is the time derivative. \mathbf{a} is the first metric tensor, \mathbf{n} is the unit normal vector, $\mathbf{c} = -\mathbf{a} \times \mathbf{n}$ is the discriminant tensor, $\boldsymbol{\mu}$, $\boldsymbol{\gamma}$ and $\boldsymbol{\kappa}$ are the tensor of in-plane strains, the vector of transverse shear strains and the tensor of the out-of-plane strains, respectively.

Limiting our discussion to the elastic behavior and small strains we assume the following constitutive equations of a plate

$$(3) \quad \begin{aligned} \mathbf{T} \cdot \mathbf{a} &= \mathbf{A} \cdot \boldsymbol{\mu} + \mathbf{B} \cdot \boldsymbol{\kappa} + \boldsymbol{\gamma} \cdot \boldsymbol{\Gamma}_1, & \mathbf{T} \cdot \mathbf{n} &= \boldsymbol{\Gamma} \cdot \boldsymbol{\gamma} + \boldsymbol{\Gamma}_1 \cdot \boldsymbol{\mu} + \boldsymbol{\Gamma}_2 \cdot \boldsymbol{\kappa}, \\ \mathbf{M}^T &= \boldsymbol{\mu} \cdot \mathbf{B} + \mathbf{C} \cdot \boldsymbol{\kappa} + \boldsymbol{\gamma} \cdot \boldsymbol{\Gamma}_2 \end{aligned}$$

\mathbf{A} , \mathbf{B} , \mathbf{C} are 4th rank tensors, $\boldsymbol{\Gamma}_1$, $\boldsymbol{\Gamma}_2$ are 3rd rank tensors, $\boldsymbol{\Gamma}$ is a 2nd rank tensor expressing the effective stiffness properties. They depend on the material properties and the cross-section geometry. In the general case the tensors contain 36 different values – a reduction is possible assuming some symmetries.

Let us consider an orthotropic material behavior and a plane mid-surface. In this case one gets

$$\begin{aligned} \mathbf{A} &= A_{11} \mathbf{a}_1 \mathbf{a}_1 + A_{12} (\mathbf{a}_1 \mathbf{a}_2 + \mathbf{a}_2 \mathbf{a}_1) + A_{22} \mathbf{a}_2 \mathbf{a}_2 + A_{44} \mathbf{a}_4 \mathbf{a}_4, \\ \mathbf{B} &= B_{13} \mathbf{a}_1 \mathbf{a}_3 + B_{14} \mathbf{a}_1 \mathbf{a}_4 + B_{23} \mathbf{a}_2 \mathbf{a}_3 + B_{24} \mathbf{a}_2 \mathbf{a}_4 + B_{42} \mathbf{a}_4 \mathbf{a}_2, \\ \mathbf{C} &= C_{22} \mathbf{a}_2 \mathbf{a}_2 + C_{33} \mathbf{a}_3 \mathbf{a}_3 + C_{34} (\mathbf{a}_3 \mathbf{a}_4 + \mathbf{a}_4 \mathbf{a}_3) + C_{44} \mathbf{a}_4 \mathbf{a}_4, \\ \boldsymbol{\Gamma} &= \boldsymbol{\Gamma}_1 \mathbf{a}_1 + \boldsymbol{\Gamma}_2 \mathbf{a}_2, \quad \boldsymbol{\Gamma}_1 = \mathbf{0}, \quad \boldsymbol{\Gamma}_2 = \mathbf{0} \end{aligned}$$

with $\mathbf{a}_1 = \mathbf{a} = \mathbf{e}_1\mathbf{e}_1 + \mathbf{e}_2\mathbf{e}_2$, $\mathbf{a}_2 = \mathbf{e}_1\mathbf{e}_1 - \mathbf{e}_2\mathbf{e}_2$, $\mathbf{a}_3 = \mathbf{c} = \mathbf{e}_1\mathbf{e}_2 - \mathbf{e}_2\mathbf{e}_1$, $\mathbf{a}_4 = \mathbf{e}_1\mathbf{e}_2 + \mathbf{e}_2\mathbf{e}_1$, $\mathbf{e}_1, \mathbf{e}_2$ are unit basic vectors.

2. Stiffness tensors identification

The individuality of each class of plates in the framework of the direct approach is expressed by the effective properties (stiffness, density, inertia terms, etc.). Let us focus our attention on the stiffness expressions. The identification of the effective stresses should be performed on the base of the properties of the real material. Let us assume the generalized Hooke's law with material properties which depend on z . The identification of the effective properties can be performed with the help of static boundary value problems (two-dimensional, three-dimensional) and the comparison of the forces and moments (in the sense of averaged stresses or stress resultants).

Finally, we get the following expressions for the stiffness tensor components [2, 4]

$$\begin{aligned}
 (A_{11}; -B_{13}; C_{33}) &= \frac{1}{4} \left\langle \frac{E_1 + E_2 + 2E_1\nu_{21}}{1 - \nu_{12}\nu_{21}}(1; z; z^2) \right\rangle, \\
 (A_{22}; B_{24}; C_{44}) &= \frac{1}{4} \left\langle \frac{E_1 + E_2 - 2E_1\nu_{21}}{1 - \nu_{12}\nu_{21}}(1; z; z^2) \right\rangle, \\
 (A_{12}; -B_{23} = B_{14}; -C_{34}) &= \frac{1}{4} \left\langle \frac{E_1 - E_2}{1 - \nu_{12}\nu_{21}} z(1; z; z^2) \right\rangle, \\
 (A_{44}; -B_{42}; C_{22}) &= \langle G_{12}(1; z; z^2) \rangle, \\
 (5) \quad \Gamma_1 = \frac{1}{2}(\lambda^2 + \eta^2) \frac{A_{44}C_{22} - B_{42}^2}{A_{44}}, \quad \Gamma_2 = \frac{1}{2}(\eta^2 - \lambda^2) \frac{A_{44}C_{22} - B_{42}^2}{A_{44}},
 \end{aligned}$$

where $\langle \dots \rangle$ is the integral over the plate thickness h , while η^2 and λ^2 are the minimal eigen-values of the following Sturm-Liouville problems

$$\frac{d}{dz} \left(G_{1n} \frac{dZ}{dz} \right) + \eta^2 G_{12} Z = 0, \quad \frac{d}{dz} \left(G_{2n} \frac{dZ}{dz} \right) + \lambda^2 G_{12} Z = 0, \quad \left. \frac{dZ}{dz} \right|_{|z|=\frac{h}{2}} = 0$$

The described above approach was applied to FGM plates made of metal or polymer foams with nonhomogeneous distribution of porosity [4, 5].

3. Conclusions

We presented the theory of FGM plates on the basis of the direct approach. The considered approach to model FGM plates within the framework of a 5-parametric theory of plates has an advantage with respect to theories of sandwich or laminated plates since many classical results can be improved without any difficulties.

- [1] L. J. Gibson and M. F. Ashby (1997). *Cellular Solids: Structure and Properties*, 2nd ed., Cambridge Solid State Science Series, Cambridge University Press, Cambridge, 1-530.
- [2] H. Altenbach (2000). An alternative determination of transverse shear stiffnesses for sandwich and laminated plates, *Int. J. Solids Struct.* **37**, 3503–3520.
- [3] P. A. Zhilin (2006). *Applied Mechanics. Foundations of the Theory of Shells (in Russian)*, St. Petersburg State Polytechnical University, 1-168.
- [4] H. Altenbach and V. Eremeyev (2008). Direct approach based analysis of plates composed of functionally graded materials, *Arch. Appl. Mech.* DOI:10.1007/s00419-007-0192-3.
- [5] H. Altenbach and V. Eremeyev (2008). Analysis of the viscoelastic behavior of plates made of functionally graded materials, *ZAMM*. (submitted).

FORMULATION OF THE INITIAL INVARIANT-BASED SHELL FINITE ELEMENT MODEL USING THE PLANE CURVE GEOMETRY

V. Kuznetsov and S. Levyakov

Novosibirsk State Technical University, Novosibirsk, Russia

A new approach is proposed for formulating a triangular finite-element of the Kirchhoff-Love thin elastic shells undergoing arbitrarily large displacements and rotations. The starting point of the approach is to represent the strain energy of the shell as a function of the invariants of the strain and curvature-change tensors of the shell middle surface. Given elongations and curvature changes of any three fibers lying on the middle surface along three independent directions, one can readily calculate these invariants. For a triangular element, it is a natural choice to take the element sides as these fibers. Thus, the strain energy is written as (summation over $m=1,2,3$)

$$\begin{aligned} \Pi &= \frac{1}{2} \int_F B [I_\varepsilon^2 - 2(1-\nu)I_{\varepsilon\varepsilon}] dF + \frac{1}{2} \int_F D [I_\kappa^2 - 2(1-\nu)I_{\kappa\kappa}] dF, \\ I_\varepsilon &= \frac{1}{8F^2} (\varepsilon_m l_m^2 l^2 - 2\varepsilon_m l_m^4), \quad I_{\varepsilon\varepsilon} = \frac{1}{16F^2} [(\varepsilon_m l_m^2)^2 - 2\varepsilon_m^2 l_m^4], \\ I_\kappa &= \frac{1}{8F^2} (\kappa_m l_m^2 l^2 - 2\kappa_m l_m^4), \quad I_{\kappa\kappa} = \frac{1}{16F^2} [(\kappa_m l_m^2)^2 - 2\kappa_m^2 l_m^4], \\ B &= Eh/(1-\nu^2), \quad D = Bh^2/12, \quad F = \frac{1}{4} (l^4 - 2l_m^2 l_m^2)^{1/2}, \quad l^2 = l_m l_m. \end{aligned}$$

where E , ν , and h are Young's modulus, Poisson's ratio, and wall thickness of the shell, respectively, I_ε and $I_{\varepsilon\varepsilon}$ (I_κ and $I_{\kappa\kappa}$) are the first and second invariants of the strain (curvature-change) tensor of the middle surface, respectively, F is the area of the middle surface of the finite element, and l_m , ε_m , and κ_m are the length, strain, and curvature change of the m th element side, respectively.

Since the normal components ε_m and κ_m have clear physical meaning of normal elongation and normal curvature change, respectively, they can be approximated without using shape functions for the displacement fields over the element. Namely, the strain and curvature-change fields are obtained by superposing approximations of ε_m and κ_m for three independent directions. For this purpose, combinations of the beam solutions can be used.

The use of the invariants allows one to avoid constructing of the local coordinate systems related to finite elements, calculate the stiffness matrix of the finite element straightforwardly for the lengths of the element sides, simplify the formulation of the shell finite-element model, and reduce the computational work.

For the shell element presented, the question of description of finite rotations is solved by associating the element with a certain geometrical object called the kinematic group [1,2] that consists of the nodal position vectors and normal vectors to the shell middle surface and possesses the property of geometrical variability. The finite element-kinematic group association implies that the strains and curvature changes of an element are related to strain parameters that characterize changes in the kinematic group configuration.

An attempt is undertaken to improve nonlinear bending capabilities of the finite element by taking into account finite curvature changes within the element. To this end, the following assumptions are used:

(a) each side of the triangular element is a plane nearly circular curve which remains plane and nearly circular during the deformation;

(b) for each element side, the normal vector to the middle surface of the shell does not deviate from the curvature plane of this side;

(c) the strains of the element sides are constant.

It should be noted that the assumption (a) imposes no restriction on the magnitude of the curvature changes of the triangle sides. The assumption (c) implies that the strain-tensor components are constant within the element. It follows that the membrane behavior of the element is modeled in a simple manner and similar to that of the constant-strain triangle.

A three-node curved triangular element with five degrees of freedom per node (three translations of the node and two rotations of the normal vector to the middle surface) is developed. The accuracy of the shell element is studied using typical geometrically nonlinear benchmark problems of thin elastic plates and shells [3]. Numerical results obtained show that the finite element provides high accuracy and convergence rate with respect to the number of finite elements thus supporting the validity of underlying assumptions. The solutions presented are in good agreement with numerical data available in the literature. Namely, the element performs very well under pure bending loading conditions: it can be rolled up so that the mutual rotation of the normal vectors within the element can be as large as 90° .

References

- [1] V.V. Kuznetsov. Kinematic groups in solid mechanics with applications, in: Proc. 6th Conf. SSTA (Shell structures, Theory and Applications), Gdansk Technical University, 1998, 177–178.
- [2] V.V. Kuznetsov and S.V. Levyakov (1994). Kinematic groups and finite elements in deformable body mechanics, *Izv. Ross. Akad. Nauk Mekh. Tverd. Tela*, **29**, 67–82 (in Russian).
- [3] K.Y. Sze, X.H. Liu and S.H. Lo (2004). Popular benchmark problems for geometric nonlinear analysis of shells, *Finite Elements Anal. Des.*, **40**, 1551-1569.

SOME PROBLEMS CONCERNING THE DEFORMATION OF ANISOTROPIC COSSERAT ELASTIC SHELLS

M. Bîrsan

Department of Mathematics, "A.I. Cuza" University of Iași, Romania

1. Introduction

We investigate the deformation of loaded cylindrical anisotropic elastic shells, in the framework of the Cosserat theory. Within the linear theory, we approach the relaxed Saint–Venant’s problem and the problem of Truesdell.

The theory of Cosserat shells is an interesting approach to the mechanics of elastic shell–like bodies, in which the thin three–dimensional body is modelled as a two–dimensional continuum (i.e. a surface) endowed with a deformable director assigned to every point. For a detailed analysis of the theory of Cosserat surfaces and its relation with other shell theories, we refer to the classical monograph of Naghdi [1] and the modern book of Rubin [2].

Due to its importance in engineering, the Saint–Venant’s problem has been studied in many articles in the context of classical theories of shells or in the theory of Cosserat surfaces [3]. For isotropic and homogeneous Cosserat shells, the solution of Saint–Venant’s relaxed problem was given in [4].

In the present work, we consider anisotropic and inhomogeneous cylindrical Cosserat shells. The cylindrical surfaces can be open or closed, and the cross–section is not necessarily circular. We assume that the constitutive coefficients of the Cosserat shell are independent of the axial coordinate.

2. The relaxed Saint–Venant’s problem

For any Cosserat shell, we denote by \mathbf{r} and \mathbf{d} the position vector and the director assigned to every point of the deformed surface. Let \mathbf{R} and \mathbf{D} designate the position vector and the director fields associated to the reference configuration \mathcal{S} of the Cosserat surface. Then, the (infinitesimal) displacement \mathbf{u} and director displacement $\boldsymbol{\delta}$ are defined by

$$(1) \quad \mathbf{u} = \mathbf{r} - \mathbf{R}, \quad \boldsymbol{\delta} = \mathbf{d} - \mathbf{D}.$$

We consider that the reference configuration \mathcal{S} is a general cylindrical surface (open or closed), and we denote by z and s the axial coordinate and the circumferential coordinate on \mathcal{S} , respectively.

The well–known Saint–Venant’s problem consists in determining the equilibrium of such shells under the action of prescribed contact forces and contact director couples distributed over its end edges. In the relaxed formulation of this problem, we consider that the terminal loads are given in the form of the resultant forces and resultant moments acting on the end edges.

We determine a solution of the relaxed Saint–Venant’s problem for anisotropic Cosserat shells using the method established by Ieșan [5] in the context of three–dimensional elasticity. Our solution is presented in the form of the displacement field $v = (\mathbf{u}, \boldsymbol{\delta})$ and it is expressed in terms of the solutions to some auxiliary boundary–value problems for ordinary differential equations (called the cross–section plane problems).

In order to obtain the solution, we separate the relaxed Saint–Venant’s problem into two problems: (P_1) the extension–bending–torsion problem, and (P_2) the flexure problem.

First, we search for a solution $v = (\mathbf{u}, \boldsymbol{\delta})$ of the problem (P_1) such that $\partial v / \partial z$ is a rigid body displacement field of the Cosserat shell. As in the three–dimensional theory, this solution is determined in terms of four constants, say a_1 , a_2 , a_3 and a_4 , which can be interpreted as the global

measures of axial curvature, axial strain and twist. We denote the solution of the extension–bending–torsion problem by $v = v\{a_1, a_2, a_3, a_4\}$, indicating thus its dependence on the constants a_k .

For the flexure problem (P_2), we obtain a solution of the form

$$(2) \quad v = \int_0^z v\{b_1, b_2, b_3, b_4\} dz + v\{c_1, c_2, c_3, c_4\} + w(s),$$

where $\{b_1, b_2, b_3, b_4\}$ and $\{c_1, c_2, c_3, c_4\}$ are constants, while $w(s)$ is a displacement field depending only on s , which are determined in the paper.

3. Truesdell's problem

We notice that the solution obtained for the relaxed Saint–Venant's problem in the theory of Cosserat shells possesses some properties which are analogous to the characteristic properties of the classical Saint–Venant's solution for cylinders. For instance, we prove that our solutions can be characterized as minimizers of the strain energy on certain classes of solutions (in correlation with the corresponding three–dimensional results for cylinders, see e.g. [5, 6]).

Further, we extend this analogy and derive a solution for the problem of Truesdell for anisotropic cylindrical shells. In [7], Truesdell proposed the following problem for the torsion of elastic cylinders: to define the functional $\tau(\cdot)$ on the set of all solutions \mathbf{u} of the torsion problem, corresponding to a scalar torque \mathcal{M} , such that

$$(3) \quad \tau(\mathbf{u}) = -\frac{\mathcal{M}}{\mu D},$$

where μD is the torsional rigidity of the cylinder. Podio–Guidugli [8] rephrased the problem for extension and bending, while Ieşan [5] considered the flexure of elastic cylinders.

We present a solution of Truesdell's problem formulated for the extension–bending–torsion problem and for the flexure problem of anisotropic cylindrical shells.

Examples are given for orthotropic cylindrical shells and for the special case of Cosserat plates.

4. References

- [1] P.M. Naghdi (1972). *The Theory of Shells and Plates*, in: Handbuch der Physik, vol. VI a/2 (C. Truesdell, ed.), pp. 425–640, Springer–Verlag, Berlin.
- [2] M.B. Rubin (2000). *Cosserat Theories: Shells, Rods, and Points*, Kluwer Academic Publishers, Dordrecht.
- [3] J.L. Ericksen (1979). On St.Venant's problem for thin–walled tubes, *Arch. Rational Mech. Anal.*, **70**, 7–12.
- [4] M. Bîrsan (2004). The solution of Saint–Venant's problem in the theory of Cosserat shells, *J. Elasticity*, **74**, 185–214.
- [5] D. Ieşan (1987). *Saint–Venant's Problem*, Lecture Notes in Mathematics no. 1279, Springer Verlag, Berlin.
- [6] J.L. Ericksen (1980). On the status of St.Venant's solutions as minimizers of energy, *Int. J. Solids Struct.*, **16**, 195–198.
- [7] C. Truesdell (1978). Some challenges offered to analysis by rational thermomechanics., in: G.M. de la Penha and L.A. Medeiros (eds.), *Contemporary Developments in Continuum Mechanics and Partial Differential Equations*, North–Holland.
- [8] P. Podio–Guidugli (1983). St.Venant formulae for generalized St.Venant problems, *Arch. Rational Mech. Anal.*, **81**, 13–20.

DEVELOPMENT OF FORMING PROCESS OF THE MUFFLER TUBE FOR HEAVY EQUIPMENTS

K.T. Han¹ and Y. Jin²

¹ *School of Mechanical Engineering, Pukyong National University, Busan, Korea*

² *Graduate School, Pukyong National University, Busan, Korea*

1. Introduction

A muffler is an important part used to reduce noise and to purify exhaust gas in cars and heavy equipments. Recently there has been a growing interest in the design and manufacturing of the muffler tube due to the strict environment regulation. In this study, we analyzed the burr and deformation of product as shear clearance, punch radius and plate holder force. The part of tube, punch, and die shape are modeled using the commercial S/W, CATIA. In analysis, using one-fourth component of the punch and die, metal forming process is simulated and Cockcroft-Latham ductile fracture theory is used. Also we studied the tube deformation, stress on punch using finite element code, DEFORMTM-3D, and analyzed the results through the simulation.

The simulation results are reflected to the forming process design for the muffler tube.

2. Development of forming process of the muffler tube

In the perforating process, the die is inserted at the inside of the tube and the punch to be put to fixed arrangement operates to the vertical. Shearing process is processed in the part that the tube contacts with the punch. At this time we simulated by a proper shear clearance. Additional, in order to optimize the simulation, a plate holder and a punch radius will be applied in the perforating process.

Through the simulation results, the optimal metal forming process for the muffler tube will be developed.

3. Finite element analysis

Ductile fracture condition is adopted to investigate the shear plane formation process of the piercing part using finite element method. Cockroft proposed a growth model of pore and ductile fracture condition by the plastic deformation energy concept.

Solving the perforating process problem by three dimensional modeling instead of two dimensional analysis is used due to tube characteristics. In the analysis of three dimensional piercing process, the stress concentration occurred at edge level needing the mesh size to make smaller. Notably, it is modeled so that the observation of the part to be sheared is simple.

In the simulation, the stroke per step is defined as one-third of the minimum element size, the friction coefficient is chosen based on the recommendable value in DEFORMTM-3D, and the punch speed is according to the real speed in the factory.

The mesh conditions for modeling are shown in Table 1.

Number of Nodes	14839
Number of Elements	66434
Surface Polygons	13986
Min Element Size	0.09 mm
Max Element Size	0.3 mm

Table 1. Mesh conditions for modeling.

The simulation conditions are shown in Table 2.

	Clearance (mm)	Stroke (mm)	Plate holder force (N)	Punch radius (mm)
Case 1	0.08	3.6	Fixed	0
Case 2	0.08	3.6	1500	0
Case 3	0.04	3.6	1500	0.05

Table 2. Simulation conditions.

4. Simulation results and discussions

In order to testify the effect of plate holder and punch radius in the process of muffler tube, three cases of the one-fourth component muffler tubes are simulated in this paper.

Case 1 is the normal case with the fixed plate holder. In case 2 the plate holder force is exerted and in case 3 a punch radius is used to optimized the design. The punch load of Case 3 is smoother than Case 2, it means when the tube is being processed the vibration is slight. Case 3 is the best among these three cases because the burr is minimized and optimal shear section is obtained.

5. Conclusions

In this study, the conditions to decide the perforating process of the muffler tube for automobiles are studied using finite element analysis. The conclusions of this study obtained can be summarized as follows:

1. When the shear clearance is 0.04mm, the value of plate holder force is 250KN, the punch radius is 0.05mm, the burr is minimized and optimal shear section is obtained.
2. The plate holder can reduce the value of die load and extend the life of it.
3. The punch radius can make the punch load smoother and reduce the value of damage, it results the process stable.
4. The analysis results by FEM are reflected in the perforating process design for the muffler tube and better products in dimension and quality are obtained.

6. References

- [1] Scientific Forming Technologies Corporation (1995). *DEFORMTM-3D User 's Manual*.
- [2] S. Kobayashi, S.I. Oh and T. Altan (1989). *Metal forming and the finite element method, Oxford University Press*.
- [3] T.C. Lee, I. C. Chan and P. F. Zheng (1997). Application of the finite element deformation method in the fine blanking process, *J. Materials Process. Tech.*, **63**, 744~749.
- [4] M. G. Cockcroft and D. J. Latham(1968). Ductility and the workability of metals, *J. Inst. Metals.*, **12**, 33~39.

COMPARISON OF NON-LINEAR STATICAL ANALYSIS OF TRUSS WITH LINEAR AND ROTATIONAL SIDE SUPPORTS AND 3D ROOF MODEL

P. Iwicki

Gdańsk University of Technology, Gdańsk, Poland

1. Introduction

The present research is devoted to study lateral buckling of truss with linear and rotational elastic side-supports. In the paper geometrically non-linear analysis of example truss with linear and rotational elastic side supports is compared with geometrically non-linear analysis of part of the roof construction with purlins and truss-bracing. The problem of bracing stiffness required to provide lateral stability of compression members is present in design codes [1], [2]. To the best of the author knowledge similar problem for trusses with elastic side supports have been investigated only in few studies as for example in experimental investigations [1] or in studies [4], [5].

2. Model description

In the present parametric study a roof truss shown in *Fig. 1* is considered. The height of the truss in the middle is 1.61 m and 0.9 m near supports. The truss is made of steel of $f_d = 305$ MPa. The connections between truss elements are stiff. It is assumed that the load is applied in the top chord joints. The top chord is laterally braced every 2.4m in joints by linear and rotational elastic side – supports and built-up top chord section is battened every 0.6m. The compressed chord of the truss is sized according code [1] for design value of axial force 700 kN, and the plastic resistance to normal force is 945 kN. The stiffness of linear elastic side supports is 50-1000 kN/m. The range of stiffness of supports has been approximated according codes [1], [2] as relation between force and limited support displacement. The stiffness of rotational side-supports is 20 kNm/deg. The part of the roof with truss bracing and purlins is also considered. The case of stiff and hinged truss-purlin connection is considered. It was assumed that upper and lower truss chord are bent in out of truss plane direction, and that the shape of imperfection is parabolic with maximal value of $L/500$, opposite in upper and lower truss chord.

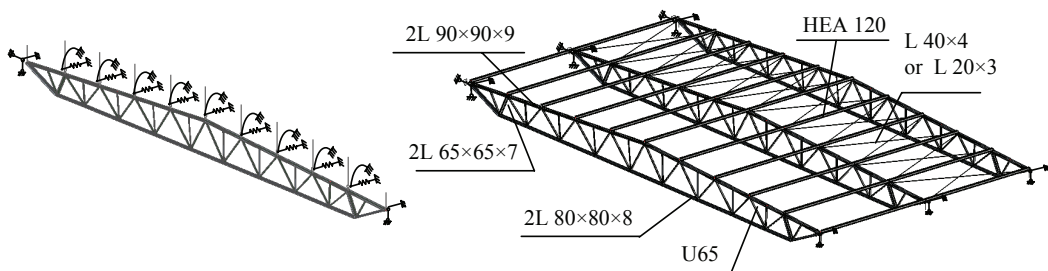


Figure 1. Truss with linear and rotational elastic side – supports and part of roof construction.

3. Results of numerical simulations, conclusions

For different stiffness of side-supports a non linear relation between normal force in compressed chord due to out of truss plane displacement has been calculated (*Fig. 2*). The limit normal force increases with increase of side support stiffness. For all of considered stiffness of linear supports excepting 50 kN/m the limit normal force of truss chord is greater than design value

of normal force. The additional rotational supports causes about 77% increase of limit normal force for support of stiffness 50 kN/m and about 20% for supports of stiffness 1000 kN/m. In the case of roof model with purlins and truss bracing, increase of limit normal force caused by stiff connection between truss and purlin is 87% for bracing of L20×3 and 104% for L40×4. Moment in rotational supports is lower than bending design moment of purlins, caused by typical gravity loads, so it is possible to consider purlins as rotational supports of the truss on condition that the connectors between the purlins and the truss are designed to carry arising moment.

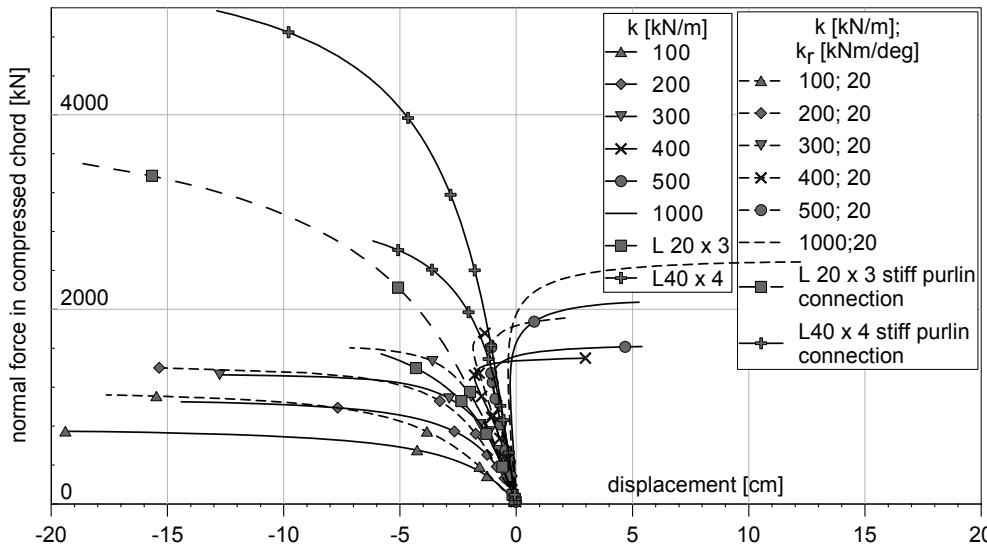


Fig.2. Normal force in compressed chord due to out of plane displacement for different stiffness of side supports

For all of side support stiffness, excepting truss bracing of L40×4 with stiff truss-purlin connection, the buckling length related to side – support distance is greater than value of relative buckling length described in code [1], so code [1] requirements are not precise and in fact predict higher critical force in compressed chord than calculated in example truss.

Relation between side supports reaction and normal force in compressed chord is non-linear. For force level corresponding to design load of the truss side support reaction is about two times lower than described by code [1].

6. References

- [1] PN-90/B-03200, *Steel structures, Design rules*.
- [2] Eurocode 3 (1992), *Design of steel structures. Part 1.1: General rules and rules for buildings*. ENV 1993-1-1, CEN.
- [3] J. Kołodziej and J. Jankowska-Sandberg (2006). Experimental research of lateral buckling of a steel truss considering the elasticity of the relevant stiffeners. *Zeszyty Naukowe Politechniki Gdańskiej 601*, **58**, 123-130.
- [4] P. Iwicki (2007), Stability of trusses with linear elastic side-supports, *Thin-Walled Structures* **45**, 849–854.
- [5] A. Biegus and D. Wojcyszyn (2004). Buckling length of chords out of the truss plane. *Inżynieria i Budownictwo II*, 607-610.
- [6] ROBOT (2007). *Millennium user's manual*. Version 20.0. Robobat.

RAISING OF A SEMI-CIRCULAR VAULT

A.V. Manzhurov and D.A. Parshin

Institute for Problems in Mechanics of Russian Academy of Sciences, Moscow, Russia

The aim of this paper is to obtain a solution of the following engineering problem: to construct a heavy circular vault on a smooth rigid horizontal base by layerwise accretion along the internal surface of an initial arc-shaped structure (see Fig.). It is assumed that the fixation of the vault to the base prevents its separation but allows for free sliding. The case under consideration is that of plane strain. The material is assumed isotropic, uniformly aging, and elastic or viscoelastic. Presented research results are based on the ideas of growing solids mechanics and mathematical theory of accreted solids (see, e.g., [1–8]).

Initial boundary value problems are formulated, in order to describe quasi-static deformation of this structure subject to its own weight combined with an arbitrary variable load on its external surface prior to, during, and after the process of its piecewise continuous accretion. These problems take into account the possibility of using prestressed structural elements in the process of accretion. For these problems analytical solutions are constructed in terms of series and quadratures. Numerical calculations are demonstrated by results obtained for various problems connected with different types and modes of raising of thin-walled and thick-walled vaults made of thin-walled elements, as well as the reinforcement of initially thick-walled vaults. It is shown that the stress-strain state of raised heavy objects essentially depends on the technique and the regime of their construction, and that the characteristics of their stress state in the process of construction may attain values that greatly exceed those at the end on this process.

The effect of creep, aging, and material weight on the deformation of a heavy vault under accretion by stress-free structural elements is studied. We single out and analyze the main tendencies whose continuous interaction determines the stress-strain state formation in the object being accreted. From the standpoint of these tendencies, some limiting regimes of accretion are considered.

Thus, if the accretion of a vault is fairly fast, a very strong load-relief is observed in its original part. However, on the initial stage of this accretion process, the vault experiences stresses that greatly exceed the original ones. In the case of a thin-walled original arc, the difference between these stresses is substantial. However, if the accretion process is slow then the material added on the final stage remains practically stress-free. In this situation, the stress level in the original part of the structure becomes much greater than the initial one. If the original arc is sufficiently thin, it is subject to very high stresses at the initial instant, and therefore, the final structure will have regions with stress levels greatly exceeding the maximal level calculated on the basis of the final configuration.

Therefore, if one fails to take into account gravity forces during the entire process of raising a heavy object, one may come to an entirely wrong picture of its current and its final state, in particular, one may obtain greatly overestimated values for the strength and the operational bearing capacity of the structure.

It is shown that for a gradually accreted vault on a sufficiently thick original arc, the final structure may have much smaller stresses than those calculated for a ready-made structure immediately installed on the base. For a vault with a thin original arc, it has been shown that if one varies the accretion rate in a suitable manner, the stresses in the final structure can be substantially decreased

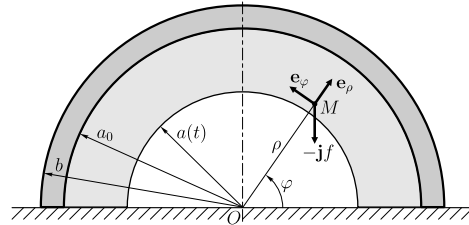


Figure. Semi-circular vault under accretion

relative to the initial state of the original arc, so that the admissible stress values in the accretion process are never achieved.

In the course of these investigations, it was found that even a fairly thick-walled original arc, being installed on a smooth base, tends to separate from the base in peripheral regions of its bottom due to its own weight. Without taking some special measures, it is impossible to get rid of these regions of separating (negative) contact stresses by subsequent reinforcement of such an arc.

Another problem under investigation is that of accretion of a vault using prestressed elements. For a vault accreted in this way, it is also impossible to ensure forces that would permanently prevent separation of the vault from the base. However, using layerwise accretion with suitable initial stresses, one can ensure a much better resulting stress state in the total structure than in the case of accretion by stress-free elements, i.e., one can minimize negative pressure on the base and the general stress level in the body.

One also considers an accretion process in which the vault vertex is fixed by suspension with controllable tension that compensates a given part of the current weight of the vault and vanishes at the end of the process. This technique leads to substantially smaller stresses in the final structure than those obtained by common accretion in the same temporal regime. In this case, it is also possible to obtain a much better final contact stress diagram than that for a ready-made vault installed on the same base. If, in addition to suspension, the elements used for accretion are subject to some initial extension, then it is even possible to construct a thin-walled vault that will exert positive pressure at all points of the base.

This research was financially supported by the Russian Foundation for Basic Research (grants Nos. 08-01-00553, 08-01-91302-IND, , and 06-01-00521), and by the Basic Research Program No. 13 of the Department of Power Engineering, Mechanical Engineering, Mechanics, and Control Processes of the Russian Academy of Sciences.

- [1] N.Kh. Arutyunyan, A.V. Manzhairov, and V.E. Naumov (1991). *Contact Problems in Mechanics of Growing Bodies*. Nauka, Moscow.
- [2] A.V. Manzhairov (1995). General noninertial initial-boundary value problem for a viscoelastic aging solid under piecewise continuous accretion, *PMM [Applied Mathematics and Mechanics]*, **59** (5), 836–848.
- [3] N.Kh. Arutyunyan and A.V. Manzhairov (1999). *Contact Problems in the Theory of Creep* [in Russian]. Izd-vo NAN RA, Yerevan.
- [4] A.V. Manzhairov and M.N. Mikhin (2004). Methods of the theory of functions of a complex variable in growing solids mechanics, *Vestnik Samarsk. Un-ta. Estestvennonauch. Ser.*, **4** (34), 82–98.
- [5] A.V. Manzhairov and D.A. Parshin (2006). Accretion of a viscoelastic ball in a centrally symmetric force field, *Mech. Solids*, **41** (1), 51–64.
- [6] A.V. Manzhairov and D.A. Parshin (2006). Accretion of solids under mass forces, *Proceedings, Indo-Russian workshop on Problems in Nonlinear Mechanics of Solids with Large Deformation, IIT Delhi, November 22–24, 2006*, IIT Delhi, New Delhi, 71–79.
- [7] A.V. Manzhairov and D.A. Parshin (2006). Modeling the accretion of cylindrical solids on a rotating mandrel with centrifugal forces taken into account, *Mech. Solids*, **41** (6), 121–134.
- [8] A.V. Manzhairov and D.A. Parshin (2007). Modeling of the deformation process of accreted conic solids, *Vestnik Samarsk. Un-ta. Estestvennonauch. Ser.*, **4** (54), 290–303.

GENERALIZED FORMULATION OF EIGENVALUE PROBLEM FOR NONLINEAR STABILITY ANALYSIS

T. Sokół

Warsaw University of Technology, Faculty of Civil Engineering, Warsaw, Poland

1. Introduction

Stability is one of the most important fields in structural designing, especially for slender and lightweight structures. The overall capacity of such structures is often limited by critical load connected with buckling or snapping instability. Calculation of critical load may be carried out in different ways. One of the most popular approaches is based on a so called initial or linearized stability and consists in solving eigenvalue problem. This classical approach is well known and was introduced in many finite element programs. Unfortunately the accuracy of solution obtained in this way may be very poor if the pre-critical behaviour of the structure is highly nonlinear. The paper presents a more flexible method for estimating of critical load based on the generalized parameterization and formulation of eigenvalue problem.

2. Generalized eigenvalue problem

Detection and calculation of critical point may be carried out using different methods [1-2]. First of all, one can distinguish “exact” methods based on “true” nonlinear equilibrium equations, from approximate methods based on some simplifications, i.e. artificial linearization of the problem. The first family of methods is especially useful as an additional tool for path following and continuation process. Precise estimation of critical load may be achieved in direct or indirect way [1]. The second family of methods enables prediction of critical load in advance (extrapolation), with or without evaluation of intermediate points on the equilibrium path. The most representative and commonly used method of this family is connected with so-called *initial buckling* eigenproblem, described as follows:

$$(1) \quad (\mathbf{K}_0 + \lambda \mathbf{K}_g) \mathbf{v} = 0$$

\mathbf{K}_0 and \mathbf{K}_g are matrices of initial and geometric stiffness respectively [3]. The solution to the above eigenproblem enables to establish both critical loads and corresponding buckling modes; however (as was stated above) the accuracy of critical load predicted in this way may be very poor. The paper discusses successive improvements to the above approach. The final conclusion of the investigation leads to the following generalized eigenvalue problem:

$$(2) \quad \left[\mathbf{K}(\eta_0) + \Delta \mathbf{K}(\eta_0) \frac{(\eta - \eta_0)}{\Delta \eta} \right] \mathbf{v} = \mathbf{0}$$

in which the consistent tangent stiffness matrix \mathbf{K} is calculated in two successive points on the equilibrium path. Contrary to classical approach, \mathbf{K} is parameterized here in different way (λ is not proper parameter in the vicinity of limit point hence the tangent stiffness matrix can not be treated as the function $\mathbf{K}(\lambda)$). Above parameterization may be based on “leading” displacement or the arc-length method.

3. Example

Consider well known von Mises truss shown in Fig. 1. The nonlinear behaviour of this structure is described by the equilibrium path shown in Fig. 2. For simplicity, the calculations were carried out

for $a = b = 1$ and $EA = 1$. Comparison of accuracy of predicted critical load using different methods is included in Tab. 1. The first column describes the applied method, starting parameter (λ_0 or η_0) and its increment. Two next columns include critical displacement (v_{cr}) and load (P_{cr}). The ratio and relative error of critical load is presented in two last columns. The table clearly shows the great improvement of accuracy using proposed approach. Contrary to classical methods the estimation is now understated (safer). More complex examples, including structures exhibiting buckling mode interaction [2], and more detailed discussion of the results will be presented in the full paper.

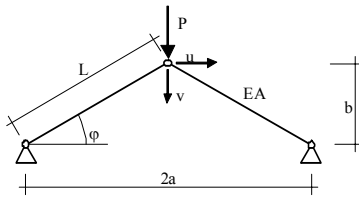


Fig. 1. Mises truss.

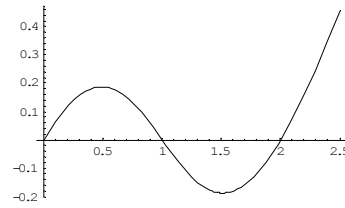


Fig. 2. Equilibrium path.

Method	v_{cr}	P_{cr}	P_{cr}/P^*	error
Exact (v^* , P^*)	0.490175	0.187403	-	-
Initial BP	-	1.414210	7.55	654.6%
Linearized BP	-	0.471405	2.52	151.5%
Quadratic BP	-	0.291344	1.55	55.5%
ULSP 0+0.1	-	0.363021	1.94	93.7%
ULSP 0.10+0.01	-	0.289520	1.54	54.5%
ULSP 0.18+.005	-	0.191697	1.02	2.3%
GSP 0+0.1	0.619114	0.173228	0.92	-7.6%
GSP 0.1+0.1	0.552731	0.184047	0.98	-1.8%
GSP 0.3+0.1	0.494929	0.187384	1.00	-0.01%
GSP 0.4+0.1	0.490080	0.187403	1.00	-4.1e-8

Tab. 1. Comparison of accuracy of critical load for different methods.

4. Conclusions

The paper has discussed different approaches for calculation of critical load. Successive improvements to the original eigenproblem describing initial buckling have been studied. The result of presented investigations is the method for estimation of critical load without complete (and time consuming) determination of equilibrium path. The numerical examples have proved its high efficiency. It may successfully be applied both in bifurcation and load limit points. It also enables early prediction of multiple critical points.

5. References

- [1] R. Seydel (1988). From equilibrium to chaos: practical bifurcation and stability analysis, Elsevier, New York.
- [2] T. Sokol (2006). On the improved predictors for compound branching problem, *First SEECCM-06*, Kragujevac, Serbia and Montenegro, vol. "Solid Mechanics", 290-296.
- [3] Z. Waszczyszyn, C. Cichoń and M. Radwańska (1994), *Stability of Structures by Finite Element Method*, Elsevier, Amsterdam.

EXPERIMENTAL INVESTIGATION OF COMPONENTS FOR FASTENING THE RAILS

J. Melcer

University of Žilina, Faculty of Civil Engineering, Slovak Republic

1. Introduction

The submitted paper is dedicated to the modelling in laboratory the operating conditions to which the tension clamps and the track panels are subjected during the operation. EWEM tension clamps are the topic of the analysis, Fig. 1. Within the installation the tension clamp is stressed, the pressing arm is picked up in vertical direction and the tension clamp starts to press on the foot of rail with the pressing force proportional to the picking up of the pressing arm. During a transport of track panels the tension clamps are stressed with additional forces from the gravity of hanging sleepers and from the inertial forces arising due to oscillating motion of track panels. The tension clamp acts as a linear element only to the certain value of picking up of the pressing arm. After the crossing of the limit value of picking up the plastic deformations come into existence. The tension clamp is weakened in this stage because of its ability to activate pressing force is reduced proportionally to the value of the permanent irreversible deformation. It was the reason for modelling in laboratory the operating conditions to which the tension clamps and the track panels are subjected during the operation. In such a way it is possible to determine the limit value of the picking up and to estimate the conditions of overloading the tension clamp and to predict its behaviour in real conditions.



Fig.1 EWEM tension clamp

2. Static and dynamic test

The set of 16 tension clamps were tested in static and dynamic load regime. The stiffness characteristics described the dependence of acting pressed force versus deformation of a clamp have been the subject of static tests. Except of static test the part of a rail was subjected to the dynamic cyclic load simulating the three years operation in real conditions, Fig. 2.



Fig. 2 Dynamical experimental testing

After the dynamic test the static test was carried out again. The influence of dynamic loading on the degradation of mechanical properties was estimated. Also the influence of additional load by the gravity forces and the inertial forces within oscillation of track panels during transport was modelled in laboratory conditions, Fig. 3. All influences were estimated and recommendations for praxis were yielded.

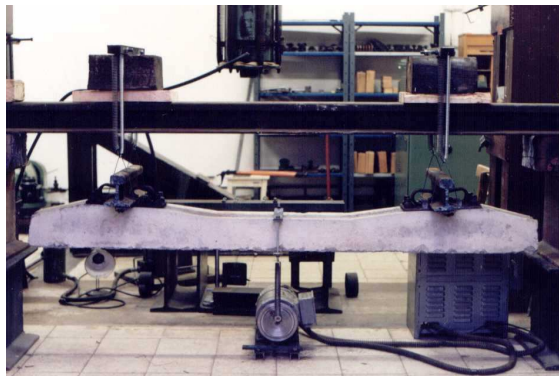


Fig. 3 Experimental modelling of additional load

3. References

- [1] Kuchárová D.: Experimental Estimation of rail response on the effect of moving vehicles. *Proceedings of the 37th International Conference on Experimental Analysis of Stress – EAN'99*, Frenštát p. Radhoštem, 1.-3-6-1999, p.91-94.
- [2] Melcer, J.: Experimental modelling of dynamic additional load of tension clamps used for fastening the rails. *Proceedings of the 39th International Conference on Experimental Stress Analysis 2001*. June 4-6, 2001, Tabor, Czech Republic, Czech Technical University, Prague, 2001, p.221-224.

SHAKING TABLE EXPERIMENTAL STUDY ON STRUCTURAL POUNDING DURING EARTHQUAKES

R. Jankowski

Gdańsk University of Technology, Gdańsk, Poland

1. Introduction

Earthquake-induced pounding between insufficiently separated buildings or bridge segments may result in some local damage at the contact points during moderate earthquakes [1] or may lead to collapse of structures during severe ground motions [2]. Structural pounding has been recently intensively studied numerically (see, for example, [3,4]). On the contrary to numerical analyses, only few experimental studies have been conducted concerning mainly the validation of the numerical models (see [5]). Therefore, the aim of the present paper is to show the results of more extensive experimental study performed on a shaking table using models of two towers equipped with colliding elements made of different building materials.

2. Setup of the experiment

A small shaking table (see Figure 1) located at the Gdańsk University of Technology was used in the experimental study. It is a unidirectional device with the platform dimensions of 0.75×0.6 m excited by the linear actuator with the stroke of 0.5 m and maximum acceleration of 10 m/s^2 . Two 1 m high model towers with different dynamic properties (see Figure 1) were built to be tested during the experiment. Each of them was constructed from four steel columns with the mid-height horizontal connections and additional skew bracings to prevent transverse as well as torsional vibrations. All elements used in the left tower had the rectangular cross section of 6×6 mm, whereas the right tower was constructed from members with the section of 8×8 mm. Additional plates made of different building materials, i.e. concrete, steel and timber were fixed at the top of each tower in order to study the pounding-involved structural response due to impacts between various materials. The top mass of the towers was kept constant for all experimental tests, apart from the material used.

3. Results of the study

The experimental study was conducted under the NS component of the El Centro earthquake (18 May 1940) for different gap size values between the towers. In this paper, the examples of the results for the gap size of 0.04 m are presented. The displacement time histories of the towers for concrete-to-concrete, steel-to-steel and timber-to-timber pounding are shown in Figure 2a, 2b and 2c, respectively. For the purposes of comparison, the displacement time histories for the independent vibrations of the towers are also presented in Figure 2d.



Figure 1. Setup of the shaking table experiment.

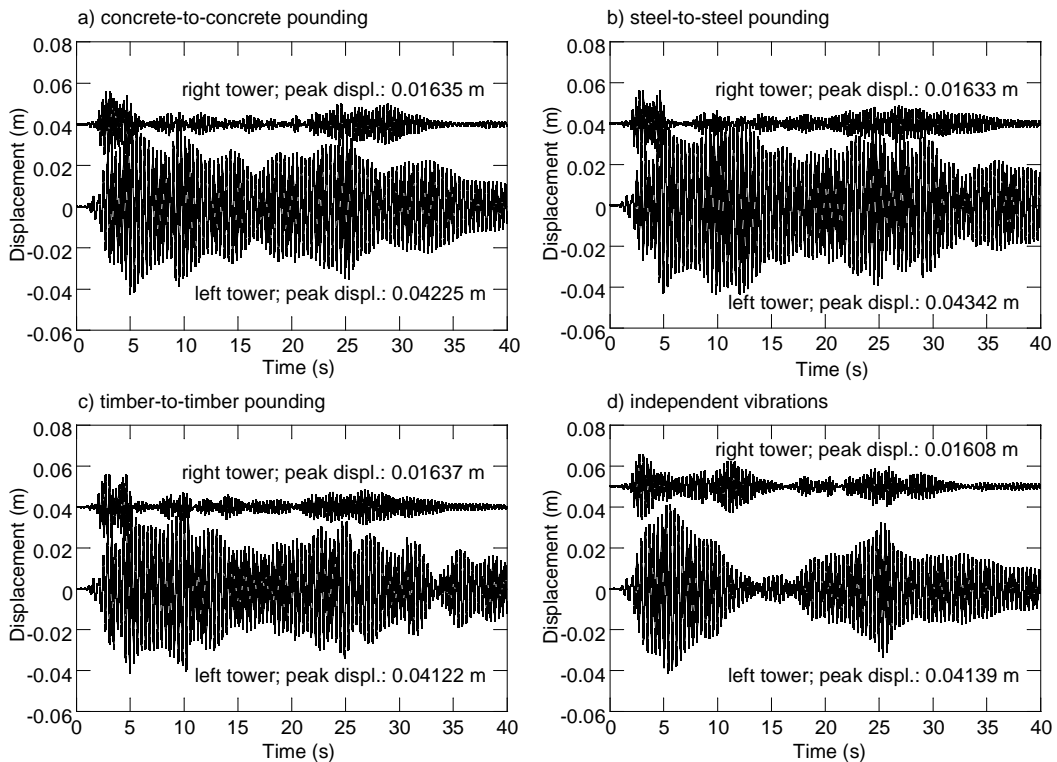


Figure 2. Displacement time histories of towers under the El Centro earthquake.

4. Conclusions

The results of the experimental study show that pounding may result in substantial increase of the structural response; however, it can also play a positive role by reducing vibrations (see reduction of the peak displacement for the left tower on Figure 2c). Moreover, the results show the considerable influence of the type of material used for colliding elements on the behaviour of structures during earthquakes.

The study described in this paper was performed using relatively small structural models. Therefore, further experimental study is planned to be conducted on larger models of real structures in order to verify the results obtained.

5. References

- [1] Z. Zembaty, A. Cholewicki, R. Jankowski and J. Szulc (2005). Earthquakes of September 21, 2004 in north-eastern Poland and their effects on structures, *Inżynieria i Budownictwo*, **1/2005**, 3-9, (in Polish).
- [2] K. Kasai and B.F. Maison (1997). Building pounding damage during the 1989 Loma Prieta earthquake, *Engineering Structures*, **19**, 195-207.
- [3] R. Jankowski (2005). Non-linear viscoelastic modelling of earthquake-induced structural pounding, *Earthquake Engineering and Structural Dynamics*, **34**, 595–611.
- [4] R. Jankowski (2006). Pounding force response spectrum under earthquake excitation. *Engineering Structures*, **28**, 1149–1161.
- [5] K.T. Chau, X.X. Wei, X. Guo and C.Y. Shen (2003). Experimental and theoretical simulations of seismic poundings between two adjacent structures, *Earthquake Engineering and Structural Dynamics*, **32**, 537-554.

PREFABRICATED STRUCTURES UNDER EARTHQUAKE EXCITATION: DAMAGE AND FAILURE OF CONNECTION JOINTS

P.H. Piotrowski^{1,2}, R. Jankowski¹

¹ *Gdańsk University of Technology, Gdańsk, Poland*

² *Ergon Poland*

1. Introduction

Prefabricated structures became more and more popular in European countries, including Poland. Many systems used in prefabrication are simply taken from countries with low seismicity, such as Finland or Belgium, and thus are not designed and tested under earthquake excitation. Although there are some recent records of earthquake activity in Poland [1], the strengthening of this type of structures is crucial when constructing in seismic countries, like Slovakia or Romania.

It has been shown, that damage of prefabricated structures during recent earthquakes is usually caused by insufficient connection strength [2]. Many of the structures have been heavily damaged, some of them completely destroyed, showing urgent necessity of further research. Therefore, the aim of this paper is to test an example of a prefabricated structure undergoing strong ground motions, and thus to prepare background for planned laboratory experiments and simulations.

2. Numerical model

The investigation has been focused on the weak points of the beam-to-column connections (see Fig.1). As the example, the behaviour of frame of 2-storey frame building with pinned beam-column connection (see Fig. 2) under the El Centro earthquake (1940) has been simulated with ABAQUS commercial software. The non-linear analysis has been conducted, which has been proven to be essential when the structural response under earthquake excitation is investigated (see, for example, [3]). In the study, the behaviour of concrete has been modelled using damaged plasticity model (see [4,5]). Reinforcement has been modelled using layered material with rebar elements embedded into concrete. A non-linear (elastoplastic) strain-hardening model has been used to simulate the reinforcing steel behaviour. All structural members have been modelled by multi-layer shell elements with multiple integration points through the thickness.

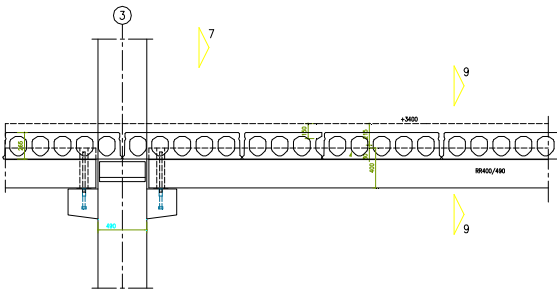


Fig. 1. Example of connection used by Ergon Company in the regions with low seismicity

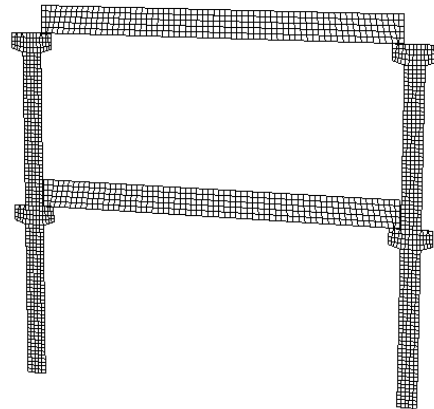


Fig. 2. FEM model of the structure

3. Response analysis

The results of the preliminary analysis in the form of stress distribution in connecting bar are shown in Fig. 3. It can be seen from the figure that failure of the structure is due to plastic flow of the connecting bars. It should be mentioned that, in the connection, neoprene bearing carries mainly compression (vertical) forces, whereas horizontal loads are acting on steel bars, which are rigidly connected with corbel and beam.

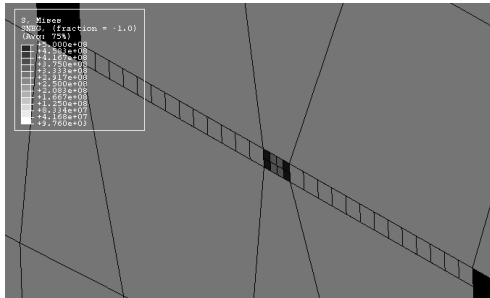


Fig. 3. Stress distribution
in connecting steel bar

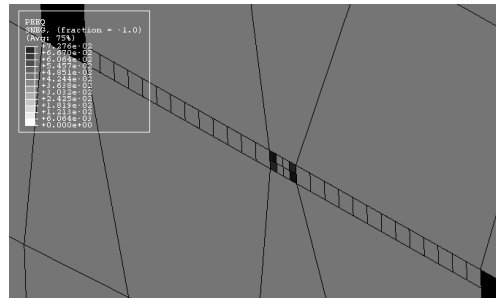


Fig. 4 Equivalent plastic strain
in connecting steel bar

4. Conclusions

The stresses in the connection between beam and column due to earthquake excitation have been assessed in this paper. The non-linear analysis has been conducted in order to enhance the accuracy of the study. The results show the need of changes in the investigated part of the structure in order to make it earthquake-resistant. Further numerical simulations and experimental studies are planned to be conducted so as to adapt the system to meet earthquake reliability.

5. Acknowledgements

The research described in this paper has been supported by Ergon Poland. This support is greatly acknowledged.

6. References

- [1] Z. Zembaty, A. Cholewicki, R. Jankowski and J. Szulc (2005). Earthquakes of September 21, 2004 in north-eastern Poland and their effects on structures, *Inżynieria i Budownictwo*, **1/2005**, 3-9 (in Polish).
- [2] M.H. Arslan, H.H. Korkmaz, F.G. Gulay (2006). Damage and failure pattern of prefabricated structures after major earthquakes in Turkey and shortfalls of the Turkish Earthquake code, *Eng. Failure Analysis*, **13**, 537-557.
- [3] R. Jankowski (2007). Assessment of damage due to earthquake-induced pounding between the main building and the stairway tower, *Key Eng. Materials*, **347**, 339-344.
- [4] J. Lubliner, J. Oliver, S. Oller, E. Oñate (1989). A plastic-damage model for concrete, *Int. J. Solids Structures*, **25**, 299-326.
- [5] J. Lee, G.L. Fenves (1998). Plastic-damage model for cyclic loading of concrete structures, *J. Eng. Mech.*, **124**, 892-900.

A HYBRID CONTINUOUS-DISCRETE APPROACH TO LARGE DISCRETE STRUCTURAL OPTIMIZATION PROBLEMS

B. Błachowski¹, W. Gutkowski²

¹ *Institute of Fundamental Technological Research, Warsaw, Poland*

² *Institute for Mechanized Construction and Rock Mining, Warsaw, Poland*

1. Introduction

Engineering systems are often composed of prefabricated elements, parameters of which are listed in professional catalogues. In the case of structural design, the catalogue is in the form of a list of available rolled profiles. The minimum weight structural design consist then in assigning to all structural members elements from the catalogue, assuring fulfilments of imposed constraints. Such a process is known as Discrete Structural Optimization (DSO). The difficulties arising in DSO come from relatively large numbers of combinations between obtained from both numbers of structural members and available parameters. These numbers can reach values of more than 10^{10} . This makes impossible to find a minimum just from a direct enumeration.

The first attempts to solve Discrete Structural Optimization were made in 1960s and 1970s. In the beginning of 1980s several stochastic approaches were applied in DSO. Most known are: Genetic Algorithm; Simulated Annealing; Evolutionary Optimization. Recently, other stochastic methods based on Particle Swarm optimization by Kitayama et al.[1] and Harmony Search by Lee et al. [2] has been applied to DSO.

The concept of controlled discrete optimization was proposed in earlier authors papers. Gutkowski proposed a controlled mutation consisting in verification of stresses at each generation of the evolutionary optimization algorithm. Also, by Gutkowski et al.[3], a control of stresses was applied in an algorithm in which redundant material is removed in elements with least stresses. This approach was then applied by Guerlement et al. [4] DSO, taking in to account EC codes.

In this study, the idea of removing redundant material is enhanced by combining the continuous and discrete solutions. At the end of the paper, several numerical examples, with numbers of combinations up to 30^8 are presented and their effectiveness is validated.

2. Formulation of the problem

The structure under consideration is of a given topology and composed of j_0 elements, which are taken from a list of available parameters as: thickness of a metal sheet h , cross section areas (CSA) A and/or moments of inertia I of a beam. Each j -th member having CSA A_j is made of linear elastic material. Small displacements and stresses within elastic range are assumed for the whole structure. The structure is subjected to q_0 multiple static loads.

The governing equations, and in the same time equality constraints, for the problem, applying Finite Element Method (FEM), are:

$$\mathbf{K}\mathbf{u}_q - \mathbf{Q}_q = \mathbf{0} \quad \text{where } q = 1; 2; \dots; q_0$$

$$\mathbf{K} - \text{stiffness matrix, } \mathbf{u}_q - \text{displacement, } \mathbf{Q}_q - \text{under } q \text{ load}$$

Inequality constraints, are imposed on:

- the largest and smallest values of listed parameters as $A_{min} \leq A \leq A_{max}$
- the maximum stresses and displacements σ_0, u_0

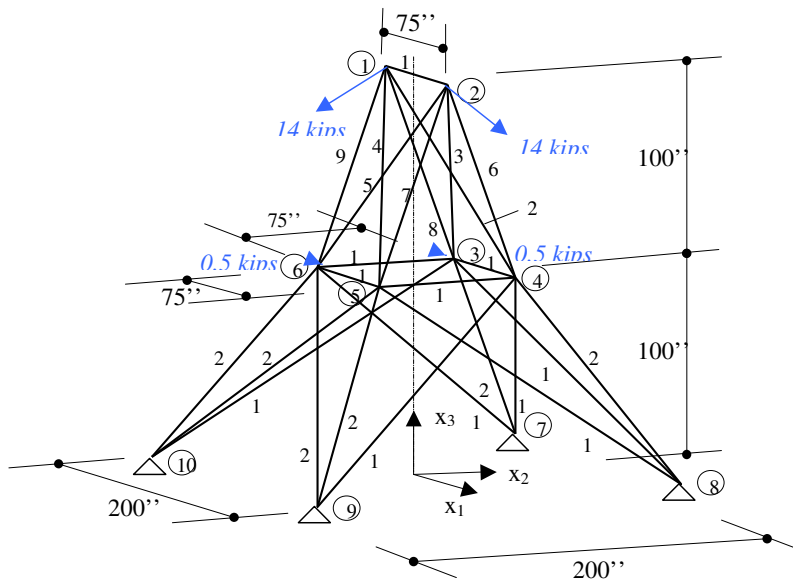
3. The outline of the hybrid method

A design of a structure (truss, frame, plates with reinforcements) has to be accomplished from a given catalogue of prefabricated elements, say rolled profiles. The design starts by finding the continuous structural optimization problem for the discussed structure, under given load and

subjected to assumed constraints. Next, a catalogue, separately for each structural member is constructed. Two parameters from the catalogue are assigned to the member. One, larger than the continuous value and one smaller. Now, a discrete solution removing redundant material is obtained. The second step consists in enlarging catalogues for all members to two larger, and two smaller values from the obtained discrete solution in the first step. Again, the discrete solution for such a set of values is obtained. The procedure of enlarging the catalogue is ended when in two successive steps the discrete solution are the same.

4. Numerical examples

In order to illustrate applicability of the method, a 25 transmission tower with 30^8 combinations, was analyzed. After calculations, it was observed that presented algorithm requires 100 FEM analyses, while for the same structure Evolutionary Optimization needs 10^4 FEM analyses.



5. References

- [1] Kitayama, S., Arakawa, M., Yamazaki, K., Penalty function approach for the mixed discrete nonlinear problems by particle swarm optimization, *Struct Multidisc Optim*, 2006, **32**(3) 191-202.
- [2] Lee, K.S., Geem, Z.W., Lee, S., Bae, K.W., The harmony search heuristic algorithm for discrete structural optimization, *Engineering Optimization*, 2005, **37**(7), 663-684.
- [3] Gutkowski, W., Bauer, J. and Zawidzka, J., An effective method for discrete structural optimization. *Engineering Computations*, 2000, **17**(4), 417-426.
- [4] Guerlement, G., Gutkowski, W., Targowski, R., Zawidzka, J., Zawidzki, J., Discrete minimum weight design of steel structures using EC3 code, *Struct Multidisc Optim*, 2001 **22**, 322 – 327.

OPTIMAL FIBERS ARRANGEMENT IN SINGLE- AND MULTILAYERED COMPOSITE MATERIALS

K. Dems and J. Wiśniewski
Łódź Technical University, Łódź, Poland

1. Introduction

The present paper constitutes the results of further investigation in the area of designing structural components made of fibre-reinforced composite materials (cf. Ref.[1-3]).

To fulfil the assumed properties of a composite structure one can modify some its structural parameters, such as mechanical properties of a matrix and fibres, fibre density, shape and arrangement of fibres etc. However, as shown in previous research, the full advantages of composite materials are obtained when the reinforcing fibres are optimally distributed and oriented or shaped in the matrix with respect to assumed objective behavioural measure under actual loading conditions of the structure. It is important particularly when the unique or important from behavioural point of view structures are considered.

The stiffness and stress optimization of fibre-reinforced composite materials is performed with the aid a hybrid evolution-gradient oriented algorithm. Such algorithm can serve as an alternative technique to classic methods applied in the optimal design of a structure made of fibre-reinforced single- or multilayered composite materials.

2. Object of analysis

A thin, two-dimensional and linearly elastic disk, made of multilayered composite material, is supported on the boundary portion S_U with prescribed displacement \mathbf{u}^0 and loaded by body forces \mathbf{f}^0 within domain its A and by external traction \mathbf{T}^0 acting along the boundary portion S_T , cf. Fig.1.

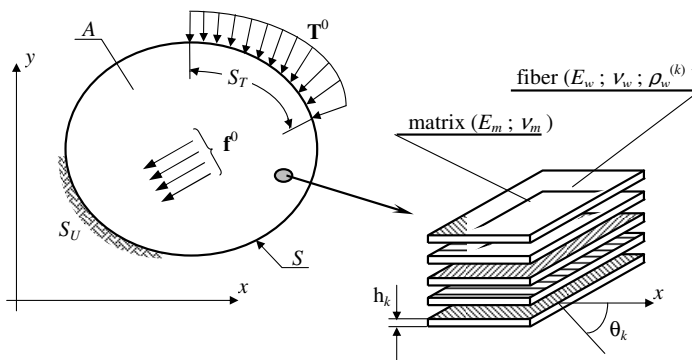


Figure 1: Two-dimensional composite disk subjected to service loading

The material of each layer is a composite made of a matrix reinforced with a ply of long and arbitrary shaped unidirectional fibres of assumed cross-section. The mechanical properties of the matrix and the fibres in k -th layer are E_{mk} , ν_{mk} and E_{wk} , ν_{wk} , respectively. The fibres are regularly spaced and perfectly aligned in the matrix with constant density ρ_{wk} , and their orientation at any point of the composite material is denoted by θ_k with respect to the global co-ordinate system x - y (see Fig. 1).

The microscopically non-homogeneous composite material is next modelled by a macroscopically homogeneous, orthotropic and linearly elastic material in the analysis step of composite structure behaviour. The purpose of this modelling process is to determine the extensional stiffness matrix \mathbf{D} for the model of the composite in the global co-ordinate system x - y and to express its components in terms of the mechanical properties of the reinforcing fibres and the matrix, fibre density as well as fibre orientation, namely

$$D_{ij} = D_{ij}(E_{wk}, \nu_{wk}, E_{mk}, \nu_{mk}, \rho_{wk}, \theta_k) \quad (1)$$

Each of these parameters influences the mechanical properties of the composite disk and then it can be treated either as constant parameter or as the design variable during the optimal design of a composite structure.

3. Optimization procedure

Let us assume that the mechanical properties of fibres and matrix as well as fibre density are given in advance, whereas orientation of rectilinear fibres or parameters defining the shape of curvilinear ones will be selected as the design variables during optimization procedure of composite layout. To describe the layout of reinforcing fibres in this last case, a polynomial, spline or Bezier function will be used.

The optimal design of fibre orientation or layout in a composite material will be discussed either for the case of the mean stiffness design for a disk subjected to service loading or for the case of stress design. Thus, in the first case, the problem can be formulated as a minimization of work done by external forces acting on structural element with the constraint imposed on total cost of composite structure and other behavioural constraints, while in the second case the objective functional will be expressed using the Tsai-Wu stress criterion.

4. Hybrid optimization system

The optimisation procedure defined in previous section will be performed with the aid of a hybrid, evolution-gradient oriented optimization system composed from two main modules.

The first module is the module of initial optimization performed using the evolution algorithm starting from randomly selecting initial solution, while the second module performs the final optimization using the gradient-oriented algorithm starting from the last, best solution generated by evolution algorithm. The finite element method is applied in both modules in order to perform the analysis step of structural behavior. In addition, this method is also used in final optimization module for performing the sensitivity analysis of state fields in order to obtain the gradient information for objective functional and behavioral constraints.

5. Acknowledgment

This research work was supported through the Ministry of Education and Science, Grant No. N501 060 32/3955.

6. References

- [1] K. Dems, Sensitivity analysis and optimal design for fibre-reinforced composite disks, *Structural Optimisation*, 11, pp.178-186, 1996.
- [2] K. Dems, J. Wiśniewski, Design of fibre layout in multilayer composites using hybrid algorithms, *Foundations of Civil and Environmental Engineering*, No.6, pp.53-77, 2006.
- [3] K. Dems, J. Wiśniewski, Stiffness optimization of fibre-reinforced composites, *Proceedings of 17th International Conference on Computer Methods in Mechanics*, Łódź-Spała, Poland, CD-Rom, 2007.

INCORPORATING TWO OPTIMIZATION ALGORITHMS INTO FEA ENVIRONMENT

K. Szajek, W. Kąkol, T. Łodygowski and M. Wierszycki

Institute of Structural Engineering, Poznań University of Technology, Poznań, Poland

1. General

Genetic algorithms (GA) have become a popular approach in design optimization in engineering applications in recent years. GAs base on the rule of the survival of fittest in natural selection. Improvement of global search can be done by employing in optimization procedure of neural networks (NN) which can learn and adapt changes over the time.

In the paper the design optimization with the use of FEA and both genetic algorithms and neural network approaches is discussed. The prepared software tool bases on existing open source libraries, namely Galileo for GA, and ffnet for NN. FE modeling, analysis and post-processing were carried out with the use of Abaqus Unified FEA suite. The optimization procedure was implemented with the use of Python (objective programming language) and the Abaqus Scripting Interface.

2. First approach - optimization using FEA and GA

The first presented approach of optimization is based on GA only. Evaluation of each individual bases on the results of FE analysis using Abaqus. The chromosomes created during genetic process constitute the starting point for evaluation procedure. For each chromosome, FE model is created and simulation is performed. The obtained results are interpreted according to a given objective function. The flow-chart of the applied algorithm is presented in Figure 1. The described approach is general one. Any nonlinear static as well as dynamic FE simulation can be used for evaluation procedure. Unfortunately, GAs are in general computationally expensive. Moreover, a random character of GAs requires a multiple usage of optimization procedure. As a result of above, this approach requires efficient and robust methods and resources and it is not used for large design optimization problems.

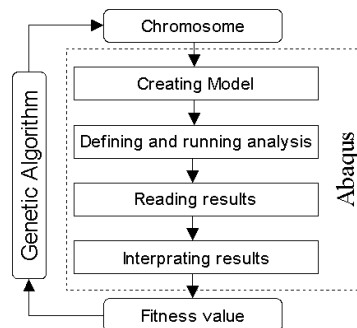


Figure 1. Chromosome evaluation using Abaqus

3. Second approach - optimization using FEA, GA and NN

The base of modification of the described above method is an assumption that GA does not demand a precise solution for each chromosome. The crucial task of evaluation mechanism is extracting features of a chromosome which improve the quality of the individual. Thus, it is

recommended to use an estimation tool which can rate the fitness less accurately but faster.

In the second presented approach of optimization it is proposed to replace the evaluation based on FE analysis with an estimation based on NN. In order to train NN, numerical analysis results for the selected and randomly generated chromosomes are used as a training set. When the learning process is terminated, an optimization attempt is carried out with the use of GA. This step corresponds to the first presented idea of optimization process with one exception; the evaluation procedure is done now with the use of NN. For each iteration of an optimization loop a training set is updated. A new training data consists of the result for the best individual obtained using GA and additionally, in the case of parallel computations, either results for random chromosomes or for created as a result of the best chromosome mutation. New training data verifies the GA solution in the first place and increases space of NN approximation on the other hand. As a result, the next GA optimal solution is calculated taking into consideration all previous attempts. The architecture of NN is changing simultaneously with the optimization process. The well-fitted architecture of NN is calculated according to a learning error. Each expensive FE analysis is used for improving an estimation tool – NN. The greater number of analyses, the better estimation of individual is expected, however, in many cases NN is able to detect advantageous features even in a small number of training data. A flow-chart of the algorithm described above is presented in Figure 2.

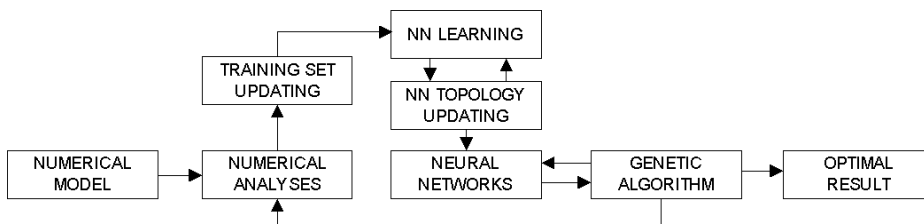


Figure 2. Flow-chart of modified optimization procedure.

4. Examples

The presented algorithms were tested and verified for several problems. The general character of GA optimization method enables us to use it in cases of a wide range of engineering applications. At the beginning very simple linear problems e.g. spanned beam with a uniformly distributed load was considered. Next, optimization of more complex nonlinear structures such as screw connection and skin-stringer structure were carried out.

5. References

- [1] D.E. Goldberg (1989), *GeneticAlgorithm in Search, Optimization and Machine Learning*, 1st ed, Addison-Wesley Professional.
- [2] T. Burczyński, Adam Długosz and W. Kuś (2006), Parallel evolutionary algorithms in shape optimization of heat radiators, *Journal of Theoretical and Applied Mechanics*, **44**, **2**, 351–366.
- [3] T. Burczyński, W. Kuś, A. Długosz and P. Orantek (2004), “Optimization and defect identification using distributed evolutionary algorithms”, *Engineering Applications of Artificial Intelligence*, **17**, **4**, 337–344.
- [4] H.K. Chao and R.E. Rowlands (2007), “Reducing tensile stress concentration in performed hybrid laminate by genetic algorithm”, *Composites Science and Technology*, **67**, **13**, 2877–2883.

**MULTI-OBJECTIVE OPTIMAL DESIGN
OF MULTI-SPAN SANDWICH PANELS WITH SOFT CORE,
ALLOWING FOR VARIABLE SUPPORT CONDITIONS**

A. Garstecki, Z. Pozorski and R. Studziński

Institute of Structural Engineering, Poznan University of Technology, Poland

1. Introduction

Sandwich panels used as the external wall cladding of industrial and storage buildings are considered in this paper. Alternative systems of wall cladding include corrugated sheets, wall cassettes and façade panels. An advantage of sandwich panels over the above mentioned systems is that they are fully prefabricated, therefore during erection on the building site they do not need additional layers, either thermal or waterproof, and can be erected in all weather conditions. High bending rigidity coupled with small weight, as well as thermal and damping properties, speak in their favour.

In this paper we are looking for pareto optimal solutions for multi-span sandwich panels with polyurethane foam core (PUR) and slightly profiled steel facings. The panels are subjected to external load of wind and to drastic changes of temperature. It is well known in the literature that the interaction of loads and distortions leads to a conflict in structural optimization [4]. The deteriorate influence of the temperature on the state of stress can be reduced by introduction of elastic supports. Therefore, the design variables vector referring to the panel is enhanced by support stiffness coefficients.

The optimization problem is non-convex [5], therefore we use distributed parallel evolutionary algorithms [2]. A large number of constraints is introduced by the way of external penalty functions. To describe the structural response of a sandwich panel we use the modified Reissner-Mindlin plate theory. According to this theory we assume that: the materials of steel facings and of the foam core are isotropic, homogeneous and linearly elastic; the facings are parallel; normal stress in the foam core is negligible ($\tau_{xz} = 0$); the shear stresses are constant in transverse direction ($\tau_{xz} = \tau_{yz} = \text{const.}$) and the in-plane strains ε_x , ε_y and γ_{xy} are small compared to unity [1].

2. Problem formulation

Thermally and mechanically loaded multi-span sandwich panels on elastic supports are considered. Mechanical load results from wind pressure with positive or negative values and is considered as uniformly distributed. The thermal distortions are induced by the temperature difference between the internal and external face sheets (1).

$$(1) \quad \Delta t = t_{\text{int.}} - t_{\text{ext.}}$$

We assumed $\Delta t = -55^\circ\text{C}$ or $\Delta t = -40^\circ\text{C}$ (for summer) and $\Delta t = 50^\circ\text{C}$ (for winter). Both face sheets have the same thermal expansion coefficient: $\alpha_T = 0.000012 \text{ } 1/^\circ\text{C}$.

The design variables are geometric parameters describing the thickness of the facings and soft core, as well as the stiffness parameters of the elastic supports. All design variables have the prescribed range (box conditions) resulting from the technology of production, transport and erection. Our objective is to find the optimal variable vector \underline{x}

$$(2) \quad \underline{x} = [t_1, t_2, D, k_1, k_2],$$

which minimizes the multi-objective function $F^*(\underline{x}, L)$, given by

$$(3) \quad F^*(\underline{x}, L) = F_1 + F_2 + F_3 = \frac{\alpha_1 \cdot (t_1 + t_2)}{\text{cost}} + \alpha_2 \cdot D + \frac{\alpha_3 \cdot L^{-1}}{\text{quality}},$$

where: t_1 and t_2 represent the thickness of the external and internal face sheets, respectively, D is the thickness of the soft core, k_1 and k_2 are the stiffness coefficients of the external and internal supports respectively and α_i are coefficients which reduce the expression to a non-dimensional form.

The aim of the optimization is to find the panel of minimum cost $C = F_1 + F_2$ for the maximum span L , i.e. (min F_3), and satisfying the set of constraints $g_i(\underline{x}, L)$. These constraints result from ultimate limit state conditions (shear stresses in the core, normal or wrinkling stresses in the facings, crushing of the core at supports) and serviceability limit state conditions (displacements). The importance of the flexural wrinkling of flat and slightly profiled sandwich panels must be stressed [3]. The external penalty function method allows to change the optimization problem with constraints into one without constraints; thus the fitness function is given by

$$(4) \quad \Psi(\underline{x}, L) = F^*(\underline{x}, L) + \sum_{i=1}^{24} G_i(\underline{x}, L),$$

where $G_i(\underline{x}, L)$ is the external penalty function. The characteristic Pareto optimal curve of the cost C for the span L is presented in Fig. 1.

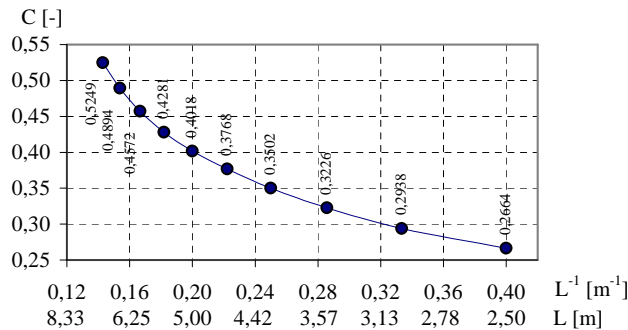


Fig. 1. Pareto optimal solutions: cost C versus L .

Elastic supports result in a redistribution of the value of the internal forces. We observed a decrease of the support reaction force and bending moment at the internal support, and an increase of the bending moment in span. Keeping in mind that flexural wrinkling is an extremely important condition [3], the above-mentioned phenomenon improves the ultimate state of stresses in those structures. Hence, introduction of optimally designed elastic supports can significantly increase the allowable spans of panels.

3. References

- [1] K. Stamm and H. Witte (1974). Sandwichkonstruktionen: Berechnung, Fertigung, Ausführung,
- [2] T. Burczyński, W. Kuś (2004). Optimization of structures using distributed and parallel evolutionary algorithms, *Lecture Notes on Computational Sciences*, **3019**, 572–579.
- [3] P. Hassinen, L. Martikainen, K. Berner (1997). On the Design and Analysis of Continuous Sandwich Panels, *Thin-Walled Structures*, **29**, 129–139.
- [4] Z. Mróz, A. Garstecki (2005). Optimal loading conditions in the design and identification of structures. Part I: Discrete formulation, *Structural Optimization*, **1**, 1-18.
- [5] I.E. Grossmann, L.T. Biegler (2004). Part II. Future perspective on optimization, *Computers and Chemical Engineering*, **28**, 1193–1218.

STATIC FEA OF MECHANICAL COMPLEX STRUCTURES

C. Iancu, A. Nioata

Department of Applied Mechanics, University "Constantin Brâncuși" Târgu-Jiu, Romania

1. Introduction

In the large category of conventional machines for plastic deformation, the mechanical presses have the largest use. So, the mechanical presses, and especially the "C"-bed presses, represent one of major trend in designing, based on several advantages.

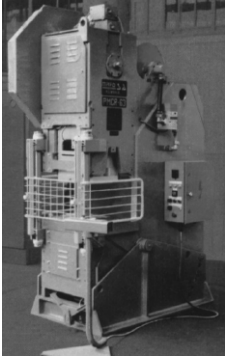


Fig.1 PMCR – 63 press

The bed is the base element of a mechanical press, having the role to sustain the cinematic assembly and to convey the pressing force from working parts to piece.

The classic calculus of the bed for crank mechanical press is based on determination of stress and deformation due to maximum load at the nominal force. So, this methodology has limitations, being impossible to estimate discrete values on different points or sections of structure. For the mentioned reasons have been developed modern analysis methods, FEA for structural calculus being hardly used lately. This method is presented on a numeric example, represented by the bed of a crank mechanical press type PMCR-63, mechanical press with open bed, with nominal force 630 kN, presented in fig.1.

2. STATIC ANALYSIS OF PMCR-63 MECHANICAL PRESS BED

The model of the analyzed structure, completed and prepared as shown in [1], is now ready for FEA. For either static or dynamic FEA, must be followed the phases: defining the mesh; defining the environment bonds; defining the loads; performing analysis and result interpretation.

2.1. Defining the mesh

The mode of obtaining the mesh was presented in [1]. The mesh have 10307 nodes, 25734 finite elements and 103590 degree of freedom (DOF), elements type SHELL 3 for discretization of all bed plates and type TETRA 4 for discretization of cantilevers and the bosses.

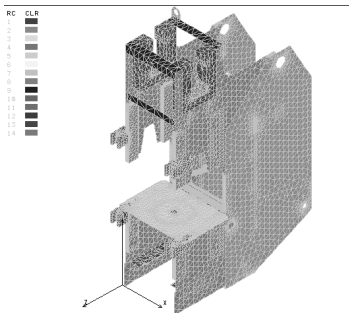


Fig.2 The discretized structure

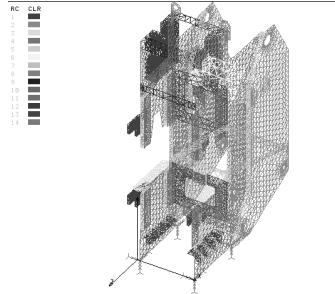


Fig.3 The environment bonds

2.2. Defining the environment bonds

The environment bonds are applied to nodes being in the zone of bed resting on foundation. In this zone are blocked all DOF (3 translations and 3 rotation). In fig.3 are presented the environment bonds.

2.3. Defining the loads

The forces developed on working are generated by rod-crank mechanism. Their effect is transmitted by superior bosses and by bed table in whole structure. So on the bed action forces on bed table, with maximum value of 63 tf and reaction forces on upper bosses, with same value, but contrasted direction. Since the action of these forces isn't concentrate, the forces on upper bosses were considered like a uniform distributed pressure on bosses width, having the value $p_1 = 63 \text{ N/mm}^2$ and the force on bed table like a distributed pressure on a surface of $\Phi 300 \text{ mm}$, $p_2 = 9,17 \text{ N/mm}^2$

2.4. Performing analysis and result interpretation

The model completed and prepared for analysis as shown, was studied with COSMOS/M software, with solving option FFE (Fast Finite Element). The results show both displacement and stress analysis, concerning maximum values and distribution on structure.

In fig.4 is presented the *displacement distribution* for the structure, observing a continuous distribution that implies a correct model. The maximum displacement is: $\delta_{\max} = 0,94727 \text{ mm}$. Also for symmetric nodes the displacement value are very similar, that confirms the model is correct.

In fig.5 is presented the *stress distribution*, (Von Mises). The admissible strength considered are:

-bending strength: 200 MPa -traction-compression strength: 180 MPa

The maximum stress is 182 MPa, and because the structure is stressed on traction-compression compound with bending, the admissible strength considered is $\sigma_{\text{Von max}} = 200 \text{ MPa}$, so the stress is bellow the admissible strength.

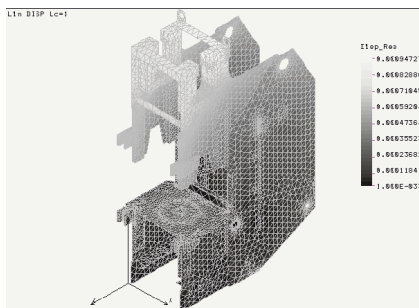


Fig.4 Displacement distribution

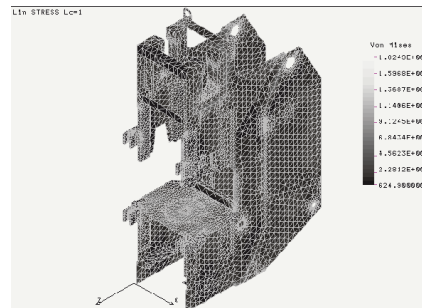


Fig.5 Stress distribution

3. Conclusions

In this paperwork are presented the steps needed in order to perform a static FEA analysis for complex structures, such as frames for mechanical presses. It was shown that the results show a continuous distribution of displacements and stresses that validate the model, proving it correct. Also, with this type of analysis it became possible knowing values in every point of the press bed that interest, and preparing the way for *the optimization of such a complex structure*.

References

- [1] Iancu, C. (2002), *Contributions to dimensional optimization of mechanical press in dynamic regime*, Ph.D. Thesis, University of Pitesti, Romania.
- [2] ★★ ★★ (2002), *Cosmos/M -Finite Element Analysis System, User Guide*, Structural Research & Analysis Corp., Los Angeles, CA, USA.

A NONASYMPTOTIC MODELLING OF HEAT CONDUCTION IN SOLIDS REINFORCED BY SHORT FIBRES WITH FUNCTIONALLY GRADATION OF FEATURES

M. Chalecki, W. Nagórko

Warsaw University of Life Sciences - SGGW, Department of Mechanics and Building Constructions,

In the paper, the model of heat conduction in solids reinforced by short fibres with a functionally gradation of effective features (functionally graded materials - FGM) will be constructed. The proposed model will contain a set of equations for an averaging temperature (describing macroscopic changes) and functions called fluctuations (describing the influence of a microstructure on the heat flow). The model will be tested on the examples of numerical solutions.

1. Conductors reinforced by fibres

We are going to consider the conductors, whose configuration in the physical space with the Cartesian orthogonal coordinate system $(x_1, x_2, x_3) \in R^3$ will be an area $\Omega = \Pi \times (-h_3, h_3)$, where $\Pi = (-h_1, h_1) \times (-h_2, h_2)$. Those conductors will be strengthened with thin fibres. We assume that the fibres are distributed parallel to the axes x_α , $\alpha = 1, 2$.

The conductors need not to be periodical, however in the area Π is possible to section off a part $I_1 \times I_2$, where $I_\alpha = [-\lambda_\alpha/2, \lambda_\alpha/2]$, $\alpha = 1, 2$ and λ_α are the quantities characterizing the structure of the reinforcement.

For any $(x_1, x_2) \in \Pi$, let us determine the functions of a saturation by the fibres $v_1 = v_1(x_1, x_2)$, $v_2 = v_2(x_2, x_1)$, such that $v_1(\cdot, x_2)$ is for every x_2 a λ_1 -periodic function, while $v_2(\cdot, x_1)$ is for every x_1 a λ_2 -periodic function.

An essential assumption from the point of view of a method of modeling which we are going to use below, is a demand, that the functions v_1, v_2 were slowly varying with respect to the coordinates x_2, x_1 , respectively, what we denote in a form: $v_1(x_1, \cdot) \in SV_\varepsilon^1(I_2)$, $v_2(x_2, \cdot) \in SV_\varepsilon^1(I_1)$. The introduced way of gradation can be a consequence of a slow variability of the length of the fibres or a slow variability of the saturation of these fibres.

In the case under consideration, the functions v_1, v_2 are not periodical and the direct application of methods of asymptotical homogenization is not effective. Therefore, we are going to use a nonasymptotic method, known as the tolerance averaging technique [1].

2. Equations of a heat conduction

For the described conductors is assumed that the heat conduction is held according to the Fourier's law, i.e. is described in the area $\Omega \times \langle t_0, t_1 \rangle$ by the equation

$$(1) \quad \partial_k (K_{kl} \partial_l \theta) - c \dot{\theta} = f, \quad k, l = 1, 2, 3$$

where $\theta = \theta(x_1, x_2, x_3, t)$ is a temperature, $f = f(x_1, x_2, x_3, t)$ – a source of heat, $c, \mathbf{K} = (K_{kl})$ – a specific heat and a tensor of a heat conduction in Ω , respectively, which assume the constant values c^M, K_{kl}^M in the matrix of the conductor, c^F, K^F in the fibres. We also assume that in the fibres a one-directional heat flow is held and $K_{kl}^M \ll K^F$.

The thermophysical features of the medium will be described with functions: $c: \Pi \rightarrow R$, $\mathbf{K}: \Pi \rightarrow R$ of the form as below:

$$\begin{aligned}
 c(x_1, x_2) &= c^M + c^F (v_1(x_1, x_2) + v_2(x_2, x_1)), \\
 K_{11}(x_1, x_2) &= K_{11}^M + K^F v_1(x_1, x_2), \quad K_{22}(x_1, x_2) = K_{22}^M + K^F v_2(x_2, x_1), \\
 (2) \quad K_{12}(x_1, x_2) &= K_{21}(x_1, x_2) = K_{12}^M
 \end{aligned}$$

where v_α are λ_α -periodic functions with respect to x_2 and x_1 , respectively, $0 \leq v_\alpha \leq 1$, $1 - v_\alpha \equiv 1$. The functional coefficients (2) are oscillating and non-continuous. They describe a micrononhomogeneity of the considered conductors.

3. Averaged model

According to the tolerance averaging technique, we carry out a micro-macro-decomposition of a temperature in a form:

$$(3) \quad \theta(x_1, x_2, t) = \vartheta(x_1, x_2, t) + \varphi^1(x_1)\psi^1(x_1, x_2, t) + \varphi^2(x_2)\psi^2(x_1, x_2, t)$$

where

$$(4) \quad \vartheta(\cdot, t), \psi^A(\cdot, t) \in SV_\varepsilon^1(\Delta) \quad A=1,2$$

for every t .

The function $\vartheta(\cdot)$, occurring in (3), can be interpreted as the macroscopic part of a temperature field $\theta(\cdot)$, whereas the functions $\psi^A(\cdot)$ describe the microfluctuations of the temperature $\theta(\cdot)$ in any part $I_1 \times I_2$. These functions are the new functions to be sought. The functions $\varphi^A(\cdot, t)$ (shape functions) are linearly independent and must be known.

According to the tolerance averaging technique, the equations for the sought functions $\vartheta(\cdot)$, $\psi^A(\cdot, t)$, $A = 1, 2$, have the form [2]:

$$\begin{aligned}
 (5) \quad & - \langle c \rangle \vartheta + \langle K_{\alpha\beta} \partial_\alpha \varphi^A \rangle \partial_\beta \psi^A + \langle K_{\alpha\beta} \rangle \partial_\alpha \partial_\beta \vartheta = \langle f \rangle \\
 & - \langle c \varphi^A \varphi^B \rangle \psi^B - \langle K_{\alpha\beta} \partial_\alpha \varphi^A \partial_\beta \varphi^B \rangle \psi^B - \langle K_{\alpha\beta} \partial_\alpha \varphi^A \rangle \partial_\beta \vartheta = \langle f \varphi^A \rangle
 \end{aligned}$$

The equations (5) have a sense only if the functions $\psi^A(\cdot, t) \in SV_\varepsilon^1(\Delta)$, i.e. they are slowly varying functions. This condition can be proved only *a posteriori* – when these functions are already known.

4. Concluding remarks

In the constructed nonasymptotic model occurs $n + 1$ equations for the temperature and fluctuations, whose determination depends on certain periodic and oscillating functions called shape functions, which must be known. In the paper will be presented such functions, according to the tolerance averaging technique. Moreover, the model will be numerically tested.

5. References

- [1] Woźniak Cz., Wierzbicki E.: *Averaging Techniques in Thermomechanics of Composite Solids*, Wyd. Politechniki Częstochowskiej, Częstochowa, 2000.
- [2] Nagórko W.: Przepływy ciepła w przewodnikach wzmocnionych siatką włókien z funkcjonalną gradacją własności materiałowych, *I Kongres Mechaniki Polskiej*, Warszawa, 2007.

A PROCEDURE FOR DEFECT IDENTIFICATION OF SUSPENSION BRIDGES CABLES BY MEANS OF OPTICAL-FIBRE STRAIN MEASUREMENTS

L. Nunziante *, M. Fraldi

Department of Structural Engineering, University of Napoli "Federico II", via Claudio 21, 80125 Napoli, Italy.

* Corresponding Author. E-mail: nunsci@unina.it ; mob.+39 338 8211 918

ABSTRACT

Recently, the use of Optical Fibre Sensors (OFS) utilising Brillouin scattering effect for reading distributed measurements of temperature and strains has been addressed. Moreover for the strain readings, a few of technical devices were proposed for connecting the optical fibre sensor to the structure, in order to obtain better results in terms of accuracy of measurements.

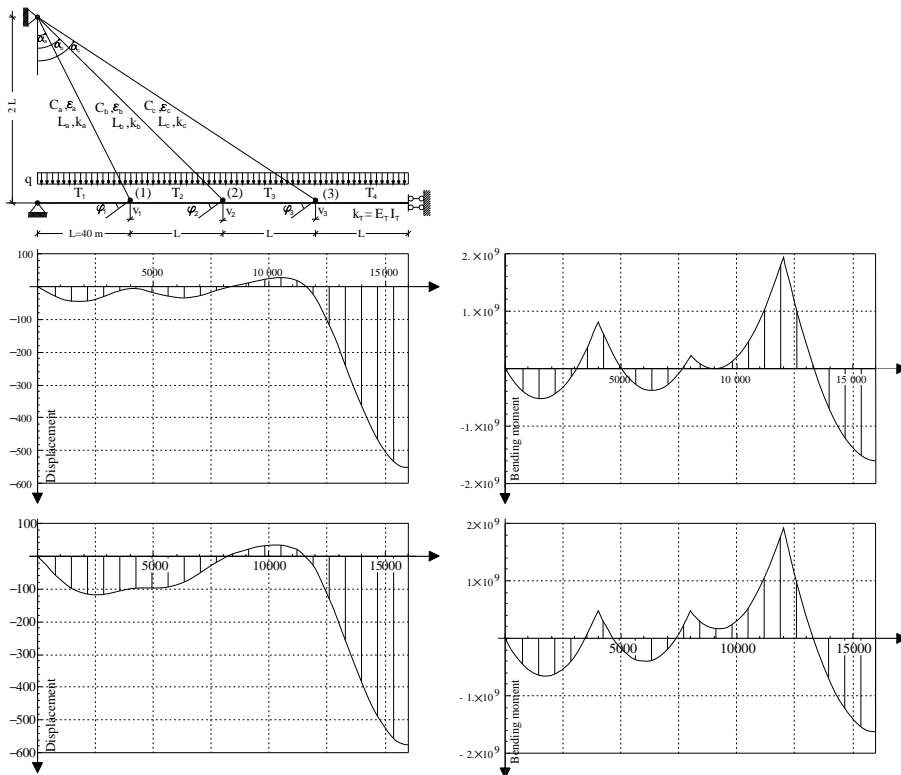
Recently, several authors have shown that, by means of distributed experimental strain readings, it is easy the safety monitoring and assessment of large structures as bridges, pipes, tall buildings, dams and tunnels. Moreover, the great utility of this new sensors were demonstrated by the authors for detection of defects rising in large structures, and accuracy and reliability of measurements were discussed. In foregoing papers some of the authors furnished the mechanical response of optical fibre, when this is embedded in a bearing support beam-like element, where OFSs are treated in the framework of elastic Functionally Graded Material Cylinders (FGMCs), under symmetrical load conditions. In this framework they obtained the complete set of the so called no-decaying solutions, which present axial strain in the system core-jacket not varying with the radius, and hence equal to the value assumed in the supporting element. Laboratory tests carried out on aluminium large rods in extension, and on wires for cables for suspended bridges, equipped with embedded-type optic fibre sensors showed the optimal accuracy of the distributed strains carried out by this new OF sensor. These results allow to facing a few of new applications, among which one of the most important is represented by the monitoring and identification of defects occurring in large structures such as trusses, suspension, or cable-stayed bridges. Namely, the problem of the identification of defects occurring in the wires constituting the cables for suspended or cable stayed bridges is one of the unsolved concern of the modern maintenance and monitoring bridge technology. As matter of fact, most part of these bridges suffers the corrosive action and the damage due to both natural and pollution agents present in the atmosphere. As already shown in several technical papers, several aggressive agents are able of strongly reducing the stiffness of the suspension cable system, and the corrosion processes are very fast being able of significant reductions of stiffness also in a few of months. The stiffness of the cables is usually due by that of thousands of wires. The reduction of cable stiffness is usually related to effects of corrosion of wires related to their cross section reduction, as well as to the decrease of the Young modulus E due to chemical agents that modify the material. In the present paper the problem of detection of corrosion or other damage effect, acting on wires for cables suspension or cable-stayed bridges, will be addressed by using structural analysis methods coupled with the results of on field experimental tests on cables.

The proposed identification procedure is based on a program of on-field test's , in which the distributed strains are measured on all the cables by means of Optical Fibre sensors. Eachone of the planned statical tests must be developed in the same conditions of temperature, without any noise effect (wind, vibration,...), and requests the application of the load distribution q over the bridge beam. The paper shows that the structural problem can be solved theoretically by means of a modified Finite Element strategy, based on a linear system of equations expressing the stationarity conditions of Total Potential Energy, in presence of the initial cable stiffnesses .

* Corresponding author: e-mail: nunsci@unina.it; Tel.: +39-081-7683727 (Office); Fax: +39-081-575 6147

After the occurrence of corrosion or other damage effects able of significantly reducing the cable stiffnesses, the experimental distributed cable's strain readings can be utilised in the same equation system, where the actual unknown cable stiffnesses are left as unknown parameters to determine. The outlined inverse procedure, by locking the cables's degrees of freedom to the values compatible with the measured cable's strains, allows to obtaining both the actual reduced values of the cable stiffnesses and the free part of the degrees of freedom. As an example, a case study of identification of corroding effects appearing in a cable stayed bridge structure is also presented.

Keywords: structural damage, defect identification, non-destructive tests, inverse structural problems, optical fibre sensor, distributed strain, rod structures, suspension bridge, cable-stayed bridge, Brillouin Scattering Effect.



References

- [1] R. Bernini, M. Fraldi, A. Minardo, V. Minutolo, F. Carannante, L. Nunziante, L. Zeni. "Damage detection in bending beams through Brillouin distributed optic-fibre sensor". *BRIDGE STRUCTURES- Assessment, Design and Construction*. Vol.1, N.3, September 2005. (355-363). Taylor&Francis. E189110. ISSN 1573-2487.
- [2] R. Bernini, M. Fraldi, A. Minardo, V. Minutolo, F. Carannante, L. Nunziante, L. Zeni. "Identification of defects and strain error estimation for bending steel beams using time domain Brillouin distributed optical fiber sensors". *Smart Materials and Structures*. 15 (2006) 1-11.
- [3] L. Nunziante, A. Gesualdo, F. Guarracino, V. Mallardo, V. Minutolo. (1997). Flaw Identification in Elastic Solids: Theory and Experiments. *EXTRACTA MATHEMATICAE*. Vol.12, No.1, Junio 1997, (61-86).
- [4] H.D. Bui, M. Tanaka et al. *Inverse Problems in Engineering Mechanics - ISIP'94*, Ed., Balkema, Rotterdam (1994).
- [5] Fraldi, M., Nunziante, L., Carannante, F. "Axis-Symmetrical Solutions for n-ply Functionally Graded Material Cylinders under Strain No-decaying Conditions". *Mechanics of Advanced Materials and Structures*, 14, 1-24, 2007.
- [6] Lekhnitskii, S. G. (1981), *Theory of Elasticity of an Anisotropic Body*, Mir, Moscow.
- [7] M. Fraldi, L. Nunziante. Solutions for optical fibres as n-ply FGM Cylinders - Theory and experiments. 2006 *Multiscale & Functionally Graded Materials Conference*. O'AHU-Hawaii. Oct. 2006.

FREE VIBRATION ANALYSIS OF STIFFENED PLATES BY THE BOUNDARY ELEMENT METHOD

R. Górski and P. Fedeliński

*Department of Strength of Materials and Computational Mechanics,
Silesian University of Technology, Gliwice, Poland*

1. Introduction

Natural frequencies, which depend on geometry, material properties and support conditions of bodies, characterize the dynamical properties of structures. For structures of complex geometry and made of different materials, natural frequencies are usually calculated by the finite element method (FEM) or the boundary element method (BEM). The methods can be coupled in order to exploit their advantages and solve the problem more efficiently.

The free vibration analysis of homogeneous plates by the dual reciprocity BEM (DRBEM) was presented for the first time by Nardini and Brebbia [2]. Albuquerque et al. [1] applied the method for the free vibration analysis of anisotropic plates. Górski and Fedeliński [3] used the DRBEM for determination of natural frequencies and mode shapes of non-homogeneous plates.

In the present paper, the formulation and application of the coupled DRBEM and FEM in the free vibration analysis of stiffened plates is presented. The generalized algebraic eigenvalue problem is transformed into the standard one and solved. One numerical example is presented and frequencies for the reinforced cantilever plate, computed by the present method and the FEM, are compared.

2. Formulation of the eigenvalue problem

Consider a plate, occupying the domain Ω^I and enclosed by the outer boundaries Γ_1^I and Γ_2^I , reinforced by a stiffener, occupying the domain Ω^{II} , as shown in Fig.1. The Γ_1^I and Γ_2^I are parts of the boundary, where displacement and traction boundary conditions are prescribed, respectively. The boundary connecting the plate and stiffener (the interface) is $\Gamma_3^I \equiv \Gamma_3^{II} \equiv \Gamma_3^{I,II}$. The translational degrees of freedom of the plate and stiffener (beam) at the $\Gamma_3^{I,II}$ are coupled and the rotational ones of the beam at the Γ_2^{II} are free. The subscripts 1, 2, 3 correspond to the fixed, free and common boundary and the superscripts I, II correspond to the plate and beam domain, respectively.

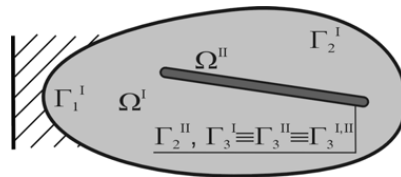


Figure 1. A plate reinforced by a stiffener.

The materials of the plate in plane stress or strain and the stiffener are linear elastic, isotropic and homogeneous. The plate is modeled by the DRBEM and the stiffener by the FEM. The numerical solution is obtained after discretization of the body into the curved boundary and straight beam finite elements. One boundary element along the $\Gamma_3^{I,II}$ is connected with two finite elements. The ideal connection at the nodes of the plate and stiffener is assumed.

The detailed transformations and the resulting matrices are presented in the full length paper. The final algebraic eigenvalue problem for the body in Fig.1 has the following form

$$\begin{bmatrix} \bar{\mathbf{H}}_{22}^I & 0 & \bar{\mathbf{H}}_{23}^I & -\bar{\mathbf{G}}_{23}^I \\ \bar{\mathbf{H}}_{32}^I & 0 & \bar{\mathbf{H}}_{33}^I & -\bar{\mathbf{G}}_{33}^I \\ 0 & \mathbf{K}_{22}^II & \mathbf{K}_{23}^II & \mathbf{T}_{23}^II \\ 0 & \mathbf{K}_{32}^II & \mathbf{K}_{33}^II & \mathbf{T}_{33}^II \end{bmatrix} \begin{bmatrix} \mathbf{u}_2^I \\ \mathbf{u}_2^II \\ \mathbf{u}_3^{I,II} \\ \mathbf{t}_3^{I,II} \end{bmatrix} = \omega^2 \begin{bmatrix} \bar{\mathbf{M}}_{22}^I & 0 & \bar{\mathbf{M}}_{23}^I & 0 \\ \bar{\mathbf{M}}_{32}^I & 0 & \bar{\mathbf{M}}_{33}^I & 0 \\ 0 & \mathbf{M}_{22}^II & \mathbf{M}_{23}^II & 0 \\ 0 & \mathbf{M}_{32}^II & \mathbf{M}_{33}^II & 0 \end{bmatrix} \begin{bmatrix} \mathbf{u}_2^I \\ \mathbf{u}_2^II \\ \mathbf{u}_3^{I,II} \\ \mathbf{t}_3^{I,II} \end{bmatrix}$$

where $\bar{\mathbf{H}}$, $\bar{\mathbf{G}}$ and $\bar{\mathbf{M}}$ are the BEM modified coefficient matrices, \mathbf{K} , \mathbf{T} and \mathbf{M} are the FEM matrices, \mathbf{u}_2 and \mathbf{u}_3 are displacements at the free boundary and at the interface, respectively, \mathbf{t}_3 are tractions at the interface.

3. Numerical example

Both sides of the plate are symmetrically reinforced by four beams of channel sections as shown in Fig.2. The length and height of the plate is $L=H=0.5$ m, the dimensions of each beam are $20 \times 10 \times 2 \times 2$ mm, and the other dimensions are $l=h=0.4$ m. The material of the plate (Ω^I) and beams (Ω^{II}) is PMMA in plane stress and aluminum, respectively. The values of mechanical properties for these materials are: modulus of elasticity $E_I=3.3$ GPa and $E_{II}=70$ GPa, Poisson's ratio $\nu_I=0.42$ and $\nu_{II}=0.34$, density $\rho_I=1180$ kg/m³ and $\rho_{II}=2700$ kg/m³.

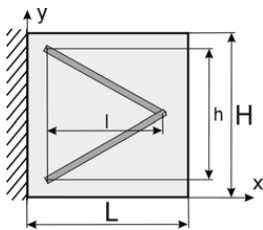


Figure 2. A stiffened plate.

No.	Frequency [Hz]		Difference [%]
	BEM/FEM	FEM	
1	398.57	398.86	0.07
2	910.94	897.93	1.45
3	902.06	902.74	0.08
4	1501.0	1500.0	0.07
5	1684.1	1672.6	0.69

Table 1. Results of analysis.

The total number of the boundary and finite elements in the BEM/FEM analysis is 112 (32 elements at the interface) and 64, respectively. The total number of 4-node quadrilateral and beam finite elements in the FEM analysis by the MSC Nastran system is 2604 and 90, respectively.

Table 1 shows the lowest five frequencies computed by the present BEM/FEM formulation and the FEM. A good agreement of the results can be observed, except of 2nd frequency, which corresponds to the longitudinal mode shape, respectively.

4. Conclusions

The coupled DRBEM and FEM is presented in the free vibration analysis of stiffened plates. This approach results in reducing the size of the final system of equations in comparison with the FEM because only the outer boundary and the interface of the body are discretized. Due to simple modification of discretization, the method can be easily used in optimization problems.

5. References

- [1] E.L. Albuquerque, P. Sollero and P. Fedelinski (2003). Free vibration analysis of anisotropic material structures using the boundary element method, *Eng. Anal. Boundary Elements*, **27**, 977–985.
- [2] D. Nardini and C.A. Brebbia (1983). A new approach to free vibration analysis using boundary elements, *Appl. Math. Modelling*, **7**, 157–162.
- [3] R. Górski and P. Fedeliński (2007). Free vibration analysis of non-homogeneous plates by the boundary element method, 17th International Conference on Computer Methods in Mechanics CMM-2007, CD-ROM Proceedings, 4 pages.

EVOLUTIONARY COMPUTING IN MULTI-OBJECTIVE OPTIMIZATION OF LAMINATES

W. Beluch¹, T. Burczyński^{1,2} and A. Długosz¹

¹*Department for Strength of Materials and Computational Mechanics, Silesian
University of Technology, Gliwice, Poland*

²*Institute of Computer Modelling, Cracow University of Technology, Cracow, Poland*

1. Formulation of the problem

The paper is devoted to the multi-objective optimization of fibre-reinforced, multi-layered laminates. Interply hybrid laminates are considered [1]. External plies of the laminates are made of a stronger and more expensive material while internal plies are made of a weaker but less expensive material.

The aim of the paper is to find the optimal set of ply angles and the number of plies made of particular materials in order to satisfy contradictory criteria. In order to solve a multi-objective optimization (MOO) task, the multi-objective evolutionary algorithm is employed. In the present paper the Pareto attitude to the multi-objective optimization is used [2]. A MOO problem can be expressed as searching for the vector of non-dominated (efficient) solutions \mathbf{x} , which minimizes the vector of k objective functions. The vector \mathbf{x} is required to satisfy the m inequality and p equality constraints.

A fibre-reinforced, symmetric hybrid laminates are considered. It is also assumed that laminates are symmetrical - as a result there is no coupling between shell and bending states. The ply orientations (fibre ply angles) and the number of external plies of the laminate are the design variables. Two objective functionals are taken into account:

1. The minimization of the structure cost. It is assumed that the thicknesses of plies h_i , the number of plies N and area of the plate A_i are fixed. The dimensionless cost C is calculated as follows:

$$(1) \quad C = [n_e c_e + (N - n_e) c_i] h_i A_i$$

where: n_e - the number of external plies; c_e, c_i - the unit costs of the external and internal ply materials, respectively [$1/m^3$].

2. The maximization of the fundamental eigenfrequency:

$$(2) \quad \arg \max\{\omega_1(\mathbf{x}); \mathbf{x} \in \mathbf{D}\}.$$

2. Multi-Objective Evolutionary Algorithm

Traditional, typically gradient optimization methods are fast and precise, but usually lead to local optima. To increase the possibility of reaching the global optimum the global optimization methods [4] are employed. Evolutionary Algorithms (EAs) are also very useful if the information about the objective function gradient is hard or impossible to obtain. The only necessary information for the EA to work is the objective (fitness) function value. As EAs work on a population of possible solutions of the problem, the searching is multidirectional. Each possible solution is called a chromosome and it consist of genes. In the real-value coding each gene typically represents one design variable.

To solve presented multi-objective optimization problem the Non-dominated Sorting Genetic Algorithm (NSGA-II) [3] has been used. In order to calculate the objective functions values the boundary-value problem for laminates must be solved. The Finite Element Method (FEM) commercial software has been used to solve the boundary-value problem for laminates.

3. Numerical example

The aim is to find the optimal number of external plies and the optimum values of ply angles to i) minimize the cost of the structure; ii) maximize the 1st eigenfrequency. A symmetric rectangular hybrid laminate plate 0.5x0.2m stacked up of 18 plies of the same thickness $h=0.0002\text{m}$ is considered. The plate is divided into 200 4-node plane finite elements. The material properties and unit costs are: i) for external material M_e : $E_1=181\text{ GPa}$, $E_2=10.3\text{ GPa}$, $\nu_{12}=0.28$, $G_{12}=7.17\text{ GPa}$, $\rho=1600\text{ kg/m}^3$, $c_e=6.0\text{ 1/m}^3$; ii) for internal material M_i : $E_1=38.6\text{ GPa}$, $E_2=8.27\text{ GPa}$, $\nu_{12}=0.26$, $G_{12}=4.14\text{ GPa}$, $\rho=1800\text{ kg/m}^3$, $c_e=1.0\text{ 1/m}^3$.

The parameters of NSGA-II are: the population size $p_s = 50$; the number of genes $n_g = 10$; the mutation probability $p_m = 0.1$; the crossover probability $p_c = 0.8$; the number of generations $gen = 100$. Each ply angle could vary in the range of $\langle -90^\circ; 90^\circ \rangle$ every 5° , 15° , 45° or continuously. The results in the form of Pareto solutions are presented in Figure 1.

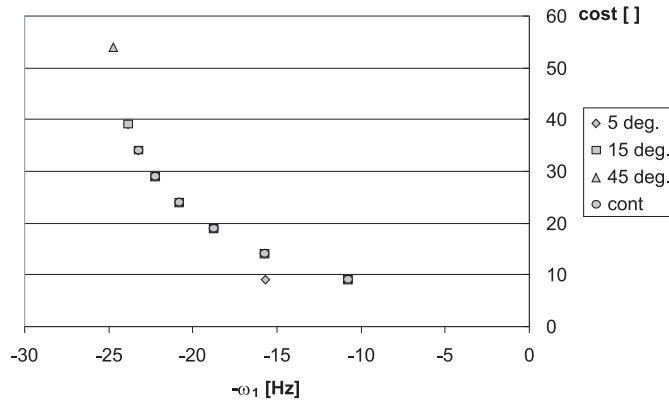


Figure 1. Optimization results for 5° , 15° , 45° and continuous variants.

4. Final conclusions

The optimization of hybrid laminates has been performed. To satisfy contradictory criteria the multi-objective optimization method in the form of multi-evolutionary algorithm has been used. Positive optimization results have been obtained for all considered variants (discrete and continuous).

5. Acknowledgments

The research is partially financed from the Polish science budget resources as the research project and the Foundation for Polish Science (2005-2008).

6. References

- [1] S. Adali et.al. Optimal design of symmetric hybrid laminates with discrete ply angles for maximum buckling load and minimum cost, *Compos. Structures*, **32**, 409–415, 1995.
- [2] J.F. Aguilar Madeiraa, H. Rodriguesa and H. Pinaa. Multi-objective optimization of structures topology by genetic algorithms, *Advances in Engineering Software*, **36**, 21–28, 2005.
- [3] K. Deb. A fast and elitist multiobjective genetic algorithm: NSGA-II. *IEEE Transactions on Evolutionary Computation*, **6**, no.2, 182–197, 2002.
- [4] J. Arabas. *Lectures on Evolutionary Algorithms*, WNT, 2001 (in Polish).

ENERGETIC APPROACH TO STABILITY OF BEAM/COLUMNS SUBJECTED TO DEFORMATION DEPENDENT LOADING

Sz. Imiełowski

Institute of Fundamental Technological Research, Warsaw, Poland

The papers presents an original approach to stability of prismatic beam/columns subjected to potential loading. In that number the force of constant direction, Euler load, as well as generalized follower force, which direction depends on actual deformation of the point of the force application are considered. The beam-column is modeled as elastic one with possible compressing deformation.. The stability analysis is applied by means of static and kinetic approach.

The static energy approach, reveals that transition from straight shape to the bend one depends directly on the energy of the system. This occurs at the point for which the bending energy is lower than energy of compressing, and it appears at the value of loading much lower than critical force. For higher values of loading the compressing proceeds with the stable bend shape until the critical state, which occurs with the stable bend shape too. The critical state is defined by the potential energy of elastic deformation which is equal to the maximum value at this point.

The analysis of kinetic approach reveals that depending on the value of loading the mode of vibration can change from the first to second one and inversely. The phenomenon of the change of the vibration mode is connected with the energy flow from the higher modes to the fundamental mode. Finally the column loss stability by divergence. Also in this case the critical state is defined by energy of the system. Moreover it is observed that, for selected set of parameters, the increase of loading can cause an increase of eigenfrequencies as in flutter systems. Such structure is called divergent pseudo-flutter systems.

The research has been supported by the MNiSzW, Poland, under the Grant nr2765/T02/2006/31

References

1. Sz. Imiełowski, Modal forms of columns subjected to generalized follower force, In: *"Theoretical Foundation of Civil Engineering, X Ukrainian-Polish Transaction"*, W.Szcześniak Ed., (2002), v.10, 141-150,.
2. J.Odorowicz, Analysis of critical and supercritical state of compressed prismatic beam-columns of large slenderness, *Drogi i Mosty*, 59-110, 2/2003,
3. Sz. Imiełowski, R.Bogacz, W.Kurnik, Fixed point in frequency domain of structures subject to generalized follower force, (2001), *Machine Dynamics Problems*, 2001, v.25, 169-182

GENETIC ALGORITHM OPTIMIZATION OF HELICOPTER BLADES VIBRATION TRANSITION

A. Gorjipoor and A. Abedian

Sharif University of Technology, Aerospace Institute, Tehran, Iran.

1. Abstract.

Helicopters suffer from high vibration relative to fixed wing aircraft because of a highly unsteady aerodynamic environment and rapidly rotating flexible blades. High vibration causes passenger discomfort, fatigue in rotor system components and increases likelihood of damage to critical avionics components in the helicopter. Vibratory hub loads are a major source of helicopter vibration and involve higher harmonic forces and moments. Passive vibration devices are often used to suppress vibration levels at some selected places in the helicopter body, such as the pilot's seat. Passive devices include pendulum absorbers, anti-resonance systems and other vibration absorbers. A drawback of passive devices is the large weight penalty and rapid performance degradation away from the tuned flight condition. [1]

In this paper, the focus is on optimizing a full three-dimensional helicopter blade structure. The passive optimization that is employed here is based on energy flow analysis models combined with Genetic Algorithm (GA) optimization technique [2]. The mentioned subject structure consists of a composite main part and a steel beam that connects main part to the hub which is completely modeled and analyzed by ANSYS. The optimization parameters include the number of layers, layer thickness, fiber orientation and the type of material for the composite constituents. These parameters are optimized with Genetic Algorithm (GA) to guarantee a minimum vibration transition from the vibratory loaded blade to the blade hub. Here, Genetic Algorithm (GA) which is a general optimization tool for searching of large, nonlinear, discrete, and poorly-understood design spaces that arise in many areas of science and engineering like the design and optimization of laminated composite structures is utilized. However, constrained optimization via the Genetic Algorithm (GA) is often a challenging endeavor, as the GA is most directly suited to unconstrained optimization problems. Note that, traditionally, external penalty functions are used to convert a constrained optimization problem into an unconstrained problem for GA-based optimization studies [3]. Therefore, here, the death, static, linear-dynamic, and a newly developed penalty function that is so called two-part penalty are employed for the GA design optimization of bending and lagging vibration transition with the minimum blade weight.

2. References

- [1] R. Ganguli, Optimum Design of a Helicopter Rotor for Low Vibration Using Aero-elastic Analysis and Surface Methods, *Journal of Sound and Vibration* (2002) 258(2), 327–344
- [2] M. Moshrefi Torbati, A.J. Keane, S.J. Elliott, M.J. Brennan, E. Rogers, Passive vibration control of a satellite boom structure by geometric optimization using genetic algorithm, *Journal of Sound and Vibration* 267 (2003) 879–892.
- [3] A. Abedian, M. H. Ghiasi, B. Dehghan-Manshadi, Comparison of Static and Dynamic Penalty Factors on Efficiency of GA in Optimization of Stiffened Composite Panels, 8th International and 12th Annual Mechanical Engineering Conference – May 2004, Tarbiat Modarres University – Tehran – I.R. Iran

LONGITUDINAL WAVE RESPONSE OF A CHIRAL SLAB INTERPOSED BETWEEN MICROPOLAR SOLID HALF-SPACES

Aarti Khurana¹ and S. K. Tomar²

¹*D. A. V. College, Sector-10, Chandigarh, India*

²*Department of Mathematics, Panjab University, Chandigarh, India*

ABSTRACT

Consider a chiral slab of uniform thickness and interposed between two different micropolar elastic solid half-spaces. Let B_1 be the plane boundary between the micropolar half-space (in which the incident wave is assumed to travel) and the chiral slab, and B_2 be the plane boundary between the chiral slab and the other micropolar elastic half-space. A plane longitudinal displacement wave propagating through one of the micropolar elastic solid half-spaces is assumed to be incident on the chiral slab. A part of the energy carried by the incident wave will be reflected back from the boundary B_1 into the incident medium and rest will be transmitted into the elastic chiral slab. A portion of the incident energy transmitted into the chiral slab will proceed to interact with the boundary B_2 . Here, again some part of the energy will be reflected and rest will be transmitted into the micropolar medium (not the incident one). These reflected waves will go back to interact with the boundary B_1 and the process will repeat.

The equations of motion without body force and body couple densities are given by

For micropolar elastic solid (see Eringen [1])

$$\begin{aligned} (\lambda + 2\mu + K)\nabla\nabla \cdot \mathbf{u} - (\mu + K)\nabla \times \nabla \times \mathbf{u} + K\nabla \times \Phi &= \rho\ddot{\mathbf{u}}, \\ (\alpha + \beta + \gamma)\nabla\nabla \cdot \Phi - \gamma\nabla \times \nabla \times \Phi + K\nabla \times \mathbf{u} - 2K\Phi &= \rho\dot{\Phi}. \end{aligned}$$

For chiral medium (see Nowacki [2])

$$\begin{aligned} (\lambda + 2\mu)\nabla\nabla \cdot \mathbf{u} - \mu\nabla \times \nabla \times \mathbf{u} + C_3\nabla\nabla \cdot \Phi - C_3\nabla \times \nabla \times \Phi &= \rho\ddot{\mathbf{u}}, \\ (\alpha + \beta + \gamma)\nabla\nabla \cdot \Phi - \gamma\nabla \times \nabla \times \Phi + 2C_3\nabla \times \Phi + C_3\nabla\nabla \cdot \mathbf{u} - C_3\nabla \times \nabla \times \mathbf{u} &= \rho\dot{\Phi}. \end{aligned}$$

The constitutive relations describing force stress tensor τ_{ij} and the couple stress tensor m_{ij} ($i, j = 1, 2, 3$) are given by

For micropolar elastic solid (see Eringen [1])

$$\begin{aligned} \tau_{ij} &= \lambda u_{k,k} \delta_{ij} + \mu (u_{i,j} + u_{j,i}) + K(u_{j,i} - e_{ijk} \Phi_k), \\ m_{ij} &= \alpha \Phi_{k,k} \delta_{ij} + \beta \Phi_{i,j} + \gamma \Phi_{j,i}, \end{aligned}$$

For chiral solid (Lakes and Benedict [3])

$$\begin{aligned} \tau_{ij} &= \lambda u_{k,k} \delta_{ij} + \mu (u_{i,j} + u_{j,i}) + C_3 \Phi_{j,i}, \\ m_{ij} &= \alpha \Phi_{k,k} \delta_{ij} + \beta \Phi_{i,j} + \gamma \Phi_{j,i} + C_3 (u_{j,i} - e_{ijk} \Phi_k). \end{aligned}$$

We shall discuss two-dimensional problem in x - z plane so that second-component of displacement vector, first and third components of the micro-rotation vector will not enter into the analysis.

There are two sets of boundary conditions possible at the micropolar - chiral interfaces, i.e., at B_1 and B_2 .

Set-I:

(i) the continuity of displacement, (ii) the continuity of traction (normal component of stress), and (iii) the continuity of micro-rotation, i.e.,

At B_1 :

$$\mathbf{u}_{(inc)}^{(1)} + \mathbf{u}_{(ref)}^{(1)} = \mathbf{u}_{(ref)}^{(2)} + \mathbf{u}_{(tr)}^{(2)}, \quad \hat{\mathbf{e}}_z \cdot (\boldsymbol{\tau}_{(inc)}^{(1)} + \boldsymbol{\tau}_{(ref)}^{(1)}) = \hat{\mathbf{e}}_z \cdot (\boldsymbol{\tau}_{(ref)}^{(2)} + \boldsymbol{\tau}_{(tr)}^{(2)}), \quad \Phi_{(ref)}^{(1)} = \Phi_{(ref)}^{(2)} + \Phi_{(tr)}^{(2)},$$

At B_2 :

$$\mathbf{u}_{(ref)}^{(2)} + \mathbf{u}_{(tr)}^{(2)} = \mathbf{u}_{(tr)}^{(3)}, \quad \hat{\mathbf{e}}_z \cdot (\boldsymbol{\tau}_{(ref)}^{(2)} + \boldsymbol{\tau}_{(tr)}^{(2)}) = \hat{\mathbf{e}}_z \cdot \boldsymbol{\tau}_{(tr)}^{(3)}, \quad \Phi_{(ref)}^{(2)} + \Phi_{(tr)}^{(2)} = \Phi_{(tr)}^{(3)},$$

Set-II:

(i) the continuity of displacement, (ii) the continuity of traction (normal component of stress), and (iii) the continuity of the normal component of couple stress, i.e.,

At B_1 :

$$\mathbf{u}_{(inc)}^{(1)} + \mathbf{u}_{(ref)}^{(1)} = \mathbf{u}_{(ref)}^{(2)} + \mathbf{u}_{(tr)}^{(2)}, \quad \hat{\mathbf{e}}_z \cdot (\boldsymbol{\tau}_{(inc)}^{(1)} + \boldsymbol{\tau}_{(ref)}^{(1)}) = \hat{\mathbf{e}}_z \cdot (\boldsymbol{\tau}_{(ref)}^{(2)} + \boldsymbol{\tau}_{(tr)}^{(2)}), \quad \hat{\mathbf{e}}_z \cdot (\mathbf{m}_{(inc)}^{(1)} + \mathbf{m}_{(ref)}^{(1)}) = \hat{\mathbf{e}}_z \cdot (\mathbf{m}_{(ref)}^{(2)} + \mathbf{m}_{(tr)}^{(2)}),$$

At B_2 :

$$\mathbf{u}_{(ref)}^{(2)} + \mathbf{u}_{(tr)}^{(2)} = \mathbf{u}_{(tr)}^{(3)}, \quad \hat{\mathbf{e}}_z \cdot (\boldsymbol{\tau}_{(ref)}^{(2)} + \boldsymbol{\tau}_{(tr)}^{(2)}) = \hat{\mathbf{e}}_z \cdot \boldsymbol{\tau}_{(tr)}^{(3)}, \quad \hat{\mathbf{e}}_z \cdot (\mathbf{m}_{(ref)}^{(2)} + \mathbf{m}_{(tr)}^{(2)}) = \hat{\mathbf{e}}_z \cdot \mathbf{m}_{(tr)}^{(3)},$$

where the superscript (1) indicates the incident micropolar elastic medium, the superscript (2) indicates the interposed chiral medium and the superscript (3) indicates the other micropolar elastic medium.

Using Helmholtz decomposition of vectors into scalar and vector potentials, the equations of motion can be reduced to some wave equations (coupled and uncoupled). Assuming the appropriate form of potentials in the respective medium and employing the above boundary conditions, it can be seen that each set of boundary conditions gives a non-homogeneous system of eighteen equations in eighteen unknown. Both the sets enable us to determine the amplitude ratios of various reflected and transmitted waves. For each set of boundary conditions, the equations satisfying them are solved numerically to obtain the reflection and transmission coefficients. Each set is found to exhibit different expressions of the reflection and transmission coefficients. Various reflection and transmission coefficients are found to be the functions of the angle of incidence, frequency of the incident wave, elastic parameters of the media and the thickness of the interposed layer. The variations in the modulus of the amplitude ratios with the angle of incidence and with the frequency ratio are computed for a peculiar model and depicted graphically. The effects of the chirality parameter and the thickness of the chiral slab on various amplitude ratios are also studied. Numerical results reveal that for very thin slab, the variations in all the amplitude ratios with the angle of incidence are found to be smooth enough. But as the thickness of the chiral slab becomes significant, we obtain more and more fluctuations in the variations of these coefficients with the angle of incidence. Comparisons in the modulus of the respective amplitude ratios obtained from the two possible sets of boundary conditions are also observed and are depicted graphically. Some results of earlier researchers [4] and [5] have also been reduced as special cases of the present formulation.

References

- [1]. A. C. Eringen (1966). *Linear theory of micropolar elasticity*, J. Math. Mech., **15**, 909-923.
- [2]. W. Nowacki (1986). *Theory of asymmetric elasticity*, Pergamon, Oxford.
- [3]. R. S. Lakes and R. L. Benedict (1982). *Noncentrosymmetry in micropolar elasticity*, Int. J. Eng. Sci., **20**, 1161-1167.
- [4]. M. J. Elphinstone and A. Lakhtakia (1994). *Plane wave response of an elastic chiral solid slab sandwiched between achiral solid half-spaces*, J. Acous. Soc. Am., **95**, 617-627.
- [5]. A. Khurana and S. K. Tomar (2007). *Transmission of longitudinal wave at a plane interface between micropolar elastic and chiral solid half-spaces: Incidence from micropolar half-space*, Available online, J. Sound Vibr.

A WEAK FORMULATION FOR THE LARGE DEFORMATION CONTACT PROBLEM WITH COULOMB FRICTION

A. Le van and T.T.H. Nguyen

*GeM (Laboratory of Civil and Mechanical Engineering), Faculty of Science - University of Nantes,
2, rue de la Houssiniere - BP 92208, 44322 Nantes Cedex 3, France*

1. Theoretical considerations

In this work, a weighted residual relationship involving both the displacements and a field of multipliers is proposed as the weak form of the large deformation contact problem with Coulomb friction in quasi-statics. It is shown that (i) the proposed weak form is equivalent to the strong form of the contact problem and (ii) the multipliers are equal to the contact tractions.

Consider two bodies, indexed by superscripts 1 and 2, undergoing motions $\phi^{(1)}$ and $\phi^{(2)}$ in the three-dimensional space during some time interval $[O, T]$. Let us assume that the bodies may come into contact with each other and formulate the contact problem using a Lagrangian description. The notations, rather standard, are summarized as follows. The reference configuration of the two bodies are represented by the regions $\Omega_o^{(1)}$ and $\Omega_o^{(2)}$. The prescribed body force per unit mass in body i is denoted $\mathbf{f}^{(i)}$. The boundary $S_o^{(i)}$ of body i is partitioned into three parts denoted $S_{oU}^{(i)}$, $S_{oT}^{(i)}$ and $S_{oc}^{(i)}$, where $S_{oU}^{(i)}$ and $S_{oT}^{(i)}$ are the parts where displacements and tractions are prescribed, respectively, and $S_{oc}^{(i)}$ is the part where contact potentially takes place. The stress state in body i is defined by the first Piola-Kirchhoff stress tensor $\mathbf{\Pi}^{(i)}$. The nominal traction vector at any point in $S_o^{(i)}$ with normal vector $\mathbf{N}^{(i)}$ is denoted $\mathbf{T}^{(i)} = \mathbf{\Pi}^{(i)} \cdot \mathbf{N}^{(i)}$. The spatial counterparts of surface $S_o^{(i)}$ is denoted $S^{(i)}$.

Given a point $\mathbf{x} \in S_c^{(1)}$ one defines a contact point $\mathbf{y} \in S_c^{(2)}$ as the closest point to \mathbf{x} via $\mathbf{y} = \arg \min_{\mathbf{x}^{(2)} \in S_c^{(2)}} \|\mathbf{x} - \mathbf{x}^{(2)}\|$, and the proximity as $g = -\nu(\mathbf{x} - \mathbf{y})$ where ν is the outward normal at point \mathbf{y} . One also defines the point $\mathbf{X} \in S_{oc}^{(1)}$ related to point \mathbf{x} in question by $\mathbf{x} = \phi^{(1)}(\mathbf{X})$ and $\mathbf{Y}(\mathbf{X}) \in S_{oc}^{(2)}$ related to point \mathbf{y} by $\mathbf{y} = \phi^{(2)}(\mathbf{Y})$. The tangential kinematics is characterized by the slip velocity $\mathbf{V}_T = \dot{\eta}^\alpha \mathbf{a}_\alpha$ which is resolved in terms of the local spatial basis $(\mathbf{a}_1, \mathbf{a}_2)$ at point $\mathbf{y} \in S_c^{(2)}$. Likewise, the nominal traction vector at any point $\mathbf{X} \in S_{oc}^{(1)}$ is resolved as $\mathbf{T} = T_N \nu - \mathbf{T}_T$. The coefficient of friction is μ .

The weak form proposed here is stated as a mixed relationship which involves both the displacement fields $\mathbf{U}^{(i)}$, $i \in \{1, 2\}$, defined in $\Omega_o^{(i)}$ and the multiplier fields λ_N and λ_T defined on $S_{oc}^{(1)}$. Accordingly, the weighting functions are the virtual displacements $\mathbf{U}^{(1)*}$, $\mathbf{U}^{(2)*}$, and the virtual multipliers λ_N^* , λ_T^* . All the functions involved in the weak form are assumed to be regular enough for the integrations and differentiations to make sense. Two positive constants ϵ_N , ϵ_T being chosen, the weighted residual relationship is given in the following proposition.

PROPOSITION 1. $\forall t \in [O, T], \forall \mathbf{U}^{(1)*}, \forall \mathbf{U}^{(2)*}, \forall \lambda_N^*, \forall \lambda_T^*$,

$$(1) \quad \begin{aligned} & \sum_{i=1}^2 \left\{ - \int_{\Omega_o^{(i)}} \mathbf{\Pi}^{(i)T} : \nabla_{\mathbf{X}^{(i)}} \mathbf{U}^{(i)*} d\Omega_o + \int_{\Omega_o^{(i)}} \mathbf{f}^{(i)} \mathbf{U}^{(i)*} d\Omega_o + \int_{S_{oU}^{(i)} \cup S_{oT}^{(i)}} \mathbf{T}^{(i)} \mathbf{U}^{(i)*} dS_o \right\} \\ & + \int_{S_{oc}^{(1)}} \left[\langle \lambda_N + \epsilon_N g \rangle \nu - \left(1 - \left\langle 1 - \frac{\mu(\lambda_N + \epsilon_N g)}{\|\lambda_T + \epsilon_T \mathbf{V}_T\|} \right\rangle \right) (\lambda_T + \epsilon_T \mathbf{V}_T) \right] \\ & (\mathbf{U}^{(1)*}(\mathbf{X}) - \mathbf{U}^{(2)*}(\mathbf{Y}(\mathbf{X}))) dS_o + \int_{S_{oc}^{(1)}} \left\{ (\lambda_N - \langle \lambda_N + \epsilon_N g \rangle) \frac{\lambda_N^*}{\epsilon_N} + \right. \\ & \left. \left[\lambda_T - \left(1 - \left\langle 1 - \frac{\mu(\lambda_N + \epsilon_N g)}{\|\lambda_T + \epsilon_T \mathbf{V}_T\|} \right\rangle \right) (\lambda_T + \epsilon_T \mathbf{V}_T) \right] \frac{\lambda_T^*}{\epsilon_T} \right\} dS_o = 0 \end{aligned}$$

where $\nabla_{\mathbf{X}^{(i)}} \mathbf{U}^{(i)*}$ is the gradient tensor of $\mathbf{U}^{(i)*}$ with respect to variables $\mathbf{X}^{(i)} \in \Omega_o^{(i)}$, $\langle \cdot \rangle$ is the Macauley

bracket: $\langle a \rangle = a$ if $a \geq 0$, $= 0$ if $a < 0$, and $\langle 1 - \frac{\mu(\lambda_N + \epsilon_T g)}{\|\lambda_T + \epsilon_T \mathbf{V}_T\|} \rangle$ must be replaced by 0 at any point on $S_{oc}^{(1)}$ where $\lambda_T + \epsilon_T \mathbf{V}_T = \mathbf{0}$.

One can readily prove the following statement which means that the strong form implies the weak one: the solution fields of the strong problem - namely $(\mathbf{U}^{(1)}, \mathbf{U}^{(2)})$ in $\Omega_o^{(1)}, \Omega_o^{(2)}$ and $(T_N, \mathbf{T}_T, \mathbf{V}_T)$ on $S_{oc}^{(1)}$ - satisfy (1), provided that one makes in that relationship $\lambda_N = T_N$ and $\lambda_T = \mathbf{T}_T$. Conversely, the following proposition shows that the weak form implies the strong one.

PROPOSITION 2. By making some smoothness assumptions, which are not specified in this abstract, it can be shown that (1) implies at any time $t \in [0, T]$ the following local equations:

- (a) The momentum balance equation for the two bodies 1 and 2.
- (b) The following relation on the boundary portion $S_o^{(i)} \setminus S_{oc}^{(i)} = S_{oT}^{(i)} \cup S_{oU}^{(i)}$: $\mathbf{\Pi}^{(i)} \mathbf{N}^{(i)} = \mathbf{T}^{(i)}$.
- (c) The equalities between the components of the nominal traction vectors and the multipliers on the contactor surface $S_{oc}^{(1)}$: $\forall \mathbf{X} \in S_{oc}^{(1)}, \mathbf{T}^{(1)} = \mathbf{\Pi}^{(1)} \mathbf{N}^{(1)} = \lambda_N \boldsymbol{\nu} - \lambda_T$. $\Leftrightarrow T_N = \lambda_N$ and $\mathbf{T}_T = \lambda_T$.
- (d) The normal and tangential contact laws: $\forall \mathbf{X} \in S_{oc}^{(1)}, g(\mathbf{X}) \leq 0$ where
 - . if $g < 0$, then $T_N = 0, \mathbf{T}_T = \mathbf{0}$
 - . if $g = 0$, then $T_N \geq 0, \|\mathbf{T}_T\| \leq \mu T_N$
 - .if $\|\mathbf{T}_T\| \leq \mu T_N$, then $\mathbf{V}_T = \mathbf{0}$ (stick)
 - .if $\|\mathbf{T}_T\| = \mu T_N$, then $\mathbf{V}_T \wedge \mathbf{T}_T = \mathbf{0}, \mathbf{V}_T \cdot \mathbf{T}_T \geq 0$ (slip)
- (e) The following relationship which expresses the equilibrium of the traction vectors at the contact interface: $\forall \mathbf{X} \in S_{oc}^{(1)}, \forall \mathbf{Y}(\mathbf{X}) \in S_{oc}^{(2)}, \mathbf{T}^{(2)}(\mathbf{Y}) dS_{oc}^{(2)} = -\mathbf{T}^{(1)}(\mathbf{X}) dS_{oc}^{(1)}$, where $dS_{oc}^{(1)}$ is a differential reference area in $S_{oc}^{(1)}$ and $dS_{oc}^{(2)}$ its counterpart in $S_{oc}^{(2)}$.

2. Numerical examples

The weak form (1) has been discretized by means of the finite element method and the contact tangent stiffness obtained by appropriately linearizing the contact terms. Several numerical examples have been investigated on solid or membrane structures subjected to dead or following loads, with hyperelastic or finite elastoplastic material models. A typical example is shown here, concerning the contact between two hyperelastic beams, one of which being subjected at one tip to a follower force.

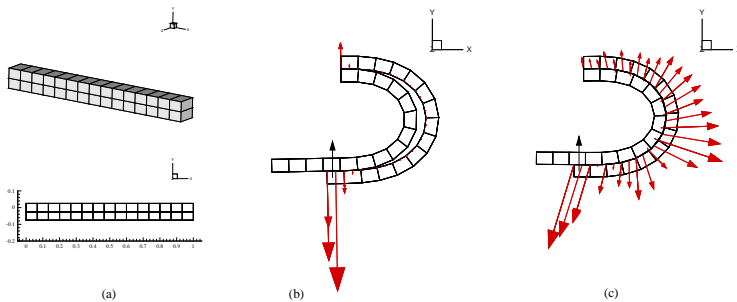


Figure 1. Contact between two beams. (a) Reference configuration, 3D view of the mesh and in-plane view. (b) Deformed shape and contact tractions at the last step in the frictionless case (c) Friction case with $\mu = 0.3$.

3. References

- P. Wriggers (2002) *Computational Contact Mechanics*, Wiley.
- T.A. Laursen (2003) *Computational Contact and Impact Mechanics*, Springer.
- G. Pietrzak and A. Curnier (1999). Large deformation frictional contact mechanics: continuum formulation and augmented Lagrangian treatment, *Comput. Methods Appl. Mech. Engrg.*, **177**, 351-381.

OFF-LINE RECONSTRUCTION OF DYNAMIC LOADS

Q. Zhang^{1,2} and Ł. Jankowski²

¹*School of Civil Engineering, Harbin Institute of Technology, Harbin, China*

²*Institute of Fundamental Technological Research, Warsaw, Poland*

1. Introduction

This research considers off-line reconstruction of spatial and temporal characteristics of dynamic loads in linear and elastoplastic systems. The motivation is the need for a technique for efficient a posteriori identification of the scenario of a sudden load, to be applied in black-box type systems.

There is an ongoing research effort in the field, see e.g. [2] for a relatively recent review. However, the structures are usually assumed to be linear and the generality of the considered loads is limited to a single pointwise load with the location known in advance or determined in an additional nonlinear optimization. Moreover, the reconstruction is often simplified by assuming stationarity of the load. If a moving force is considered, it has a constant velocity. A number of papers deals with single pointwise impact loads only and disregards all load characteristics besides the location. Papers that do consider multiple independent loads, assume superfluous number of sensors.

The approach proposed here is aimed at the fully general case. In the so-called underestimated case it allows to use a limited number of sensors to reconstruct general dynamic loads of unknown locations, including simultaneous multiple impacts, freely moving and diffuse loads. However, this is at the cost of the uniqueness of reconstruction, which can be attained only with additional heuristic assumptions. This way an equivalent load is identified, which is observationally indistinguishable from the actual load and optimum in a given sense. Additionally, the problem of optimum sensor location is discussed.

2. Response to dynamic load and load reconstruction

At zero initial conditions, the discretized response ε of a linear system can be expressed by means of a simple convolution equation $\varepsilon = \mathbf{B}\mathbf{p}$, where the vector \mathbf{p} collects the discretized loads in all load-exposed degrees of freedom (DOF) and \mathbf{B} is the system transfer matrix. The elastoplastic behavior is included by combining the Virtual Distortion Method (VDM) [1] with the return mapping algorithm. The convolution equation takes into account the effects of the plastic distortions β of the yielding elements, $\varepsilon = [\mathbf{B}\mathbf{B}^P] [\mathbf{p}^T \beta^T]^T$. The distortions β have to satisfy the constitutive law and are nonlinearly dependent on the unknown load \mathbf{p} [3]. Load reconstruction amounts to a deconvolution: compare the measured ε^M and the modeled ε system responses, and obtain the excitation by solving the resulting system of equations. For a linear system, it leads to a large and intrinsically ill-conditioned system of linear equations, while an elastoplastic system yields nonlinear equations.

If the system is linear overdetermined, a unique load can be found relatively easily. In underdetermined linear systems, the unknown load can be split into two complimentary components: the reconstructible component which can be reconstructed from the measurement, and the unreconstructible component. All information about the latter is lost in the measurement process, hence it cannot be reconstructed, but can be assumed using heuristic postulates. In an elastoplastic system, three cases are possible: strongly overdetermined case, in which there are more sensors than load-exposed DOFs and yielding elements, overdetermined case and underdetermined case, in which there are fewer equations than unknowns. In the strongly overdetermined case, the load \mathbf{p} and the distortions β can be treated as uncoupled; the resulting equation can be considered linear and solved directly. The other two cases lead to nonlinear problems, which can be solved by gradient-based optimization techniques.

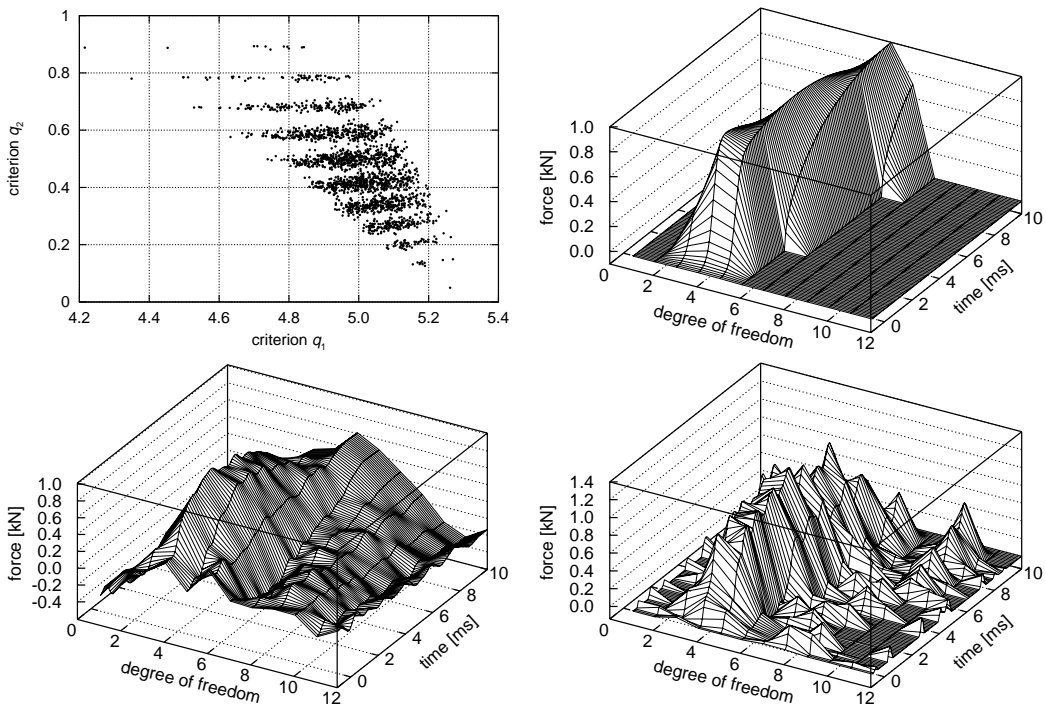


Figure 1. Numerical example: (top left) correlation plot for the two proposed sensor location criteria. Each dot corresponds to one of 2047 considered locations of 1 to 11 sensors; (top right) assumed actual load evolution; (bottom left) identification result for the linear system, four sensors and 5 % rms noise level; (bottom right) identification result for the elastoplastic system, five sensors and 5 % rms noise level

3. Optimum sensor location

Optimum sensor location is crucial for the accuracy of the reconstruction. Two sensor location criteria are proposed, based either on the dimension of the unreconstructible load subspace or on its coincidence with a given set of expected or typical loads. These criteria tend to be negatively correlated, thus a third, compound criterion is proposed, which can be seen as a single *a priori* measure of reconstruction accuracy.

4. Numerical example

In the numerical example a 119 element truss structure is used. There are 100 measurement time steps (of 0.1 ms) and 110 reconstruction time steps. Since 12 DOFs are load-exposed and four (or five) sensors are used, the resulting system is a strongly underdetermined (1320 unknowns and 400 or 500 equations). The assumed testing load and the results are shown in Figure 1.

- [1] J. Holnicki-Szulc, ed. (2008), *Smart Technologies for Safety Engineering*, John Wiley & Sons, Ltd, Chichester, in press.
- [2] E. Jacquelin, A. Bennani, P. Hamelin (2003), Force reconstruction: analysis and regularization of a deconvolution problem, *Journal of Sound and Vibration*, **265**, 81107.
- [3] Ł. Jankowski (2008), Off-line identification of dynamic loads, *Structural and Multidisciplinary Optimization*, in press.

SPARSE GRID AND EVOLUTION-TYPE ALGORITHM IN SHAPE OPTIMIZATION FOR BECK'S COLUMN

*K. Lisowski*¹

¹*Technical University of Koszalin, Koszalin, Poland*

1. Introduction

The Beck column is defined as a column clamped at one end and subjected to a certain follower force at the other. The force in this system is always tangent to the deflection line on a free end. After passing critical value of acting force, the Beck column loses its stability in an oscillatory manner. The problem was first investigated theoretically by Pfluger (1950) and solved by Beck (1952). The solution was confirmed by several authors (Pfluger 1950, Leipholz 1962, Deineko & Leonov 1955, Kordas & Zyckowski 1963). Nowadays the follower force play important role in civil engineering, vehicle dynamics and aeronautics. In this paper a new approach for finding columns with a higher value of the critical force is presented.

2. New approach in optimization

The equation of motion for the Beck column is described in the following manner [2]:

$$(1) \quad (Su'' + Pu)'' = -\rho\ddot{u}.$$

where:

$u = u(z, t)$ - the unknown displacement function, P - the given constant longitudinal compressing force, $S = S(z)$ - the bending stiffness, $\rho = \rho(z)$ - the mass density.

For the optimization of the parameters describing the shape, eg.1 has to be studied with appropriate boundary conditions. We look for the maximum P , such that solution to (1) remain stable, cf. [1], [3], [4]. Well known procedures are the steepest-descent, gradient method and Newton's method. In this paper a new approach for finding optimal shape of a column is applied. The evolution algorithms (EA) [3] are used with sparse grid interpolation to speed up the calculation of objective function. A process of calculating each combination of decision variable is time consuming.

The main idea consists of adapting a form of evolution for finding extrema of functions. At the beginning, the algorithm creates an initial population of individuals. Then operations of differentiation are performed on the population. Those operations are selection and mutation. The individuals are then evaluated by the objective function, which is called here the fitness function. The best-fitted individuals are propagated to the next generation. The process is being repeated until suitable stopping criteria are met.

The sparse grids interpolate the objective function with a special discretization technique thus a smooth multivariate function can be approximated with a suitable interpolation formula. The reason for involved sparse grids is to speed up the calculation of objective function and restrict the area where the EA searches for a optimal solution.

The object of optimization is the two-segment column jointed with a passive hinge. Below graphs show a plot of interpolated function and the plot of errors function i.e. the difference between real and interpolated values.

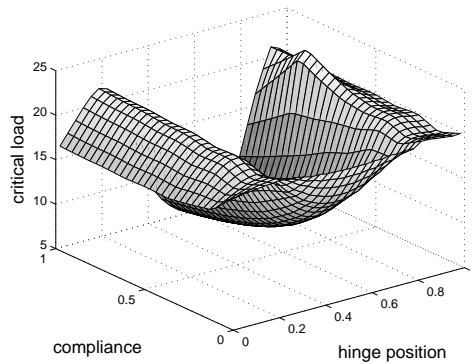


Figure 1. Graph of interpolated critical load vs. position and the compliance of hinge.

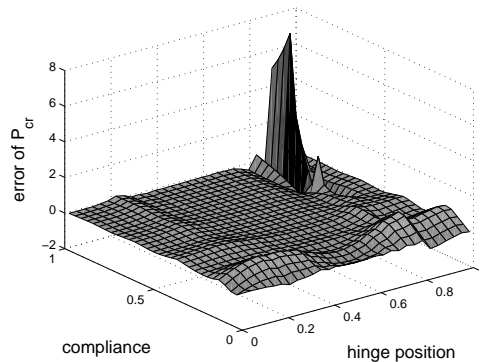


Figure 2. Graph of errors (the difference real and interpolated values) of objective function.

An application of sparse grids with combination of evolution algorithms is a new concept in the optimization of column profile. On the future a column with more number of elements (with mutable cross-section) are going to be analyzed.

3. References

- [1] Bogacz, R., Frischmuth K., 2005, Transient Behavior of Columns under Follower Forces, *Machine Dynamics Problems*, Vol. 29 No. 4, pp. 7–20.
- [2] Bogacz R., Janiszewski R.: *Zagadnienia analizy i syntezy kolumn obciążonych siłami śledzącymi ze względu na stateczność*. Warszawska Drukarnia Naukowa, Warszawa 1986
- [3] Price K. V., Storn R. M., Lampinen J. A.: *Differential Evolution: A Practical Approach to Global Optimization*. I edition, Springer 2005
- [4] Lisowski K., Frischmuth K.: Shape optimization for Beck's column by evolution-type algorithms. *Zeszyty Naukowe Wydziału Mechanicznego nr 40*, Wydawnictwo Uczelniane Politechniki Koszalińskiej, str. 186-193, Koszalin 2007

GEOMETRIC SENSITIVITY ANALYSIS OF TRUSS AND FRAME STRUCTURES

D. Bojczuk, M. Jabłoński

*Kielce University of Technology, Faculty of Management and Computer Modelling,
Kielce, Poland*

1. Introduction

The problem of manufacturing imperfections and their influence on structural configuration is discussed in the paper. When a structure is composed of members with dimension imperfections, states of stresses, strains and displacements induced by external load will vary and additionally in hyperstatic structures self-equilibrated states of stresses will arise. The influence of these effects on the optimal design was analyzed in [3] and [4]. However, length imperfections even in unloaded structure may induce variations of geometry. The problem of determination of these changes for selected points of a structure, which can be called *geometric sensitivity analysis*, is studied in this paper. It is extension of the previous considerations presented in [2], and here also geometrically nonlinear case is analyzed. It is important to notice, that the cumulative change in point position may be far greater than it would appear from the value of members tolerances and it even may cause that the structure will reach unstable state corresponding to the limit point.

2. Geometric sensitivity analysis – linear case

Let us consider a truss or a frame composed of members, which have nominal lengths l_1, l_2, \dots, l_n , where n is the number of members. It is assumed that member lengths may deviate from their nominal values by tolerances $t_1^{(l)}, t_2^{(l)}, \dots, t_n^{(l)}$. The change of i -th member length arising directly from the tolerance can be expressed in the form $\Delta l_i^{(t)} = \alpha_i t_i^{(l)}$, where $|\alpha_i| \leq 1$, $i = 1, 2, \dots, n$.

The first problem analyzed here is to determine maximal translation w in fixed direction of certain point (node) induced by considered tolerances. Let us introduce the adjoint structure without any dimension imperfections and with the same boundary conditions as the primary structure but subjected to force λP^a applied in direction of the analyzed displacement w , where λ is the load parameter and P^a denotes the reference load. Now, the virtual work equation for the primary and adjoint structures can be written in the form

$$(1) \quad \lambda P^a w = \sum_{i=1}^n \left(N_i^a \Delta l_i^{(c)} + \int_{l_i} M_g^a \kappa^{(c)} dx_i \right),$$

where $\Delta l_i^{(c)}$, $\kappa^{(c)}$ are the total elongations of members and the total curvatures in the primary structure, while N_i^a , M_g^a denote the normal forces and the bending moments in the adjoint structure. Let us notice, that analyzed tolerances induce self-equilibrated state of stress with elastic elongations $\Delta l_i^{(el)} = \Delta l_i^{(c)} - \Delta l_i^{(t)}$ and elastic curvatures $\kappa^{(el)} = \kappa^{(c)}$. Using for this state and for the adjoint structure the virtual work principle, we get

$$(2) \quad \sum_{i=1}^n \left(N_i^a \Delta l_i^{(el)} + \int_{l_i} M_g^a \kappa^{(el)} dx_i \right) = 0.$$

In order to obtain relationship for the translation w in the selected direction we should substitute equation (2) into (1). Now, it is easy to notice, that the maximal translation occurs, when $\Delta l_i^{(t)}$ attain extreme values i.e. when $\alpha_i = 1$ or $\alpha_i = -1$ and when for all members it has simultaneously the same (or simultaneously the opposite) sign as corresponding force N_i^a . So, taking $\lambda P^a = 1$, the

maximal translation in fixed direction can be written as follows

$$(3) \quad |w|_{max} = \max_{\alpha_i} \left| \sum_{i=1}^n N_i^a \alpha_i t_i^{(l)} \right| = \sum_{i=1}^n |N_i^a t_i^{(l)}|.$$

Now, let us consider problem of determination of maximal translation w_c of certain point (node) in arbitrary direction. We assume, that this direction forms unknown angle β with axis x of the rectangular coordinate system x, y . The translation w_c can be determined using translations in x and y directions. Then, we have

$$(4) \quad \lambda P^a w_c = \lambda P^a \cos \beta \cdot w_x + \lambda P^a \sin \beta \cdot w_y = \sum_{i=1}^n (N_i^{a(x)} \cos \beta + N_i^{a(y)} \sin \beta) \alpha_i t_i^{(l)},$$

where $N_i^{a(x)}, N_i^{a(y)}$ denote forces in i -th member induced by unit loads $\lambda P^a = 1$ applied respectively in x and y direction. Finally, maximal translation can be determined as the solution of the following problem

$$(5) \quad |w_c|_{max} = \max_{\beta} \left[\sum_{i=1}^n \left| (N_i^{a(x)} \cos \beta + N_i^{a(y)} \sin \beta) t_i^{(l)} \right| \right].$$

3. Geometric sensitivity analysis – non-linear case

In this case the adjoint problem is introduced by analogy to the incremental problem for the primary structure related to perturbation of the current equilibrium state. Then, using finite element notation, equilibrium equation for the adjoint structure can be written in the form $\mathbf{K}^t \mathbf{u}^a = \dot{\lambda} P^a$ (cf. [1]), where \mathbf{K}^t is the tangent stiffness matrix and \mathbf{u}^a denotes vector of displacements. The load $\dot{\lambda} P^a$ is applied, as previously, in direction of the analyzed displacement w , where point over the symbol denotes increment of the quantity. Using approach analogous as for the linear case, we get

$$(6) \quad \dot{\lambda} P^a w = \sum_{i=1}^n N_i^a \alpha_i t_i^{(l)}.$$

In order to obtain the maximal translation, non-linear equation (6) should be solved with respect to w , where values α_i are chosen analogously as in (3). It is important to notice that during incremental process of solving the problem (6), situation when $\dot{\lambda} = 0$ may appear and it corresponds to structure geometric instability related to the limit point.

4. Concluding remarks

The problem of maximal translation determination for certain points (nodes) of truss or frame structures induced by length imperfections of their members, is discussed in the paper. Apart from the linear analysis, in order to reveal possible geometric instabilities of the limit point type, the considerations are also developed for the non-linear case.

5. References

- [1] D. Bojczuk (1999). *Analiza wrażliwości i optymalizacja konstrukcji prętowych* (in Polish). Wydawnictwo Politechniki Świętokrzyskiej, Kielce.
- [2] D. Bojczuk, M. Jabłoński (2007). Optymalizacja konstrukcji prętowych przy zastosowaniu pochodnej topologicznej i skończonych modyfikacji topologii (in Polish). *Proc. I Congress of Polish Mechanics*, Warszawa, on CD.
- [3] K. Dems, W. Gutkowski (2003). Optimal shape and configuration optimization of multi-loaded structures with manufacturing tolerances. *Proc. V World Congress on Struct. Multidisc. Optim.*, Lido di Jesolo, on CD.
- [4] W. Gutkowski, J. Latalski (2005). Structural optimization with member dimensional imperfections. *Struct. Multidisc. Optim.*, **30**, 1-10.

**APPLICATION OF THE STABILIZATION METHOD FOR ANALYSIS
OF GEOMETRICALLY NON-LINEAR FORCED VIBRATIONS OF ELASTIC BEAMS
ON UNILATERAL WINKLER FOUNDATION**

A. Bobylov and A. Zubko

Dniepropetrovsk national university, Dniepropetrovsk, Ukraine

The computational model of geometrically non-linear elastic beam is frequently used for analysis of dynamics of one-dimensional distributed systems on unilateral elastic foundation. The problems of forced vibrations of deformable solids under unilateral constraints are nonlinear problems with conditions expressed in the form of inequalities. Besides, in most cases it is necessary to take into account the dissipation of energy that is caused by external viscous resistance.

As a rule, capabilities of analytical methods for solving this type of problems are limited to discrete systems with a small number of freedoms. That's why the principal role in solving forced vibrations of deformable solids under unilateral constraints belongs to numerical methods. A stabilization method for computational modeling of geometrically non-linear forced vibrations of elastic beams on unilateral Winkler foundation is presented. This method was used earlier for computational modeling of forced vibrations of viscoelastic solids under unilateral contact [1] and geometrically non-linear forced vibrations of elastic beams without unilateral constraints [2].

It is well known, that if damping is present in a system then initial conditions have considerable effect on forced vibrations of the deformable solids only during a limited period of time after which the system moves to a steady-motion state. Therefore, the main idea of this approach is that the T-periodical solution of the original problem can be found as a solution of the Cauchy problem when damping is present in the system. In this case initial conditions can be chosen arbitrarily.

Beam deformation is described by the Timoshenko model. It is proposed that a value of resistance forces is proportional to velocity. Geometrically nonlinear equations of motion for Timoshenko beam on unilateral Winkler foundation are as follows

$$\frac{\partial Q}{\partial x} + \frac{\partial}{\partial x} \left(N \frac{\partial w}{\partial x} \right) + q - c \cdot H(w - \phi) \cdot (w - \phi) - \varepsilon \frac{\partial w}{\partial t} - \rho F \frac{\partial^2 w}{\partial t^2} = 0,$$

$$\frac{\partial M}{\partial x} - Q - \rho J \frac{\partial^2 \gamma}{\partial t^2} = 0, \quad \frac{\partial N}{\partial x} - \rho F \frac{\partial^2 u}{\partial t^2} = 0,$$

where w is the transverse displacement; γ is the angle of rotation of the normal relatively to the axis of the beam; u is the longitudinal displacement; M is the bending moment; Q is the shear force; N is the normal force; ρ is the mass per unit of length; F is the area of the cross section; J is the moment of inertia of the cross section; q is T-periodic transversal distributed load; c is the foundation stiffness; ϕ is the clearance between the beam and the foundation; $H(\cdot)$ is Hevyside function; ε is the viscous damping coefficient per unit of length.

The forces Q , N and the bending moment M are related to the displacements w , u and the angle of rotation γ by the constitutive relations

$$M = EJ \frac{\partial \gamma}{\partial x}, \quad Q = k^2 GF \left(\frac{\partial w}{\partial x} + \gamma \right), \quad N = EF \left(\frac{\partial u}{\partial x} + \frac{1}{2} \left(\frac{\partial w}{\partial x} \right)^2 \right),$$

where E is Young's modulus of the beam material; G is the shearing modulus; $k^2 = 5/6$ for a rectangular cross section.

For definiteness the boundary conditions have the following form:

$$w(0) = w(l) = 0; \quad M(0) = M(l) = 0; \quad u(0) = u(l) = 0.$$

Through a standard variational procedure, we obtain the following variational equation:

$$\begin{aligned} & \int_0^l \left(\rho F \frac{\partial^2 w}{\partial t^2} (\tilde{w} - w) + \rho J \frac{\partial^2 \gamma}{\partial t^2} (\tilde{\gamma} - \gamma) + \rho F \frac{\partial^2 u}{\partial t^2} (\tilde{u} - u) + \varepsilon \frac{\partial w}{\partial t} (\tilde{w} - w) \right) dx + \\ & + \int_0^l \left(k^2 G F \left(\frac{\partial w}{\partial x} + \gamma \right) \left(\frac{\partial \tilde{w}}{\partial x} + \tilde{\gamma} - \frac{\partial w}{\partial x} - \gamma \right) + E J \frac{\partial \gamma}{\partial x} \left(\frac{\partial \tilde{\gamma}}{\partial x} - \frac{\partial \gamma}{\partial x} \right) + E F \frac{\partial u}{\partial x} \left(\frac{\partial \tilde{u}}{\partial x} - \frac{\partial u}{\partial x} \right) \right) dx + \\ & + \int_0^l E F \left(\frac{\partial u}{\partial x} + \frac{1}{2} \left(\frac{\partial w}{\partial x} \right)^2 \right) \frac{\partial w}{\partial x} \left(\frac{\partial \tilde{w}}{\partial x} - \frac{\partial w}{\partial x} \right) dx + \frac{1}{2} \int_0^l E F \left(\frac{\partial w}{\partial x} \right)^2 \left(\frac{\partial \tilde{u}}{\partial x} - \frac{\partial u}{\partial x} \right) dx - \\ & - \int_0^l q (\tilde{w} - w) dx + \int_0^l c \cdot H(w - \phi) \cdot (w - \phi) (\tilde{w} - w) dx = 0, \quad \forall (\tilde{w}, \tilde{\gamma}, \tilde{u}) \in K. \end{aligned}$$

where K is the set of the kinematically admissible beam displacements.

This equation expresses the principle of admissible displacements for the elastic beam on unilateral Winkler foundation and includes only first spatial derivatives of the displacements.

The finite difference method is used for time semi-discretization of the variational equation. The second and the first time derivatives are approximated with three-point central differences. As a result an explicit three-layer scheme is used for numerical time integration. The minimization problem which is equivalent to the obtained variational problem on each time step is derived.

The finite element method is used for the spatial discretization of the minimization problem. Two-nodal and three-nodal Lagrange finite elements are used.

A software package based on the described computational algorithm was developed. Numerical solutions of a number of problems were obtained and convergence of the computational algorithms was investigated. The influence of foundation compliance on the solution behavior was investigated. Specifics of amplitude-frequency dependencies of stresses and displacements were researched. It is known that an amplitude-frequency dependency for the elastic beam is not unique due to geometrical nonlinearity, i.e. a few values of the amplitude can correspond to the one value of the frequency near a resonance. It is a difficulty for numerical solving. In this study the continuation method is used to derive the amplitude-frequency curves. The frequency of forced vibrations is chosen as a continuation parameter. The calculation was performed in two stages. On the first stage the frequency of forced vibrations was increased in the range under investigation. On the second stage the frequency was decreased from the maximum to the minimum values. The solution for the previous value of the frequency was used for the initial condition.

Performed computational experiments confirmed effectiveness of suggested methods for solving problems of geometrically non-linear forced vibrations of elastic beams on unilateral Winkler foundation.

- [1] A. Bobylov and E. Suturin (2005). Application of the stabilization method for analysis of forced vibrations of viscoelastic solids under unilateral constraints. *8th Conference on Dynamical Systems – Theory and Applications, Lodz, Poland, 269-276.*
- [2] A. Bobylov and A. Zubko (2007). Application of the stabilization method for analysis of geometrically nonlinear forced vibrations of an elastic beam. *9th Conference on Dynamical Systems – Theory and Applications, Lodz, Poland, 553-560.*

LEVEL SET METHOD IN STRUCTURAL OPTIMIZATION

A. Myśliński

Systems Research Institute, Warsaw, Poland

1. Introduction

The paper is concerned with the numerical solution of a structural optimization problem for an elastic body in unilateral contact with a rigid foundation. Shape optimization of contact problems is considered, among others, in [3, 7] where necessary optimality conditions and numerical results are provided. The material derivative method is employed in monograph [7] to calculate the sensitivity of solutions to contact problems as well as the derivatives of domain depending functionals with respect to variations of the boundary of the domain occupied by the body. Topology optimization deals with the optimal material distribution within the body resulting in its optimal shape [1, 5, 8]. The topological derivative [8] is employed to account variations of the solutions to state equations or shape functionals with respect to emerging of small holes in the interior of the domain occupied by the body. The notion of topological derivative and results concerning its application in optimization of elastic structures are reported in many papers (see references in [8]).

2. Problem formulation

In the paper the elastic contact problem with a given friction, described by Coulomb law, is considered. The displacement field of the body in unilateral contact is governed by an elliptic variational inequality of the second order [2]. The structural optimization problem for the elastic body in contact consists in finding such topology of the domain occupied by the body and the shape of its boundary that the normal contact stress along the boundary of the body is minimized. The volume of the body is assumed to be bounded.

3. Necessary optimality condition

Introducing an adjoint system and using the material derivative method we calculate shape derivative of the cost functional in direction of the velocity field V with respect to perturbations of the boundary of the domain occupied by the body. Asymptotic expansion method is used to calculate topological derivative of this cost functional with respect to the inserting of a small ball at a point inside the optimized domain. Formulae of these derivatives are provided [4]. These derivatives are employed to formulate a necessary optimality condition for simultaneous shape and topology optimization problem and to calculate descent direction in the numerical algorithm.

4. Level set method

In structural optimization the level set method [6] is employed in numerical algorithms for tracking the evolution of the domain boundary on a fixed mesh and finding an optimal domain. This method is based on an implicit representation of the boundaries of the optimized structure, i.e., the position of the boundary of the body is described as an isocountour of a scalar function of a higher dimensionality. While the shape of the structure may undergo major changes the level set function remains to be simple in its topology. The evolution of the domain boundary is governed by Hamilton - Jacobi equation. The speed vector field driving the propagation of the level set function is given by the Eulerian derivative of the cost functional with respect to the variations of the free boundary. Applications of the level set methods in structural optimization can be found, among others, in [1].

Recently [9], different numerical improvements of the level set method employed for the numerical solution of the structural optimization problems are proposed and numerically tested.

5. Numerical Methods and Results

The structural optimization problem is solved numerically as the simultaneous shape and topology optimization problem. Contact system as well as the adjoint system are discretized and numerically solved using finite element method and primal - dual algorithm with active set strategy. Lagrange multiplier method is used to solve the structural optimization problem. First this problem is solved as topology optimization problem and at grid points where the topology derivative is negative the holes are created. Next shape optimization problem is solved. During this step in Hamilton - Jacobi equation velocity field V is set equal to the calculated shape gradient of the cost functional. Finite difference method and explicit up - wind scheme are used to solve Hamilton - Jacobi equation. Numerical examples indicating that the proposed numerical algorithm allows for significant improvements of the structure from one iteration to the next are provided and discussed.

- [1] G. Allaire, F. Jouve, A. Toader (2004). Structural Optimization Using Sensitivity Analysis and a Level Set Method. *Journal of Computational Physics*, **194**, 363-393.
- [2] I. Hlaváček, J. Haslinger, J. Nečas, J. Lovíšek (1988). *Solution of Variational Inequalities in Mechanics*, Springer, New York.
- [3] A. Myśliński (2006). *Shape Optimization of Nonlinear Distributed Parameter Systems*, Academic Printing House EXIT, Warsaw, Poland.
- [4] A. Myśliński (2007). Level Set Method for Optimization of Contact Problems, *Research Report RB/78/2007*, Systems Research Institute, Warsaw, Poland.
- [5] A.A. Novotny, R.A. Feijóo, C. Padra, E. Tarocco (2005). Topological Derivative for Linear Elastic Plate Bending Problems. *Control and Cybernetics*, **34**, 339-361.
- [6] S. Osher, R. Fedkiw (2003). *Level Set Methods and Dynamic Implicit Surfaces*, Springer, New York, New York.
- [7] J. Sokołowski, J.P. Zolesio (1992). *Introduction to Shape Optimization. Shape Sensitivity Analysis*, Springer, Berlin.
- [8] J. Sokołowski, A. Żochowski (2004). On topological derivative in shape optimization, In: *Optimal Shape Design and Modelling*, T. Lewiński, O. Sigmund, J. Sokołowski, A. Żochowski eds., Academic Printing House EXIT, Warsaw, Poland, 55-143.
- [9] S.Y. Wang, K.M. Lim, B.C. Khao, M.Y. Wang (2007). An extended level set method for shape and topology optimization, *Journal of Computational Physics*, **221**, 395-421.

INERTIAL MOVING LOADS

B. Dyniewicz and C. Bajer

Institute of Fundamental Technological Research, Warsaw, Poland

1. Introduction

The problem of bridge spans under a moving inertial load [1, 2] has existed since the beginning of the railways development. Together with increasing velocity of trains, the influence of the wave phenomenon is rising as well. Dynamic effects are generated by the load of train current collectors, travelling through the power supply cable of the overhead contact line. Solutions of inertial moving load applied to discrete systems unfortunately are practically not reported. Inertial force, which should be considered as a couple of a force and a mass is usually replaced by a spring-mass system. Finally the problem is solved as a problem with a massless force. We must also emphasize that the ad-hoc mass distribution between neighbouring nodes simply fails. In the case of the beam at low speed ranges and low ratio of the moving mass to the beam mass results exhibit errors. Unfortunately, such formulations exist in spite of a wrong formulation and analysis.

In this presentation the differential equations of the motion of a string and beams were derived from the Lagrange equation of the 2nd kind. Moreover, the direct solution of the differential equation was obtained as an alternative solution. Both results coincide. We also present the numerical approach to the moving inertial load problem. Classical finite element method with Newmark time integration scheme mentioned in fails. The space-time finite element method is the only method which enables us to describe the mass passing through the spatial finite element in a continuous way. We present the solution in the case of a string and a Bernoulli-Euler beam.

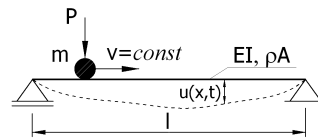


Figure 1. The point mass moving on the beam.

2. Formulation

The motion equation of the beam under a moving mass m coupled with a force P can be written as follows

$$(1) \quad EI \frac{\partial^4 u(x,t)}{\partial x^4} + \rho A \frac{\partial^2 u(x,t)}{\partial t^2} = \delta(x-vt) P - \delta(x-vt) m \frac{\partial^2 u(vt,t)}{\partial t^2},$$

where EI is the beam stiffness, N is a tensile force and ρA is a linear mass density. Taking into account beam terms, we impose four boundary conditions

$$(2) \quad u(0,t) = 0, \quad u(l,t) = 0, \quad \left. \frac{\partial^2 u(x,t)}{\partial x^2} \right|_{x=0} = 0, \quad \left. \frac{\partial^2 u(x,t)}{\partial x^2} \right|_{x=l} = 0,$$

and two initial conditions $u(x,0) = 0$, $\partial u(x,t)/\partial t|_{t=0} = 0$. The equation can not be easily solved and we must integrate it in a numerical way. We use the matrix notation here

$$(3) \quad \mathbf{M} \begin{bmatrix} \ddot{\xi}_1(t) \\ \ddot{\xi}_2(t) \\ \vdots \\ \ddot{\xi}_n(t) \end{bmatrix} + \mathbf{C} \begin{bmatrix} \dot{\xi}_1(t) \\ \dot{\xi}_2(t) \\ \vdots \\ \dot{\xi}_n(t) \end{bmatrix} + \mathbf{K} \begin{bmatrix} \xi_1(t) \\ \xi_2(t) \\ \vdots \\ \xi_n(t) \end{bmatrix} = \mathbf{P},$$

which results in a short form $M\ddot{\xi} + C\dot{\xi} + K\xi = P$, where M , C and K are square matrices for $i = j = 1, 2, \dots, n$.

When we calculate the value of general coordinates $\xi_i(t)$ for each i to n . Finally we can compute displacements of the string-beam $u(x, t)$

$$(4) \quad u(x, t) = \sum_{i=1}^{\infty} \xi_i(t) \sin \frac{i\pi x}{l}.$$

Displacements given in the example below are dimensionless. They were calculated in relation to the static deflection u_0 of the string-beam loaded in the mid point by the point force P : $u_0 = u_{0s} u_{0b} / (u_{0s} + u_{0b})$. u_{0s} and u_{0b} are static deflections in the case of a string and a beam, respectively. The mass trajectory is depicted in Fig. 2.

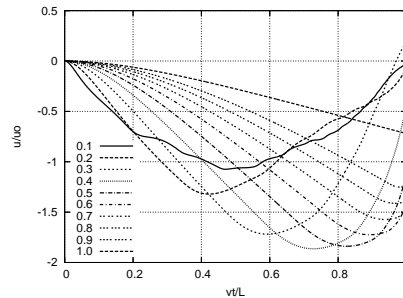


Figure 2. Mass trajectory for different speeds v (bending neglected).

3. Conclusions

We deal with the problem of the numerical treatment of the moving mass problem. The solution presented in the paper shows the way of mathematical analysis which results in a universal time stepping procedure. It enables us to solve the problem with the arbitrary speed. The solution in the case of the string exhibits discontinuous mass trajectory [3, 4] at the end support. This fact influences high gradients of the solution at the final stage of the motion. This phenomenon is the paradoxical property of the differential equation since considering boundary conditions we intuitively expect smooth curves. Numerical results of the string vibrations exhibit good accuracy, comparing with semi-analytical solution. In the case of the beam the coincidence of both curves is perfect.

- [1] C.E. Inglis. *A Mathematical Treatise on Vibrations in Railway Bridges*. Cambridge University Press, 1934.
- [2] L. Fryba. *Vibrations of solids and structures under moving loads*. Academia, Prague, 1972.
- [3] B. Dyniewicz i C.I. Bajer. Paradox of the particle's trajectory moving on a string. *Arch. Appl. Mech.*, 2008. DOI: 10.1007/s00419-008-0222-9.
- [4] C.I. Bajer i B. Dyniewicz. Space-time approach to numerical analysis of a string with a moving mass. *Int. J. Numer. Meth. Engng.*, 2008. DOI: 10.1002/nme.2372.

PHYSICS, CHEMISTRY AND MECHANICS ARE GROWING TOGETHER - THE ROLE OF NONEQUILIBRIUM THERMODYNAMICS

F.D. Fischer¹, J. Svoboda²

¹*Institute of Mechanics, Montanuniversität Leoben, Leoben, Austria*

²*Institute of Physics of Materials, Academy of Sciences of the Czech Republic*

1. Introduction

Materials are rather complex systems described by a number of characteristic parameters (CPs), conservation laws and phenomenological equations, together with boundary and contact conditions. All these relations are engaged to simulate the development of the material system, mostly under simplified conditions. The extraction of the time evolution of the CPs from the solution is often impossible. Therefore, we start with the Thermodynamic Extremal Principle (TEP), proposed by Onsager in 1931 for heat conduction and 1945 for diffusion, which allows a direct derivation of the evolution equations for CPs in the case of slow processes at elevated temperatures, e.g. diffusive processes, dealing with linear non-equilibrium thermodynamics.

2. The Thermodynamical Extremal Principle (TEP)

The TEP is outlined shortly as following, for details see e.g. [1]. We have CPs denoted as $q_i, (i=1, \dots, N)$, e.g. concentrations etc., and their rates \dot{q}_i . The total Gibbs energy of the system is supposed to be $G(q_1, \dots, q_N)$ with its rate $\dot{G} = \sum_{i=1}^N (\partial G / \partial q_i) \dot{q}_i$. Linear constraints exist in the form

$C_k = \sum_{i=1}^N a_{ik} \dot{q}_i = 0, k=1, \dots, m$. We define a dissipation Q_h as a positive homogeneous function of the $\dot{q}_1, \dots, \dot{q}_N, h$ with h being the order homogeneity. This dissipation function Q_h reflects the power generated by the evolution of the internal variables. We look now for a maximum of Q_h constrained by $\dot{Q}_h + G = 0$ and the constraints $C_k = 0, i=1, \dots, m$. The result are evolution equations for the \dot{q}_i as

$$(1) \quad \sum_{j=1}^N U_{ij} \dot{q}_j + \sum_{k=1}^m a_{ik} \beta_k = -\frac{\partial G}{\partial q_i}, i=1, \dots, N,$$

if Q_h is a quadratic function $\sum_{i,j=1}^N U_{ij} (q_1, \dots, q_N) \dot{q}_i \dot{q}_j$. The β_k are Lagrange multipliers.

It is interesting to note that the TEP may be equivalent to the minimization of $\dot{G} + \Delta(q_1, \dots, q_N; \dot{q}_1, \dots, \dot{q}_N)$ with Δ being a dissipation potential for a wide class of functions as shown by Hackl and Fischer [2], yielding for homogeneous functions $Q_h = h\Delta$.

3. Application of the TEP

The first application of TEP is demonstrated on grain coarsening both with grain boundary motion and additionally diffusion in the matrix in the case of coarsening of precipitates, for details see [3]. If the grain radii are chosen as those parameters, the application of the TEP reproduces Hillert's classical evolution equations for the radii of individual grains (multigrain concept). The observed or calculated ensemble of grains is usually classified by a grain radii distribution function involving a certain number of parameters. A new concept [4] is now represented by the direct

application of the TEP to the radii distribution function by derivation of the evolution equations for its parameters (distribution concept). The kinetics of systems with bimodal and different monomodal starting distribution functions are calculated by means of both multigrain and distribution concepts and the results of simulations are compared and discussed. The dissipation of the grain coarsening process is evaluated, and it is shown that the width of the distribution function decisively influences the coarsening kinetics.

The second application deals with a chemically driven inelastic deformation in systems with non-ideal sources and sinks for vacancies. As thermodynamic forces generalized chemical potentials including both chemical and mechanical terms appear together with an evolution law for the vacancies, [5]. As a representative example the inelastic deformation state in a Fe-Mn-C bamboo-structured wire is demonstrated in dependence on the activity of sources and sinks for vacancies at dislocation jogs in the bulk. Sources and sinks for vacancies are supposed to be ideal at grain boundaries. Fig. 1 shows the axial strain along a wire with the dimension-free length 2 and two grain boundaries ($\bar{x} = 0.5, \bar{x} = 1.5$) at a certain time instant for different jog densities ρL^2 ; details can be taken from [6].

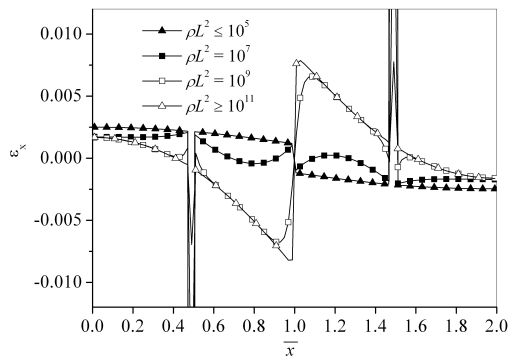


Figure 1. Chemically driven longitudinal strain in a wire.

4. References

- [1] J. Svoboda, I. Turek, F.D. Fischer (2005). Application of the Thermodynamic Extremal Principle to Modeling of Thermodynamic Processes in Material Sciences, *Phil. Mag.*, **85**, 3699-3707.
- [2] K. Hackl and F.D. Fischer (2007). On the Relation between the Principle of Maximum Dissipation and Inelastic Evolution Given by Dissipation Potentials, to be published *Proc. R. Soc. A*.
- [3] F.D. Fischer, J. Svoboda, P. Fratzl (2003). A Thermodynamical Approach to Grain Growth and Coarsening, *Phil. Mag. A*, **83**, 1075-1093.
- [4] J. Svoboda and F.D. Fischer (2007). A New Approach to Modelling of Non-Steady Grain Growth, *Acta mater.*, **55**, 4467-4474.
- [5] J. Svoboda, F.D. Fischer, P. Fratzl (2006). Diffusion and Creep in Multi-Component Alloys with Non-Ideal Sources and Sinks for Vacancies, *Acta mater.*, **54**, 3043-3053.
- [6] J. Svoboda, F.D. Fischer, E. Gamsjäger (2007). Simulation of Chemically Driven Inelastic Strain in Multi-Component Systems with Non-Ideal Sources and Sinks for Vacancies, to be published *Acta mater.*

MICROMECHANICAL MODELLING OF PSEUDOELASTIC SMA POLYCRYSTALS UNDER NON-PROPORTIONAL LOADING

S. Stupkiewicz and H. Petryk

Institute of Fundamental Technological Research (IPPT), Warsaw, Poland

1. Introduction

This work is concerned with micromechanical modelling of polycrystalline shape memory alloys (SMA) undergoing stress-induced martensitic transformations. In our previous papers [1, 2, 3], a micromechanical model of stress-induced phase transformation in SMA single crystals has been developed, starting from transformations of the atomic lattice structure and using exact compatibility conditions on the interfaces. In this model, sequential application of the micro-macro transition for rank-one laminates combined with a local phase transformation criterion provides overall response of a single crystal of a higher-rank laminated microstructure varying with the overall deformation. The transformation criterion is rate-independent with a threshold value for the thermodynamic driving force acting on a phase transformation front, including in this way the intrinsic dissipation due to phase transition. Selection of an optimal microstructure for the actual type of loading, from a number of different possibilities, is based on the transformation criterion, and the corresponding procedure can be interpreted as minimization of the incremental energy supply [4]. That approach is extended here to the scale of a polycrystalline aggregate, with the focus on the effect of interaction between neighbouring grains. The proposed grain-to-polycrystal transition scheme bears a resemblance to that developed recently in [5] in a different context, namely, for the prediction of texture development in plastically deforming metals.

2. Multi-scale model

The stress-induced martensitic transformation is assumed to proceed by the formation and evolution of microstructure at several scales, starting from the scale of the crystalline lattice, through the intermediate scales of martensite–martensite and austenite–martensite laminates, up to the scale of a single grain with complex multi-variant martensitic microstructures. The response of a single grain is fully defined by specifying the average Helmholtz free energy $\bar{\phi}$ (e.g. [6]) and dissipation function $\bar{\mathcal{D}}$. Selection of the active transformation mechanisms, i.e. the evolution of the microstructure, is then performed by minimization of the incremental energy supply [4],

$$(1) \quad \Delta E \rightarrow \min \quad \text{subject to kinematical constraints,}$$

where $\Delta E = \Delta \bar{\phi} + \Delta \bar{\mathcal{D}} + \Delta \Omega$, the prefix Δ denotes a virtual increment from a given state, corresponding to a given increment of an external control parameter, and $\Delta \Omega$ is the increment in the potential energy of external loads.

In order to realistically describe the pseudoelastic response on non-proportional loading paths, the dissipation is assumed to comprise two components,

$$(2) \quad \Delta \bar{\mathcal{D}} = f_c |\Delta \bar{\eta}| + f_r |\Delta \bar{\eta}_r|,$$

associated with the increment $\Delta \bar{\eta}$ in the volume fraction of martensite due to the forward or reverse austenite–martensite transformation, and with the volume fraction $\Delta \bar{\eta}_r$ of reoriented martensite.

Interaction of grains is accounted for by assuming that the polycrystal is an aggregate of bi-crystals, each formed by a grain boundary, of fixed orientation, and by parts of two adjacent grains.

Compatibility conditions (equilibrium and displacement continuity) on the grain boundary are enforced on the average stresses and strains within each sub-grain. The average stress and strain of a bi-crystal can be further averaged over the aggregate of differently oriented bi-crystals using any of the available grain-to-polycrystal transition schemes. At this stage, the effect of crystallographic texture can be easily included in the model by choosing preferential orientations of the grains.

3. Model predictions

The model has been applied to predict the pseudoelastic response of polycrystalline NiTi on proportional and non-proportional loading paths. Sample results are presented in Fig. 1. For instance, from Fig. 1(a) it is seen that the bounds corresponding to the Taylor and Sachs models are significantly improved when these schemes are combined with the bi-crystal model.

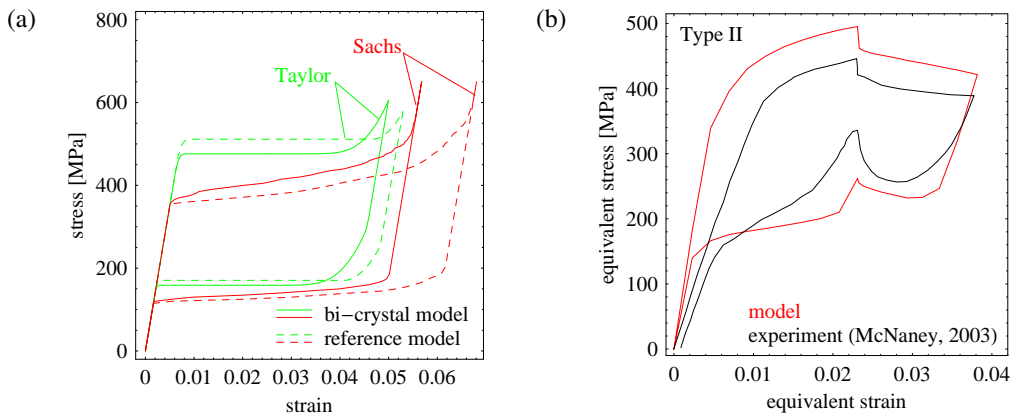


Figure 1. Predictions of the pseudoelastic response of polycrystalline NiTi for (a) uniaxial compression and (b) non-proportional tension–torsion loading (compared to the experimental results of McNaney et al. [7]).

Acknowledgement This work was supported by the KMM-NoE project.

References

- [1] S. Stupkiewicz and H. Petryk. Modelling of laminated micro-structures in stress-induced martensitic transformation. *J. Mech. Phys. Solids*, 50:2303–2331, 2002.
- [2] S. Stupkiewicz and H. Petryk. Micromechanical modelling of stress-induced martensitic transformation and detwinning in shape memory alloys. *Journal de Physique IV*, 115:141–149, 2004.
- [3] S. Stupkiewicz and H. Petryk. Finite-strain micromechanical model of stress-induced martensitic transformations in shape memory alloys. *Mater. Sci. Eng. A*, 438–440:126–130, 2006.
- [4] H. Petryk. Incremental energy minimization in dissipative solids. *C. R. Mecanique*, 331:469–474, 2003.
- [5] P. Van Houtte, S. Li, M. Seefeldt, and L. Delannay. Deformation texture prediction: from the Taylor model to the advanced Lamel model. *Int. J. Plasticity*, 21:589–624, 2005.
- [6] E. Patoor, D.C. Lagoudas, P.B. Entchev, L.C. Brinson, and X. Gao. Shape memory alloys, Part I: General properties and modeling of single crystals. *Mech. Mater.*, 38:391–429, 2006.
- [7] J.M. McNaney, V. Imbeni, Y. Jung, P. Papadopoulos, and R.O. Ritchie. An experimental study of the superelastic effect in a shape-memory Nitinol alloy under biaxial loading. *Mech. Mater.*, 35:969–986, 2003.

TORSIONAL DEFORMATION AND ROTARY DRIVING CHARACTERISTICS OF SMA THIN STRIP

H. Tobushi¹, E. A. Pieczyska², W. K. Nowacki², T. Sakuragi¹ and Y. Sugimoto¹

¹ *Department of Mechanical Engineering, Aichi Institute of Technology, 1247, Yachigusa, Yakusa-cho, Toyota, 470-0392, Japan*

² *Institute of Fundamental Technological Research, Polish Academy of Sciences, Swietokrzyska 21, Warsaw, 00-049, Poland*

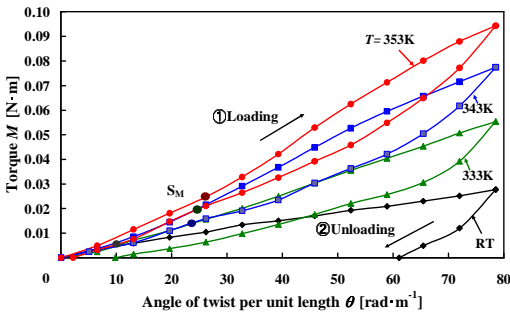
1. Introduction

Shape-memory alloys (SMAs) have played a leading part in research into smart materials. The main characteristics of SMAs are the shape memory effect (SME) and superelasticity (SE). Using the torsional deformation of a TiNi SMA tube, twist in the blades of rotor aircraft was investigated in order to improve the flight performance. In practical applications making use of SMA thin strips, torsional deformation can be obtained simply by gripping both ends without any mechanical process. In the present study, the torsional deformation properties of a TiNi SMA thin strip are investigated. The characteristics of energy storage, dissipated work and fatigue are also investigated.

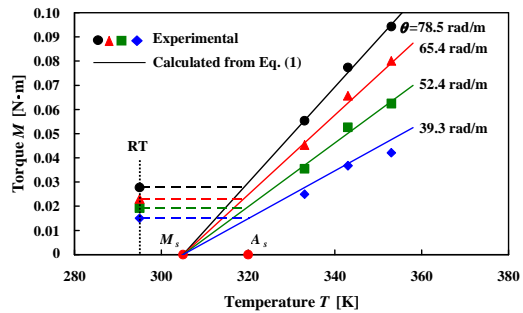
2. Relationship between torque and angle of twist

The relationship between torque M and angle of twist per unit length θ for the heat-treated material as obtained from the torsion test is shown in Fig.1. As can be seen from Fig.1(a), M increases with an increase in θ . At room temperature, a large residual angle of twist per unit length appears after unloading, giving evidence of the SME. At $T = 333\text{K}$, since T is $A_s < T < A_f$ and therefore there is a partial effect of superelasticity in which the reverse transformation does not completely occur, a residual angle of twist appears after unloading. At temperatures above 343K , the angle of twist recovers during unloading and no residual angle of twist appears. As can be seen from the relationship between torque and temperature in the loading process, shown in Fig.1(b), torque M increases in proportion to temperature rise T - M_s for the same angle of twist per unit length θ at temperatures above A_s . The slope increases in proportion to θ .

I shall next discuss the relationship between torque M and angle of twist ϕ based on the evidence of the elastic deformation due to torsion. In the case of torsion in a bar of rectangular cross-section of width w and thickness t , the angle of twist per unit length θ is expressed by using modulus of rigidity G .



(a) Relation between torque and angle of twist.



(b) Relation between torque and temperature in the loading process.

Fig.1. Results of torsion test for heat-treated material.

Considering the fact that the $M-\theta$ and $M-(T-M_s)$ curves in the loading process are close to straight lines, the relation becomes

$$(1) \quad M = awt^3 G \theta (T - M_s)$$

where the factor a depends on the ratio w/t . The values of G at temperatures above and below A_s differ in a ratio of about 3 : 1. By taking the average value $G = 20\text{GPa}$ and $a = 1.61 \times 10^{-2}\text{K}^{-1}$, the calculated results can be found as shown by the solid lines in Fig.1(b).

3. Energy storage and dissipation

The area under the loading curve of the relation between the torque and the angle of twist corresponds to work done during loading. The area under the unloading curve corresponds to the recoverable strain energy E_r . The area inside the hysteresis loop during loading and unloading corresponds to the dissipated work W_d .

The relations between E_r and W_d and temperature T at $\theta = 78.5\text{rad}\cdot\text{m}^{-1}$ (total angle of twist $\phi = \pi$) for the heat-treated materials are shown in Fig.2. As can be seen, E_r increases markedly in proportion to T as the torque during unloading increases with increasing temperature. The relation between E_r and T is expressed by a linear equation: $E_r = b(T - A_s)$ for $b = 3.68\text{mJ}\cdot\text{K}^{-1}$, where A_s denotes the reverse transformation starting temperature under no stress and $A_s = 295\text{K}$.

On the other hand, as can be seen in Fig.2, the dissipated work W_d decreases gradually with an increase in temperature T . The rate of decrease in W_d is small and W_d is only slightly dependent on T .

4. Torsion fatigue properties

The relations between amplitude of the twisting angle per unit length θ_a and the number of cycles to failure N_f for the as-received and heat-treated materials obtained from the torsion fatigue test are shown in Fig.3, expressed on a logarithmic scale.

As can be seen in Fig.3, the number of cycles to failure N_f decreases with an increase in the amplitude of the twisting angle per unit length θ_a . This relation is approximated by a straight line on the logarithmic graph. The fatigue life curve in the region of low-cycle fatigue seems therefore to be expressible in an equation similar to that already obtained for the fatigue life curve of TiNi SMA wires under bending. This can be seen in Eq.(2)

$$(2) \quad \theta_a \cdot N_f^\beta = \alpha \quad \text{for} \quad \begin{cases} \beta = 0.20, \alpha = 580 \text{ rad} \cdot \text{m}^{-1} : \text{Heat - treated} \\ \beta = 0.15, \alpha = 280 \text{ rad} \cdot \text{m}^{-1} : \text{As - received} \end{cases}$$

where α and β represent θ_a where $N_f = 1$ and the slope of the $\log \theta_a - \log N_f$ curve, respectively. The calculated results obtained from Eq.(2) are shown by solid lines in Fig.3.

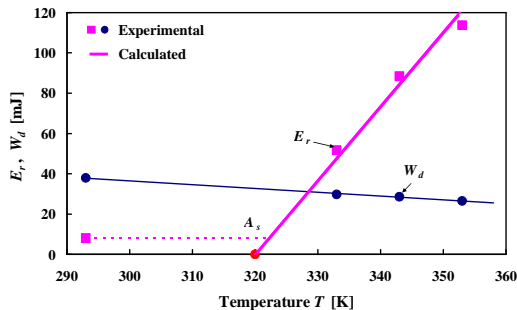


Fig.2. Dependence of E_r and W_d on temperature at $\theta = 78.5\text{rad}\cdot\text{m}^{-1}$ ($\phi = \pi$) for heat-treated material

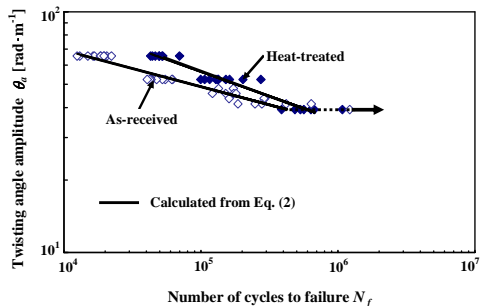


Fig.3. Fatigue life curves of SMA thin strip for torsion.

STRESS-INDUCED MARTENSITE TRANSFORMATION IN TINI SMA - EXPERIMENTAL ESTIMATION OF ENERGY BALANCE

E.A. Pieczyska

Institute of Fundamental Technological Research, Warsaw, Poland

An equation for energy balance of the martensite forward and reverse transformation in shape memory alloy (SMA) on the basis of the laws of thermodynamics, applied to homogeneous thermodynamical processes [1], under some assumptions was obtained:

$$c_p dT + dq = \frac{\gamma \sigma(z)}{\rho} dz + \frac{1}{2} \gamma \frac{c_M}{\rho} (M_s + A_s) dz - \alpha \frac{T \Delta \sigma}{\rho}, \text{ where:}$$

$c_p dT$ - the heat related to the SMA specific heat; dq - the heat exchange with surroundings;

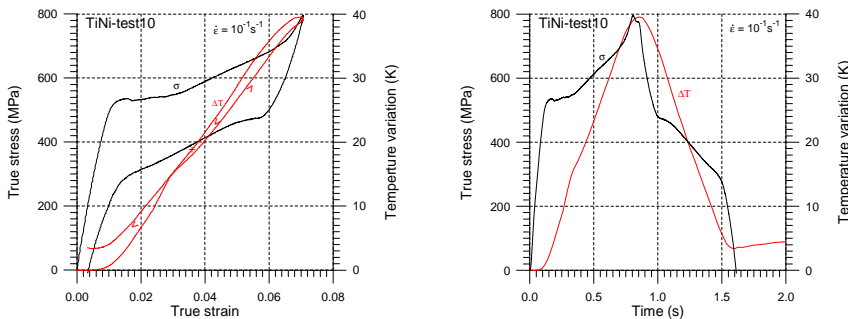
$\gamma(\sigma/\rho) dz$ - the work done by testing machine in order to deform the specimen;

$\frac{1}{2} \gamma \frac{c_M}{\rho} (M_s + A_s) dz$ - the term of thermomechanical couplings, related to martensite formation.

The last part of the equation, called piezocalorimetric effect, is neglected in the analysis, since its value is not significant. For example, for 39K, recorded for the highest strain rate 10^{-1}s^{-1} , is as follows: $-10 \times 10^{-6} / \text{K} \times 312 \text{K} \times 800 \text{MPa} / 6.45 \text{g/cm}^3 = 0.38 \text{ [J/g]}$. So as average contribution, 0.19 [J/g].

Parameters of the martensite transformation; c_M, M_s, A_s, γ were identified from tension test carried out on the TiNi shape memory alloy at three various temperatures with very low strain rate. As a result, it was found: $c_M = 5.62 \text{MPa/K}, M_s = 228 \text{K}, A_s = 282 \text{K}, \gamma = 0.07$. The value of $\alpha = 10 \times 10^{-6} / \text{K}$ has been given by the TiNi SMA producer - Furukawa Electric Co., while the material density $\rho = 6.45 \text{g/cm}^3$ was measured by the author. Basing on the above equation, completed by the estimated material parameters as well as by the thermomechanical data found for the TiNi shape memory alloy tension tests performed with various strain rates, an energy balance for the stress-induced martensite transformation has been calculated. Thermal data, namely the temperature increase accompanying the exothermic martensite forward transformation, and the temperature decrease, accompanying the reverse endothermic transformation, were recorded in contact-less way by a high quality infrared camera. The calculations have been made for three various strain rates; $10^{-1} \text{s}^{-1}, 10^{-2} \text{s}^{-1}$ and 10^{-4}s^{-1} . Finally, the following data, depending on the strain rate, were estimated.

$$\dot{\epsilon} = 10^{-1} \text{s}^{-1}; \Delta T_{\text{MARTENSITE}} = 39 \text{K}, \Delta T_{\text{REVERSE}} = 36 \text{K}, \gamma = 0.07, z = 0.95, c_M = 5.62 \text{MPa/K}, M_s = 228 \text{K}, A_s = 282 \text{K}$$



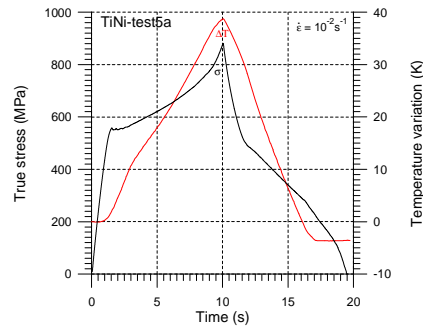
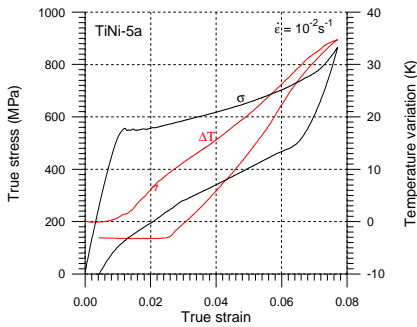
During the martensite transformation:

$$17.94 \text{ [J/g]} + q = 6.17 \text{ [J/g]} + 14.77 \text{ [J/g]}; \text{ so the estimated heat exchange } q = 3.0 \text{ [J/g]}.$$

During the reverse transformation:

$$-16.56 \text{ [J/g]} + q = -3.28 \text{ [J/g]} - 14.77 \text{ [J/g]}; \text{ so the estimated heat exchange } q = -1.49 \text{ [J/g]}.$$

$$\dot{\epsilon}=10^{-2}\text{s}^{-1}; \Delta T_{\text{MARTENSITE}}=34\text{K}, \Delta T_{\text{REVERSE}}=35\text{K}, \gamma=0.07, z=0.95, c_M=5.62\text{MPa/K}, M_s=228\text{K}, A_s=282\text{K}$$



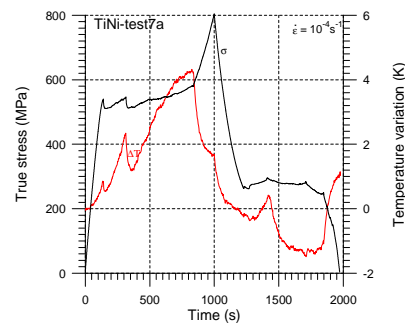
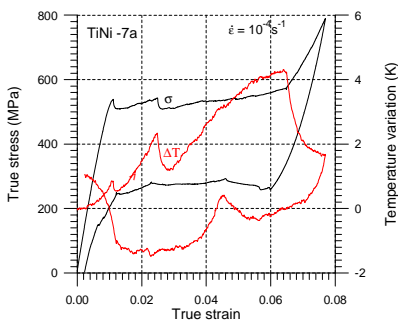
During the martensite transformation:

$$15.64 \text{ J/g} + q = 5.89 \text{ J/g} + 14.77 \text{ [J/g]}; \text{ so the estimated heat exchange } q = 5.02 \text{ [J/g]}.$$

During the reverse transformation:

$$-16.1 \text{ [J/g]} + q = -2.89 \text{ [J/g]} - 14.77 \text{ [J/g]}; \text{ so the estimated heat exchange } q = -1.56 \text{ [J/g. K]}.$$

$$\dot{\epsilon}=10^{-4}\text{s}^{-1}; \Delta T_{\text{MARTENSITE}}=4.2\text{K}, \Delta T_{\text{REVERSE}}=-1, \gamma=0.07, z=1, c_M=5.62 \text{ MPa/K}, M_s=228\text{K}, A_s=282\text{K}$$



During the martensite transformation:

$$1.93 \text{ [J/g]} + q = 4.59 \text{ [J/g]} + 15.55 \text{ [J/g]}; \text{ so the estimated heat exchange } q = 18.21 \text{ [J/g]}.$$

During the reverse transformation:

$$-0.46 \text{ [J/g]} + q = -1.17 \text{ [J/g]} - 15.55 \text{ [J/g]}; \text{ so the estimated heat exchange } q = -16.25 \text{ [J/g]}.$$

One can notice that irrespective of the strain rate applied, the heat of the new phase formation is much higher than those, supplied by the testing machine in order to deform the TiNi specimen, so the obtained results confirm the prediction of the phase transformation in SMA theory [1]. Furthermore, as it was found from comparison of the obtained results, the higher the strain rate, the higher the temperature changes and the lower the heat that transfers to the surroundings. So the obtained data of the martensite transformation energy balance seem to be reasonable.

Acknowledgments: The research has been partly carried out with the financial support of the Polish Ministry of Science and Higher Education under Grant No. N N501 0106 33. The experiments were performed with contribution of W.K. Nowacki and S.P. Gadaj to whom author gave her gratitude. Author also wishes to extend her thanks to B. Raniecki for scientific advice and fruitful comments.

References

- [1] B. Raniecki, Ch. Lexcellent and K. Tanaka (1992). Thermodynamic models of pseudoelastic behavior of shape memory alloys, Arch. Mech., 44, 3, 261-284.
- [2] E.A. Pieczyska, S.P. Gadaj, W.K. Nowacki and H. Tobushi (2006). Phase transformation front evolution for stress- and strain-controlled test in TiNi SMA, Experimental Mechanics, Vol.46, No4, 531-542.

INFLUENCE OF PLASTIC DEFORMATION ON STRUCTURAL CHARACTERISTICS AND LONG-RANGE ORDER IN Ni₃Al ALLOY

S. Starenchenko, I. Radchenko, V. Starenchenko

Tomsk State University of Architecture and Building, Tomsk, Russia

1. Introduction

The interest in the intermetallic alloy Ni₃Al due to its unique properties is kept up for a long time. Properties of alloy are connected with a high ordering energy. The long-range order remains up to the melting temperature. However, plastic deformation essentially can change a structural state of alloy Ni₃Al [1], decrease the long-range order degree and even can lead to its full destruction.

2. Experimental procedure

In this work the study of structural characteristics of the coarse-crystalline alloy Ni₃Al deformed by cold-rolling at a room temperature is presented.

The X-ray diffraction was used to determine the average internal strain, the crystallite sizes and the average size of antiphase domains based on the Hall-Williamson analysis of peak broadening [2]. The degree of the long-range order was determined from the ratios of the intensities I_{ss} of the superlattice reflections (100) and (110) to the intensities I_f of the fundamental reflections (200) and (220), respectively, with allowance for necessary factors such as the multiplicity factor P , angular factor Φ and structure factor F :

$$\eta^2 = I_{ss}(P\Phi F^2)_f / I_f(P\Phi F^2)_{ss}$$

The long-range order parameter, the average size of the antiphase domains, the average size of the areas of coherent dispersion, microstresses and parameters of a crystal lattice are measured with the X-ray methods. Change of these characteristics during deformation gives the information necessary for understanding the phenomena, occurring at deformation of alloys, and also mechanisms of deformation-induced disordering.

3. Results and discussion

Experimental study has showed that the initial state of the alloy Ni₃Al was the two-phase ($\gamma + \gamma'$). The reflexes (220), (311) и (222) of the ordered ($\gamma' \rightarrow L1_2$ superstructure) and the disordered ($\gamma \rightarrow A1$ structure) phases overlap each other. The volume fraction of the ordered phase is about 0.75. It is suitable to the binary constitutional diagram of system Ni-Al. The effective long-range order parameter is $\eta = 0.86 \pm 0.05$ whereas the long-range order parameter within of the ordered phase is $\eta = 1.00 \pm 0.05$. During deformation the effective long-range order parameter decreases (fig. 1.a.1). This decrease occurs because of destruction of the long-range order in local places. Fig.1.a.2 shows the change in the long-range order parameter within of the ordered phase. It will be observed it is accompanied with the emergence of the defective disordered phase. The volume fraction of the disordered phase, which appears in the deformed alloy, is shown in fig. 1.b. The phase composition of the deformed material becomes more complex. There are three different phases. The secondary

disordered phase occurs besides the initial ordered and disordered phases. It exhibits that the strain-induced order-disorder phase transition is heterogeneous.

During deformation there is the increase of the defects within the material, growth of microstresses, reduction of size of the areas of crystallites and antiphase domains, increase in a crystal lattice parameter. The dependence between the effective long-range order parameter and density of the deformation antiphase boundaries is obtained. It is noticed that full destruction of the long-range order in the alloy Ni₃Al even after deformation $\varepsilon=0.95$ does not occur. It is possibly connected with a high value of the ordering energy of the alloy. The effect of the plastic deformation on the state of this alloy is carried out under the following scheme:

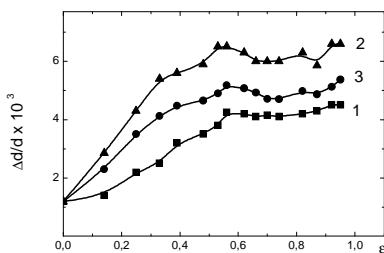


Fig. 2. Dependence of microdistortions $\Delta d/d$ in the [111] (1), [100] (2) directions and average in all directions (3) on the degree of strain in the Ni₃Al alloy

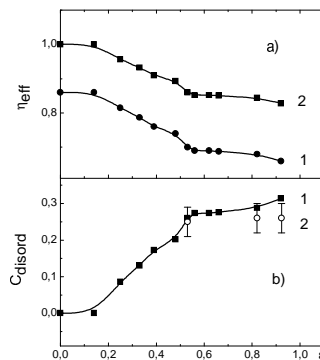


Fig. 1. Dependence: a) 1 - the effective long-range order parameter; 2 - the effective long-range order parameter of ordered phase; b) 1 - the volume fraction of disordered phase (experimental); 2 - the volume fraction of disordered phase (calculated) on the degree of strain in the Ni₃Al alloy

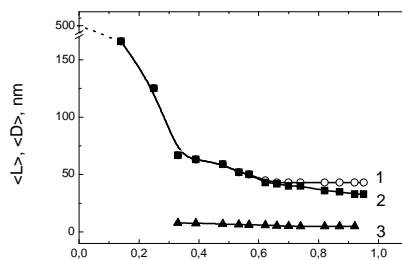


Fig. 3. Dependence of the average size of the crystallites (1), the average size of the antiphase domains (2), the average size of the fine antiphase domains (3) on the degree of strain in the Ni₃Al alloy

A mathematics model of strain-induced destruction of the long-range order in the alloys with $L1_2$ superstructure [2] demonstrated that among different mechanisms of the generation of the antiphase boundaries, such as 1) the accumulation of thermal APBs by means of the intersection of moving dislocations; 2) the formation of APB tubes; 3) the multiplication of superdislocations; 4) the movement of single dislocations; 5) the accumulation APBs at the climb of edge dislocations, only the movement of single dislocations and the formation of APB tubes play the more important role for destruction of the long-range order. However every other mechanism is needed to prepare the action of the most effective mechanisms.

6. References

- [1] S.C. Jang and C.C. Koch (1990). Amorphization and disordering of the Ni₃Al ordered intermetallic by mechanical milling, *J. Mater.Res.* **5**, 498-510.
- [2] G.K. Williamson and W.H. Hall (1953), *Acta Metall.* **1**, 22-31.
- [3] V.A. Starenchenko, O.D. Pantyukhova and S.V. Starenchenko (2002). Simulation of the process of deformation – induced destruction of long-range order in alloys with an $L1_2$ superstructures, *Physics of the Solid State (Russian)*, **44**, No 5, 994-1002.

ESTIMATION OF MATERIAL EFFORT DURING DRYING PROCESSES

S.J. Kowalski and A. Rybicki

*Poznań University of Technology, Institute of Technology and Chemical Engineering,
Poznań, Poland*

ABSTRACT

One of the main problems accompanying drying of saturated porous materials (e.g. ceramics, wood, and others) is the problem of cracking initiated by the drying induced stresses. This destructive effect appears very often at the surface of dried products, but not always. Sometimes cracks occur in a strange place inside the material. The reason for that is of different nature as, for example, the pre-existing flaws, the stress reverse phenomenon, or the accumulation of energy coming from several components of the stress tensor.

The aim of this paper is to discuss in more detail the problem of mechanical energy accumulation as well as the effort of material under drying according to the energetic hypothesis. This hypothesis allows calculating the overall stress, which is necessary to formulate the strength condition for a given material. Such an approach is always necessary when more components of the stress tensor appear in a dried sample.

The problem of energy effort in dried materials is very complex as the mechanical properties of such materials change themselves during the process. In order to grasp adequately this problem one has to use a mechanistic model of drying, in which the mechanical coefficients have to be depended on the moisture content. Only such a model may allow to obtain the adequate values of the stress components and to calculate properly the overall stress.

On the other hand the admissible stress, which has to be determined for the purpose of the strength condition, also changes itself along with the moisture content variation. This stress has to be determined in separate experimental tests for given material, similarly as the mechanical coefficients that are involved in the drying model.

The objective of the present consideration is the analysis of the stress state in a cylindrically shaped sample made of kaolin-clay and subjected to convective drying. The distribution of stress components throughout the cylinder and their evolution in time is determined. These stress components allow calculating the overall stress as a function of place and moisture content. The map of the cylinder space presenting the points of possibly violated strength condition is given.

Distributions and time evolutions of liquid content X (dry basis) and temperature T are determined for the first and second period of drying using the differential equations that include the phase transitions of liquid into vapour and the diffusive and thermodiffusive moisture transport, [1]:

$$\dot{X} = D_X \nabla^2 (c_T T + c_X X) - \Omega (c_T T + c_X X), \quad \dot{T} = D_T \nabla^2 T - l \frac{\Omega}{\rho^s c_v} (c_T T + c_X X) \quad (1)$$

where D_X and D_T denote the mass and thermal diffusivity, c_X and c_T express the ratio of diffusion and thermodiffusion, Ω expresses the intensity of phase transition of liquid into vapour, l is the latent heat of evaporation, c_v is the specific heat, ρ^s is the density of dry body, and ∇^2 denotes the Laplace operator in cylindrical coordinates.

The boundary conditions for the heat and mass transfer express the convective exchange of heat and vapour between cylinder and the ambient air, and the symmetry conditions with respect to the middle of the cylinder. The initial conditions assume the uniform distribution of moisture and temperature.

The following system of two coupled equations is used for determination of radial and longitudinal displacements u_r and u_z

$$M\nabla^2 u_r + \frac{\partial}{\partial r} [(M+A)\varepsilon - \gamma_T T - \gamma_X X] = M \frac{u_r}{r^2}, \quad M\nabla^2 u_z + \frac{\partial}{\partial z} [(M+A)\varepsilon - \gamma_T T - \gamma_X X] = 0 \quad (2)$$

where $\gamma_T = (2M+3A)\kappa^{(T)}$, $\gamma_X = (2M+3A)\kappa^{(X)}$, $\kappa^{(T)}$ and $\kappa^{(X)}$ are the coefficients of linear thermal and humid expansion, ε is the volumetric strain, $M(X)$ and $K(X)$ are the elastic shear and bulk modulus dependent on moisture content.

Since no any external surface forces acting on the cylindrical sample the radial and longitudinal stresses on the external surfaces equal zero. The other two boundary conditions assume zero-valued radial and longitudinal displacements at cylinder axis and at the bottom of the cylinder, that is

$$\sigma_{rr}|_{r=R} = 0, \quad \sigma_{zz}|_{z=H} = 0, \quad u_r|_{r=0} = 0 \quad \text{and} \quad u_z|_{z=0} = 0 \quad (3)$$

The state of stress in the cylinder is fully described by the components σ_{rr} , $\sigma_{\varphi\varphi}$, σ_{zz} , σ_{rz} , where

$$\sigma_{ij} = 2M\varepsilon_{ij} + (A\varepsilon - \gamma_T T - \gamma_X X)\delta_{ij}, \quad \varepsilon_{ij} = \frac{1}{2}(u_{i,j} + u_{j,i}), \quad \varepsilon = \frac{\partial u_r}{\partial r} + \frac{u_r}{r} + \frac{\partial u_z}{\partial z} \quad (4)$$

The overall (reduced) stress and admissible stress [2] read.

$$\sigma_{red} = \frac{1}{\sqrt{2}} \sqrt{(\sigma_{rr} - \sigma_{zz})^2 + (\sigma_{rr} - \sigma_{\varphi\varphi})^2 + (\sigma_{\varphi\varphi} - \sigma_{zz})^2 + 6\sigma_{rz}^2}, \quad \sigma_{adm} = \sigma_0 + \sigma_X \exp(-C_\sigma X) \quad (4)$$

Figure 1 presents the mapping of stress difference between σ_{adm} and σ_{red} in quarter plane of the cylinder

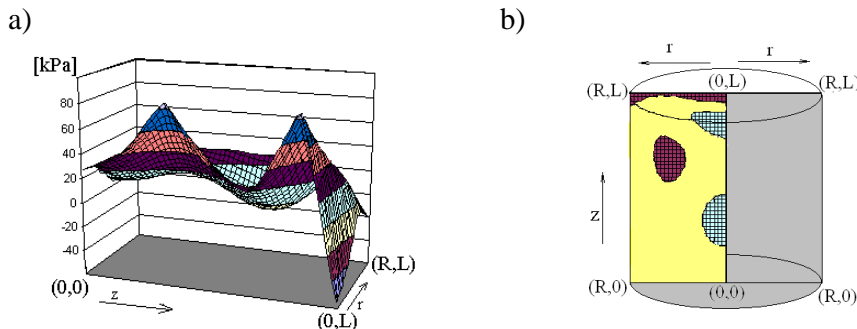


Fig. 1. Difference ($\sigma_{adm} - \sigma_{red}$) in a quarter plane of the cylinder: a) spatial mapping, b) flat visualization of the places with violated strength condition.

The places in which $(\sigma_{adm} - \sigma_{red}) < 0$ denote violation of the material strength (dark area in Fig. 1b).

References

- [1] KOWALSKI S.J., RYBICKI A., Residual Stresses in Dried Bodies, *Drying Technology*, **25** (4), 2007.
- [2] MUSIELAK G., Modelling and numerical simulations of transport phenomena and drying stresses in capillary-porous materials, Ed. Poznań University of Technology, 2004, (in Polish.)

STRESS-STRAIN CURVE AND STORED ENERGY DURING UNIAXIAL DEFORMATION OF POLYCRYSTALS

W. Oliferuk, M. Maj

Institute of Fundamental Technological Research, Warsaw, Poland

1. Introduction

A portion of the mechanical energy expended on plastic deformation is released as a heat and the remainder is stored in the material. The stored energy is an essential feature of cold worked state and represents the change in the internal energy of the material.

The measurement of the stored energy is usually laborious and complicated therefore many authors have tried to calculate the stored energy from stress-strain curve though the curve does not contain information about the energy converted into a heat [1-3]. On the other hand both the strain hardening and stored energy of cold work are associated with the creation of lattice imperfections. Thus an attempt to find connection between stored energy and stress-strain curve seems to be justified.

The aim of this work is to answer the question what information about the stored energy can be derived from stress-strain curve. Results of theoretical study will be interpreted in terms of energy storage mechanisms and will be compared with stored energy determined experimentally during uniaxial tension.

2. Energy balance during deformation

The theoretical analysis of energy balance for elastic-perfectly plastic material has been performed. The curve shown in Fig. 1 is typical for 'load-unload cycle' for elastic-perfectly plastic material subjected to the load F .

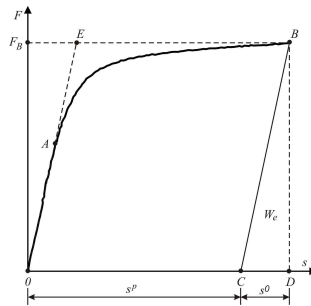


Fig. 1. Generalized load versus generalized displacement curve.

It has been shown that in the case of elastic-perfectly plastic material the total stored energy is equal to:

$$(1) \quad E_s = W_{AEB} - \int_V \int_0^{\sigma_B} \hat{\epsilon}^{ip} : d\hat{\sigma} dV,$$

where $\hat{\epsilon}^{ip}$ is the local ideal plastic strain, what means that the total energy expended on this strain is converted into a heat, $\hat{\sigma}$ is the local stress tensor and V is the volume of the gauge part of the specimen.

It should be noticed that the energy W_{AEB} can be calculated directly from experimentally obtained stress-strain curve (area AEB in Fig. 1).

It has been shown that the energy W_{AEB} is connected with internal stress field generated during non-homogeneous plastic deformation. Performed analysis has shown that, on the basis of the stress-strain curve, it is impossible to derive the energy stored during homogeneous deformation (the energy of statistically stored dislocations).

3. Experimental results

The stored energy e_s was determined as a difference between the mechanical energy expended on plastic deformation w_p and the energy dissipated as a heat q_d

$$(2) \quad e_s = w_p - q_d,$$

where e_s , w_p , q_d are specific quantities.

The plastic work was determined on the basis of stress strain-curve. The energy q_d was determined by simulating the process of specimen heating during deformation by means of controlled supply of electrical power in such a way that the temperature increase with time during the simulation was identical to that measured during the tensile test [4]. The temperature distribution on the specimen surface was determined using IR thermographic system.

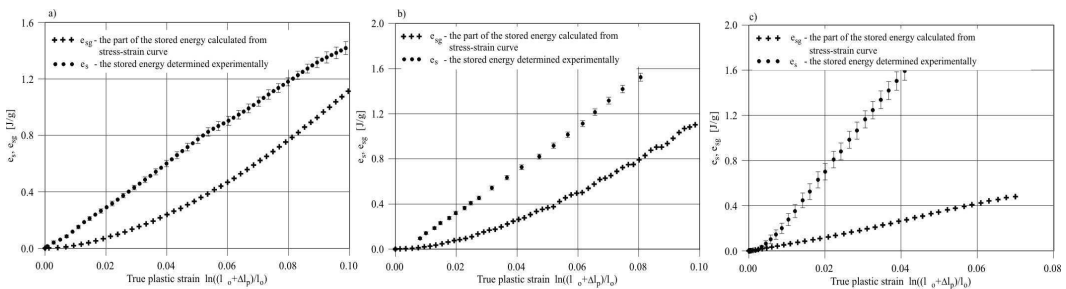


Fig. 2. The part of stored energy calculated from stress-strain curve and the measured total stored energy versus plastic strain for: a) 316L, b) 304L and c) Ti.

The results of total stored energy measurements performed on the 316L and 304L austenitic stainless steels and titanium, were compared with that obtained on the basis the theoretical analysis (Fig. 2). It is shown that the stored energy, connected with non-homogeneous plastic deformation, calculated from stress-strain curve for all tested materials is smaller than the total stored energy determined experimentally.

4. References

- [1] V. Kafka (1979). Strain hardening and stored energy. *Acta Tech. CSAV*, **24**, 199-216.
- [2] N. Aravas, K.S. Kim, F.A. Leckie (1990). On the calculation of the stored energy of cold work. *J. Eng. Mater. Techn.*, **112**, 465-470.
- [3] W. Szczepiński (2001). The stored energy in metals and the concept of residual microstresses in plasticity. *Arch. Mech.*, **53**, 615-629.
- [4] W. Oliferuk, A. Korbel, M.W. Grabski (1996). Mode of deformation and the rate of energy storage during uniaxial tensile deformation of austenitic steel. *Mater. Sci. Eng.* **A220**, 123-128.

DEFORMATION BEHAVIOR OF TiNi SMA OBSERVED BY LOCAL STRAIN, THERMOGRAPHY AND TRANSFORMATION BAND

E. A. Pieczyska¹, H. Tobushi², W. K. Nowacki¹, T. Sakuragi² and Y. Sugimoto²

¹ *Institute of Fundamental Technological Research, Polish Academy of Sciences, Swietokrzyska 21, Warsaw, 00-049, Poland*

² *Department of Mechanical Engineering, Aichi Institute of Technology, 1247, Yachigusa, Yakusa-cho, Toyota, 470-0392, Japan*

1. Introduction

In shape memory alloys (SMAs), strain of 6% is recovered by heating or unloading: shape memory effect (SME) or superelasticity (SE), respectively. In the loading process, strain appears due to the stress-induced martensitic transformation (SIMT) and diminishes due to the reverse transformation (RT) by heating or unloading. The deformation properties due to the SIMT differ depending on temperature and loading rate. The loading rate is designated by strain rate and stress rate. In the present paper, the influence of loading rate on the deformation behaviors is investigated for TiNi SMA. The deformation behaviors are observed by local strain, temperature variation by the thermography and transformation band on the surface of specimen.

2. Dependence of deformation behavior on loading rate

The stress-strain curves obtained by tension tests for an SME-NT wire under various strain rate at temperature $T=353\text{K}$ are shown in Fig.1. As can be seen, the overshoot and undershoot and stress plateau appear clearly in the case of strain rate $d\varepsilon/dt=1.67 \times 10^{-4}\text{s}^{-1}$. These phenomena do not appear in the case of $d\varepsilon/dt$ higher than $1.67 \times 10^{-3}\text{s}^{-1}$. The MT stress increases and the RT stress decreases with an increase in strain rate. The MT is exothermic and the RT endothermic process. Therefore, temperature of the specimen increases in the loading process and decreases in the unloading process with increasing strain rate. In the case of high strain, there is not enough time for temperature to be constant, and deformation processes, resulting in large variation in the MT stress.

3. Behavior of local strain

The relation between local strain $\Delta l/l$ and accumulated total axial strain $\Sigma|\Delta L/L|$ obtained by tension test for an SE-NT wire at strain rate $d\varepsilon/dt=8.33 \times 10^{-5}\text{s}^{-1}$ is shown in Fig.2. The local strain expresses a ratio of variation Δl to gauge length l at each divided position ①-⑩ in the specimen. The

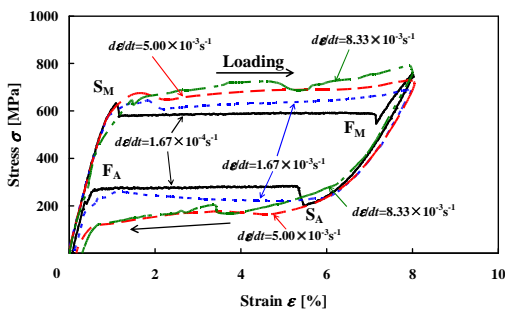


Fig.1. Relation between stress and strain under constant strain rates in SE-NT wire at $T=353\text{K}$

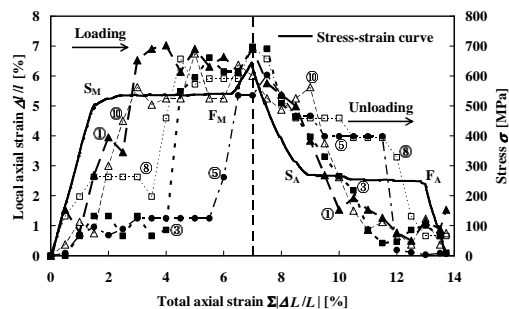


Fig.2. Relation between local strain and accumulated total axial strain in the SE test

accumulated total axial strain expresses the sum of absolute value of variation in total axial strain $\Delta L/L$ in the loading and unloading process. In Fig.2, the stress-strain curves in the loading and unloading processes are shown by the solid lines. As can be seen Fig.2, local strain $\Delta l/l$ in one end position ① increases markedly at total strain $\Sigma|\Delta L/L|=1.5\%$, and $\Delta l/l$ in another end position ⑩ increases by 4.5% at $\Sigma|\Delta L/L|=2.0\%$. The variation of $\Delta l/l$ appears in turn into central part of the specimen thereafter. The variation in $\Delta l/l$ finishes in the central part ⑤ at $\Sigma|\Delta L/L|=6\%$. In the unloading process, $\Delta l/l$ in both ends ① and ⑩ of the specimen decreases by 4.0% at $\Sigma|\Delta L/L|=9\%$ where the RT starts. The variation in $\Delta l/l$ during the unloading process appears in the similar order as the loading process.

4. Transformation behavior observed by thermography

The temperature distributions on the surface of the SE-NT tape (width of 10mm and thickness of 0.7mm) through the images obtained by an infrared camera in tension test at strain rate $d\varepsilon/dt = 1.67 \times 10^{-3} \text{ s}^{-1}$ are shown in Fig.3. As can be seen Fig.3, a transformation band with high temperature due to the MT appears in an upper end of the specimen at strain of 1.83% (Fig.(a)). The transformation bands appear in a bottom end and the central part of the specimen at strain of 2.15% (Fig.(b)). Temperature increases thereafter in many parts of the specimen (Fig.(d)), and the MT grows in the whole parts of the specimen till maximum strain (Figs.(e)-(l)). The reason why the temperature rise is small in both ends of the specimen is heat flow from the specimen into the grippers. The lowest temperature in the unloading process is 283K and maximum temperature change is -12.2K.

5. Transformation band on the surface of the specimen

The photographs on the surface of the SE-NT tape obtained by the tension test under strain rate $d\varepsilon/dt=1.67 \times 10^{-4} \text{ s}^{-1}$ are shown in Fig.4. As can be seen, variation does not appear on the surface of the specimen till strain of 1%. The band due to the SIMT occurs in an upper end of the specimen at strain of 2%. The transformation band grows thereafter from the upper part into the central part and occurs also in a bottom part at strain of 4%. The martensitic phase band occurred in both ends of the specimen grows toward the central part with an increase in strain. At strain of 8%, the parent phase with a narrow band remains in the central part of the specimen.

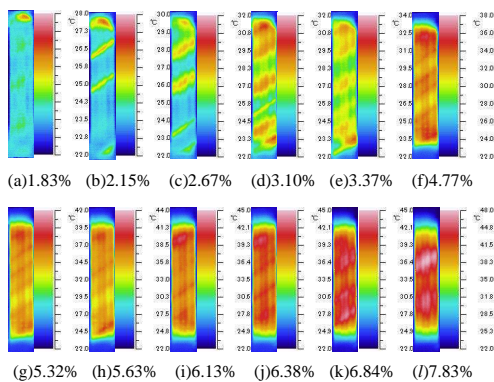


Fig.3. Temperature distributions on the tape specimen in the loading process during tension test

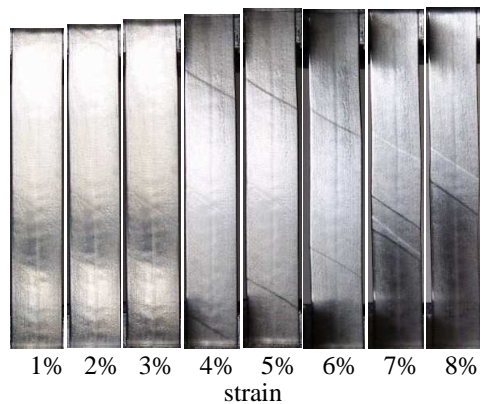


Fig.4. Deformation patterns on the surface of the tape specimen due to phase transformation in the loading process

TRANSFORMATION PLASTICITY THE MECHANISM, CONSTITUTIVE EQUATION AND APPLICATIONS

T. Inoue

Department of Mechanical Systems Engineering, Fukuyama, Japan

1. Introduction

The transformation plasticity is known to contribute a drastic effect on the simulation of some practical engineering courses of thermo-mechanical processes, such as heat treatment, welding, casting and so on involving phase transformation of steels. Most constitutive laws for transformation plasticity have been treated to be independent of ordinal thermo-plasticity. Considering that the mechanisms for both strains are essentially with no difference from metallurgical viewpoint, the constitutive equation for transformation plastic strain rate is expected to be described in relation with plasticity theory.

A phenomenological mechanism of transformation plasticity is discussed, in the first part of the paper, why the transformation plastic deformation takes place under a stress level even lower than the characteristic yield stress of mother phase: This is principally based on the difference in thermal expansion coefficient of mother and new phases. Bearing in mind that it is also a kind of plastic strain, a unified plastic flow theory is derived by introducing the effect of progressing new phase into the yield function of stress, temperature and plasticity related parameters. Thus obtained strain rate reveals to include the transformation plastic part in addition to mechanical and thermal plastic components.

Application of the theory is carried out to simulate some complicated cases of varying stress and temperature, and the results are compared with experimental data.

2. A phenomenological model

Consider that the material is composed of mother and new phases, say austenite and pearlite, or martensite, being connected parallelly each other [1]. Since the thermal expansion coefficient of *mother phase* α_m is larger than that of *new phase* α_n in most case, tensile thermal stress is essentially induced in the mother phase. External stress in addition to the tensile thermal and phase transformation stresses brings out to large value sometimes beyond the yield stress, which is the initiation of plastic deformation, or transformation plasticity. Simple numerical calculation will be illustrated how the stresses in mother and new phases vary during phase transformation, and the dependence of applied stress is discussed.

3. Unified transformation and thermoplasticity constitutive equation

In order to formulate a constitutive equation of a body under phase transformation, we assume that the material point focused is composed of N kinds of phases, which include all phases with the volume fraction ξ_i ($i=1,2,3,\dots,N$) and that the mechanical and thermophysical property χ is represented by the *mixture law* such that $\chi = \sum \xi_i \chi_i$, with $\sum \xi_i = 1$. Stress state related to the yielding of the I -th phase (say, mother phase, or austenite) is assumed to be affected by other phases (new phase, or pearlite) with the volume fraction ζ_j ($J=1,2,3,\dots,M$) [2]. Then, the plastic state of the I -th phase is controlled by the yield function in the form,

$$F_I = F_I(\sigma_{ij}, T, \epsilon_{ij}^p, \kappa_i, \zeta_j), \quad (I=1,2,\dots,N ; J=1,2,\dots,M) \quad (1)$$

Here, σ_{ij} , T and κ_i are respectively stand for uniform stress, temperature and plastic hardening parameter.

Applying the normality rule for the plastic strain rate, we finally have

$$\dot{\varepsilon}_{ij}^p = \Lambda_I \frac{\partial F_I}{\partial \sigma_{ij}} = \hat{G}_I \left[\left(\frac{\partial F_I}{\partial \sigma_{kl}} \dot{\sigma}_{kl} + \frac{\partial F_I}{\partial T} \dot{T} \right) + \sum_{N=1}^{\bar{N}} \frac{\partial F_I}{\partial \xi_J} \dot{\xi}_J \right] \frac{\partial F_I}{\partial \sigma_{ij}}, \quad (2)$$

in which the first term is the ordinal thermo-mechanical strain rate while the second corresponds to the TP strain rate. The TP strain rate possibly reveals to so-called Greenwood-Johnson type formula [3] in the special case of two phase.

$$\dot{\varepsilon}^{tp} = 3K(1-\xi)\dot{\xi}\sigma. \quad (3)$$

4. Application to the strain response for stress-temperature variation

The theory developed is now applied to some cases under varying stress and temperature [4]. Total strain in such cases of varying temperature reads

$$\varepsilon(T) = \varepsilon^e + \varepsilon^{th} + \varepsilon^m + \varepsilon^{tp} = \frac{\sigma}{E} + \int_{T_s}^T \left\{ \left[\alpha_m(1-\xi) + \alpha_n \xi \right] + \beta \frac{\partial \xi}{\partial T} \right\} dT + 3 \int_0^{\xi(T)} K(1-\xi)\sigma d\xi. \quad (4)$$

The first case example of application is to draw so-called temperature-elongation diagram depending on applied stress, and the second is related to fire extinguishment of structure made of a fire resistant steel (FR490A) heated and cooled between room temperature and 900 °C with decreasing and increasing stress. The results of simulation are compared with some experimental data to verify the theory developed.

5. Summary

A discussion on the mechanism from thermo-mechanical viewpoint is carried out, and the constitutive law is derived for unified thermomechanical-transformation plasticity theory. Application of the theory is made to some processes under varying temperature and stress.

Acknowledgement The author is indebted to express his gratitude to IMS-Japan, NEDO and METI for their financial supports to this project. Thanks are also due to my student, T. Tanaka, K. Sato, A. Nishimura and E. Wakamatsu, Fukuyama University, for their cooperation with experiments.

REFERENCES

- [1] T. Inoue(2007), *Unified transformation-thermoplasticity and the Application* (in Japanese), J. Soc. Materials Science, Japan, 56 p. 354-359.
- [2] T. Inoue(2008), On Phenomenological Mechanism of Transformation Plasticity and Inelastic Behavior of a Steel subjected to Varying Temperature and Stress --- Application of Unified transformation-thermoplasticity Theory (in Japanese), J. Soc. Materials Science, Japan, 57 pp.225-230.
- [3] T. Inoue(2007), A Phenomenological Mechanism of Transformation Plasticity and the Unified Constitutive Equation of Transformation-thermo-mechanical Plasticity, Proc. APCOM'07 Kyoto, JAPAN CD published.
- [4] G.W. Greenwood and R.H. Johnson (1965), *The deformation of metals under small stresses during phase transformations*, Proc. Roy. Soc., 283A p.403-422.

IDENTIFICATION OF BOUNDARY HEAT FLUX ON THE EXTERNAL SURFACE OF CASTING

E. Majchrzak¹, B. Mochnacki² and J.S. Suchy³

¹ *Silesian University of Technology, Gliwice, Poland*

² *Czestochowa University of Technology, Czestochowa, Poland*

³ *AGH, Cracow, Poland*

1. Introduction

The thermal processes in the system casting-mould are considered. In particular, the inverse problem consisting in the estimation of boundary heat flux flowing from casting sub-domain to the mould sub-domain is analyzed. To solve the problem the global function specification method is applied. The additional information necessary to solve an inverse problem results from the knowledge of cooling curves at the point selected from casting sub-domain. The solidification model bases on the equation corresponding to the one domain method. As an example, the 1D system created by steel casting and sand mix mould is considered. On the stage of numerical solution of direct problem and additional one the finite difference method has been applied.

2. Governing equations

The thermal processes proceeding in the casting sub-domain are described by the following energy equation

$$C(T) \frac{\partial T}{\partial t} = \text{div}[\lambda(T) \text{grad} T]$$

where $C(T) = c(T) - L df_s / dT$ [J/m³·K] is called a volumetric substitute thermal capacity [1], $c(T)$ is a volumetric specific heat of casting material, f_s is a volumetric solid state fraction at the point considered, L is a latent heat. From the mathematical point of view the equation determines the transient temperature field in the entire, conventionally homogeneous casting domain and this approach is called 'a one domain method' [1].

A similar equation, namely

$$c_m(T_m) \frac{\partial T_m}{\partial t} = \text{div}[\lambda_m(T_m) \text{grad} T_m]$$

determines a temperature field in a mould sub-domain (c_m is a volumetric specific heat of mould, λ_m is a thermal conductivity of the mould).

On a contact surface between casting and mould the continuity condition is given

$$x \in \Gamma_c : -\lambda \bar{n} \cdot \text{grad} T = -\lambda_m \bar{n} \cdot \text{grad} T_m, \quad T = T_m$$

while on the fragments of external boundary the Dirichlet, Neumann or Robin conditions can be accepted [1]. The initial temperatures (pouring temperature and initial mould temperature) are also known. The simpler model of heat exchange between casting and mould consists in the approximation of mould influence by the Neumann condition (in this way the mould sub-domain is conventionally neglected).

To determine the time dependent substitute Neumann condition the cooling curves at the points selected from the casting domain are applied and they constitute the additional information necessary to solve the inverse problem considered.

3. Global function specification method

It is assumed that the time dependent boundary heat flux $q(t)$ on the external surface of casting is unknown. The time interval $[0, t^F]$ is divided into intervals $[t^{f-1}, t^f]$ with constant step $\Delta t = t^f - t^{f-1}$ and for $t \in [t^{f-1}, t^f]$: $q(t) = q(t^f) = q^f$. In the global function specification method [2] the unknown values $q^1, q^2, \dots, q^{f-1}, q^f, \dots, q^F$ are identified simultaneously.

Let us assume that the temperatures T_{di}^f at the points x_i are given. Applying the least squares criterion [2] one obtains

$$S(q^1, q^2, \dots, q^F) = \sum_{f=1}^F \sum_{i=1}^M (T_i^f - T_{di}^f)^2 \rightarrow \text{MIN}$$

where M is the number of sensors, T_i^f are the calculated temperatures obtained from the solution of the direct problem by using the current available estimate for the unknown values $q^f, f=1, 2, \dots, F$.

At first the direct problem should be solved under the assumption that $q^f = q^{fk}, f=1, 2, \dots, F$ at the same time q^{fk} for $k=0$ are the arbitrary assumed values of heat fluxes, while for $k > 0$ they result from the previous iteration. The solution obtained this means the temperature distribution at the points x_i for times $t^f, f=1, 2, \dots, F$ will be denoted as T_i^{fk} .

Function T_i^f is expanded into Taylor series at the neighbourhood of this solution, and using the necessary condition of several variables function minimum, after the certain mathematical manipulations one obtains

$$\sum_{f=p}^F \sum_{i=1}^M \sum_{s=1}^f z_i^{f,s} z_i^{f,p} (q^s - q^{sk}) = \sum_{f=p}^F \sum_{i=1}^M z_i^{f,p} (T_{di}^f - T_i^{fk}), \quad p=1, 2, \dots, F$$

where $z_i^{f,s} = \partial T_i^f / \partial q^s$, $z_i^{f,p} = \partial T_i^f / \partial q^p$ are the sensitivity coefficients [2]. This system of equations allows to find the values q^1, q^2, \dots, q^F .

4. Example of computations

The 1D system casting - mould is considered. The dimensions of layers corresponding to casting and mould: $2L_1 = 0.03$ m, $L_2 - L_1 = 0.045$ m. Initial temperatures equal $T_p = 1550$ °C (casting) and $T_{m0} = 20$ °C (mould). The remaining data have been taken from [1]. In Figure 1 the cooling curves from casting domain are shown, while Figure 2 illustrates the course of real and identified boundary heat flux.

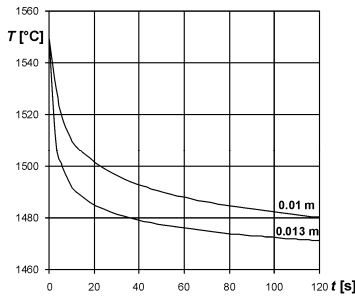


Fig. 1. Cooling curves

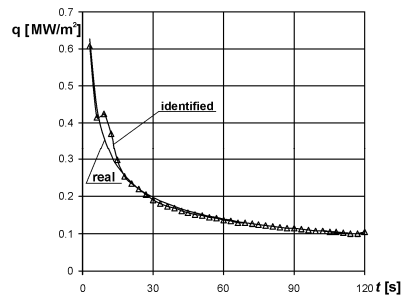


Fig. 2. Real and identified heat flux

5. References

- [1] E.Majchrzak, B.Mochnacki (2007). Identification of thermal properties of the system casting - mould, *Materials Science Forum*, 539-543, 2491-2496.
- [2] B.Mochnacki, E.Majchrzak, R.Szopa, J.S.Suchy (2006). Inverse problems in the thermal theory of foundry, *Scientific Research of the Institute of Mathematics and Computer Science*, Czestochowa, 1(5), 154-179.

TiNi SMA - INVESTIGATION OF STRESS-INDUCED MARTENSITE REVERSE TRANSFORMATION, INDEPENDENT OF THERMAL INFLUENCES OF THE FORWARD ONE

*E.A. Pieczyska, W.K. Nowacki, S.P. Gadaj and H. Tobushi**

Institute of Fundamental Technological Research, Warsaw, Poland

** Aichi Institute of Technology, Toyota-city, Japan*

Goal of the study was investigation of stress-induced reverse transformation behavior in shape memory alloy (SMA), independent of thermal influences of the martensite one. To this end, specimens of TiNi SMA were subjected to tension test performed on testing machine with stress rate 12.5 MPa/s to strain limit 8 %, followed by cooling the specimen to its initial temperature, and unloading with the same stress rate. Furthermore, an infrared camera was used in order to measure the infrared radiation from the specimen surface and to find the temperature changes, accompanying the phase transformation processes. The experiments have been carried out in room conditions.

The obtained results, namely the stress and the temperature changes vs. strain are presented in Fig.1, while the stress and the temperature changes vs. time in Fig. 2.

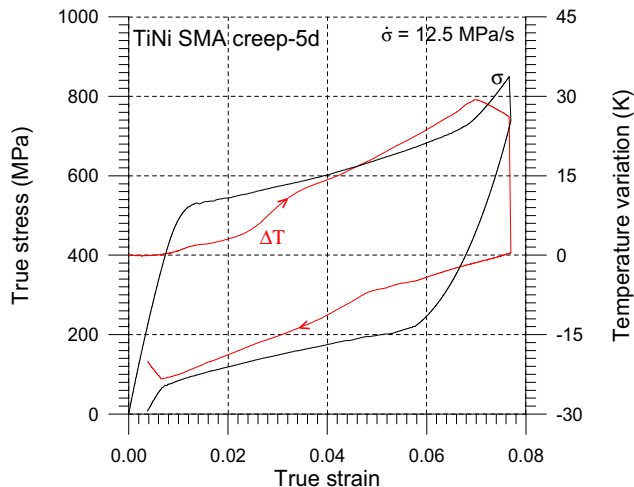


Fig. 1. Stress and temperature changes vs. strain during tension test of TiNi SMA with stress rate 12.5 MPa/s, followed by cooling the specimen to its initial temperature and unloading.

Looking at the figures one can notice that during the loading with such a stress rate, the stress increases up to 850 MPa which results in temperature increase up to 30K. Exothermic martensite transformation starts at of about 1% and develops with increasing stresses above 700 MPa till the strain limit 7%. At this strain value, the processes related to the heat flow to the surroundings are higher than the processes related to the heat production, so the specimen temperature drops. The drop in temperature, observed during the SMA loading manifests that at this level of deformation the exothermic main martensite transformation in the specimen is completed.

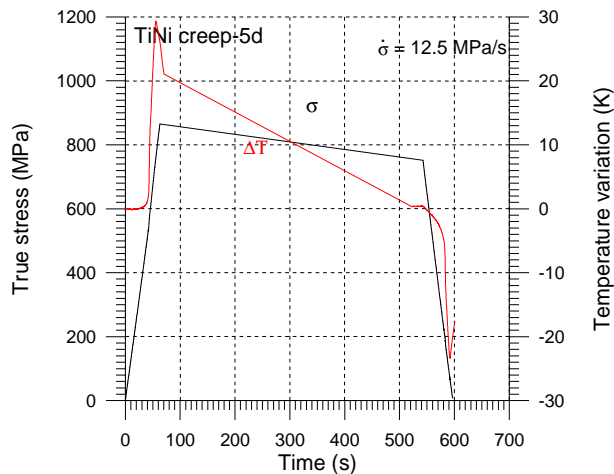


Fig. 2. Stress and temperature changes vs. time during tension test of TiNi SMA with stress rate 12.5 MPa/s, followed by cooling the specimen to its initial temperature and unloading.

During the subsequent cooling process, the temperature decreases to the initial room temperature due to the heat exchange with surroundings, while the stress decreases from 860 MPa to 740 MPa. It means that the stress relaxation under constant strain is induced due to the delayed martensite transformation when the specimen was under cooling process.

During the unloading, the main reverse transformation appears at stress of 220 MPa with strain of 6 % and finishes at stress of 80 MPa with strain of 0.6 %. The temperature drops due to the endothermic reverse transformation, up to -20K at the end of the process. However, one can notice that in this case the temperature drops from the same beginning of the unloading, which is probably caused by a "preceding" reverse transition.

Furthermore, there is not symmetry between the martensite forward and the reverse transformations. This is caused by the fact that the run of the martensite transformation is related to the instantaneous strain rate applied [1]. For the stress-controlled tension test the strain rate is not constant during the loading and the unloading processes [1-3].

Acknowledgments:

The research has been partly carried out with the financial support of the Polish Ministry of Science and Higher Education under Grant No. N N501 0106 33.

References

- [1] E.A. Pieczyska, S.P. Gadaj, W.K. Nowacki and H. Tobushi (2006). Phase transformation front evolution for stress- and strain-controlled test in TiNi Shape Memory Alloy, *Experimental Mechanics*, Vol. 46, No 4, 531-542.
- [2] Elżbieta A. Pieczyska, Hisaaki Tobushi, Wojciech K. Nowacki, Stefan P. Gadaj and Toshimi Sakuragi (2007). Subloop Deformation Behavior of TiNi Shape Memory Alloy Subjected to Stress-Controlled Loadings, *Materials Transactions*, Vol. 48, 2679-2686.
- [3] E. Pieczyska, W. Nowacki, T. Sakuragi and H. Tobushi (2007). Superelastic deformation properties of SMA, *Key Engineering Materials*, Vols. 340-341, 1211-1216.

FEATURES OF THE TEMPERATURE-INDUCED AND DEFORMATION-INDUCED ORDER-DISORDER PHASE TRANSITION

S.V. Starenchenko

Tomsk State University of Architecture and Building, Tomsk, Russia

1. Introduction

Phase transformations of different types are important way to be in control of properties of materials. The order-disorder transformation is one of them. It is able to change parameters of alloys changing a long-range order degree. A variation of antiphase domains sizes effects on properties of alloys as well. Despite a fact that atomic ordering has been studied many decades it will pay attention long time due to a great number problems demanding their decision.

2. Experimental procedure

Experimental results of the X-ray study are presented in this work. Binary alloys based on fcc lattice with superstructures $L1_2$, $L1_2(M)$, $L1_2(MM)$, $D1_a$ have been used for research. The alloys were obtained by inductional melting in an argon atmosphere. The ingots were homogenized at high temperatures. The samples were annealed near T_{melt} and quenched into ice water. The specimens of different alloys were annealed for ordering at various temperatures for different periods of time. X-ray diffraction was performed with DRON-1,5 and DRON-3 diffractometers using CuK_{α} - radiation.

The temperature-induced order-disorder phase transition has been studied in the alloys shown in the table 1. The lattice parameter, the antiphase period M , the degree of tetragonal or orthorhombical distortions, average long range order parameter, the long range order parameter far from and near the antiphase boundary were obtained to study the temperature-induced order-disorder phase transition.

The deformation-induced order-disorder phase transition has been researched in the alloys presented in the table 2. The well-ordered samples were deformed by cold rolling in this case. The long-range order parameter, the average size of the antiphase domains, the average size of the areas of coherent dispersion, microstresses and parameters of a crystal lattice are measured.

Table 1.

Studied alloys and their characteristics.

	Alloy	Superstructure	$T_k, ^\circ C$	η_{max}	η_{Tk}	$\langle D \rangle, nm$
1	Au ₃ Cu I (polycrystal)	$L1_2$	208	0.95-1.0	0,6	15-20
2	Au ₃ Cu II (polycrystal)	$L1_2(MM)$	204	0.9-1.0	0,1	10
3	Au ₃ Cd polycrystal	DO_{23} - $L1_2(M=2)$	422	1,0	0,65	45
4	Au ₄ Zn (polycrystal)	$L1_2 (MM)$	305	1,0	0,5	60-80
5	Au ₄ Cr (polycrystal)	$D1_a$	360	0,82	0,66	33
6	Au ₄ V (polycrystal)	$D1_a$	565	0,94	0,9	85

Table 2.

Studied alloys and their characteristics.

	Alloy	Superstructure	$T_K, ^\circ\text{C}$	η_{\max}	η_{TK}	$\langle D \rangle, \text{nm}$
1	Au ₃ Cu (polycrystal)	$L1_2$	208	0.95-1.0	0,6	15-20
2	Cu-22%Pt (polycrystal)	$L1_2$	685	0,8	0,6	80-130
3	Ni ₃ Fe (single crystal)	$L1_2$	535	1,0	0,44	13
4	Ni ₃ Al (polycrystal)	$L1_2$		1,0	1,0	$\gg 100$
5	Au ₄ Zn (polycrystal)	$L1_2$ (MM)	305	1,0	0,5	60-80
6	Cu ₃ Pd (polycrystal)	$L1_2$ (M)	468	0,8	0,54	50-150

3. Results and discussion

Studying of the temperature-induced and the deformation-induced order-disorder phase transformation has given possibility of establishing of their mechanisms, and has pointed at the role of antiphase boundaries, finding of their generality and difference. Some results of this study are presented in [1-4]. Increasing of the degree of the temperature or the deformation influence has brought on increasing amount of the defects in the alloys. The accumulation of defects has led up to the destruction of the long-range order in alloys. The antiphase boundaries play a particular role in the order-disorder transformation. Different nature of driving-forces of the order-disorder transformation determines differential peculiarity of every type of transformation. Essential disagreement of driving-forces defines the difference of mechanisms of the antiphase boundaries accumulation. The main features of the temperature-induced and the deformation-induced order-disorder phase transformation are shown in the table 3.

Table 3.

The features of the temperature-induced and the deformation-induced order-disorder phase transformation

	T- transformation	ϵ -transformation
1.	a) homogeneous disordering (LRO) at $T < T_K$. b) heterogeneous disordering (LRO+SRO) at $T \leq T_K$.	heterogeneous disordering - (LRO+SRO) at $\epsilon > 0$.
2.	a) SRO-phase is absent at $T < T_K$. b) SRO-phase appears at $T \leq T_K$.	SRO-phase appears at $\epsilon > 0$.
3.	a) $\langle D \rangle = \text{const}$ at $T < T_K$. b) $\langle D \rangle$ decreases at $T \leq T_K$.	$\langle D \rangle$ decreases monotonically at $\epsilon > 0$.

4. References

- [1] S.V. Starenchenko., E.V. Kozlov. (1999).The order-disorder transition in alloys with long period. *Mat. Science Forum.* V.321-324. P. 641-646.
- [2] S.V.Starenchenko, E.V. Kozlov (1999).X-ray study of the order-disorder transition in alloys with long period. *Proceedings of International Conference on Solid- Solid Phase Transformation '99, (JIMIC-3)*. The Jap. Institute of Metals - Ed. M. Koiwa, K.Otsuka and T.Miyazaki, P. 45-48.
- [3] S.V.Starenchenko, E.V.Kozlov, V.A.Starenchenko (2000). X-ray study of the order – disorder transformation by the plastic deformation, *42 Advances in Structure Analysis*. Ed. R. Kuzel, J. Hasek. CSCA. Praha, ISBN: 80 – 901748 – 5 – x, P. 449 – 455.
- [4] V.A. Starenchenko, O.D. Pantyukhova and S.V. Starenchenko (2002). Simulation of the process of deformation–induced destruction of long-range order in alloys with an $L1_2$ superstructures, *Physics of the Solid State (Russian)*, **44**, No 5, 994–1002.

STRESS REVERSE AND RESIDUAL STRESSES IN DRIED MATERIALS

S.J. Kowalski and A. Rybicki

*Poznań University of Technology, Institute of Technology and Chemical Engineering,
Poznań, Poland*

ABSTRACT

Non-uniform shrinkage of saturated materials subjected to drying is the main reason for generation of internal stresses. The drying induced stresses in elastic materials are of temporary character and disappear after drying. This is however not the case when the stresses cause local inelastic strains [1]. In such circumstances the phenomenon of *stress reverse* may take place when the material dries and the drier surface attempts to shrink but is restrained by the wet material core. Then, the surface is stressed in tension and the core in compression and large inelastic tensional strain occur at the surface. Later, under the surface with reduced shrinkage, the core dries and attempts to shrink causing the stress state to reverse. The reversed tensional stresses inside the material cause often internal cracks.

Another phenomenon that may occur in dried materials is called *the locked-up or residual stresses*. They arise when the material changes its mechanical properties during drying. Such stresses may occur, for example, in saturated clay-like materials that are viscoplastic, and in the course of drying become elasto-visco-plastic, elastoplastic, elastic and even brittle at the end of the process. If the change of mechanical properties is non-uniform throughout the body, the residual stresses mostly are present in materials after drying. Such stresses may have a substantial influence on the mechanical behaviour of materials during their utilization.

The residual stresses may elucidate, for example, why some dry materials shrink instead swelling during rehydration [1]. It was stated that the compressive properties are related to the morphology of the material. Loss of water and segregation of components that occur during drying makes the cell walls rigid. The outer layer becomes rigid and acquires considerable mechanical strength while the interior of the material is still of weak tensile strength. Amorphous domains are formed which add substantially to the mechanical strength of the material.

Similar phenomenon arises during quenching of steel. This process changes the structure and physical properties of carbon steel because a new structure called *martensite* arises in some domains. The accompanied to this process morphological phase transitions cause volume changes and induce internal stresses responsible in many cases for cracks of the material.

The above statements lead to the conclusion that residual stresses in saturated bodies may arise during hydro-thermal processes if the material suffers shrinkage and its physical properties are changed in some domains. That means that for description of residual stresses should be applied a drying model, the material coefficients of which reflect changes of mechanical properties.

In this paper we present a mechanistic model of drying which allows to describe the mechanical changes of elastic and viscoelastic materials under drying [3]. Both materials reveal drying-induced stresses, however, the stress history in these two materials differ from each other both qualitatively and quantitatively. We want to show that none of these two materials will reveal residual stresses if the material coefficients are assumed to be constant. In order to describe the residual stresses, the material properties have to vary in the course of drying, that is, the material coefficients ought to be functions of moisture content.

We shall illustrate the problem of residual stresses on an example of kaolin-clay cylinder dried convectively. The system of differential equations was established for description of the heat and mass transfer as well as the drying stresses during both the constant and the falling rate periods. The

constructed on the basis of these equations numerical algorithm enable evaluation of the distribution of moisture content, temperature, and stresses in the dried body and their evolution in time in all stages of drying. The most relevant meaning of this model is that it enables description of a complete history of the drying induced stresses during the whole process up to residual stresses at the end.

A number of experimental tests were carried out to observe the variation of mechanical behaviour of the kaolin-clay material during drying and to determine the material coefficients as a function of moisture content. In this way we have expressed the changeability of physical properties of the material during drying, what enabled us to describe the residual stresses at the final stage of drying.

Figure 1a presents the time evolution of maximum circumferential stresses in the elastic and viscoelastic cylinder with constant shear and bulk moduli $M = 450$ kPa and $A = 600$ kPa and relaxation time $\tau = 5 \cdot 10^4$ min by drying in air humidity 35 % and temperature 70 °C .

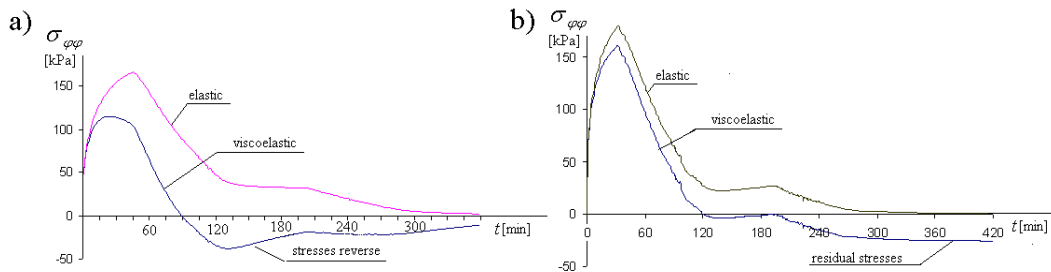


Fig. 1. Time evolution of maximum circumferential stresses in elastic and viscoelastic cylinder: a) with constant material coefficients, b) with material coefficients dependent on moisture content

It is seen that the plot of stress evolution for viscoelastic cylinder is different as that for elastic one. The stresses in elastic cylinder reach maximum in some instant of time and then tend to zero, while those in viscoelastic cylinder reach also maximum but of smaller value, next tend to negative values (stress reverse), and finally tend to zero. Figure 1b presents the time evolution of maximum circumferential stresses in the elastic and viscoelastic cylinder with variable material coefficients. It is seen that the circumferential stresses in viscoelastic cylinder become compressive and permanent in the final stage of drying. They do not tend to zero as those for elastic or viscoelastic cylinder with constant coefficients. This is because of change of material properties at the cylinder surface from viscoelastic to rigid at the final stage of drying. The relaxation time τ is near to zero for totally wet material (moisture content about 40%) and becomes very large ($\approx 10^6$ min) for dry body (moisture content about 6 %).

References

- [1] Kowalski, S.J.; Rybicki, A. The vapour-liquid interface and stresses in dried bodies, *Transport in Porous Media*, **2007**, *66*(1-2).
- [2] LEWICKI P.P., WITROWA-RAJCHERT D., MARIAK J., Changes of structure during rehydration of dried apples, *Journal of Food Engineering* 1997, *32*, 347-350.
- [3] Kowalski, S.J. *Thermomechanics of drying processes*. Springer Verlag Heilderberg-Berlin, **2003**, p. 365.

DESCRIPTION OF CYCLIC HARDENING OF MATERIAL WITH PLASTICITY INDUCED MARTENSITIC TRANSFORMATION

G.Ziętek¹, Z.Mróz²

¹ *Wrocław University of Technology, Wrocław, Poland*

² *Institute of Fundamental Technological Research, Warsaw, Poland*

1. Introduction

The martensitic transformation takes place in the wide group of austenitic steels mainly with high manganese or nickel content and may be caused by various reasons like: temperature, stress or plastic strain. The phase transition process may substantially affect strength properties such as: monotonic and cyclic hardening, corrosion resistance, fatigue life, magnetic sensitivity, etc. The phenomenon of mechanically induced martensite evolution was extensively investigated mostly by Olson and Cohen [1]. They assumed that there are two modes of transformation: *stress-assisted* and *strain-induced martensite*. These modes correspond to different generation of the nucleation sites and to different morphologies of martensite in a form of plate or lathlike structures. The range of temperature variation specifies the area of process of a suitable type.

- *Stress-assisted martensite* – The plates of martensite form at the presence of stress. The process is similar to that occurring spontaneously during cooling at the stress level not exceeding the yield point of the austenite, [2].
- *Strain-induced martensite* – The lathlike martensite [2, 3] forms as a consequence of plastic straining. This process may take place at a higher temperature above M_s level than that occurring during martensite formation in the cooling process (about $200C^\circ$ higher [2]).

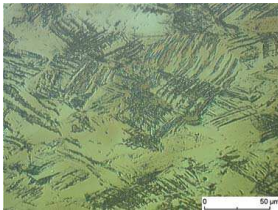


Fig.1. The lathlike martensite – AISI 304 steel [3]

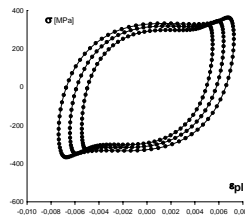


Fig.2. Experimental hysteresis loops [4]

The microscopic picture of the lathlike structure of martensite induced during cyclic deformation is presented in Fig. 1 and the hysteresis loops are shown in Fig.2. The examined cylindrical specimens were made of AISI 304 steel.

The present work aims at description of inelastic material response with plasticity induced martensitic transformation during cyclic deformation. The appearance of martensite changes not only the strength and cyclic properties but also deformation response of material under external load i.e., the form of hysteresis loop, (Fig. 2.). The constitutive equations are required to simulate deformation response of material for complex deformation paths and the related evolution of martensitic phase.

2. Material model – main assumptions

Phenomenological constitutive equations are formulated within the framework of irreversible thermodynamics with internal state variables. The volume fraction of martensite (ξ) is the most

popular macroscopic internal variable specifying the growth of martensitic phase [5]. The evolution equation for this parameter together with suitable model of plastic deformation provides description of the response under monotonic and variable loading. The two-phase material is treated as a thermodynamic system with two coupled irreversible processes namely, plastic deformation and phase transformation. Thus, two conditions of process occurrence must be formulated.

$$(1) \quad F_p = \sqrt{\frac{3}{2}(s_{ij} - X_{ij} - f_{ij}(Y, \xi))(s_{ij} - X_{ij} - f_{ij}(Y, \xi))} - R_p \leq 0 \quad \text{the yield condition.}$$

$$(2) \quad F_{tr} = \sqrt{\frac{3}{2}(X_{ij} - Y_{ij})(X_{ij} - Y_{ij})} - R_{tr}(\Sigma) \leq 0 \quad \text{the transformation condition.}$$

Where s_{ij} is the stress deviator. The yield condition (1) takes a familiar Huber-Mises form, but the tensor representing the additional translation of yield surface is specified by the deviatoric tensor f_{ij} related to the back stress X_{ij} . Equation (2) represents the transformation condition. The radius of the transformation surface depends on the generalized force Σ conjugated to the internal parameter ξ . The translation of the yield surface depends on the deviatoric tensor Y_{ij} which represents the center of transformation surface. The proposed model was analyzed assuming the tensor f_{ij} in the form:

$$(3) \quad f_{ij} = a(\xi) \left(\sqrt{\frac{3}{2} Y_{kl} Y_{kl}} \right)^n Y_{ij} = a(\xi) (Y_e)^n Y_{ij}.$$

3. Identification of model parameters and simulation

The identification of model parameters was carried out for austenitic steel AISI 304, on the basis of experimental data for the steady state of cyclic tension and compression. Next, the simulation for uniaxial and biaxial states was performed taking into account first cycles of loading. Examples of identification and simulation are presented in Fig. 3.

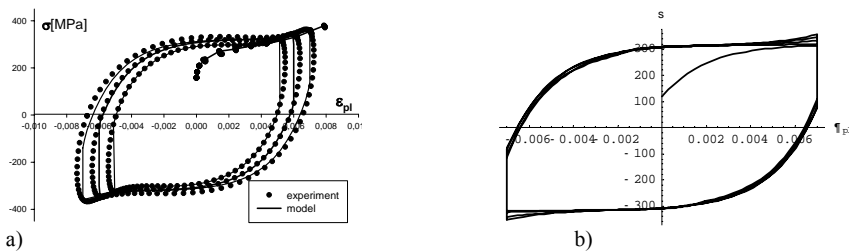


Fig. 3. Hysteresis loops: a) the experiment and identification, b) the simulation.

4. References

- [1] G.B. Olson and M. Cohen (1975). Kinetics of Strain-Induced Martensitic Nucleation, *Metallurgical Transactions A*, **6A**, p. 791.
- [2] P. C. Maxwell, A. Goldberg and J. C. Shyne (1974), Stress-assisted and strain-induced martensites in FE-Ni-C alloys, *Metallurgical Transactions*, **5**, 1305-1318.
- [3] B. Fassa, J. Kaleta and W. Wiśniewski (2004). Examination of athermal martensitic transformation induced by cyclic deformation in austenite, *21st Symposium on Experimental Mechanics of Solids*, 201-206.
- [4] J. Kaleta and G. Ziętek (1998). Representation of cyclic properties of austenitic steels with plasticity-induced martensitic transformation (PIMT), *Fatigue & Fracture of Engineering Materials & Structures*, **21**, p. 955-964.
- [5] Z. Mróz and G. Ziętek (2007). Modeling of cyclic hardening of metals coupled with martensitic transformation, *Archiwum Mechaniki Stosowanej*, **59**, 1-20.

THERMAL CYCLING EFFECT ON DIFFERENT TWO WAY SHAPE MEMORY TRAINING METHODS IN NiTi SHAPE MEMORY ALLOYS

C. Urbina , S. De la Flor, F. Ferrando
Department of Mechanical Engineering,
University Rovira i Virgili, Tarragona, Spain

1. Introduction

The two-way shape memory effect (TWSME) is the reversible and spontaneous shape change of the alloys subject to thermal cycling. The TWSME is not an intrinsic property of a shape memory alloy (SMA): it is only observed after some training procedures [1]. The TWSME developed by the alloy depends on its previous thermomechanical history, the training method applied and the training parameters used. Several training routes have been reported to be associated with the B2→B19' transformation, but little work has been done on training methods that consider R-phase transformation to be an essential part of the training process. In fact, different opinions are published [2, 3] concerning the influence of R-phase on the TWSME. The aim of this work is to study experimentally the influence of R-phase on the development of the two way memory strain (ϵ_{tw}) and on the transformation temperatures (TTs). Constant load thermal cycling (L) and tensile deformation below M_f (D) are used as training procedures.

2. Materials and Experimental procedures

A binary near-equiatomic NiTi wire (diameter 1 mm) manufactured by Euroflex (SME 495) is used. Two different thermomechanical treatments (A, B) are applied in order to ensure different R-phase presence on the alloys. Treatment A consists of a heat treatment at 500°C for 1 hour, and subsequent quenching in water. Treatment B consists of the same heat treatment as A, but the R-phase is then enhanced and stabilized by a repeated thermal cycling at zero stress in the temperature transformation range. The TTs (M_s , M_f , R_s , R_f , A_s , A_f) are obtained by measuring the changes in electrical resistivity (ER) due to temperature. The A and B samples trained by L are A_L and B_L ; the A and B samples trained by D are A_D and B_D . To perform L training, a constant training stress of $\sigma_{tr}=103.7$ MPa is applied to the sample in the martensitic state, and then it is repeatedly thermally cycled through the transformation range. D training is carried out in three subsequent steps: (a) tension test at a training strain of $\epsilon_{tr} = 4.5\%$ in the martensitic state, (b) the sample is completely unloaded, (c) the sample is heated to above A_f . These σ_{tr} and ϵ_{tr} guarantee the complete martensite reorientation in accordance with [2]. Then, repeated thermal cycling is performed on A_L , B_L , A_D and B_D to measure the ϵ_{tw} and determine the evolution of TTs. A small force of 5 N is applied to keep the samples stretched during TWSME tests.

3. Results

Figure 1 presents the TTs measured for treatments A and B, (showing R-phase); the TTs after L training (A_L , B_L) and the TTs after D training (A_D , B_D). Taking temperatures A and B as initial reference values, the R-phase transformation does not appear in all the trained samples because the M_s increases considerably during the training cycles. ER profiles during training have not resistivity peaks associated with the R-phase. L training increases both martensitic temperatures and decreases A_s . D training decreases M_f but increases M_s , and decreases A_s and A_f for both samples equally. Figure 2 shows the TWSME behavior for samples A_L and B_L , trained by the L method. The evolution of the reversibility of the deformation (ϵ_R) during training illustrates that, after an initial

rise, ϵ_R reaches a fairly constant rate after four cycles. Thermally cycled sample B_L develops ϵ_{tw} values that are similar to those of A_L , but the accumulation of plastic strain (ϵ_P) is lower, suggesting that the dislocations introduced by prior thermal cycling can help the formation of preferentially oriented martensite [3], which is an essential factor to obtain a substantial ϵ_{tw} .

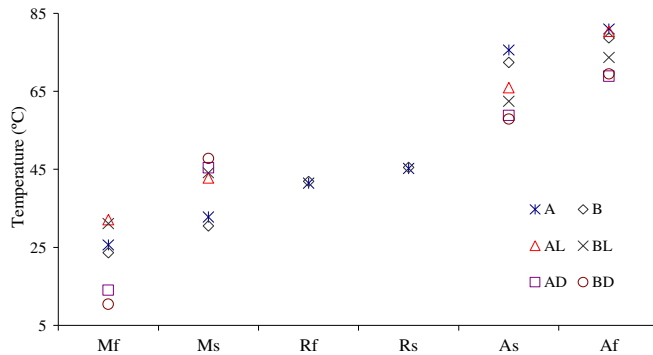


Figure 1. Effect of thermal treatments and training methods on the transition temperatures.

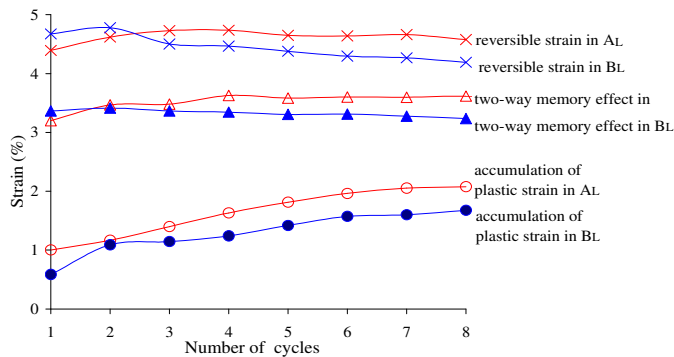


Figure 2. ϵ_R , ϵ_P and ϵ_{tw} evolution for constant load training (L).

4. Conclusions

D and L training enlarge TT intervals. The increase in M_S and decrease in A_S narrows the hysteresis width, and this effect is stronger in the B samples. A_L and B_L show resistivity peaks on ER curves measured after thirty TWSME tests, suggesting that the applied training parameters do not help to make the complete R-phase vanishment. Prior thermal cycling leads to lower ϵ_P for values of ϵ_{tw} similar to A_L . L training shows similar ϵ_{tw} than D.

5. References

- [1] X. M. Zhang and J. Fernandez (2006). Role of external applied stress on the two-way shape memory effect, *Mater. Sci. Eng. A*, **438-440**, 431-435.
- [2] Y. Liu and P.G. McCormick (1990). Factors influencing the development of two-way shape memory in NiTi, *Acta Metall. Mater.*, **38**, 1321-1326.
- [3] C. Chang and D. Vokoun (2001). Two-Way shape memory effect of NiTi alloy induced by constraint aging treatment at room temperature, *Metall. Mater. Trans. A*, **A32**, 1629-1634.

INELASTIC BEHAVIOR AND NUMERICAL ANALYSIS IN TWIN-ROLL CASTING PROCESS OF AZ31 ALLOY

D.Y. Ju^{1,2}, X.D. Hu¹ and Z.H. Zhao²

¹ *Saitama Institute of Technology, Fukaya, Japan email: dyju@sit.ac.jp*

² *University of Science and Technology Liaoning, China*

1. Introduction

Twin-roll casting process is a rapid solidification process combining with hot rolling. In the process molten metal was solidified starting at the point of first metal-roll contact and ending before the kissing point. This near-net-shape process can directly produce thin strips in one step. It has more advantages due to its higher productivity, low cost and energy saving. Therefore more and more researchers have concentrated their studies on the processes [1].

In twin roll casting process rolling action play an important role and the liquid metal will be squeezed out from the mush zone, which is very different from the conventional continuous casting process. In this work, we focus the research work on the constitutive equation, stresses and deformation study, other aspects will be simplified. A 2D FEM model was employed and use sequential coupled analysis method to simulate the thermal mechanical behavior during twin-roll casting process of Mg alloy AZ31. Here, the Anand's model, a temperature and rate dependent model for high temperature deformation, was employed to calculate the thermal mechanical stress in the casting process. Based on the stresses analysis and experimental tests, it reveals that separating force should be strictly controlled in the twin roll casting process in order to avoid cracks caused by thermal and deformation stresses.

2. Inelastic constitute equation

In twin-roll thin strip casting process, stresses primarily arise due to high thermal gradient and rolling deformation. The total strain rate can be decomposed as:

$$\dot{\varepsilon}_{ij} = \dot{\varepsilon}_{ij}^e + \dot{\varepsilon}_{ij}^p + \dot{\varepsilon}_{ij}^{Th} \quad (1)$$

where $\dot{\varepsilon}_{ij}^e$, $\dot{\varepsilon}_{ij}^p$, $\dot{\varepsilon}_{ij}^{Th}$ were elastic, plastic and thermal strain rate, respectively. Elastic strain rate, thermal strain rate are given by:

$$\dot{\sigma}_{ij} = E_{ijkl}(T)\dot{\varepsilon}_{kl}^e \quad (2)$$

$$\dot{\varepsilon}_{ij}^{Th} = \alpha \Delta T \dot{\delta}_{ij} \quad (3)$$

where $E_{ijkl}(T)$ is the temperature dependent elastic modulus. And ΔT is the change rate of current temperature and the reference temperature at the point, α is thermal coefficient of expansion. The plastic strain rate $\dot{\varepsilon}_{ij}^p$ is described by Anand model, which is a temperature and rate dependent model for high temperature large deformation process. A set of internal type constitutive equations for large elastic-viscoplastic deformation at high temperature was proposed by Anand and Brown [2]. The specific functional form for the flow equation:

$$\dot{\varepsilon}^p = A \exp\left(-\frac{Q}{R\theta}\right) \left[\sinh\left(\xi \frac{\tilde{\sigma}}{s}\right) \right]^{1/m} \quad (4)$$

and the specific functional form of evolution equation for the internal variable s

$$\dot{s} = \left\{ h_0 \left[\left(1 - \frac{s}{s^*} \right) \right]^a \text{sign} \left(1 - \frac{s}{s^*} \right) \right\} \dot{\epsilon}^p; \quad a > 1 \quad (5)$$

$$s^* = \tilde{s} \left[\frac{\dot{\epsilon}^p}{A} \exp \left(\frac{Q}{RT} \right) \right]^n \quad (6)$$

where h_0 is the hardening constant, A is the strain rate sensitivity of hardening, s^* is the saturation value of s , \tilde{s} is a coefficient, and n is the strain rate sensitivity for the saturation value of deformation resistance, respectively. The nine parameters of Anand constitutive model A , Q , ξ , m , h_0 , \tilde{s} , n , a and s_0 (the initial value of s) can be obtained from curve-fitting of compression tests, by which large strain and fully developed plastic flow can be achieved due to the absence of necking. Isothermal constant true strain rate tests of AZ31 with different strain rates and temperatures were carried out, the true strain versus stress curves were shown in Fig. 1. The parameters of Anand model regressed from comparison tests are A : $3.5 \times 10^7 \text{s}^{-1}$, Q : 160kJ/mol , ξ : 8.5 , m : 0.28 , h_0 : $3.038 \times 10^9 \text{Pa}$, n : 0.018 , a : 1.07 , s_0 : $3.5 \times 10^7 \text{Pa}$, \tilde{s} : $5 \times 10^7 \text{Pa}$. Fig.3. show the prediction and experimental strain vs. stress curves.

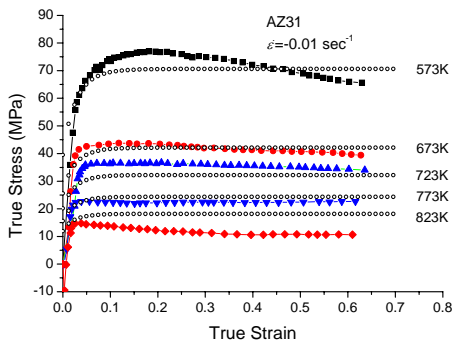


Fig. 1. Prediction and experimental compression true strain vs. stress curves at different temperatures

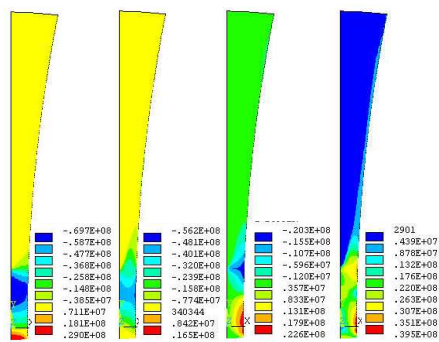


Fig. 2. Contours of σ_x (a), σ_y (b), σ_{xy} (c) and von Mises stress (d)

3 Thermal Stresses

In this study, the simulation model was employed to calculate stresses. The thermal flow result of temperature field was imposed as body load and the reference temperature was set as the average temperature of strip surface. The strip surface set as free surface because solidifying shrinkage. To simulate rolling action in twin-roll casting process, displacement load along roller tangent direction was imposed. The results of stresses and deformations were shown in Fig. 2. The stress status of strip surface along casting direction was tensile stress; this is one of main reasons causing strip crack defects.

4. Conclusion

The deformation of twin-roll casting process is non-uniformed because of high temperature gradient; the backward squeeze zone and the exit zone are the two dangerous regions for cracks. Rolling actions is much dangerous than thermal stress. Control the solidification end near the kissing point can decrease rolling deformation and decrease the crack tendency.

References

- [1] D. Y. Ju, H. Y. Zhao, X. D. Hu, Mater. Sci. Forum Vols. 488-489 (2005) p. 439.
- [2] S. B. Brown, K. H. Kim and L. Anand, International Journal of Plasticity, Vol. 5, PP. 95-130, 1989

Mechanical behaviour of TRIP steels subjected to low impact velocity at wide range of temperatures

J. A. Rodríguez-Martínez¹, A. Rusinek², D. A. Pedroche¹, A. Arias¹, J. R. Klepaczko²

¹Department of Continuum Mechanics and Structural Analysis, University Carlos III of Madrid, Avda. de la Universidad 30, 28911 Leganés, Madrid, Spain

²Laboratory of Physics and Mechanics of Materials, UMR CNRS 7554, University Paul Verlaine of Metz, Ile du Saucy, 57000 Metz, France

1. Introduction

The response of materials under impact loading has a considerable interest. It allows for clarification of several problems in different application fields such as civil, military, aeronautical and automotive engineering, [1-2]. The use of TRIP steels is widespread in the industry as a structural element responsible for the absorption of energy during an eventual impact or accident as for example in crashworthiness application. Thus, in the present work mechanical behaviour of **TRIP 600** and **TRIP 1000** sheets subjected to low impact velocity at different initial temperatures is analyzed.

2. Experimental setup

For this task a drop weight tower has been used. Thus, it was possible to perforate the TRIP steel sheets for initial velocities $V_0 \leq 5\text{m/s}$ in a wide range of initial temperatures $173\text{K} \leq T_0 \leq 373\text{K}$. The dimensions of the square sheets impacted are 100×100 mm. The steel sheets of thickness $t = 1.0$ mm and $t = 0.5$ mm in the case of **TRIP 600** and **TRIP 1000** respectively. The impactor used had a shape of conical nose with diameter of $\phi_p = 20\text{mm}$ and mass of $M_p = 18.7\text{kg}$. The experimental set-up allows to obtain measurements of the force-time history and both, the initial and residual velocities. Finally, the process has been filmed using a high speed camera.

3. Mechanical characterization of TRIP 600 and TRIP 1000

The mechanical behaviour of both, **TRIP 600** and **TRIP 1000**, has been defined using different strain rates and initial temperatures, Figs 1-2. In Fig. 1 experimental results are reported for **TRIP 600** and **TRIP 1000** at room temperature for different strain rates. For **TRIP 1000** a Lüders' band propagation is also observed corresponding to a plateau of stress at the beginning of loading, Fig. 1-b.

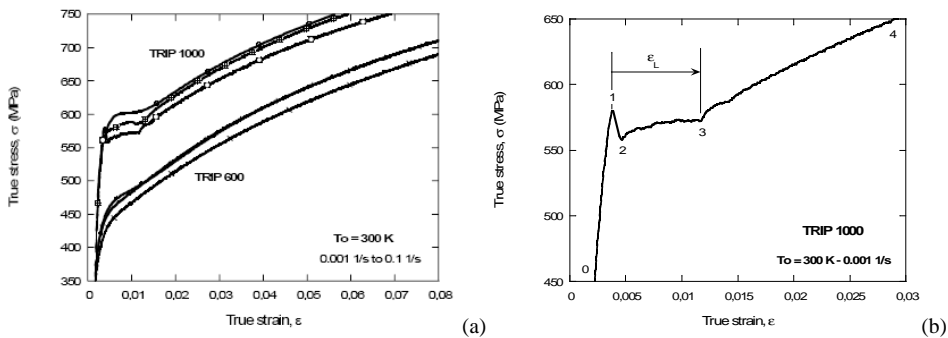


Fig. 1. Experimental results for **TRIP 600** and **TRIP 1000** steels at room temperature and different strain rates

The influence of the temperature on the behaviour of the materials studied is shown in Fig. 2. It is observed a strong dependency of the strain hardening with temperature

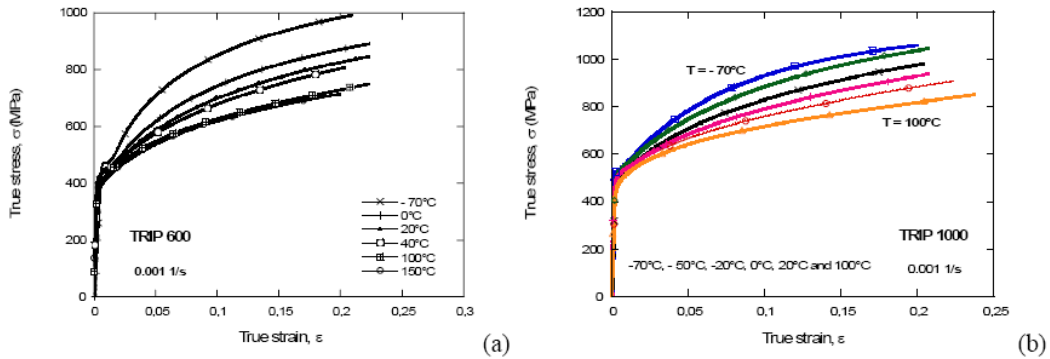


Fig.2 Experimental results in quasi-static loading at different temperatures for (a) TRIP 600 and (b) TRIP 1000

It is also observed during experiments, due to high stress levels and large ductility, a substantial increase of temperature, Fig. 3-a. This observation is also true for the quasi-static loading, $\dot{\epsilon} > 10^{-3} \text{ s}^{-1}$, where the temperature increase near the necking zone is close to $\Delta T \approx 100\text{K}$. Thus, the process of phase transformation is reduced for quasi-static loading and does not exist in the case of dynamic loading. On the contrary for low temperature, phase transformation is observed reducing strain hardening Fig 2-a-b. An analytical approach is proposed to describe the temperature increase along the specimen. Analytical predictions are compared with experimental results, Fig. 3-a.

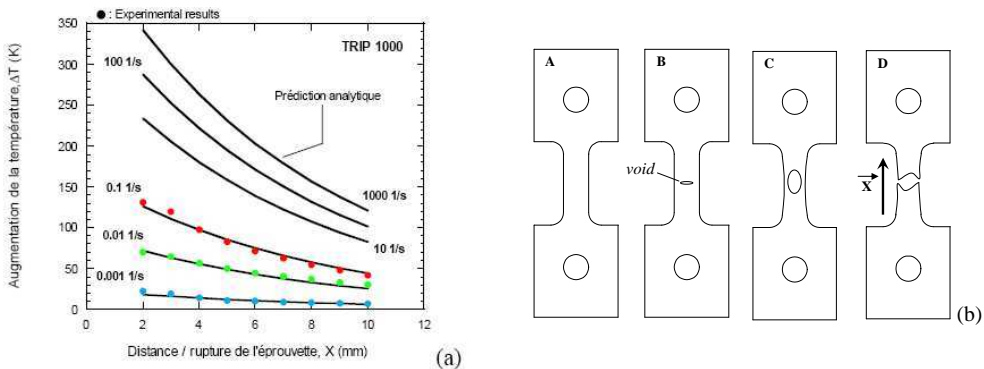


Fig.3 (a) Analytical predictions of RK model and comparison with experimental results in the case of TRIP 1000 steel (b) Definition of failure during tension test due to necking appearance

4. Analysis of the perforation process for high strength steels

The perforation tests have revealed that the failure mode of the steel sheets is due to ductile hole enlargement with presence of petalling, Fig. 4, more accentuated in the case of TRIP 1000 due to the reduced thickness of the plates in comparison with TRIP 600, Fig. 5. The experimental observations in terms on number of petals have been compared with the analytical predictions reported in [4] and a good agreement has been found between them.

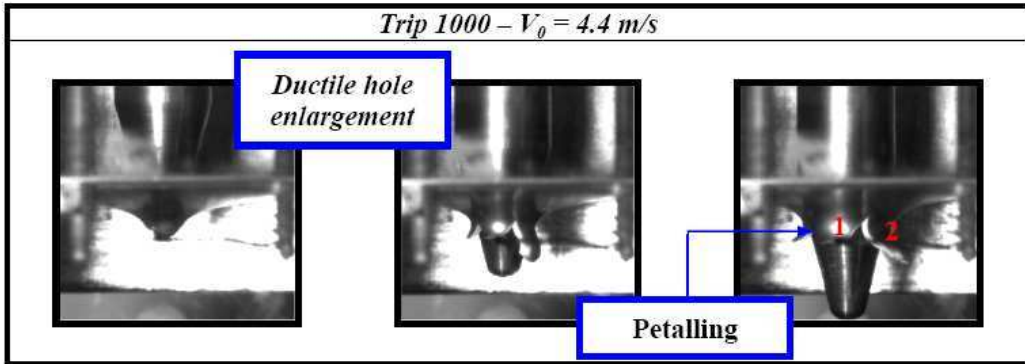


Fig.4 Sequence of the perforation process of TRIP 1000 steel sheet for $V_0 = 4.4$ m/s and $T_0 = 300$ K.

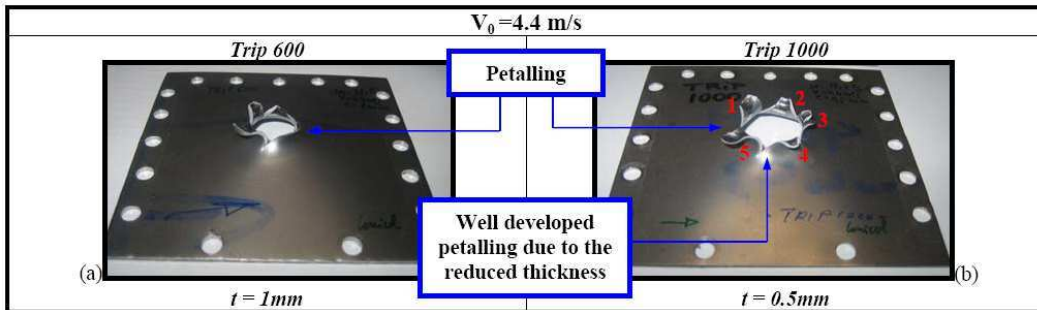


Fig.5 Failure mode of the steel sheets for $V_0 = 4.4$ m/s and $T_0 = 300$ K. (a) TRIP 600 (b) TRIP 1000

The ballistic limit in the case of room temperature for both steels has been found close to $V_{bl} \approx 3.5$ m/s. This value is reduced in the case of higher temperatures, for example $T_0 = 373$ K, due to the thermal softening of the material and considerably augmented for low temperature, $T_0 = 173$ K, due to the transformation of the austenitic phase into martensite.

Acknowledgements

The authors thank to IPPT group, including Dr. P. Gadaj and Prof. W. K. Nowacki for a possibility of temperature measurements.

References

- [1] Rusinek, A., Klepaczko, J.R. Shear testing of sheet steel at wide range of strain rates and a constitutive relation with strain-rate and temperature dependence of the flow stress. *Int. J. Plasticity*. 2001; 17, 87–115.
- [2] Rusinek A., Rodríguez-Martínez J.A., Zaera R., Klepaczko J. R., Sauvelet C., Arias A. Experimental and numerical analysis of failure process of mild steel sheets subjected to perpendicular impact by hemispherical projectiles. *Int. J. Impact Eng.* (submitted)
- [3] Arias A, Rodríguez-Martínez J.A. Rusinek A. Numerical simulations of impact behaviour of thin steel to cylindrical, conical and hemispherical non-deformable projectiles, *Eng. Fracture Mech.* 75 (2008) 1635–1656
- [4] Wierzbicki T. Petalling of plates under explosive and impact loading. *Int. J. Impact Eng.* 1999;22:935-954

Index of Authors

- Abedian A., 387
Abramovich H., 292
Abushawashi Y.M., 68
Akbari M.A., 266
Altenbach H., 348
Anand L., 254
Anghel C.R., 226
Arias A., 436
Asanov V., 202
Atchonouglo K., 286
Attarnejad R., 296
Ayuga F., 338
- Bacigalupo A., 138
Bajer C., 402
Balevičius R., 220
Banach Z., 258
Ban M., 286
Bartosz K., 260
Basista M., 160, 238
Bauer E., 192
Bayandin Yu., 274
Bednarek T., 82
Beluch W., 54, 384
Bessoud A.L., 332
Bîrsan M., 352
Błachowski B., 368
Bobiński J., 162, 216
Bobylov A., 398
Bochenek B., 228
Bojczuk D., 396
Budak V.D., 310
Burczyński T., 54, 56, 90, 384
- Canteli J.A., 86
Cantero J.L., 86
Chalecki M., 378
Chamera S., 26
Chen X., 226
Chernyakov Yu., 270
Chernyakov Yu.A., 282
- Chiba N., 226
Chróścielewski J., 52, 318
Chudzicka-Adamczak M., 110
Cieszko M., 16, 28, 112, 122
Colak O.U., 8
Cudmani R., 194
Czarnecki S., 66
- Danielewski M., 100
Dąbrowska-Tkaczyk A., 42
De Baets P., 48
De la Flor S., 432
De Waele W., 48
Dems K., 370
Dinkler D., 294
Długosz A., 90, 384
Dłużewski P., 96, 224
Doliński K., 150
Duan H.L., 222
Duhame D., 250
Dunajewski I., 130
Dyniewicz B., 402
Dziatkiewicz G., 84
- Edalat P., 300, 326
Ehret A.E., 6
Eremeyev V.A., 242, 290, 348
Erzar B., 146
Eshtewi S.H., 68
Eslaminia M., 296
Evseev A., 202
- Fedeliński P., 50, 182, 382
Ferrando F., 432
Fialko S., 60
Fischer F.D., 404
Forquin P., 146
Fortune D., 286
Foryś U., 36
Fraldi M., 380
Frischmuth K., 102
- Gadaj S.P., 256, 424
Gallego E., 338
Gałka A., 44, 46
Gambarotta L., 138
Gambin B., 44, 46
Gambin W., 24
Garstecki A., 374
Garwolińska A., 80
Gavrilova E., 116
Gavrylenko G.D., 346
Geymonat G., 302
Ghaffari H.O., 190
Gilewicz J., 126
Gladskyi M., 170
Glema A., 262
González I.M., 70
González-Montellano C., 338
Gorjipoor A., 387
Górski J., 216, 312
Górski R., 382
Grigorenko A.Ya., 310
Grigorenko Ya., 304
Gross D., 238
Gutkowski W., 368
Gzik M., 40
- Hackl K., 98
Haftbaradaran H., 264
Hammoud M., 250
Han K.T., 354
Hara K., 288
Harutyunyan E., 336
Hassan T., 8
Hoang V.N., 64
Hoffmann T.J., 110
Hosseini A.V., 266
Hu X.D., 434
- Iancu C., 376
Ilic S., 98
Imiełowski Sz., 386

- Inoue T., 420
Itskov M., 6
Iwicki P., 356
- Jabłoński M., 396
Jach K., 94
Jankowiak T., 186
Jankowski Ł., 392
Jankowski R., 364, 366
Janus-Michalska M., 252
Jański L., 172
Jia W.P., 188
Jiang Q.H., 210
Jin Y., 354
John A., 10, 18, 58
Jurczak G., 96
Ju D.Y., 188, 434
- Kaczmarek M., 4, 32, 80
Kaczyński A., 174
Kačianauskas R., 136, 220
Kałuża G., 12
Karihaloo B.L., 222
Kazakov K.E., 248
Kąkol W., 372
Kempiński M., 122
Khedmati M.R., 300, 326
Kholghi M., 132
Khoroshun L., 140
Khurana A., 388
Klepaczko J.R., 146, 168, 436
Klinkel S., 308
Kłosowski P., 178, 316
Knabel J., 64
Kochmann D., 230
Kokot G., 58
Kolanek K., 64
Kopernik M., 22
Kosiński W., 102
Kotulski Z., 130
Kovács A., 166
Kovács Á., 166
Kovalev V., 298
Kowalczyk P. (IPPT), 30
Kowalczyk P. (PW), 20, 24
Kowalczyk-Gajewska K., 236, 276
Kowalski S.J., 414, 428
- Kozicki J., 158, 200
Krasucki F., 332
Kreja I., 318, 334
Kret S., 96
Kriese W., 16
Kruzelecki J., 330
Krzyzyski T., 26, 246
Kubik J., 112
Kuna M., 172
Kurpa L., 322
Kursa M., 234
Kuś W., 58
Kuziak R., 76
Kuznetsov V., 350
- Lachowicz C.T., 152
Larecki W., 258
Lazarus V., 164
Le K.C., 230
Le van A., 390
Leblond J.B., 164
Lekszycki T., 34
Lerintiu C., 286
Leu S.-Y., 268
Levyakov S., 350
Liaghat G.H., 266
Lisowski K., 394
Loktev A., 340
Loktev D., 340
Luckner H.J., 256
Lychev S.A., 118
Lyubitsky K., 322
- Łodygowski T., 186, 262, 372
Łukasiak T., 88
- Maciejewski I., 26
Magier M., 94
Maj M., 416
Majchrzak E., 12, 422
Manzhurov A.V., 248, 358
Marciniak Z., 152
Mardare C., 328
Marín N.C., 86
Marzec I., 176
Matsner V.I., 346
Mejak G., 148
Melcer J., 362
- Miguélez H., 70
Miguélez M.H., 86
Mikulski T., 312
Milenin A., 62
Mochacki B., 422
Monastyrskyy B., 174
Morán J., 338
Morland L.W., 195
Movaggar A., 170
Mróz K.P., 150
Mróz Z., 74, 220, 430
Müller W.H., 140
Münch A., 302
Munoz A., 70
Musielak G., 128
Myślecki K., 320
Myśliński A., 400
- Naghavi M., 132
Nagórko W., 378
Naimark O., 144, 202, 274
Nazarenko L., 140
Neubauer M., 246
Nguyen T.T.H., 390
Nioata A., 376
Nowacki W.K., 256, 272, 408, 418, 424
Nowak B., 32
Nowak J., 22
Nowak M., 38
Nowak Z., 272
Nunziante L., 380
- Ogasawara N., 226
Oleńkiewicz J., 320
Oleśkiewicz R., 246
Oliferuk W., 104, 416
Orantek P., 10, 18, 54, 56, 90
Othman A.M., 68
- Páczelt I., 74
Palin-Luc T., 144
Pamin J., 204, 276
Panasovskiy K., 170
Panasz P., 344
Pankov I., 202
Panteleev I., 202
Parshin D.A., 358
Pedroche D.A., 436

- Perzyna P., 262, 272
 Petrescu F., 114
 Petryk H., 234, 240, 406
 Pęcherski R.B., 272
 Pidvysotsky V., 76
 Piechór K., 14
 Pieczyńska E.A., 408, 410,
 418, 424
 Pietraszkiewicz W., 242,
 290, 314
 Pietrzyk M., 76
 Pindra N., 164
 Pinheiro M., 208
 Piotrowski P.H., 366
 Plekhov O., 144, 202
 Płochocki Z., 104
 Pol M.H., 266
 Polishchuk A.S., 282
 Poniznik Z., 238
 Pontow J., 294
 Poteralska J., 12
 Pozorski Z., 374
 Ptaszny J., 50
 Puzyrev S.V., 310
 Pyrz R., 228
 Pyrzowski Ł., 178

 Radchenko I., 412
 Radulescu A.V., 114
 Radulescu I., 108, 114
 Rahaei M., 132
 Rahaei M.B., 106, 120, 132,
 134
 Rastani M., 300, 326
 Rec T., 62
 Ritchie R.O., 2
 Rodríguez-Martínez J.A.,
 168, 436
 Rojek J., 214
 Rozumek D., 152
 Rucka M., 52, 196
 Rusinek A., 168, 436
 Ruterana P., 96
 Rybicki A., 414, 428

 Sab K., 250
 Sabik A., 318
 Saintier N., 144
 Sakuragi T., 408, 418
 Salit V., 238

 Sargsyan S.H., 342
 Sawicki A., 212
 Scherzer M., 172
 Schlebusch R., 324
 Sembiring P., 230
 Semenova I., 144
 Serpilli M., 332
 Shafiye A., 132
 Shahba A., 296
 Shariff M.H.B.M., 180
 Sherbakov S., 154, 280, 284
 Shimizu S., 288
 Shneider V., 270
 Shodja H.M., 264
 Shukayev S., 170
 Sielamowicz I., 220
 Sielicki P., 186
 Slominski C., 194
 Sokół T., 360
 Sosnovskiy L., 154, 284
 Sosnowski W., 82
 Souchet R., 278
 Stankiewicz A., 204
 Starenchenko S., 412
 Starenchenko S.V., 426
 Starenchenko V., 412
 Staroszczyk R., 232
 Stepanova L., 142
 Stocki R., 64
 Studziński R., 374
 Stupkiewicz S., 406
 Suchy J.S., 422
 Sugimoto Y., 408, 418
 Sumelka W., 262
 Svanadze M., 244
 Svoboda J., 404
 Szajek K., 372
 Szczepański Z., 28
 Szwabowicz M.L., 314
 Szybiński B., 78

 Świdziński W., 212
 Świerczyński R., 94
 Świt B., 128

 Tanton S.F., 192
 Tazowski P., 64
 Tejchman J., 92, 158, 162,
 176, 196, 198,
 200, 206, 216

 Tejszerska D., 40
 Teslenko D., 270
 Tobushi H., 408, 418, 424
 Tokarzewski S., 126
 Tomar S.K., 388
 Trybuła D., 330
 Turska E., 306

 Urbina C., 432

 Valiev R., 144
 Vallée C., 286, 314
 Vízváry Z., 166

 Wagner W., 308
 Wang C.H., 156
 Wang J., 222
 Wang J.G., 188
 Wang X.T., 206
 Wan R., 208
 Wegleński W., 160
 Wierszycki M., 372
 Wilde K., 52, 196
 Wille R., 140
 Wisniewski K., 306, 344
 Wiśniewski J., 370
 Witkowski W., 52, 318
 Wittenberghe J.V., 48
 Wojnar R., 124
 Wójcik M., 92
 Wróblewski A., 78
 Wrana B., 218
 Wu W., 198, 206
 Wysocka O., 104
 Wysota P., 18

 Yaremchenko S., 304
 Yeung M.R., 210

 Zaitsev A.V., 184
 Zarutsky V., 292
 Zastrau B., 324
 Zhang Q., 392
 Zhao Z.H., 434
 Zhou C.B., 210
 Ziętek G., 430
 Zmitrowicz A., 72
 Zubko A., 398

 Żebro T., 276